BEILSTEIN JOURNAL OF NANOTECHNOLOGY

Self-assembly of nanostructures and nanomaterials

Edited by Isabelle Berbezier and Maurizio De Crescenzi

Imprint

Beilstein Journal of Nanotechnology
www.bjnano.org
ISSN 2190-4286
Email: journals-support@beilstein-institut.de

The *Beilstein Journal of Nanotechnology* is published by the Beilstein-Institut zur Förderung der Chemischen Wissenschaften.

Beilstein-Institut zur Förderung der
Chemischen Wissenschaften
Trakehner Straße 7–9
60487 Frankfurt am Main
Germany
www.beilstein-institut.de

BEILSTEIN JOURNAL OF NANOTECHNOLOGY

Self-assembly of nanostructures and nanomaterials

Isabelle Berbezier*[1] and Maurizio De Crescenzi[2]

Editorial

Open Access

Address:
[1]CNRS-AMU, Im2np, Faculté des Sciences et Techniques, Avenue Escadrille Normandie Niemen, 13397 Marseille Cedex 20, France and [2]Department of Physics, University of Roma Tor Vergata, Via della Ricerca Scientifica, 1, 00133 Roma, Italy

Email:
Isabelle Berbezier* - isabelle.berbezier@im2np.fr

* Corresponding author

Keywords:
nanomaterials; nanostructures; self-assembly phenomena

Beilstein J. Nanotechnol. **2015,** *6,* 1397–1398.
doi:10.3762/bjnano.6.144

Received: 10 June 2015
Accepted: 11 June 2015
Published: 24 June 2015

This article is part of the Thematic Series "Self-assembly of nanostructures and nanomaterials".

Editor-in-Chief: T. Schimmel

Presently, most microelectronic devices are fabricated using top-down approaches. According to Moore's law, with the predicted ultimate reduction in size over the next years, these processes will reach the limits of technological instrument resolution. In addition, a major bottleneck in top-down approaches is the prohibitive cost due to the large number of technological steps required to reduce the device size. Furthermore, a broad range of applications require ultrasmall, complex devices that cannot be produced using top-down methods. New processes building on the natural self-organization of matter should therefore be conceived and developed, along with adequate characterization methods in order to allow for their application in innovative devices. Such self-organization processes are already implemented in various materials such as biological materials, soft matter, metals and semiconductors. Self-assembly is a process that builds an ordered structure, brick-by-brick, starting from disordered building blocks, using simple key ingredients. Self-assembly is commonly controlled by certain intrinsic material parameters (e.g., composition, strain, thickness, phase transformation, structural changes) and results from the interaction between different factors (e.g., deposit/substrate, liquid/gas/solid phases, crystals). Besides these intrinsic parameters, a number of extrinsic factors, including thermal treatment, chemical and electrochemical reactions, mechanical stress, electric or magnetic fields, can strongly influence the self-assembled morphologies.

Self-assembly processes are generally low cost, large-scale techniques, which can be suitable for various industrial environments. Identified as one of the key topics in nanoscience with potential to shape future scientific research, self-assembly is the most promising path to breakthroughs in nanoelectronics, optoelectronics, spintronics, molecular nanotechnology, biology, materials science, software, robotics, manufacturing, transportation, energy harvesting, infrastructure and construction.

Research on self-assembled nanostructures encompasses fundamental issues in chemical synthesis, crystal growth and self-organization of 0D, 1D and 2D nanostructures, nanopatterning, lithographic techniques, nanocharacterization, scaling of materials properties down to molecular dimensions, quantum properties and applications of nanoscale assemblies to advanced devices. The main topics of interest involve 2D nanomaterials such as nanomembranes, graphene, silicene and ordered mesoporous oxides, 1D nanomaterials such as nanowires and nanotubes, and 0D nanomaterials such as quantum dots, nanocrystals and Q-bits.

Focusing on this dynamic new field, self-assembly “the science of things that put themselves together” explores the physics of nanostructures, new synthesis approaches, in addition to size-, shape- and composition-dependent properties. The major obstacles concern the reproducibility and control of the basic mechanisms in order to predict and produce patterns with tunable size, periodicity and position and the new physical properties resulting from low dimensionality.

The goal of this Thematic Series is to bring together studies in the broad field of research on self-assembled nanostructures, which may seem far away, but are expected to promote an extraordinary exchange of ideas appropriate to conceive multidisciplinary processes suitable for various materials with the aim to produce exceptional new nanomaterials with revolutionary properties.

This Thematic Series covers the physics of nanostructures at the nanoscale including:

- large-scale patterning obtained by spontaneous structuring as well as local probe nanopatterning for nanostructure size and position control;
- theoretical and experimental efforts dedicated to a better understanding of the formation, evolution, and organization of nanoscale systems;
- fundamental and new issues in nucleation, crystal growth, surface and interface atomistic mechanisms; and
- new optical, electrical, magnetic, and mechanical properties of self-assembled systems.

Isabelle Berbezier and Maurizio De Crescenzi

Marseille and Rome, June 2015

License and Terms

The definitive version of this article is the electronic one which can be found at:
doi:10.3762/bjnano.6.144

BEILSTEIN JOURNAL OF NANOTECHNOLOGY

Photodetectors based on carbon nanotubes deposited by using a spray technique on semi-insulating gallium arsenide

Domenico Melisi*[1,2], Maria Angela Nitti[2], Marco Valentini[1,2], Antonio Valentini[1,2], Teresa Ligonzo[1,2], Giuseppe De Pascali[1,2] and Marianna Ambrico[3]

Full Research Paper

Open Access

Address:
[1]INFN – Sezione di Bari, Via Orabona 4, 70126, Italy, [2]Department of Physics, University of Bari "A. Moro", Via Orabona 4, 70126, Italy and [3]CNR IMIP, UoS di BARI, via Orabona 4, Bari, 70126, Italy

Email:
Domenico Melisi* - domenico.melisi@ba.infn.it

* Corresponding author

Keywords:
multi-wall carbon nanotubes; photodetectors; spray technique; UV–NIR

Beilstein J. Nanotechnol. **2014,** *5,* 1999–2006.
doi:10.3762/bjnano.5.208

Received: 18 July 2014
Accepted: 16 October 2014
Published: 05 November 2014

This article is part of the Thematic Series "Self-assembly of nanostructures and nanomaterials".

Guest Editor: I. Berbezier

Abstract

In this paper, a spray technique is used to perform low temperature deposition of multi-wall carbon nanotubes on semi-insulating gallium arsenide in order to obtain photodectors. A dispersion of nanotube powder in non-polar 1,2-dichloroethane is used as starting material. The morphological properties of the deposited films has been analysed by means of electron microscopy, in scanning and transmission mode. Detectors with different layouts have been prepared and current–voltage characteristics have been recorded in the dark and under irradiation with light in the range from ultraviolet to near infrared. The device spectral efficiency obtained from the electrical characterization is finally reported and an improvement of the photodetector behavior due to the nanotubes is presented and discussed.

Introduction

Fast photoconductive detectors (PCD) are widely used for the characterization of sub-nanosecond pulses generated from infrared (IR) to ultraviolet (UV) light, X-ray and gamma-ray photons, as well as charged particles [1-3]. Applications of carbon nanotubes (CNTs) in this field have shown interesting results, in particular in new technologically advanced nanoelectronic devices [4,5]. Photodetectors based on films of CNTs (both bundle and carpet distribution) on silicon, have been previously analyzed in the visible and IR spectral regions [6,7]. Moreover the chemical, mechanical and electrical properties make CNTs also suitable to fabricate a wide range of radiation detectors for space applications, high energy physics and medical instrumentation [7-9].

The common technique obtain CNT films is chemical vapour deposition (CVD), but some deposition requirements, such as high temperatures of the substrates, the necessity of a catalyst and, as a consequence, the necessity of a barrier layer between the latter and the substrate, limit the applications of this technique [10-12]. In our previous work we have already shown the potential of a spray deposition technique for depositing CNTs on silicon, starting from a powder, at low temperatures, without catalyst and an intermediate layer [7]. By using this spray technique, CNT films on silicon-based photodetectors were prepared, achieving quantum efficiency (QE) values in the visible light range comparable with those obtained for similar detectors with CNTs deposited by CVD [7,13-15]. In this work results from a photodetector based on CNTs spray-deposited on semi-insulating gallium arsenide (SI GaAs) are reported.

In order to perform the morphological characterization of the resulting films, electron microscopy, in scanning (SEM) and transmission (TEM) modes, was used.

Current–voltage (I–V) characterizations under dark and illuminated conditions, from NIR to UV region, were performed with two different device configurations. The resulting QE and the photocurrent spectral measurements are reported and discussed. Finally, the effect of the nanotubes on the charge generation and collection in the detector is analyzed.

Experimental

The multi-wall CNT (MWCNT) powder, with a purity degree greater than 95 wt %, was provided by COMETOX. The nanotubes are 5–15 µm long, and the diameters are between 10 and 30 nm. The procedure for the preparation of the solution is reported elsewhere [7]. The only difference is that an ultrasonic atomizer NS60K50-Sonaer 60 kHz system has been used in place of an airbrush, in order to obtain a better film uniformity. Due to the low deposition temperature (60 °C), custom-made transparent Mylar masks were used to better confine the CNT deposition area. SI GaAs substrates (350 ± 25 µm, resistivity $5.4 \cdot 10^7$–$9.1 \cdot 10^7$ Ω·cm, Hall mobility 5692–6025 $cm^2 \cdot V^{-1} \cdot s^{-1}$, carrier concentration $1.2 \cdot 10^7$–$2.1 \cdot 10^7$ cm^{-3}), produced by Wafer Technology LTD, were used for the fabrication of the photodetectors. In order to obtain the final devices, the substrates were first degreased in acetone and methanol, after that they were etched for 30 s in a fresh solution of $H_2SO_4/H_2O_2/H_2O$ (4:1:1), then rinsed in methanol and double-distilled water and finally dried with nitrogen. Two different layouts were used for the realization of the photodetectors (Figure 1). The first configuration, named single face sample (SFS), has a CNT layer sprayed on one face and a titanium/gold layer (30/50 nm), deposited by ion beam sputtering (IBS) [16], on the other face. The second one, named double face sample (DFS), consists of a CNT layer sprayed on both sides. The SFS configuration with the presence of a Schottky contact (Ti/Au layer) on the GaAs substrate [16] was chosen as the final device, while the DFS has been realized and analyzed only to study the electrical characteristics of CNTs on the gallium arsenide. After the spray process, in the SFS device configuration, an interdigitated 50 nm thick indium tin oxide (ITO) film was deposited from an ITO target on CNTs by means of IBS. An ITO/GaAs/Ti/Au device was also prepared as control sample.

Transmission electron microscopy (FEI Tecnai G^2 Spirit, 120 kV energy) was used to preliminarily evaluate the degree of dispersion of the CNTs in the spray solution performing few spray on TEM grids. Scanning electron microscopy (Zeiss-

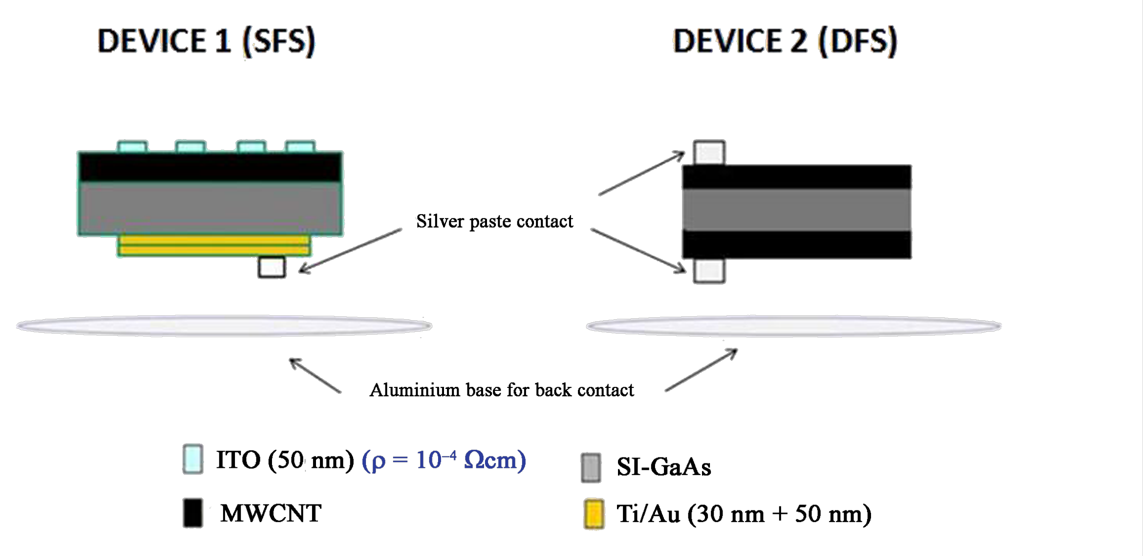

Figure 1: Schematic image of the two device layouts used: single face sample (SFS) and double face sample (DFS).

Sigma microscope with in-lens detector, 20 µm aperture, 10 kV energy) was used to obtain informations about the thickness of the CNT film and about the uniformity of its distribution on the GaAs substrate.

In order to perform the electrical characterization, all the samples were mounted gluing the back side on an aluminium disk by using a silver paste, leaving the front side covered with CNTs for the light exposure. The voltage supply was connected to the top ITO contact whereas the sample was grounded at the rear through the aluminium support.

For the calculation of QE, a typical configuration for spectral photocurrent measurements with a light source, wavelength selector and reference diode has been used. Specifically, a Thorlabs OSL1 white light source with optical fiber and a focusing lens were used to obtain a light spot on the photodetector while single wavelengths (400, 500, 600 and 700 nm) in the visible light range were selected by means of a filter set. For the UV characterization in the spectral range of 150–210 nm the measurements were performed under vacuum by using a McPherson 30 W Deuterium lamp coupled with a monochromator (Mc Pherson TM/Div. of S.I. Corp. mod. 234/302) as spectral light source. In this configuration the response of an UV-calibrated NIST diode (International Radiation Detectors, serial no. 97-527) was used for the QE calculation. An Agilent source/monitor unit was used to record the current–voltage characteristics.

To obtain more detailed information of the photodetector in the range of vis–NIR, photocurrent spectra of the SFS and of the ITO/GaAs/Ti/Au control sample were also performed in air, in the range of 350–1050 nm at various DC voltages, collected by means of a Stanford Research 850 lock-in amplifier equipped with a current preamplifier. Monochromatic, chopped (at a frequency of 13Hz) light impinging on the ITO/CNTs side of the samples was obtained by a tungsten halogen lamp coupled with an Acton Reasearch Spectra Pro 300i monochromator. The photocurrent response as a function of the light intensity at given DC voltages and wavelengths were obtained by inserting neutral filters of various optical density on the light path towards the sample. A calibrated THOR Labs photodiode (Thorlabs PM100D with a silicon photodiode S120VC) was used to normalize the sample photocurrent to the incident light intensity for all the measurements in the vis–NIR region.

Results and Discussion

TEM images acquired at 120 kV of the spray dispersions obtained with both the atomizer (Figure 2a) and the airbrush (Figure 2b), show a more uniform distribution of the layer deposited with the atomizer uniform than that of the layer deposited with the airbrush. The uniformity of a thicker layer deposited on GaAs is also confirmed by the SEM image reported in Figure 3.

In Figure 4 the dark-current–voltage (I–V) characteristics for the SFS, DFS and ITO/GaAs/Ti/Au photodetector configurations are reported. The inset reports the negative part of the I–V, showing the same trend for SFS and DFS samples. From the positive part a different behaviour of the SFS and DSF, due to the rectifying effect of Ti with respect to the ohmic effect of CNTs is observed. Good ohmic behaviour is demonstrated for the ITO/CNT/GaAs top contact of the SFS device. In fact, by comparing the rectifying and non-rectifying behaviour, respectively, of the SFS and of the ITO/GaAs/Ti/Au it can be deduced that the poor ohmic behaviour of the ITO/GaAs contact acts mostly as a counter barrier with respect to the GaAs/Ti/Au contact (Figure 4). In fact, for a positive applied voltage, the

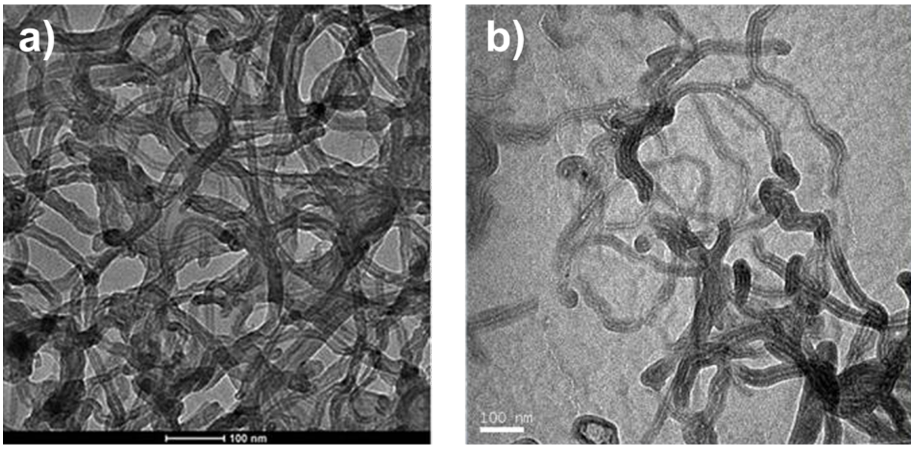

Figure 2: TEM micrographs of CNTs dispersion spray obtained by means of: the ultrasonic atomizer a); the airbrush b). Scale bars: 100 nm.

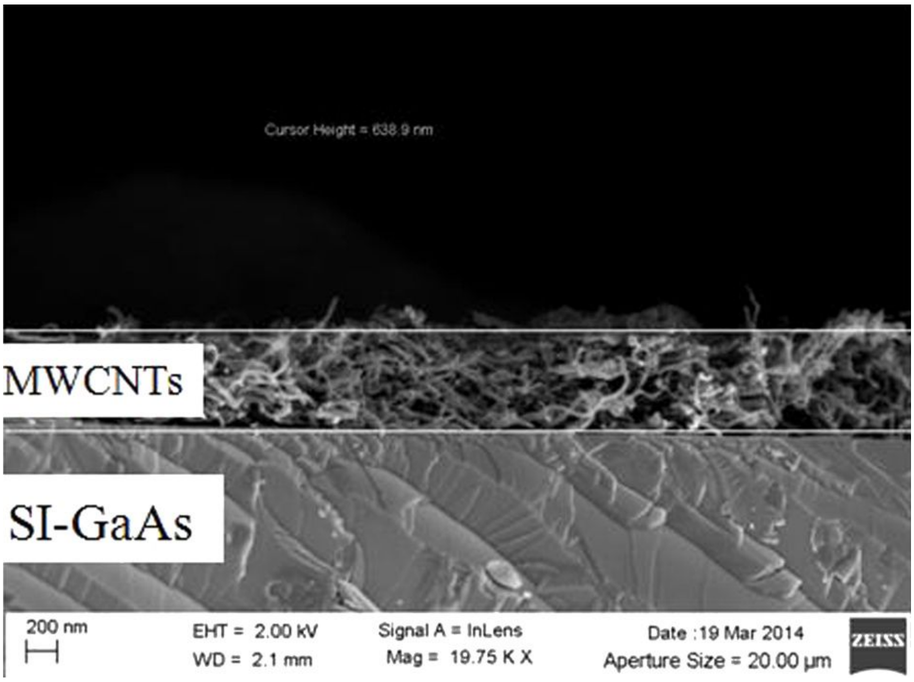

Figure 3: SEM image of the MWCNT film on a semi-insulating gallium arsenide substrate.

ITO/GaAs equivalent resistance increases, thus limiting the forward bias voltage drop at the GaAs/Ti/Au Schottky contact with subsequent reduction of the forward current. Then evidently the insertion of the CNT layer improves the ohmic behaviour with respect to the ITO/GaAs interface and consequently the diode performance.

The net photocurrents for negative bias of the devices in the vis–UV spectral region have been used to obtain the photoconductive absolute QE by means of the following formula:

$$\mathrm{QE}\left[\%\right] = \eta \cdot \left(I_{\mathrm{sam}} / I_{\mathrm{ref}}\right) \cdot 100\,,$$

where I_{sam} [A] is the sample current, I_{ref} [A] is the calibrated photodiode current, and η is the internal quantum efficiency of the calibrated photodiode.

The resulting calculation trends, at a bias voltage of −6 V, are reported for SFS and DFS in Figure 5 and Figure 6 for the visible and the UV range, respectively. The higher QE of SFS with respect to DFS at lower wavelengths in the visible light range (Figure 5) can be attributed to the contribution to the photo-generated charges from the near-band-gap light absorption of ITO [17]. Furthermore, the interdigitated ITO contact of the SFS covers half of the active surface of the device, and its ultraviolet absorption gives rise to the halving of the QE values in this region (Figure 6).

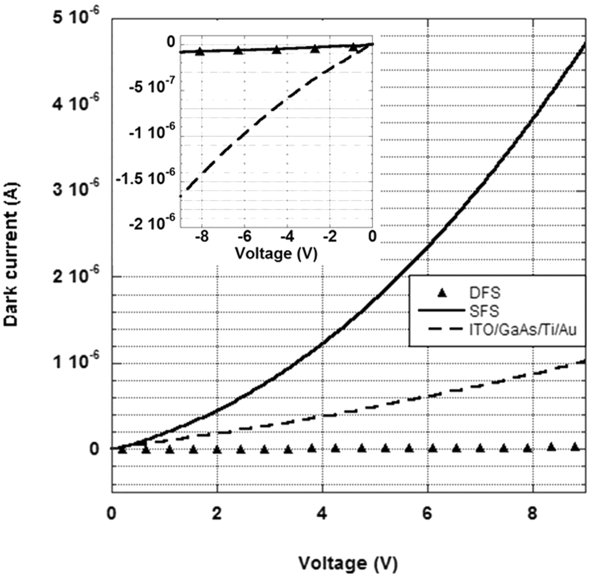

Figure 4: Dark-current–voltage characteristics for the SFS, DFS and ITO/GaAs/Ti/Au photodetector configurations. The inset reports the negative part of the dark-current–voltage characteristics.

To better understand the detector QE results in the range UV–vis that were analyzed so far, in Figure 7 [7] the expected responsivity of a gallium arsenide photodetector and, for comparison, a photodetector based on CNTs are reported. It is clear from the figure that the response in the UV of the CNTs/GaAs

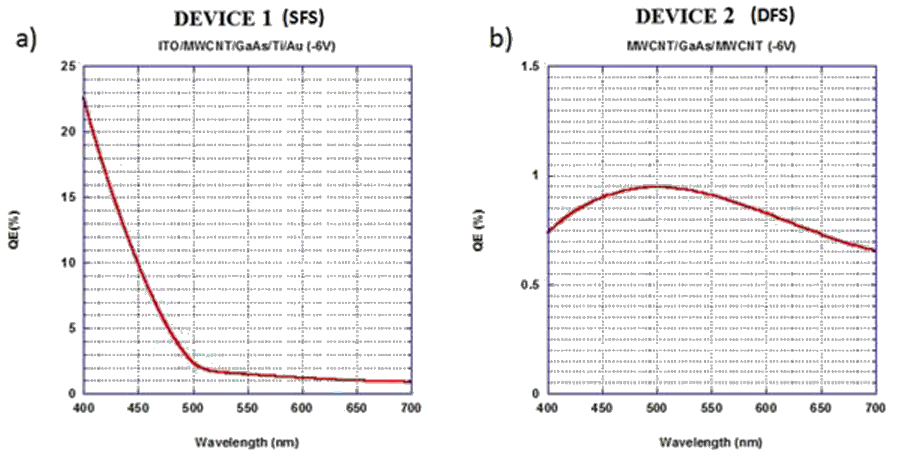

Figure 5: Absolute quantum efficiency trend in the visible light range, calculated at a bias voltage of −6 V for the devices SFS a) and DFS b).

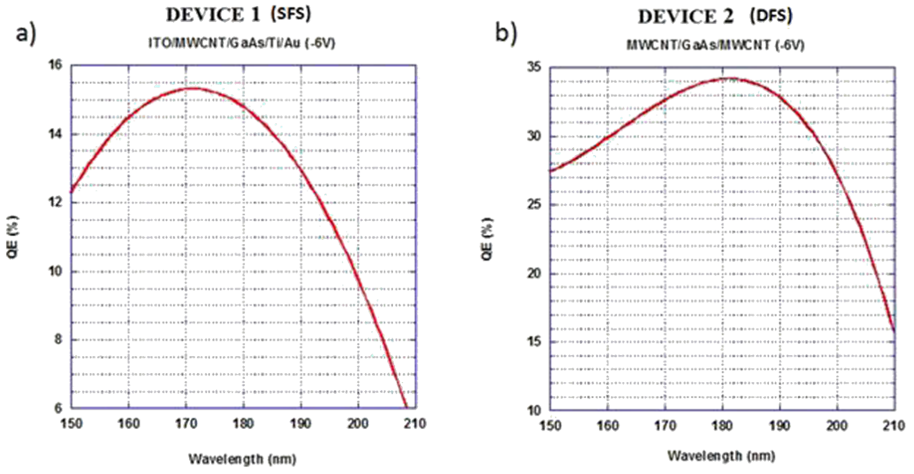

Figure 6: Absolute quantum efficiency trend in the UV range, calculated at a bias voltage of −6 V for the devices SFS a) and DFS b).

detector is due to the absorption of the CNTs in this region, to which, in the visible, the contribution of gallium arsenide is added.

In Figure 8 the normalized photocurrent spectra, measured at various voltages, in the 350–1050 nm region are reported. In spite of the evident voltage-dependence of the spectra, all of them exhibit a steep increase in the IR range, between 900 and 1000 nm. Assuming the photocurrent directly proportional to the GaAs absorption coefficient and direct gap transitions, an absorption edge of 1.38 eV has been obtained for all the spectra. This value is slightly lower than the energy gap of GaAs at room temperature (1.42 eV) [18]. As mentioned above, the spectral response of the device is voltage-dependent and particularly the photocurrent increases linearly with the voltage in the NIR region, although at different rates for the various wavelengths: The closer to the GaAs absorbtion edge (1.38 eV), the more the photocurrent increases with voltage. This characteristic, with respect to what was observed in analogous photocurrent spectra of the ITO/GaAs/Ti/Au device (not shown), is more pronounced so that at the maximum investigated voltages (+10 and −10 Volts) the SFS spectra become nearly flat (Figure 8a and Figure 8b) in the whole vis–NIR range except for the pronounced peak at the absorption edge. This peculiarity and especially the fact that, for positive voltages only, the photocurrent onset at 900–1000 nm is greatly enhanced with respect to the whole investigated spectral range, is still under investigation. As a further observation it must be pointed out that, with respect to the ITO/GaAs/Ti/Au comparison sample, at the maximum of the absorption edge (890 nm), the photocurrent exhibits a linear dependence on the incident light intensity (i.e., $I_{\mathrm{ph}} \propto P^{\gamma}$ with $\gamma \approx 1$) over many order of magnitude, as shown in Figure 9a and Figure 9b, for both negative and positive voltages. At 800 nm, only for positive voltage, the dependence

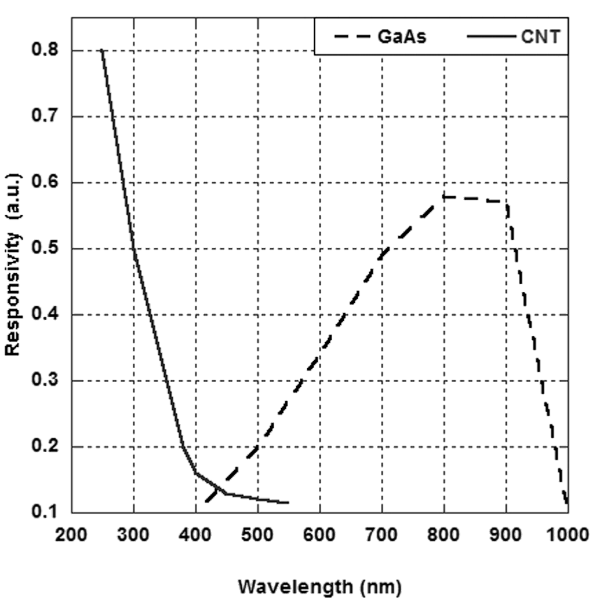

Figure 7: Responsivity trend of GaAs and CNTs based photodetectors.

turns out to be sublinear (γ = 0.82), as shown in Figure 9b. This result has to be compared with γ ranging between 0.67 and 0.91, obtained for the ITO/GaAs/Ti/Au in the same experimental conditions. To have a linear dependence of the photocurrent on the light intensity is an important achievement in a photodetector. Nevertheless in such devices (either p-i-n or Schottky diodes) the value of the exponent γ depends not only on the intrinsic properties of the photoactive material (traps and recombination centres distribution) but also on the properties of the contacts. Generally, the photocurrent [19] can be expressed as $I_{\mathrm{ph}} = e \cdot G \cdot F$, where F is the number of electron–hole pairs photogenerated per unit time and G is the photoconductive gain representing the number of carriers passing between electrodes in the unit time for each absorbed photon in the unit time. In fact, depending on the type of the contacts (blocking, ohmic or injecting), while the photogenerated charge is swept away by the electric field, the photoconductor volume can be replenished with other carriers (secondary photocurrent). If both mobile photogenerated electrons and holes are not replenished at the electrodes [19], e.g., in a reverse-biased photodiode, G is at most unity and it occurs when the one photogenerated electron–hole pair per photon is swept out before recombining via a recombination centre. In this case γ = 1 as for the reverse-biased SFS diode (Figure 9a). Conversely, for a direct-biased SFS diode (Figure 9b) the ITO/CNT ohmic contact supplies extra majority carriers to the GaAs volume (possibly the forward-biased Ti/Au Schottky contact might also inject minority carriers). In this case G can be nominally larger than unity but the detector is less sensitive to the light intensity, i.e., $\gamma \leq 1$ [20]. This occurs also for the ITO/GaAs/Ti/Au device as shown in the insets of Figure 9a inset and Figure 9b. As mentioned above for the dark-current–voltage characteristics, the ITO/GaAs contacts constitutes a counter barrier with respect to the GaAs/Ti/Au Schottky contact, so for a reverse bias of the latter the former is forward biased and viceversa, with secondary photocurrent generation [19,20] and $\gamma < 1$.

Conclusion

In this work we have shown the capability to produce photodetectors based on MWCNTs/semi-insulating GaAs by using a spray technique to deposit the nanotube film. Two different configurations have been analysed. The first with a Ti/Au back contact (SFS) and a CNT film on the other face. The second with CNTs on both sides (DFS). Furthermore an ITO/GaAs/Ti/

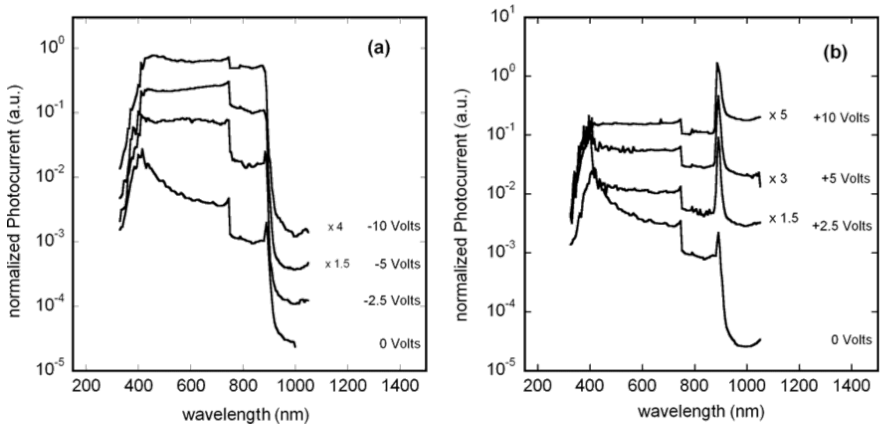

Figure 8: Normalized photocurrent spectra measured at: (a) negative voltages, (b) positive voltages applied to the ITO top contact with respect to the bottom Ti/Au contact. For the sake of clarity, some spectra were shifted up in the plots multiplying them by a factor, as indicated in the figure. The step shown in all the spectra at 750 nm is due to the change of the gratings of the monochromator.

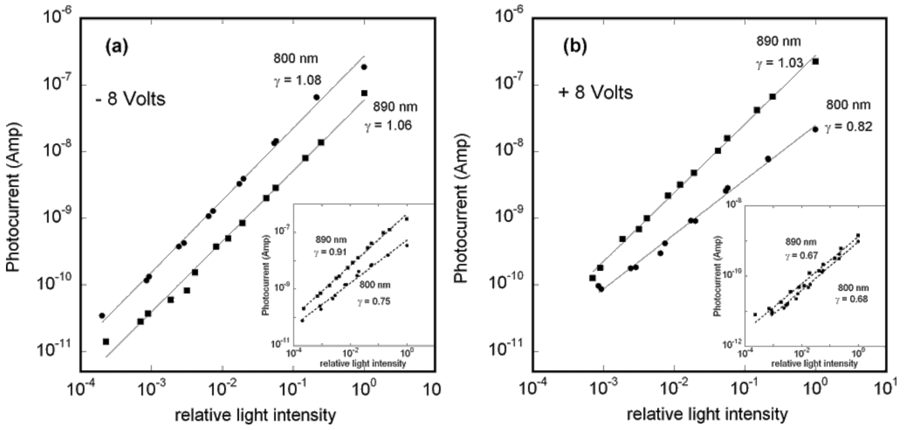

Figure 9: Photocurrent as a function of the relative monochromatic light intensity at λ = 800 and 890 nm for (a) −8 V and (b) +8 V applied to the top device contact. The best power-law fits are shown along with the resulting exponent γ. The full light intensity was approximately 10^{-5} W/cm^2. In the insets (a) and (b) the results obtained for a similar device without CNTs (ITO/GaAs/Ti/Au) under the same experimental conditions are shown for comparison.

Au device was prepared to better understand some experimental results obtained for the SFS.

The *I–V* measurements under illumination evidence, in both configurations, the contribution of the responsivity of the CNTs in the UV as photoactive layer to the detector performance. Furthernore, in the vis–NIR spectral range photocurrent appears to be more field-dependent in the device with CNTs, so that at maximum applied voltages photocurrent spectra of the SFS (differently from the ITO/GaAs/Ti/Au) gets nearly flat. This aspect is still under investigation.

The comparison of the dark-current–voltage characteristics of the ITO/CNT/GaAs/Ti/Au (SFS) and of the ITO/GaAs/Ti/Au demonstrates the good ohmic behaviour of the ITO/CNT/GaAs contact with respect to the bare ITO/GaAs one. This peculiarity improves the rectifying properties of the SFS device and, as a further consequence, its linear photocurrent-dependence behaviour, especially in reverse-bias mode.

Acknowledgements

This work was carried out in the frame of HP3 (Hadron Physics 3) european Project and GR.V-INFN SinPhoNIA (Single Photon Nanotechnology Innovative Approach) Collaboration.

References

1. Smith, F. W.; Le, H. Q.; Diadiuk, V.; Hollis, M. A.; Calawa, A. R.; Gupta, S.; Frankel, M.; Dykaar, D. R.; Mourou, G. A.; Hsiang, T. Y. *Appl. Phys. Lett.* **1989,** *54,* 890–892. doi:10.1063/1.100800
2. Moglestue, C.; Rosenzweig, J.; Kuhl, J.; Klingenstein, M.; Lambsdorff, M.; Axmann, A.; Schneider, J.; Hülsmann, A. J. *J. Appl. Phys.* **1991,** *70,* 2435–2448. doi:10.1063/1.349395
3. Decrossas, E. High frequency characterization of carbon nanotube for device application. Ph.D. Thesis, University of Arkansas, Fayetteville, AR, USA, 2012.
4. Tans, S. J.; Verschueren, A. R. M.; Dekker, C. *Nature* **1998,** *393,* 49–52. doi:10.1038/29954
5. Kamat, P. V. *Nano Today* **2006,** *1,* 20–27. doi:10.1016/S1748-0132(06)70113-X
6. Moon, J. S.; Park, J. H.; Lee, T. Y.; Kim, Y. W.; Yoo, J. B.; Park, C. Y.; Kim, J. M.; Jin, K. W. *Diamond Relat. Mater.* **2005,** *14,* 1882–1887. doi:10.1016/j.diamond.2005.07.015
7. Melisi, D.; Nitti, M. A.; Valentini, M.; Valentini, A.; Ditaranto, N.; Cioffi, N.; Di Franco, C. *Thin Solid Films* **2013,** *543,* 19–22. doi:10.1016/j.tsf.2013.03.079
8. Ruffini, G.; Dunne, S.; Farrés, E.; Pallares, J. M.; Ray, C.; Mendoza, E.; Silva, R.; Grau, C. *Sens. Actuators, A* **2006,** *132,* 34–41. doi:10.1016/j.sna.2006.06.013
9. Artru, X.; Fomin, S. P.; Shul'ga, N. F.; Ispirian, K. A.; Zhevago, N. K. *Phys. Rep.* **2005,** *412,* 89–189. doi:10.1016/j.physrep.2005.02.002
10. Ren, Z. F.; Huang, Z. P.; Xu, J. W.; Wang, J. H.; Bush, P.; Siegal, M. P.; Provencio, P. N. *Science* **1998,** *282,* 1105–1107. doi:10.1126/science.282.5391.1105
11. Che, G.; Lakshimi, B. B.; Martin, C. R.; Fisher, R. *Chem. Mater.* **1998,** *10,* 260–267. doi:10.1021/cm970412f
12. Kumar, M.; Ando, Y. *J. Nanosci. Nanotechnol.* **2010,** *10,* 3739–3758. doi:10.1166/jnn.2010.2939
13. Ambrosio, A.; Aramo, C.; Battiston, R.; Castrucci, P.; Cilmo, M.; De Crescenzi, M.; Fiandrini, E.; Grossi, V.; Guarino, F.; Maddalena, P.; Nappi, E.; Passacantando, M.; Pignatel, G.; Santucci, S.; Scarselli, M.; Tinti, A.; Valentini, A.; Ambrosio, M. *J. Instrum.* **2012,** *7,* P08013. doi:10.1088/1748-0221/7/08/P08013
14. Ambrosio, A.; Ambrosio, M.; Ambrosone, G.; Carillo, V.; Coscia, U.; Grossi, V.; Maddalena, P.; Passacantando, M.; Perillo, E.; Raulo, A.; Samtucci, S. *Nucl. Instrum. Methods Phys. Res., Sect. A* **2008,** *589,* 398–403. doi:10.1016/j.nima.2008.03.004
15. Aramo, C.; Ambrosio, A.; Ambrosio, M.; Castrucci, P.; Cilmo, M.; De Crescenzi, M.; Fiandrini, E.; Guarino, F.; Grossi, V.; Nappi, E.; Passacantando, M.; Pignatel, G.; Santucci, S.; Scarselli, M.; Tinti, A.; Valentini, A. *Nucl. Instrum. Methods Phys. Res., Sect. A* **2012,** *695,* 150–153. doi:10.1016/j.nima.2011.12.098

16. Cola, A.; Lupo, G.; Vasanelli, L.; Valentini, A. *J. Appl. Phys.* **1992,** *71,* 4966–4971. doi:10.1063/1.350594
17. Mridha, S.; Basak, D. *J. Appl. Phys.* **2007,** *101,* 083102. doi:10.1063/1.2724808
18. Madelung, O. *Semiconductors: data handbook;* Springer, 2004.
19. Bube, R. H. *Photoconductivity of solids;* John Wiley & Sons, Inc, 1960.
20. Sze, S. M.; Kwok, K. N. *Physics of semiconductor devices,* 3rd ed.; John Wiley & Sons, 2007.

License and Terms

The definitive version of this article is the electronic one which can be found at:
doi:10.3762/bjnano.5.208

BEILSTEIN JOURNAL OF NANOTECHNOLOGY

Si/Ge intermixing during Ge Stranski–Krastanov growth

Alain Portavoce*[1], Khalid Hoummada[2], Antoine Ronda[1], Dominique Mangelinck[1]
and Isabelle Berbezier[1]

Full Research Paper

Address:
[1]CNRS, IM2NP, Faculté des Sciences de Saint-Jérôme case 142, 13397 Marseille, France and [2]Aix-Marseille University, IM2NP, Faculté des Sciences de Saint-Jérôme case 142, 13397 Marseille, France

Email:
Alain Portavoce* - alain.portavoce@im2np.fr

* Corresponding author

Keywords:
atom probe tomography; germanium islands; Stranski–Krastanov growth

Beilstein J. Nanotechnol. **2014,** *5,* 2374–2382.
doi:10.3762/bjnano.5.246

Received: 16 July 2014
Accepted: 19 November 2014
Published: 09 December 2014

This article is part of the Thematic Series “Self-assembly of nanostructures and nanomaterials”.

Associate Editor: P. Ziemann

Abstract

The Stranski–Krastanov growth of Ge islands on Si(001) has been widely studied. The morphology changes of Ge islands during growth, from nucleation to hut/island formation and growth, followed by hut-to-dome island transformation and dislocation nucleation of domes, have been well described, even at the atomic scale, using techniques such as scanning tunneling microscopy and transmission electron microscopy. Although it is known that these islands do not consist of pure Ge (due to Si/Ge intermixing), the composition of the Ge islands is not precisely known. In the present work, atom probe tomography was used to study the composition of buried dome islands at the atomic scale, in the three-dimensional space. The core of the island was shown to contain about 55 atom % Ge, while the Ge composition surrounding this core decreases rapidly in all directions in the islands to reach a Ge concentration of about 15 atom %. The Ge distribution in the islands follows a cylindrical symmetry and Ge segregation is observed only in the {113} facets of the islands. The Ge composition of the wetting layer is not homogeneous, varying from 5 to 30 atom %.

Introduction

The nucleation and growth of Ge islands on a Si(001) substrate have been the subject of numerous investigations with the aim of understanding the fundamental processes involved in the Stranski–Krastanov growth process and to produce original devices based on a Ge dot assembly [1-7]. The focus of these investigations was devoted to understanding the shape of the islands and density variations versus stress (or strain) or substrate surface modifications (e.g., patterning, Si(Ge) buffer or surfactant variations) [6-11], using characterization techniques such as atomic force microscopy (AFM), scanning tunneling microscopy (STM), transmission electron microscopy (TEM) and X-ray diffraction (XRD), as well as photoluminescence spectroscopy (PL). Consequently, the control of the Ge island shape and density, as well as the control of Ge island assembly, has significantly progressed over the last years [6,12]. However, few studies have been devoted to the understanding of the Ge island composition [13-33]. This is related to the difficulty of experimentally analyzing the composition of three-dimensional (3D) nano-objects. In general, the investigations performed on Ge dot compositions involve indirect methods, often coupled with calculations. These studies shown that Ge dots do not consist of pure Ge, but rather contain a significant amount of Si in addition. However, contradicting interpretations were made concerning the atomic distribution in the islands, where some measurements led to the conclusion that the islands are made of a Si-rich core and a Ge-rich shell, and others led to the opposite conclusion [23,26,28,30,32]. It was only very recently that the calculations made by Georgiou et al. [34] resolved this controversy, showing that formation of islands with a Si-rich core is related to near-equilibrium processes and inter-island diffusion, while formation of islands exhibiting a Ge-rich core is strain driven and kinetically limited. It is important to stress that the Ge dot composition can have a significant impact on Ge-dot-based device properties, such as electron confinement and optical properties, for example. Consequently, the measurement of the Ge island composition versus growth conditions is of great interest for: (1) understanding the fundamental processes occurring at the atomic scale during growth, and (2) the control of Ge dot composition versus growth conditions or surface state for device fabrication. In addition, despite the fact that Ge islands are known to nucleate after the deposition of 3 to 6 Ge monolayers (MLs) [1-6,35], the composition and the thickness of the wetting layer (WL) are still under discussion due to Si/Ge intermixing during growth [10,11,25].

In the present work, pulsed laser atom probe tomography (APT) has been used to quantitatively study (at the atomic scale and in the 3D space) the composition of large Ge dome islands grown by gas-source molecular beam epitaxy (GS-MBE) and buried under a Si cap [36]. APT measurements show that these islands are made of a more Ge-rich core (≈55 atom % Ge) and an increasingly Ge-deficient shell (≈15 atom % Ge). Despite the strong Si/Ge intermixing during Ge island formation, the Si cap or Si substrate/island interface is abrupt, exhibiting weak Si/Ge intermixing during Si deposition. The islands keep their usual {111} and {113} surface facets under the Si cap, and Ge segregation is observed only in {113} facets. The thickness and the Ge composition of the WL are not homogeneous and fluctuate between 1 to 4.5 nm, and between 5 to 30 atom % Ge, respectively.

Results and Discussion

The goal of this study is to quantitatively measure the composition of Ge islands in the three-dimensional space at the atomic scale using pulsed laser APT [37]. APT uses structures shaped by dual beam focus ion beam (FIB) as tips exhibiting a tip diameter between 50 nm (top of the tip) and 200 nm [38,39]. Figure 1 presents the different steps leading to the formation of APT samples by FIB. After the deposition of a Ni cap for the protection of the sample surface, the sample is loaded into a dual beam FIB. Here, an additional protective Pt layer is deposited by FIB (Figure 1a) and a wedge is cut (Figure 1b) and lifted off using an in situ tungsten finger (Figure 1c). Next, several pieces (approximately 3 × 3 µm^2) of the sample wedge are glued onto preshaped Si pillars (Figure 1d) using FIB Pt deposition before being shaped as tips by FIB (Figure 1e–g).

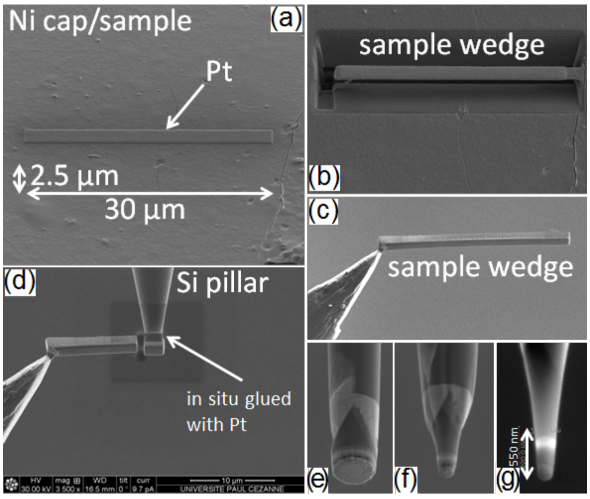

Figure 1: SEM images acquired during APT sample preparation in a dual-beam FIB process. The image sequence (a to f) corresponds to the chronological steps required for the fabrication of an APT tip.

Generally, the surface density of Ge islands is between 1 × 10^9 to 5 × 10^{10} cm^{-2}, their lateral size is between 100 and 1000 nm, and their height is between 10 and 100 nm [40]. Therefore, the difficulty lies in locating a single island in the APT sample. This is especially true for the case of small islands with a low surface density. Such islands cannot be observed by scanning electron microscopy (SEM) or FIB and the probability of shaping a tip exactly on an island is quite low. For these reasons, the island growth procedure was designed to produce large Ge islands (domes) occupying a large proportion of the sample surface. Two identical layers of islands were grown on the sample, where the first was buried by a Si layer before growing the second layer on top. Figure 2 presents AFM measurements performed on the second layer of islands, located on the surface. The island surface density is ≈6 × 10^8 cm^{-2}, and the average island height and average width are ≈72 nm and ≈430 nm, respectively.

The sample size presented in Figure 2a corresponds to the typical size of the initial wedge piece deposited on the preshaped Si pillar (Figure 1d). The goal of steps e, f, and g presented in Figure 1e–g, is to form the apex of the tip used for APT measurements in the center of the sample in Figure 2a.

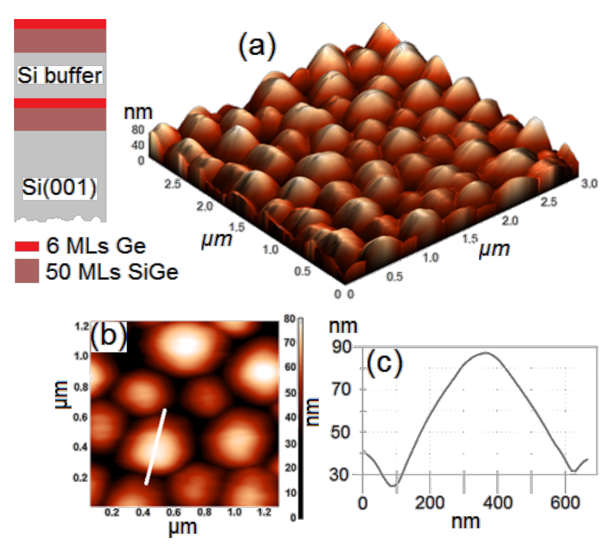

Figure 2: Sketch of the sample structure and AFM measurements performed on the sample surface after MBE growth: (a) 3 × 3 µm^2 3D image, b) 2D image, and c) height variations measured along the white line in (b).

Consequently, due to their lateral size, it is difficult to get an entire island in a single APT sample. However, due to the reduced distance between islands, the probability to obtain part of an island in an APT sample is high. Figure 3 presents a typical sample volume analyzed by APT. The size of the volume is 100 × 100 × 90 nm^3. Each dot corresponds to a single atom: green, gray, red and blue dots correspond to Ni, Si, Ge and O atoms, respectively. In addition, the dark red surfaces correspond to 2 atom % Ge isoconcentration surfaces. This allows for easier delimiting of the WL and the island interfaces.

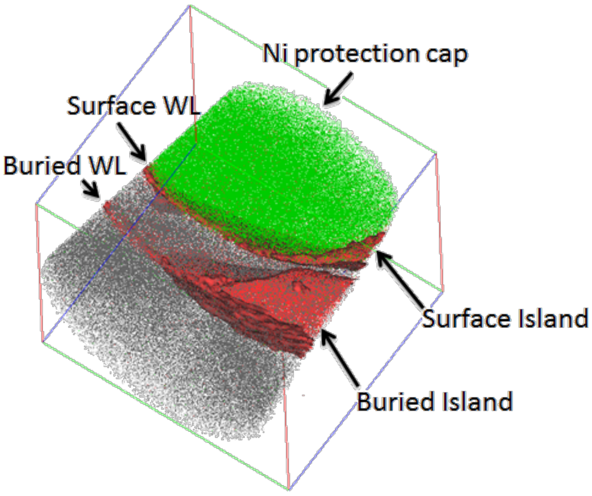

Figure 3: APT volume (100 × 100 × 90 nm^3) obtained from the sample. Green, gray, red and blue dots correspond to Ni, Si, Ge and O atoms, respectively. 2 atom % Ge isoconcentration surfaces are also shown (dark red surfaces).

From this analysis, one can recognize the structure of the sample: the Ni cap deposited for APT sample preparation, the second layer of islands (the WL and a small part of a surface island are recognizable), the Si buffer, the first layer of islands, and the Si substrate. APT analysis allows one-dimensional (1D) atomic composition profiles to be determined in any direction in the analyzed volume.

Figure 4 shows the composition variation measured in two different APT samples through the surface WL and the buried WL in a region between islands. The surface WL and the buried WL were found to be similar (both are inhomogeneous). Their thickness and their composition vary in the sample from 1 to 4.5 nm (with an average thickness ≈2.7 nm) and from 5 to 30 atom % Ge, respectively.

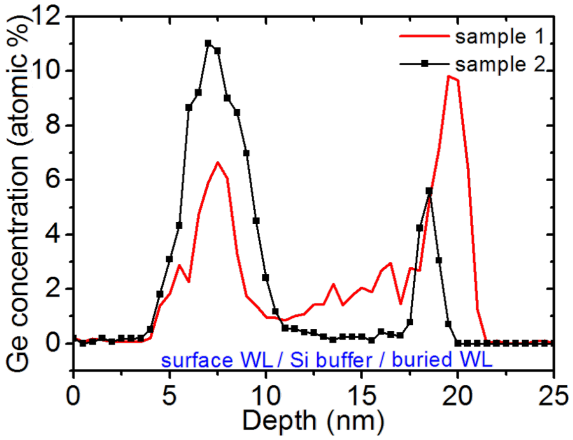

Figure 4: Top-down, 1D Ge concentration profiles measured between the islands in two different samples. The profiles go through the surface WL, the Si buffer, the buried WL, and end in the Si substrate.

Figure 5a shows a TEM cross-sectional view of a typical dome island exhibiting {111} and {113} facets forming an angle of 54.7° and 25.2°, respectively, with the (001) surface of the Si substrate [40]. Figure 5b,c presents only the Ge atoms of buried islands in two different 3D APT volumes. As expected, the interface between the Si substrate and the islands is flat. However, one can observe facets at the island/Si cap interface. Actually, two types of facets were observed, exhibiting angles of approximately 55 ± 5° and 25 ± 5° with the Si substrate, respectively. These angles are in good agreement with the usual {111} and {113} facets of Ge dome islands [40]. The facets underneath the Si cap remained intact. In addition, as can be seen in Figure 5b,c the Si/Ge intermixing between the island base and the substrate, as well as between the island top and the Si cap is insignificant. In Figure 5c one can observe an increase of the Ge atom fraction on top of the island.

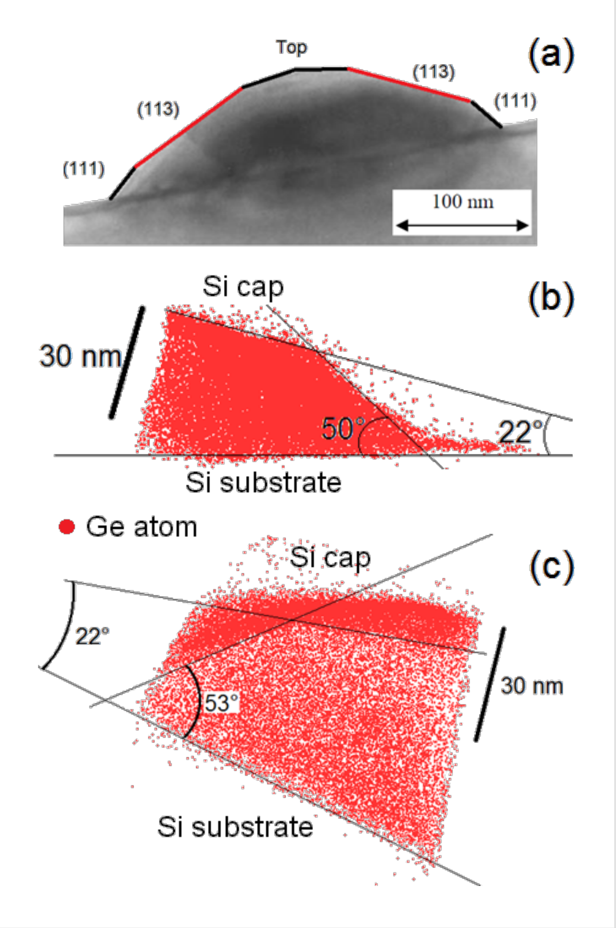

Figure 5: Cross-sectional TEM image of a typical dome island (a), and side-views of two different APT volumes showing only the Ge atoms they contain (b and c).

This result is further emphasized in Figure 6 by reducing the number of atoms shown in the APT volume. Due to the superimposed effect of the 3D APT data (Figure 5 and Figure 6) it is necessary to analyze 1D composition profiles perpendicular to the facets in order to observe that Ge segregation actually only occurs on the {113} facets. For example, Figure 7 presents two different 1D composition profiles measured perpendicular to a {111} facet (squares) and perpendicular to a {113} facet (solid line). In both profiles, the surface wetting layer, with a Ge composition of about 10 atom %, can be observed. In the case of the {111} facet, the Ge concentration in the island is almost constant, at approximately 14 atom %. The {113} facet also exhibits a constant Ge concentration of approximately 14% within the island bulk. This is preceded by a region of increased Ge concentration of up to 23 atom % at the Si cap/island interface.

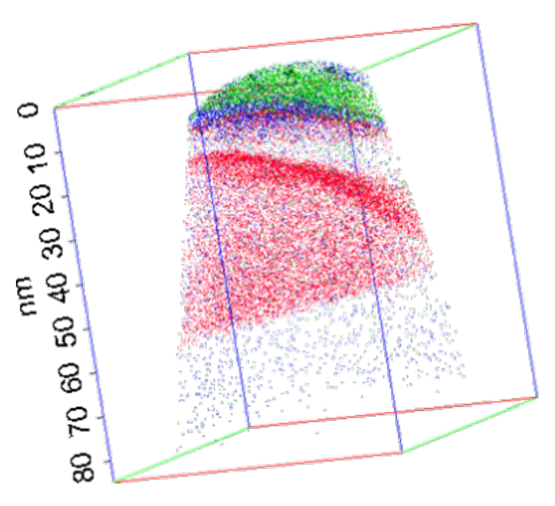

Figure 6: APT volume showing 2% of the Ni atoms, 5% of the Ge atoms, and 100% of the O atoms (the Si atoms are not shown). The O atoms detected in the bulk of the sample are actually due to noise.

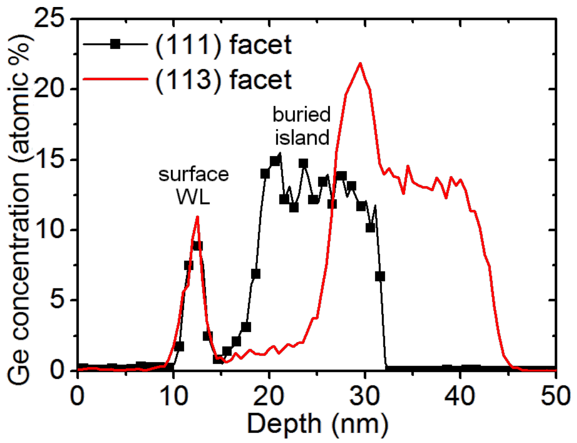

Figure 7: Top-down 1D Ge concentration profiles measured in two different APT volumes, one in the direction perpendicular to a (111) facet (black solid squares), and the other in the direction perpendicular to a (113) facet (red solid line).

The Ge concentration in the segregation layer of the {113} facets was found to vary from 23 to 35 atom %. Figure 8a presents another APT volume (120 × 120 × 100 nm^3) containing the core of a Ge island. Figure 8b and Figure 8c present a 2D map and a 1D profile (top-down), respectively, of the Ge concentration in the island core. The island core is not localized in the center of the island but at the bottom, close to the Si substrate/island interface. On average, the Ge concentration in the island core is about 55 atom %.

Figure 9a shows an APT volume (90 × 90 × 130 nm^3) in which the 1D Ge and Si concentration profiles presented in Figure 9b have been measured. The purpose of Figure 9c is to qualitatively show where in the island the profiles in Figure 9b were measured.

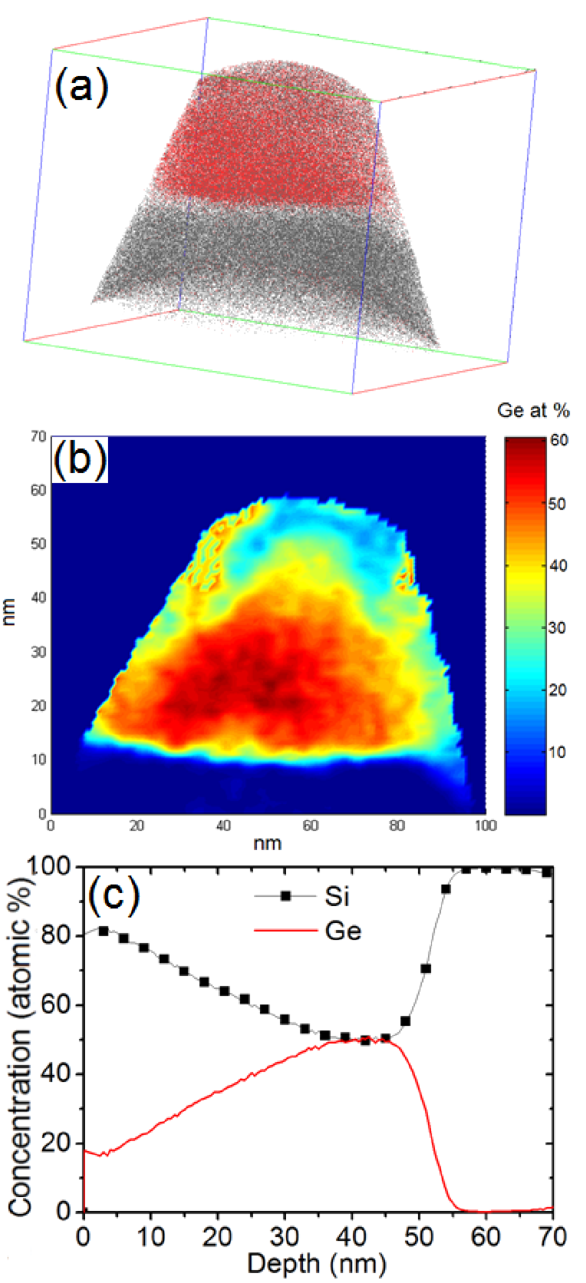

Figure 8: APT analysis: (a) 3D volume (120 × 120 × 100 nm^3), (b) 2D map of the Ge concentration distribution in the center of the volume presented in Figure 8a, and (c) top-down 1D Si and Ge concentration profiles measured in the volume presented in Figure 8a.

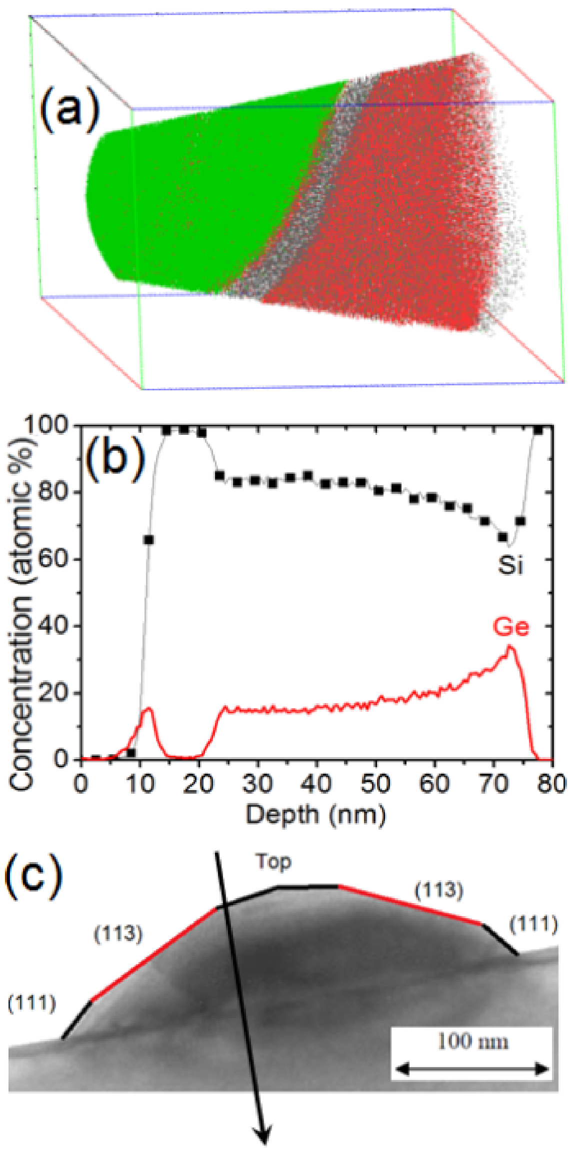

Figure 9: (a) APT volume (90 × 90 × 130 nm^3) and (b) Si and Ge 1D concentration profiles measured in (a). Figure 9c indicates the direction in which the concentration profiles were measured in the island.

We observed the surface wetting layer, followed by the Si buffer and no Ge segregation at the Si buffer/island interface. Within the island, the Ge concentration is constant (≈15 atom %) on ≈20 nm before and progressively increases until reaching the base of the island. This profile (as shown in Figure 9c) corresponds to the part of the island between the (113) facet and the top of the island. Figure 10 is similar to Figure 9, but presents an APT volume (70 × 70 × 85 nm^3) corresponding to the part of an island just below a (113) facet. In this case, one can observe the Ge segregation at the Si cap/island interface and a constant Ge composition of ≈15 atom % in the entire island up to the island/Si substrate interface. Together, Figure 9 and Figure 10 with Figure 8 show how the Ge concentration decreases from the island core in all directions to reach a quasi-constant concentration of ≈15 atom %. It is interesting to note that the island core composition (≈55 Ge atom %) and the island shell composition (≈15 Ge atom %) appear to be independent of the size of the islands, since the APT measurements were acquired in a random distribution of islands (see Figure 2).

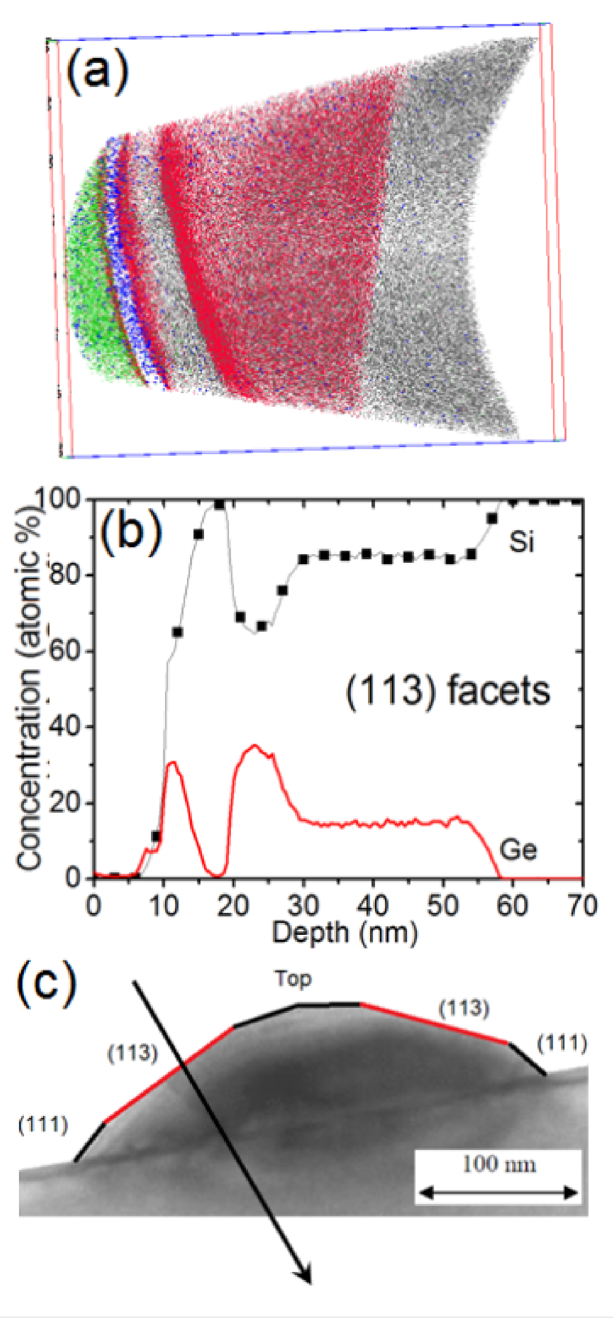

Figure 10: (a) APT volume (70 × 70 × 85 nm^3) and (b) Si and Ge 1D concentration profiles measured in this volume. Figure 10c indicates the direction in which the concentration profiles were measured in the island.

In an attempt to give an overall picture of a half-island, four APT volumes corresponding to different part of islands were combined in Figure 11. This figure shows how the different APT volumes were associated (in red and green the shape of the associated tips), as well as a Ge isoconcentration surface of 1 atom % which delimits the buried Ge island. In this image, the white arrow in the Ge segregation region is revealed by the isoconcentration surface. In order to show how the Ge concentration varies in the island, three isoconcentration surfaces are presented in Figure 11b, corresponding to the Ge concentrations of 53, 40 and 10 atom %. The Ge concentration profile along the direction shown by the red arrow in this image is presented in the Figure 11c. In this last figure, one can observe a Ge concentration plateau of ≈55 atom % in the island core and a rapid decrease of the Ge concentration reaching ≈15 atom % in the rest of the island.

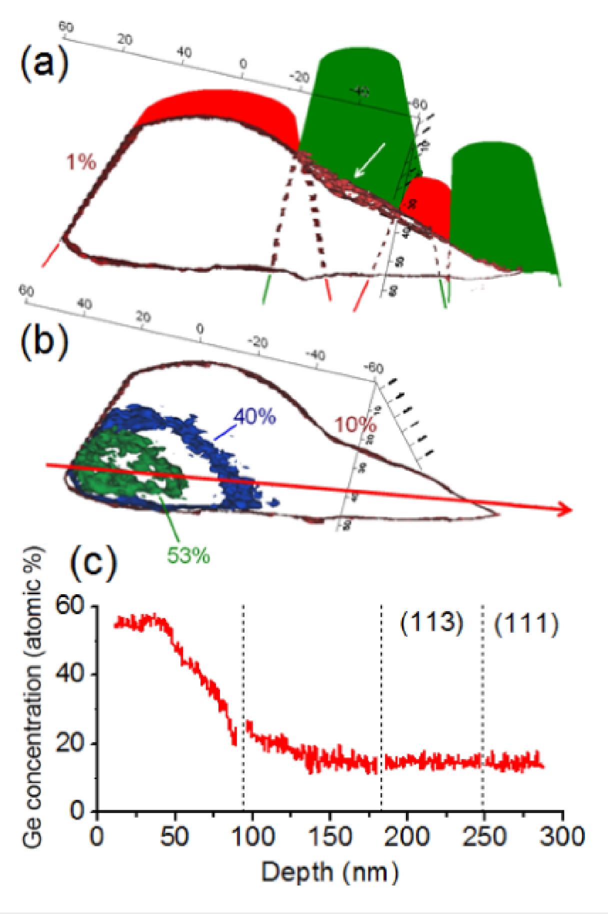

Figure 11: APT measurements obtained for four APT volumes (green and red surfaces) which form almost half of a Ge island: (a) Ge isoconcentration surface of 1 atom %, (b) Ge isoconcentration surfaces of 53, 40 and 10 atom %, and (c) Ge 1D concentration profile measured in the direction indicated by the red arrow in (b).

The composition of Ge islands depends on the growth conditions. Ge islands exhibiting a Si-rich core were shown to correspond to growth conditions allowing for near-equilibrium states to be reached, which is more typical for the case of chemical vapor deposition [34]. Ge islands exhibiting a Ge-rich core were shown to be related to growth conditions promoting far-from-equilibrium states, controlled by kinetic processes, which is more typical for the case of MBE growth [34]. Equilibrium is reached through free energy minimization, taking into account the minimization of the surface energy, the strain energy, the alloy mixing energy and the configurational entropy [22]. In the case of a pure Ge dome island (no intermixing with Si), the stress was shown to be compressive in the interior of the island, and tensile at the edges of the island [34]. Thus, in the case of island formation close to equilibrium, the Si-rich core is attributed to the compressive conditions prevailing in the island core, and the Ge-rich outer shell is attributed to the lower surface energy of Ge and the tensile conditions prevailing at the island edges. From a kinetic point of view, it was shown that the main limiting factor of atomic redistribution is atomic diffusion (maximum diffusion length ≈1 nm normal to the facets). Atomic transport is mainly strain-driven. The diffusion path of atoms is determined by the distribution of diffusion barriers, and can explain the atomic distribution found in the islands having a Ge-rich core. In particular, Si diffusion is easier at the island border and in a thin sub-surface layer parallel to the facets (where the island composition exhibits a cylindrical symmetry), and Si atoms cannot reach the island core, while the sides of the island can experience significant strain-driven alloying. Our observations are in agreement with strain-driven and diffusion-limited atomic redistribution during MBE growth of dome islands. However, our results lie somewhat between the two extreme cases shown in [34], namely: (1) near-equilibrium islands with a Si-rich core and a Ge-rich outer-shell, exhibiting strong composition gradients in the two directions parallel and normal to the surface, and (2) kinetically-controlled islands with a core rich in Ge and border rich in Si (lateral composition variations), with negligible composition variations in the direction normal to the surface (bottom to top). Indeed, in our case, the islands exhibit a more Si-rich periphery and a more Ge-rich core, as expected for kinetically limited island growth. However, significant Ge composition gradients are found in both directions parallel and normal to the surface, with a core located at the bottom of the island, and an increase of Ge concentration can be observed on the island surface (Ge segregation on {113} facets), as expected for near-equilibrium islands.

X-ray diffraction measurements revealed the existence of atomically ordered Si/Ge domains in dome islands and the WL [41]. Ordered domains were shown to be located in a limited region of the islands, and LeGoues et al. [42] showed that Si/Ge ordering is likely linked to surface reconstruction. Recently, atom-scale Monte Carlo simulations showed that ordering domains in dome islands could indeed correspond to a surface-related phenomenon driven by surface equilibrium [43]. The calculations emphasized that ordering should be stronger in the vicinity of {15 3 23} facets and should be weak for the {105} and {113} facets. The APT instrument used for this experiment was able to measure only 40% of all the atoms in the sample, thus assessment of atomic ordering would be difficult to evidence in the APT volumes. In addition, {15 3 23} facets (contact angle ≈36°) and {105} facets (contact angle ≈11°, i.e., the facets on top of the island in Figure 5a) were not clearly identified in our measurements. However, one can note that surface segregation usually involves only one to two atomic planes, while the Ge increase observed on the {113} facets of the islands seems to concern a relatively thick subsurface layer of several nanometers in depth, as can be seen in Figures 5c, 6, 7, and 10. Thus, considering that ordered domains are due to a surface effect located in a limited region, the APT measurements suggest that Si/Ge ordering takes place at the {113} facets.

Conclusion

Pulsed laser APT revealed the Si and Ge atomic distributions in large Ge dome islands buried by Si. The bulk composition of the islands exhibits a cylindrical symmetry. The islands are composed of a ≈55 atom % Ge core located close to the Si substrate/island interface, surrounded by a shell containing ≈15 atom % Ge. Between the islands, the thickness of the WL and its composition are not homogeneous, varying between 1 and 4.5 nm (average thickness ≈2.7 nm) and between 5 and 30 atom % Ge, respectively. The Si/Si–Ge interface is abrupt, and the islands maintain their equilibrium {111} and {113} facets under the Si cap. Ge segregation is observed only in the {113} facets, with a Ge accumulation up to 23–35 atom %. These results are in agreement with recent calculations showing that the composition of Ge islands grown by MBE should be mainly driven by strain minimization and limited by atomic diffusion kinetic barriers.

Experimental

The sample was grown in a VG Semicon gas source MBE chamber using disilane and germane, exhibiting a base pressure in the 10^{-11} mbar range. The Si(001) substrate was chemically cleaned using a modified Radio Corporation of America (RCA) process before introduction in the MBE setup. First, the disilane gas was introduced into the growth chamber while increasing the substrate temperature (*T*) up to 850 °C in order to grow a 100 nm thick Si buffer. Then, the temperature was decreased to T = 700 °C and a 50 monolayer (ML) thick $Si_{0.7}Ge_{0.3}$ layer was deposited before the deposition of 6 MLs of pure Ge. These layers were then buried with a pure Si buffer before another layer (50 MLs-$Si_{0.7}Ge_{0.3}$/6 MLs-Ge) was grown (see the sketch of the sample structure in Figure 2). The entire growth was performed without interruption. Sample preparation for APT was performed using a Helios NanoLab DualBeam Ga^+ FIB from FEI. A 100 nm thick Ni film was deposited by magnetron sputtering on each sample for protection before the samples were processed by FIB. Two types of samples were prepared: either the Ni cap was deposited without removing the surface native oxide of the sample (Figure 6, for example) or the sample was dipped in a 5% HF solution for 1 min in order to remove the native oxide (Figure 3, for example) before capping with Ni. The same results were obtained for the two types of samples. APT analysis was performed using a LEAP 3000X HR microscope in the pulsed laser mode. The analysis was carried out at 50 K, with a laser pulse frequency of 100 kHz, using a laser power between 0.5 and 0.6 nJ, corresponding to a I_{Si}^{2+} /I_{Si}^{1+} ratio between 100 and 10, and a I_{Ge}^{2+} /I_{Ge}^{1+} ratio between 7 and 2.5.

References

1. Voigtländer, B. *Surf. Sci. Rep.* **2001,** *43,* 127–254. doi:10.1016/S0167-5729(01)00012-7
2. Berbezier, I.; Ronda, A.; Portavoce, A. *J. Phys.: Condens. Matter* **2002,** *14,* 8283–8331. doi:10.1088/0953-8984/14/35/306
3. Teichert, C. *Phys. Rep.* **2002,** *365,* 335–432. doi:10.1016/S0370-1573(02)00009-1
4. Stangl, J.; Holý, V.; Bauer, G. *Rev. Mod. Phys.* **2004,** *76,* 725–783. doi:10.1103/RevModPhys.76.725
5. Baribeau, J.-M.; Wu, X.; Rowell, N. L.; Lockwood, D. J. *J. Phys.: Condens. Matter* **2006,** *18,* R139–R174. doi:10.1088/0953-8984/18/8/R01
6. Berbezier, I.; Ronda, A. *Surf. Sci. Rep.* **2009,** *64,* 47–98. doi:10.1016/j.surfrep.2008.09.003
7. Portavoce, A.; Kammler, M.; Hull, R.; Reuter, M.; Ross, F. M. *Nanotechnology* **2006,** *17,* 4451–4455. doi:10.1088/0957-4484/17/17/028
8. Volpi, F.; Portavoce, A.; Ronda, A.; Shi, Y.; Gay, J. M.; Berbezier, I. *Thin Solid Films* **2000,** *380,* 46–50.
9. Portavoce, A.; Berbezier, I.; Gas, P.; Ronda, A. *Phys. Rev. B* **2004,** *69,* 155414. doi:10.1103/PhysRevB.69.155414
10. Portavoce, A.; Kammler, M.; Hull, R.; Reuter, M. C.; Copel, M.; Ross, F. M. *Phys. Rev. B* **2004,** *70,* 195306. doi:10.1103/PhysRevB.70.195306
11. Portavoce, A.; Hull, R.; Reuter, M. C.; Ross, F. M. *Phys. Rev. B* **2007,** *76,* 235301. doi:10.1103/PhysRevB.76.235301
12. Schmidt, O. G. *Lateral alignment of epitaxial quantum dots;* Springer: Berlin, Heidelberg, New York, 2007.
13. Regelman, D. V.; Magidson, V.; Beserman, R.; Dettmer, K. *Thin Solid Films* **1998,** *336,* 73–75. doi:10.1016/S0040-6090(98)01272-3
14. Liao, X. Z.; Zou, J.; Cockayne, D. J. H.; Jiang, Z. M.; Wang, X.; Leon, R. *Appl. Phys. Lett.* **2000,** *77,* 1304–1306. doi:10.1063/1.1290384
15. Stangl, J.; Daniel, A.; Holý, V.; Roch, T.; Bauer, G.; Kegel, I.; Metzger, T. H.; Wiebach, T.; Schmidt, O. G.; Eberl, K. *Appl. Phys. Lett.* **2001,** *79,* 1474–1476. doi:10.1063/1.1392975
16. Sonnet, P.; Kelires, P. C. *Phys. Rev. B* **2002,** *66,* 205307. doi:10.1103/PhysRevB.66.205307
17. Floyd, M.; Zhang, Y.; Driver, K. P.; Drucker, J.; Crozier, P. A.; Smith, D. J. *Appl. Phys. Lett.* **2003,** *82,* 1473–1475. doi:10.1063/1.1558215
18. Denker, U.; Stoffel, M.; Schmidt, O. G. *Phys. Rev. Lett.* **2003,** *90,* 196102. doi:10.1103/PhysRevLett.90.196102
19. Denker, U.; Sigg, H.; Schmidt, O. G. *Mater. Sci. Eng., B* **2003,** *101,* 89–94. doi:10.1016/S0921-5107(02)00660-8
20. Sonnet, P.; Kelires, P. C. *Appl. Phys. Lett.* **2004,** *85,* 203–205. doi:10.1063/1.1771452
21. Denker, U.; Sigg, H.; Schmidt, O. G. *Appl. Surf. Sci.* **2004,** *224,* 127–133. doi:10.1016/j.apsusc.2003.09.009
22. Hadjisavvas, G.; Kelires, P. C. *Phys. Rev. B* **2005,** *72,* 075334. doi:10.1103/PhysRevB.72.075334
23. Lang, C.; Cockayne, D. J. H.; Nguyen-Manh, D. *Phys. Rev. B* **2005,** *72,* 155328. doi:10.1103/PhysRevB.72.155328
24. De Seta, M.; Capellini, G.; Di Gaspare, L.; Evangelisti, F.; D'Acapito, F. *J. Appl. Phys.* **2006,** *100,* 093516. doi:10.1063/1.2362929
25. De Seta, M.; Capellini, G.; Evangelisti, F. *Phys. Rev. B* **2008,** *77,* 045431. doi:10.1103/PhysRevB.77.045431
26. Leite, M. S.; Malachias, A.; Kycia, S. W.; Kamins, T. I.; Williams, R. S.; Medeiros-Ribeiro, G. *Phys. Rev. Lett.* **2008,** *100,* 226101. doi:10.1103/PhysRevLett.100.226101
27. De Seta, M.; Capellini, G.; Evangelisti, F. *Superlattices Microstruct.* **2009,** *46,* 328–332. doi:10.1016/j.spmi.2008.10.004
28. Leite, M. S.; Kamins, T. I.; Medeiros-Ribeiro, G. *Appl. Phys. Lett.* **2009,** *94,* 053118. doi:10.1063/1.3078289
29. Chang, H. T.; Lee, C.-H.; Lee, S. W. The Compositional Distribution of Ge Islands Grown by Ultra-High Vacuum Chemical Vapor Deposition. In *Proceedings of the 218th Meeting of The Electrochemical Society,* Las Vegas, Nevada, Oct 10–15, 2010.
30. Montoro, L. A.; Leite, M. S.; Biggemann, D.; Peternella, F. G.; Batenburg, K. J.; Medeiros-Ribeiro, G.; Ramirez, A. J. *J. Phys. Chem. C* **2009,** *113,* 9018–9022. doi:10.1021/jp902480w
31. Lee, S. W.; Lee, C.-H.; Chang, H. T.; Cheng, S. L.; Liu, C. W. *Thin Solid Films* **2009,** *517,* 5029–5032. doi:10.1016/j.tsf.2009.03.041
32. Ogawa, Y.; Toizumi, T.; Minami, F.; Baranov, A. V. *Phys. Rev. B* **2011,** *83,* 081302. doi:10.1103/PhysRevB.83.081302
33. Biasiol, G.; Heun, S. *Phys. Rep.* **2011,** *500,* 117–173. doi:10.1016/j.physrep.2010.12.001
34. Georgiou, C.; Leontiou, T.; Kelires, P. C. *AIP Adv.* **2014,** *4,* 077135. doi:10.1063/1.4891935
35. Portavoce, A.; Berbezier, I.; Ronda, A. *Phys. Rev. B* **2004,** *69,* 155416. doi:10.1103/PhysRevB.69.155416
36. Portavoce, A.; Hoummada, K.; Berbezier, I.; Ronda, A.; Mangelinck, D. *Appl. Phys. Lett.* **2012,** *100,* 164105. doi:10.1063/1.4704150
37. Miller, M. K.; Forbes, R. G. *Atom-Probe Tomography: The Local Electrode Atom Probe;* New York: Springer, 2014. doi:10.1007/978-1-4899-7430-3
38. Thompson, K.; Lawrence, D.; Larson, D. J.; Olson, J. D.; Kelly, T. F.; Gorman, B. *Ultramicroscopy* **2007,** *107,* 131–139. doi:10.1016/j.ultramic.2006.06.008
39. Miller, M. K.; Russell, K. F.; Thompson, G. B. *Ultramicroscopy* **2005,** *102,* 287–298. doi:10.1016/j.ultramic.2004.10.011
40. Portavoce, A.; Ronda, A.; Berbezier, I. *Mater. Sci. Eng., B* **2002,** *89,* 205–210. doi:10.1016/S0921-5107(01)00853-4
41. Malachias, A.; Schülli, T. U.; Medeiros-Ribeiro, G.; Cançado, L. G.; Stoffel, M.; Schmidt, O. G.; Metzger, T. H.; Magalhães-Paniago, R. *Phys. Rev. B* **2005,** *72,* 165315. doi:10.1103/PhysRevB.72.165315
42. LeGoues, F. K.; Kesan, V. P.; Iyer, S. S.; Tersoff, J.; Tromp, R. *Phys. Rev. Lett.* **1990,** *64,* 2038–2041. doi:10.1103/PhysRevLett.64.2038
43. Vantarakis, G.; Remediakis, I. N.; Kelires, P. C. *Phys. Rev. Lett.* **2012,** *108,* 176102. doi:10.1103/PhysRevLett.108.176102

License and Terms

The definitive version of this article is the electronic one which can be found at:
doi:10.3762/bjnano.5.246

BEILSTEIN JOURNAL OF NANOTECHNOLOGY

SERS and DFT study of copper surfaces coated with corrosion inhibitor

Maurizio Muniz-Miranda*[1], Francesco Muniz-Miranda[2] and Stefano Caporali[1]

Full Research Paper

Open Access

Address:
[1]Department of Chemistry “Ugo Schiff”, University of Florence, Via Lastruccia 3, 50019 Sesto Fiorentino, Italy and [2]Department of Chemistry and Geology, University of Modena and Reggio Emilia, Via Campi 183, 41125 Modena, Italy

Email:
Maurizio Muniz-Miranda* - muniz@unifi.it; Francesco Muniz-Miranda - francesco.munizmiranda@unimore.it

* Corresponding author

Keywords:
copper corrosion; DFT; inhibitor film; 1,2,4-triazole; SERS

Beilstein J. Nanotechnol. **2014,** *5,* 2489–2497.
doi:10.3762/bjnano.5.258

Received: 17 July 2014
Accepted: 25 November 2014
Published: 29 December 2014

This article is part of the Thematic Series "Self-assembly of nanostructures and nanomaterials".

Guest Editor: I. Berbezier

Abstract

Azole derivatives are common inhibitors of copper corrosion due to the chemical adsorption occurring on the metal surface that gives rise to a protective film. In particular, 1,2,4-triazole performs comparable to benzotriazole, which is much more widely used, but is by no means an environmentally friendly agent. In this study, we have analyzed the adsorption of 1,2,4-triazole on copper by taking advantage of the surface-enhanced Raman scattering (SERS) effect, which highlights the vibrational features of organic ligand monolayers adhering to rough surfaces of some metals such as gold, silver and copper. To ensure the necessary SERS activation, a roughening procedure was implemented on the copper substrates, resulting in nanoscale surface structures, as evidenced by microscopic investigation. To obtain sufficient information on the molecule–metal interaction and the formation of an anticorrosive thin film, the SERS spectra were interpreted with the aid of theoretical calculations based on the density functional theory (DFT) approach.

Introduction

Copper has a long history in a variety of industrial uses due to its large electrical and thermal conductivity, mechanical workability and durability (due to its endurance to weathering). These properties, however, can be compromised by the occurrence of corrosion. In fact, copper undergoes severe corrosion in the presence of ions such as chlorides, which can be present in high amount in the environment, aqueous solutions or soil. A very efficient way to protect copper surfaces is by creating an anticorrosive thin film by chemisorption of organic inhibitors. Heterocycles containing sulphur or nitrogen atoms, available for bonding with the copper surface, are widely employed for such a purpose. A class of very efficient corrosion inhibitors for copper and its alloys in different media is formed by 1,2,4-triazole and its derivatives [1-6]. In particular, 1,2,4-triazole exhibits comparable corrosion inhibition [7] as compared to benzotriazole, which is much more widely but is not environmentally friendly.

The adsorption of various organic ligands onto smooth surfaces of copper was previously studied by means of surface-enhanced Raman scattering (SERS) spectroscopy [8]. Due to the huge amplification of the Raman signal of the adsorbed molecules, this technique allows detailed information on the vibrational behavior of molecules adhering to rough surfaces of metals (such as silver, gold, or copper), as well as on the type of interaction with the active sites of the metal substrate to be obtained. In the case of smooth surfaces of copper, however, the SERS activation was ensured by the deposition of silver colloidal nanoparticles on the copper substrate where the organic molecules were already stable and present due to chemisorption [9-11]. Regardless, it must be taken into account that the deposited silver particles, in addition to promoting the SERS enhancement, could to some extent change the ligand adsorption to copper. Hence, a roughening procedure of smooth copper plates was developed to ensure a suitable SERS activation without the aid of silver nanoparticles. The SERS spectra of 1,2,4-triazole adsorbed on nanostructured copper surfaces are interpreted with the aid of density functional theory (DFT) calculations, which were able to provide useful information on the adsorption of different ligands on metal surfaces, including corrosion inhibitors [12-15]. Combining spectroscopic and theoretical results leads to the conclusion that an anticorrosive film coating can be formed by neutral molecules linked to the Cu^+ active sites of the rough metal surface.

Results and Discussion

SEM analysis and profilometry

In order to exploit the Raman enhancement effect of a monolayer of adsorbed molecules on a copper plate, the substrate must exhibit a surface roughness at the nanometer level. In these nanoscale structures, the excitation of electrons from the metal surface by laser irradiation can be confined, resulting in plasmon resonance [16]. The existence of this resonance is a necessary condition to observe a SERS signal by adsorbed species on the metal surface. In order to obtain a suitable surface roughness from a smooth copper substrate, etching in nitric acid was performed (as previously demonstrated [17]), followed by immersion in ammonia solution. The reducing environment limits the oxidation of the copper surface (which takes place very quickly) in order to preserve the metallic nanostructures necessary for the SERS activation by removing oxides by formation of water-soluble complexes with ammonia. Next, the copper plate was immersed in a solution of 1,2,4-triazole, which acts as a corrosion inhibitor by adsorption onto the metallic substrate. The scanning electron microscopy (SEM) images (Figure 1) show that the smooth surface is eroded by the etching treatment to a different extent depending upon the size and orientation of the copper grains in the lamina.

A higher magnification SEM micrograph (Figure 2) of the etched sample surface reveals a fine surface arrangement, showing the formation of submicrometer dendritic structures, typical of rapid growth crystals.

The existence of these nanostructures is additionally proved by measuring the surface roughness. A line profile was obtained on the etched sample surface as shown in Figure 3. In addition to

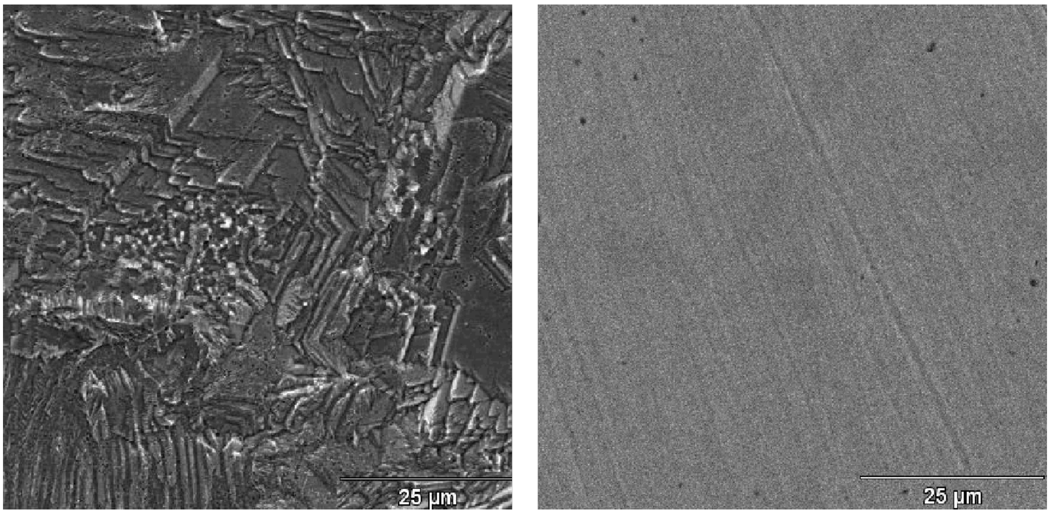

Figure 1: Comparison between the SEM images of an etched copper surface (left) and a smooth copper surface (right).

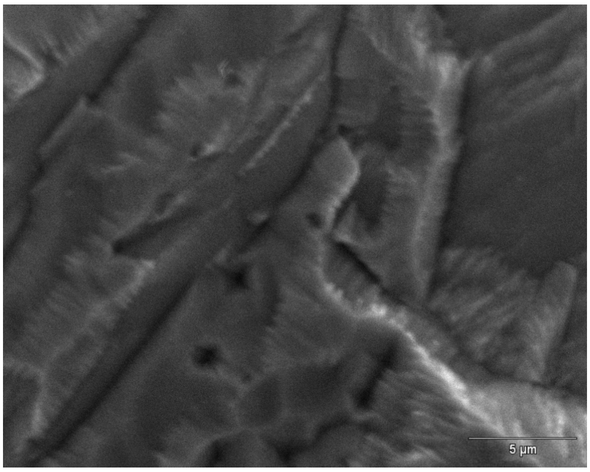

Figure 2: High magnification SEM image of an etched copper surface, showing the fine dendritic structure.

profile variations of a few micrometers due to the copper grains, additional submicrometer variations can be observed and are likely attributable to the dendritic, nanometer-sized structures, which could confer a suitable SERS activation to the metal substrate.

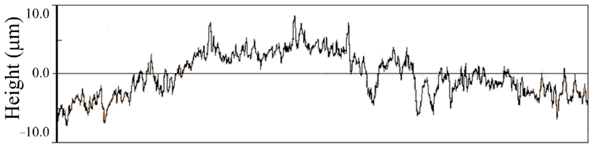

Figure 3: Line profile (profilometry) of an etched copper surface. Total scan length 4.8 mm.

Raman spectra and DFT analysis

The investigation on the layer of adsorbed ligands is based on the analysis of the SERS spectra, in addition to a computational approach using the DFT method. This study is complicated by the fact that the molecule in question is a heterocyclic ring that can bind to the metal via two different molecular sites, namely, the sp^2-type nitrogen atoms, N2 and N4, which have electronic lone pairs capable of interacting with the active sites of the copper surface. A further complication arises from the existence of two possible tautomers of 1,2,4-triazole [18-20], which hereafter are denoted as 1*H* and 4*H*, with regard to the presence of a hydrogen atom linked to the nitrogen atom N1 or N4, respectively. In order to interpret the SERS spectra of the adsorbed molecules, it is first necessary to perform a preliminary vibrational analysis of the isolated molecule.

Figure 4 shows a typical FT-Raman spectra of 1,2,4-triazole in ethanol and water solutions. They are quite similar except for the band observed in water at 1291 cm^{-1} and in ethanol at 1284 cm^{-1}. These observed frequencies can be calculated for the isolated molecule by DFT.

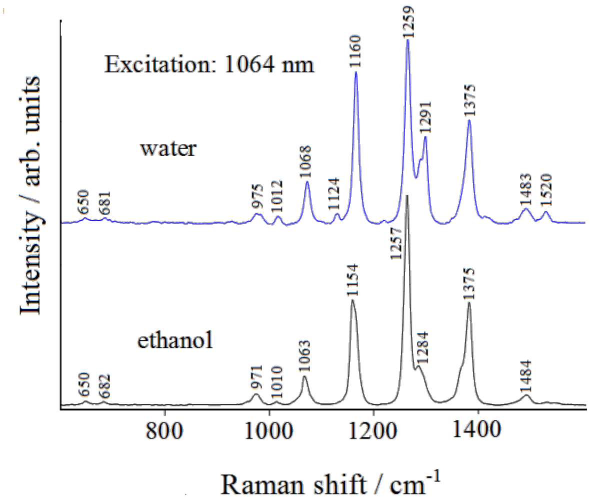

Figure 4: Normal FT-Raman spectra of 1,2,4-triazole in solution. Solvent subtracted.

The DFT calculations show that the 1*H* tautomer is more stable than the 4*H* having an energy of −242.320444 Hartree and −242.309585 Hartree, respectively, as discussed in the literature [18]. In addition, the calculated free energy difference indicates that the 1*H* tautomer is more stable than 4*H*, resulting in ΔG = 6.22 kcal/mol, the same value found by Jimenez and Alderete [21] using the same theory level (B3LYP/6-311++G(d,p)) with a different computational package. Table 1 shows the observed Raman frequencies of the 1,2,4-triazole solution, as compared with those calculated for the 1*H* and 4*H* tautomers, along with an approximate assignment.

From the inspection of Table 1 one can see that the calculated frequencies of the 1*H* tautomer agree well with the intense Raman bands observed in solution. The weak Raman band at 1480 cm^{-1} can be attributed to the 4*H* tautomer which is present in a small amount.

The optimized geometry of the 1*H* tautomer, along with the vibrational modes corresponding to the strongest Raman bands, are shown in Figure 5.

The N2–C3 and N4–C5 bonds are the shortest double bonds according to the experimental structure [22,23]. In general, the calculated distances are very similar to the experimental values, which have been reproduced here better than with previous computational approaches [12,24,25].

Table 1: Observed and calculated Raman shifts (cm^{-1}) of 1,2,4-triazole.

Obs. Raman water	Obs. Raman ethanol	Calc. 1*H* tautomer	Calc. 4*H* tautomer	Description[a]
		541	509	o.p. H bending
650 vw	650 vw	663	644	ring torsion
681 vw	682 vw	682	672	ring torsion
			777	
		827	814	o.p. H bending
		878		o.p. H bending
		943	922	ring bending
975 w	971 w	980	951	ring bending
1012 w	1010 vw		999	
1068 m	1063 m	1056	1071	N1-N2 stretching
1124 w		1115	1087	i.p. H bending
1160 s	1154 m/s	1156		N1–N2, C3–N4 stretching
1213 vw			1204	
1259 vvs	1257 vvs	1250	1278	ring breathing
1291 m	1284 sh	1291		N4–C3 stretching, i.p. H bending
1375 m/s	1375 m/s	1359	1377	N2–C3, N4–C5 stretching
1414 vw		1432		i.p. H bending
1483 w	1484 w		1488	
			1490	
1520 w	1522 vw	1520		N2–C3 stretching

[a]For 1*H* tautomer (see Figure 5); o.p. = out-of-plane; i.p. = in-plane.

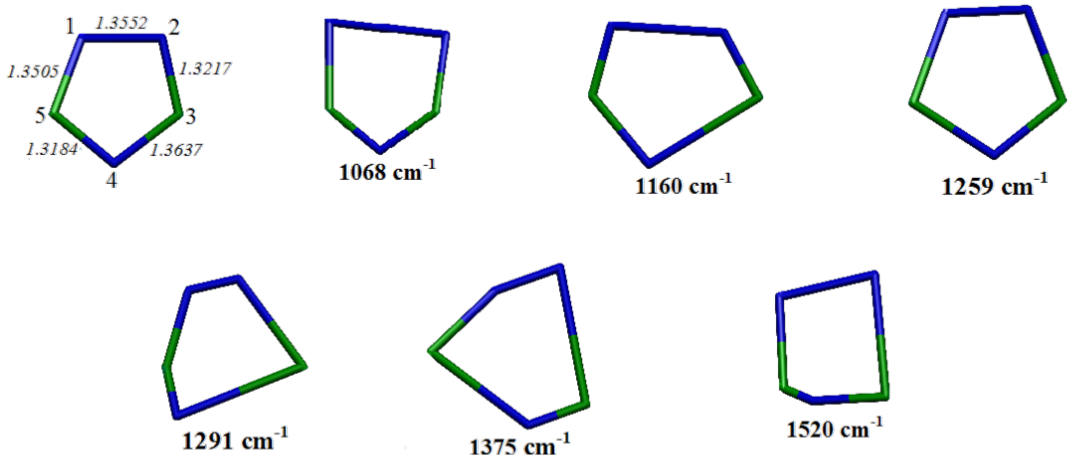

Figure 5: Optimized geometry of 1*H*-1,2,4-triazole (upper left) with the calculated distances (angstroms), along with the vibrational modes corresponding to the strongest Raman bands. Hydrogen atoms are hidden.

The vibrational normal modes shown in Figure 5, which correspond to the most intense Raman bands, are all ring deformations: the Raman bands at 1068, 1291 and 1520 cm^{-1} are mainly attributable to N1–N2, N4–C3 and N2–C3 stretching modes, respectively, whereas those observed at 1160, 1259 and 1375 cm^{-1} can be described as N1–N2/C3–N4 stretching mode, ring breathing mode and N2–C3/N4–C5 stretching mode, respectively. It should be noted that the modes that involve the stretching of two bonds, namely those at 1160 and 1375 cm^{-1}, along with the ring breathing mode at 1259 cm^{-1}, result in a larger increase of the ring size and consequently of the molecular polarizability, resulting stronger Raman intensities, as well as was experimentally observed. In Figure 6, we show the calculated Raman spectra of the two tautomers with their relative intensities. The observed Raman spectrum of triazole is better reproduced as compared to that simulated for the 1*H* tautomer, where only the band around 1380 cm^{-1} appears overestimated.

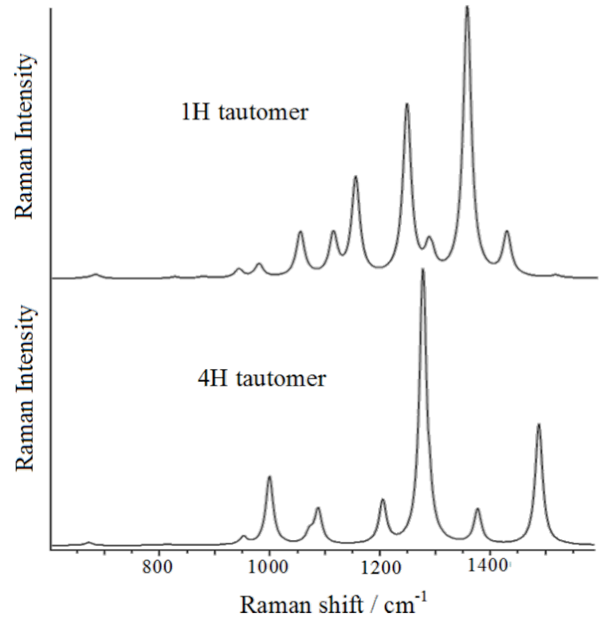

Figure 6: Simulated Raman spectra of the two tautomers of 1,2,4-triazole.

SERS investigation

On the basis of these structural and vibrational results on the isolated molecule, we can assume that the DFT calculations (at the B3LYP/6-311++G(d,p) level of theory, as described in the Computational details section) are reliable, such that they can be applied to the models of triazole/copper complexes. However, a prediction regarding the molecular sites of interaction with the copper surface can already be made. In fact, in the 1*H* tautomer, the nitrogen atom N4 is more negatively charged than N2, based on evaluation of the Mulliken atomic charges (−0.2059·|*e*| for N4, −0.1450·|*e*| for N2, where |*e*| is the elementary electric charge). Consequently, it is expected to be more favorably linked to metal. The 4*H* tautomer, instead, has the opportunity to interact with one or two atoms of copper. Figure 7 shows the Raman spectra recorded on the copper plates upon excitation at 785 nm.

In this figure, (A) is the spectrum of the smooth plate of copper exposed to air, (B) is that of the plate exposed to air after the etching treatment, before immersion in a triazole solution. In both cases, only two broad Raman bands occur around 530 and 620 cm^{-1}, which are related to the presence of Cu(I) oxide, as reported in the literature [26-28]. These bands, visible on both the smooth and etched copper surfaces, can be related to the formation of a Cu_2O multilayer. On the contrary, the oxidation reaction of the etched copper surface is not evidenced when adsorbed triazole is present. Spectrum C in Figure 7 corresponds to the etched copper plate after immersion in an ethanol solution of triazole and air-drying: the Raman bands attributable to the presence of adsorbed triazole are observed, with sizeable frequency shifts with respect to the corresponding normal Raman bands of triazole in solution (see Table 1). This indicates that the etching treatment provides the necessary SERS activation of the copper surface and that triazole is chemisorbed on the copper surface. Without this surface treatment, no Raman signal from the adsorbed ligand could be detected. The same SERS bands are also observed with larger intensities for the etched plate immersed in an aqueous solution of triazole (spectra D). Again, in this case, the spectrum does not show Raman bands due to the formation of cuprous oxide, which is related to the initial stage of the corrosion process of the metal. Therefore, the SERS findings highlight the corrosion inhibition effect by the layer of adsorbed triazole.

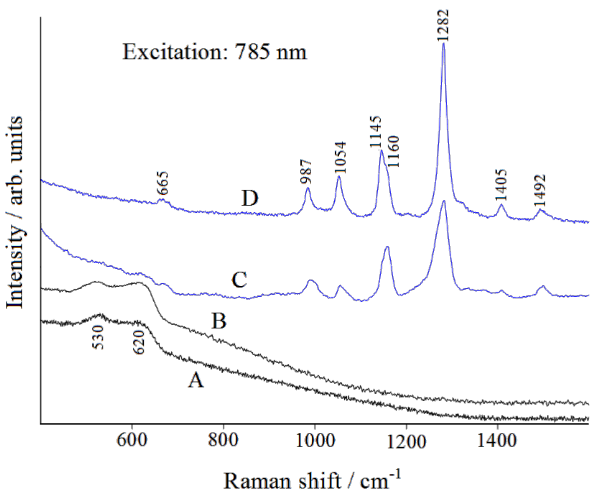

Figure 7: Micro-Raman spectra (excitation 785 nm): smooth copper plate (A); etched copper plate (B); etched copper plate, after immersion in an ethanol (C) or a water (D) solution of 1,2,4-triazole and air-drying.

To understand this effect and to obtain information on the inhibiting layer, it is possible to obtain additional information from the SERS data using the DFT computational approach. This approach is based on model systems formed by the ligand molecules and the active sites of the copper surface (see Figure 8), which can be formed by Cu^0 neutral atoms or Cu^+ cations.

Here, we have considered the complexes of the 1*H* tautomer interacting through the N2 or N4 atom (Figure 8, upper panel) with a Cu^+ ion or with a Cu^0 neutral atom. In addition, the complexes of the 4*H* tautomer interacting with a Cu^+ ion or with a Cu^0 neutral atom have been taken into account, as well

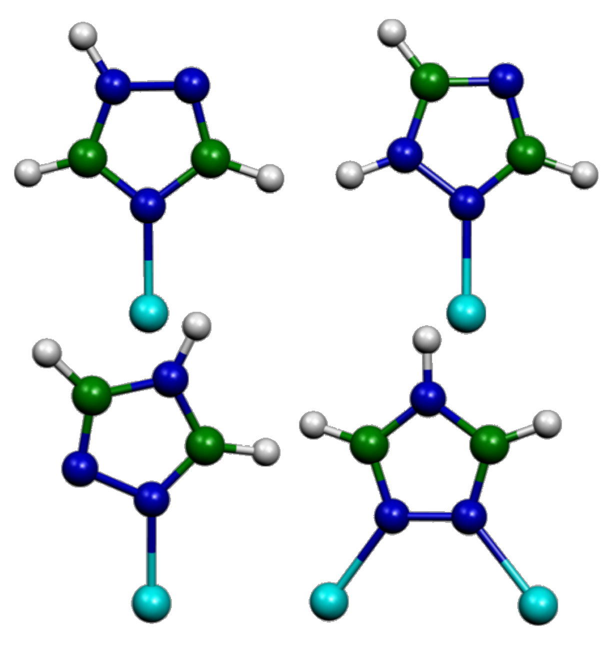

Figure 8: Model systems for 1*H*/copper (upper panel) and 4*H*/copper (lower panel) complexes; carbon, nitrogen and copper atoms are represented as green, dark blue and light blue spheres, respectively.

as with two Cu^+ ions or with a Cu^+/Cu^0 couple (Figure 8, lower panel). The structure of the 4*H* complex with two neutral copper atoms did not converge and even adopted a more relaxed configuration for the structural optimization.

Table 2 shows the comparison between the observed SERS bands and those calculated for the different model systems by DFT calculations. Only the complex formed by the 1*H* tautomer bound to a Cu^+ ion through the N4 atom provided calculated frequencies that reasonably agree with those observed in the SERS spectra. Moreover, even the calculations on the isolated molecule led favored the 1*H* tautomer interacting with the N4 atom rather than with the N2 atom. The interaction with Cu^+ ions is indeed possible, considering the oxidation facility of the copper surface; moreover, in the DFT calculations, the interaction of ligand molecules with Cu^+ ions always leads to the formation of complexes in singlet electronic states (spin multiplicity 1). These are more stable than those with neutral copper atoms, with spin multiplicity 2. Indeed, it should be noted that the interaction with a Cu^+ ion provides a stronger electronic charge-transfer from molecule to metal with respect to the interaction with a neutral copper atom, about $0.5 \cdot |e|$ versus $0.3 \cdot |e|$.

Table 2: Observed SERS wavenumbers (cm^{-1}) of adsorbed 1,2,4-triazole compared with the calculated Raman wavenumbers of the surface complexes[a].

Obs. SERS on Cu	Calc. 1*H* Cu^+(4)	Calc. 1*H* Cu^+(2)	Calc. 4*H* Cu^+	Calc. 4*H* $2Cu^+$	Calc. 4*H* Cu^+/Cu^0	Calc. 4*H* Cu^0	Calc. 1*H* Cu^0(4)	Calc. 1*H* Cu^0(2)
		514				545	570	545
	626	639	609	618	608	641	659	656
665 w	665	655	667	661	669	669	673	668
	701		674	721	671			
	851	877	839	875	844	798	838	840
	869	895	861	895	867	828	878	882
	950	932	950	940	951	942	958	944
987 m	1002	1007	958	1002	968	951	974	984
						1014		
1054 m	1059	1088	1043	1051	1023	1079	1052	1066
			1087	1136	1108		1133	1118
1145 s	1137	1122	1137	1148	1118	1100	1145	1168
1160 s	1167	1194						
			1213	1228	1215	1205		
1282 vs	1265	1252	1302			1288	1253	1247
1282 vs	1275	1319		1306	1310		1289	1304
1405 w	1393	1351	1397	1410	1401	1391	1370	1356
1492 w	1483	1458	1503	1515	1514	1492	1452	1441
	1538	1511	1530	1541	1523	1504	1528	1513

[a] 1*H* Cu^+(4): 1*H* tautomer linked to Cu^+ via N4; 1*H* Cu^+(2): 1*H* tautomer linked to Cu^+ via N2; 1*H* Cu^0(4): 1*H* tautomer linked to Cu^0 via N4; 1*H* Cu^0(2): 1*H* tautomer linked to Cu^0 via N2; 4*H* Cu^+: 4*H* tautomer linked to Cu^+; 4*H* Cu^+: 4*H* tautomer linked to two Cu^+; 4*H* Cu^+/Cu^0: 4*H* tautomer linked to Cu^+ and Cu^0; 4*H* Cu^0: 4*H* tautomer linked to Cu^0.

Corrosion inhibition effect

Considering the interaction of the molecule with the metal surface via the N4 atom, the possibility to form chains of adsorbed molecules linked by hydrogen bonds exists, as proposed in Figure 9. This creates a compact, adsorbed triazole layer which can impair surface corrosion and explains the absence of the Raman bands at 530 and 620 cm^{-1} in the SERS spectrum, which would be due to the formation of a Cu(I) oxide multilayer (indicating the initial stage of the corrosion process of the metal).

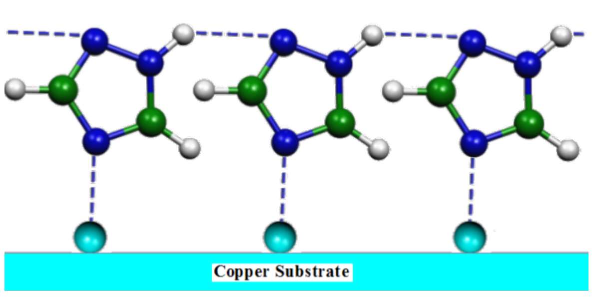

Figure 9: Adsorption model of the 1,2,4-triazole molecules on the copper substrate.

As a further confirmation of this surface arrangement of adsorbed triazole molecules acting as protective film for copper, we report in Figure 10 the SERS spectrum of another azole, imidazole (structurally quite similar to triazole), obtained by following the same experimental procedures adopted for triazole. The SERS spectra of the two azoles appear similar, which is reasonable considering the same adsorption geometry on copper, however, the SERS spectrum of imidazole shows the occurrence of strong Raman bands around 530 and 620 cm^{-1}. These are attributed to a multilayer of cuprous oxide, which are absent in the SERS spectra of triazole. Hence, the adsorbed imidazole molecules, which are unable to interact by hydrogen bonding, do not allow for the excellent inhibition action provided by the compact thin film of adsorbed molecules of triazole, which is capable of isolating the metallic surface from the oxidative action of the atmosphere.

Conclusion

An etching process was performed on smooth copper surfaces using nitric acid followed by immersion in an ammonia solution, resulting in SERS-active substrates. This activation was validated by the SEM and profilometry investigations of the roughened surface, which show submicrometer structures after etching. The presence of absorbed 1,2,4-triazole molecules is highlighted by the examination of the SERS spectra, obtained by simple incubation of the copper plate in ligand solutions and air-drying. This treatment inhibits the oxidation of the copper surface, as was evidenced by the absence of typical bands of Cu(I) oxide in the Raman spectra. Additionally, the observed frequency shifts of the SERS spectral peaks with respect to the corresponding non-SERS Raman spectral peaks of triazole in solution suggest chemisorption of the ligand molecules on the copper surface. The DFT calculations on molecule/metal model systems assisted in the interpretation of the spectroscopic data and provided information on both the tautomeric form of 1,2,4-triazole adsorbed on copper, and the nature of the surface active sites interacting with the ligand molecules. A model of adsorption based on a compact molecular film was proposed, thus justifying the inhibiting action of 1,2,4-triazole with respect to the corrosion of the copper surface. The SERS study of imidazole, similar to triazole but unable to bind the adsorbed molecules among them, confirms this conclusion.

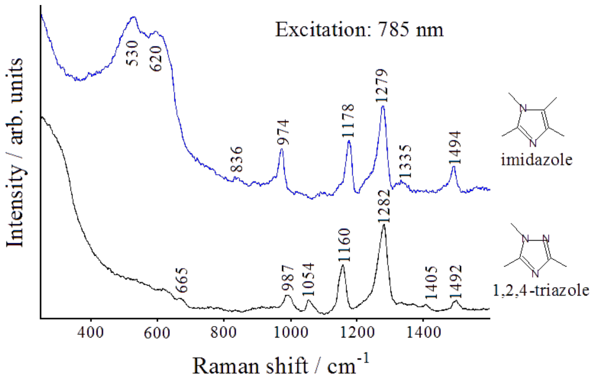

Figure 10: Comparison between the SERS spectra of 1,2,4-triazole and imidazole absorbed on etched copper surfaces, after immersion in ethanol solutions and air-drying.

Experimental

A hot-rolled plate of copper, as supplied by Aldrich (purity 99.98%), was first mechanically polished with alumina powder to a mirror finish then carefully washed with water and ethanol in an ultrasonic bath. The smooth plate was immersed for one minute in a concentrated solution of nitric acid in order to obtain a discernable etching and then the plate was immersed in a concentrated solution of ammonia to eliminate the presence of copper oxides from the surface. After a quick washing with water and ethanol as running solvents, the etched plate was immersed for one day in a diluted solution (10^{-2} M) of 1,2,4-triazole, then carefully washed with ethanol to leave behind only the chemisorbed ligand. Sample morphology was observed by SEM (Hitachi S-2300) operating at 20 kV. The surface roughness was measured by collecting line profiles using a Hommel Tester W55 profilometer, scanning 4.8 mm at a 0.2 mm s^{-1} scan rate. The parameters employed were λ_c = 0.8 mm and λ_c/λ_s = 300 using a filter ISO 11562(MI).

Raman spectra of 1,2,4-triazole (10^{-1} M concentration) in ethanol or water solutions were collected with a Fourier transform (FT)-Raman spectrometer (Bruker Optics, Model MultiRam), equipped with a broad range quartz beamsplitter, an air-cooled Nd:YAG laser excitation source (1064 nm) and a Ge diode detector cooled with liquid nitrogen. The instrument provided a spectral range of 3600–50 cm^{-1} (Stokes shift). The experiments were performed in a 180° geometry, with 200 mW of laser power.

Raman spectra on copper plates were measured using a Renishaw RM2000 microRaman apparatus, equipped with a diode laser emitting at 785 nm. Sample irradiation was accomplished by using the 50× microscope objective of a Leica Microscope DMLM. The backscattered Raman signal was filtered by a double holographic notch filter system and detected by an air-cooled CCD. All spectra were calibrated with respect to a silicon wafer at 520 cm^{-1}.

Computational details

All calculations were carried out using the Gaussian 09 package [29]. Optimized geometries, vibrational frequencies and other molecular properties of 1,2,4-triazole and its investigated copper complexes were obtained using the hybrid B3LYP exchange-correlation function [30-33]. The 6-311++G(d,p) basis set was used for all atoms, including copper. The integral grid was set to "ultrafine" and the optimization criteria to "very tight". By allowing all the parameters to relax, the calculations converged to optimized geometries corresponding to true energy minima, as revealed by the lack of imaginary values in the vibrational mode calculations. A scaling factor of 0.98 for all calculated vibrational wavenumbers was adopted, as performed for similar molecular systems [13,15,34-36].

References

1. Fox, P. G.; Bradley, P. A. *Corros. Sci.* **1980,** *20,* 643–649. doi:10.1016/0010-938X(80)90100-6
2. Sherif, E.-S. M.; Erasmus, R. M.; Comins, J. D. *J. Colloid Interface Sci.* **2007,** *306,* 96–104. doi:10.1016/j.jcis.2006.10.029
3. Sherif, E.-S. M.; Erasmus, R. M.; Comins, J. D. *J. Colloid Interface Sci.* **2007,** *309,* 470–477. doi:10.1016/j.jcis.2007.01.003
4. Sherif, E.-S. M.; Erasmus, R. M.; Comins, J. D. *J. Colloid Interface Sci.* **2007,** *311,* 144–151. doi:10.1016/j.jcis.2007.02.064
5. Khiati, Z.; Othman, A. A.; Sanchez-Moreno, M.; Bernard, M.-C.; Joiret, S.; Sutter, E. M. M.; Vivier, V. *Corros. Sci.* **2011,** *53,* 3092–3099. doi:10.1016/j.corsci.2011.05.042
6. John, S.; Joseph, A. *Mater. Chem. Phys.* **2012,** *133,* 1083–1091. doi:10.1016/j.matchemphys.2012.02.020
7. Jiang, L.; Lan, Y.; He, Y.; Li, Y.; Li, Y.; Luo, J. *Thin Solid Films* **2014,** *556,* 395–404. doi:10.1016/j.tsf.2013.12.047
8. Schlücker, S. *Surface Enhanced Raman Spectroscopy: Analytical, Biophysical and Life Science Applications;* Wiley-VCH: Weinheim, Germany, 2011. doi:10.1002/9783527632756.index
9. Muniz-Miranda, M. *J. Raman Spectrosc.* **1996,** *27,* 435–437. doi:10.1002/(SICI)1097-4555(199605)27:5<435::AID-JRS990>3.0.CO;2-0
10. Muniz-Miranda, M.; Puggelli, M.; Ricceri, R.; Gabrielli, G. *Langmuir* **1996,** *12,* 4417–4420. doi:10.1021/la960098o
11. Pergolese, B.; Muniz-Miranda, M.; Bigotto, A. *J. Phys. Chem. B* **2006,** *110,* 9241–9245. doi:10.1021/jp0605698
12. Lesar, A.; Milošev, I. *Chem. Phys. Lett.* **2009,** *483,* 198–203. doi:10.1016/j.cplett.2009.10.082
13. Muniz-Miranda, M.; Pergolese, B.; Bigotto, A. *Phys. Chem. Chem. Phys.* **2010,** *12,* 1145–1151. doi:10.1039/b913014d
14. Pagliai, M.; Caporali, S.; Muniz-Miranda, M.; Pratesi, G.; Schettino, V. *J. Phys. Chem. Lett.* **2012,** *3,* 242–245. doi:10.1021/jz201526v
15. Muniz-Miranda, M.; Pergolese, B.; Muniz-Miranda, F.; Caporali, S. *J. Alloys Compd.* **2014,** *615* (Suppl. 1), S357–S360. doi:10.1016/j.jallcom.2013.12.063
16. Le Ru, E. C.; Etchegoin, P. G. *Principles of Surface-Enhanced Raman Spectroscopy and Related Plasmonic Effects;* Elsevier: Oxford, U.K., 2009.
17. Shin, K. S.; Lee, H. S.; Joo, S. W.; Kim, K. *J. Phys. Chem. C* **2007,** *111,* 15223–15227. doi:10.1021/jp073053c
18. Cox, J. R.; Woodcock, S.; Hillier, I. H.; Vincent, M. A. *J. Phys. Chem.* **1990,** *94,* 5499–5501. doi:10.1021/j100377a016
19. Davarski, K. A.; Khalachev, N. K.; Yankova, R. Z.; Raikov, S. *Chem. Heterocycl. Compd.* **1998,** *34,* 568–574. doi:10.1007/BF02290940
20. Balabin, R. M. *J. Chem. Phys.* **2009,** *131,* 154307. doi:10.1063/1.3249968
21. Jiménez, V.; Alderete, J. B. *J. Mol. Struct.: THEOCHEM* **2006,** *775,* 1–7. doi:10.1016/j.theochem.2006.06.010
22. Bolton, K.; Brown, R. D.; Burden, F. R.; Mishra, A. *J. Mol. Struct.* **1975,** *27,* 261–266. doi:10.1016/0022-2860(75)87034-7
23. Chiang, J. F.; Lu, K. C. *J. Mol. Struct.* **1977,** *41,* 223–229. doi:10.1016/0022-2860(77)80064-1
24. Billes, F.; Endrédi, H.; Keresztury, G. *J. Mol. Struct.: THEOCHEM* **2000,** *530,* 183–200. doi:10.1016/S0166-1280(00)00340-7
25. Gutowski, K. E.; Rogers, R. D.; Dixon, D. A. *J. Phys. Chem. A* **2006,** *110,* 11890–11897. doi:10.1021/jp0643698
26. Chan, H. Y. H.; Takoudis, C. G.; Weaver, M. J. *J. Phys. Chem. B* **1999,** *103,* 357–365. doi:10.1021/jp983787c
27. Niaura, G. *Electrochim. Acta* **2000,** *45,* 3507–3519. doi:10.1016/S0013-4686(00)00434-5
28. Brandão, C. R. R.; Costa, L. A. F.; Breyer, H. S.; Rubim, J. C. *Electrochem. Commun.* **2009,** *11,* 1846–1848. doi:10.1016/j.elecom.2009.07.034
29. *Gaussian 09,* Revision C.01; Gaussian, Inc.: Wallingford, CT, 2010.
30. Becke, A. D. *J. Chem. Phys.* **1993,** *98,* 5648–5652. doi:10.1063/1.464913
31. Lee, C.; Yang, W.; Parr, R. G. *Phys. Rev. B* **1988,** *37,* 785–789. doi:10.1103/PhysRevB.37.785
32. Vosko, S. H.; Wilk, L.; Nusair, M. *Can. J. Phys.* **1980,** *58,* 1200–1211. doi:10.1139/p80-159
33. Stephens, P. J.; Devlin, F. J.; Chabalowski, C. F.; Frisch, M. J. *J. Phys. Chem.* **1994,** *98,* 11623–11627. doi:10.1021/j100096a001
34. Muniz-Miranda, M.; Pagliai, M.; Muniz-Miranda, F.; Schettino, V. *Chem. Commun.* **2011,** *47,* 3138–3140. doi:10.1039/c0cc05217e
35. Pagliai, M.; Muniz-Miranda, F.; Schettino, V.; Muniz-Miranda, M. *Progr. Colloid Polym. Sci.* **2012,** *139,* 39–44. doi:10.1007/978-3-642-28974-3_8

36. Muniz-Miranda, M.; Pagliai, M. *J. Phys. Chem. C* **2013,** *117,* 2328–2333. doi:10.1021/jp309600p

License and Terms

The definitive version of this article is the electronic one which can be found at:
doi:10.3762/bjnano.5.258

BEILSTEIN JOURNAL OF NANOTECHNOLOGY

Bright photoluminescence from ordered arrays of SiGe nanowires grown on Si(111)

D. J. Lockwood*[1], N. L. Rowell[1], A. Benkouider[2], A. Ronda[2], L. Favre[2] and I. Berbezier[2]

Full Research Paper

Open Access

Address:
[1]Measurement Science and Standards, National Research Council, 1200 Montreal Road, Ottawa, Ontario K1A 0R6, Canada and [2]CNRS, Institut Matériaux Microélectronique Nanosciences de Provence, AMU, Avenue Normandie Niemen, 13397 Marseille Cedex 20, France

Email:
D. J. Lockwood* - david.lockwood@nrc-cnrc.gc.ca

* Corresponding author

Keywords:
bandgap; germanium; nanowires; near field; silicon; photoluminescence

Beilstein J. Nanotechnol. **2014,** *5,* 2498–2504.
doi:10.3762/bjnano.5.259

Received: 18 July 2014
Accepted: 24 November 2014
Published: 30 December 2014

This article is part of the Thematic Series "Self-assembly of nanostructures and nanomaterials".

Associate Editor: A. J. Meixner

Abstract

We report on the optical properties of SiGe nanowires (NWs) grown by molecular beam epitaxy (MBE) in ordered arrays on SiO_2/Si(111) substrates. The production method employs Au catalysts with self-limited sizes deposited in SiO_2-free sites opened-up in the substrate by focused ion beam patterning for the preferential nucleation and growth of these well-organized NWs. The NWs thus produced have a diameter of 200 nm, a length of 200 nm, and a Ge concentration $x = 0.15$. Their photoluminescence (PL) spectra were measured at low temperatures (from 6 to 25 K) with excitation at 405 and 458 nm. There are four major features in the energy range of interest (980–1120 meV) at energies of 1040.7, 1082.8, 1092.5, and 1098.5 meV, which are assigned to the NW-transverse optic (TO) Si–Si mode, NW-transverse acoustic (TA), Si–substrate–TO and NW-no-phonon (NP) lines, respectively. From these results the NW TA and TO phonon energies are found to be 15.7 and 57.8 meV, respectively, which agree very well with the values expected for bulk $Si_{1-x}Ge_x$ with $x = 0.15$, while the measured NW NP energy of 1099 meV would indicate a bulk-like Ge concentration of $x = 0.14$. Both of these concentrations values, as determined from PL, are in agreement with the target value. The NWs are too large in diameter for a quantum confinement induced energy shift in the band gap. Nevertheless, NW PL is readily observed, indicating that efficient carrier recombination is occurring within the NWs.

Introduction

Semiconductor nanowires (NWs) are thought of as promising building blocks for opto-electronic devices that exploit their novel electronic band structures generated by two-dimensional (2D) quantum confinement in conjunction with their associated optical properties [1-6]. However, in order to fully implement these new properties, strict control is needed over the NW location, uniformity, composition, and size. By exploiting such band gap engineering, directly allowed transitions have been demonstrated for specific core/shell NW configurations with an ultimate control over the NW shape, aspect ratio and radial multishell composition [7]. A major asset of Si/Ge core/shell [8] and axial [9] NW heterostructures is also their ease of integration in CMOS technology, which allows the fabrication of opto-electronic devices with an increased photon absorption over a wider range of wavelengths and with an improved efficiency of electron generation. In addition, by combining the extraordinary technological know-how that has been developed for Si with direct-gap Si/Ge heterostructures, the fabrication of various NWs for applications such as photovoltaic tandem solar cells has been enabled [10-12]. Most of the device specifications require a low cost fabrication process with good control over the NW reproducibility and uniformity [13].

A variety of different NW growth methods have been reported including vapor–liquid–solid [14-17], solid–liquid–solid [18,19], vapor–solid–solid [20-22], oxide-assisted [23], and others [24-27]. Many of these growth methods have lead to NWs possessing non-uniform diameters and lengths and that are haphazardly oriented and randomly positioned [28]. We have evolved an efficient and simple electrochemical process that joins focused-ion-beam (FIB) lithography and galvanic reaction to selectively prepare gold nanoparticles in well-defined locations. Afterwards these nanoparticles are used for the molecular beam epitaxy (MBE) growth of ordered SiGe NW arrays with predefined NW positions and diameters. Here we report on the optical properties of such MBE grown NWs.

Experimental

A schematic overview of the various steps used in the growth process is given in Figure 1. The steps consisted of: (a) rapid thermal oxidation (RTO); (b) FIB patterning; (c) galvanic selective deposition of Au; (d) induced phase transition in AuSi catalysts; and (e) selective growth of SiGe NWs. With this method we have produced $Si_{1-x}Ge_x$ NWs with diameters in the range 50–200 nm, although the size can potentially be tuned between 30 and 300 nm, and with Ge concentration x in the range $0 \leq x \leq 0.15$.

Prior to the substrate patterning (Figure 1a), the Si(111) substrates, which were either 5 cm diameter wafers or wafer sections of dimensions 2 × 2 cm^2 and 1 × 1 cm^2, were first systematically cleaned by a modified Shiraki ex situ process and then capped with an ultra-thin (5 nm thick) SiO_2 thermal oxide (UTO) that was obtained by rapid thermal oxidation (RTO) in a clean vacuum.

In the second step (Figure 1b), 2D arrays of small windows (with diameters in the range 50–200 nm) were opened in the UTO by FIB milling using a Tescan LYRA1 XMH dual-beam FIB workstation having an Orsay Physics mass filtered ion column operated at 30 keV. A liquid metal alloy ion source (LMAIS) of Au_4Si ([Si] = 19%, [Au] = 81%) heated at 450 °C was used for the milling step; a Au^{2+} or Si^+ ion beam was selected independently by a Wien filter. The patterns in the Si/SiO_2 substrate were milled with the Au^{2+} ion beam at an incident angle of ≈10° from the normal: Regarding the choice of incident angle, we have shown in another study [29] that the sputtering rate is larger when working at 10° from the normal. The FIB milling process should be performed with a low current dose to minimize the surface roughening of the substrate and the density of defects formed; typically, the emission current used was about 10 pA and the ion dose = 10^{16} PA/cm^2/s. This point is essential to provide an efficient selectivity during the last NW growth step.

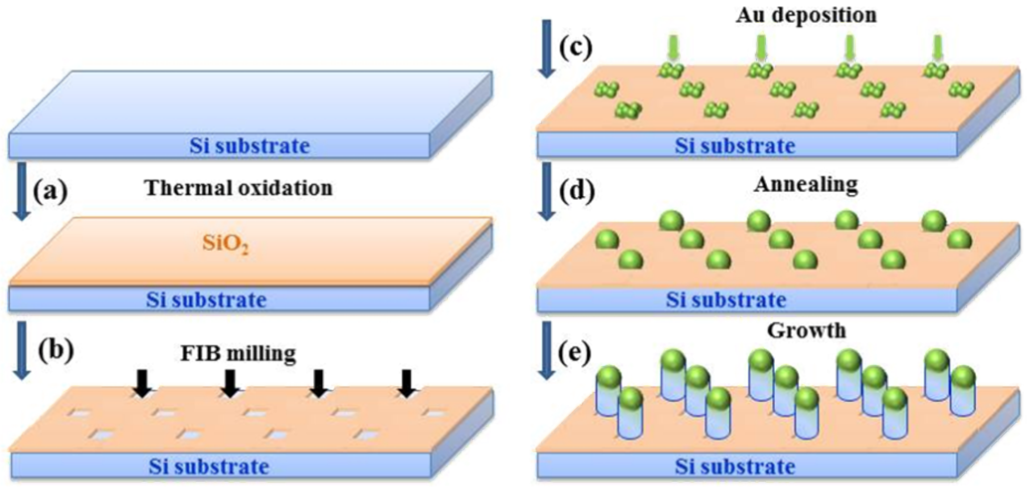

Figure 1: Schematic representation of the process steps: (a) formation of SiO_2 (5 nm thick) by RTO; (b) opening of SiO_2-free windows by FIB milling; (c) Au deposition by oxido-reduction of gold salts; (d) phase transition of Au in AuSi clusters by annealing at temperature T_A; and (e) MBE growth of SiGe NWs at T_A.

After the FIB etching, the samples were immediately dipped into a gold salt ($H^+Au^{3+}Cl_4^-$) aqueous solution at room temperature. Since the freshly FIB etched nanopits on silicon are then SiH_x^- terminated, while the original surface remains coated with the inert thermal SiO_2 layer, the interiors of the nanopits are ready for the electrochemical step. The latter step, called galvanic deposition, is based on the spontaneous oxido-reduction reactions between the semiconductor surface (the substrate) and the metallic ions in the solution. Upon contact with the Si surface, the solution spontaneously reduces and precipitates into Au nanocrystals, according to the following equation:

$$\mathrm{AuCl_4^-} + 3e^- \rightarrow \mathrm{Au}(s) + 4\mathrm{Cl}^- \quad \textit{with } E^0_{\mathrm{Au^{3+}/Au}} = 0.94\ \mathrm{V} \qquad (1)$$

In parallel, in the aqueous solution, as a result of the high reduction potential of gold ions, the Si surface, which provides the electrons to reduce the gold ions to metallic gold, oxidizes into SiO_2 as per the following equation:

$$\mathrm{Si} + 2\mathrm{H_2O} \rightarrow \mathrm{SiO_2} + 4e^- \quad \textit{with } E^0_{\mathrm{Si^{2+}/Si}} = 0.84\ \mathrm{V} \qquad (2)$$

This spontaneously formed silicon dioxide prevents further metal ion reduction. Since the gold salt reduction process is not possible on SiO_2, the reaction immediately stops after the formation of SiO_2 [30].

After the selective galvanic deposition of gold clusters on the substrate, the samples were loaded into the MBE chamber. The phase transformation from the small Au nanoclusters located within the SiO_2-cover-free nanopits to the $Au_{0.18}Si_{0.82}$ eutectic alloy is obtained by thermal annealing at 550 °C for 30 min.

The annealing and growth experiments were performed in the MBE growth chamber of a Riber SIVA32 system with a base pressure of 10^{-11} Torr. The silicon flux was obtained from an electron beam evaporator and maintained constant during the deposition at 0.03 nm/s, while germanium was deposited from an effusion cell. The growth temperatures were varied between 380 and 600 °C and were controlled in real time using an infrared pyrometer. The silicon substrate was rotated during the experiments to maintain a thickness and composition uniformity over the whole wafer or wafer section (the results obtained were similar for all substrates). Figure 2 displays SEM images of representative Si NWs grown at 550 °C on the positionally-ordered $Au_{0.18}Si_{0.82}$ catalysts. The main advantage of this growth method is the control of the NW position (related to site selectivity) and its size; a homogeneous size is obtained due to the regular network of Au nanocrystals (see Figure 2). Also, SiGe NWs can be grown and then transformed in a second step into core-shell NWs using a condensation process that we have developed.

Three NW samples were prepared for this study: Sample (A), where the NWs are grown randomly across the Si substrate; sample (B), where the nanowires decorate the edges of 400 × 400 μm^2 boxes; and sample (C), where the NWs fill 400 × 400 μm^2 boxes in ordered arrays, as described above. These samples have NWs that have a nominal Ge concentration of $x = 0.15$ and that are 200 nm in diameter and 200 nm long, with a morphology similar to the Si NWs shown in Figure 2.

The photoluminescence (PL) spectra were measured at low temperatures (from 6 to 25 K) using a Bomem DA3 FTIR spectrometer equipped with a cooled Ge (Applied Detector Corporation) detector, and the samples were excited with loosely-

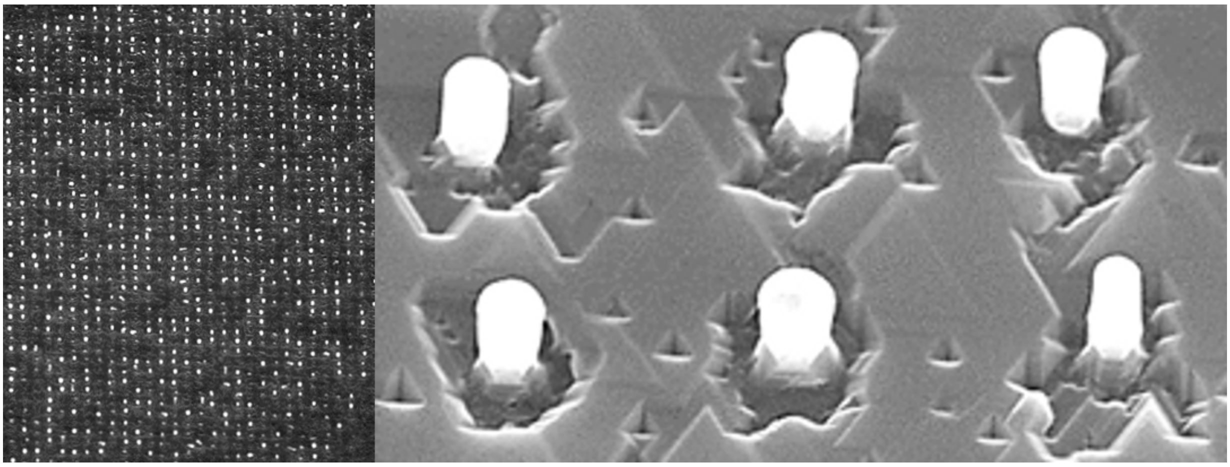

Figure 2: Scanning electron microscope (SEM) images of the ordered arrays of Si NWs showing (left) a NW array and (right) individual 200 nm long NWs.

focused light from a GaN-based semiconductor laser (70 mW at 405 nm) or from an argon ion laser (35 mW at 458 nm).

Results and Discussion

The PL spectra obtained for sample (C) with excitation at 405 and 438 nm are compared in Figure 3. The two spectra exhibit the same features, most of which arise from the Si substrate together with a few arising from instrumental effects. The main difference between them, as also observed for the other two samples at 6 K, lies in their overall intensity: the spectrum excited at 458 nm is much more intense than the 405 nm one. This is a consequence of the exciting light at 438 nm penetrating beyond the NWs further into the substrate than the 405 nm light and thus enhancing the Si PL intensity. The NW features we are interested in overlap the Si PL, and thus to help minimize the substrate signal we consider next only results obtained using excitation at 405 nm.

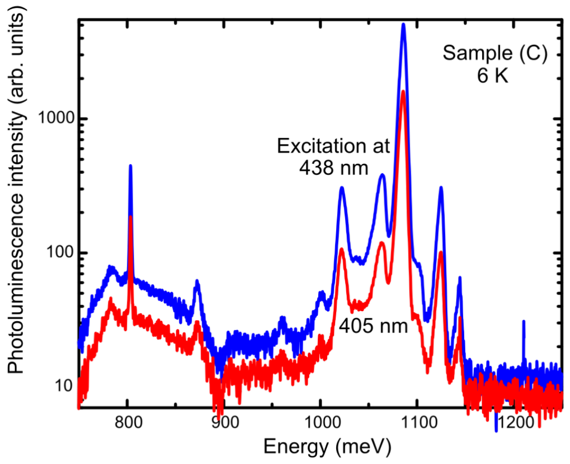

Figure 3: The raw PL spectrum obtained from sample (C) at 6 K with excitation at 405 and 458 nm.

The temperature dependence of the PL spectrum obtained from sample (C) is shown in Figure 4. PL spectra with similar temperature dependences were obtained from the other samples. Figure 4 shows that the NW spectral region of interest (from approximately 950 to 1050 meV) is dominated by the boron ($\approx 10^{17}$ cm^{-3})-doped Si substrate phonon-replica spectrum at the lowest temperatures (6 and 10 K). On increasing the sample temperature up to 20 K, the Si substrate PL becomes sufficiently quenched from the increasing dissociation of multiple-donor bound excitons within the substrate [31] that the underlying NW PL is more readily seen. By 25 K, only the sharp line at 1092.5 meV due to the Si substrate remains. From now on we shall consider only the PL obtained from the samples at 25 K to avoid the overlapping substrate signal as much as possible.

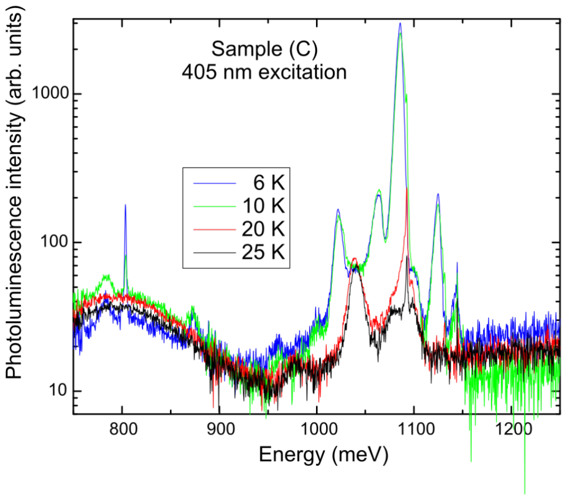

Figure 4: Temperature dependence of the instrument-response-corrected PL spectrum obtained from sample (C) with excitation at 405 nm.

The instrument-response-corrected PL spectra obtained from all three samples at 25 K with excitation at 405 nm are given in Figure 5. At energies below the range of interest for the NWs, broad features are seen at ≈800, 940, and 975 meV that are due to the Si substrate. At higher energies, there is a very sharp peak at 1144 meV associated with an instrumental emission line that should be ignored. The overall intensity of the NW PL varied from sample to sample, as can be seen in Figure 5; sample (C), with a higher density of NWs distributed within the array, was the strongest, while sample (A) with a random distribution of NWs was the weakest. Nevertheless, the spectra are quite similar overall.

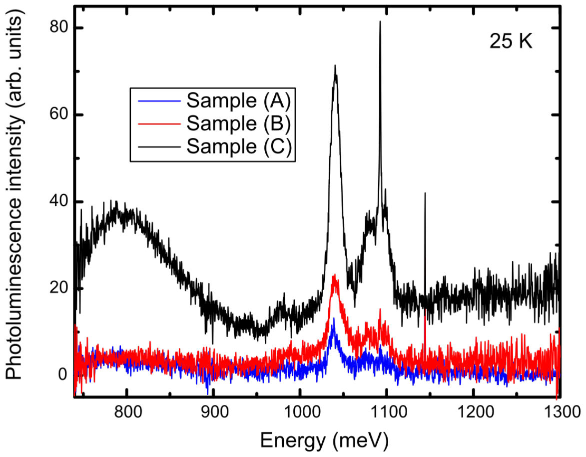

Figure 5: Instrument-response-corrected PL spectra obtained with 405 nm excitation from the (A), (B), and (C) samples at 25 K.

The NW PL is strong considering that the volume of NW material is so small (each wire has a volume of 0.006 μm^3) and thus the carriers have to be recombining efficiently within the wires to produce this light emission at the SiGe-alloy band gap energy. We know from earlier studies of SiGe etched wires [32] and dots [33] that just the spatial confinement of carriers is sufficient to produce the readily-observed PL found here, which implies that the carriers in these samples are not being lost in large numbers to the substrate or recombining in large quantities at defects inside or on the surface of the NWs. The wires are too large in diameter for a quantum confinement induced energy shift in the band gap, but the phonon energies could be affected slightly by confinement and surface effects [34]. The wires are grown free-standing and thus there should be no internal strain (i.e., bulk-like energy values should be observed).

Further details about the PL spectra can be obtained from spectral curve resolving, Such an analysis using a Gaussian line shape revealed that there are four major features in the energy range of interest (see Figure 6 for results obtained for the three samples at 25 K). The fitted peak energies, line widths, and amplitudes for the three samples are given in Table 1. In order of increasing energy, they are readily assigned to the NW free-exciton transverse-optic (TO) Si–Si vibrational mode, NW free-exciton transverse-acoustic (TA) phonon, Si–substrate-bound-exciton TO phonon and NW free-exciton no-phonon (NP) lines, respectively [31,35]. The peak amplitude data given in Table 1 can be used to estimate the amplitude ratios of the NW lines relative to the strongest line (the NW TO mode) for each sample and the results are given in Table 2. Given the uncertainties in the fits obtained from curve resolving, the amplitude ratio for the TO/TA peaks is much the same in the three samples (see Table 2), as would be expected if both lines arose just from the NWs and that the NWs were of similar composition in all samples. The good agreement obtained between the TO/TA peak amplitude ratios for Samples (B) and (C) is not as good for Sample (A), whose PL was much weaker than the other two samples resulting in greater errors in the peak amplitudes from the fits. The fitted frequencies and line widths for the respective NW and Si TO mode lines vary slightly between the three samples, but are essentially the same within error (see Table 1). Interestingly, the free-exciton NP line intensity relative to its phonon replicas (TA and TO lines) in these NWs is much more intense than that found in bulk Si, but is somewhat lower compared to what is observed in bulk alloy material of a similar composition [35], which may reflect on the action of NW surface effects as opposed to the usual alloy disorder effect resulting in a breakdown in the wave vector selection rules.

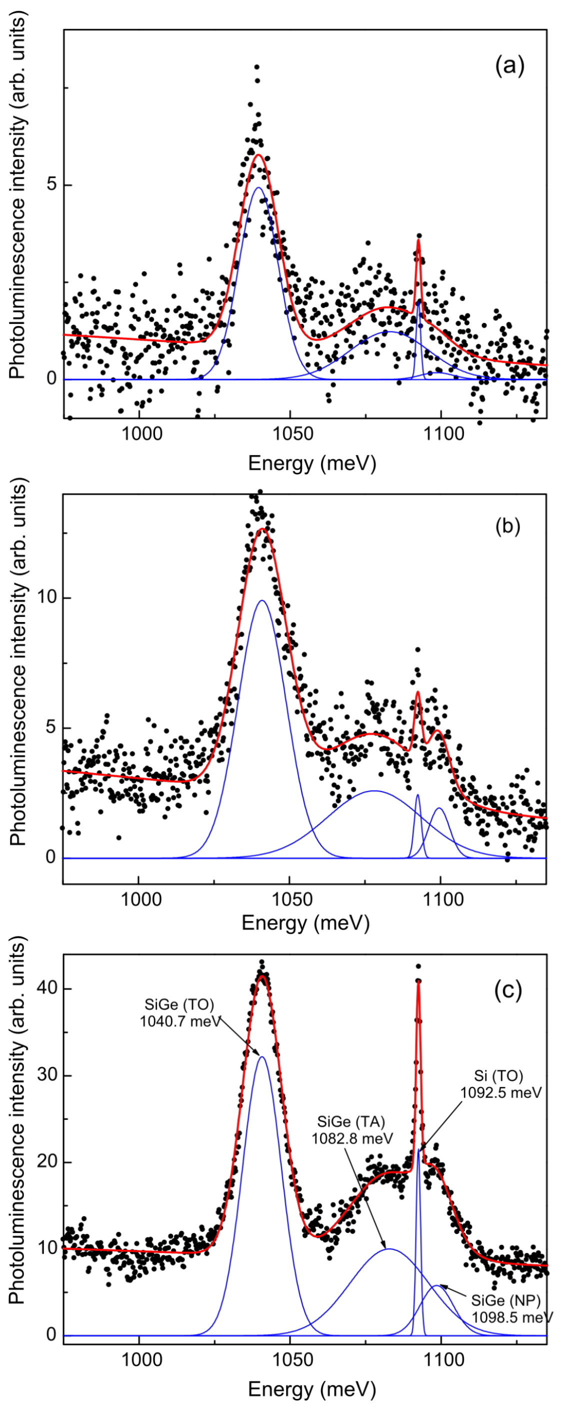

Figure 6: Curve-resolved PL spectrum of (a) sample (A), (b) sample (B), and (c) sample (C) at 25 K obtained with 405 nm excitation. The solid line shows the overall fit to the PL data, while the three SiGe NW component lines are shown beneath the fitted spectrum. The very sharp line at 1092.5 meV arises from the Si substrate.

Using the results obtained from the fits to the sample with the strongest PL (sample (C)), the NW TA and TO phonon energies are found to be 15.7 (1.8) and 57.8 (0.6) meV, respectively, which agree very well with the values expected for bulk $Si_{1-x}Ge_x$ with $x = 0.15$ of 18 (1) and 58 meV, respectively [35]. The measured NW free-exciton NP energy of 1099 meV would

Table 1: Results of curve resolving the PL spectra excited with 405 nm excitation for the three NW samples at 25 K. The fitted band frequencies ω_i and widths γ_i are given in millielectronvolts for the four Gaussians (i = 1–4) used in the fit. The peak height (h_i) is given in arbitrary units. The uncertainties in the parameter values from the fits are given in parentheses.

sample	ω_1	γ_1	h_1	ω_2	γ_2	h_2	ω_3	γ_3	h_3	ω_4	γ_4	h_4
(A)	1039.49	15.20	4.94	1082.84	30.66	1.23	1092.46	1.73	2.00	1098.52	12.93	0.18
	(0.12)	(0.30)	(0.08)	(3.91)	(7.14)	(0.17)	(0.10)	(0.27)	(0.24)	(5.05)	(20.31)	(0.39)
(B)	1040.94	18.76	9.92	1078.12	36.73	2.59	1092.48	2.64	2.45	1099.53	8.12	1.93
	(0.16)	(0.36)	(0.14)	(1.12)	(3.74)	(0.11)	(0.20)	(0.50)	(0.37)	(0.48)	(1.51)	(0.27)
(C)	1040.69	15.06	32.19	1082.81	30.58	10.01	1092.46	1.73	21.62	1098.51	12.95	5.83
	(0.06)	(0.15)	(0.26)	(1.29)	(2.11)	(0.40)	(0.03)	(0.08)	(0.82)	(0.48)	(1.88)	(1.07)

Table 2: Amplitude ratios h_{TO}/h_{TA} and h_{TO}/h_{NP} of the NW TA and NP lines, respectively, relative to the strongest line of the three NW lines (the NW TO mode) for each sample.

sample	h_{TO}/h_{TA}	h_{TO}/h_{NP}
(A)	4.02 (0.62)	27.44 (59.90)
(B)	3.83 (0.22)	5.14 (0.79)
(C)	3.22 (0.15)	5.52 (1.06)

indicate a Ge concentration of $x = 0.14$ (this concentration gives an X-point energy gap of 1099 meV in bulk SiGe) [35]. Thus the positions in energy of the NP peak and those of the accompanying phonon replicas independently confirm the alloy concentration as being $x = 0.15 \pm 0.01$.

Conclusion

The readily-observed PL seen from the SiGe NWs indicates they are clean (i.e., contain few growth defects and impurities) and are electrically isolated from the substrate. They are not strained to any significant extent and x for these samples is confirmed from the PL to be 0.15. These NWs with their well-controlled position, composition, and size and their efficient luminescence exhibit relevant features that are a significant improvement in quality over those produced by other vapor-solid-solid growth methods and that could be useful for applications in optoelectronic nanodevices. However, their mass production in current CMOS production lines would be problematic.

References

1. Xiang, J.; Lu, W.; Hu, Y.; Wu, Y.; Yan, H.; Lieber, C. M. *Nature* **2006,** *441,* 489. doi:10.1038/nature04796
2. Lu, W.; Lieber, C. M. *Nat. Mater.* **2007,** *6,* 841. doi:10.1038/nmat2028
3. Conibeer, G. *Mater. Today* **2007,** *10,* 42. doi:10.1016/S1369-7021(07)70278-X
4. Conibeer, G.; Green, M.; Corkish, R.; Cho, Y.; Cho, E.-C.; Jiang, C.-W.; Fangsuwannarak, T.; Pink, E.; Huang, Y. D.; Puzzer, T.; Trupke, T.; Richards, B.; Shalav, A.; Lin, K.-L. *Thin Solid Films* **2006,** *511,* 654. doi:10.1016/j.tsf.2005.12.119
5. Nelson, J. *The Physics of Solar Cells;* Imperial College Press: London, U.K., 2003.
6. Werner, P.; Zakharov, N. D.; Gerth, G.; Schubert, L.; Gösele, U. *Int. J. Mater. Res.* **2006,** *97,* 1008. doi:10.3139/146.101332
7. Zhang, L.; d'Avezac, M.; Luo, J.-W.; Zunger, A. *Nano Lett.* **2012,** *12,* 984. doi:10.1021/nl2040892
8. Tian, B.; Zheng, X.; Kempa, T. J.; Fang, Y.; Yu, N.; Yu, G.; Huang, J.; Lieber, C. M. *Nature* **2007,** *449,* 885. doi:10.1038/nature06181
9. Chang, H.-Y.; Tsybeskov, L.; Sharma, S.; Kamins, T. I.; Wu, X.; Lockwood, D. J. *Appl. Phys. Lett.* **2009,** *95,* 133120. doi:10.1063/1.3240595
10. Goldthorpe, I. A.; Marshall, A. F.; McIntyre, P. C. *Nano Lett.* **2008,** *8,* 4081–4086. doi:10.1021/nl802408y
11. Peng, X.; Tang, F.; Logan, P. *J. Phys.: Condens. Matter* **2011,** *23,* 115502. doi:10.1088/0953-8984/23/11/115502
12. Palummo, M.; Amato, M.; Ossicini, S. *Phys. Rev. B* **2010,** *82,* 073305. doi:10.1103/PhysRevB.82.073305
13. Green, M. A. *Third Generation Photovoltaics: Advanced Solar Energy Conversion;* Springer-Verlag: Berlin, Germany, 2003.
14. Wu, Y.; Cui, Y.; Huynh, L.; Barrelet, C. J.; Bell, D. C.; Lieber, C. M. *Nano Lett.* **2004,** *4,* 433. doi:10.1021/nl035162i
15. Duan, X.; Lieber, C. M. *Adv. Mater.* **2000,** *12,* 298. doi:10.1002/(SICI)1521-4095(200002)12:4<298::AID-ADMA298>3.0.CO;2-Y
16. Wu, Y.; Yang, P. *J. Am. Chem. Soc.* **2001,** *123,* 3165. doi:10.1021/ja0059084
17. Ge, S.; Jiang, K.; Lu, X.; Chen, Y.; Wang, R.; Fan, S. *Adv. Mater.* **2005,** *17,* 56. doi:10.1002/adma.200400474
18. Trentler, T. J.; Hickman, K. M.; Goel, S. C.; Viano, A. M.; Gibbons, P. C.; Buhro, W. E. *Science* **1995,** *270,* 1791. doi:10.1126/science.270.5243.1791
19. Yan, H. F.; Xing, Y. J.; Hang, Q. L.; Yu, D. P.; Wang, Y. P.; Xu, J.; Xi, Z. H.; Feng, S. Q. *Chem. Phys. Lett.* **2000,** *323,* 224. doi:10.1016/S0009-2614(00)00519-4
20. Berbezier, I.; Ayoub, J. P.; Favre, L.; Ronda, A.; Morresi, L.; Pinto, N. *Surf. Sci.* **2011,** *605,* 7. doi:10.1016/j.susc.2010.09.014
21. Wang, Y.; Schmidt, V.; Senz, S.; Gösele, U. *Nat. Nanotechnol.* **2006,** *1,* 186. doi:10.1038/nnano.2006.133
22. Chen, S. Y.; Chen, L. J. *Thin Solid Films* **2006,** *508,* 222. doi:10.1016/j.tsf.2005.07.322
23. Zhang, R.-Q.; Lifshitz, Y.; Lee, S.-T. *Adv. Mater.* **2003,** *15,* 635. doi:10.1002/adma.200301641
24. Chen, C.-Y.; Wu, C.-S.; Chou, C.-J.; Yen, T.-J. *Adv. Mater.* **2008,** *20,* 3811. doi:10.1002/adma.200702788
25. Peng, K. Q.; Hu, J. J.; Yan, Y. J.; Wu, Y.; Fang, H.; Xu, Y.; Lee, S. T.; Zhu, J. *Adv. Funct. Mater.* **2006,** *16,* 387. doi:10.1002/adfm.200500392

26. Holmes, J. D.; Johnston, K. P.; Doty, R. C.; Korgel, B. A. *Science* **2000,** *287,* 1471. doi:10.1126/science.287.5457.1471
27. Yu, D. P.; Lee, C. S.; Bello, I.; Sun, X. S.; Tang, Y. H.; Zhou, G. W.; Bai, Z. G.; Zhang, Z.; Feng, S. Q. *Solid State Commun.* **1998,** *105,* 403. doi:10.1016/S0038-1098(97)10143-0
28. Sutter, E.; Ozturk, B.; Sutter, P. *Nanotechnology* **2008,** *19,* 435607. doi:10.1088/0957-4484/19/43/435607
29. Benkouider, A.; Berbezier, I.; Ronda, A.; Favre, L.; Ruiz Gomes, E.; Marcus, I. C.; Alonso, I.; Delobbe, A.; Sudraud, P. *Thin Solid Films* **2013,** *543,* 69–73. doi:10.1016/j.tsf.2013.02.119
30. Benkouider, A.; Ronda, A.; Gouyé, A.; Herrier, C.; Favre, L.; Lockwood, D. J.; Rowell, N. L.; Delobbe, A.; Sudraud, P.; Berbezier, I. *Nanotechnology* **2014,** *25,* 335303. doi:10.1088/0957-4484/25/33/335303
31. Nöel, J.-P.; Rowell, N. L.; Greene, J. E. *J. Appl. Phys.* **1995,** *77,* 4623–4631. doi:10.1063/1.359428
32. Tang, Y. S.; Wilkinson, C. D. W.; Sotomayor Torres, C. M.; Smith, D. W.; Whall, T. E.; Parker, E. H. C. *Solid State Commun.* **1993,** *85,* 199. doi:10.1016/0038-1098(93)90437-R
33. Lockwood, D. J.; Tsybeskov, L. Light Emission in Si/SiGe Nanostructures. In *Handbook of Silicon Photonics;* Vivien, L.; Pavesi, L., Eds.; CRC Press: Boca Raton, FL, U.S.A., 2013; pp 354–371.
34. Barbagiovanni, E. G.; Lockwood, D. J.; Simpson, P. J.; Goncharova, L. V. *Appl. Phys. Rev.* **2014,** *1,* 011302. doi:10.1063/1.4835095
35. Weber, J.; Alonso, M. I. *Phys. Rev. B* **1989,** *40,* 5683–5693. doi:10.1103/PhysRevB.40.5683

License and Terms

BEILSTEIN JOURNAL OF NANOTECHNOLOGY

Formation of stable Si–O–C submonolayers on hydrogen-terminated silicon(111) under low-temperature conditions

Yit Lung Khung[*1,§], Siti Hawa Ngalim[2], Andrea Scaccabarozzi[1] and Dario Narducci[1]

Letter

Open Access

Address:
[1]University of Milan-Bicocca, Department of Materials Science, Via R. Cozzi 53, I-20125 Milan, Italy and [2]Regenerative Medicine Cluster, Advanced Medical and Dental Institute (AMDI), Universiti Sains Malaysia, Penang, Malaysia

Email:
Yit Lung Khung[*] - yit.khung@unimib.it

[*] Corresponding author
§ Phone: +39-02-6448-5143, Fax: +39-02-6448-5400

Keywords:
hydrogen abstraction; thermal hydrosilylation; UV-initated hydrosilylation; X-ray photoelectron spectroscopy

Beilstein J. Nanotechnol. **2015,** *6,* 19–26.
doi:10.3762/bjnano.6.3

Received: 16 July 2014
Accepted: 28 November 2014
Published: 05 January 2015

This article is part of the Thematic Series "Self-assembly of nanostructures and nanomaterials".

Guest Editor: I. Berbezier

Abstract

In this letter, we report results of a hydrosilylation carried out on bifunctional molecules by using two different approaches, namely through thermal treatment and photochemical treatment through UV irradiation. Previously, our group also demonstrated that in a mixed alkyne/alcohol solution, surface coupling is biased towards the formation of Si–O–C linkages instead of Si–C linkages, thus indirectly supporting the kinetic model of hydrogen abstraction from the Si–H surface (Khung, Y. L. et al. *Chem. – Eur. J.* **2014,** *20,* 15151–15158). To further examine the probability of this kinetic model we compare the results from reactions with bifunctional alkynes carried out under thermal treatment (<130 °C) and under UV irradiation, respectively. X-ray photoelectron spectroscopy and contact angle measurements showed that under thermal conditions, the Si–H surface predominately reacts to form Si–O–C bonds from ethynylbenzyl alcohol solution while the UV photochemical route ensures that the alcohol-based alkyne may also form Si–C bonds, thus producing a monolayer of mixed linkages. The results suggested the importance of surface radicals as well as the type of terminal group as being essential towards directing the nature of surface linkage.

Introduction

Forming covalently-attached organic submonolayers on silicon remains one of the challenges in surface science. In order to gain access to the electronic properties of silicon, it is imperative that the organic layer on the top surface be kept thin enough to avoid a masking of the intrinsic properties of silicon, especially in biosensing application [1]. So far, hydrosilylation is among the most commonly accepted techniques to graft organics onto silicon surfaces [2-6]. It is the process during which unsaturated carbon reacts with hydrogen-terminated silicon (SiH) to form a stable submonolayer through covalent

Si–C linkages at the surface. The reaction can typically be mediated through catalysts or Lewis acids [3,4], through an intermediate halogenation followed by Grignard chemistry [7], through UV irradiation on the surface [8] or thermally driven [9,10]. In recent years, thermal hydrosilylation has emerged as an attractive alternative due to the lack of potentially contaminating catalysts as well as the low process costs. The general consensus on the mechanism of hydrosilylation of the bulk silicon surface proposed by Linford et al. suggests a self-propagating chain mechanism that ultimately leads to densely packed layers. It is considered to be a self-repeating three-step reaction [11] after the initial radicalization of the silicon surface:

$$\mathrm{R{-}CH{=}CH_2 + {\bullet}Si(111) \rightarrow R{-}(CH{\bullet})CH_2Si(111)} \quad (1)$$

$$\begin{gathered}\mathrm{R{-}(CH{\bullet})CH_2Si(111) + R{-}CH_2CH{=}CH_2} \\ \mathrm{\rightarrow R{-}(CH_2)_2Si(111) + R{-}CH{\bullet}CH{=}CH_2}\end{gathered} \quad (2)$$

$$\begin{gathered}\mathrm{R{-}(CH{\bullet})_2Si(111) + HSi(111)} \\ \mathrm{\rightarrow R{-}(CH_2)_2Si(111) + Si(111)}\end{gathered} \quad (3)$$

The conditions by which Linford et al. performed the reaction were very stringent and regardless of variations in the experimental approach in later studies by other authors, the basis of a silyl radical reacting with unsaturated C–C bonds remained undisputed. However, as early as 2005, Wood et al. brought to attention that the cleavage of Si–H to form initial silyl radicals might not be the only mode for hydrosilylation to occur [12]. Typically, the commonly accepted notion is that thermal hydrosilylation requires temperatures above 150 °C in order to cleave the silicon–hydrogen bond at the surface to form surface radicals. However previous studies had shown that hydrosilylation could also proceed at a lower temperature (110 °C). Wood et al. further suggested a reaction mechanism in which trace oxygen is involved in the extraction of hydrogen off from the hydrogenated silicon surface.

One question to address would be the actual reaction preference of the Si–H surface when exposed to both an alkyne and an alcohol at lower temperatures, i.e., whether the surface would still undergo hydrogen abstraction in the presence of a competing reactant. One of the classical competitor to alkynes forming Si–C on Si–H are alcohols. They were previously reported to react with Si–H to form stable Si–O–C linkages [13]. To examine this point, we proposed a comparative study between two modes of hydrosilylation (thermal and UV photochemical) for a bifunctional alkyne. Alkynes were deliberately chosen due to their higher reactivity towards hydrogen-terminated silicon compared to alkenes. The main theme of this study is to examine whether hydrogen extraction is a probable mechanism for surface reaction at low temperatures. Two alkynes were selected, namely 4-ethynyl-α,α,α-trifluorotoluene (trifluoroalkyne), whose trifluoride functional group serves both as both a surface marker (in the C 1s reaction) and as a means of raising the surface hydrophobicity upon functionalization of the alkyne, and 4-ethynylbenzyl alcohol (ethynylbenzyl alcohol) whose hydroxy (OH) group may initiate a nucleophilic attack on the Si–H surface [9] while the alkyne termination can present itself for reaction to the same surface through hydrogen abstraction [12,14]. The hypothesis is that, for thermal hydrosilylation, at low temperature, two mechanisms may potentially occur to form two different linkage (Si–O–C and Si–C) [12,14], namely hydrogen abstraction through trace oxygen or a nucleophilic attack on the silicon surface for the ethynylbenzyl alcohol. On the other hand, if the surface is activated through UV irradiation, both mechanisms can be deemed to be unneccesary, thus facilitating the grafting reaction of the molecule through the alkyne end, in turn, forming a stable Si-C linkage. On the other hand, a trifluoroalkyne was also selected to demonstrate the viability of the hydrogen abstraction model by observing the nature of the linkage formed considering that this molecule could only react at the alkyne end. Thus, the eventual presence of Si–O–C and Si–C from surface analysis in our controlled setup would give impetus towards the acceptance of the hydrogen abstraction model for low-temperature hydrosilylation. The role of oxygen in the low-temperature hydrosilylation reaction can then be better understood from this experimental approach.

Result and Discussion

To help understand the role of oxygen during hydrosilylation, a direct comparison of the reactivity between both thermal and UV-initiated hydrosilylation was made for two different alkyne species. Trifluoroalkyne was employed to demonstrate the formation of Si–C linkages through hydrogen abstraction by trace oxygen and the level of oxygen was greatly reduced by a series of degassing steps similar to those described by Ciampi et al. [15]. On the other hand, ethynylbenzyl alcohol was used to react with the surface via a nucleophilic route from the hydrogen-terminated surface during low-temperature hydrosilylation. It is envisaged that at low temperatures (<150 °C), the Si–C bonds at the surface are not cleaved to form radicals. Thus, in order for surface grafting to form Si–C linkages, it is necessary for the hydrogen to be abstracted from the surface via oxygen species present in solution (Figure 1). In our deliberate thermal setup, there is also the possibility of grafting via Si–O–C linkages instead of the nominal Si–C linkages typically associated with thermal hydrosilylation. However, we envisage that under UV irradiation, the surface would be preactivated to form silyl radicals and surface grafting could proceed to form both the Si–O–C and the Si–C as Hacker et al. had previously demonstrated the viability of creating thin Si–O–C films with saturated alcohol through UV irradiation [13]. Such observation would further reinforce hydrogen abstraction as a viable mechanism for low temperature hydrosilylation. It is important to note that the film produced on the silicon surface can only described as a sub-monolayer as attaining a full surface coverage in which every silicon atom is occupied would be technically impossible due to steric hindrances and this has been well discussed in literature [12,16].

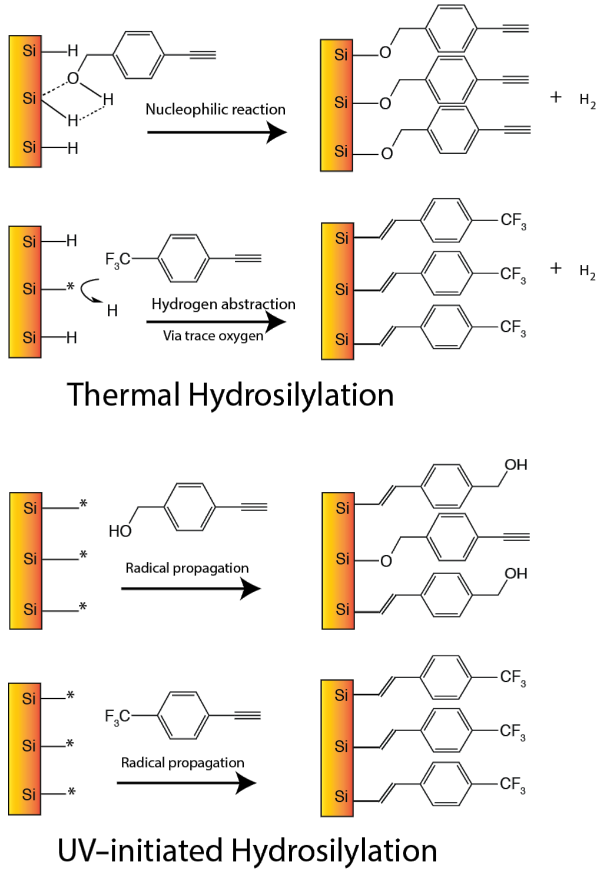

Figure 1: Hypothetical reaction pathways of ethynylbenzyl alcohol and trifluroalkyne during thermal and UV-initiated hydrosilyation.

High-resolution XPS analyses were performed on thermally grafted as well as UV-irradiated surfaces well for both trifluoroalkyne and ethynylbenzyl alcohol (Figure 2). The Si 2p spectra for thermally treated trifluoroalkyne and ethynylbenzyl alcohol exhibited the characteristic peaks (Si 2p$_{3/2}$ (99.7–99.9 eV) and Si 2p$_{1/2}$ (100.2–100.7 eV)) for elemental silicon while the broad distribution at 103.5–104.2 eV was attributed to the various Si–O$_x$ species [17,18]. Interestingly, for the trifluoroalkyne samples, the oxidation (Si–O$_x$) was observed to be higher for the UV-irradiated surfaces (Figure 2b) as compared to that from thermal hydrosilylation (Figure 2a). This could be interpreted as a consequence of the higher concentration of surface radicals under UV exposure that rendered the surface more susceptible towards oxidation from residual oxygen (O$_2$) in solution. As the temperature of the thermal hydrosilylation setup was less than 150 °C, there were no radicals formed at the silicon surface that was thus more stable towards oxidation during the reaction time. XPS analysis on the ethynylbenzyl alcohol revealed that for thermal hydrosilylation, the elemental Si peak intensities were reduced (99.6 eV and 100.1 eV) while an intense peak at 102.1 eV was observed in turn. Considering its position, it was unlikely to be oxide (≈103.7 eV) and previous reports had reported this position to be a strong indicator for the Si–O–C linkage. This is the first evidence that surface grafting of ethynylbenzyl alcohol had occurred through the Si–O–C linkage instead of the Si–C linkage.

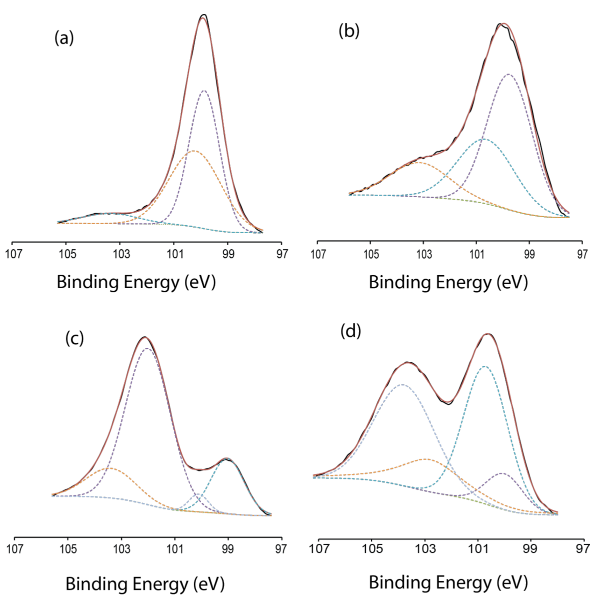

Figure 2: High-resolution XPS Si 2p spectra of the surface (a) thermally functionalized with trifluoroalkyne, (b) functionalized with trifluoroalkyne through UV-irradiation, (c) thermally functionalized with ethynylbenzyl alcohol and (d) functionalized with ethynylbenzyl alcohol though UV-irradiation.

When the surface underwent UV irradiation (Figure 2d), the level of oxidation (103.7–104.7 eV) increased significantly. The broad peak centered at 102.5 eV was attributed to Si–O–C [19,20]. The intensity of the elemental Si (99.8 eV and 100.3 eV) had also increased in comparison to that of the thermal hydrosilylation samples (Figure 2c). Coincidentally, Si–C was normally observed in the literature at 100.2–100.4 eV [21,22] and often overlapped with the Si 2p$_{3/2}$ and Si 2p$_{1/2}$ signatures. Therefore the observed increment at the 100.0–100.4 eV in conjunction with assignment at 102.5 eV could be taken as an indication that the UV-initiated grafting of ethynylbenzyl alcohol yielded two linkages, Si–C and Si–O–C. The increase in oxidation as highlighted by the broad peak at 103.7–104.7 eV may also be explained by the UV-initiated surfaces being more susceptible towards oxidation.

To study the nucleophilic reaction that gave rise to the Si–O–C linkage, high-resolution C 1s spectra were taken after both the thermal and UV-initiated hydrosilylation of ethynylbenzyl alcohol. The C 1s scan of the trifluoroalkyne would not serve any purpose considering the end product would be a Si–C linkage and cannot be used to examine the nucleophilic reactions as mentioned. Thus, as shown in Figure 3a, upon thermal grafting, a broad peak centering at 284.6 eV was attributed to that of sp^2 C–C (as evident from aromaticity of the ethynylbenzyl alcohol) as well as adventitious C–C from the exposure of the surface to air [23-25]. Interestingly, the peak at 286.3 eV could be attributed to the epoxy type linkage (C–O–R) as previously reported in literature [26]. In view of the possible Si–O–C linkage at the surface, this assignment was deemed as representation of this linkage. The broad peak at 287.7 eV could be assigned to π–π carbon satellites, possibly arising from the aromatic stacking of the benzyl rings [27]. On the other hand, the high-resolution C 1s spectra of the UV-initiated functionalization with ethynylbenzyl alcohol yielded several peaks suggesting the presence of both Si–C and Si–O–C. While the peaks at 284.2 eV and 285.3 eV could be attributed to sp^2 C–C and adventitious C–C, the most important peak assignment belongs to the signal centered at 282.6 eV [23,28,29], which gave the strongest evidence for Si–C linkages [30]. On the other hand, the peak at 286.3 eV proposed the presence of Si–O–C linkages on the same surface. Nonetheless, the Si 2p spectra suggested that under UV irradiation of ethynylbenzyl alcohol, due to the reactivity of the surface, an OH-terminated alkyne might react from both ends to the surface. Furthermore, by measuring the area under the peaks after a Shirley background subtraction and an automatically assigned Gaussian–Lorentzian fit with the XPS peaks software for both Si–O–C and the Si–C peaks, we found that the surface had been decorated at a Si–O–C (286.3) ratio of 2:1 relative to Si–C (282.6 eV). Hence, only a third of the surface had been functionalized through Si–C linkages.

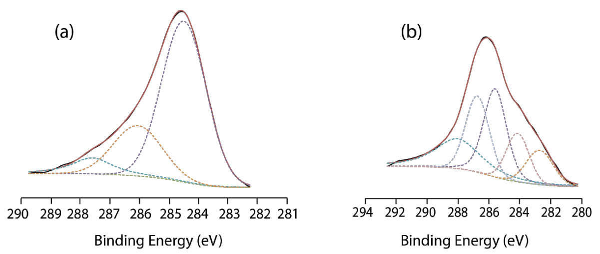

Figure 3: High-resolution XPS C 1s spectra of surfaces (a) thermally functionalized with ethynylbenzyl alcohol and (b) functionalized with ethynylbenzyl alcohol through UV initiation.

High-resolution O1s spectra also helped to explain further the nature of the oxide on the surface, whether the oxide was inherent to the silicon surface or whether the oxide is bound to carbon or silicon as in the Si–O–C linkage. As shown in Figure 4a, on the thermally functionalized surface for the ethynylbenzyl alcohol, the main O 1s peak was observed centered at 531.9 eV. The main peak of the UV-functionalized surface (Figure 4b) was positioned at 532.4 eV. This peak can easily be assigned to the characteristic C–OH bond [31-33] of the hydroxy end groups of the ethynylbenzyl alcohol molecules that were linked to the surface through the alkyne end. The upshift of 0.4 eV for the main O 1s peaks between the two different reactions suggested that the OH-group of the ethynylbenzyl alcohol has different environments with respect to the surface. During thermal hydrosilylation, the lower binding energy can only suggest that OH had been cleaved to form a linkage to the surface as previously reported by Shao et al. [34]. Although in both of the mentioned linkages (Si–O–C and C–OH) in this paper, the carbon atoms are technically sp^3 hybridized. Yet, the environment of the bond is considered to be very different. Compared to the exposed C–OH group of the ethynylbenzyl alcohol molecule bound to the surface through the alkyne group, an oxygen atom in the Si–O–C linkage would experience a difference in electronegativity (silicon is marginally less electronegative compared to hydrogen). The arrangement of an oxygen atom sandwiched between a silicon and a carbon atom would result in an increase in overall electrostatic repulsion and this will subsequently decrease the bonding energy, as was reported previously in literature [35]. From the O 1s spectra, we were able to observe this reduction in binding energy of O 1s in the thermal hydrosilylation samples and thus concluded that the predominant oxygen species in these samples had been associated with the Si–O–C linkage while those produced from UV-initiated hydrosilylation were C–OH. The secondary peak for the thermal hydrosilylation (Figure 4a) at 533.3 eV was indicative of SiO_2 from oxidation [36] while the secondary peak for the UV-initiated hydrosilylation (Figure 4b) was centered at 534.3 eV, which was nominally linked to absorbed water on the surface [37]. What was interesting was that despite the wide FWHM for both samples (2.81 for thermal hydrosilylation and 2.07 for UV-irradiated surfaces), the absorbance of the water peak was only observable for the UV-irradiated surfaces. Considering that the exposed end groups on the surface of the UV-irradiated samples were C–OH, the reason for the absorbance of water is considered to be a more hydrophilic surface.

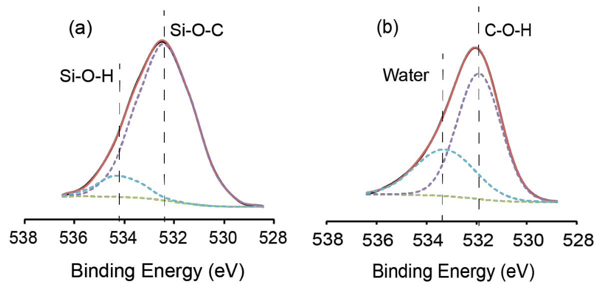

Figure 4: High-resolution XPS O 1s spectra of surfaces (a) thermally functionalized with ethynylbenzyl alcohol and (b) functionalized with ethynylbenzyl alcohol through UV irradiation.

To further examine the nature of the grafting, contact angle (CA) measurements were performed and the results were are shown in Table 1. The values for the trifluoroalkyne, both after thermal and UV-initiated hydrosilylation, were very similar, namely (84.0 ± 1.5)° and (83.5 ± 0.5)° (Table 1). But this was not the case for the ethynylbenzyl alcohol. After the thermal hydrosilylation, the CA value was 89.6 ± 3.0°, higher than for the CF_3-terminated trifluoroalkyne. One would imagine that the trifluoroalkyne would exhibit a higher hydrophobicity due to its fluoro-group termination while the higher values observed for the ethynylbenzyl alcohol could only be explained by the formation of Si–O–C bonds, with the free alkyne group exposed from the surface. On the other hand, upon UV irradiation of the surface, the CA values for the ethynylbenzyl alcohol were clearly reduced to (67.4 ± 4.1)°. Together with the XPS C 1s and O 1s high-resolution spectra obtained on these surfaces, the only sensible explanation for this was that both Si–O–C and Si–C linkages were formed on the surface, thus creating a patchy surface with an intimate mixture of moieties exposing hydroxy or alkyne groups. This would certainly reduce the surface wettability as reported in previous reports on heterogeneous monolayer-like assemblies on surfaces [38,39]. What was also interesting was that the atomic concentration, listed in Table 1, had revealed that the level of oxidation (O 1s) was significantly higher at UV-irradiated surfaces for trifluoroalkyne compared to the thermally treated surfaces and one possible explanation was that the UV-initiated hydrosilylation was carried out at room temperature while thermally treated surfaces were performed at 130 °C which would likely exclude

Table 1: Sessile droplet contact angle measurements of the two surfaces hydrosilylated with the two alkynes. The atomic concentration (atom %) from XPS survey spectra is also as listed below for the two different reaction mechanisms.

contact angle				
	thermal hydrosilylation		UV-inititated hydrosilylation	
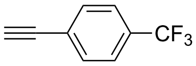	(84.0 ± 1.5)°		(83.5 ± 0.5)°	
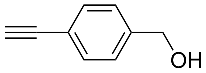	(89.6 ± 3.0)°		(67.4 ± 4.1)°	
atomic concentration (atom %) after thermal hydrosilylation				
	C 1s	Si 2p	O 1s	F 1s
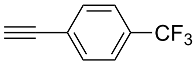	14.63	66.18	15.21	3.97
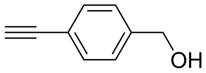	68.32	15.40	16.19	—
atomic concentration (atom %) after UV-initiated hydrosilylation				
	C 1s	Si 2p	O 1s	F 1s
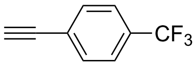	14.21	50.39	32.18	3.22
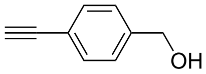	19.13	34.72	48.15	—

water from the reaction system. This may allow for more extensively oxidation to occur since the radicalized surface was highly susceptible to oxidation. The O 1s spectra from the ethynylbenzyl alcohol had been already discussed in the previous section with C–O contributing to the high percentage of oxygen observed.

Conclusion

From the XPS analysis and the contact angle measurements, several conclusions can be drawn from this study. Firstly, the efficacy of the low-temperature thermal hydrosilylation was heavily dependent on the presence of oxygen species. In the absence of oxygen carrying organics, it was possible that trifluoroalkyne was grafted through Si–C linkages because of trace amounts of oxygen. Despite the thorough degassing method used, it was not possible to remove all oxygen in a non-vacuum environment. Secondly, it was noticed that the UV-irradiation had created a highly reactive surface that was reacted with both OH-terminations and alkyne-terminations of the molecules. In the thermal setup for the ethynylbenzyl alcohol, a strong predominance of Si–O–C was observed. This suggested that the role of hydrogen abstraction from the surface through residual oxygen in the thermal setup is minimal as the absence of Si–C bonds from XPS also indicated that the reaction only yielded Si–O–C linkages despite the long reaction time of 18 h. The results reported here shed light on the issues related to OH reactivity at low temperatures as well as on the indiscriminate reactivity of the Si radicals formed at the surface. This information is important with regard to the hydrosilylation of OH bearing species to a silicon surface.

Experimental

Materials

Silicon wafers (111), were boron-doped (resistivity of 0.01–0.018 Ω·cm) and were used in this experiment. Sulfuric acid (Aldrich) and hydrogen peroxide (BDH Prolabo) were of semiconductor grade. 4-ethynylbenzyl alcohol and 4-ethynyl-α,α,α-trifluorotoluene were purchased from Sigma-Aldrich. All other chemicals, unless stated otherwise were used as received without further purification.

Thermal reaction protocol

Similar to the methodology as described by Ciampi et al [15], silicon wafers approximately 20 × 20 mm^2 were cleaned for 30 min in hot Piranha solution (95 °C, hydrogen peroxide (33%)/conc. sulfuric acid, 1:3 (v/v)). The samples were then submerged in a solution of 2.5% hydrofluoric acid for 1.5 min. Subsequently, the samples were placed to a degassed (through a minimum of 20 freeze-pump-thaw cycles) solution of 4-ethynyl-α,α,α-trifluorotoluene (0.3 M in mesitylene). The sample was kept under a stream of nitrogen while the reaction vessel was immersed in an oil bath set to 130 °C for 18 h. After the reaction, the flask was carefully opened and the functionalized surface samples were exposed to the atmosphere and subsequently rinsed and sonicated in copious amounts of chloroform, ethyl acetate, and then ethanol before being analyzed.

For the 4-ethynylbenzyl alcohol-based layer, the silicon surface was also functionalized in similar fashion and with the same molar concentrations. The functionalized surface samples were rinsed consecutively with copious amounts of chloroform, ethyl acetate, and then ethanol before being analyzed.

UV-initiated hydrosilylation

Silicon wafers were pre-prepared in similar fashion to that in the thermal hydrosilylation protocol. Subsequently, the surfaces were transferred, taking care to completely exclude air from in the reaction vessel (a custom-made fused silica flask), to a degassed (through a minimum of 20 freeze-pump-thaw cycles) sample of 4-ethynyl-α,α,α-trifluorotoluene (0.3 M in mesitylene). The surface was irradiated with 254 nm (4.88 eV) UV radiation was provided by a commercial 6 W Hg tube. Any shorter wavelength component from the lamp (typically the 185 nm line) was filtered out by using a coloured glass filter with a transmittance of lower than 1% outside the 220–400 nm band. The choice of custom-made quartz Schlenk flask made of fused silica ensures a very high transmittance of the 254 nm light to the sample, up to 90%.

The experimental setup is arranged with the UV lamp held in vertical position with an adjustable distance from the reaction vessel, so that the UV light impinges perpendicularly to the sample surface and the power density can be easily varied. Vessel and lamp are enclosed in a dark box so that no light other than that from the UV lamp can reach the sample.

A calibration of the light intensity was performed by using a large area calibrated silicon photodiode from Hamamatsu photonics, showing that the experimental setup is capable to deliver 254 nm UV light intensities from 1.2 mW/cm^2 down to 100 μW/cm^2 (lower values can be easily obtained by inserting other filters). The lamp-to-sample distance was adjusted in order to have a power density of 700 μW/cm^2. The surfaces were exposed to the UV irradiation for 2 h, then rinsed consecutively with copious amounts of chloroform, ethyl acetate, and then ethanol before being analyzed.

Contact angle measurements

The water contact angle (CA) values were acquired on a Dataphysics OCA-20 goniometer setup at room temperature in ambient atmosphere. This instrument consists of a CCD video camera with a resolution of 768 × 576 pixels that can take up to

50 images per second. For each sessile droplet measurement three separate 5 μL droplets were dispensed onto the selected sample and the drop images were recorded. All drop images were then processed by an image analyzer that calculated both the left and right contact angles from the droplet shape with an accuracy of ±0.1°.

X-ray photoelectron spectroscopy (XPS)

The XPS wide scan spectra were acquired by using an AXIS Ultra DLD, Kratos, equipped with an Al Kα X-ray source (1486.6 eV) at 10 mA, 15 kV, analyzing a 300 × 700 μm area under ultra-high vaccum ($3.9 \cdot 10^{-9}$ Torr). Analyses were performed in the hybrid lens mode with the slot aperture and the pass energy of the hemispherical analyzer set to 100 eV for the survey scan. High-resolution spectra were obtained for the C 1s, F 1s, Si 2p and O 1s energies for all samples. The spectra were subsequently analyzed by using the built-in Kratos Vision 1.5 software.

Acknowledgements

Authors gratefully acknowledge the support given by Prof. Claudia Riccardi through the PlasmaPrometeo Center, University of Milano Bicocca, for contact angle measurements

References

1. Khung, Y. L.; Narducci, D. *Biosens. Bioelectron.* **2013,** *50,* 278–293. doi:10.1016/j.bios.2013.06.033
2. Boukherroub, R.; Morin, S.; Bensebaa, F.; Wayner, D. D. M. *Langmuir* **1999,** *15,* 3831–3835. doi:10.1021/la9901478
3. Buriak, J. M.; Allen, M. J. *J. Am. Chem. Soc.* **1998,** *120,* 1339–1340. doi:10.1021/ja9740125
4. Buriak, J. M.; Stewart, M. P.; Geders, T. W.; Allen, M. J.; Choi, H. C.; Smith, J.; Raftery, D.; Canham, L. T. *J. Am. Chem. Soc.* **1999,** *121,* 11491–11502. doi:10.1021/ja992188w
5. Cicero, R. L.; Linford, M. R.; Chidsey, C. E. D. *Langmuir* **2000,** *16,* 5688–5695. doi:10.1021/la9911990
6. Stewart, M. P.; Buriak, J. M. *Angew. Chem., Int. Ed.* **1998,** *37,* 3257–3260. doi:10.1002/(SICI)1521-3773(19981217)37:23<3257::AID-ANIE3257>3.0.CO;2-1
7. Webb, L. J.; Lewis, N. S. *J. Phys. Chem. B* **2003,** *107,* 5404–5412. doi:10.1021/jp0222752
8. Wang, X.; Ruther, R. E.; Streifer, J. A.; Hamers, R. J. *J. Am. Chem. Soc.* **2010,** *132,* 4048. doi:10.1021/ja910498z
9. Boukherroub, R.; Morin, S.; Sharpe, P.; Wayner, D. D. M.; Allongue, P. *Langmuir* **2000,** *16,* 7429–7434. doi:10.1021/la991678z
10. Ng, A.; Ciampi, S.; James, M.; Harper, J. B.; Gooding, J. J. *Langmuir* **2009,** *25,* 13934–13941. doi:10.1021/la901526e
11. Linford, M. R.; Fenter, P.; Eisenberger, P. M.; Chidsey, C. E. D. *J. Am. Chem. Soc.* **1995,** *117,* 3145–3155. doi:10.1021/ja00116a019
12. Woods, M.; Carlsson, S.; Hong, Q.; Patole, S. N.; Lie, L. H.; Houlton, A.; Horrocks, B. R. *J. Phys. Chem. B* **2005,** *109,* 24035–24045. doi:10.1021/jp052542e
13. Hacker, C. A.; Anderson, K. A.; Richter, L. J.; Richter, C. A. *Langmuir* **2005,** *21,* 882–889. doi:10.1021/la048841x
14. Cleland, G.; Horrocks, B. R.; Houlton, A. *J. Chem. Soc., Faraday Trans.* **1995,** *91,* 4001–4003. doi:10.1039/ft9959104001
15. Ciampi, S.; Böcking, T.; Kilian, K. A.; James, M.; Harper, J. B.; Gooding, J. J. *Langmuir* **2007,** *23,* 9320–9329. doi:10.1021/la701035g
16. Sieval, A. B.; van den Hout, B.; Zuilhof, H.; Sudhölter, E. J. R. *Langmuir* **2001,** *17,* 2172–2181. doi:10.1021/la001494g
17. de Villeneuve, C. H.; Pinson, J.; Bernard, M. C.; Allongue, P. *J. Phys. Chem. B* **1997,** *101,* 2415–2420. doi:10.1021/jp962581d
18. Grunthaner, F. J.; Grunthaner, P. J.; Vasquez, R. P.; Lewis, B. F.; Maserjian, J.; Madhukar, A. *J. Vac. Sci. Technol., A* **1979,** *16,* 1443–1453. doi:10.1116/1.570218
19. Avila, A.; Montero, I.; Galán, L.; Ripalda, J. M.; Levy, R. *J. Appl. Phys.* **2001,** *89,* 212–216. doi:10.1063/1.1332796
20. Li, N.; Hu, P.; Zhang, X.; Liu, Y.; Han, W. *Corros. Sci.* **2013,** *73,* 44–53. doi:10.1016/j.corsci.2013.03.023
21. Gómez, F. J.; Prieto, P.; Elizalde, E.; Piqueras, J. *Appl. Phys. Lett.* **1996,** *69,* 773–775. doi:10.1063/1.117887
22. Wang, Y. X.; Wen, J.; Guo, Z.; Tang, Y. Q.; Tang, H. G.; Wu, J. X. *Thin Solid Films* **1999,** *338,* 93–99. doi:10.1016/S0040-6090(98)01004-9
23. Armstrong, J. L.; White, J. M.; Langell, M. *J. Vac. Sci. Technol., A* **1997,** *15,* 1146–1154. doi:10.1116/1.580445
24. Kwon, S.; Lee, E.-S.; Seo, H.; Jeon, K.-J.; Hwang, C. C.; Kim, Y.-H.; Park, J. Y. *Surf. Sci.* **2013,** *612,* 37–41. doi:10.1016/j.susc.2013.02.010
25. Yao, H.; Chu, C.-C.; Sue, H.-J.; Nishimura, R. *Carbon* **2013,** *53,* 366–373. doi:10.1016/j.carbon.2012.11.023
26. Wang, Y.-S.; Yang, S.-Y.; Li, S.-M.; Tien, H.-W.; Hsiao, S.-T.; Liao, W.-H.; Liu, C.-H.; Chang, K.-H.; Ma, C.-C. M.; Hu, C.-C. *Electrochim. Acta* **2013,** *87,* 261–269. doi:10.1016/j.electacta.2012.09.013
27. Riga, J.; Snauwaert, P.; De Pryck, A.; Lazzaroni, R.; Boutique, J. P.; Verbist, J. J.; Bredas, J. L.; Andre, J. M.; Taliani, C. *Synth. Met.* **1987,** *21,* 223–228. doi:10.1016/0379-6779(87)90090-7
28. Contarini, S.; Howlett, S. P.; Rizzo, C.; De Angelis, B. A. *Appl. Surf. Sci.* **1991,** *51,* 177–183. doi:10.1016/0169-4332(91)90400-E
29. Rao, N. P.; Tymiak, N.; Blum, J.; Neuman, A.; Lee, H. J.; Girshick, S. L.; McMurry, P. H.; Heberlein, J. *J. Aerosol Sci.* **1998,** *29,* 707–720. doi:10.1016/S0021-8502(97)10015-5
30. Jiang, L. D.; Cheung, R.; Brown, R.; Mount, A. *J. Appl. Phys.* **2003,** *93,* 1376–1383. doi:10.1063/1.1534908
31. Attard, G. A.; Chibane, K.; Ebert, H. D.; Parsons, R. *Surf. Sci.* **1989,** *224,* 311–326. doi:10.1016/0039-6028(89)90917-5
32. Weston, M.; Britton, A. J.; O'Shea, J. N. *J. Chem. Phys.* **2011,** *134,* 054705. doi:10.1063/1.3549573
33. Chen, C.-M.; Huang, J.-Q.; Zhang, Q.; Gong, W.-Z.; Yang, Q.-H.; Wang, M.-Z.; Yang, Y.-G. *Carbon* **2012,** *50,* 659–667. doi:10.1016/j.carbon.2011.09.022
34. Shao, Y. X.; Dong, D.; Cai, Y. H.; Wang, S.; Ang, S. G.; Xu, G. Q. *J. Phys. Chem. C* **2010,** *114,* 17159–17165. doi:10.1021/jp103945m
35. Simonsen, M. E.; Sønderby, C.; Li, Z.; Søgaard, E. G. *J. Mater. Sci.* **2009,** *44,* 2079–2088. doi:10.1007/s10853-009-3270-9
36. Wu, J. X.; Wang, Z. M.; Li, F. Q.; Ma, M. S. *Appl. Surf. Sci.* **2004,** *225,* 229–234. doi:10.1016/j.apsusc.2003.10.019
37. Wu, Z.; Zhang, W.; Xiong, F.; Yuan, Q.; Jin, Y.; Yang, J.; Huang, W. *Phys. Chem. Chem. Phys.* **2014,** *16,* 7051–7057. doi:10.1039/c4cp00697f

38. Kulkarni, S. A.; Ogale, S. B.; Vijayamohanan, K. P. *J. Colloid Interface Sci.* **2008,** *318,* 372–379. doi:10.1016/j.jcis.2007.11.012
39. Bittoun, E.; Marmur, A.; Ostblom, M.; Ederth, T.; Liedberg, B. *Langmuir* **2009,** *25,* 12374–12379. doi:10.1021/la9016992

License and Terms

The definitive version of this article is the electronic one which can be found at:
doi:10.3762/bjnano.6.3

BEILSTEIN JOURNAL OF NANOTECHNOLOGY

Morphology, structural properties and reducibility of size-selected CeO_{2-x} nanoparticle films

Maria Chiara Spadaro[*1,2], Sergio D'Addato[1,2], Gabriele Gasperi[1,2], Francesco Benedetti[1,2], Paola Luches[1], Vincenzo Grillo[1,3], Giovanni Bertoni[3] and Sergio Valeri[1,2]

Full Research Paper

Open Access

Address:
[1]CNR-NANO, Centro di Ricerca S3, via G. Campi 213/a, Modena, Italy, [2]Dipartimento FIM, Università di Modena e Reggio Emilia, Via G. Campi 213/a, Modena, Italy and [3]CNR-IMEM, Parco Area delle Scienze 37/A - 43124 Parma, Italy

Email:
Maria Chiara Spadaro[*] - mariachiara.spadaro@unimore.it

[*] Corresponding author

Keywords:
CeO_2 ultra-thin films; ceria nanoparticles; magnetron sputtering; reduction and oxidation; size-dependent properties; size-selected nanoparticles; X-ray photoelectron spectroscopy

Beilstein J. Nanotechnol. **2015,** *6,* 60–67.
doi:10.3762/bjnano.6.7

Received: 02 August 2014
Accepted: 26 November 2014
Published: 07 January 2015

This article is part of the Thematic Series "Self-assembly of nanostructures and nanomaterials".

Guest Editor: I. Berbezier

Abstract

Non-stoichiometric ceria nanoparticles (NPs) were obtained by a gas aggregation source with a magnetron and were mass-selected with a quadrupole mass filter. By varying magnetron power, Ar gas flow, and the length of the aggregation tube, NPs with an average diameter of 6, 9, and 14 nm were synthesized and deposited onto a substrate, thus obtaining NP films. The morphology of the films was studied with scanning electron microscopy, while high resolution transmission electron microscopy was used to gain a deeper insight into the atomic structure of individual NPs. By using X-ray photoelectron spectroscopy we analyzed the degree of reduction of the NPs of different diameters, before and after thermal treatments in vacuum (reduction cycle) and in O_2 atmosphere (oxidation cycle) at different temperatures. From this analysis we inferred that the size is an important parameter only at intermediate temperatures. As a comparison, we evaluated the reducibility of an ultra-thin ceria film with the same surface to volume ratio as the 9 nm diameter NPs film, observing that NPs are more reducible than the ceria film.

Introduction

The main property of cerium oxide that attracts scientific attention is its ability to store and release oxygen depending on the ambient conditions [1]. In particular, ceria in the form of nanoparticles (NPs) is important in industrial catalysis [2] and in biomedical applications to prevent the oxidation of human cells [3]. Doped cerium oxide films are also promising candidates as electrolytes in solid oxide fuel cells [4].

A lot of studies have been performed on ceria NPs while varying their diameter: NPs with diameter less than 5 nm have larger oxygen storage capacity than the ones with higher diameter; this is related to the larger surface area exposed by the smaller NPs [5].

It is well known that in CeO_{2-x} NPs the lattice parameter increases when the particle size is decreased. Tsunekawa et al. [6], analyzing NPs with diameter between 2 nm and 4 nm, suggested that the reduction of the Ce ion charge from 4+ to 3+ leads to an increase of the lattice parameter because of the decrease in the electrostatic force. With the assumption that the increase of the lattice parameter is also due to a higher concentration of oxygen vacancies, Tsunekawa results are complementary with the ones of Zhou et al. [7], obtained for NP diameters between 4 and 60 nm. These results led to the conclusion that the lattice parameter increase is related to the formation of oxygen vacancies and Ce^{3+} ions.

Following this approach, Deshpande et al. [8] correlated the lattice parameter expansion with the concentration of Ce^{3+} ions (measured by X-ray photoelectron spectroscopy, XPS), ascribing it to the higher ionic radius of Ce^{3+}, compared to the Ce^{4+}, and to the introduction of oxygen vacancies, which in turn induces a distortion of the local symmetry. In the last years a ‘Madelung model’ has been proposed to describe the properties of ionic crystals as a function of their surface to volume ratio. Here, the balance between long range Coulomb attractive and short range repulsive interactions is broken, leading to an effective negative pressure and thus to an increase of the lattice parameter [9]. Actually, a proper combination of all these factors, namely the increase of concentration of Ce^{3+} ions, oxygen vacancies and Madelung pressure, can explain the observed phenomena.

It is not yet clear if the presence of Ce^{3+} ions is an intrinsic characteristic of the NP [10] or if it is related to the synthesis procedure. Paun et al. [11] synthesized ceria NPs with different diameters and identical polyhedral shapes, by means of different chemical synthesis procedures. The concentration of Ce^{3+} ions was found to be quite different even for NPs with the same diameter, showing that the presence of Ce^{3+} ions is also related to the synthesis procedure and not only to the particle size.

Few works have been performed with NPs synthetized by magnetron sputtering, the technique used in this study. Tschöpe et al. [12] studied ceria NPs realized by magnetron sputtering from pure and mixed metal target and inert gas condensation, observing the high non-stoichiometry of these systems due to the particular synthesis method. The non-stoichiometry is due to the presence of Ce^{3+} ions. Non-stoichiometric NPs grown in this way exhibit a higher catalytic activity than stoichiometric material, mainly because of surface defects and chemisorbed oxygen [13,14]. A new interpretation for the redox activity of CeO_{2-x} NPs has been recently proposed, based on the increase of electron density in delocalized mixed cerium and oxygen orbitals, rather than on localized surface reduction of Ce^{4+} to Ce^{3+} ionic species [15].

In this work we present the results of the study of CeO_{2-x} NPs produced by combining magnetron sputtering with a gas aggregation source. We investigated NPs reducibility as a function of their diameter (ranging from 6 to 14 nm) under reduction and oxidation conditions, and in comparison with a ultra-thin ceria film of the same surface to volume ratio as the 9 nm diameter NPs film. The NPs have been characterized with regard to morphology and structure by scanning electron microscopy (SEM) and high resolution transmission electron microscopy (HRTEM). The thermal stability of the NPs was investigated by XPS. The aim of this work is to investigate the fundamental relationship between NPs chemical and physical properties, in order to improve the understanding of the basic processes, which are fundamental for the ceria NPs applications.

Experimental

The ceria NPs were synthesized at the SESAMo Laboratory [16-18], with an experimental system composed of three interconnected vacuum chambers (schematic view in Figure 1); the deposition chamber (C) is connected on one side to the NPs source chamber (A), equipped also with a quadrupole mass filter (B), and on the other side to the XPS chamber (D) for in situ chemical characterization. Ceria NPs were obtained by DC magnetron sputtering and inert gas (Ar) aggregation method, from a pure Ce target (99.9%).

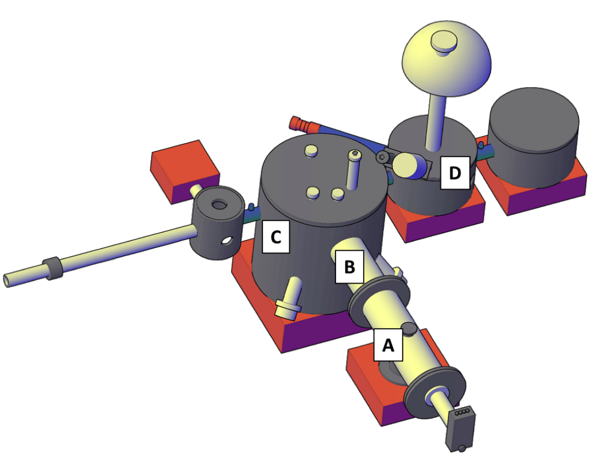

Figure 1: Sketch of the experimental set up: the NPs are created by the NC200 source (A), they are mass selected by the QMF (B) and they are deposited on the substrate in the deposition chamber (C). The chemical characterization is performed in situ in the XPS chamber (D).

Most of the clusters were charged, so that they could be mass selected by the quadrupole mass filter (QMF). The NP beam reached the deposition chamber, where a NP film was grown on a Si/SiO$_x$ substrate. Depositions were carried out in oxygen atmosphere ($p_{O2} = 5 \cdot 10^{-6}$ mbar) and post-oxidation for 30 min ($p_{O2} = 4 \cdot 10^{-5}$ mbar), to fully oxidize the NPs. The nominal film thickness was fixed to 10 nm (the evaporation rate was measured by a quartz microbalance in the deposition chamber) for all samples described in this work. The amount values of deposited NPs are given in terms of nominal thickness of an equivalent continuous film with the same density as CeO$_2$. By changing the length of the aggregation tube, the electrical power applied to the target and the Ar gas flux, we obtained NPs with different average lateral sizes: 6, 9 and 14 nm.

In particular the magnetron discharge power (P), Ar flux (f) and aggregation length conditions (l) used were: 1) 6 nm NPs: $P = 67$ W, $f = 10$ sccm, $l = 50$ mm; 2) 9 nm NPs: $P = 30$ W, $f = 40$ sccm; $l = 50$ mm; 3) 14 nm NPs: $P = 99$ W, $f = 56$ sccm, $l = 150$ mm. The NPs diameter is controlled by the QMF monitor during the deposition, in fact it is possible to check the NPs diameter distribution scanning the quadrupole voltage whilst monitoring the NPs beam ion current. We also check the diameter distribution by ex situ SEM measurements, with a dual beam system (FEI Strata DB235M), in order to perform a statistical analysis and to have information on the mean diameter value and the full width at half maximum (FWHM) of the size distribution.

After deposition the samples were analyzed with in situ XPS, by using a twin anode X-ray source (XR50, Specs), generating Al Kα photons and a hemispherical electron analyzer (Phoibos 150, Specs). The reduction and oxidation cycles were performed in a different UHV apparatus, described in the second part of this section. After transferring the sample to the second apparatus the Ce^{3+} concentration in the NPs slightly increased from its original value measured immediately after growth, because of air exposure (almost 4% for all samples). We do not expect this modification to affect the oxygen transport in the NPs. For the reduction process the samples were heated in UHV at $T = 520$ K, $T = 770$ K and $T = 1020$ K for 30 min; for the oxidation process the samples were heated at $T = 1020$ K in O$_2$ ($p = 10^{-7}$ mbar) for 30 min. To estimate the contribution to the XPS spectra due to Ce^{3+} and Ce^{4+} ions we performed a fit with a linear combination of the Ce^{3+} and Ce^{4+} reference spectra, and by using the fitting equation

$$a \cdot I\left(Ce^{3+}\right) + \left(1 - a\right) \cdot I\left(Ce^{4+}\right) \qquad (1)$$

From the fit we evaluated the parameter a, which represents an estimate of the Ce^{3+} concentration. The error was estimated through the fitting procedure.

The Ce^{3+} and Ce^{4+} reference spectra were obtained from NP films treated with the following procedures:

To obtain the Ce^{4+} reference sample the deposited NPs were oxidized during their growth, injecting oxygen in the aggregation chamber (A region in Figure 1). The obtained NPs had an average lateral size $<d> = 9$ nm. A post-annealing at 1020 K in a rich oxygen atmosphere (10^{-7} mbar) was also performed. The reference spectrum for the reduced component I(Ce^{3+}) was obtained from a film of NPs with $<d> = 9$ nm grown under high vacuum conditions, without the presence of oxygen. The ’as deposited’ sample was then annealed at $T = 1020$ K in UHV.

HRTEM experiments were performed by using a JEOL JEM-2200FS instrument working at 200 keV and equipped with a Schottky emitter. The instrument has an objective lens spherical aberration coefficient of 0.5 mm, providing a point-to-point resolution of 0.19 nm. The images were subsequently elaborated by using the STEM_CELL software [19]. Concerning the ultra-thin films we evaluated the morphology with in situ STM measurements by using an OMICRON room temperature SPM. The STM images have been processed by using the Image SXM software [20].

A second UHV apparatus was used to grow both epitaxial and non-epitaxial cerium oxide ultrathin films for comparison. The system is equipped with facilities for substrate preparation, film growth, in situ XPS, and scanning tunnelling microscopy (STM) analysis. The substrate used for film growth was a Pt(111) single crystal prepared by repeated cycles of sputtering (1 keV, 1 μA) and annealing (1040 K).

A 2 ML cerium oxide epitaxial film with the same surface-to-volume ratio of the NPs with 9 nm diameter ($S/V = 0.6$ nm^{-1}), was grown with the procedures described in [21], i.e., reactive Ce electron-beam deposition in $p_{O2} = 1 \cdot 10^{-7}$ mbar at room temperature and post-growth annealing at $T = 1040$ K under the same O$_2$ partial pressure. A non-epitaxial cerium oxide film grown on Pt(111) with nominal thickness $t = 2$ ML, was obtained with the same procedures as the epitaxial film, without the post-growth annealing in O$_2$, and it was studied for further comparison.

Reducing thermal treatments were performed by using an electron bombardment heater. The samples were heated in UHV to the desired temperature, kept at that temperature for 30 min, and cooled to room temperature, following [22]. The oxidizing thermal treatments were performed under an oxygen partial pressure of $p_{O2} = 1{\cdot}10^{-7}$ mbar. XPS measurements were performed using an Al Kα X-ray source and a hemispherical electron analyzer. The STM was operated at room temperature in constant current mode, by using electrochemically etched tungsten tips, degassed by thermal treatments and sputtered by ion bombardment before the measurements.

Results and Discussion

Figure 2 shows SEM images of NPs with different size values, and STM images of the epitaxial and non-epitaxial film. The 9 nm NPs (Figure 2b) are clearly visible and well dispersed, and it was possible to obtain the lateral size distribution shown in Figure 2b. The size distribution was obtained by measuring the area of 125 different NPs from SEM images and by evaluating the corresponding diameters, which range between 8.5 nm and 10.5 nm. By fitting the diameter histogram with a lognormal distribution we estimated the mean diameter value to be <*d*> = 9.19 nm (FWHM = 0.65 nm). Concerning the 6 nm and the 14 nm samples, the size has been evaluated from 25 different NPs in different areas. These images show that the density of NPs in the samples is clearly decreasing with increasing the NPs diameter. This is because for every sample we deposited an amount of NPs in order to have the same nominal film thickness of 10 nm. In Figure 2d a STM image of the non-epitaxial film is shown; the substrate is completely covered with a disordered film with a structured surface showing grains of a few nanometers in lateral size and a few angstroms in average height. After annealing the film up to *T* = 1040 K in O_2 we obtained an epitaxial ceria thin film as shown in Figure 2e, in which the islands have atomically flat surfaces. In this case 45% of the Pt(111) substrate is covered and the islands have a mean height of 0.6 nm and a lateral size of 20–30 nm.

To gain a deeper insight into the atomic structure of the NPs, STEM and HR TEM measurements have been performed on 9 nm NPs deposited on a Lacey support grid, as shown in Figure 3a and Figure 3b respectively. Ce lattice fringes are also clearly visible. The NPs on the sample exhibit single crystalline

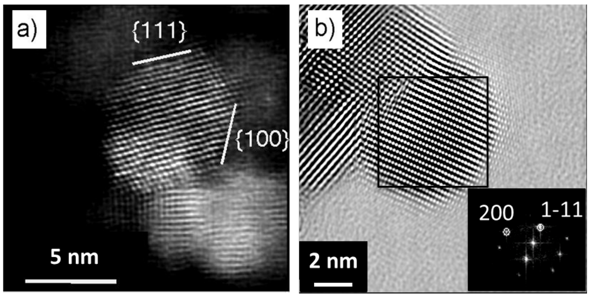

Figure 3: STEM (a) and HRTEM (b) images of ceria NPs corresponding to the sample with average diameter of 9 nm, the inset in (b) shows the FFT of the selected area with indicated the corresponding planes.

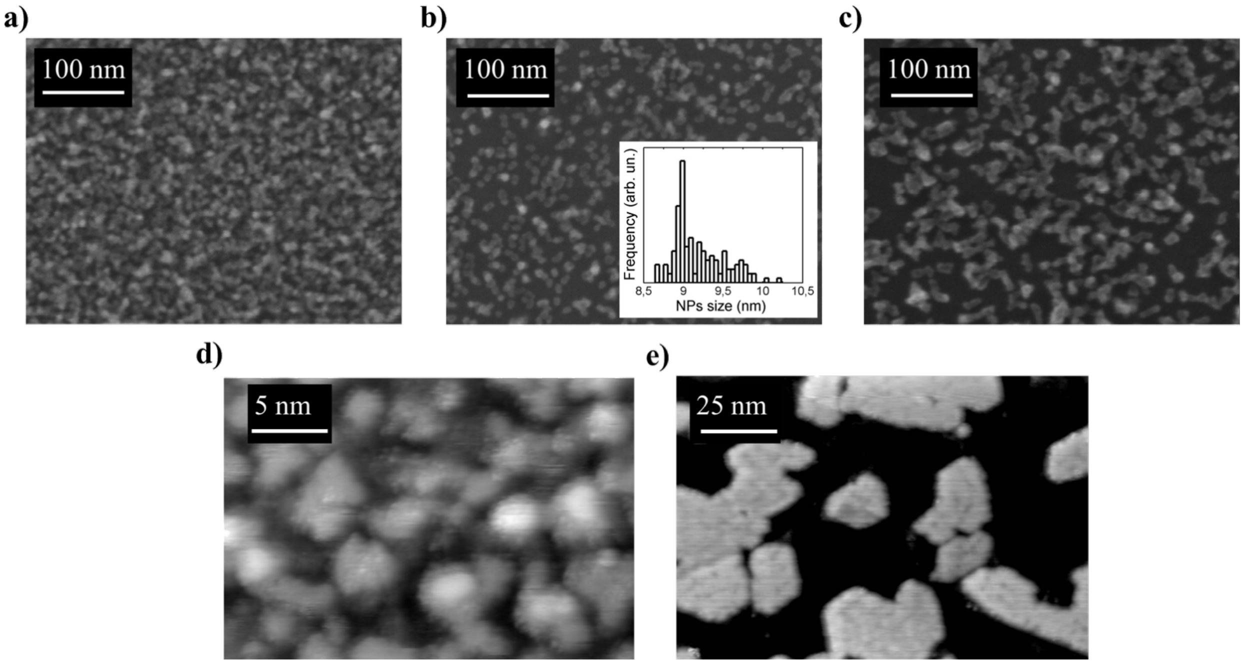

Figure 2: SEM images of NPs films: NPs diameter 6 nm (a), NPs diameter 9 nm (lateral size distribution in the inset) (b) and NPs diameter 14 nm (c). STM images of the non-epitaxial (d) and epitaxial (e) ultra-thin ceria films acquired at 1.5 V and 0.04 nA.

structure (cubic CeO_2, space group 225, $Fm{-}3m$), exposing frequently {111}, {220} and {100} facets, as evidenced in Figure 3a and Figure 3b. The (111) surface is indeed the most stable for cerium dioxide [1] and the (220) has the next lowest surface energy; at variance, the (100) surface is not as stable as the (111), but it is the most frequently exposed plane in ceria NPs after the (111) [23] probably because of the low dimensionality effects.

In Figure 4a a typical Ce 3d XPS spectrum of non-stoichiometric ceria NPs, with $<d>$ = 6 nm, after annealing in O_2 at T = 1020 K, is shown. In the spectrum it is possible to observe features from both Ce^{3+} and Ce^{4+} ionic species, as already observed for ceria NPs. In fact a core–shell model was proposed [24,25] for the oxidation state of the CeO_{2-x} NPs, which assumes that the core of the nanoparticle is composed of CeO_2 while the shell is composed of one layer of Ce_2O_3. This model well agrees with the observation in NPs with different size and shape for every synthesis procedures.

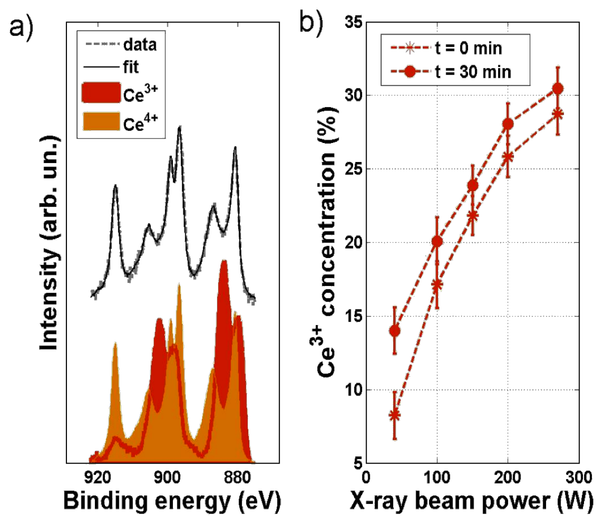

Figure 4: (a) Ce 3d XPS spectra and corresponding fit of the 9 nm sample acquired at 40 W, in the bottom region Ce^{3+} and Ce^{4+} XPS spectra, respectively, measured on NPs grown without oxygen in the system and then annealed in UHV at 1020 K, and on NPs oxidized directly in the aggregation chamber and then annealed in O_2 at 1020 K; (b) Ce^{3+} concentration at different X-ray power acquired on the sample at the beginning of the acquisition for each X-ray power, t = 0 min, (red circle) and after 30 min (red star) of X-ray exposure, t = 30 min.

In the same figure the Ce 3d Ce^{3+} and Ce^{4+} reference spectra are also shown. It can be observed that Ce^{3+} reference spectrum shows a minor trace of Ce^{4+} related feature: in fact the peak present at binding energy value BE = 915 eV (see Figure 4a bottom panel red curve) is related with Ce^{4+} ions contribution. Because of the presence of this small peak, it was not possible to obtain an absolute value of the Ce^{3+} concentration, but the variation in the amount of Ce^{3+} ions as a function of size and annealing temperature could be monitored. It is also important to observe that UHV conditions and exposure to X-ray can reduce the samples, and thus Ce^{3+} concentration from XPS analysis can be overestimated [26]. The fitting curve obtained by using Equation 1 is also shown in the same figure; it can be observed that it is in good agreement with the experimental data.

As mentioned before CeO_{2-x} NPs can be reduced under X-ray irradiation [26]. We performed an XPS analysis of the 9 nm sample while increasing the X-ray power and observed a progressive reduction of the NPs, and we evaluated the change of the concentration of the Ce^{3+} ions by performing the previously described fitting procedure. For each acquisition, the sample was kept under the flux for 30 min, and the Ce 3d spectrum was acquired at the beginning and at the end of each exposure for every value of the X-ray source operating power, in order to detect if the longer exposure affected the oxidation state. Fit results are shown in Figure 4b. Five different power values have been used: 40 W, 100 W, 150 W, 200 W, 270 W, the last one being the one that was used conventionally to perform XPS analysis. It is possible to observe that for low X-ray power contribution to the spectra coming from Ce^{3+} ions is very small (a = 8%, Table 1), and that it increases with the X-ray power; in particular for 270 W a value a = 30% was obtained. This reduction under UHV conditions and X-ray exposure at increasing power was not observed for the epitaxial film. In spite of the difficulties in obtaining absolute values of the concentration of Ce^{3+}, it was possible to monitor the behavior of NPs in reduction and oxidation conditions.

Table 1: Ce^{3+} XPS intensity resulting from the fitting of the XPS spectra acquired at different X-ray power after different irradiation times.

power (W)	Ce^{3+} XPS intensity (%)	
	t = 0 min	t = 30 min
40	8.24 ± 1.59	14 ± 1.59
100	17.14 ± 1.59	20.09 ± 1.59
150	21.81 ± 1.32	23.93 ± 1.32
200	25.83 ± 1.39	28.05 ± 1.39
270	28.73 ± 1.39	30.48 ± 1.39

In Figure 5a, Ce 3d spectra for a complete reduction and oxidation cycle are shown. One can observe that the Ce^{3+}-related features become more evident at increasing annealing temperatures. Performing the previously described fitting procedure, we monitored the intensity of the Ce^{3+} component in the XPS data as a function of the annealing temperature for all samples. Fit

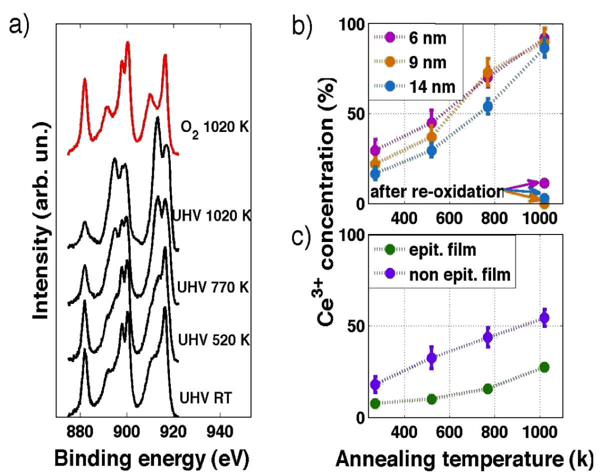

Figure 5: (a) Ce 3d XPS spectra for a complete reduction (black curves) and oxidation (red curve) cycle. (b) Intensity of the Ce^{3+} component at different annealing temperature and after re-oxidation on NPs of diameter of 6 nm (pink dots), 9 nm (orange dots), and 14 nm (blue dots), and (c) on the ultra-thin epitaxial (green dots) and non-epitaxial (violet dots) ceria film.

results are reported in Table 2, and they are plotted in Figure 5b for the NPs and in Figure 5c for the ultra-thin films.

The intensity of the Ce^{3+} component strongly depends on the NP size at room temperature (RT) and after thermal treatments at temperatures up to 770 K: NPs with average sizes of $<d> = 6$ nm and $<d> = 14$ nm present, respectively, the highest and lowest values of Ce^{3+} intensity, corresponding to the highest and lowest Ce^{3+} concentration, while 9 nm NPs with $<d> = 9$ nm exhibit an intermediate value. The reason for this behavior can be ascribed to the strong difference in the surface to volume ratio and to the oxygen vacancy energy formation [27]. After a thermal treatment at 1020 K, these differences in the Ce^{3+} component intensities are less significant; in agreement with the results reported in [27], the oxygen vacancy formation energy is related with NPs size, in particular it decreases with increasing the NPs size. It seems that the dimensionality has a strong contribution up to $T = 770$ K while at $T = 1020$ K the Ce^{3+} concentration is not related to the size.

In contrast, XPS from epitaxial film shows a very small concentration of Ce^{3+} ions already at RT, which increases with thermal treatments in vacuum. Moreover, the maximum value obtained for the intensity of Ce^{3+} component after thermal treatment at $T = 1020$ K is significantly lower with respect to the other samples (NPs and non-epitaxial film). Since the film has been chosen to have a comparable surface to volume ratio as the 9 nm NP, the lower degree of reduction is possibly due to the fact that the film exposes mainly (111) surfaces, which are the most stable ones. The non-epitaxial film instead shows a behavior closer to the NPs for thermal treatments up to $T = 520$ K, while for higher temperatures the Ce^{3+} concentration is lower than in the NPs. This significant difference can be ascribed to structural and morphological changes occurring in the non-epitaxial film at increasing temperature, as shown in Figure 6 in which STM images of the non-epitaxial film before and after the reduction cycle are reported. It is possible to observe that the as-grown film (Figure 6a) completely covers the substrate as a granular ultra-thin film (as in Figure 2d). After annealing in UHV at 1020 K it is possible to observe that the film becomes non-continuous with the formation of single quasi-hexagonal

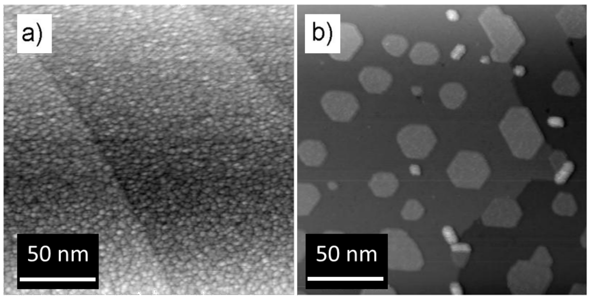

Figure 6: STM images of a cerium oxide ultrathin film on Pt(111) (a) as grown, acquired at 2.0 V and 0.03 nA, and (b) after annealing in UHV at 1020 K, acquired at 2.5 V and 0.03 nA.

Table 2: Ce^{3+} XPS intensity resulting from the fitting of the XPS spectra acquired at different annealing temperatures for NPs with different size and ultra-thin films under reduction and oxidation conditions.

annealing temperature (K)	Ce^{3+} XPS intensity (%) 6 nm	9 nm	14 nm	epitaxial film	non-epitaxial film
RT (UHV)	29.49 ± 5.87	21.84 ± 3.80	16.6 ± 3.35	7.57 ± 0.80	17.90 ± 4.33
520 (UHV)	44.82 ± 6.89	37.16 ± 6.12	29.57 ± 3.78	10.07 ± 1.23	32.47 ± 3.91
770 (UHV)	70.13 ± 5.43	72.89 ± 7.60	53.86 ± 4.17	15.64 ± 1.23	43.70 ± 5.21
1020 (UHV)	91.97 ± 5.12	89.95 ± 7.60	86.62 ± 5.35	27.37 ± 1.23	54.36 ± 4.62
1020 (O_2)	11.31 ± 0.23	0 ± 0.25	2.87 ± 0.40		

islands that cover almost 40% of the Pt(111) surface. So, because of the UHV annealing, the previously disordered ultrathin film arranges in an ordered one exposing mainly the (111) surface, in analogy with previous studies investigating the changes of morphology after annealing the granular films in O_2 [21].

Conclusion

Non-stoichiometric ceria NPs have been synthetized through magnetron sputtering with a gas aggregation source. With a quadrupole filter NPs have been mass-selected obtaining a narrow size distribution, and three different lateral sizes have been selected. The morphology and stoichiometry of the NPs have been investigated and it was demonstrated that the concentration of Ce^{3+} ions decreases as a function of particle size for this kind of synthesis method. We investigated in detail how the combination of X-ray power, exposure and UHV conditions influence the oxidation state of the NPs and observed a partial reduction of the NPs. The variation of the Ce^{3+} concentration with thermal treatments was monitored with XPS, performing an analysis of the line shape of the Ce 3d spectrum. The oxidation state stability after thermal treatments in vacuum and in oxygen atmosphere has been studied for different particle sizes, and it has been compared with the epitaxial and non-epitaxial films. In this way the easier oxygen release in NPs synthetized by sputtering technique with respect to the films has been demonstrated. Such reducibility could affect the catalytic properties of ceria NPs.

Acknowledgements

The authors thank G. C. Gazzadi and C. Menozzi for the SEM measurements. The work has been financially supported by the Italian Ministry of Education, Universities and Research through the FIRB Project RBAP115AYN “Oxides at the nanoscale: multifunctionality and applications”, by the COST Action CM1104 “Reducible oxide chemistry, structure and functions”, and by a grant from the University of Modena and Reggio Emilia entitled “The role of cerium oxidation state in bioactive glasses used as biomaterials of 3rd generation”.

References

1. Trovarelli, A.; Fornasiero, P. *Catalysis by Ceria and Related Materials;* Imperial College Press: London, 2012.
2. Sayle, T. X. T.; Parker, S. C.; Sayle, D. C. *Phys. Chem. Chem. Phys.* **2005,** *7,* 2936–2941. doi:10.1039/b506359k
3. Pirmohamed, T.; Dowding, J. M.; Singh, S.; Wasserman, B.; Heckert, E.; Karakoti, A. S.; King, J. E. S.; Seal, S.; Self, W. T. *Chem. Commun.* **2010,** *46,* 2736–2738. doi:10.1039/b922024k
4. Steele, B. C. H.; Heinzel, A. *Nature* **2001,** *414,* 345–352. doi:10.1038/35104620
5. Imagawa, H.; Suda, A.; Yamamura, K.; Sun, S. *J. Phys. Chem. C* **2011,** *115,* 1740–1745. doi:10.1021/jp109878j
6. Tsunekawa, S.; Ishikawa, K.; Li, Z.-Q.; Kawazoe, Y.; Kasuya, A. *Phys. Rev. Lett.* **2000,** *85,* 3440. doi:10.1103/PhysRevLett.85.3440
7. Zhou, X.-D.; Huebner, W. *Appl. Phys. Lett.* **2001,** *79,* 3512. doi:10.1063/1.1419235
8. Deshpande, S.; Patil, S.; VNT Kuchibhatla, S.; Seal, S. *Appl. Phys. Lett.* **2005,** *87,* 133113. doi:10.1063/1.2061873
9. Perebeinos, V.; Chan, S.-W.; Zhang, F. *Solid State Commun.* **2002,** *123,* 295–297. doi:10.1016/S0038-1098(02)00266-1
10. Dutta, P.; Seehra, M. S.; Shi, Y.; Eyring, E. M.; Ernst, R. D. *Chem. Mater.* **2006,** *18,* 5144–5146. doi:10.1021/cm061580n
11. Paun, C.; Safonova, O. V.; Szlachetko, J.; Abdala, P. M.; Nachtegaal, M.; Sa, J.; Kleymenov, E.; Cervellino, A.; Krumeich, F.; van Bokhoven, J. A. *J. Phys. Chem. C* **2012,** *116,* 7312–7317. doi:10.1021/jp300342b
12. Tschöpe, A.; Ying, J. Y. *Nanostruct. Mater.* **1994,** *4,* 617–619. doi:10.1016/0965-9773(94)90071-X
13. Tschöpe, A.; Liu, W.; Flytzanistepahanopoulos, M.; Ying, J. Y. *J. Catal.* **1995,** *157,* 42–50. doi:10.1006/jcat.1995.1266
14. Tschöpe, A.; Schaadt, D.; Birringer, R.; Ying, J. Y. *Nanostruct. Mater.* **1997,** *9,* 423–432. doi:10.1016/S0965-9773(97)00095-0
15. Cafun, J.-D.; Kvashnina, K. O.; Casals, E.; Puntes, V. F.; Glatzel, P. *ACS Nano* **2013,** *7,* 10726–10732. doi:10.1021/nn403542p
16. D’Addato, S.; Gragnaniello, L.; Valeri, S.; Rota, A.; di Bona, A.; Spizzo, F.; Panozaqi, T.; Schifano, S. F. *J. Appl. Phys.* **2010,** *107,* 104318. doi:10.1063/1.3374467
17. D’Addato, S.; Grillo, V.; Altieri, S.; Tondi, R.; Valeri, S.; Frabboni, S. *J. Phys.: Condens. Matter* **2011,** *23,* 175003. doi:10.1088/0953-8984/23/17/175003
18. D’Addato, S.; Spadaro, M. C.; Luches, P.; Grillo, V.; Frabboni, S.; Valeri, S.; Ferretti, A. M.; Capetti, E.; Ponti, A. *Appl. Surf. Sci.* **2014,** *306,* 2–6. doi:10.1016/j.apsusc.2014.02.060
19. STEM_CELL | TEM GROUP. http://tem-s3.nano.cnr.it/?page_id=2 (accessed Aug 1, 2014).
20. Image SXM. http://www.ImageSXM.org.uk (accessed Aug 1, 2014).
21. Luches, P.; Pagliuca, F.; Valeri, S. *J. Phys. Chem. C* **2011,** *115,* 10718–10726. doi:10.1021/jp201139y
22. Luches, P.; Pagliuca, F.; Valeri, S. *Phys. Chem. Chem. Phys.* **2014,** *16,* 18848–18857. doi:10.1039/C4CP02723J
23. Zhang, F.; Jin, Q.; Chan, S.-W. *J. Appl. Phys.* **2004,** *95,* 4319–4326. doi:10.1063/1.1667251
24. Wu, L.; Wiesmann, H. J.; Moodenbaugh, A. R.; Klie, R. F.; Zhu, Y.; Welch, D. O.; Suenaga, M. *Phys. Rev. B* **2004,** *69,* 125415. doi:10.1103/PhysRevB.69.125415
25. Turner, S.; Lazar, S.; Freitag, B.; Egoavil, R.; Verbeeck, J.; Put, S.; Strauvend, Y.; Van Tendeloo, G. *Nanoscale* **2011,** *3,* 3385. doi:10.1039/c1nr10510h
26. Zhang, F.; Wang, P.; Koberstein, J.; Khalid, S.; Chan, S.-W. *Surf. Sci.* **2004,** *563,* 74–82. doi:10.1016/j.susc.2004.05.138
27. Migani, A.; Vayssilov, G. N.; Bromley, S. T.; Illas, F.; Neyman, K. M. *J. Mater. Chem.* **2010,** *20,* 10535–10546. doi:10.1039/c0jm01908a

License and Terms

The definitive version of this article is the electronic one which can be found at:
doi:10.3762/bjnano.6.7

BEILSTEIN JOURNAL OF NANOTECHNOLOGY

Strain distribution due to surface domains: a self-consistent approach with respect to surface elasticity

Javier Fuhr[1] and Pierre Müller*[2]

Full Research Paper

Address:
[1]Centre Atomico Bariloche, CNEA and CONICET, Bustillo 9500, 8400, Bariloche, Argentina and [2]Aix Marseille Université, CNRS, CINaM UMR 7325, 13288 Marseille, France

Email:
Pierre Müller* - muller@cinam.univ-mrs.fr

* Corresponding author

Keywords:
surface strain; surface elasticity; strain field

Beilstein J. Nanotechnol. **2015,** *6,* 321–326.
doi:10.3762/bjnano.6.30

Received: 07 July 2014
Accepted: 19 December 2014
Published: 29 January 2015

This article is part of the Thematic Series "Self-assembly of nanostructures and nanomaterials".

Guest Editor: I. Berbezier

Abstract

Elastically mediated interactions between surface domains are classically described in terms of point forces. Such point forces lead to local strain divergences that are usually avoided by introducing a poorly defined cut-off length. In this work, we develop a self-consistent approach in which the strain field induced by the surface domains is expressed as the solution of an integral equation that contains surface elastic constants, S_{ij}. For surfaces with positive S_{ij} the new approach avoids the introduction of a cut-off length. The classical and the new approaches are compared in case of 1-D periodic ribbons.

Introduction

The classical approach used to calculate the strain field that surface domains induce in their underlying substrate consists of modeling the surface by a distribution of point forces concentrated at the domain boundaries [1-3], the force amplitude being proportional to the difference of surface stress between the surface domains [3-6]. However, point forces induce local strain divergences, which are avoided by the introduction of an atomic cut-off length. Hu [7,8] stated that the concept of concentrated forces is only an approximation valid for infinite stiff substrates. Indeed if the substrate becomes deformed by the point forces acting at its surface, the substrate in turn deforms the surface and then leads to a new distribution of surface forces so that the surface forces have to be determined by a self-consistent analysis. In this paper, we show that when elastic surface properties are properly considered, the strain field induced by the surface domains may be expressed as the solution of a self-consistent integro-differential equation.

Results and Discussion

Let us consider (see Figure 1a) a semi-infinite body whose surface contains two domains (two infinite ribbons) A and B characterized by their own surface stress s^{A} and s^{B}. The 1D domain boundary is located at $x_{\mathrm{o}} = 0$. Note that for the sake of simplicity only the surface stress components s_1^i are taken to be different from zero (see Appendix I for the Voigt notation of tensors).

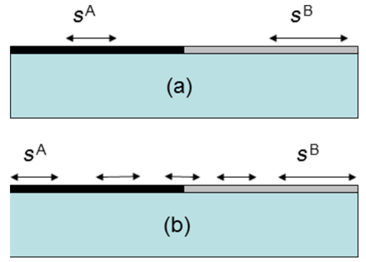

Figure 1: (a) Classical model in which each domain is characterized by its own supposedly constant surface stress. (b) When taking into account surface elasticity, the surface stress at mechanical equilibrium is no longer constant except far from the boundary.

In the classical approach [6-8] the strain field generated in the substrate is assumed to be generated by a line of point forces $\vec{f}(\vec{r}) = (f_x,0,0)\delta(x-x_0)$ (with $\delta(x)$ being the Dirac function) and is given by:

$$\varepsilon_1(x,z) = \int D_{xx}(x/x',z)\, f_x(x')\,dx' , \tag{1}$$

where $D_{xx}(x/x',z)$ is the xx component of the Green tensor and where the component $f_x(x) = \Delta s_1$ originates from the surface-stress difference $\Delta s_1 = s_1^{\mathrm{A}} - s_1^{\mathrm{B}}$ at the boundary between the two surface domains. The Green tensor valid for a semi-infinite isotropic substrate can be found in many text books [1,2,9] so that the deformation at the surface $\varepsilon_1(x,z = 0)$ finally reads:

$$\varepsilon_1(x,z=0) = -\frac{h\Delta s_1}{x}, \tag{2}$$

where $h = \left[2(1-\nu_{\mathrm{subs}}^2)\right]/(\pi E_{\mathrm{subs}})$ with E_{subs} and ν_{subs} being the Young modulus and the Poisson coefficient of the substrate (supposed to be cubic). The strain at the surface (Equation 2) exhibits a local divergence at the boundary $x = x_0 = 0$. The elastic energy can thus be calculated after introduction of an atomic cut-off length to avoid this local divergence [6,10].

However, the concept of point forces is only an approximation. If the substrate is deformed by point forces acting at its surface, the substrate in turn deforms the surface and then leads to a new distribution of surface forces. In the following, we consider that, due to the elastic relaxation, the surface stress at equilibrium exhibits a Hooke's-law-like behavior along the surface [9,11,12]:

$$s_1(x) = s_1^i + S_{11}^i\varepsilon_1(x,z=0), \tag{3}$$

with i = A, B according to whether x lies in region A or B. In Equation 3, s_1^i is the surface stress far from the domain boundary (or in other words the surface stress before elastic relaxation) and S_{11}^i the surface elastic constants properly defined in terms of excess quantities (see Appendix). The surface force distribution due to the surface stress variation (see Figure 1b) is obtained from force balance and reads $f_x(x,z = 0) = ds_1/dx$.

By using the Green formalism again, we obtain at the surface, $z = 0$:

$$\varepsilon_1(x,z=0) = -h\int_{-\infty}^{\infty} \frac{S_{11}\varepsilon_{1,x}(x',z=0)}{x-x'}dx' , \tag{4}$$

where $\varepsilon_{1,x} = d\varepsilon_1/dx$.

This equation replaces the classical result of Equation 2. Equation 4 is an integro-differential equation that has to be solved numerically. At mechanical equilibrium the absence of surface stress discontinuity at the domain boundary, $s_1(x_0^+) = s_1(x_0^-)$ combined to the constitutive Equation 3 leads to the following boundary condition

$$S_{11}^B\varepsilon_1(x_0^-) - S_{11}^A\varepsilon_1(x_0^+) = s_1^A - s_1^B . \tag{5}$$

When the elastic constants of the surface are positive, Equation 4 can be easily numerically integrated. Figure 2a shows (black dots) the result obtained by integration of Equation 4 with the boundary condition

$$\varepsilon_1(x_0^-) - \varepsilon(x_0^+) = (s_1^A - s_1^B)/S_{11}$$

that means for $S_{11}^A = S_{11}^B \equiv S_{11}$. We also plot in Figure 2a the classical result calculated from Equation 2 (continuous red curve). It is clearly seen that the new expression avoids the local strain divergence that is now replaced by a local strain jump $\Delta s_1/S_{11}$ at $x_0 = 0$.

Since the solutions of Equation 4 depend on the values of hS_{11} and Δs_1 we report in Figure 2b the results obtained for different typical values of hS_{11} and Δs_1 data obtained from [11]. More precisely, since the classical expression scales as $1/x$, we plot ln ε versus x. As can be seen, in the limit of large x all solutions tends towards the classical one (common red asymptote in Figure 2b). Moreover we can clearly see that the classical approach is recovered in the limit $S_{11} \rightarrow 0$.

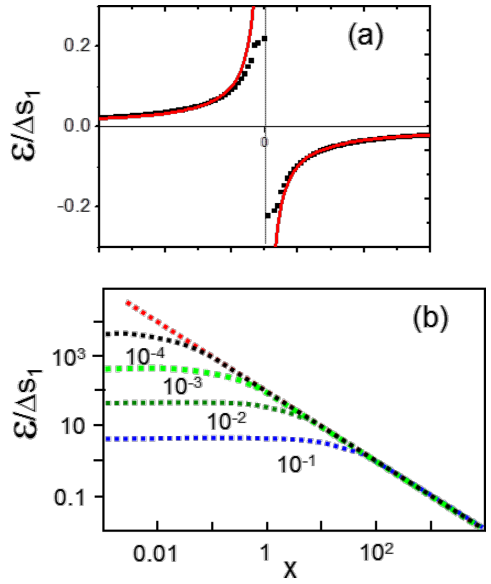

Figure 2: (a) Continuous (red) curve: normalised strain field $\varepsilon/\Delta s_1$ calculated with Equation 2, Black dots: normalised strain field $\varepsilon/\Delta s_1$ calculated from Equation 4 with $\Delta s_1/S_{11} = 0.4$ (b) ln–ln diagram of the normalised strain field $\varepsilon/\Delta s_1$ calculated from Equation 4 for hS_{11} varying from 10^{-1} to 10^{-4} (arbitrary units). The common asymptote is the classical result calculated from Equation 2.

The elemental solution of Equation 4 enables to describe more complex experimental configurations as the one that corresponds to the spontaneous formation of 1D periodic stripes by a foreign gas adsorbed on a surface (as for instance O/Cu(110) [13]). In the classical model each stripe (width $2d$) is modeled by two lines of point forces one located at d and the other at $-d$ with the opposite sign $f_x(x) = \Delta s_1(\delta(x - d) - \delta(x + d))$ so that for a set of periodic ribbons of the period L the elastic field is obtained by a simple superposition of the elemental solutions given in Equation 2. In the classical case it reads

$$\varepsilon_1(x, z=0) = h\Delta s_1 \frac{\pi}{L}\left\{\cot\left[\frac{\pi(x+d)}{L}\right] - \cot\left[\frac{\pi(x-d)}{L}\right]\right\}, \quad (6)$$

whereas within the new approach the elastic field is solution of the integral equation:

$$\varepsilon_1(x, z=0) = h\frac{\pi}{L}\int_0^{L/2} S_{11}\varepsilon_{1,x}(x', z=0)\times \left\{\cot\left[\frac{\pi(x+x')}{L}\right] - \cot\left[\frac{\pi(x-x')}{L}\right]\right\}dx'. \quad (7)$$

The results are shown in Figure 3 in which two cases are reported. In the first case $d/L = 1/2$, whereas in the second case $d/L = 3/10$. Again both solutions (classical and new approach) are quite similar since the only difference lies in the local divergences of the classical model (red curves in Figure 3) that are now replaced by local strain jumps.

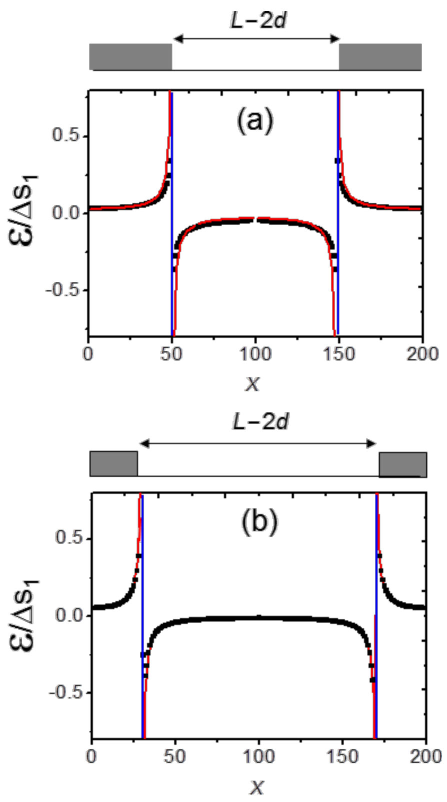

Figure 3: Normalised strain fields $\varepsilon/\Delta s_1$ calculated for 1-D periodic stripes. (a) $d/L = 1/2$, (b) $d/L = 3/10$. In both cases the continuous (red) curve corresponds to the classical solution of Equation 6 and black dots to the numerical solution of Equation 7. (Vertical blue lines correspond to the location of the ribbons edges sketched in grey in the upper part of the figures)

For surfaces with negative surface elastic constants Equation 4 does not present stable solutions. It is quite normal since in this case, the surface is no more stable by itself but is only stabilized by its underlying layers (see Appendix I). From a physical point of view it means that, for mechanical reasons, we have to consider a “thick surface” or, in other terms, that the surface has to be modeled as a thin film the thickness a of which corresponds to the smaller substrate thickness necessary to stabilize the body (bulk + surface). It can be shown that this is equivalent to modify the integro-differential equation for $S_{11} < 0$, by changing the kernel:

$$\bar{\varepsilon}_1(x) \approx -h\int_{-\infty}^{\infty} S_{11}(x')\bar{\varepsilon}_{1,x}(x')\frac{x-x'}{(x-x')^2+a^2}dx'. \quad (8)$$

In Figure 4 we show the result obtained from numerical integration of Equation 8 for the test value $hS_{11} = -0.01$. In this case $a = |2hS_{11}|$ is the minimum value necessary to stabilize Equation 8. Since s_1 is positive but S_{11} is negative, there is a sign inversion of ε close to the boundary. For vanishing a this local oscillation propagates on the surface and is at the origin of the instabilities that do not allow to find stable solutions to Equation 4. However we cannot exclude that the total energy of materials with $s_1S_{11} < 0$ could be reduced by some local morphological modifications of their surface. In such a case, the Green tensor used for this calculation should be inadequate.

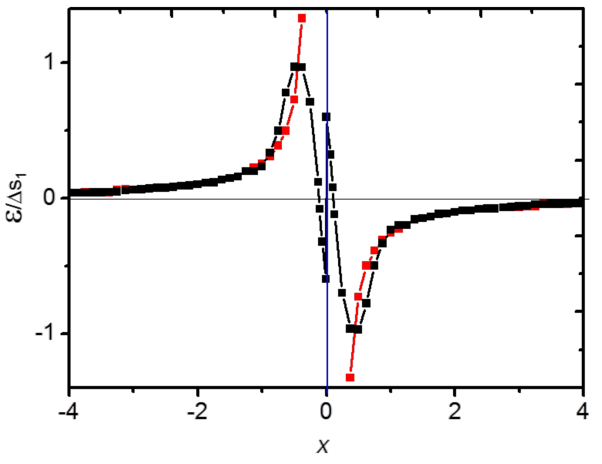

Figure 4: Black squares: normalised strain $\varepsilon/\Delta s_1$ solution of Equation 8 calculated for $\Delta s_1/S_{11} = 0.5$, red squares: classical solution plotted from Equation 2. (arbitrary units, vertical blue line corresponds to the location of the ribbons edges sketched in grey in the upper part of the figures).

In conclusion, the self-consistent approach expressed in terms of surface elastic constants is more satisfactory than the classical approach, particularly in the case of stable surfaces (characterized by positive surface elastic constants) for which there is no need to introduce a cut-off length. In case of unstable surfaces (negative surface elastic constants) a cut-off length is still necessary, its value is connected to the minimum substrate thickness necessary to stabilize the body (surface + underlying bulk). Even if the model only deals with 1D structures it can be generalized to other structures such as 2D circular domains. The so-obtained equations are less tractable but the main result remains the same (see Appendix II).

Appendix I: Surface elasticity

From a thermodynamic point of view all extensive quantities may present an excess at the interface between two media (for a review see [9]). For a system formed by a body facing vacuum the following excess quantities can be defined [9]:

the surface energy density: $$\gamma_0 = \frac{1}{A_0}\left(E\big|_{\varepsilon=0} - E^{\text{bulk}}_{\varepsilon=0}\right),$$

the surface stress components: $$s_{ij}^{(0)} = \frac{1}{A_0}\left(\left.\frac{\partial E}{\partial \varepsilon_{ij}}\right|_{\epsilon=0} - V_0\sigma_{ij}^{(0)}\right),$$

the surface elastic constants: $$S_{ijkl} = \frac{1}{A_0}\left(\left.\frac{\partial^2 E}{\partial \varepsilon_{ij}\partial \varepsilon_{kl}}\right|_{\epsilon=0} - V_0C_{ijkl}\right),$$

where

$$E = E_0 + \sum_{ij}\left.\frac{\partial E}{\partial \varepsilon_{ij}}\right|_{\varepsilon=0}\varepsilon_{ij} + \frac{1}{2}\sum_{ijkl}\left.\frac{\partial^2 E}{\partial \varepsilon_{ij}\partial \varepsilon_{kl}}\right|_{\varepsilon=0}\varepsilon_{ij}\varepsilon_{kl} \qquad (9)$$

is the second order strain development of the energy of a body of volume V_0 limited by a surface of area A_0 and

$$E^{\text{bulk}} = E_0^{\text{bulk}} + V_0\sum_{ij}\sigma_{ij}^{(0)}\varepsilon_{ij} + \frac{V_0}{2}\sum_{ijkl}C_{ijkl}\varepsilon_{ij}\varepsilon_{kl} \qquad (10)$$

is the second order development of a piece of body of same volume V_0 but without any surface. In these expressions $\sigma_{ij}^{(0)}$ are the bulk stress components and C_{ijkl} the bulk elastic constant.

The so-defined surface quantities depend on a typical length scale at which surface effects are disentangled from bulk effects. Actually, in surface energy calculations, this length is unambiguoulsy determined by a Gibbs dividing surface construction [14]. Surface stress and surface elastic constants values can thus be calculated from strain derivatives of the well-defined surface energy quantity [11].

In contrast to surface energy density and bulk elastic constants, surface stress components and surface elastic constants do not need to be positive. [9,11]. This does not violate the thermodynamical stability condition since actually a surface can only exist when it is supported by a bulk material. Hence the stability of the solid is ensured only by the total energy (surface + volume).

Finally, in the body of the paper we use the Voigt notation so that the surface stress can be written as the components of a 3D vector s = $(s_{xx},s_{yy},s_{xy}) = (s_1,s_2,s_6)$, while surface and bulk elastic constants are written as the components of 3D matrices S_{ij} and C_{ij}, respectively.

Appendix II: 2D circular domains

In case of a circular domain of radius R, the classical approach considers a force distribution $f_r(r) = \Delta s_0 \delta(r-R)$ that generates a displacement field expressed in terms of complete elliptic integrals $K(x)$ and $E(x)$ as:

$$u(r) = \frac{1-\nu^2}{\pi E} 4\Delta s_0 \begin{cases} \dfrac{R}{r}\left[K\left(\dfrac{r}{R}\right) - E\left(\dfrac{r}{R}\right)\right] & \text{if } r < R\,, \\ \left[K\left(\dfrac{R}{r}\right) - E\left(\dfrac{R}{r}\right)\right] & \text{if } r > R\,. \end{cases} \tag{11}$$

In the distributed force model, we use the stress-strain relations valid at the surface expressed in polar coordinates:

$$s_{rr} = s_{0,rr} + S_{11}\varepsilon_{rr} + S_{12}\varepsilon_{\theta\theta}\,, \tag{12}$$

$$s_{\theta\theta} = s_{0,\theta\theta} + S_{12}\varepsilon_{rr} + S_{11}\varepsilon_{\theta\theta}\,, \tag{13}$$

again with the Voigt notation in polar coordinates $A_{rr} \equiv A_r$, $A_{\theta\theta} \equiv A_\theta$.

By using the classical mechanical equilibrium equation $f_r + (s_{rr} - s_{\theta\theta}/r) + \partial s_{rr}/\partial r = 0$ and strain–displacement relations expressed in polar coordinates we obtain the following force distribution

$$f(r) = -f_r(r) = S_{11}\left\{u''(r) + \frac{u'(r)}{r} - \frac{u(r)}{r^2}\right\}. \tag{14}$$

The displacement can thus be obtained from the self-consistent equation (which replaces Equation 11)

$$u(r) = \frac{1-\nu^2}{\pi E} 4\Delta s_0 \begin{cases} \displaystyle\int_0^r ds f(s)\left[K\left(\frac{s}{r}\right) - E\left(\frac{s}{r}\right)\right] \\ \displaystyle + \int_r^R ds f(s)\frac{s}{r}\left[K\left(\frac{r}{s}\right) - E\left(\frac{r}{s}\right)\right] & \text{if } r < R\,, \\ \displaystyle\int_0^R ds f(s)\left[K\left(\frac{s}{r}\right) - E\left(\frac{s}{r}\right)\right] & \text{if } r > R\,. \end{cases} \tag{15}$$

The necessary boundary conditions, analog to Equation 5, must now be written for normal and tangential strains

$$s_{rr}\left(R^+\right) = s_{rr}\left(R^-\right), \tag{16}$$

$$s_0^A - s_0^B = S_{11}^A u'\left(R^-\right) + S_{12}^A \frac{u\left(R^-\right)}{R} - S_{11}^B u'\left(R^+\right) - S_{12}^B \frac{u\left(R^+\right)}{R}. \tag{17}$$

The integral equation for the displacement field, Equation 15, only needs the surface elastic constant S_{11}, but the edge condition introduces the need of the other surface elastic constant S_{12}. Qualitatively the result is similar to the one shown in Figure 2.

Acknowledgments

We thank A. Saul for fruitful discussions. This work has been done thanks to PICS grant No. 4843 and ANR 13 BS-000-402 LOTUS Grant.

References

1. Mindlin, R. D. *J. Appl. Phys.* **1936,** *7,* 195–202. doi:10.1063/1.1745385
2. Landau, L.; Lifshitz, E. *Theory of elasticity;* Pergamon Press: Oxford, United Kingdom, 1970.
3. Maradudin, A. A.; Wallis, R. F. *Surf. Sci.* **1980,** *91,* 423. doi:10.1016/0039-6028(80)90342-8
4. Marchenko, V. I. *J. Exp. Theor. Phys.* **1981,** *54,* 605–607.
5. Marchenko, V. I. *J. Exp. Theor. Phys.* **1981,** *33,* 381–383.
6. Alerhand, O. L.; Vanderbilt, D.; Meade, R. D.; Joannopoulos, J. D. *Phys. Rev. Lett.* **1988,** *61,* 1973–1976. doi:10.1103/PhysRevLett.61.1973
7. Hu, S. M. *J. Appl. Phys.* **1979,** *50,* 4661–4666. doi:10.1063/1.326575
8. Hu, S. M. *Appl. Phys. Lett.* **1978,** *32,* 5–7. doi:10.1063/1.89840
9. Müller, P.; Saúl, A. *Surf. Sci. Rep.* **2004,** *54,* 157. doi:10.1016/j.surfrep.2004.05.001
10. Kern, R.; Müller, P. *Surf. Sci.* **1997,** *392,* 103–133. doi:10.1016/S0039-6028(97)00536-0
11. Shenoy, V. B. *Phys. Rev. B* **2005,** *71,* 094104. doi:10.1103/PhysRevB.71.094104
12. Müller, P. Fundamentals of Stress and Strain at the Nanoscale Level: Toward Nanoelasticity. In *Mechanical Stress on the Nanoscale;* Hanbrücken, M.; Müller, P.; Wehrspohn, R. B., Eds.; Wiley-VCH Verlag GmbH & Co. KGaA: Weinheim, Germany, 2011; pp 27–59.
13. Kern, K.; Niehus, H.; Schatz, A.; Zeppenfeld, P.; Goerge, J.; Comsa, G. *Phys. Rev. Lett.* **1991,** *67,* 855–858. doi:10.1103/PhysRevLett.67.855
14. Nozières, P.; Wolf, D. E. *Z. Phys. B: Condens. Matter* **1988,** *70,* 399–407. doi:10.1007/BF01317248

License and Terms

BEILSTEIN JOURNAL OF NANOTECHNOLOGY

Nanoporous Ge thin film production combining Ge sputtering and dopant implantation

Jacques Perrin Toinin*[1,2], Alain Portavoce[2], Khalid Hoummada[1], Michaël Texier[1], Maxime Bertoglio[2], Sandrine Bernardini[1], Marco Abbarchi[1] and Lee Chow[3]

Full Research Paper

Open Access

Address:
[1]Aix-Marseille University, IM2NP, Faculté des Sciences de Saint-Jérôme case 142, 13397 Marseille, France, [2]CNRS, IM2NP, Faculté des Sciences de Saint-Jérôme case 142, 13397 Marseille, France and [3]Department of Physics, University of Central Florida, Orlando, FL 32816, USA

Email:
Jacques Perrin Toinin* - jacques.perrin-toinin@im2np.fr

* Corresponding author

Keywords:
germanium; ion implantation; porous material

Beilstein J. Nanotechnol. **2015,** *6,* 336–342.
doi:10.3762/bjnano.6.32

Received: 29 July 2014
Accepted: 12 January 2015
Published: 30 January 2015

This article is part of the Thematic Series "Self-assembly of nanostructures and nanomaterials".

Guest Editor: I. Berbezier

Abstract

In this work a novel process allowing for the production of nanoporous Ge thin films is presented. This process uses the combination of two techniques: Ge sputtering on SiO_2 and dopant ion implantation. The process entails four successive steps: (i) Ge sputtering on SiO_2, (ii) implantation preannealing, (iii) high-dose dopant implantation, and (iv) implantation postannealing. Scanning electron microscopy and transmission electron microscopy were used to characterize the morphology of the Ge film at different process steps under different postannealing conditions. For the same postannealing conditions, the Ge film topology was shown to be similar for different implantation doses and different dopants. However, the film topology can be controlled by adjusting the postannealing conditions.

Introduction

Porous materials are of great interest for a large scope of industrial applications dealing with adsorption, catalysis, or molecular filtration and isolation. Furthermore, porous semiconductors can exhibit interesting properties for optoelectronic applications. For example, porous Si was shown to exhibit an increased band gap compared to bulk Si due to quantum (Q) size effects, related either to the formation of pseudo Q-wires or Q-dots in the porous structure, depending on the production method [1].

Generally, porous Si photoluminescence data can be interpreted either with a Q-wire model, or a model between the Q-wire and Q-dot models [2]. Porous Si optoelectronic properties were shown to be mainly determined by the "skeleton size" of the material and not by the pore sizes. However, in some cases, controlling the pore size allows for the control of the skeleton size, and thus should allow semiconductor band gap engineering, where the aim is the design of devices able to absorb or emit light at a tunable wavelength. Efficient visible electroluminescence has been achieved with porous Si for different wavelengths (red–green). Si and Ge are indirect gap materials, requiring phonon scattering for optical absorption/emission to take place. However, Q-size effects present in porous semiconductors can promote optical transitions without the need of phonons by breaking the momentum conservation rules and/or by making the material quasi-direct through the process of Brillouin zone folding [3]. For example, non-phonon processes were shown to dominate in the case of porous Si under strong confinement potential [4-6]. In addition, Q-effects in porous semiconductors can be interesting for photovoltaic applications, since they can lead to multiple exciton generation [7]. In particular, multiple exciton generation has been previously demonstrated in Si nanostructures [8].

Ge has a similar structure to Si, however, it offers several benefits compared to Si such as faster carrier mobility, smaller band gap and lower process temperatures [9]. In addition, the Ge exciton Bohr radius (≈24 nm) is significantly larger than that of Si (≈4.5 nm), allowing for quantum effects to appear in nanostructures exhibiting larger sizes [10], and allowing the k-selection rules to be broken. For example, lasing has only been observed in Ge for the case of strained [11] and doped [12] Ge layers. Furthermore, in addition to its small indirect band gap (≈0.66 eV), Ge exhibits a larger direct band gap (≈0.80 eV) that could promote non-phonon optical transitions if n-type doping of about 10^{20} cm^{-3} could be achieved in Ge. Since Ge is compatible with complementary metal oxide semiconductor (CMOS) technology, the production of porous Ge thin films could be used for integration of optoelectronic devices in Si microelectronic technology.

The production of porous Ge can be performed using several techniques such as anodization and electrochemical etching, spark processing or inductively coupled plasma chemical vapor deposition [13-15].

Ion implantation is a well-known technique used in the microelectronic industry to dope the active regions of semiconductor devices. Generally, implantation leads to the formation of defects of different nature in the material (vacancy, dislocation, amorphization, etc.). High-dose implantations in Ge (>10^{15} atoms/cm^2) have been reported to induce the formation of nanoporous structures [16-25]. Thus, ion implantation may be a simple way to produce a nanoporous semiconductor.

In the present work, the impact of high dose selenium and tellurium (3.5×10^{15} atoms/cm^2) implantations on the morphology of polycrystalline Ge thin films is presented, as well as the evolution of the film morphology with thermal annealing conditions (temperature and time).

Results and Discussion

340 nm thick Ge layers were deposited on the native oxide layer of a silicon substrate at room temperature (RT), under high vacuum, by magnetron sputtering. Recrystallization was then performed by rapid thermal annealing at 600 °C under vacuum ($P \approx 3 \times 10^{-5}$ mbar) and the Ge layer was implanted under vacuum ($P \approx 2 \times 10^{-6}$ mbar). Three types of implantations were performed: (i) the first set of samples were implanted with a 3.6×10^{15} atoms/cm^2 dose of Se atoms with an energy of 130 keV, (ii) the second set of samples were implanted with a 3.1×10^{15} atoms/cm^2 dose of Te atoms with an energy of 180 keV, and (iii) the last set of samples were co-implanted with both Se and Te atoms under the same conditions as previously mentioned. Figure 1 shows the predicted dopant and vacancy concentration profiles induced by implantation using the Stopping and Range of Ions in Matter (SRIM) software. This software is used in the ion implantation research and technology community to predict implantation profiles as well as implantation-induced defect distributions given the implantation energy, the nature of the implanted species, and the nature of the substrate [26]. The calculations are based on the classical theories of the stopping of ions in matter and Monte Carlo simulations: the energy loss of ions in matter are calculated and used to provide stopping powers, range and straggling distributions of implanted ions. In addition, the kinetic effects associated with the physics of implantation-mediated defects are also taken into account, allowing the distribution of point defects created in the target material to be obtained [27,28].

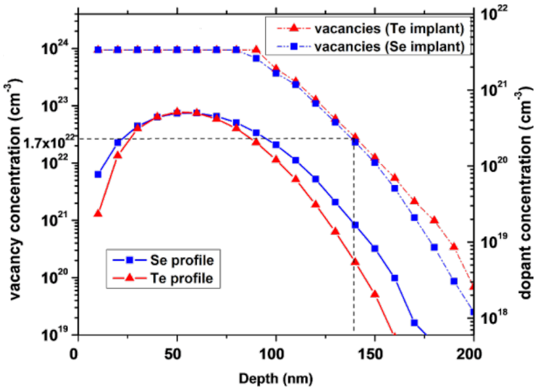

Figure 1: SRIM calculations of the implant distribution of Te (red) and Se (blue) atoms in Ge. The distributions of implanted ions are shown using straight lines on the right axis and the vacancies distributions are shown using dashed lines on the left axis.

Table 1: Surface density and average lateral size of the different implantation-induced defects versus implanted species.

Defect type	Property	Cluster	Hole	Porous structure
Se implantation	Average size (nm)	360 ± 2	70 ± 4	32 ± 2
	Density (×10^6 cm^{-2})	$4.2 \times 10^1 \pm 3.5$	$1 \times 10^3 \pm 70$	$5.49 \times 10^4 \pm 2.5 \times 10^2$
Te implantation	Average size (nm)	520 ± 8	120 ± 1	33 ± 2
	Density (×10^6 cm^{-2})	3 ± 1	$5.7 \times 10^2 \pm 90$	$4.35 \times 10^4 \pm 2.5 \times 10^2$
Se and Te co-implantation	Average size (nm)	540 ± 3	130 ± 3	40 ± 1
	Density (×10^6 cm^{-2})	$3.7 \times 10^1 \pm 4$	$5.69 \times 10^2 \pm 90$	$3.70 \times 10^4 \pm 1 \times 10^2$

The dopant distributions follow a Gaussian distribution with a maximum concentration of 5×10^{20} atoms/cm^3 located at a depth of 55 nm. Given that the more Ge-rich, Ge–Se compound is GeSe [29] and the only Ge–Te compound is GeTe [30], the presently studied implantations (exhibiting a maximum concentration level of about 1%) are not expected to allow the formation of a full compound layer. However, the formation of small Ge-dopant clusters is possible (the Se–Te binary system is fully miscible, corresponding to an ideal solution [31]). Usually, a damage energy higher than 5 eV/atoms[1] corresponding to a vacancy concentration of $\approx 1.7 \times 10^{22}$ vac/cm^3 leads to Ge amorphization [32]. Thus, the SRIM calculations predict the formation of an amorphous Ge layer from the surface of the Ge film up to a depth of 140 nm. One can observe in Figure 1 that no dopants and no vacancies are expected to be found at a depth larger than 220 nm. Consequently, the implantation-induced defects should be confined in the Ge layer thickness.

Figure 2 presents scanning electron microscopy (SEM) plan-view images of the as-implanted Se sample. The implantation induces the formation of three types of defects, randomly distributed on or in the germanium layer: (i) large clusters of Ge oxide with an average lateral size of ≈400 nm (composition analyzed by atom probe tomography, not reported here), (ii) holes with an average lateral size of ≈100 nm, and (iii) a nanoporous structure exhibiting pores with an average lateral size of ≈35 nm. The same three types of defects are observed in all the three sets of samples.

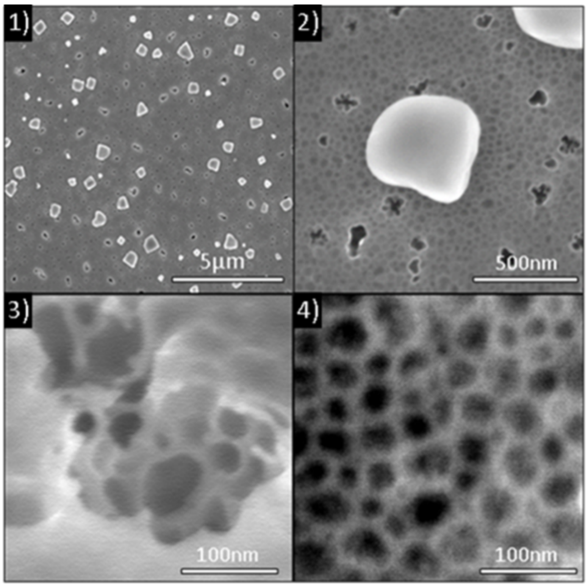

Figure 2: SEM plan-view images of the as-implanted Se sample: (1) low resolution view showing the different types of defects; (2) a single GeO$_x$ cluster; (3) the structure of holes; and (4) the nanoporous structure.

The average size and the density of these defects are reported in Table 1. An increase of the size of holes and of the clusters can be noticed between the Se-only implanted sample and the other sets of samples (60% for holes and 70% for clusters). However, the impact of the co-implantation is limited compared to the individual implantations. Furthermore, it can be noted that the porous structure is independent of the implantation type. Thus, variation in the defects appears to be dependent on the mass and the energy of the implanted species, but independent of the implanted dose.

Various thermal postannealing treatments were performed after ion implantation. For a better understanding of the evolution of the film morphology with the thermal treatments, the different annealing treatments are compared using a reference scale defined as the thermal budget (TB) based on the surface diffusion length of Ge atoms on the silicon (111) surface described by:

$$L = \sqrt{D(T) \times t}, \qquad (1)$$

where L is the Ge surface diffusion length (cm), and $D = 0.06 \times \exp(-2.47\ \text{eV}/kT)$ is the Ge surface diffusion coefficient (cm^2 s^{-1}) on Si [33], depending on both the temperature and the annealing time, t. Table 2 presents the annealing parameters. One can distinguish three ranges of thermal treatments: (i) a low annealing TB with TB = 3.1 µm, (ii) an intermediate TB between 3.9 µm and 4.8 µm, and (iii) a high TB = 8.7 µm.

Table 2: Thermal annealing conditions (temperature and time), and corresponding thermal budgets.

Thermal budget	Low → High				
Temperature (°C)	525	625	675	575	725
Time (h)	168	5	1	48	1
Diffusion length (µm)	3.1	3.9	4.1	4.8	8.7

Figure 3 presents the influence of the thermal annealing on the morphology of the co-implanted Se/Te sample. Thermal treatments induce large modifications of the implantation-induced defect morphology. For 4.1 ≤ TB ≤ 4.8 µm (Figure 3.2 and 3.3), the GeO_x clusters initially observed on the as-implanted film surface (Figure 3.1) vanished during annealing. Instead, large holes can be observed (Figure 3.2), with a depth as deep as the Ge film thickness. These holes exhibit the same size and the same surface density as the initial clusters, leading to the conclusion that they are actually located on the surface sites initially occupied by a GeO_x cluster. The initial holes present in the as-implanted film still exist after annealing. However, the initial nanoporous structure experienced a morphology modification leading to an increase of the pore size. In addition, new types of clusters appeared on the surface (Figure 3.3). They are characterized by a surrounding trench that is typical of crystal growth which uses the surrounding material and is limited by atomic surface diffusion. At this thermal budget, a three-scale porous structure is obtained with (i) large holes linked to the disappearance of the GeO_x clusters (average lateral size ≈500 nm), (ii) the holes initially present in the as-implanted samples (average lateral size ≈100 nm), and (iii) the modified nanoporous structure (average lateral size ≈50 nm). For the highest thermal budget (TB = 8.7 µm, Figure 3.4), the structure of the Ge film is greatly modified. One can observe the disappearance of both the holes and the nanoporous structure. Instead, the SEM plan-view analysis (Figure 3.4) reveals the growth of faceted crystallites, with an average lateral size of 700 nm for the Se-implanted sample and of 1600 nm for the co-implanted sample, and a complex surface structure between these crystallites. Indeed, some parts of the surface exhibit large roughness, while some others appear completely flat (black contrast in Figure 3.4). This phenomenon can be explained considering that these crystallites result from the Ge dewetting mechanism occurring on the buried SiO_2 layer already observed in Figure 3.3. The general dewetting phenomenon is due to surface/interface energy minimization between the film and the substrate, leading to island formation or agglomeration at a temperature below the melting temperature of the film material. This phenomenon is generally undesirable in the field of micro- or nano-technology [34] yet has been reported to be interesting for the fabrication of nanocrystals. A wide range of materials can be used for the fabrication of nanocrystals by dewetting, such as metals or semiconductors. In addition, the structure of the dewetted layers can be controlled using several techniques such as pulsed laser annealing [35,36] or a substrate patterned by focused ion beam. The study of Ge dewetting on SiO_2 [37] has already been reported in the literature, however, only in the case of very thin amorphous Ge layers (5−15 nm thick) [38-40]. For a large TB, the atomic diffusion length on the surface is significant, and during dewetting, Ge atoms can form large crystallites. In this case, between the crystallites, the very flat parts of the surface correspond to the flat SiO_2 layer that is revealed due to the dewetting phenomenon, while the rough parts of the surface correspond to the surface regions where the dewetting phenomenon is incomplete.

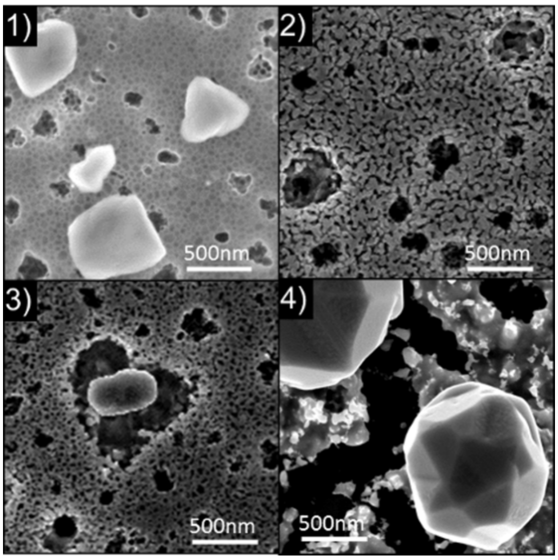

Figure 3: Thermal annealing effects on the co-implanted Se/Te sample: (1) as-implanted, (2) TB = 4.1 µm; (3) TB = 4.8 µm; and (4) TB = 8.7 µm.

The cross-sectional analysis shown in Figure 4 gives interesting information about the observed implantation-induced defects, and confirms the evolution of the nanoporous structure and the holes between the lowest thermal budget (TEM analysis, Figure 4.1 and 4.2) and TB = 4.8 µm (SEM analysis, Figure 4.3).

A detailed analysis of the images indicates that the brightest areas (identified as being GeO_x clusters) correspond to amorphous materials that are in contact with the buried native SiO_2

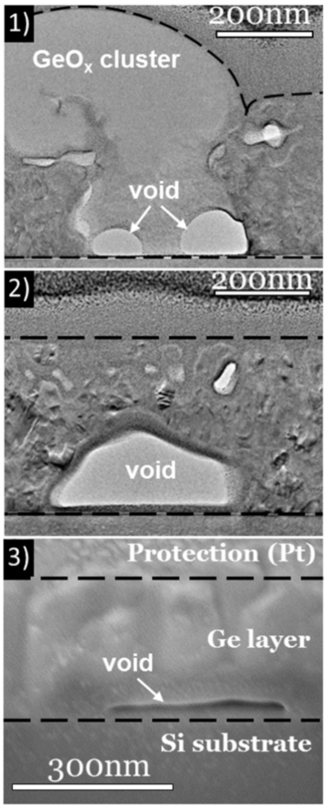

Figure 4: (1) and (2) TEM cross-sectional view of the Se-implanted sample after annealing with TB = 3.1 µm. (3) SEM cross-sectional view of the Se-implanted sample after annealing with TB = 4.8 µm.

layer, present through the entire Ge layer thickness. Therefore, the disappearance of the GeO$_x$ clusters can be explained by the complete evaporation of the GeO$_x$ during annealing, leaving deep holes in the Ge film. The image contrast is affected by the variation of both local diffraction conditions and absorption. The moiré pattern visible in various areas of the deposited layer confirms its polycrystalline structure. The pores are difficult to observe in the cross-sectional view due to the superimposition of the structure in the analysis and due to the filling of the pores by the protective Pt layer, however, the various Ge nanograins (≤50 nm) exhibiting different orientations are easily observed. The SEM cross-sectional view of the sample with a TB = 4.8 µm (Figure 4.3) shows the porosity enlargement of the porous structure compared to lower TB (Figure 4.2). In addition to the implantation-induced defects identified in plan-view observations, cross-sectional observations show the existence of cavities at the Ge/SiO$_2$ interface (Figure 4.1 and 4.2). These cavities present facets when in contact with polycrystalline Ge, and present a spherical shape when in contact with amorphous GeO$_x$. They can be related to the initial Ge dewetting mechanism, and thus, are expected to form during annealing.

Figure 5.1 presents an SEM plan-view image obtained on a 340 nm thick Ge film without implantation, but annealed in an RTP furnace at $T \approx 650$ °C for 20 min. One can note that even without implantation, the Ge film is dewetted on the SiO$_2$ layer, exhibiting a net shape. Consequently, the dewetting phenomenon should play a significant role in the atomic redistribution observed during annealing of implanted films. However, the structure obtained with the as-deposited Ge films (Figure 5.1) is quite different from the structure obtained with implanted films (Figure 3 and Figure 5.2). Consequently, the implantation process, and possibly the nature of the implanted dopants (Ge-dopant cluster formation, surface and interface segregation, etc.) as well as their atomic diffusion mechanism in the bulk and on the surface of the Ge film, have a significant effect on the Ge dewetting phenomenon. For example, the cavity formation at the Ge/SiO$_2$ interface could be also related to the diffusion mechanism of Se and Te atoms [41].

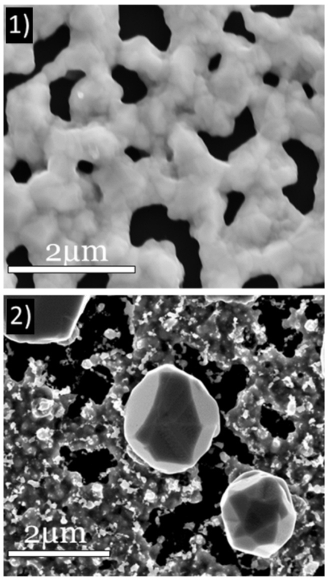

Figure 5: SEM plan-view image obtained after annealing a 340 nm thick Ge layer sputtered on the native Si oxide of a Si(001) substrate: (1) without implantation and TB = 0.64 µm; and (2) with Se implantation and TB = 8.7 µm.

Conclusion

The fabrication of highly-doped, porous Ge thin films (which are of high potential use for optoelectronic device fabrication) was successfully achieved using experimental techniques compatible with Si CMOS technology.

High-dose (>10^{15} atoms/cm^2) dopant implantations (Se and Te) have been performed in polycrystalline Ge films deposited on the native Si oxide. These implantations induced the formation of three types of defects in the Ge film: (i) large GeO$_x$ clusters,

(ii) holes, and (iii) nanopores (≈35 nm wide). Under thermal annealing (i) the large GeO_x clusters disappear leaving large pores (≈400 nm wide) in the film, (ii) the initial holes stay quasi-unchanged in the film, forming ≈100 nm wide pores, and (iii) the size of the nanopores increases (≈50 nm wide). In addition, cavities can form at the Ge/SiO_2 interface with a lateral size of between 100 and 200 nm. At high thermal budget, the film is completely fragmented with the formation of large Ge islands (≈1 µm wide). These phenomena can be explained by the combination of several mechanisms. Among them, the Ge dewetting on the SiO_2-buried layer is the most obvious. However, the influence of the nature of the implanted dopants (bulk and surface diffusion) and the possible formation of Ge-dopant nanoclusters can also have a significant effect on the observed atomic redistribution. The careful control of thermal annealing conditions should allow the control of the size and of the distribution of the pores, allowing for the production of Ge nanoporous films exhibiting characteristic skeleton sizes smaller (≈10 nm, without annealing) or larger (≈50 nm, annealing at 675 °C for 1 h) than the Ge-exciton Bohr radius, depending on the desired applications.

Experimental

The Ge layers were deposited on the native silicon oxide of a (001) silicon wafer by magnetron sputtering in a commercial set up with a deposition chamber exhibiting a base pressure of $\approx 10^{-8}$ mbar. The first thermal annealing executed after Ge deposition was performed in a commercial Jetfirst 600 Rapid Thermal Annealing furnace under a vacuum of 2×10^{-5} mbar at $T = 600$ °C for 20 min. The samples were implanted with a dose of 3.6×10^{15} atoms/cm^2 using the industrial implanter IMC200 developed by the company IBS. The implantations were performed under a pressure of 2×10^{-6} mbar at an angle of 7° with respect to the normal of the sample surface, and with an ion beam energy of 130 keV for Se^+ ions and of 180 keV for Te^+ ions. After implantation, the samples were annealed in different conditions ($1 \leq t \leq 168$ h and $525 \leq T \leq 725$ °C) in a custom-built furnace under a pressure of 1×10^{-7} mbar during annealing.

TEM images were performed using a FEI Titan 80-300 Cs-corrected microscope operating at 200 kV under multibeam conditions with the Ge substrate aligned along the <110> crystallographic direction. The spherical aberration was tuned to −15 µm to both optimize the spatial resolution and reduce the spatial delocalization [42].

SEM images were performed using a FEI Helios 600 Nanolab microscope in the secondary electron (SE) mode with an accelerating voltage of 5 kV, using either an Everhart–Thornley Detector (ETD) located below the objective lens for imaging at low magnifications, or using a through lens detector (TLD) placed within the objective lens for capturing high-resolution images. In this mode, the image contrast is mainly affected by topographic variations allowing the presence of holes and asperities at the sample surface to be evidenced. The lateral size and the density were analyzed manually from the SEM images using the ImageJ software developed at the National Institute of Health. The errors in the measurements can be estimated with the original SEM image resolution.

Acknowledgements

The authors thank Marion Descoins for technical support. This work was supported by the French National Agency for Research (ANR) through the Program “Science de l’ingénierie” (Project DoGeTec, No. ANR-12-JS09-0015-1).

References

1. Schuppler, S.; Friedman, S. L.; Marcus, M. A.; Adler, D. L.; Xie, Y.-H.; Ross, F. M.; Chabal, Y. J.; Harris, T. D.; Brus, L. E.; Brown, W. L.; Chaban, E. E.; Szajowski, P. F.; Christman, S. B.; Citrin, P. H. *Phys. Rev. B* **1995,** *52,* 4910. doi:10.1103/PhysRevB.52.4910
2. Barbagiovanni, E. G.; Lockwood, D. J.; Simpson, P. J.; Goncharova, L. V. *Appl. Phys. Rev.* **2014,** *1,* 011302. doi:10.1063/1.4835095
3. Iyer, S. S.; Xie, Y.-H. *Science* **1993,** *260,* 40. doi:10.1126/science.260.5104.40
4. Hybertsen, M. S. *Phys. Rev. Lett.* **1994,** *72,* 1514. doi:10.1103/PhysRevLett.72.1514
5. Kovalev, D.; Heckler, H.; Ben-Chorin, M.; Polisski, G.; Schwartzkopff, M.; Koch, F. *Phys. Rev. Lett.* **1998,** *81,* 2803. doi:10.1103/PhysRevLett.81.2803
6. Kovalev, D.; Heckler, H.; Polisski, G.; Diener, J.; Koch, F. *Opt. Mater.* **2001,** *17,* 35. doi:10.1016/S0925-3467(01)00017-9
7. Nozik, A. J. *Nat. Photonics* **2012,** *6,* 272. doi:10.1038/nphoton.2012.78
8. Beard, M. C.; Knutsen, K. P.; Yu, P.; Luther, J. M.; Song, Q.; Metzger, W. K.; Ellingson, R. J.; Nozik, A. J. *Nano Lett.* **2007,** *7,* 2506. doi:10.1021/nl071486l
9. Sze, S. M. *Physics of Semiconductor Devices,* 2nd ed.; Wiley-VCH: Berlin, 1981.
10. Barbagiovanni, E. G.; Lockwood, D. J.; Simpson, P. J.; Goncharova, L. V. *J. Appl. Phys.* **2012,** *111,* 034307. doi:10.1063/1.3680884
11. Süess, M. J.; Geiger, R.; Minamisawa, R. A.; Schiefler, G.; Frigerio, J.; Chrastina, D.; Isella, G.; Spolenak, R.; Faist, J.; Sigg, H. *Nat. Photonics* **2013,** *7,* 466. doi:10.1038/nphoton.2013.67
12. Liu, J.; Sun, X.; Camacho-Aguilera, R.; Kimerling, L. C.; Michel, J. *Opt. Lett.* **2010,** *35,* 679. doi:10.1364/OL.35.000679
13. Choi, H. C.; Buriak, J. M. *Chem. Commun.* **2000,** 1669–1670. doi:10.1039/B004011H
14. Chang, S.-S.; Hummel, R. E. *J. Lumin.* **2000,** *86,* 33–38. doi:10.1016/S0022-2313(99)00179-9
15. Ko, T. S.; Shieh, J.; Yang, M. C.; Lu, T. C.; Kuo, H. C.; Wang, S. C. *Thin Solid Films* **2008,** *516,* 2934–2938. doi:10.1016/j.tsf.2007.06.023.
16. Wilson, I. H. *J. Appl. Phys.* **1982,** *53,* 1698. doi:10.1063/1.331636
17. Wang, L. M.; Birtcher, R. C. *Appl. Phys. Lett.* **1989,** *55,* 2494. doi:10.1063/1.102009

18. Stritzker, B.; Elliman, R. G.; Zou, J. *Nucl. Instrum. Methods Phys. Res., Sect. B 175–177,* 193–196. doi:10.1016/S0168-583X(00)00597-8
19. Wang, L. M.; Birtcher, R. C. *Philos. Mag. A* **1991,** *64,* 1209. doi:10.1080/01418619108225344
20. Holland, O. W.; Appleton, B. R.; Narayan, J. *J. Appl. Phys.* **1983,** *54,* 2295. doi:10.1063/1.332385
21. Ottaviano, L.; Verna, A.; Grossi, V.; Parisse, P.; Piperno, S.; Passacantando, M.; Impellizzeri, G.; Priolo, F. *Surf. Sci.* **2007,** *601,* 2623–2627. doi:10.1016/j.susc.2006.11.075
22. Romano, L.; Impellizzeri, G.; Tomasello, M. V.; Giannazzo, F.; Spinella, C.; Grimaldi, M. G. *J. Appl. Phys.* **2010,** *107,* 084314. doi:10.1063/1.3372757
23. Janssens, T.; Huyghebaert, C.; Vanhaeren, D.; Winderickx, G.; Satta, A.; Meuris, M.; Vandervorst, W. *J. Vac. Sci. Technol., B* **2006,** *24,* 510. doi:10.1116/1.2151904
24. Romano, L.; Impellizzeri, G.; Bosco, L.; Ruffino, F.; Miritello, M.; Grimaldi, M. G. *J. Appl. Phys.* **2012,** *111,* 113515. doi:10.1063/1.4725427
25. Darby, B. L.; Yates, B. R.; Rudawski, N. G.; Jones, K. S.; Kontos, A.; Elliman, R. G. *Thin Solid Films* **2011,** *519,* 5962–5965. doi:10.1016/j.tsf.2011.03.040
26. Particle interactions with matter. http://srim.org (accessed Dec 8, 2014).
27. Ziegler, J. F.; Biersack, J. P.; Littmark, U. *The Stopping and Range of Ions in Solids;* Pergamom: New York, 1985.
28. Ziegler, J. F. *Nucl. Instrum. Methods Phys. Res., Sect. B* **2004,** *219–220,* 1027. doi:10.1016/j.nimb.2004.01.208
29. Ipser, H.; Gambino, M.; Schuster, W. *Monatsh. Chem.* **1982,** *113,* 389–398. doi:10.1007/BF00799914
30. Okamoto, H. *J. Phase Equilib.* **2000,** *21,* 496. doi:10.1361/105497100770339789
31. Ghosh, G.; Sharma, R. C.; Li, D. T.; Chang, Y. A. *J. Phase Equilib.* **1994,** *15,* 213–224. doi:10.1007/BF02646370
32. Claverie, A.; Koffel, S.; Cherkashin, N.; Benassayag, G.; Scheiblin, P. *Thin Solid Films* **2010,** *518,* 2307–2313. doi:10.1016/j.tsf.2009.09.162
33. Allen, C. E.; Ditchfield, R.; Seebauer, E. G. *Phys. Rev. B* **1997,** *55,* 13304. doi:10.1103/PhysRevB.55.13304
34. Thompson, C. V. *Annu. Rev. Mater. Res.* **2012,** *42,* 1–36. doi:10.1146/annurev-matsci-070511-155048
35. Trice, J.; Thomas, D.; Favazza, C.; Sureshkumar, R.; Kalyanaraman, R. *Phys. Rev. B* **2007,** *75,* 235439. doi:10.1103/PhysRevB.75.235439
36. Ruffino, F.; Pugliara, A.; Carria, E.; Romano, L.; Bongiorno, C.; Spinella, C.; Grimaldi, M. G. *Nanotechnology* **2012,** *23,* 045601. doi:10.1088/0957-4484/23/4/045601
37. Abbarchi, M.; Naffouti, M.; Vial, B.; Benkouider, A.; Lermusiaux, L.; Favre, L.; Ronda, A.; Bidault, S.; Berbezier, I.; Bonod, N. *ACS Nano* **2014,** *8,* 11181–11190. doi:10.1021/nn505632b
38. Szkutnik, P. D.; Karmous, A.; Bassani, F.; Ronda, A.; Berbezier, I.; Gacem, K.; El Hdiy, A.; Troyon, M. *Eur. Phys. J.: Appl. Phys.* **2008,** *41,* 103–106. doi:10.1051/epjap:2008006
39. Gacem, K.; El Hdiy, A.; Troyon, M.; Berbezier, I.; Ronda, A. *Nanotechnology* **2010,** *21,* 065706. doi:10.1088/0957-4484/21/6/065706
40. Berbezier, I.; Aouassa, M.; Ronda, A.; Favre, L.; Bollani, M.; Sordan, R.; Delobbe, A.; Sudraud, P. *J. Appl. Phys.* **2013,** *113,* 064908. doi:10.1063/1.4790713
41. De Luca, A.; Portavoce, A.; Texier, M.; Grosjean, C.; Burle, N.; Oison, V.; Pichaud, B. *J. Appl. Phys.* **2014,** *115,* 013501. doi:10.1063/1.4859455
42. Texier, M.; Thibault-Pénisson, J. *Micron* **2012,** *43,* 516. doi:10.1016/j.micron.2011.09.014

License and Terms

BEILSTEIN JOURNAL OF NANOTECHNOLOGY

Carrier multiplication in silicon nanocrystals: ab initio results

Ivan Marri*[1], Marco Govoni*[2,3] and Stefano Ossicini[1]

Full Research Paper

Open Access

Address:
[1]Department of Science and Methods for Engineering (DISMI), via Amendola 2, Pad. Morselli, 42122 Reggio Emilia, Italy, [2]Department of Physics, University of Modena and Reggio Emilia, via Campi 213/a, 41125 Modena, Italy and [3]present address: Institute for Molecular Engineering, The University of Chicago, 5555 South Ellis Avenue, Chicago, Illinois 60637, United States

Email:
Ivan Marri* - marri@unimo.it; Marco Govoni* - mgovoni@uchicago.edu

* Corresponding author

Keywords:
carrier multiplication; nanocrystals; silicon; solar cells

Beilstein J. Nanotechnol. **2015,** *6,* 343–352.
doi:10.3762/bjnano.6.33

Received: 17 July 2014
Accepted: 30 December 2014
Published: 02 February 2015

This article is part of the Thematic Series "Self-assembly of nanostructures and nanomaterials".

Guest Editor: I. Berbezier

Abstract

One of the most important goals in the field of renewable energy is the development of original solar cell schemes employing new materials to overcome the performance limitations of traditional solar cell devices. Among such innovative materials, nanostructures have emerged as an important class of materials that can be used to realize efficient photovoltaic devices. When these systems are implemented into solar cells, new effects can be exploited to maximize the harvest of solar radiation and to minimize the loss factors. In this context, carrier multiplication seems one promising way to minimize the effects induced by thermalization loss processes thereby significantly increasing the solar cell power conversion. In this work we analyze and quantify different types of carrier multiplication decay dynamics by analyzing systems of isolated and coupled silicon nanocrystals. The effects on carrier multiplication dynamics by energy and charge transfer processes are also discussed.

Introduction

An important challenge in modern day scientific research is the establishment of clean, inexpensive, renewable energy sources. Based on the extraction of energy from the solar spectrum, photovoltaics (PV) is one of the most appealing and promising technologies in this regard. Intense effort is focused on increasing solar cell performance through the minimization of loss factors and the maximization of solar radiation harvesting. This is accomplished by improving the optoelectronic properties of existing devices and by realizing new schemes for innovative solar cell systems. For optimal energy conversion in PV devices, one important requirement is that the full energy of the solar spectrum is used. In this context, the development of third generation nanostructured solar cells appears as a promising way to realize new systems that can overcome the limitations of traditional, single junction PV devices. The possibility of exploiting features that derive from the reduced dimensionality of the nanocrystalline phase, and in particular, features induced by the quantum confinement effect [1-5] can lead to a better use of the carrier excess energy, and can increase solar cell thermodynamic conversion efficiency over the Shockley–Queisser (SQ) limit [6]. In this context, carrier multiplication (CM) can be exploited to maximize solar cell performance, promoting a net reduction of loss mechanisms. CM is a Coulomb-driven, recombination process that occurs when a highly excited carrier (excess energy of the excited carrier is higher than the band gap energy, E_g) decays to a lower energy state by transferring its excess energy to generate extra e–h pairs. When CM involves states of the same nanostructure, the effect is termed one-site CM. Because of the restrictions imposed by energy and momentum conservation and by fast phonon relaxation processes, CM is often inefficient in bulk semiconductors. On the nanoscale, CM is favored (a) by quantum confinement that enhances the carrier–carrier Coulomb interaction [7], (b) by the lack of restrictions imposed by the conservation of momentum [8] and, in some cases, (c) by the so-called “phonon bottleneck” effect [9,10] that reduces the probability of exciton relaxation by phonon emission. These conditions make the formation of multiple e–h pairs after absorption of high energy photons more likely to occur in low-dimensional nanostructures. Consequently, at the nanoscale CM can be as fast as (or faster than) phonon scattering processes and Auger cooling mechanisms [11]. Therefore, CM represents an effective way to minimize energy loss factors and constitutes a possible route for increasing solar cell photocurrent, and hence, to increase solar cell efficiency. Effects induced by CM on the excited carrier dynamics have been observed in a wide range of systems, for instance PbSe and PbS [12-16], CdSe and CdTe [17-19], PbTe [20], InAs [21], InP [22] and Si [23]. These effects have been studied using different theoretical approaches [21,24-30] although only recently was a full ab initio interpretation of CM proposed [31]. Recently, a relevant photocurrent enhancement arising from CM was observed in a PbSe-based, quantum dot (QD) solar cell [32], which proves the possibility of exploiting CM effects to improve solar cell performance. In this context, the possibility to use the non-toxic and largely diffused silicon instead of lead-based materials can be advantageous to the future development of QD-based solar cell devices. A new CM scheme was recently hypothesized by Timmerman et al. [33-35] and by Trinh et al. [36] in order to explain results obtained in photoluminescence (PL) and induced absorption (IA) experiments conducted on dense arrays of silicon nanocrystals (Si-NCs, NC–NC separation ≤ 1 nm). In the first set of experiments, the authors proved that although the excitation cross-section is wavelength-dependent and increases for shorter excitation wavelengths, the maximum time-integrated PL signal for a given sample saturates at the same level independent of the excitation wavelength or the number of generated e–h pairs per NC after a laser pulse. In this case, saturation occurs when every NC absorbs at least one photon. This process was explained by considering a new energy transfer-based CM scheme, space-separated quantum cutting (SSQC). CM by SSQC is driven by the Coulomb interaction between carriers of different NCs and differs from traditional CM dynamics because the generated e–h pairs are localized onto different interacting NCs. By distributing the excitation among several nanostructures, CM by SSQC represents one of the most suitable routes for solar cell loss minimization. Subsequent experiments conducted by Trinh et al. [36] pointed out the lack of fast decay components in the IA dynamics for high energy excitations ($h\nu > 2E_g$). For such photoexcitation events, the intensity of the IA signal was proven to be twice that recorded at an energy below the CM threshold ($h\nu \approx 1.6E_g$); this argument was used to prove the occurrence of CM effects in dense arrays of Si-NCs. Experimental results were interpreted by hypothesizing a direct formation of e–h pairs localized onto different NCs by SSQC. The measured quantum yield was proven to be very similar to that measured in the PL experiments conducted by Timmerman et al. [33-35], pointing to a similar microscopic origin of the recorded PL and IA signals.

In this work, we investigate effects induced on CM dynamics using first principles calculations. One-site CM, Coulomb-driven charge transfer (CDCT) and SSQC processes are evaluated in detail and a hierarchy of CM lifetimes are noted.

Theory

In this work we investigate CM effects in systems of isolated and interacting Si-NCs. Structural and electronic properties are calculated within the density functional theory (DFT) using the local density approximation, as implemented in the Quantum-ESPRESSO package [37]. Energy levels are determined by considering a wavefunction cutoff of 20 Hartree. Following Rabani et al. [29], CM rates are calculated by applying first order perturbation theory (Fermi’s golden rule, impact ionization decay mechanism) by separating processes ignited by electrons (h spectator) and holes (e spectator), that is:

$$R^{\mathrm{e}}_{n_\mathrm{i},\mathbf{k}_\mathrm{i}}(E_\mathrm{i}) = \left[\sum_{n_\mathrm{c},n_\mathrm{d}}^{\text{cond.}} \sum_{n_\mathrm{b}}^{\text{val.}} \sum_{\mathbf{k}_\mathrm{b},\mathbf{k}_\mathrm{c},\mathbf{k}_\mathrm{d}}^{\text{1BZ}} 4\pi \left[|\mathbf{M}_\mathrm{D}|^2 + |\mathbf{M}_\mathrm{E}|^2 + |\mathbf{M}_\mathrm{D} - \mathbf{M}_\mathrm{E}|^2 \right] \delta(E_\mathrm{i} + E_\mathrm{b} - E_\mathrm{c} - E_\mathrm{d}) \right] \tag{1}$$

and

$$R^{\mathrm{h}}_{n_\mathrm{i},\mathbf{k}_\mathrm{i}}(E_\mathrm{i}) = \left[\sum_{n_\mathrm{c},n_\mathrm{d}}^{\text{val.}} \sum_{n_\mathrm{b}}^{\text{cond.}} \sum_{\mathbf{k}_\mathrm{b},\mathbf{k}_\mathrm{c},\mathbf{k}_\mathrm{d}}^{\text{1BZ}} 4\pi \left[|\mathbf{M}_\mathrm{D}|^2 + |\mathbf{M}_\mathrm{E}|^2 + |\mathbf{M}_\mathrm{D} - \mathbf{M}_\mathrm{E}|^2 \right] \delta(E_\mathrm{i} + E_\mathrm{b} - E_\mathrm{c} - E_\mathrm{d}) \right], \tag{2}$$

where the superscripts “e” and “h” identify mechanisms ignited by relaxation of an electron and a hole, respectively. In Equation 1 and Equation 2, the rates are expressed as a function of the energy of the initial carrier, without considering the lattice vibration (a detailed ab initio calculation of phonon-assisted CM processes currently represents, for the considered systems, an unattainable task that goes beyond the scope of this work). The label $n_\mathrm{i}\mathbf{k}_\mathrm{i}$ denotes the Kohn–Sham (KS) state of the carrier that ignites the transition, while $n_\mathrm{b}\mathbf{k}_\mathrm{b}$, $n_\mathrm{c}\mathbf{k}_\mathrm{c}$ and $n_\mathrm{d}\mathbf{k}_\mathrm{d}$ identify the final states (see Figure 1). $\mathbf{M}_\mathrm{D}$ and $\mathbf{M}_\mathrm{E}$ are the two particle direct and exchange Coulomb matrix elements [38] calculated between KS states. Energy conservation is imposed by the presence of the delta function (it is implemented in the form of a Gaussian distribution with a full width at half maximum of 0.02 eV). The screened Coulomb potential, which is the basis of the calculation of both $\mathbf{M}_\mathrm{D}$ and $\mathbf{M}_\mathrm{E}$, is obtained by solving Dyson's equation in the random phase approximation, as implemented in the many-body YAMBO code [39]. In reciprocal space, the Fourier transform of the zero-frequency screened Coulomb potential is given by:

$$\mathbf{W}_{\mathbf{GG}'}(\mathbf{q}) = \frac{4\pi}{|\mathbf{q}+\mathbf{G}|^2}\delta_{\mathbf{GG}'} + \frac{4\pi}{|\mathbf{q}+\mathbf{G}|^2}\chi_{\mathbf{GG}'}(\mathbf{q},\omega=0)\frac{4\pi}{|\mathbf{q}+\mathbf{G}'|^2}, \quad (3)$$

where **G** and **G**' are vectors of the reciprocal lattice, $\mathbf{q} = (\mathbf{k}_\mathrm{c} - \mathbf{k}_\mathrm{i})_\mathrm{1BZ}$, and $\chi_{\mathbf{GG}'}$ is the reducible, zero frequency, density–density response function. The first term on the right-hand side of Equation 3 represents the bare part of the Coulomb potential, and the second term defines the screened part. The presence of off-diagonal elements in the solution of Dyson's equation is related to the inclusion of local fields. CM lifetimes are then obtained as a reciprocal of rates, that is

$$\tau^{(\mathrm{e/h})}_{n_\mathrm{i}\mathbf{k}_\mathrm{i}}(E_\mathrm{i}) = \frac{1}{R^{(\mathrm{e/h})}_{n_\mathrm{i}\mathbf{k}_\mathrm{i}}(E_\mathrm{i})} \quad (4)$$

found by calculating the inverse of the sum of all CM rates able to connect the initial $n_\mathrm{i}\mathbf{k}_\mathrm{i}$ state with the final states, satisfying the energy conservation law within 0.05 eV. Spurious Coulomb interactions among nearby replicas are avoided thanks to the use of the box-shaped, exact cutoff technique [40].

When two NCs are placed in close proximity, wavefunctions are able to delocalize on the entire system and new CM effects emerge from NC–NC interaction. In this condition, the total CM rate can be split in two parts: (a) one-site CM processes, where initial and final states are localized onto the same NC and (b) two-site CM effects, where initial and final states are localized onto different NCs, that is, SSQC and CDCT. SSQC is a Coulomb-driven, energy transfer process that occurs when a high energy electron (hole) decays toward the conduction (valence) band CB (VB) edge by promoting the formation of an extra e–h pair in a nearby NC. CDCT, instead, is a Coulomb-driven, charge transfer mechanism that occurs when an electron (hole) decays toward the CB (VB) of a nearby NC where an extra e–h pair is generated (see Figure 1).

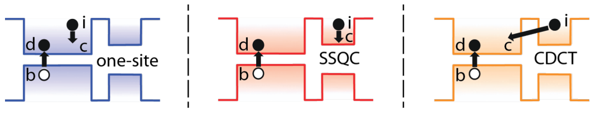

Figure 1: A schematic representation of one-site CM, SSQC and CDCT (for more details see [41]). When SSQC occurs, a highly excited carrier decays to lower energy states, transferring its excess energy to a close NC where an extra e–h pair is generated.

One of the simplest way to represent a system of interacting NCs is to place two different NCs in the same simulation box, at a tunable separation, *d*. In our work, the largest NC is placed in the left part of the box while the smaller NC is placed into the right part of the cell. The NCs are equidistant with respect the center of the cell. In order to quantify both the one-site and two-site CM lifetimes, we introduce a new parameter, the spill-out parameter $s_{n_\mathrm{x}\mathbf{k}_\mathrm{x}}$, which defines the localization of a specific KS state $n_\mathrm{x}\mathbf{k}_\mathrm{x}$ onto the smaller NC. This parameter is obtained by integrating the wavefunction square modulus $|\Psi_{n_\mathrm{x}\mathbf{k}_\mathrm{x}}(x,y,z)|^2$ over the volume of the cell that is occupied by the smaller NC, that is:

$$s_{n_\mathrm{x}\mathbf{k}_\mathrm{x}} = \int_{L_x/2}^{L_x} dx \int_0^{L_y} dy \int_0^{L_z} dz\, |\Psi_{n_\mathrm{x}\mathbf{k}_\mathrm{x}}(x,y,z)|^2$$

where L_x, L_y and L_z are the box cell edges. When the electronic state $s_{n_\mathrm{x}\mathbf{k}_\mathrm{x}}$ is completely localized on the smallest (largest) NC then $s_{n_\mathrm{x}\mathbf{k}_\mathrm{x}} = 1$ ($s_{n_\mathrm{x}\mathbf{k}_\mathrm{x}} = 0$). Otherwise, when the state $n_\mathrm{x}\mathbf{k}_\mathrm{x}$ is spread over both NCs, then $0 < s_{n_\mathrm{x}\mathbf{k}_\mathrm{x}} < 1$. For a system of interacting NCs, the one-site CM rate is given by

$$\frac{1}{\tau^{(\mathrm{e/h})}_{\text{one-site}}(E_\mathrm{i})} = \sum_{n_\mathrm{b}\mathbf{k}_\mathrm{b}} \sum_{n_\mathrm{c}\mathbf{k}_\mathrm{c}} \sum_{n_\mathrm{d}\mathbf{k}_\mathrm{d}} \Big[s_{n_\mathrm{i}\mathbf{k}_\mathrm{i}} s_{n_\mathrm{b}\mathbf{k}_\mathrm{b}} s_{n_\mathrm{c}\mathbf{k}_\mathrm{c}} s_{n_\mathrm{d}\mathbf{k}_\mathrm{d}} + \left(1-s_{n_\mathrm{i}\mathbf{k}_\mathrm{i}}\right)\left(1-s_{n_\mathrm{b}\mathbf{k}_\mathrm{b}}\right)\left(1-s_{n_\mathrm{c}\mathbf{k}_\mathrm{c}}\right)\left(1-s_{n_\mathrm{d}\mathbf{k}_\mathrm{d}}\right)\Big] \times \frac{1}{\tau^{(\mathrm{e/h})}_{(\mathrm{i,b})\to(\mathrm{c,d})}(E_\mathrm{i})}, \quad (5)$$

where $\tau^{\mathrm{e/h}}_{\text{one-site}}$ (E_i) is the one-site CM lifetime for a process ignited by a carrier of energy E_i. $1/\tau^{(\mathrm{e/h})}_{(\mathrm{i,b})\to(\mathrm{c,d})}(E_\mathrm{i})$ is the total CM rate for the generic, single, CM decay path (i,b) → (c,d) (see Figure 1).

$$\frac{1}{\tau^{(\mathrm{e/h})}_{(\mathrm{i,b})\to(\mathrm{c,d})}(E_\mathrm{i})} = 4\pi\left[|\mathrm{M_D}|^2 + |\mathrm{M_E}|^2 + |\mathrm{M_D} - \mathrm{M_E}|^2\right]\delta\left(E_\mathrm{i} + E_\mathrm{b} - E_\mathrm{c} - E_\mathrm{d}\right)$$

and the weighting factors $s_{n_\mathrm{i}\mathbf{k}_\mathrm{i}}$, $s_{n_\mathrm{b}\mathbf{k}_\mathrm{b}}$, $s_{n_\mathrm{c}\mathbf{k}_\mathrm{c}}$, and $s_{n_\mathrm{d}\mathbf{k}_\mathrm{d}}$ are the spill-out parameters of the states *i*, *b*, *c* and *d*.

Equation 5 is obtained by weighting the single CM rate $1/\tau^{(\mathrm{e/h})}_{(\mathrm{i,b})\to(\mathrm{c,d})}(E_\mathrm{i})$ of a permitted CM decay path (i,b) → (c,d) with the product of the spill-out parameters and by summing over all possible final states [42]. At the same time the SSQC rate is obtained by considering the portion of the wavefunctions of the states i and c that are localized onto the smallest (largest) NC and the portion of the states b and d that are localized onto the largest (smallest) NC, that is:

$$\frac{1}{\tau^{(\mathrm{e/h})}_{\mathrm{SSQC}}(E_\mathrm{i})} = \sum_{n_\mathrm{b}\mathbf{k}_\mathrm{b}} \sum_{n_\mathrm{c}\mathbf{k}_\mathrm{c}} \sum_{n_\mathrm{d}\mathbf{k}_\mathrm{d}} \Big\{ \Big[\big(1 - s_{n_\mathrm{i}\mathbf{k}_\mathrm{i}}\big) s_{n_\mathrm{b}\mathbf{k}_\mathrm{b}} + s_{n_\mathrm{i}\mathbf{k}_\mathrm{i}} \big(1 - s_{n_\mathrm{b}\mathbf{k}_\mathrm{b}}\big) \Big] \times \\ \Big[s_{n_\mathrm{c}\mathbf{k}_\mathrm{c}} \big(1 - s_{n_\mathrm{d}\mathbf{k}_\mathrm{d}}\big) + s_{n_\mathrm{d}\mathbf{k}_\mathrm{d}} \big(1 - s_{n_\mathrm{c}\mathbf{k}_\mathrm{c}}\big) \Big] \Big\} \frac{1}{\tau^{(\mathrm{e/h})}_{(\mathrm{i,b})\to(\mathrm{c,d})}(E_\mathrm{i})}. \tag{6}$$

The CDCT rate can be trivially obtained by:

$$\frac{1}{\tau^{(\mathrm{e/h})}_{\mathrm{CDCT}}(E_\mathrm{i})} = \frac{1}{\tau^{(\mathrm{e/h})}_{n_\mathrm{i}\mathbf{k}_\mathrm{i}}(E_\mathrm{i})} - \frac{1}{\tau^{(\mathrm{e/h})}_{\mathrm{SSQC}}(E_\mathrm{i})} - \frac{1}{\tau^{(\mathrm{e/h})}_{\text{one-site}}(E_\mathrm{i})}. \tag{7}$$

In our work, we consider four different isolated Si-NCs: ($Si_{35}H_{36}$, $Si_{87}H_{76}$, $Si_{147}H_{100}$ and $Si_{293}H_{172}$), and a couple of interacting NCs ($Si_{87}H_{76}$ × $Si_{293}H_{172}$). For all of the systems considered, the NCs are always assumed in vacuum.

Results and Discussion

CM effects in isolated and interacting Si-NCs were investigated for the first time by first-principles calculations by Govoni et al. [31], who simulated CM decays in systems of isolated and interacting Si-NCs. CM lifetimes were calculated in four different spherical and hydrogenated systems, that is the $Si_{35}H_{36}$ ($E_\mathrm{g}^{\mathrm{Si_{35}H_{36}}} = 3.42$ eV, 1.3 nm of diameter), the $Si_{87}H_{76}$ ($E_\mathrm{g}^{\mathrm{Si_{87}H_{76}}} = 2.50$ eV, 1.6 nm diameter), the $Si_{147}H_{100}$ ($E_\mathrm{g}^{\mathrm{Si_{147}H_{100}}} = 2.21$ eV, 1.9 nm diameter) and the $Si_{293}H_{172}$ ($E_\mathrm{g}^{\mathrm{Si_{293}H_{172}}} = 1.70$ eV, 2.4 nm diameter).

Systems of strongly coupled Si-NCs ($Si_{35}H_{36}$ × $Si_{293}H_{172}$ and $Si_{147}H_{100}$ × $Si_{293}H_{172}$) were then analyzed in order to define effects induced by NC interplay on CM effects.

In this work we investigate new aspects of CM dynamics in both isolated and interacting Si-NCs. For the first step, we reconsider the systems $Si_{35}H_{36}$, $Si_{87}H_{76}$, $Si_{147}H_{100}$ and $Si_{293}H_{172}$ and we analyze the dependence of CM lifetimes on NCs size. The role played by local fields (and in general by the screened part of the Coulomb potential) on CM dynamics is successively analyzed. The system of strongly coupled NCs ($Si_{87}H_{76}$ × $Si_{293}H_{172}$) was then studied to investigate effects induced by NC interplay on CM decay processes. The resulting CM lifetimes are then compared with those obtained in [31] for the systems $Si_{35}H_{36}$ × $Si_{293}H_{172}$ and $Si_{147}H_{100}$ × $Si_{293}H_{172}$ in order to investigate the dependence of the two-site CM effect on NC size. The role played by reciprocal NCs orientation is finally briefly analyzed.

CM lifetimes calculated for the isolated Si-NC systems are reported in Figure 2 as a function of both the energy of the initial carrier ((b) absolute energy scale) and the ratio between the energy of the initial carrier and the energy gap of the system ($E_\mathrm{i}/E_\mathrm{g}$, (d), relative energy scale). In both cases, CM lifetimes are obtained by omitting vacuum states, which are conduction levels above the vacuum energy.The calculated CM lifetimes for Si-NCs are then compared with those obtained for Si-bulk (yellow points). The results of Figure 2 indicate that CM is forbidden when the excess energy, E^exc, of the initial carrier is lower than E_g. On the contrary, when $|E^\mathrm{exc}| > |E_\mathrm{g}|$, CM is permitted and the calculated CM lifetime, after initial fluctuations, decreases when the energy of the initial carrier increases. When an absolute energy scale is adopted (Figure 2b) and low energy dynamics are analyzed, CM is strongly influenced by the energy gap of the system and is faster in systems with lower E_g, that is, the Si-bulk (energy range of approximately -2.5 eV $< E_\mathrm{i} < 2.5$ eV). However, under these conditions, CM is generally not sufficiently fast to dominate over concurrent decay mechanisms and can only weakly affect the time evolution of the excited carrier. For Si-NCs, thermalization processes are expected to range from a few picoseconds to a fraction of a picosecond [43,44]. In the ranges -3.8 eV $< E_\mathrm{i} < -2.5$ eV and 2.5 eV $< E_\mathrm{i} < 3.8$ eV, the CM lifetimes calculated for the $Si_{293}H_{172}$ are lower than those obtained for the Si-bulk. For the remainder of the plot, that is, approximately for $E_\mathrm{i} < -3.8$ eV and $E_\mathrm{i} > 3.8$ eV, CM is faster in Si-NC systems than in Si-bulk and is observed to be independent of the NC size. In this range of energies, CM is sufficiently fast to compete with concurrent non-CM processes and, playing a fundamental role in the determination of the excited carrier dynamics, can be exploited to improve solar cell performance. Analysis of high energy, CM decay paths is therefore fundamental and can have a strong impact on the engineering of new PV devices. The behavior recorded at high energies (where CM lifetimes are independent of the NC size) can be interpreted by reformulating Equation 1 and Equation 2 in order to point out the dependence of the CM rate on the density of final states. Following Allan et al. [24]:

$$\frac{1}{\tau_{n_\mathrm{i}\mathbf{k}_\mathrm{i}}(E_\mathrm{i})} = \frac{2\pi}{\hbar} \left| \mathrm{M_{eff}}(E_\mathrm{i}) \right|^2 \rho^{f}_{n_\mathrm{i}\mathbf{k}_\mathrm{i}}(E_\mathrm{i}) \tag{8}$$

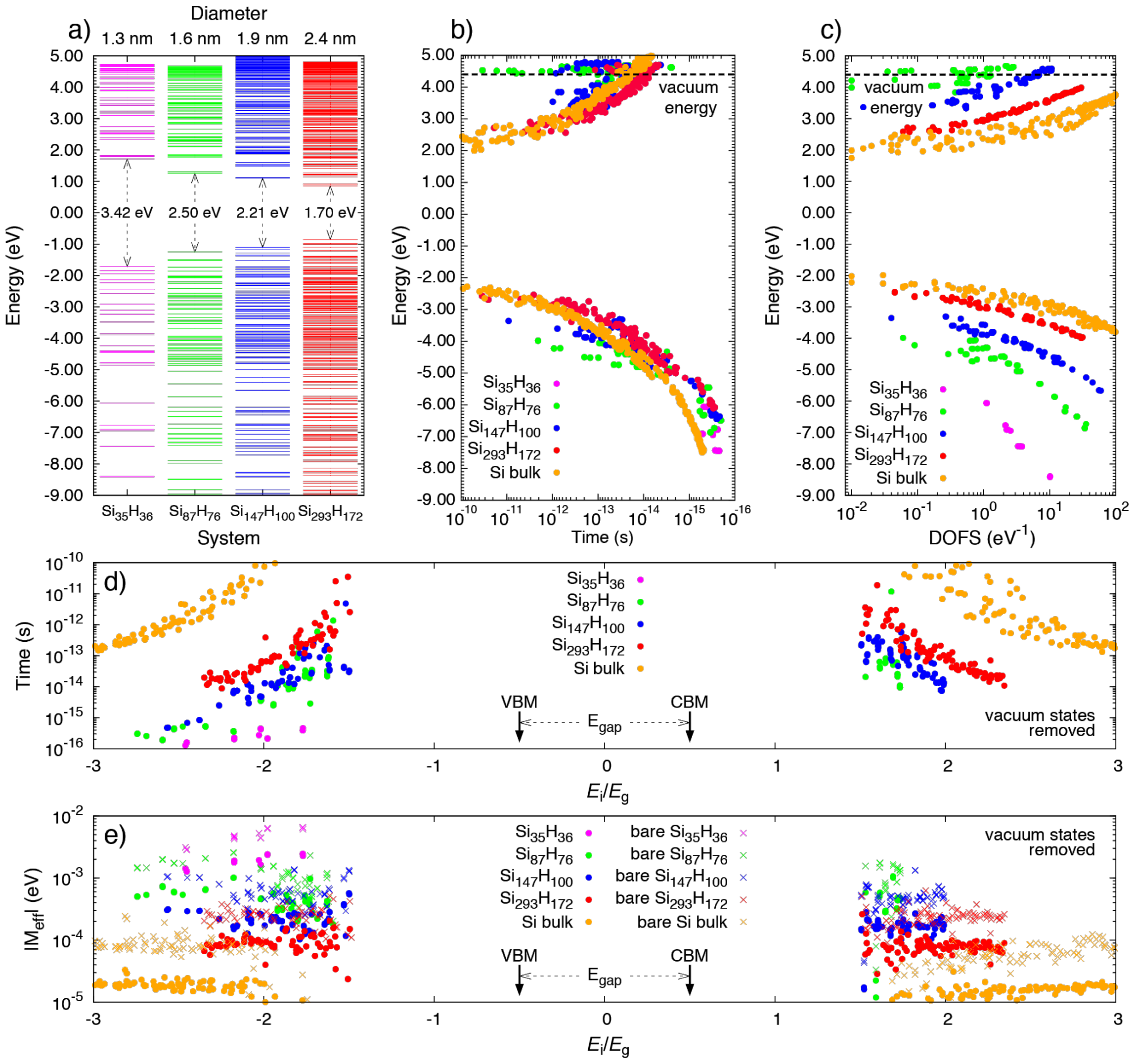

Figure 2: Electronic structures of $Si_{35}H_{36}$, $Si_{87}H_{76}$, $Si_{147}H_{100}$ and $Si_{293}H_{172}$ are reported in (a). CM lifetimes calculated for the considered Si-NC systems and for the Si-bulk are reported in (b) and (d). Both mechanisms which are ignited by electron relaxation (positive energy) and hole relaxation (negative energy) are considered. In (b), CM lifetimes are given as a function of the energy of the the initial carrier, E_i. In (d) CM lifetimes are expressed in terms of the ratio E_i/E_g. The zero of the energy scale is set at the half band gap for each NC system. Dashed horizontal lines in (b) and (c) denote the vacuum energy level. In our calculations, we omit vacuum states, that is, conduction band states with an energy higher than the vacuum energy. The calculated density of final states are reported in (c). The results were obtained considering a broadening of 5 meV. The effective Coulomb matrix elements are given in (e). The filled circle data points represent results obtained by including both bare and screened terms in Equation 3 and colored crosses represent only the bare terms of Equation 3.

where $|M_{\text{eff}}(E_\text{i})|$ is the effective two-particle, Coulomb matrix element and $\rho^{f}_{n_\text{i}\mathbf{k}_\text{i}}(E_\text{i})$ is the density of final states. Calculations of $\rho^{f}_{n_\text{i}\mathbf{k}_\text{i}}(E_\text{i})$ *and* $|M_{\text{eff}}(E_\text{i})|$ are reported in Figure 2c and Figure 2e for both Si-NCs and Si-bulk (Coulomb matrix elements are calculated for both by including and neglecting the screened term, indicated by the dot-type and cross-type points, respectively, of Figure 2e). Our results indicate that, while the effective Coulomb matrix elements (and therefore their squared modulus) decrease with increasing NC size, the density of final states increases with increasing NC size. Far from the activation threshold (approximately $-3.8\ \text{eV} < E_\text{i}$ and $E_\text{i} > 3.8\ \text{eV}$) we observe a sort of exact compensation between the trends of $|M_{\text{eff}}(E_\text{i})|^2$ and of $\rho^{f}_{n_\text{i}\mathbf{k}_\text{i}}(E_\text{i})$ that make $\tau_{n_\text{i}\mathbf{k}_\text{i}}(E_\text{i})$ almost NC-size-independent. Again, from Figure 2e, we observe that due to the strong discretization of NC electronic states near the VB and CB, the effective Coulomb matrix elements scatter among different orders of magnitude when they are calculated at energies near the CM thresholds. Such oscillations strongly affect the CM lifetimes at low energies and generate fluctuations that are clearly visible in both the plots of Figure 2b and Figure 2d. Instead, at high energies, the effective Coulomb matrix elements stabilize at constant values that depend only on the NC size. Therefore, in this portion of the energy range, the typical trend of $\tau_{n_i\mathbf{k}_i}(E_i)$, which decreases when the energy of the initial state increases, is only ascribable to the monotonically increasing behavior of $\rho^{f}_{n_i\mathbf{k}_i}(E_i)$.

A realistic estimation of CM lifetimes requires a detailed evaluation of the carrier–carrier Coulomb interaction. Due to the required computational and theoretical efforts necessary to solve Equation 3, the Coulomb potential is often approximated by considering only the bare term. The inclusion of the screened part of the Coulomb potential, which requires a detailed estimation of the many-body interacting polarizability, is often neglected in order to make the procedure that leads to the calculation of the dielectric function more manageable. In order to quantify the role played by the screened part of the Coulomb potential, we calculate effective Coulomb matrix elements by adopting two different procedures: firstly, by omitting and then, by including the second term on the right-hand side of Equation 3. The results of Figure 2e illustrate that the inclusion of the screened part of the Coulomb potential leads to effective Coulomb matrix elements that are up to one-order of magnitude smaller that those obtainable by only considering the bare Coulomb interaction. As a consequence, a simplified procedure that avoids the complete calculation of Equation 3 (and therefore also neglects the inclusion of local field effects) leads to an overestimate of the efficiency of CM decay mechanisms and does not allow for a realistic determination of high energy, excited carrier dynamics. It is thus evident that a detailed estimation of $\tau_{n_i\mathbf{k}_i}(E_i)$ requires an accurate description of the atomistic properties of the systems that, especially for nanostructures, can be obtained only through a parameter-free, ab initio investigation of the electronic properties of the considered materials.

A clear dependence of CM lifetimes on NC size appears when a relative energy scale is adopted (plot of Figure 2d), that is, when the CM lifetimes are related to E_i/E_g. As proven by Beard et al. [45], this scale is the most appropriate to predict the possible implication of the CM for PV applications. Thus, from this perspective, there are clear advantages which are induced by size reduction, that is, when moving from the Si-bulk scale to the nanoscale for $Si_{35}H_{36}$, as supported by results of Figure 2d.

In order to study the effects induced by NCs on the interplay of CM dynamics, we consider the system $Si_{87}H_{76} \times Si_{293}H_{172}$ that is obtained by placing in the same simulation box (box size 9.0 × 4.8 × 4.8 nm) two different NCs placed at a tunable separation. As illustrated in Equation 5, Equation 6 and Equation 7, the wavefunction delocalization plays a fundamental role in the determination of one-site CM, CDCT and SSQC lifetimes when systems of strongly interacting NCs are considered. As discussed in [31], the wavefunction delocalization processes (and the effects induced by them) become relevant for NC–NC separations of $d \le 1.0$ nm. As a consequence, we analyze the effects induced by NC interplay on CM decay processes by only considering NC–NC separations that fall in the sub-nm regime, and in particular by assuming $d = 0.8$ nm and $d = 0.6$ nm. In our work, the NC–NC separation is the distance between the nearest Si atoms that are localized on different NCs. The calculated CM lifetimes obtained by summing the contributions of Equation 5, Equation 6 and Equation 7 are reported in Figure 3a as a function of the energy of the initial carrier and of the NC–NC separation, d (total CM lifetimes).

The calculated SSQC and CDCT lifetimes (mathematically characterized by Equation 6 and Equation 7) are depicted in Figure 3b and Figure 3c. Only mechanisms ignited by electron relaxation are considered. The analysis of the results of Figure 3 leads to the conclusions which are outlined in the following.

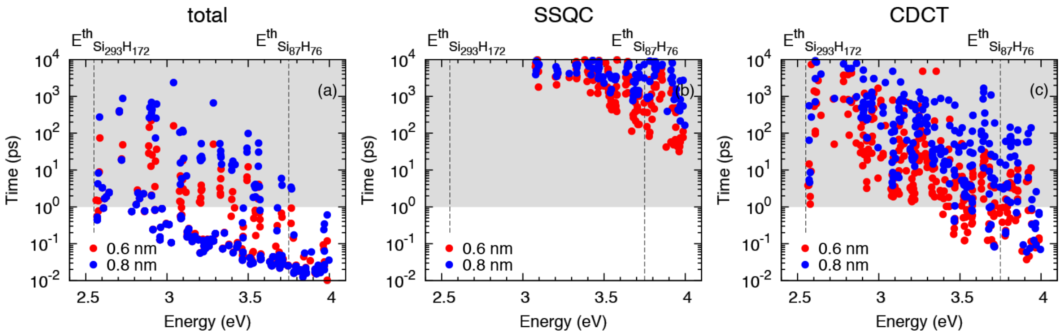

Figure 3: Calculated total CM, SSQC and CDCT lifetimes are reported in (a), (b) and (c), respectively, for the system $Si_{87}H_{76} \times Si_{293}H_{172}$, where NC–NC separations of 0.8 and 0.6 nm (blue and red points, respectively) are given. $E^{th}_{Si_{293}H_{172}}$ and $E^{th}_{Si_{87}H_{76}}$ denote the CM energy threshold of the isolated NCs, that is for the $Si_{293}H_{172}$ and the $Si_{87}H_{76}$ NCs.

First, by changing the separation from *d* = 0.8 to *d* = 0.6 nm, some changes emerge in the plot of the CM lifetimes (Figure 3a). As a result of the improved NC–NC interaction, we observe the drift of some points toward reduced lifetimes. Such changes essentially concern the portion of the plot delimited by the energies $E^{\mathrm{th}}_{\mathrm{Si_{293}H_{172}}}$ and $E^{\mathrm{th}}_{\mathrm{Si_{87}H_{76}}}$ (i.e., the CM energy threshold of the isolated NCs) and by the lifetimes of 1–100 ps. At *d* = 0.6 nm, the distribution of the points is less scattered than for *d* =0.8 nm and moves toward that of an isolated, unique, large system (a similar behavior also characterizes the system $\mathrm{Si_{147}H_{100}} \times \mathrm{Si_{293}H_{172}}$, see [41]).

Additionally, NC interplay does not significantly alter the faster CM decay processes. This conclusion can be obtained by analyzing the region of Figure 3a that takes into account the CM relaxation mechanisms with a lifetime less than 0.1 ps. Here we observe that blue (*d* = 0.8 nm) and red (*d* = 0.6 nm) points are almost identical. The number of CM decay paths recorded in this region of the plot does not improve when we move from *d* = 0.8 nm to *d* = 0.6 nm.

When the NC–NC separation is reduced, the NC interplay increases, and two-site CM mechanisms become fast. At high energy, τ_{CDCT} ranges from tens of ps to a fraction of a ps, while τ_{SSQC} ranges from hundreds of picoseconds to a few tens of picoseconds. Both the CDCT and SSCQ lifetimes decrease when the NC separation decreases, as a consequence of both the augmented Coulomb interaction between carriers of different NCs and the increased delocalization of wavefunctions.

Another conclusion reached is that CDCT processes are in general faster than SSQC mechanisms. In order to be efficient, CDCT requires a noticeable delocalization of only the initial state while SSQC requires a significant delocalization of all the states involved in the transition; as a consequence, the CDCT decay processes are in general favored with respect to the corresponding SSQC mechanisms.

Finally, despite the fact that NC interplay can enhance the two-site CM processes, the $\mathrm{Si_{87}H_{76}} \times \mathrm{Si_{293}H_{172}}$ satisfies the typical hierarchy of lifetimes $\tau_{\mathrm{one-site}} \leq \tau_{\mathrm{CDCT}} \leq \tau_{\mathrm{SSQC}}$ expected. As a consequence, the system $\mathrm{Si_{87}H_{76}} \times \mathrm{Si_{293}H_{172}}$ also follows this recently identified trend for the $\mathrm{Si_{35}H_{36}} \times \mathrm{Si_{293}H_{172}}$ and the $\mathrm{Si_{147}H_{100}} \times \mathrm{Si_{293}H_{172}}$ systems. Thus, for a given energy of the initial state, one-site CM mechanisms result faster than CDCT processes, and CDCT processes result faster than SSQC mechanisms.

Remarkably, the relevance of the two-site CM processes are expected to benefit from experimental conditions where the formation of minibands (the presence of molecular chains that interconnect different NCs and for multiple interacting NCs) amplify the importance of both the energy and charge CM dynamics. Again, by comparing the results of Figure 3b with the corresponding CM lifetimes calculated in [31], we can say that the efficiency of SSQC processes tends to increase with increasing NC size. In general, experiments are conducted on nanostructured systems that are larger than those considered in this work. As a consequence, in a realistic system, both SSQC and CDCT dynamics could be faster than those computed herein, although these effects should not give rise to changes in the previously discussed hierarchy of lifetimes. The CM is driven by Coulomb interaction and therefore its relevance is maximized when the effect involves carriers localized onto the same NC.

To support the general validity of our results, we analyzed CM effects considering two different additional systems. The first one is obtained by assuming a different configuration of $\mathrm{Si_{87}H_{76}} \times \mathrm{Si_{293}H_{172}}$, where the $\mathrm{Si_{87}H_{76}}$ is rotated around one of axis of symmetry. In this new setup, denoted as $\mathrm{Si_{87}H_{76}^{tilted}} \times \mathrm{Si_{293}H_{172}}$, the NCs show a different reciprocal surface orientation that affects both wavefunction delocalization and spill-out parameters. The second one is obtained by placing in the same simulation box two identical Si-NCs, that is, $\mathrm{Si_{87}H_{76}} \times \mathrm{Si_{87}H_{76}}$, placed at a tunable separation (*d* = 0.9, 0.7, 0.5, 0.3, 0.1 nm). Calculated total CM, SSQC and CDCT lifetimes for the system $\mathrm{Si_{87}H_{76}^{tilted}} \times \mathrm{Si_{293}H_{172}}$ are depicted in Figure 4a–c. Simulated total CM lifetimes for the system $\mathrm{Si_{87}H_{76}} \times \mathrm{Si_{87}H_{76}}$ are reported in Figure 4d.

Despite the fact that the reciprocal NC orientation slightly affects both CDCT and SSQC lifetimes, we do not observe significant changes in CM dynamics from the $\mathrm{Si_{87}H_{76}} \times \mathrm{Si_{293}H_{172}}$ to the $\mathrm{Si_{87}H_{76}^{tilted}} \times \mathrm{Si_{293}H_{172}}$ systems. Also, in this case, one-site processes dominate CM decay mechanisms and CDCT processes are faster than SSQC events.

Our conclusions do not change when we move from a system of differently coupled Si-NCs to a system of identically coupled Si-NCs. Also, in this case, NC interplay does not significantly affect sub-ps CM events that are dominated by the occurrence of one-site CM processes, that is, by processes that are only weakly influenced by NC–NC interaction. As a result, only CM decay paths with a lifetime greater than 1 ps are influenced by NC interplay and are then pushed to lower lifetimes.

As a result of ab initio calculations based on the first-order perturbation theory (weak coupling scheme), which is the one-site the dominant CM decay process, after absorption of a single photon we have always the formation of Auger-affected multi-

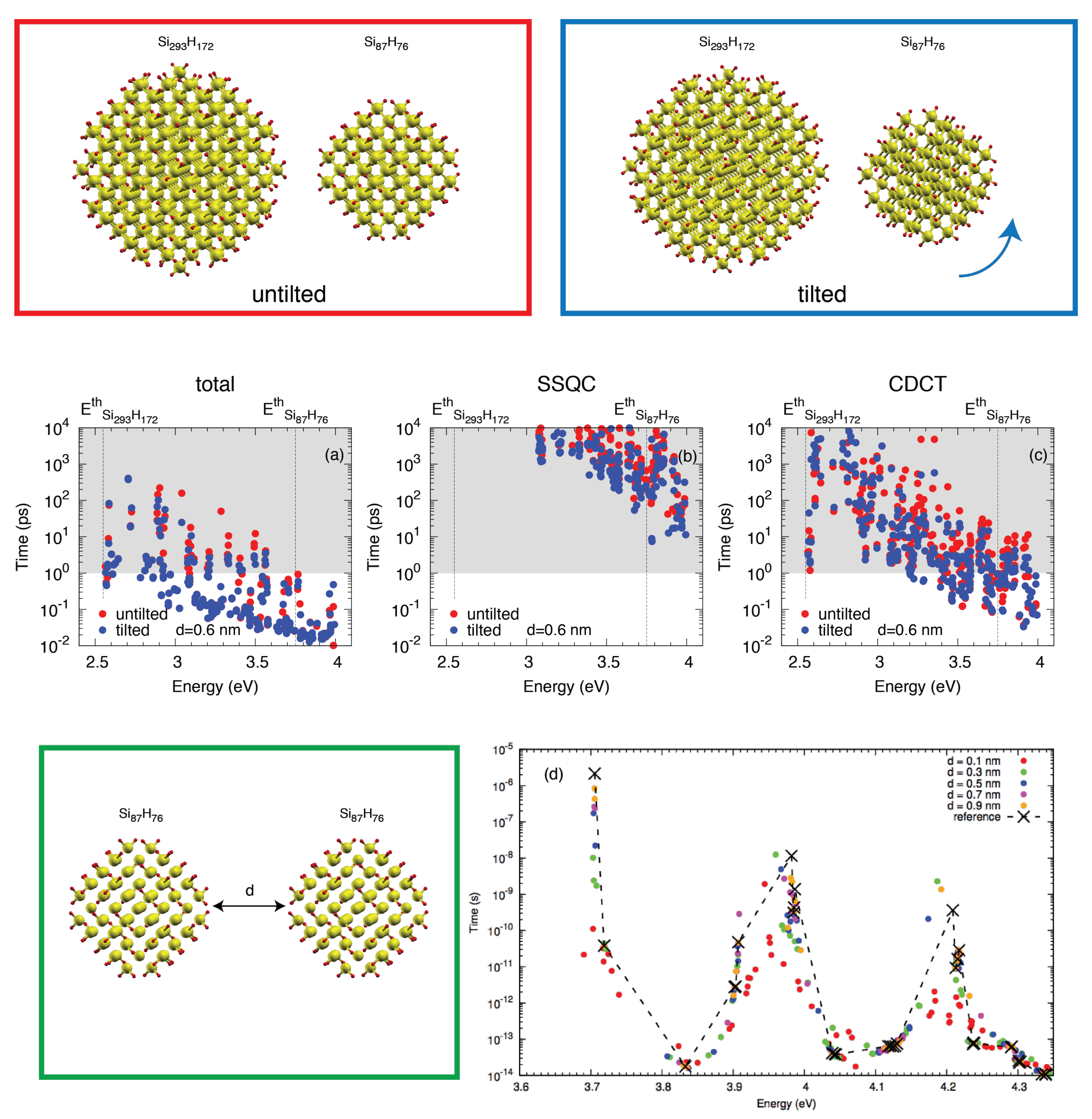

Figure 4: A representation of the systems $Si_{87}H_{76}$ × $Si_{293}H_{172}$ and $Si_{87}H_{76}^{tilted} \times Si_{293}H_{172}$ is given in the upper part of the figure. Calculated total CM, SSQC and CDCT lifetimes are reported in (a), (b) and (c), respectively, for the systems $Si_{87}H_{76}$ × $Si_{293}H_{172}$ and $Si_{87}H_{76}^{tilted} \times Si_{293}H_{172}$, assuming d = 0.6 nm, for untilted and tilted systems (red and blue points, respectively). The size of the simulation box was 9.0 nm × 4.8 nm × 4.8 nm. The system $Si_{87}H_{76}$ × $Si_{87}H_{76}$ is depicted in the bottom-left part of the figure. Calculated total CM lifetimes for the system $Si_{87}H_{76}$ × $Si_{87}H_{76}$ are reported in (d) by assuming a NC–NC separation ranging from 0.9 to 0.1 nm. The reference (cross-type points) denotes the total CM lifetimes calculated for the isolated system ($Si_{87}H_{76}$). The size of the simulation box was 9.0 nm × 4.8 nm × 4.8 nm.

excitons localized in single NCs, even when systems of strongly coupled NCs are considered. A direct separation of e–h pairs onto space separated nanostructures by SSQC is therefore not compatible with our theoretical results. Therefore, in our opinion, more complicated dynamics, where for instance SSQC effects are assisted by exciton recycling mechanisms [31,41], must be hypothesized in order to explain results of [36].

Conclusion

In this work, we have calculated CM lifetimes for systems of isolated and interacting Si-NCs. As a first step, we have considered four different, free-standing NCs ($Si_{35}H_{36}$, $Si_{87}H_{76}$, $Si_{147}H_{100}$ and $Si_{293}H_{172}$) with diameters (energy gaps) ranging from 1.3 nm (3.42 eV) to 2.4 nm (1.70 eV). Calculated CM lifetimes have been reported using both an absolute and a relative energy scale. Recorded trends have been interpreted in terms of two-particle, effective Coulomb matrix elements, $|M_{\mathrm{eff}}(E_{\mathrm{i}})|$, and of the density of final states, $\rho^{f}_{n_{\mathrm{i}}\mathbf{k}_{\mathrm{i}}}(\mathrm{E_i})$ by dividing plots in two parts: a near CM energy threshold region (low energy region) and a far CM energy threshold region (high energy region). In this manner, we have proven that oscillations detected in the CM lifetimes plots at low energy are induced by fluctuations in the effective Coulomb matrix elements, while trends recorded at high energy are mainly connected with the monotonically increasing behavior of $\rho^{f}_{n_{\mathrm{i}}\mathbf{k}_{\mathrm{i}}}(\mathrm{E_i})$. The role played by the screened part of the Coulomb potential (and by local fields) was then clarified.

The effects induced by NC interplay on CM dynamics have been investigated considering a system formed by two NCs placed in close proximity, that is, $\mathrm{Si_{87}H_{76}} \times \mathrm{Si_{293}H_{172}}$. One-site CM, SSQC and CDCT lifetimes have been quantified by first principles calculations and reported as a function of the energy of the initial carrier. The obtained results point out that one-site CM mechanisms always dominate over two-site CM processes and that the resulting lifetimes follow the hierarchy $\tau_{\mathrm{one-site}} \le \tau_{\mathrm{CDCT}} \le \tau_{\mathrm{SSQC}}$. As a consequence, Auger affected multiexciton configurations are always formed in single NCs after absorption of high energy photons. A direct separation of e–h pairs in space-separated NCs is thus not compatible with our results. The role played by reciprocal NCs surface orientation has been investigated by rotating the $\mathrm{Si_{87}H_{76}}$ system around one axis of symmetry. The obtained results indicated that although reciprocal NC orientation affects wavefunction delocalization (and thus the relevance of two-site CM processes, suggesting interaction between non-spherical NCs), it does not alter the hierarchy of lifetimes previously discussed. The same conclusions can be obtained when systems of identical, interacting, NCs are investigated. Moreover, in this case, the effects induced by NC interplay can only modify the efficiency of CM transitions with lifetimes higher than 1 ps.

Acknowledgements

The authors thank the Super-Computing Interuniversity Consortium CINECA for support and high-performance computing resources under the Italian Super-Computing Resource Allocation (ISCRA) initiative, PRACE for awarding us access to resource IBM BG/Q based in Italy at CINECA, and the European Community Seventh Framework Programme (FP7/2007-2013; grant agreement 245977).

References

1. Ossicini, S.; Bisi, O.; Degoli, E.; Marri, I.; Iori, F.; Luppi, E.; Magri, R.; Poli, R.; Cantele, G.; Ninno, D.; Trani, F.; Marsili, M.; Pulci, O.; Olevano, V.; Gatti, M.; Gaal-Nagy, K.; Incze, A.; Onida, G. *J. Nanosci. Nanotechnol.* **2008,** *8,* 479. doi:10.1166/jnn.2008.A009
2. Iori, F.; Degoli, E.; Luppi, E.; Magri, R.; Marri, I.; Cantele, G.; Ninno, D.; Trani, F.; Ossicini, S. *J. Lumin.* **2006,** *121,* 335. doi:10.1016/j.jlumin.2006.08.062
3. Guerra, R.; Marri, I.; Magri, R.; Martin-Samos, L.; Pulci, O.; Degoli, E.; Ossicini, S. *Phys. Rev. B* **2009,** *79,* 155320. doi:10.1103/PhysRevB.79.155320
4. Iori, F.; Degoli, E.; Magri, R.; Marri, I.; Cantele, G.; Ninno, D.; Trani, F.; Pulci, O.; Ossicini, S. *Phys. Rev. B* **2007,** *76,* 085302. doi:10.1103/PhysRevB.76.085302
5. Priolo, F.; Gregorkiewicz, T.; Galli, M.; Krauss, T. F. *Nat. Nanotechnol.* **2014,** *9,* 19–32. doi:10.1038/nnano.2013.271
6. Shockley, W.; Queisser, H. J. *Appl. Phys. Lett.* **1961,** *32,* 510–519. doi:10.1063/1.1736034
7. Klimov, V. I.; Mikhailovsky, A. A.; Xu, S.; Malko, A.; Hollingsworth, J. A.; Leatherdale, C. A.; Eisler, H.-J.; Bawendi, M. G. *Science* **2000,** *290,* 314–317. doi:10.1126/science.290.5490.314
8. Beard, M. C. *J. Phys. Chem. Lett.* **2011,** *2,* 1282–1288. doi:10.1021/jz200166y
9. Benisty, H.; Sotomayor-Torrès, C. M.; Weisbuch, C. *Phys. Rev. B* **1991,** *44,* 10945–10948. doi:10.1103/PhysRevB.44.10945
10. Nozik, A. J. *Phys. E (Amsterdam, Neth.)* **2002,** *14,* 115–120. doi:10.1016/S1386-9477(02)00374-0
11. Califano, M.; Zunger, A.; Franceschetti, A. *Nano Lett.* **2004,** *4,* 525–531. doi:10.1021/nl049869w
12. Ellingson, R. J.; Beard, M. C.; Johnson, J. C.; Yu, P.; Micic, O. I.; Nozik, A. J.; Shabaev, A.; Efros, A. L. *Nano Lett.* **2005,** *5,* 865–871. doi:10.1021/nl0502672
13. Schaller, R. D.; Klimov, V. I. *Phys. Rev. Lett.* **2004,** *92,* 186601. doi:10.1103/PhysRevLett.92.186601
14. Trinh, M. T.; Houtepen, A. J.; Schins, J. M.; Hanrath, T.; Piris, J.; Knulst, W.; Goossens, A. P. L. M.; Siebbeles, L. D. A. *Nano Lett.* **2008,** *8,* 1713–1718. doi:10.1021/nl0807225
15. Schaller, R. D.; Petruska, M. A.; Klimov, V. I. *Appl. Phys. Lett.* **2005,** *87,* 253102. doi:10.1063/1.2142092
16. Schaller, R. D.; Sykora, M.; Pietryga, J. M.; Klimov, V. I. *Nano Lett.* **2006,** *6,* 424–429. doi:10.1021/nl052276g
17. Nair, G.; Bawendi, M. G. *Phys. Rev. B* **2007,** *76,* 081304. doi:10.1103/PhysRevB.76.081304
18. Schaller, R. D.; Sykora, M.; Jeong, S.; Klimov, V. I. *J. Phys. Chem. B* **2006,** *110,* 25332–25338. doi:10.1021/jp065282p
19. Gachet, D.; Avidan, A.; Pinkas, I.; Oron, D. *Nano Lett.* **2010,** *10,* 164–170. doi:10.1021/nl903172f
20. Murphy, J. E.; Beard, M. C.; Norman, A. G.; Ahrenkiel, S. P.; Johnson, J. C.; Yu, P.; Mićić, O. I.; Ellingson, R. J.; Nozik, A. J. *J. Am. Chem. Soc.* **2006,** *128,* 3241–3247. doi:10.1021/ja0574973
21. Schaller, R. D.; Pietryga, J. M.; Klimov, V. I. *Nano Lett.* **2007,** *7,* 3469–3476. doi:10.1021/nl072046x
22. Stubbs, S. K.; Hardman, S. J. O.; Graham, D. M.; Spencer, B. F.; Flavell, W. R.; Glarvey, P.; Masala, O.; Pickett, N. L.; Binks, D. J. *Phys. Rev. B* **2010,** *81,* 081303. doi:10.1103/PhysRevB.81.081303
23. Beard, M. C.; Knutsen, K. P.; Yu, P.; Luther, J. M.; Song, Q.; Metzger, W. K.; Ellingson, R. J.; Nozik, A. J. *Nano Lett.* **2007,** *7,* 2506–2512. doi:10.1021/nl071486l
24. Allan, G.; Delerue, C. *Phys. Rev. B* **2006,** *73,* 205423. doi:10.1103/PhysRevB.73.205423
25. Franceschetti, A.; An, J. M.; Zunger, A. *Nano Lett.* **2006,** *6,* 2191–2195. doi:10.1021/nl0612401
26. Allan, G.; Delerue, C. *Phys. Rev. B* **2009,** *79,* 195324. doi:10.1103/PhysRevB.79.195324

27. Shabaev, A.; Efros, A. L.; Nozik, A. J. *Nano Lett.* **2006,** *6,* 2856–2863. doi:10.1021/nl062059v
28. Schaller, R. D.; Agranovich, V. M.; Klimov, V. I. *Nat. Phys.* **2005,** *1,* 189–194. doi:10.1038/nphys151
29. Rabani, E.; Baer, R. *Nano Lett.* **2008,** *8,* 4488–4492. doi:10.1021/nl802443c
30. Rabani, E.; Baer, R. *Chem. Phys. Lett.* **2010,** *496,* 227. doi:10.1016/j.cplett.2010.07.059
31. Govoni, M.; Marri, I.; Ossicini, S. *Nat. Photonics* **2012,** *6,* 672–679. doi:10.1038/nphoton.2012.206
32. Semonin, O. E.; Luther, J. M.; Choi, S.; Chen, H.-Y.; Gao, J.; Nozik, A. J.; Beard, M. C. *Science* **2011,** *334,* 1530–1533. doi:10.1126/science.1209845
33. Timmerman, D.; Izeddin, I.; Stallinga, P.; YassievichI, I. N.; Gregorkiewicz, T. *Nat. Photonics* **2008,** *2,* 105–109. doi:10.1038/nphoton.2007.279
34. Timmerman, D.; Izeddin, I.; Gregorkiewicz, T. *Phys. Status Solidi A* **2010,** *207,* 183–187. doi:10.1002/pssa.200925363
35. Timmerman, D.; Valenta, J.; Dohnalová, K.; de Boer, W. D. A. M.; Gregorkiewicz, T. *Nat. Nanotechnol.* **2011,** *6,* 710–713. doi:10.1038/nnano.2011.167
36. Trinh, M. T.; Limpens, R.; de Boer, W. D. A. M.; Schins, J. M.; Siebbeles, L. D. A.; Gregorkiewicz, T. *Nat. Photonics* **2012,** *6,* 316–321. doi:10.1038/nphoton.2012.36
37. Giannozzi, P.; Baroni, S.; Bonini, N.; Calandra, M.; Car, R.; Cavazzoni, C.; Ceresoli, D.; Chiarotti, G. L.; Cococcioni, M.; Dabo, I.; Corso, A. D.; de Gironcoli, S.; Fabris, S.; Fratesi, G.; Gebauer, R.; Gerstmann, U.; Gougoussis, C.; Kokalj, A.; Lazzeri, M.; Martin-Samos, L.; Marzari, N.; Mauri, F.; Mazzarello, R.; Paolini, S.; Pasquarello, A.; Paulatto, L.; Sbraccia, C.; Scandolo, S.; Sclauzero, G.; Seitsonen, A. P.; Smogunov, A.; Umari, P.; Wentzcovitch, R. M. *J. Phys.: Condens. Matter* **2009,** *21,* 395502. doi:10.1088/0953-8984/21/39/395502
38. Govoni, M.; Marri, I.; Ossicini, S. *Phys. Rev. B* **2011,** *84,* 075215. doi:10.1103/PhysRevB.84.075215
39. Marini, A.; Hogan, C.; Grüning, M.; Varsano, D. *Comput. Phys. Commun.* **2009,** *180,* 1392. doi:10.1016/j.cpc.2009.02.003
40. Rozzi, C. A.; Varsano, D.; Marini, A.; Gross, E. K. U.; Rubio, A. *Phys. Rev. B* **2006,** *73,* 205119. doi:10.1103/PhysRevB.73.205119
41. Marri, I.; Govoni, M.; Ossicini, S. *J. Am. Chem. Soc.* **2014,** *136,* 13257–13266. doi:10.1021/ja5057328
42. The contribution given by the smallest [largest] NC is obtained by multiplying $1/\tau^{(\mathrm{e/h})}_{(\mathrm{i,b})\to(\mathrm{c,d})}\left(E_\mathrm{i}\right)$ by $s_{n_\mathrm{i}\mathbf{k}_\mathrm{i}}s_{n_\mathrm{b}\mathbf{k}_\mathrm{b}}s_{n_\mathrm{c}\mathbf{k}_\mathrm{c}}s_{n_\mathrm{d}\mathbf{k}_\mathrm{d}}$ [by $(1-s_{n_i\mathbf{k}_i})(1-s_{n_b\mathbf{k}_b})(1-s_{n_c\mathbf{k}_c})(1-s_{n_d\mathbf{k}_d})$] and by summing over all possible final states.
43. de Boer, W. D. A. M.; Timmerman, D.; Dohnalová, K.; Yassievich, I. N.; Zhang, H.; Buma, W. J.; Gregorkiewicz, T. *Nat. Nanotechnol.* **2010,** *5,* 878–884. doi:10.1038/nnano.2010.236
44. Lioudakis, E.; Othonos, A.; Nassiopoulou, A. G. *Appl. Phys. Lett.* **2007,** *90,* 171103. doi:10.1063/1.2728756
45. Beard, M. C.; Midgett, A. G.; Hanna, M. C.; Luther, J. M.; Hughes, B. K.; Nozik, A. J. *Nano Lett.* **2010,** *10,* 3019–3027. doi:10.1021/nl101490z

License and Terms

The definitive version of this article is the electronic one which can be found at:
doi:10.3762/bjnano.6.33

BEILSTEIN JOURNAL OF NANOTECHNOLOGY

Exploiting the hierarchical morphology of single-walled and multi-walled carbon nanotube films for highly hydrophobic coatings

Francesco De Nicola*[1,2], Paola Castrucci[1,2], Manuela Scarselli[1,2], Francesca Nanni[3], Ilaria Cacciotti[4] and Maurizio De Crescenzi[1,2,5]

Full Research Paper

Open Access

Address:
[1]Dipartimento di Fisica, Universitá di Roma Tor Vergata, Via della Ricerca Scientifica 1, 00133 Roma, Italy, [2]Istituto Nazionale di Fisica Nucleare, Universitá di Roma Tor Vergata (INFN-Roma Tor Vergata), Via della Ricerca Scientifica 1, 00133 Roma, Italy, [3]Dipartimento di Ingegneria dell’Impresa, Universitá di Roma Tor Vergata (INSTM-UdR Roma Tor Vergata), Via del Politecnico 1, 00133 Roma, Italy, [4]Universitá di Roma Niccolò Cusano (INSTM-UdR), Via Don Carlo Gnocchi 3, 00166 Roma, Italy and [5]Istituto di Struttura della Materia, Consiglio Nazionale delle Ricerche (ISM-CNR), Via del Fosso del Cavaliere 100, 00100 Roma, Italy

Email:
Francesco De Nicola* - fdenicola@roma2.infn.it

* Corresponding author

Keywords:
hierarchical structures; hydrophobic surfaces; multi-walled carbon nanotube; single-walled carbon nanotube; wetting transitions

Beilstein J. Nanotechnol. **2015,** *6,* 353–360.
doi:10.3762/bjnano.6.34

Received: 12 September 2014
Accepted: 13 January 2015
Published: 02 February 2015

This article is part of the Thematic Series "Self-assembly of nanostructures and nanomaterials".

Guest Editor: I. Berbezier

Abstract

Self-assembled hierarchical solid surfaces are very interesting for wetting phenomena, as observed in a variety of natural and artificial surfaces. Here, we report single-walled (SWCNT) and multi-walled carbon nanotube (MWCNT) thin films realized by a simple, rapid, reproducible, and inexpensive filtration process from an aqueous dispersion, that was deposited at room temperature by a dry-transfer printing method on glass. Furthermore, the investigation of carbon nanotube films through scanning electron microscopy (SEM) reveals the multi-scale hierarchical morphology of the self-assembled carbon nanotube random networks. Moreover, contact angle measurements show that hierarchical SWCNT/MWCNT composite surfaces exhibit a higher hydrophobicity (contact angles of up to 137°) than bare SWCNT (110°) and MWCNT (97°) coatings, thereby confirming the enhancement produced by the surface hierarchical morphology.

Introduction

In general, the surface morphology [1] is a crucial parameter for the fabrication of artificial hydrophobic surfaces and may be enhanced especially by hierarchical [2-7] and fractal structures [7,8], possibly allowing for the formation of air pockets to further impede the penetration of water [9].

In particular, hierarchical surface morphologies are a recent concept introduced to explain the wetting properties of surfaces such as plant leaves [2,3], bird feathers [10], and insect legs [11]. These surfaces are made of a hierarchical micro- and nanomorphology which improves their wettability.

It is indeed well-established [12,13] that on composite rough surfaces a hierarchical morphology may induce a wetting transition from Wenzel [1] to Cassie–Baxter [9] state owing to air trapping. Moreover, this transition may occur by passing through thermodynamically metastable states [13-16], where the free energy surface presents one absolute minimum and one or more local minima separated from the former by large free energy barriers, as compared to the thermal energy. Metastability can also have a technological importance, as in practice, it represents a way of extending the range of stability of the Cassie–Baxter state [14,17]. Conversely, a negative consequence of metastability is that it might prevent or slow down the transition between Wenzel and Cassie–Baxter states [14,17].

Moreover, biomimetics [18,19] may be exploited in order to realize cutting edge artificial surfaces [2,3,5] that mimicking natural surface. In this way these surfaces can be optimized for hydrophobic (lipophilic) and/or hydrophilic (lipophobic) applications.

Motivated by this concept, we report here the fabrication of highly hydrophobic coatings of self-assembling SWCNTs on MWCNTs. Since the former are smaller than the latter (about one order of magnitude), we observed that a surface hierarchy naturally occurs by depositing layer by layer a SWCNT film upon a MWCNT film. The particular two-fold hierarchical morphology of the surface, resembling that observed in lotus leaves [3] and rose petals [2] in which micropapillae are made of nanopapillae, improves the hydrophobic behavior of carbon nanotube coatings compared to bare SWCNT and MWCNT films. Moreover, we report for the first time the experimental Wenzel/Cassie–Baxter phase diagram [8,12,17] for a carbon nanotube surface, showing that the transition between the Wenzel and Cassie–Baxter states occurs by passing through metastable states.

Generally, carbon nanotubes [20,21] are the one-dimensional allotropic form of carbon with cylindrical symmetry and a sp^2 lattice. Carbon nanotubes may be single-walled or multi-walled depending on the number of coaxially arranged graphite planes. Moreover, owing to their honeycomb lattice, carbon nanotubes are inherently hydrophilic (the contact angle of graphite with water being approx. 86° [22]) but apolar. However, by surface functionalization or textured arrangement it can be possible to realize carbon nanotube films which offer versatility, high stability, and multi-functionality owing to their exceptionally unique properties [21], making their usage widespread in hydrophobic surface applications [4,5,23-35].

Furthermore, self-assembly hierarchical nanostructured materials [36-39] are nowadays investigated as a consequence of their tunable peculiar properties and the easy, highly reproducible, and low-cost fabrication. In addition, they are ideal low-dimensional materials for the fabrication of high aspect ratio and large area devices [40].

Results and Discussion

The films obtained from the process described in the Experimental section are porous random networks of SWCNTs and MWCNTs that exhibit a hierarchical morphology made of micro- and nanostructures, as evident from SEM micrographs in Figure 1. From SEM image analysis (see Experimental section), we estimated the pore radius ρ and the bundle diameter d of the SWCNT and MWCNT random networks. The obtained results are reported in Table 1 together with the SWCNT microstructure area S and height h. However, in the case of MWCNT films, no microstructures were observed. It is noteworthy that the characteristic dimension d of MWCNTs is bigger by about one order than that of SWCNTs.

In particular, we considered the microstructures shown in Figure 1c as ripples randomly distributed within the film. Such self-assembly occurs by an out-of-plane bending process during evaporative drying of single-walled carbon nanotube film during its preparation [36,37,41]. The out-of-plane assembly is the result of the competition between attractive capillary forces and bending stress due to the elasticity of SWCNT film. Once the liquid is completely evaporated, a pattern of micrometer-sized randomly shaped islands is formed. If, after complete evaporation, there is a balance between adhesion and elastic energy, the microstructures are in a stable bent configuration with respect to further wetting–dewetting cycles. This self-assembly leads to an intrinsic hierarchical microstructured (ripples) and nanostructured (carbon nanotubes) roughness able to enhance the wetting properties of the SWCNT film. Conversely, the MWCNT sample (Figure 1d) just aligned vertically out of plane.

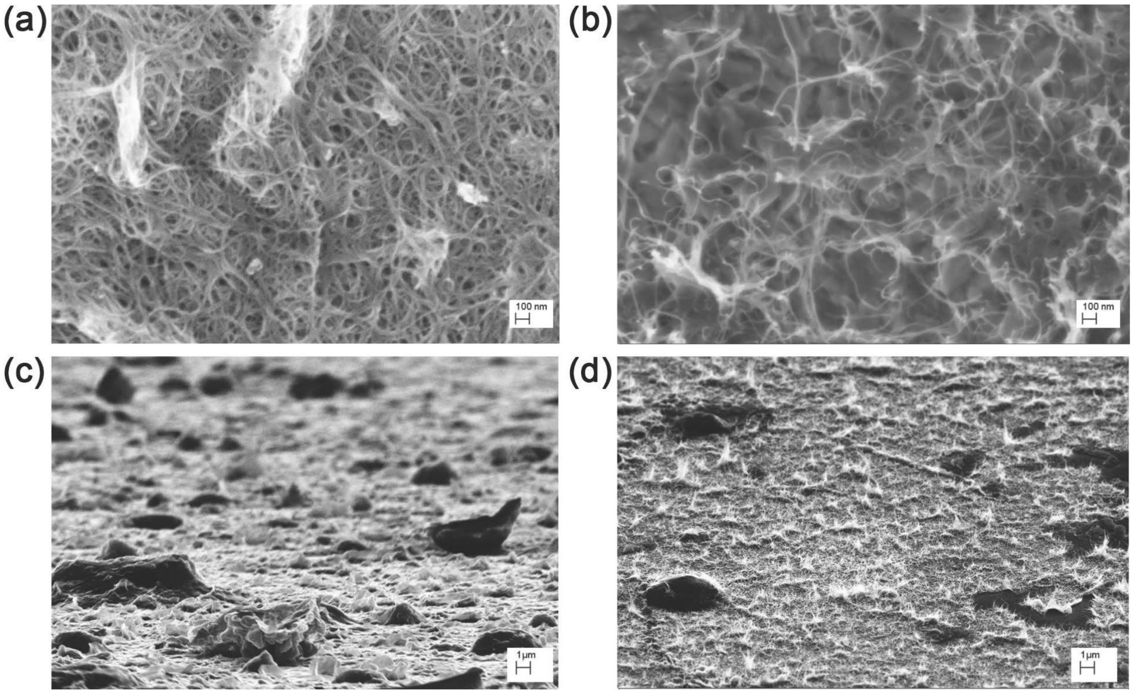

Figure 1: Scanning electron micrographs of SWCNT (a,c) and MWCNT (b,d) films at different magnifications 200,000× (a,b), and 10,000× (c,d). In the images taken at grazing incidence (c,d) it is possible to observe that SWCNTs (c) self-assemble in ripples forming several microstructures, while MWCNTs (d) just aligned in the out-of-plane vertical direction. (d) Black areas are holes in the film.

Table 1: Experimental results of SEM analysis and contact angle measurements.

sample	ρ (nm)	*d* (nm)	*S* (μm^2)	*h* (μm)	θ (°)
SWCNT	2–8	4–8	0.003–0.007	1.6–11.7	110 ± 3
MWCNT	40–44	34–84	—	—	97 ± 8
SWCNT/MWCNT	47–51	—	7.3–13.7	3.2–61.6	129 ± 8
MWCNT/SWCNT	5–7	—	7.7–14.3	2.3–76.2	103 ± 7

Furthermore, we induced an extrinsic hierarchical architecture by depositing a SWCNT film on a MWCNT film (SWCNT/MWCNT) and in reverse order (MWCNT/SWCNT), as shown in Figure 2. From SEM image analysis, we obtained the two film pore diameters, microstructure areas and heights, as reported in Table 1. In both cases, a self-assembly led to the formation of several huge microstructures as compared to the those of the SWCNT films.

Moreover, in Figure 3a and Figure 3b, images of water droplets cast on our SWCNT and MWCNT films are shown, with average contact angle values of θ = 110 ± 3° and θ = 97 ± 8°, respectively. These results can be ascribed to the particular morphology of both the films induced by the inherent properties of the carbon nanotubes (e.g., self-assembly, nanotube diameter and spatial orientation) and film preparation method. We also found that for the SWCNT/MWCNT sample the extrinsic surface hierarchy increased the hydrophobicity of the MWCNT sample, exhibiting a highly hydrophobic average contact angle value of θ = 129 ± 8° (Figure 3c), comparable to the values of PTFE (Teflon) of 108–118° [22,42]. Conversely, for the MWCNT/SWCNT sample (Figure 3d) a slightly decrease of the average contact angle value (θ = 103 ± 7°) with respect to the bare SWCNT sample was encountered.

Our results, summarized in Table 1, may be interpreted on the basis of the microstructure characteristic dimensions *S* and *h*. In both the SWCNT/MWCNT and MWCNT/SWCNT samples the microstructure characteristic dimensions are comparable with those of lotus and rose micropapillae [2,3]. Nevertheless, in the latter the extrinsic hierarchical morphology is reversed (bigger MWCNT scale superimposed on the smaller SWCNT scale), thereby losing the hierarchical fakir effect [7,43]. Therefore, the SWCNT/MWCNT sample has the best hydrophobic behavior

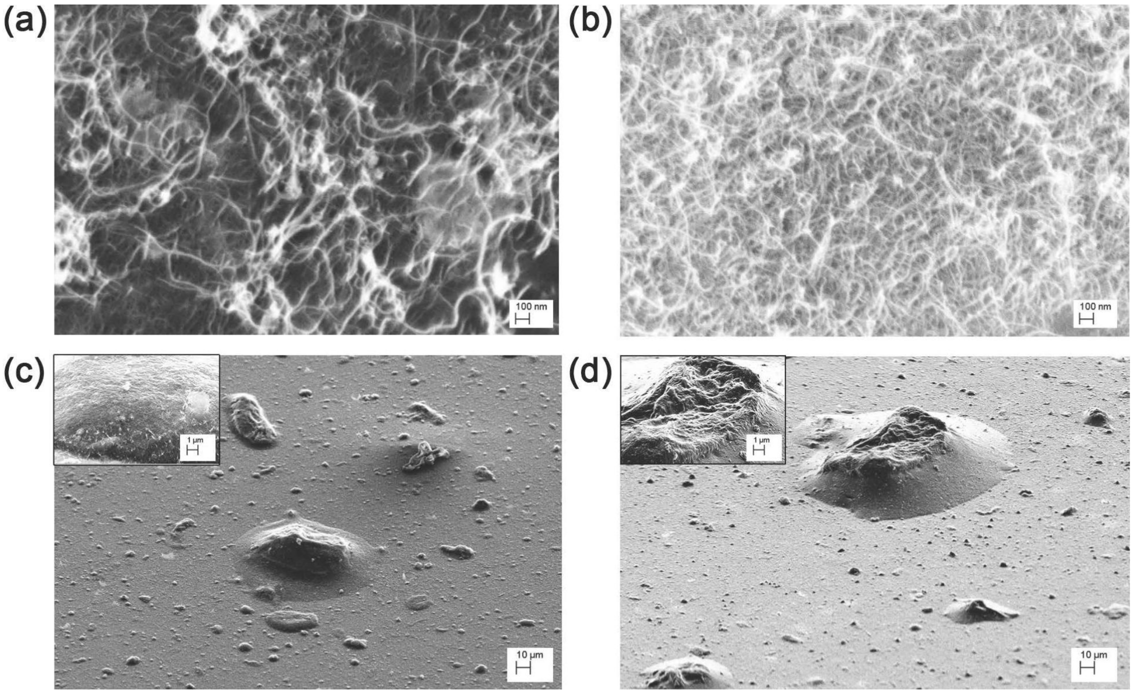

Figure 2: Scanning electron micrographs of SWCNT/MWCNT (a,c) and MWCNT/SWCNT (b,d) films at different magnifications 200,000 × (a,b), 1,000× (c,d), and 10,000× (c,d insets). In the images taken at grazing incidence (c,d and insets), it is possible to observe that in both cases the self-assembly forms several huge microstructures. (c,d insets) Details of the microstructures showing a hierarchical morphology very similar to that of lotus leaves and rose petals.

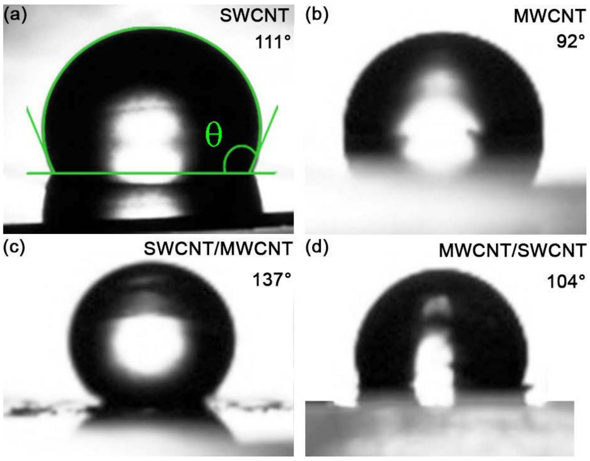

Figure 3: Water droplets cast on SWCNT (a), MWCNT (b), SWCNT/MWCNT (c), and MWCNT/SWCNT (d) films. Owing to the rough and porous surface of the samples, water drops exhibit different contact angle values, depending on the exact place at the surface on which they are cast. In this case, the contact angle can be only defined on average.

because is the most biomimetic. We remark that the large deviation of the average value of the contact angle is due to the highly rough and porous surface of our samples. In addition, no roll-off angle value could be measured, evidently due to the high contact angle hysteresis, which pinned the droplets to the surface [2].

In order to better understand the origin of the enhancement provided by the SWCNT/MWCNT film over the MWCNT film, we characterized the wetting state of the former composite surface with respect to the latter. In Figure 4a, we report the contact angle of both films as a function of the concentration in volume percent of ethanol in water. It is possible to observe that since ethanol has a lower liquid–vapor surface tension ($\gamma_{LV} = 22$ mJ·m^{-2}) than water ($\gamma_{LV} = 72$ mJ·m^{-2}), the higher the ethanol concentration in water, the lower the surface tension of the solution. Furthermore, the contact angle is generally proportional to the liquid surface tension by the Young's relation

$$\cos\theta = \frac{\gamma_{SV} - \gamma_{SL}}{\gamma_{LV}}, \qquad (1)$$

where γ_{SV} and γ_{SL} are the solid–vapor and solid–liquid surface tensions, respectively. Therefore, also the contact angles of the carbon nanotube films decrease with the decrease in surface tension of the liquid droplet. This phenomenon is connected to the lipophilicity of the apolar surface of the carbon nanotube. Indeed, on our carbon nanotube films no contact angle ($\theta \approx 0$) can be measured for pure ethanol droplets. Therefore, we

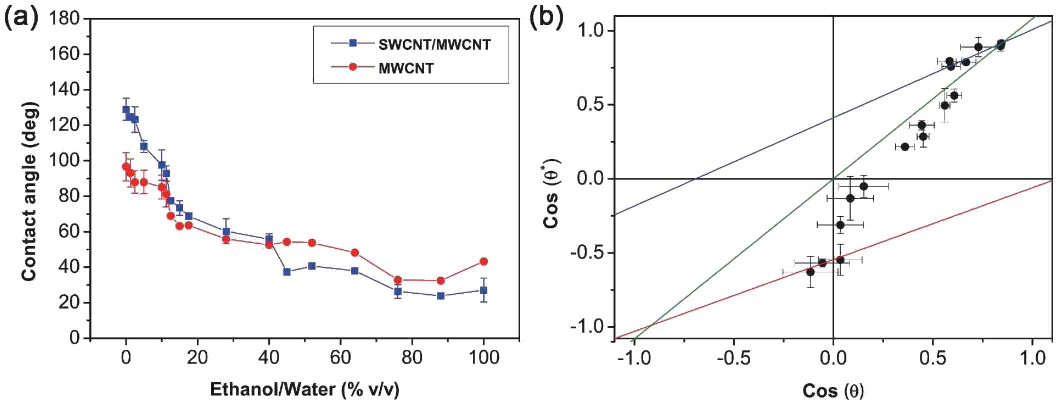

Figure 4: (a) Contact angle of the SWCNT/MWCNT (blue squares) and MWCNT (red dots) films as a function of ethanol concentration in water. (b) Wenzel/Cassie–Baxter phase diagram of the SWCNT/MWCNT surface respect to the MWCNT surface. Wetting states are studied changing the liquid surface tension by adding different ethanol concentrations in water. Wenzel regime (green solid line) fit reports a roughness factor *r* = 1.08 ± 0.01, while lipophilic (blue solid line) and hydrophobic (red solid line) Cassie–Baxter regime fits report respectively a liquid fraction $\phi_+ = 0.41 \pm 0.04$ and an air fraction $\phi_- = 0.54 \pm 0.02$. The Wenzel/Cassie–Baxter transition point in the hydrophobic regime is the intersection between the red and green solid lines, while in the lipophilic regime it is the intersection between the blue and green solid lines. Error bars are standard deviations.

investigated all the wetting phenomena occurring on our carbon nanotube surface, exploring all the wetting states. We further noted that for θ ≈ 56°, (cos θ ≈ 0.56) there is an intersection point between the two curves in Figure 4a, beyond which the SWCNT/MWCNT surface becomes more lipophilic than the MWCNT surface. That point corresponds to the transition point from Wenzel to Cassie–Baxter state in the lipophilic region of the Wenzel/Cassie–Baxter phase diagram, as confirmed from the plot (first quadrant) in Figure 4b. However, the plot in Figure 4b shows that the transition occurs by passing through metastable states with an abrupt change in the wetting state. We fitted our data with the lipophilic Cassie–Baxter's equation [9]

$$\cos\theta^* = \left(1-\phi_+\right)\cos\theta + \phi_+, \quad 1 = \phi + \phi_+ , \tag{2}$$

with ϕ the surface solid fraction, ϕ_+ the surface fraction wetted by the liquid, θ^* the SWCNT/MWCNT surface contact angle and θ the MWCNT surface contact angle. We obtained from fit a liquid fraction $\phi_+ = 0.41 \pm 0.04$ in contact with the droplet. However, we remark that these metastable Cassie–Baxter states coexist with the Wenzel states, which are stable because lower in surface free energy.

Moreover we fitted our data in Figure 4b with Wenzel's equation [1]

$$\cos\theta^* = r\cos\theta, \quad r \geq 1 , \tag{3}$$

where *r* is the roughness factor (i.e, the ratio between the actual wet surface area and its projection on the plane). Interestingly, the fit returned *r* = 1.08 ± 0.01, which means that substantially the SWCNT/MWCNT sample has the same roughness of the MWCNT sample. It is noteworthy that in our case *r* ≈ 1 does not mean that the surface is smooth, because we are not comparing the SWCNT/MWCNT with its corresponding smooth surface with the same chemistry, such as plain graphite. However, in the latter case we would have had a high roughness factor [41]. Therefore, we can exclude a roughness enhancement, which we did not observe, as the reason of a such improvement in hydrophobic behavior the SWCNT/MWCNT sample over the MWCNT sample. In addition, from the relation [44]

$$\cos\theta' = \frac{1-\phi_+}{r-\phi_+} , \tag{4}$$

we can infer that the lipophilic Wenzel/Cassie–Baxter transition point is cos θ′ = 0.88 (the intersection between the blue and green solid lines in Figure 4b), which is beyond the measured data, thus confirming that the achieved lipophilic Cassie–Baxter states are metastable.

Conversely, in the hydrophobic region (third quadrant of the plot) we observe a sharp discontinuity beyond cos θ = 0, confirming again that the transition between the Wenzel and Cassie–Baxter states is not continuous, but it undergoes metastable states which slow down the dewetting process. Actually, by fitting our data in Figure 4b with the hydrophobic Cassie–Baxter's equation

$$\cos\theta^* = \left(1-\phi_-\right)\cos\theta - \phi_-, \quad 1 = \phi + \phi_- , \tag{5}$$

we obtained an air surface fraction $\phi_{-} = 0.54 \pm 0.02$ below the liquid droplet. Furthermore, by the relation [44]

$$\cos\theta'' = \frac{\phi_{-} - 1}{r - \phi_{-}}, \tag{6}$$

we can infer that the hydrophobic Wenzel/Cassie–Baxter transition point is cos θ″ = −0.85 (the intersection between the red and green solid lines in Figure 4b), which is beyond the measured data, thus confirming that the achieved hydrophobic Cassie–Baxter states are metastable. Nevertheless, this result suggests a consistent air pocket formation [9].

Therefore, we can assert that the only cause of the improved hydrophobicity/lipophilicity of the SWCNT/MWCNT film over the MWCNT film, is the fakir effect induced by the two-fold hierarchical morphology given by the SWCNT film superimposed on the MWCNT film. This particular morphology induces the formation of air pocket when the interaction with the liquid is hydrophobic, otherwise it favourites the formation of a precursor liquid film [44] that enhances the wettability of the carbon nanotube surface, when the interaction with the liquid is lipophilic.

Furthermore, we studied the stability of our carbon nanotube films over time by performing suction experiments. Figure 5 reports the variations of the contact angle value as a function of the elapsed time from dropping the liquid on the SWCNT, MWCNT, SWCNT/MWCNT, and MWCNT/SWCNT coatings. In such suction experiment, we show that although the samples are porous, the contact angle trend is quite constant. In particular, we demonstrated the stability over time of the hydrophobic Cassie–Baxter metastable state for the SWCNT/MWCNT sample. However, the slight linear decrease of the contact angle in time is both due to liquid evaporation and suction by the porous films. Our results are particularly remarkable, since the water contact angle of carbon nanotube films has been reported [45] so far to linearly decrease with time, from an initial value of approx. 146° to about zero within 15 min.

Conclusion

Single-walled and multi-walled carbon nanotube films were prepared by vacuum filtration of an aqueous dispersion. Such coatings were deposited by dry-transfer printing on glass, at room temperature. Furthermore, SEM images revealed the intrinsic hierarchical nature of carbon nanotube random networks owed to a dry-induced out-of-plane self-assembly phenomenon. Moreover, static contact angles of sessile water drops cast on carbon nanotube composite surfaces were measured, finding that our SWCNT random network films are more hydrophobic than our MWCNT random network films.

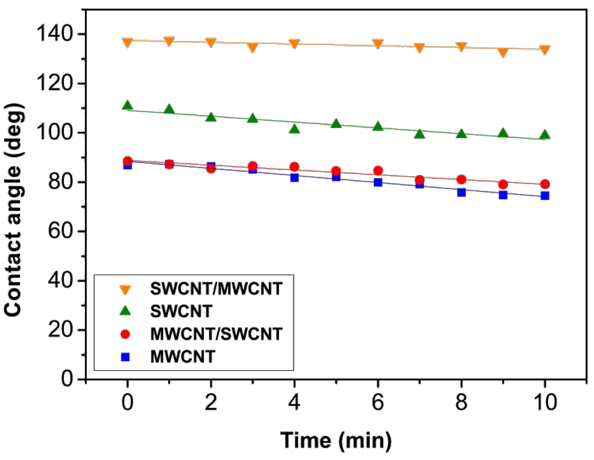

Figure 5: Variations of the contact angle as a function of the elapsed time from drop cast on the porous SWCNT (green triangles), MWCNT (blue squares), SWCNT/MWCNT (orange inverted triangles), MWCNT/SWCNT (red dots) films. The quite constant trend of the SWCNT/MWCNT contact angle value shows the stability in time of the carbon nanotube hydrophobic Cassie–Baxter metastable state.

This behavior may be ascribed to remarkable differences in the two film morphology induced by our preparation method. However, since the characteristic dimension of SWCNT is one order of magnitude smaller than MWCNT, when a SWCNT film is placed on a MWCNT film an extrinsic hierarchical morphology occurs making the resulting composite surface highly hydrophobic (θ = 129 ± 8°). We showed that our results are due to two main reasons: (i) The characteristic dimension of the self-assembly microstructures in the SWCNT/MWCNT samples are comparable with those of micropapillae in hydrophobic plant leaves. (ii) The hierarchical surface morphology lead to the formation of a consistent amount of air pockets, as a consequence of the transition from the hydrophobic Wenzel state to the hydrophobic Cassie–Baxter metastable state. In addition, we observed that the latter state is fairly stable in time. Such highly hydrophobic hierarchical carbon nanotube coatings may be very attracting for several industrial applications such as waterproof surfaces [23], anti-sticking [31], anti-contamination [4], self-cleaning [46], anti-fouling [47], anti-fogging [48], low-friction coatings [5], adsorption [30], lubrication [22], dispersion [44], and self-assembly [49].

Experimental

Fabrication of carbon nanotube films

Highly pure SWCNT powder (Sigma-Aldrich, assay >90%, diameter: 0.7–0.9 nm) and MWCNT powder (Nanocyl, NC7000, assay >90%, diameter: 5–50 nm) were dispersed in aqueous solution (80 μg·mL^{-1}) with 2% w/v sodium dodecyl sulfate (Sigma-Aldrich, assay >98.5%) anionic surfactant. In addition, to better disperse the suspension, the carbon nanotubes were tip-ultrasonicated (Branson S250A, 200 W, 20% power, 20 kHz) in an ice-bath for an hour and the unbundled supernatant was collected through a pipette. The result was a well-dispersed suspension that is stable for several months. Carbon nanotube films were fabricated by a vacuum filtration process of 1 mL in volume of the dispersion cast on mixed cellulose ester filters (Pall GN6, 1 in diameter, 0.45 μm pore diameter). In order to prepare hierarchical MWCNT/SWCNT films, after filtering 1 mL of the SWCNT dispersion, 1 mL of the MWCNT dispersion was filtered. This process was also carried out in reverse order to produce SWCNT/MWCNT films. In this way, a stack of two different film layers were obtained. Subsequently, rinsing in water and in a solution of ethanol, methanol and water (15:15:70) to remove as much surfactant as possible was performed. Samples were made uniformly depositing by the dry-transfer printing method carbon nanotube films on Carlo Erba soda-lime glass slides. More details about this novel deposition technique without chemical deposition processes have been reported elsewhere [41].

Sample characterization

Scanning electron microscopy micrographs were acquired with Zeiss Leo Supra 35 field emission scanning electron microscope (FEG-SEM) and analyzed in order to measure carbon nanotube bundle diameter, network pore, and microstructure feature (height and area) distributions. A statistical analysis of these quantities was performed and the values reported in Table 1 were estimated by taking the quantity distribution mode values and standard deviations. In particular, we performed microstructure area measurements through analyzing the SEM micrographs of the films at a magnification of 30,000× with a threshold algorithm and considering their irregular shape. The analysis of microstructure height was carried out on SEM images acquired at a magnification of 10,000× at grazing angle, i.e., by tilting the sample to an angle very close to 90° with respect to the sample normal. In such a way, the height of film microstructures can be estimated by trigonometric measurements. The film pore area defined as the area of the irregular empty regions delimited by the intersection among carbon nanotube bundles was quantified by the statistical analysis with a threshold algorithm of film SEM images at the highest magnification (200,000×), at which pores are clearly observable. The radius of the pore was calculated by considering the pore area as that of a circle.

Contact angle measurements

Images of sessile water drops cast on carbon nanotube films were acquired by a custom setup with a CCD camera. Static advanced contact angles were measured by increasing the volume of the drop by steps of 1 μL, and a plugin [50] for the open-source software ImageJ was exploited to estimate the contact angle values. This plugin exploits an algorithm based on a small-perturbation solution of the Young–Laplace equation [22]. Furthermore, the presented method is applied to a continuous image of the droplet by using cubic B-Spline interpolation of the drop contour to reach subpixel resolution. Every contact angle value reported is the average over five measures of images of droplets cast on five different points of the film (namely in the center, north, south, east, and west part). The deionized water (18.2 MΩ·cm) drop volume used to achieve the contact angles of samples was $V = 10$ μL. Moreover, every contact angle was measured 15 s after drop casting to ensure that the droplet reached its equilibrium position.

Acknowledgements

The authors thank R. De Angelis, F. De Matteis, and P. Prosposito (Universitá di Roma Tor Vergata, Roma, Italy) for their courtesy of contact angle instrumentation. This project was financial supported by the European Office of Aerospace Research and Development (EOARD) through the Air Force Office of Scientific Research Material Command, USAF, under Grant No. FA9550-14-1-0047.

References

1. Wenzel, R. N. *Ind. Eng. Chem.* **1936,** *28,* 988–994. doi:10.1021/ie50320a024
2. Feng, L.; Zhang, Y.; Xi, J.; Zhu, Y.; Wang, N.; Xia, F.; Jiang, L. *Langmuir* **2008,** *24,* 4114–4119. doi:10.1021/la703821h
3. Sun, M.; Luo, C.; Xu, L.; Ji, H.; Ouyang, Q.; Yu, D.; Chen, Y. *Langmuir* **2005,** *21,* 8978–8981. doi:10.1021/la050316q
4. Li, Y.; Huang, X. J.; Heo, S. H.; Li, C. C.; Choi, Y. K.; Cai, W. P.; Cho, S. O. *Langmuir* **2007,** *23,* 2169–2174. doi:10.1021/la0620758
5. Jung, Y. C.; Bhushan, B. *ACS Nano* **2009,** *3,* 4155–4163. doi:10.1021/nn901509r
6. Egatz-Gomez, A.; Majithia, R.; Levert, C.; Meissner, K. E. *RSC Adv.* **2012,** *2,* 11472–11480. doi:10.1039/c2ra22267a
7. Bittoun, E.; Marmur, A. *Langmuir* **2012,** *28,* 13933–13942. doi:10.1021/la3029512
8. Shibuichi, S.; Onda, T.; Satoh, N.; Tsujii, K. *J. Phys. Chem.* **1996,** *100,* 19512–19517. doi:10.1021/jp9616728
9. Cassie, A. B. D.; Baxter, S. *Trans. Faraday Soc.* **1944,** *40,* 546–551. doi:10.1039/tf9444000546
10. Bormashenko, E.; Bormashenko, Y.; Stein, T.; Whyman, G.; Bormashenko, E. *J. Colloid Interface Sci.* **2007,** *311,* 212–216. doi:10.1016/j.jcis.2007.02.049
11. Gao, X.; Jiang, L. *Nature* **2004,** *432,* 36. doi:10.1038/432036a
12. Lafuma, A.; Quéré, D. *Nat. Mater.* **2003,** *2,* 457–460. doi:10.1038/nmat924
13. Giacomello, A.; Chinappi, M.; Meloni, S.; Casciola, C. M. *Phys. Rev. Lett.* **2012,** *109,* 226102. doi:10.1103/PhysRevLett.109.226102
14. Giacomello, A.; Meloni, S.; Chinappi, M.; Casciola, C. M. *Langmuir* **2012,** *28,* 10764–10772. doi:10.1021/la3018453
15. Savoy, E. S.; Escobedo, F. A. *Langmuir* **2012,** *28,* 16080–16090. doi:10.1021/la303407r
16. Murakami, D.; Jinnai, H.; Takahara, A. *Langmuir* **2014,** *30,* 2061–2067. doi:10.1021/la4049067

17. Bico, J.; Thiele, U.; Quéré, D. *Colloids Surf., A* **2002,** *206,* 41–46. doi:10.1016/S0927-7757(02)00061-4
18. Bhushan, B. *Philos. Trans. R. Soc. London, Ser. A* **2009,** *367,* 1445–1486. doi:10.1098/rsta.2009.0011
19. Bar-Cohen, Y. *Biomimetics Biologically Inspired Technologies;* CRC Press: Boca Raton, 2005.
20. Iijima, S. *Nature* **1991,** *354,* 56–58. doi:10.1038/354056a0
21. Jorio, A.; Dresselhaus, G.; Dresselhaus, M. S. *Carbon Nanotubes Advanced Topics in the Synthesis, Structure, Properties and Applications;* Springer: New York, 2008.
22. Adamson, A. W.; Gast, A. P. *Physical Chemistry of Surfaces;* John Wiley & Sons: New York, 1997.
23. Georgakilas, V.; Bourlinos, A. B.; Zboril, R.; Trapalis, C. *Chem. Mater.* **2008,** *20,* 2884–2886. doi:10.1021/cm7034079
24. Wang, N.; Xi, J.; Wang, S.; Liu, H.; Feng, L.; Jiang, L. *J. Colloid Interface Sci.* **2008,** *320,* 365–368. doi:10.1016/j.jcis.2008.01.005
25. Yang, J.; Zhang, Z.; Men, X.; Xu, X.; Zhu, X. *J. Colloid Interface Sci.* **2010,** *346,* 241–247. doi:10.1016/j.jcis.2010.02.040
26. Kakade, B. A.; Pillai, V. K. *J. Phys. Chem. C* **2008,** *112,* 3183–3186. doi:10.1021/jp711657f
27. Nasibulin, A. G.; Kaskela, A.; Mustonen, K.; Anisimov, A. S.; Ruiz, V.; Kivistö, S.; Rackauskas, S.; Timmermans, M. Y.; Pudas, M.; Aitchison, B.; Kauppinen, M.; Brown, D. P.; Okhotnikov, O. G.; Kauppinen, E. I. *ACS Nano* **2011,** *5,* 3214–3221. doi:10.1021/nn200338r
28. Wang, C.-F.; Chen, W.-Y.; Cheng, H.-Z.; Fu, S.-L. *J. Phys. Chem. C* **2010,** *114,* 15607–15611. doi:10.1021/jp1047985
29. Wang, K.; Hu, N.-X.; Xu, G.; Qi, Y. *Carbon* **2011,** *49,* 1769–1774. doi:10.1016/j.carbon.2010.12.063
30. Li, J.; Wang, L.; Jiang, W. *Carbon* **2010,** *48,* 2668–2671. doi:10.1016/j.carbon.2010.03.038
31. Wang, Z.; Koratkar, N.; Ci, L.; Ajayan, P. M. *Appl. Phys. Lett.* **2007,** *90,* 143117. doi:10.1063/1.2720761
32. Zhang, L.; Resasco, D. E. *Langmuir* **2009,** *25,* 4792–4798. doi:10.1021/la8040264
33. Bu, I. Y. Y.; Oei, S. P. *Appl. Surf. Sci.* **2010,** *256,* 6699–6704. doi:10.1016/j.apsusc.2010.04.073
34. Kakade, B.; Mehta, R.; Durge, A.; Kulkarni, S.; Pillai, V. *Nano Lett.* **2008,** *8,* 2693–2696. doi:10.1021/nl801012r
35. Li, S.; Li, H.; Wang, X.; Song, Y.; Liu, Y.; Jiang, L.; Zhu, D. *J. Phys. Chem. B* **2002,** *106,* 9274–9276. doi:10.1021/jp0209401
36. Li, Q.; DePaula, R.; Zhang, X.; Zheng, L.; Arendt, P. N.; Mueller, F. M.; Zhu, Y. T.; Tu, Y. *Nanotechnology* **2006,** *17,* 4533–4536. doi:10.1088/0957-4484/17/18/001
37. Chakrapani, N.; Wei, B.; Carrillo, A.; Ajayan, P. M.; Kane, R. S. *Proc. Natl. Acad. Sci. U. S. A.* **2004,** *101,* 4009–4012. doi:10.1073/pnas.0400734101
38. Bohn, S.; Platkiewicz, J.; Andreotti, B.; Adda-Bedia, M.; Couder, Y. *Phys. Rev. E* **2005,** *71,* 046215. doi:10.1103/PhysRevE.71.046215
39. Fusi, M.; Di Fonzo, F.; Casari, C. S.; Maccallini, E.; Caruso, T.; Agostino, R. G.; Bottani, C. E.; Bassi, A. L. *Langmuir* **2011,** *27,* 1935–1941. doi:10.1021/la103955q
40. Sauvage, F.; Di Fonzo, F.; Li Bassi, A.; Casari, C. S.; Russo, V.; Divitini, G.; Ducati, C.; Bottani, C. E.; Comte, P.; Graetzel, M. *Nano Lett.* **2010,** *10,* 2562–2567. doi:10.1021/nl101198b
41. De Nicola, F.; Castrucci, P.; Scarselli, M.; Nanni, F.; Cacciotti, I.; De Crescenzi, M. *Sci. Rep.* **2014,** in press.
42. Clark, M. D.; Krishnamoorti, R. *Thin Solid Films* **2012,** *520,* 4332–4338. doi:10.1016/j.tsf.2012.02.067
43. Quéré, D. *Nat. Mater.* **2002,** *1,* 14–15. doi:10.1038/nmat715
44. De Gennes, P.-G.; Brochard-Wyart, F.; Quéré, D. *Capillarity and wetting phenomena;* Springer: New York, 2003.
45. Huang, L.; Lau, S. P.; Yang, H. Y.; Leong, E. S. P.; Yu, S. F. *J. Phys. Chem. B* **2005,** *109,* 7746–7748. doi:10.1021/jp046549s
46. Fürstner, R.; Barthlott, W.; Neinhuis, C.; Walzel, P. *Langmuir* **2005,** *21,* 956–961. doi:10.1021/la0401011
47. Zhang, H.; Lamb, R.; Lewis, J. *Sci. Technol. Adv. Mater.* **2005,** *6,* 236–239. doi:10.1016/j.stam.2005.03.003
48. Lai, Y.; Tang, Y.; Gong, J.; Gong, D.; Chi, L.; Lin, C.; Chen, Z. *J. Mater. Chem.* **2012,** *22,* 7420–7426. doi:10.1039/c2jm16298a
49. Huang, Y.; Zhou, J.; Su, B.; Shi, L.; Wang, J.; Chen, S.; Wang, L.; Zi, J.; Song, Y.; Jiang, L. *J. Am. Chem. Soc.* **2012,** *134,* 17053–17058. doi:10.1021/ja304751k
50. Stalder, A. F.; Melchior, T.; Müller, M.; Sage, D.; Blu, T.; Unser, M. *Colloids Surf., A* **2010,** *364,* 72–81. doi:10.1016/j.colsurfa.2010.04.040

License and Terms

BEILSTEIN JOURNAL OF NANOTECHNOLOGY

In situ scanning tunneling microscopy study of Ca-modified rutile TiO_2(110) in bulk water

Giulia Serrano*[1], Beatrice Bonanni[1], Tomasz Kosmala[1,2], Marco Di Giovannantonio[1,3], Ulrike Diebold[4], Klaus Wandelt[2] and Claudio Goletti[1]

Full Research Paper

Open Access

Address:
[1]Department of Physics, Università degli Studi di Roma “Tor Vergata”, Via della Ricerca Scientifica 1, 00133 Rome, Italy, [2]Institut für Physikalische und Theoretische Chemie, Wegelerstraße 12, 53115 Bonn, Germany, [3]Istituto di Struttura della Materia (ISM), Consiglio Nazionale delle Ricerche (CNR), Via Fosso del Cavaliere 100, 00133 Rome, Italy and [4]Institute of Applied Physics, Vienna University of Technology, Wiedner Hauptstraße 8–10/134, 1040 Vienna, Austria

Email:
Giulia Serrano* - serrano@roma2.infn.it

* Corresponding author

Keywords:
alkali earth metals; scanning probe microscopy; solid/liquid interface; titanium dioxide reconstruction

Beilstein J. Nanotechnol. **2015,** *6,* 438–443.
doi:10.3762/bjnano.6.44

Received: 29 September 2014
Accepted: 15 January 2015
Published: 12 February 2015

This article is part of the Thematic Series "Self-assembly of nanostructures and nanomaterials".

Guest Editor: I. Berbezier

Abstract

Despite the rising technological interest in the use of calcium-modified TiO_2 surfaces in biomedical implants, the Ca/TiO_2 interface has not been studied in an aqueous environment. This investigation is the first report on the use of in situ scanning tunneling microscopy (STM) to study calcium-modified rutile TiO_2(110) surfaces immersed in high purity water. The TiO_2 surface was prepared under ultrahigh vacuum (UHV) with repeated sputtering/annealing cycles. Low energy electron diffraction (LEED) analysis shows a pattern typical for the surface segregation of calcium, which is present as an impurity on the TiO_2 bulk. In situ STM images of the surface in bulk water exhibit one-dimensional rows of segregated calcium regularly aligned with the [001] crystal direction. The in situ-characterized morphology and structure of this Ca-modified TiO_2 surface are discussed and compared with UHV-STM results from the literature. Prolonged immersion (two days) in the liquid leads to degradation of the overlayer, resulting in a disordered surface. X-ray photoelectron spectroscopy, performed after immersion in water, confirms the presence of calcium.

Introduction

Metal oxide surfaces (in particular titanium dioxide (TiO_2) surfaces) covered by an alkaline-earth-metal overlayer have been investigated in recent years in experiments [1-5] and theoretical studies [6], considering applications ranging from nanotechnology [7] to gas sensing [8], as well as catalysis [9] and biomedicine [10,11]. In particular, the high corrosion resistance of titanium to biological environments has stimulated the study of this metal and its oxide for in vivo or in vitro calcium phosphate ceramic growth [12-15]. Recently, the deposition of a thin calcium layer onto TiO_2 substrates resulted in a prototypical model of the interface responsible for the bone growth by apposition in medical implants [16].

The experiments reported in the literature mostly concern Ca overlayers on a $TiO_2(110)$ rutile surface prepared under ultra-high vacuum (UHV) conditions, which is considered to be a model system [10,11]. Ordered Ca layers have been obtained by thermally activated segregation from the bulk [1-5], where calcium was a common bulk impurity in the TiO_2 samples [10]. A $c(6 \times 2)$ structure has been proposed for the resulting Ca overlayer based on low energy electron diffraction (LEED) and scanning tunneling microscopy (STM) measurements [1]. Segregation has been reported to produce an additional, differently ordered Ca layer, namely a $p(3 \times 1)$ structure [2-4]. More controlled and homogeneous Ca overlayers have been grown on a TiO_2 surface by metal vapor deposition (MVD) technique [5], showing that both MVD and segregation methods can produce a $c(6 \times 2)$ Ca structure. Finally, theoretical calculations have provided insight into possible preferential adsorption sites for Ca atoms on this surface [6].

The study of the Ca/TiO_2 interface in ideal (UHV) conditions lacks information about the electronic and structural modifications occurring under more realistic conditions, in particular, in an aqueous environment. Such a study would be an essential step towards a more thorough understanding of the system, leading to the optimization of many related applications. As an example, it was recently demonstrated that a low surface calcium coverage may increase the wetting energy and therefore the surface hydrophilicity of TiO_2 surfaces [17]. This has very interesting implications for the application of Ti-based biomaterials, since the augmented wettability would enhance the interaction between the implant surface and the biological environment.

In this paper we present an in situ STM investigation of a Ca overlayer thermally grown in UHV on the $TiO_2(110)$ rutile surface and then immersed in water. The $c(6 \times 2)$ LEED pattern observed after UHV preparation and the subsequent X-ray photoelectron spectroscopy (XPS) measurements confirm that high-temperature annealing produces a Ca layer by thermal segregation from the bulk. After immersion in high purity water, STM images show quasi one-dimensional rows of bright protrusions aligned with the [001] direction of the $TiO_2(110)$ surface. The stability of this overlayer in water is discussed.

Results and Discussion

The $TiO_2(110)$ surface was prepared in UHV with sputtering/annealing cycles, as described in detail in the Experimental section, and the surface quality was examined using LEED. In Figure 1, we report the LEED pattern of the TiO_2 surface: (a) after the usual preparation in UHV resulting in the 1 × 1 clean phase [10] and (b) after calcium segregation due to a higher annealing temperature [1-5].

In the latter case, two sets of diffraction patterns are visible, which is in agreement with the patterns previously observed by other groups for $TiO_2(110)$ covered with approximately one monolayer (ML) of Ca [1,5]. More intense spots form the rectangular pattern (green, solid line in Figure 1b) characteristic of the clean $TiO_2(110)$ surface, and correspond to the 1 × 1 termination as shown in Figure 1a. Marked streaks appear along

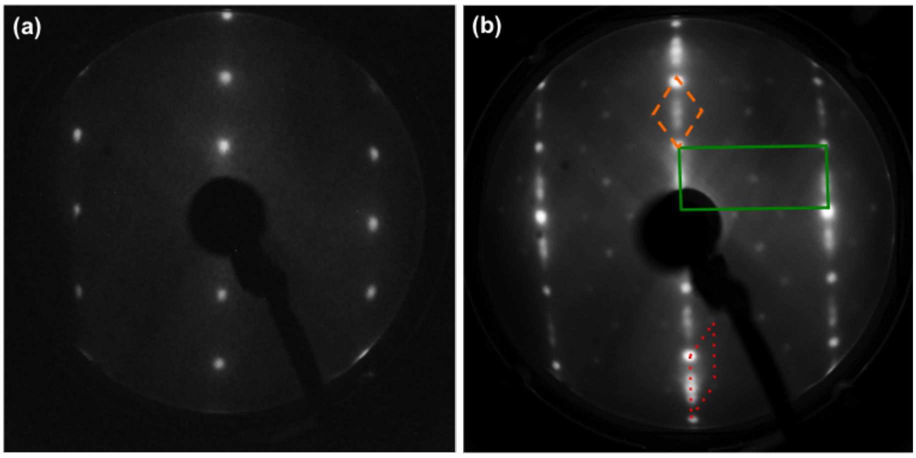

Figure 1: LEED pattern of (a) the clean $TiO_2(110)$ surface showing the 1 × 1 termination (electron beam energy E = 56 eV); (b) the $TiO_2(110)$ surface after Ca segregation from the bulk, after annealing in UHV at a higher temperature (electron beam energy E = 65 eV). Both the 1 × 1 unit cell of the substrate (green, solid line) and the $c(6 \times 2)$ unit cell of the Ca overlayer are shown. The orange, dashed and red, dotted lines indicate two possible choices for the $c(6 \times 2)$ unit cell.

the columns of spots aligned in the $[1\bar{1}0]$ direction, indicating the lack of in-phase correlation as a consequence of some degree of disorder in this direction. This is likely related to oxygen deficiencies in the surface layer caused by UHV preparation [1,10]. Between the primary pattern and the streaks a second set of weaker spots can be observed that form a $c(6 \times 2)$ superstructure. As proposed by Zhang et al. [1], two possible unit cells,

$$\begin{bmatrix} 3 & 1 \\ 3 & -1 \end{bmatrix}$$

(orange, dashed line) and

$$\begin{bmatrix} 6 & 0 \\ 3 & 1 \end{bmatrix}$$

(red, dotted line) are also shown.

The sample was transferred from the UHV chamber to the STM cell and then immersed in high purity water (see Experimental section for details). STM images of the surface shown in Figure 2 were recorded in water after approximately two hours of immersion. In the chosen tip polarity (the sample is grounded), electrons tunnel into empty surface states. The TiO_2 sample exhibits a terraced surface with a terrace width of about 100 nm, and step height of 3.2 ± 0.5 Å (Figure 2a). This was the expected value for the interplanar distance perpendicular to the (110) surface, and confirms previous STM observations of the clean TiO_2 surface immersed in bulk water [18]. On the terraces (Figure 2b), rows of ordered bright spots run along the [001] direction of the crystal, their length ranging from a few to tens of nanometers.

Similar rows aligned in the [001] direction were previously observed by STM after Ca deposition or bulk segregation in UHV [1,5]. These are typically up to tens of nanometers long and spaced about three times the periodicity of the substrate in the perpendicular $[1\bar{1}0]$ direction. Depending on the surface coverage, these Ca-related, linear features also show different spacings of two, four, or five (and even higher) times the substrate periodicity [1,5]. For a single ML coverage, a $c(6 \times 2)$ honeycomb lattice was observed on the rutile (110) surface [5]. Additional structures, perpendicular to the primary rows (namely, along the $[1\bar{1}0]$ direction) and forming a bi-dimensional network, have been also imaged in UHV on the Ca/TiO_2 surface below one ML [1,5].

We conclude that the rows imaged in water by STM are consistent with the Ca-related structures due to impurity segregation

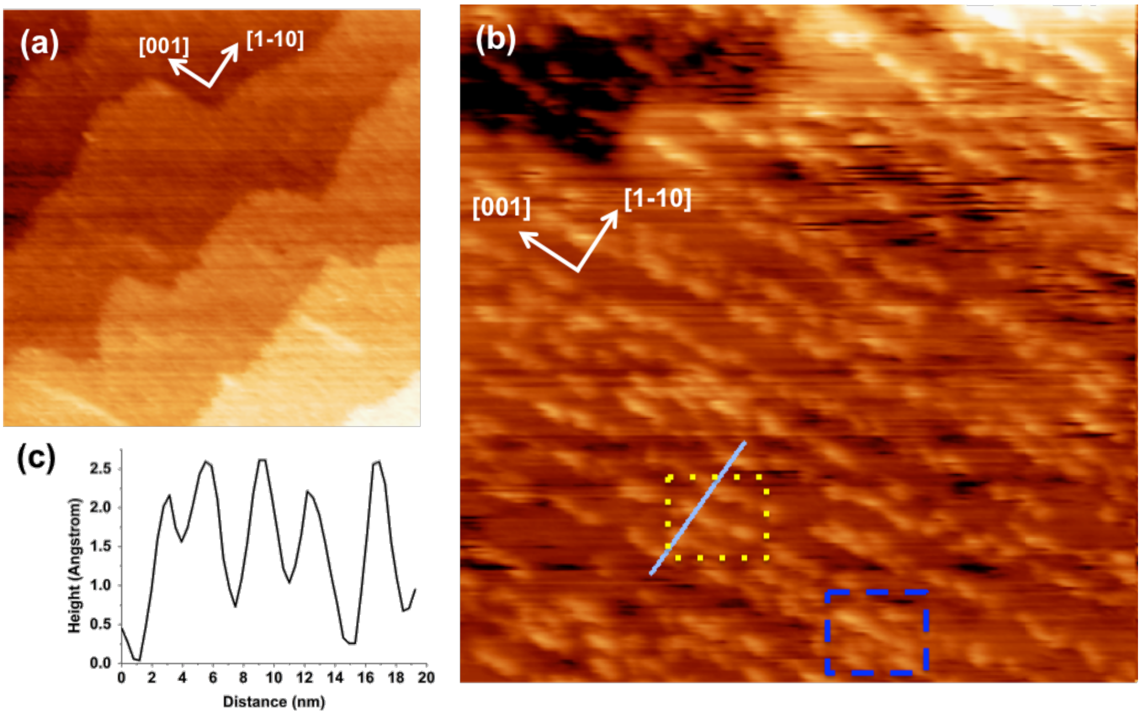

Figure 2: STM images in water of the $TiO_2(110)$ surface after Ca segregation (a) 370.5 × 370.5 nm^2, $V_{bias} = -1$ V, $I_{tunnel} = 1$ nA; (b) 81.8 × 81.8 nm^2, $V_{bias} = -1$ V, $I_{tunnel} = 1$ nA; (c) line profile corresponding to the full line in (b). Ca-related rows of 5× and 3× the spacing (with respect to the $TiO_2(110)$ periodicity) along the $[1\bar{1}0]$ directions are shown in the yellow, dotted and the blue, dashed marked areas, respectively.

seen in UHV (see discussion below). In water the mean distance is 3.3 ± 0.2 nm, corresponding to about five times the $TiO_2(110)$ periodicity along the $[1\bar{1}0]$ direction ($a_{[1-10]}$ = 0.65 nm). Distances equal to three or four, and up to about eight times the substrate periodicity along the $[1\bar{1}0]$ direction were also observed, in agreement with previous UHV results [1,5]. The colored boxes in Figure 2b identify areas where 5× (yellow dotted) and 3× (blue dashed) -spaced rows are present. The resulting irregularity in spacing between Ca-related rows explains the lack of order along the $[1\bar{1}0]$ direction in the LEED pattern. From the STM profile of five adjacent Ca structures (Figure 2c, along the full line of Figure 2b) approximately 3 nm apart, a Full Width Half Maximum (FWHM) of 1.2 ± 0.2 nm, and an apparent height of 2.0 ± 0.5 Å were measured, again, in good agreement with previous UHV studies [1,5].

In contrast to the STM studies in UHV, the elongated features along the $[1\bar{1}0]$ direction were not observed, connecting the rows in a quasi-2D network [1,5]. This could be the consequence of a different quantity of bulk impurities segregated onto the surface in this experiment. This quantity is difficult to control as it depends on the heating temperature and the impurity concentration in the bulk (the latter is unknown in our case). Nevertheless, Bikondoa et al. [5] have reported that in UHV experiments, row-like structures are already visible in the low coverage regime (0.3 ML) along both the [001] and $[1\bar{1}0]$ crystallographic directions, below the coverage value we estimate in our images (about 0.5 ML). Thus, we propose that the quasi-one-dimensional appearance of the rows in our data is most likely related to the immersion in water. Dissolution of segregated atoms in liquid very likely depends upon the surface site. Therefore, we hypothesize that the Ca row-like structures along the $[1\bar{1}0]$ direction [5] are dissolved and transferred into solution before the same process happens for Ca in rows along the [001] direction. We will comment on this assumption below.

At higher resolution, the rows appear to consist of discrete, elongated or circular, protrusions aligned in the [001] direction (Figure 3), with a length ranging between 1 and 5 nm, and a minimum width of about 1 nm. The smallest protrusions well-exceed atomic dimensions, therefore, a single nanostructure, constituting the row building block, very likely corresponds to a cluster of segregated impurity atoms.

The surface is not completely covered by the nanostructured overlayer: substrate areas free of calcium are visible. We have reported that in atomically resolved images of the rutile (110) surface in water, a 2× periodicity is measured along the [001] direction, suggesting the presence of an adsorbed overlayer (very likely water molecules) [18]. In the present experiment, the quality of the images does not allow for observation of these details. Nevertheless, in the areas free of calcium, weak rows are visible on the substrate and their spacing matches the expected value for the clean $TiO_2(110)$ 1 × 1 surface (7.0 ± 0.5 Å) [10,18]. In some areas (see for instance the highlighted black square in Figure 3), the Ca-related structures appear to be centered with these substrate rows, as in the UHV experiments [1,5].

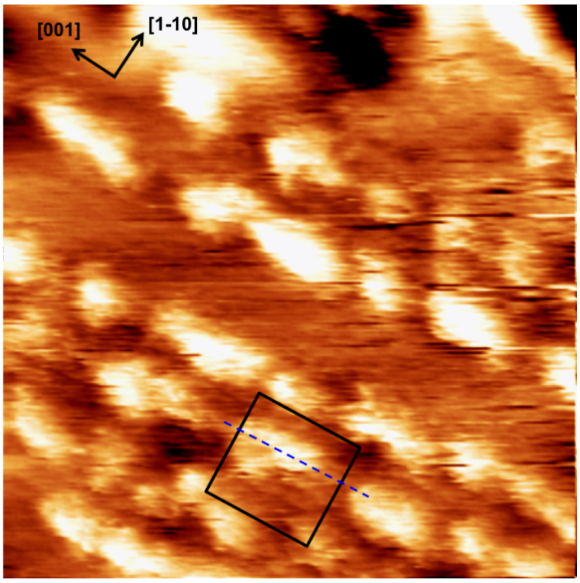

Figure 3: STM image in water of the Ca/$TiO_2(110)$ surface after Ca segregation, 27.3 × 27.3 nm^2, V_{bias} = −1 V, I_{tunnel} = 1 nA. The alignment of the Ca-related rows with $TiO_2(110)$ substrate rows (dashed, blue line) is highlighted by the black square.

The STM images in Figure 2 and Figure 3 were recorded within a few hours of immersion in the liquid. After longer immersion in the aqueous environment, a clear degradation effect of the Ca-related rows in the [001] direction was observed. In Figure 4 we report the resulting images after more than 48 h of continuous immersion in high purity water: the ordered and aligned structures are no longer present on the surface. Although a weak directionality is still discernible in some areas of the surface (see Figure 4a), most of the rounded structures (whose diameter is in the 1–3 nm range) also visible in Figure 3 are now randomly distributed (Figure 4b). A line profile measured across two adjacent protrusions (solid line in Figure 4b) is presented in Figure 4c and shows height and FWHM values very similar to those of the structures assigned to the Ca clusters previously discussed.

XPS analysis carried out after re-entry of the sample in the UHV chamber confirms that calcium is still present on the TiO_2

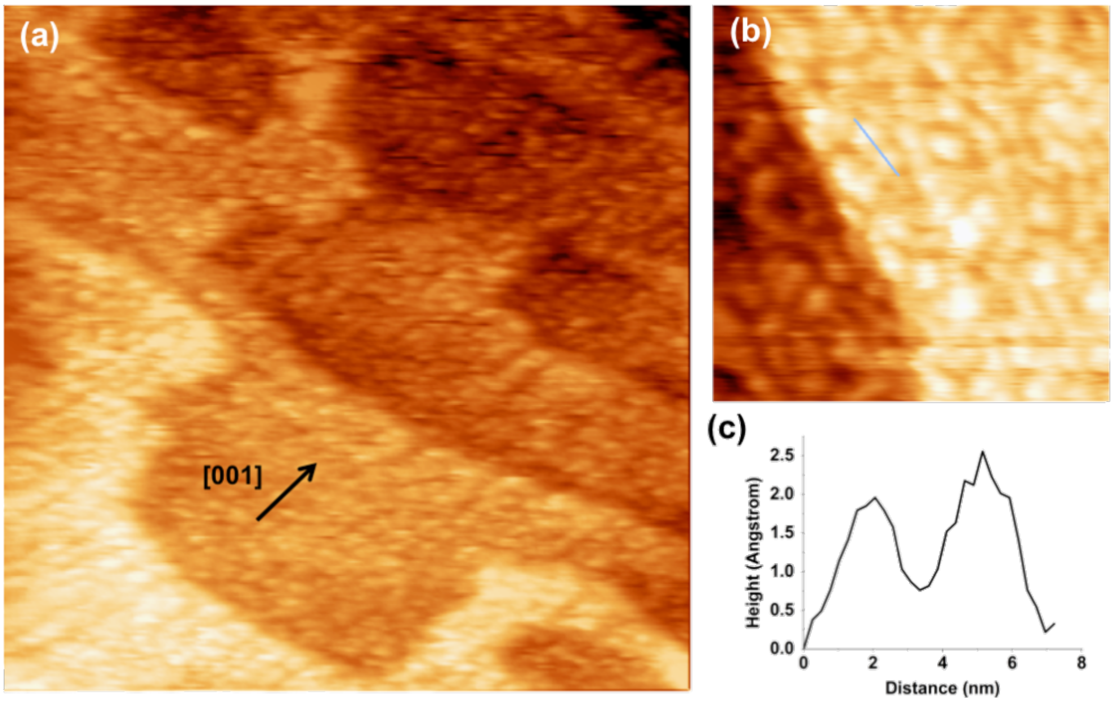

Figure 4: STM images in water of the Ca/TiO_2(110) surface recorded after a 48 h immersion in the liquid (a) 146.9 × 146.9 nm^2, V_{bias} = −1 V, I_{tunnel} = 1 nA; (b) 40.3 × 40.3 nm^2, V_{bias} = −1 V, I_{tunnel} = 1 nA; (c) line profile corresponding to the blue line in (b).

surface. Although we did not determine the quantity originally present before immersion in water, this result supports that calcium had segregated to the surface after thermal annealing in UHV, thus enforcing the interpretation of the rows as being Ca-induced.

At present, it is not known which surface sites Ca is preferentially bound to on the rutile TiO_2(110) surface. Recently, density functional theory (DFT) calculations have shown that, among the possible sites originally proposed on the basis of STM investigations [1], bridging oxygen (BO) atoms and in-plane oxygen (IO) atoms represent minima in the potential energy surface, thus providing more stable sites for adsorption [6]. Interestingly, San Miguel et al. [6] report that from increasing the surface coverage of the surface as well as reducing the proximity to an oxygen vacancy, a significant reduction of the adsorption energy for Ca results. This means that calcium dissolution from the TiO_2 surface into water should be favored at these sites. Therefore, Ca segregated near a defect site or in the branches directed along the [$1\bar{1}0$] directions (the latter occurring with increasing coverage [6]) disappears first, at the early stages of immersion in water (in our experiment, within 2 h). We note that the average density of surface defects (about 10% [10]) is sufficient to provide the adsorption sites necessary to produce the 2D network observed in UHV [1,5]. The rows which are still on the surface after the first stage of immersion in water are thus formed by Ca bound to the preferred adsorption sites, BO and IO, possibly involving both the Ti and O atoms of the surface layers, and producing a certain degree of local structural deformation [6].

Conclusion

The Ca-modified TiO_2(110) rutile surface was investigated in UHV conditions after preparation using sputtering and annealing cycles to produce calcium segregation. The final LEED surface pattern was in agreement with previous studies of calcium overlayers on TiO_2(110). After transfer from UHV to the liquid cell and immersion in high purity water, STM images in water show a terraced surface with monoatomic steps, in addition to rows aligned with the [001] direction, as expected for Ca segregation in UHV. In contrast to previous UHV results, additional elongated structures in the perpendicular [$1\bar{1}0$] direction are not present, possibly a consequence of a water-induced modification. More than 48 h of continuous exposure to high purity water resulted in a disordered surface with rounded protrusions irregularly distributed over the whole investigated area. The presence of calcium on the surface was confirmed by XPS after reentry of the sample into the UHV chamber.

Experimental

The TiO_2 rutile (110) single crystal was purchased from Pi-Kem LTD. The sample was made conductive via bulk reduction in a UHV chamber ($P < 1 \times 10^{-10}$ mbar) by means of repeated Ar^+ sputtering (1 keV) and annealing cycles. This preparation procedure is known to result in the 1 × 1 clean surface [10]. Prolonged sputtering cycles and a higher sample temperature (in our case 1000 ± 50 K) during annealing can cause surface segregation of calcium from the bulk [1-5]. The temperature was monitored by a thermocouple and an infrared pyrometer. The surface structure was examined by LEED. The UHV chamber is equipped with an XPS system. A Mg source and a pass energy of 50 eV were used for the measurements. Peak positions were calibrated according to the O1s position.

After UHV preparation, the sample was taken out of the vacuum chamber and transferred into the STM cell under ultrapure Argon flux. The STM cell was then filled with high purity water (milli-Q purification system, resistivity = 18.2 MΩ·cm). In order to avoid contamination by oxygen and other gaseous molecules in solution, the milli-Q water was degassed prior to the Argon flux for 1 h. STM measurements were performed using an electrochemical STM [19] equipped with an electrochemical cell positioned in a compact “BEETLE”-type setup [20]. The STM housing was filled with Argon gas in order to ensure an inert atmosphere. Tungsten tips were used for the STM measurements. The tips were prepared by chemical etching (2 M KOH solution) and then coated with hot glue to minimize the faradaic current contribution in the case of electrochemical measurements. The STM images were analyzed with the WSxM software [21].

Acknowledgements

We gratefully acknowledge "Polo Solare Organico–Regione Lazio" for financial support. UD acknowledges support by the ERC Advanced Grant ”Oxide Surfaces”.

References

1. Zhang, L. P.; Li, M.; Diebold, U. *Surf. Sci.* **1998,** *412,* 242–251. doi:10.1016/S0039-6028(98)00432-4
2. Nörenberg, H.; Harding, J. H. *Appl. Surf. Sci.* **1999,** *142,* 174–176. doi:10.1016/S0169-4332(98)00670-9
3. Nörenberg, H.; Harding, J. H. *Phys. Rev. B* **1999,** *59,* 9842. doi:10.1103/PhysRevB.59.9842
4. Nörenberg, H.; Harding, J. H. *Surf. Sci.* **2001,** *473,* 151–157. doi:10.1016/S0039-6028(00)00961-4
5. Bikondoa, O.; Pang, C. L.; Muryn, C. A.; Daniels, B. G.; Ferrero, S.; Michelangeli, E.; Thornton, G. *J. Phys. Chem. B* **2004,** *108,* 16768–16771. doi:10.1021/jp048143l
6. San Miguel, M. A.; Oviedo, J.; Sanz, J. F. *J. Phys. Chem. C* **2009,** *113,* 3740–3745. doi:10.1021/jp809680h
7. Fu, Q.; Wagner, T. *Surf. Sci. Rep.* **2007,** *62,* 431–498. doi:10.1016/j.surfrep.2007.07.001
8. Sun, Y.-F.; Liu, S.-B.; Meng, F.-L.; Liu, J.-Y.; Jin, Z.; Kong, L.-T.; Liu, J.-H. *Sensors* **2012,** *12,* 2610–2631. doi:10.3390/s120302610
9. Henderson, M. A. *Surf. Sci. Rep.* **2011,** *66,* 185–297. doi:10.1016/j.surfrep.2011.01.001
10. Diebold, U. *Surf. Sci. Rep.* **2003,** *48,* 53–229. doi:10.1016/S0167-5729(02)00100-0
11. Pang, C. L.; Lindsay, R.; Thornton, G. *Chem. Rev.* **2013,** *113,* 3887–3948. doi:10.1021/cr300409r
12. Hanawa, T.; Ota, M. *Appl. Surf. Sci.* **1992,** *55,* 269–276. doi:10.1016/0169-4332(92)90178-Z
13. Sutherland, D. S.; Forshaw, P. D.; Allen, G. C.; Brown, I. T.; Williams, K. R. *Biomaterials* **1993,** *14,* 893–899. doi:10.1016/0142-9612(93)90130-T
14. Healy, K. E.; Ducheyne, P. *Biomaterials* **1992,** *13,* 553–561. doi:10.1016/0142-9612(92)90108-Z
15. Healy, K. E.; Ducheyne, P. *J. Colloid Interface Sci.* **1992,** *150,* 404–417. doi:10.1016/0021-9797(92)90210-D
16. Jones, F. H. *Surf. Sci. Rep.* **2001,** *42,* 75–205. doi:10.1016/S0167-5729(00)00011-X
17. Posternak, M.; Berner, S.; Baldereschi, A.; Delley, B. *J. Phys. Chem. C* **2013,** *117,* 26013–26020. doi:10.1021/jp406817k
18. Serrano, G.; Bonanni, B.; Di Giovannantonio, M.; Kosmala, T.; Schmid, M.; Diebold, U.; Di Carlo, A.; Chen, J.; VandeVondele, J.; Wandelt, K.; Goletti, C. *J. Phys. Chem. Lett.* **2015,** submitted.
19. Wilms, M.; Kruft, M.; Bermes, G.; Wandelt, K. *Rev. Sci. Instrum.* **1999,** *70,* 3641–3650. doi:10.1063/1.1149971
20. Besocke, K. *Surf. Sci.* **1987,** *181,* 145–153. doi:10.1016/0039-6028(87)90151-8
21. Horcas, I.; Fernández, R.; Gómez-Rodríguez, J. M.; Colchero, J.; Gómez-Herrero, J.; Baro, A. M. *Rev. Sci. Instrum.* **2007,** *78,* 013705. doi:10.1063/1.2432410

License and Terms

The definitive version of this article is the electronic one which can be found at:
doi:10.3762/bjnano.6.44

BEILSTEIN JOURNAL OF NANOTECHNOLOGY

Electrical properties of single CdTe nanowires

Elena Matei[1], Camelia Florica[1], Andreea Costas[1], María Eugenia Toimil-Molares[2] and Ionut Enculescu*[1]

Full Research Paper

Open Access

Address:
[1]National Institute for Materials Physics, Magurele, Ilfov, Romania, 77125 and [2]GSI, Planckstraße 1, 64291 Darmstadt, Germany

Email:
Ionut Enculescu* - encu@infim.ro

* Corresponding author

Keywords:
CdTe; electrodeposition; nanowires; transport properties

Beilstein J. Nanotechnol. **2015,** *6,* 444–450.
doi:10.3762/bjnano.6.45

Received: 17 September 2014
Accepted: 16 December 2014
Published: 12 February 2015

This article is part of the Thematic Series "Self-assembly of nanostructures and nanomaterials".

Guest Editor: I. Berbezier

Abstract

Ion track, nanoporous membranes were employed as templates for the preparation of CdTe nanowires. For this purpose, electrochemical deposition from a bath containing Cd and Te ions was employed. This process leads to high aspect ratio CdTe nanowires, which were harvested and placed on a substrate with lithographically patterned, interdigitated electrodes. Focused ion beam-induced metallization was used to produce individual nanowires with electrical contacts and electrical measurements were performed on these individual nanowires. The influence of a bottom gate was investigated and it was found that surface passivation leads to improved transport properties.

Introduction

Nanowires, which are quasi one-dimensional structures, are considered an extremely important class of nanostructures, regarded as highly effective building blocks for future electronic devices [1-4]. In addition to their specific dimensions and high aspect ratio (which enable ultraminiaturization, due to the high surface-to-volume ratio), nanowires provide increased functionality for electronic devices which contain them [5-7].

There are numerous ways to fabricate nanowires, with methods ranging from simple and straightforward wet chemistry approaches, to complex multistep approaches that were developed over the past two decades. The main goal in all experiments involving such nanostructure preparation is to control both the morphological properties and the structural and compositional characteristics, in order to control the functionality of the nanowires. It is also important that the fabrication method leads to reproducible results and is highly scalable, thus increasing the efficiency of the preparation step.

The template approach is a method which enables the fabrication of nanowires with excellent reproducibility and a narrow distribution of the geometrical characteristics [8-13]. The method typically makes use of a nanoporous membrane as a template along with a method for filling its pores. As templates, most used are polymer ion track membranes, anodic alumina and diblock copolymer templates, while the filling methods range from electrochemical or electroless deposition, to atomic layer deposition or molten metal injection.

The nanoporous polymer ion track membranes are obtained by polymer foil irradiation with swift heavy ions and further chemical etching of the ion tracks [13]. This method allows for control of pore density by taking into account that each ion leaves a single, cylindrical track and pore size throughout the etching process. These parameters are usually chosen in connection with the desired final nanowire size and quantity.

Electrochemical deposition is a well-established method of plating conductive substrates with a specific metal or alloy. During the last decades, semiconductor electrodeposition became more and more attractive, as it may represent a viable alternative to more expensive fabrication methods [14-16]. CdTe electroplating is an excellent example of semiconductor electrodeposition for both film and nanostructure fabrication [14]. By employing a bath containing both cadmium and telluride, their controlled reduction at the working electrode leads to the formation of a high quality, stoichiometric, compound semiconductor.

In this work, a template approach for fabricating CdTe nanowires by electrodeposition inside ion track polycarbonate nanoporous membranes was employed. It was recently proved that one can easily control the characteristic of the nanowires prepared in this way by controlling the electrodeposition overpotential [15]. However, the number of reports dealing with the electrical properties of individual CdTe nanowires are very few.

In the present report, in addition to basic characterization regarding morphology, structure and composition determination, the nanowires were connected with electrical contacts by means of a combination of lithography and focused ion beam-induced metallization (FIBIM). The electrical properties were determined for individual nanowires prepared under different conditions. Further, the effect of a bottom gate on the charge carriers transported through the nanowire channel was examined. It was also found that (similar to other cases of semiconductor nanowires) the surface passivation leads to an improvement in the electrical properties [16,17].

Results and Discussion

Electrochemical deposition of CdTe is a process that has been studied over several decades, and is one of the first reports of an electrodeposited semiconductor. The mechanism leading to the formation of the stoichiometric compound was thermodynamically explained based on the free energy corresponding to the compound formation reaction. In the case of this particular compound, this free energy opens up the possibility to obtain the stoichiometric composition for a rather wide range of electrode potentials and the ability to tune the bath composition over a rather wide range. Practically, the electrodeposition of multicomponent materials (either alloys or compounds) is related to the differences in reduction potentials for each component. In order to reach the desired composition, the deposition conditions must be adjusted in order to reach the desired reaction rate for each component. The procedure typically involves a deposition bath containing a high ratio of the element that is reduced at more electronegative values to the element that is reduced at less electronegative values. For the electrodeposition of CdTe, a bath containing $CdSO_4$ as a source of Cd ions and TeO_2 as a source of Te ions was employed at a ratio of 100 (considering that Cd is reduced at a far more negative electrode potential than Te). Consequently, the electrochemical polarization curves show a plateau in current over a range covering approximately 300 mV.

Electrodeposition inside nanoporous membranes has several particularities, which are a consequence of the fact that the process takes place in a restricted geometry ([13] gives a detailed description of the process). In this regard, the diffusion of ions through the nanopores is different from typical diffusion in an open bath when plating on a typical two-dimensional electrode. As a consequence, the current versus time curve shows a strong current increase when the pore is completely filled and during switching from deposition inside the nanopore to deposition on the surface. This effect was used to determine the time necessary for complete filling whereby the process can be stopped earlier. The nanowires growing from caps on the surface (indicating complete pore filling) are more difficult to harvest and contact, and therefore, the deposition process should be stopped before cap formation.

The deposition was performed in membranes with 10^8 and 10^9 pores/cm^2 and different pore diameters. In order to characterize the nanowires, the template membrane was dissolved by immersing the template containing the nanowires in chloroform and the process was repeated at least 5 times. The process was started with p.a.-grade chloroform and for the last two washing steps, semiconductor-grade chloroform was used. Thorough washing is important for precise electrical characterization since template remnants can influence the characteristics of the metal–semiconductor interface.

In Figure 1 one can observe SEM images of such arrays of nanowires prepared at different electrode potentials, shown after

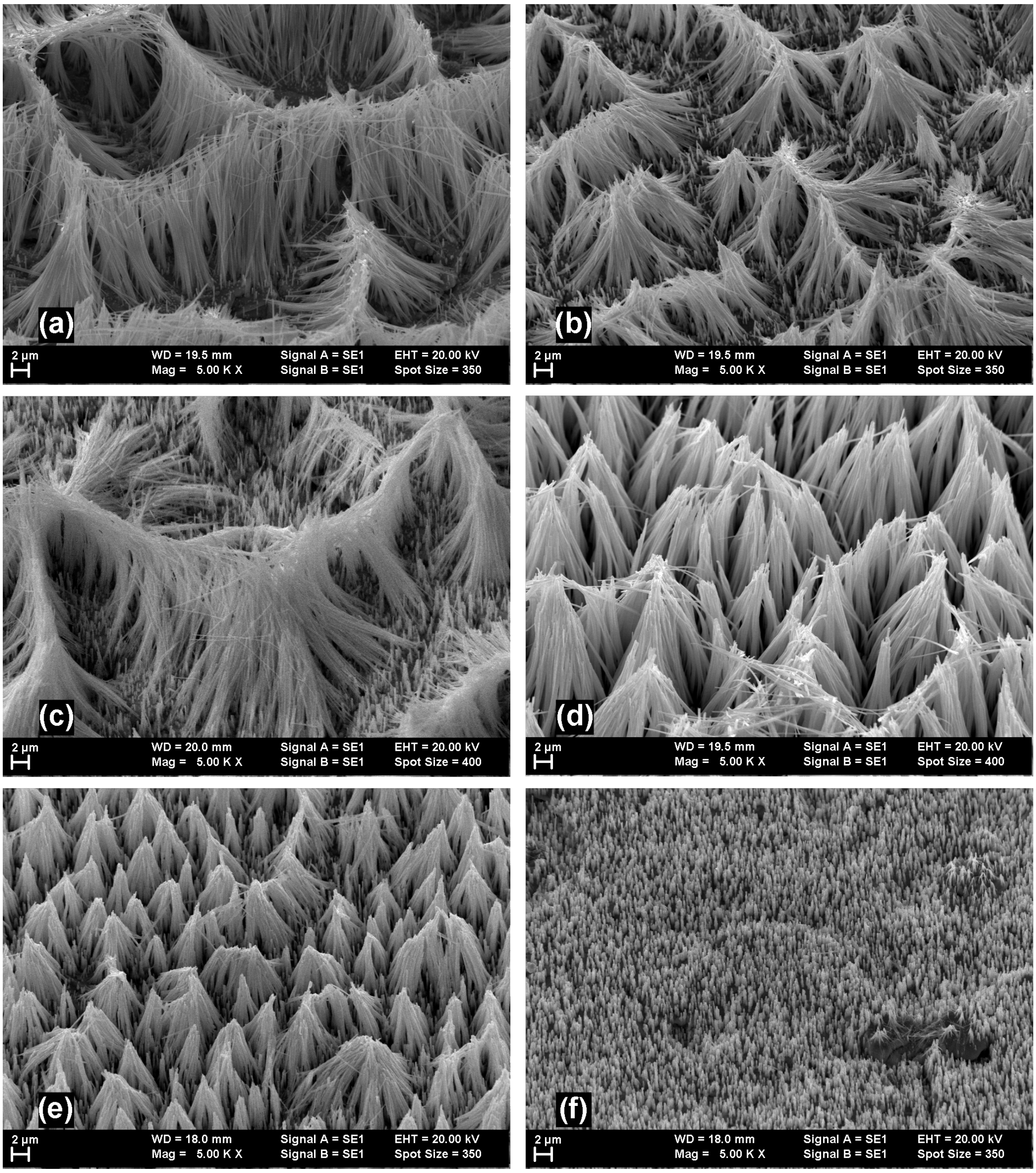

Figure 1: SEM micrographs of CdTe nanowires deposited at (a) −400 mV; (b) −500 mV; (c) −550 mV; (d) −600 mV; (e) −650 mV; (f) −700 mV.

the host membrane was dissolved. As can be seen from the micrographs, the morphology of the cylindrical nanowires corresponds to the template pore characteristics.

EDX spectra deconvolution was employed to determine the composition of the nanowires for different working electrode voltages and the dependence of the composition on the working electrode potential is presented in Figure 2b. A quasi-plateau of the potential for the compound nanowires ranging from −500 to −650 mV vs SCE was found.

The optical properties of compound semiconductors are of high interest since optoelectronic devices are a straightforward application. CdTe is an example of a semiconductor that is extensively employed as an active layer in solar cells and its high absorption coefficient makes it extremely efficient. Figure 3 gives the optical reflection spectra for arrays of CdTe nanowires prepared at different overvoltages. The band gap of the semiconductor was determined to be 1.49 eV by employing the Kubelka–Munk function. This value is in accordance with literature data at approximately 1.45–1.5 eV [18].

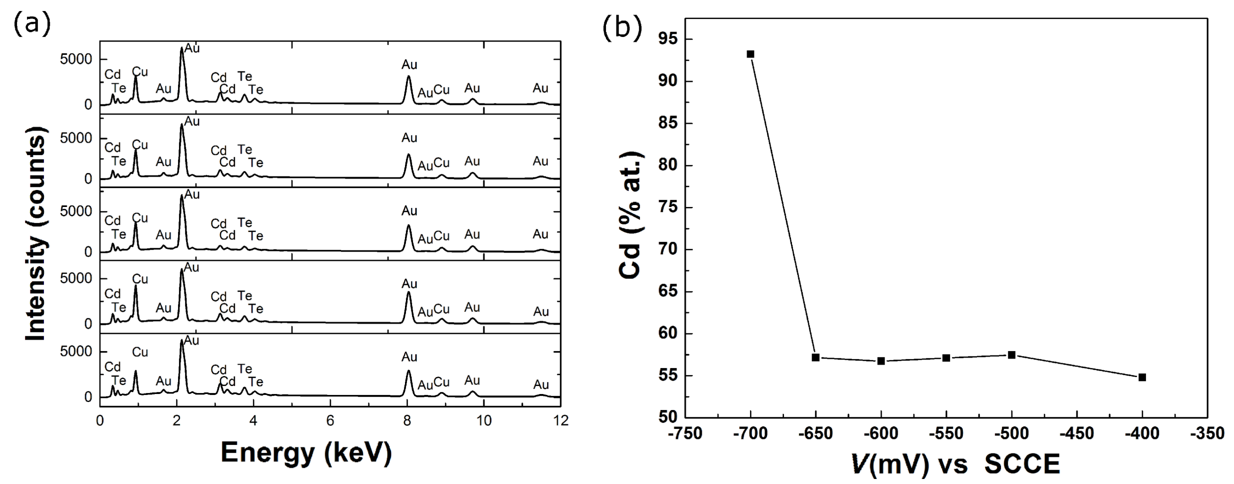

Figure 2: (a) EDX spectra for a series of samples prepared at different electrode potentials; (b) Cd content versus working electrode potential.

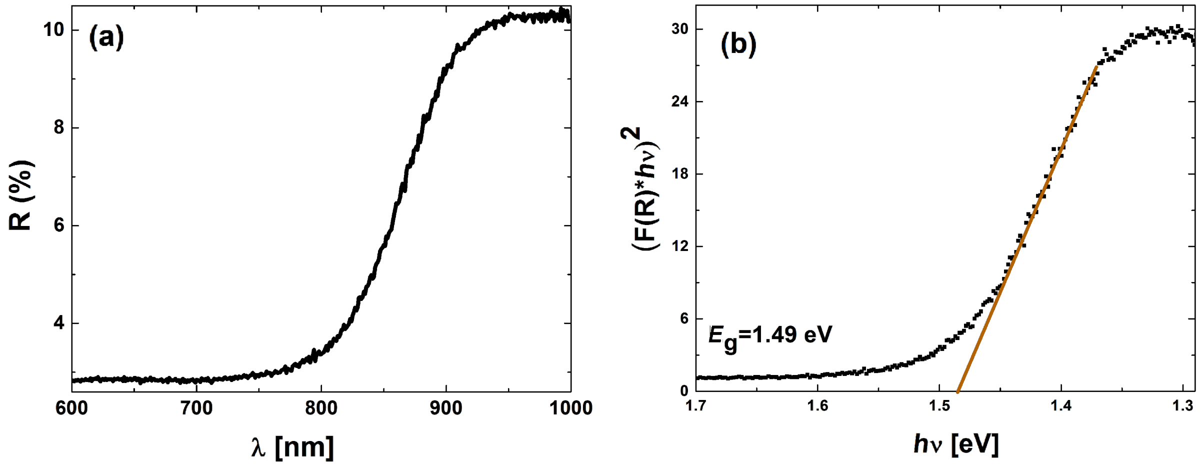

Figure 3: (a) Spectral reflectance curve and (b) Kubelka–Munk representation for band gap determination of CdTe deposited at −500 mV.

The nanowires were further harvested in chloroform by ultrasonication. Taking into account the brittleness of the semiconducting nanostructure, the ultrasonication step was performed for only a few seconds. Further, a droplet of nanowire suspension was placed on Si/SiO_2 substrates on which interdigitated Ti/Au electrodes were patterned by photolithography (Figure 4).

FIBIM is a direct patterning method employed for the design of metallic nanostructures. The method is based on the interaction of an ion beam with the surface-adsorbed, metal–organic molecules corresponding to the working gas. The decomposition leads to a patterned metallic layer with precisely tailored geometry. In our case, a platinum pattern was formed in order to connect the CdTe nanowires to the photolithographically designed, interdigitated contact (Figure 4b). The drawback of this method is that the metal deposited in this way has a lower conductivity as compared to other deposition methods. This is a direct result of the approach and is due to the presence of carbon in the metal layer. This carbon is a residue due to the organic component of the precursor gas.

Further electrical measurements revealed a slightly nonlinear current–voltage characteristic. When a voltage was applied to the silicon substrate, this gate potential influenced the current through the nanowire.

For ZnO it was previously reported [17,19] that a thin layer of polymer covering the nanowire drastically improved the transport properties. This was tested in this work and to our knowledge, only one previous paper dealt with the electrical transport of individual nanowires [20]. No observation of passivation effects on CdTe nanowires was previously reported. We also

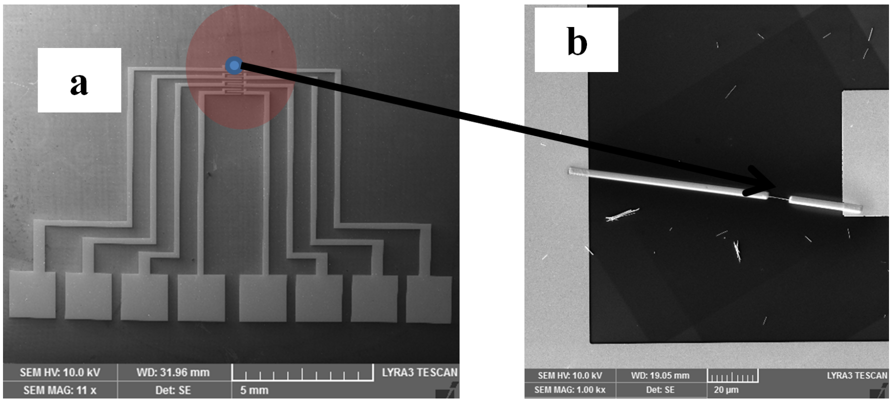

Figure 4: (a) The system of electrodes produced by lithography for contacting the nanowire; (b) an image of an individual nanowire contacted by FIBIM to the larger lithographically prepared electrodes.

observed a similar behavior for CdTe, as would be expected for objects with similar geometries. In Figure 5 current–voltage characteristics are presented for a nanowire contacted by this approach before and after poly(methyl methacrylate) (PMMA) passivation.

A difference of almost an order of magnitude between the sample before and after PMMA covering was observed. This increase in current observed when adding the polymer layer has a potential source: the passivation of surface states, which may be responsible for a decrease in the number of the free charge carriers available in the nanowire.

Conclusion

CdTe nanowires were prepared by electrochemical deposition inside ion track, nanoporous membranes. Substrates with interdigitated electrodes were fabricated by employing a photolithographic approach. After the growth of the nanowires, they were placed onto the substrate and FIBIM was employed to make contacts between the nanowire and the electrodes. The contacts were not pure platinum, but rather a mixture of platinum and carbon, which was the residual phase from the organic component of the gaseous precursor used.

The electrical characteristics were measured and nonlinear I–V characteristics were observed. A strong increase in current was measured when the nanowire was covered with a thin polymer layer. One possible explanation for this phenomenon is that the surface states, which are extremely important for high surface-to-volume ratios, were passivated through the process.

CdTe is an important semiconductor for optoelectronics and this approach to CdTe nanowire fabrication gives the opportunity to measure electrical properties of individual nanostructures and to

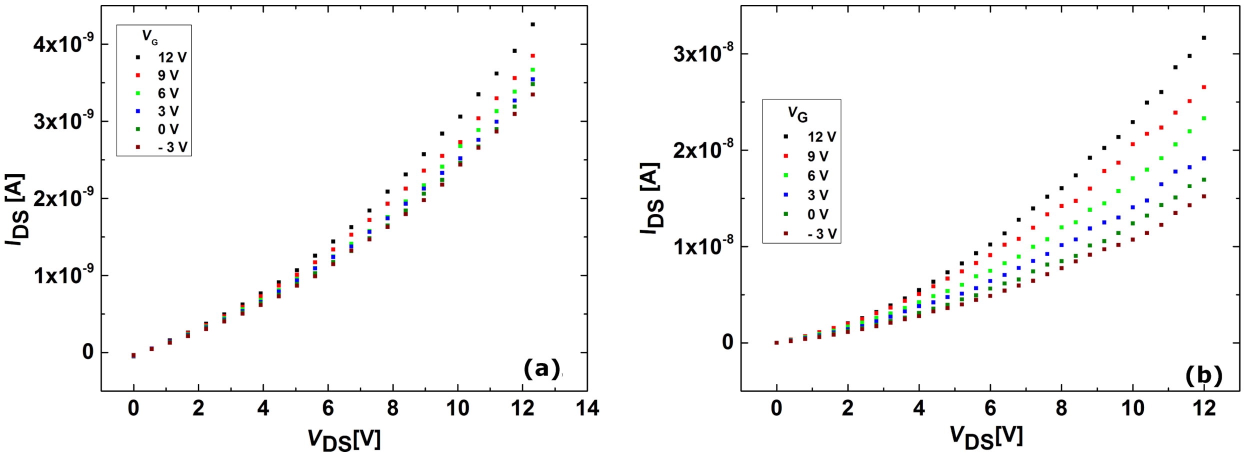

Figure 5: (a) Current–voltage characteristics for a CdTe nanowire contacted by FIBIM; (b) Current–voltage characteristics for a CdTe nanowire contacted by FIBIM after PMMA passivation.

better understand them in correlation with the preparation methods.

Experimental

Polycarbonate foils of 30 µm thickness were irradiated with swift heavy ions from the linear accelerator UNILAC at the Gesellschaft für Schwerionenforschung (GSI). The ions (Au, Pb or U) were accelerated at a specific kinetic energy of 11.4 MeV/nucleon. When passing through the polymer foil, each ion leaves a cylindrical defect track as a consequence of its interaction with the target. Further, these tracks were chemically etched, leading to the formation of cylindrical pores. An aqueous solution of 5 M NaOH and 10 vol % methanol was employed for the etching process at a temperature of 50 °C. The etching rate was 2 µm/h, at three minutes of etching, resulting in cylindrical pores of approximately 100 nm diameter.

On one face of the membrane, a thin (50 nm) gold electrode is deposited by means of DC sputtering. This is further strengthened by the electrodeposition of a thick (10 µm) copper film. This membrane was then inserted into an electrochemical cell, with the uncovered side facing the electrolyte.

A potentiostat (Parstat 2272) was employed for controlling the deposition process in a three-electrode setup. The reference electrode was a commercial, saturated calomel electrode and the counter electrode was a 4 cm^2 platinum foil. A double-walled glass beaker was employed as an electrochemical cell, and a deposition temperature of 80 °C was maintained by means of an external water circulator.

The deposition bath contained $CdSO_4$ and TeO_2 as the sources of the two ions. The pH was adjusted to 2 using sulfuric acid and sodium hydroxide. Higher pHs led to tellurium oxide precipitation.

After nanowire growth, the membrane was dissolved with chloroform leaving the nanowires exposed. The arrays of nanowires fabricated in this manner were investigated by means of scanning electron microscopy, energy dispersive X-ray analysis and optical spectroscopy.

Further, the wires were harvested by ultrasonication into a suspension in chloroform. A droplet of nanowire suspension in semiconductor-grade chloroform was placed on a n^{++} Si/SiO_2 substrate with patterned, interdigitated contracts. These were obtained by photolithography and sequential deposition of 20 nm of Ti and 200 nm Au. A dual-beam, FIB/FEG machine was employed to connect the individual nanowire with the existing interdigitated contacts. During this FIBIM process, a metal–organic gas containing platinum was injected through a nozzle close to the surface of the sample and decomposed in a precise pattern determined by the Ga ion beam. The result is a stripe of a mixture of Pt–C–Ga with the desired geometry determined by the ion beam scanning pattern.

A probe station was employed for performing the electrical characterization of individual nanowires. In order to investigate the effect of a gate on the transport through the nanowire, a third electrical contact was made to the n^{++} Si substrate. A comparison of the transport properties of the nanowires with and without a passivated thin layer of PMMA was performed. This polymer passivation layer was deposited onto the wire by means of spin coating.

Acknowledgements

The authors acknowledge the financial support of the Romanian Government through UEFISCDI contract 24/2013. Andreea Costas was supported by the strategic grant POSDRU/159/1.5/S/137750, “Project Doctoral and Postdoctoral programs support for increased competitiveness in Exact Sciences research”, which is cofinanced by the European Social Foundation within the Sectorial Operational Program Human Resources Development 2007–2013.

References

1. Li, D.; Xia, Y. *Adv. Mater.* **2004,** *16,* 1151–1170. doi:10.1002/adma.200400719
2. Huang, M. H.; Mao, S.; Feick, H.; Yan, H.; Wu, Y.; Kind, H.; Weber, E.; Russo, R.; Yang, P. *Science* **2001,** *292,* 1897–1899. doi:10.1126/science.1060367
3. Morales, A. M.; Lieber, C. M. *Science* **1998,** *279,* 208–211. doi:10.1126/science.279.5348.208
4. Lu, W.; Lieber, C. M. *Nat. Mater.* **2007,** *6,* 841–850. doi:10.1038/nmat2028
5. Cui, Y.; Wei, Q.; Park, H.; Lieber, C. M. *Science* **2001,** *293,* 1289–1292. doi:10.1126/science.1062711
6. Yan, H.; Choe, H. S.; Nam, S.; Hu, Y.; Das, S.; Klemic, J. F.; Ellenbogen, J. C.; Lieber, C. M. *Nature* **2011,** *470,* 240–244. doi:10.1038/nature09749
7. Rogers, J. A.; Lagally, M. G.; Nuzzo, R. G. *Nature* **2011,** *477,* 45–53. doi:10.1038/nature10381
8. Martin, C. R. *Science* **1994,** *266,* 1961–1966. doi:10.1126/science.266.5193.1961
9. Liang, H.-W.; Liu, S.; Yu, S.-H. *Adv. Mater.* **2010,** *22,* 3925–3937. doi:10.1002/adma.200904391
10. Kline, T. R.; Tian, M.; Wang, J.; Sen, A.; Chan, M. W. H.; Mallouk, T. E. *Inorg. Chem.* **2006,** *45,* 7555–7565. doi:10.1021/ic0601384
11. Li, L.; Pan, S.; Dou, X.; Zhu, Y.; Huang, X.; Yang, Y.; Li, G.; Zhang, L. *J. Phys. Chem. C* **2007,** *111,* 7288–7291. doi:10.1021/jp0711242
12. Matei, E.; Enculescu, I.; Toimil-Molares, M. E.; Leca, A.; Ghica, C.; Kuncser, V. *J. Nanopart. Res.* **2013,** *15,* 1863. doi:10.1007/s11051-013-1863-3
13. Toimil-Molares, M. E. *Beilstein J. Nanotechnol.* **2012,** *3,* 860–883. doi:10.3762/bjnano.3.97

14. Lincot, D. *Thin Solid Films* **2005,** *487,* 40–48. doi:10.1016/j.tsf.2005.01.032
15. Matei, E.; Ion, L.; Antohe, S.; Neumann, R.; Enculescu, I. *Nanotechnology* **2010,** *21,* 105202. doi:10.1088/0957-4484/21/10/105202
16. Jeong, S. S.; Mittiga, A.; Salza, E.; Masci, A.; Passerini, S. *Electrochim. Acta* **2008,** *53,* 2226–2231. doi:10.1016/j.electacta.2007.09.030
17. Hong, W.-K.; Song, S.; Hwang, D.-K.; Kwon, S.-S.; Jo, G.; Park, S.-J.; Lee, T. *Appl. Surf. Sci.* **2008,** *254,* 7559–7564. doi:10.1016/j.apsusc.2008.01.070
18. Sarkar, S.; Pal, S.; Sarkar, P. *J. Mater. Chem.* **2012,** *22,* 10716–10724. doi:10.1039/c2jm16810c
19. Florica, C.; Matei, E.; Costas, A.; Toimil Molares, M. E.; Enculescu, I. *Electrochim. Acta* **2014,** *137,* 290–297. doi:10.1016/j.electacta.2014.05.124
20. Kum, M. C.; Yoo, B. Y.; Rheem, Y. W.; Bozhilov, K. N.; Chen, W.; Mulchandani, A.; Myung, N. V. *Nanotechnology* **2008,** *19,* 325711. doi:10.1088/0957-4484/19/32/325711

License and Terms

The definitive version of this article is the electronic one which can be found at:
doi:10.3762/bjnano.6.45

BEILSTEIN JOURNAL OF NANOTECHNOLOGY

Raman spectroscopy as a tool to investigate the structure and electronic properties of carbon-atom wires

Alberto Milani[1,2], Matteo Tommasini[1,2], Valeria Russo[2,3], Andrea Li Bassi[2,3],
Andrea Lucotti[1,2], Franco Cataldo[4,5] and Carlo S. Casari*[2,3]

Review

Open Access

Address:
[1]Department of Chemistry, Materials and Chemical Engineering "G. Natta", Politecnico di Milano, Piazza Leonardo da Vinci 32, 20133 Milano, Italy, [2]NEMAS – Center for NanoEngineered Materials and Surfaces, Politecnico di Milano, via Ponzio 34/3, 20133 Milano, Italy, [3]Department of Energy, Politecnico di Milano, via Ponzio 34/3, 20133 Milano, Italy, [4]Dipartimento di Scienze Ecologiche e Biologiche, Università della Tuscia, Via Camillo de Lellis, Viterbo, Italy and [5]Actinium Chemical Research srl, Via Casilina 1626A, 00133 Roma, Italy

Email:
Carlo S. Casari* - carlo.casari@polimi.it

* Corresponding author

Keywords:
carbon nanostructures; cumulenes; polyynes; Raman spectroscopy; sp-hybridized carbon systems

Beilstein J. Nanotechnol. **2015,** *6,* 480–491.
doi:10.3762/bjnano.6.49

Received: 17 September 2014
Accepted: 14 January 2015
Published: 17 February 2015

This article is part of the Thematic Series "Self-assembly of nanostructures and nanomaterials".

Guest Editor: I. Berbezier

Abstract

Graphene, nanotubes and other carbon nanostructures have shown potential as candidates for advanced technological applications due to the different coordination of carbon atoms and to the possibility of π-conjugation. In this context, atomic-scale wires comprised of sp-hybridized carbon atoms represent ideal 1D systems to potentially downscale devices to the atomic level. Carbon-atom wires (CAWs) can be arranged in two possible structures: a sequence of double bonds (cumulenes), resulting in a 1D metal, or an alternating sequence of single–triple bonds (polyynes), expected to show semiconducting properties. The electronic and optical properties of CAWs can be finely tuned by controlling the wire length (i.e., the number of carbon atoms) and the type of termination (e.g., atom, molecular group or nanostructure). Although linear, sp-hybridized carbon systems are still considered elusive and unstable materials, a number of nanostructures consisting of sp-carbon wires have been produced and characterized to date. In this short review, we present the main CAW synthesis techniques and stabilization strategies and we discuss the current status of the understanding of their structural, electronic and vibrational properties with particular attention to how these properties are related to one another. We focus on the use of vibrational spectroscopy to provide information on the structural and electronic properties of the system (e.g., determination of wire length). Moreover, by employing Raman spectroscopy and surface enhanced Raman scattering in combination with the support of first principles calculations, we show that a detailed understanding of the charge transfer between CAWs and metal nanoparticles may open the possibility to tune the electronic structure from alternating to equalized bonds.

Review

Introduction

Over the last decades carbon nanostructures have been widely investigated for their unique properties and for their potential technological applications [1]. For instance, single wall carbon nanotubes represent quasi-1D systems whose electronic properties are strongly related to the nanotube structure (i.e., chirality), while graphene is a 2D system with appealing electronic and optical properties [2-4]. In addition to structures based on sp^2 hybridization of carbon atoms, sp-hybridized carbon-atom wires (CAWs) are intriguing systems with structure-, length- and termination-dependent properties [5]. Similar to graphene (which today is considered the ultimate 2D system (1-atom-thick)), CAWs represent a true 1D system (1-atom-large) which can display either semiconducting or metallic properties due to the conjugation and electron–phonon coupling effects of their delocalized π electrons.

In addition to many examples in organic chemistry, the occurrence of sp-hybridized carbon has been observed in many carbon-based materials and structures, embedded in cold gas matrices, in free carbon clusters in the gas phase, as pure sp-sp^2 systems, in liquids, inside carbon nanotubes and connecting graphene sheets [5-13]. The research on sp carbon dates back to the last century when the carbon community was in search of a new carbon allotrope based on linear carbon. The first papers claiming observations of sp-hybridized carbon as a new allotrope (named carbyne, and the mineral form was called chaoite) date back to the sixties by Kudryavtsev and co-workers [14], by El Goresy and Donnay [15] and by Whittaker [16,17]. Criticism on the interpretation of these results was raised in the eighties by Smith and Buseck and were the objects of debate [18-20]. In the same period the search for linear carbon in interstellar medium for astrophysics studies drove the discovery of fullerenes by Kroto, Smalley and Curl, as reported in the Nobel lecture by Kroto [21]. Even though a new allotrope based on sp carbon has still yet to be found, sp-hybridized carbon nanostructures (or large molecules) in the form of linear atomic wires can be now produced and investigated. Great interest has been shown in the theoretical prediction of the electronic and transport properties of carbon wires connected to metal electrodes and to other carbon nanostructures such as graphene and nanotubes, while detailed experimental work is still needed to unveil the structure and properties of these systems.

Raman spectroscopy is a powerful tool for the characterization of carbon materials and nanostructures due to its sensitivity to the vibration of C–C bonds. For instance, strong electron–phonon coupling and resonance effects allow for the measurement of single carbon nanostructures and together with confinement effects, provides information on their structure, hybridization state, defects, presence of functionalization and/or doping, and can even quantify the nanotube chirality, the number of layers and the edge structure in graphene [22,23].

In this review we discuss how Raman spectroscopy can be utilized to obtain a wealth of information on the structure of CAWs including length, stability behavior and electronic structure changes induced by charge transfer effects. In particular, for different CAWs, the results of a combined standard Raman spectroscopy and surface enhanced Raman spectroscopy investigation at different excitation wavelengths with the support of first principles calculations will be reviewed. We begin by discussing the structure of ideal and as-synthesized CAWs with particular focus on π-conjugation effects and the change in electronic properties as a result of the wire length and termination. Then we review the various CAWs synthesis techniques and strategies to improve stability. Finally we present Raman and SERS characterizations of selected CAW systems.

Structure of carbon-atom wires

The ideal model of sp-hybridized carbon wires is an infinite chain comprised of two different geometric arrangements of atoms, as depicted in Figure 1. One possibility is a sequence of double bonds in a completely equalized geometry (also called cumulene), and the other is a series of alternating triple and single bonds in a dimerized geometry (also called polyyne). The two configurations are physically related by stability issues since the 1D atomic equalized structures tend to change into the alternating triple–single bond structures to reach a minimum energy configuration (i.e., due to the onset of a Peierls distortion). Such structural change has a direct effect on the electronic properties.

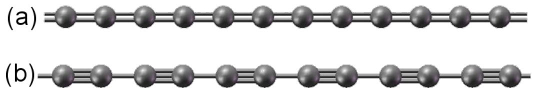

Figure 1: Schematic structures of infinite, linear, sp-carbon wires: (a) equalized wire with all double bonds (cumulene) and (b) alternating single–triple bond wire structure (polyyne).

Infinite cumulenes have one atom per unit cell, providing one electron from each $2p_z$ orbital, thus forming a half-filled band of a 1D metal. As a consequence of Peierls distortion (driven by electron–phonon coupling and dimerization of the structure), an energy gap opens and the metallic character of cumulenes changes into the semiconducting behavior of polyynes, which corresponds to a lower energy of the ideal sp-carbon chain.

Along this metal-to-semiconductor transition the vibrational properties are strongly modified. One of the major effects is the appearance of an optical phonon branch, which is otherwise absent in an equalized, monoatomic, infinite chain, such as the ideal cumulene.

Moving from ideal to real, as-synthesized structures, finite length effects and termination of the chain play a fundamental role. The end groups can affect the overall configuration and their effect becomes more significant with decreasing wire length. The control of the electronic properties such as the band gap and the conducting character by tuning the wire structure may open new opportunities for the realization of nanoscale cables and devices, as demonstrated by theoretical predictions [24,25] however still not experimentally demonstrated. Indeed, this possibility exploits the connection between the molecular structure, the electronic properties and the vibrational properties, which is well documented for all π-conjugated carbon systems [26-29]. The infinite wire model affords a reliable interpretation of the experimental data, portraying the main trends observed in both the electronic and vibrational features, and offering a unified framework for the analysis of the different linear carbon chains synthetized to date. Indeed, many works [29-35] have offered a detailed theoretical interpretation of the relation between the chain structure, band gap and Raman activity of the infinite chain, thus fostering the interpretation of the behavior of the existing finite length carbon chains. However, this approach also has some limitations due to non-negligible end effects. Such limitations may require the relaxation of the assumption of an infinite, atomic chain for the detailed discussion of real, finite-length systems, where the Peierls distortion effect, the stability of cumulenic versus polyynic chains and the vibrational structure (i.e., IR and Raman signals) must be considered.

Beginning with the structural properties, the most significant parameter in this context is the bond length alternation (BLA). The BLA is the difference between the average length of quasi-single and quasi-triple bonds in the chain. It is well-known that an increase in the length of the sp (or sp^2) carbon chain induces an increase in the π-electron conjugation, corresponding to a decrease in the BLA [26,28,36-39], which can be easily rationalized by a straightforward application of the Hückel method. Therefore, longer chains will tend to have an even more equalized structure with a smaller BLA [27,30,31,39-42], even if the occurrence of Peierls distortion would make the perfectly equalized chain unstable. Given this, the markedly polyynic structure found in most of the synthetized sp-carbon chains is usually related to the influence of Peierls distortion. Indeed, the BLA decreases with increasing chain length (π-conjugation) for both polyynes and cumulenes (see Figure 2), similar to many other polyconjugated materials. In contrast, a detailed computational analysis on long sp-carbon chains [42] clearly demonstrated that Peierls distortion dominates over the decrease of the BLA caused by the increasing degree of π-electron delocalization only in relatively long chains. It was verified that C_N chains possess a cumulenic structure determined by end effects for $N < 52$, while in longer chains, the onset of Peierls distortion imposes the alternating structure. This is consistent with the fact that Peierls distortion may be rigorously defined only for an infinite chain. Hence in shorter sp chains, the presence of end effects cannot be overlooked [41,42] and the structure (BLA) of finite sp chains is determined mainly by the chemical nature of the end-capping groups. In Figure 2, the BLA and C–C bond

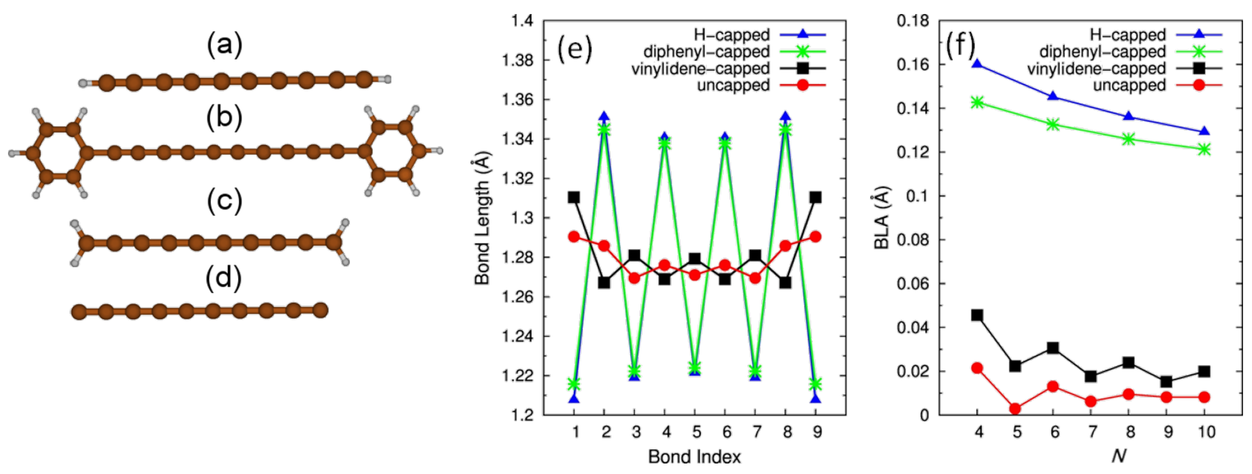

Figure 2: (a–d) carbon-atom wires with different terminations: hydrogen-capped (a), phenyl-capped (b), vinylidene-capped (c) and uncapped (d). The bond length and the bond length alternation (BLA) as a function of the number of carbon atoms comprising the wire are reported in panels (e) and (f), respectively. The data are from DFT calculations.

lengths (computed with DFT) are reported for a selection of differently capped sp chains [40]. In hydrogen-capped chains, the H-terminal forces the formation of a triple bond on the adjacent C–C bond, thus a single bond is formed on the next C–C bond, inducing a polyynic structure. A vinylidene cap (i.e., $=CH_2$) induces a C=C bond on the sp-chain end, thus promoting a much more equalized, cumulene-like, structure. For the same number of C atoms in the sp chain, the vinylidene-capped chains exhibit a much more equalized structure with respect to hydrogen-capped chains, highlighting that the geometry of finite sp carbon chains is not dictated by Peierls distortion but is completely due to end effects. This property paves the way for the design of new sp-carbon compounds where, by a proper choice of the end groups, it is possible to modify the chain structure, possibly down to very low BLAs, thus forming structures that can be practically considered as cumulenic. By consequence, the electronic properties of the conjugated system can be modulated from a semiconducting to a metallic behavior. On these grounds, the recent works by Tykwinski et al. [43,44] are particularly useful. Long sp-carbon chains, containing up to nine cumulated C=C bonds were synthesized by a proper choice of the end-capping groups. They represent, to the best of the authors' knowledge, the first long cumulenes obtained by rational chemical synthesis.

Synthesis techniques and stabilization strategies

Various physical and chemical techniques can be used to produce sp carbon wires in several forms, mainly by bottom-up approaches [5]. Physical techniques are mostly based on the rapid quenching of a carbon vapor in various environments. Supersonic carbon cluster sources based on the arc discharge between graphite electrodes (i.e., the pulsed microplasma cluster source (PMCS) developed by Milani and co-workers) resulted in sp–sp^2 hybrid amorphous carbon films with an estimated sp content up to 40% [45,46]. Unfortunately, the sp phase easily undergoes rearrangement to the sp^2 phase when the sample is exposed to air due to oxidative and cross-linking effects and thus requires in situ characterization techniques, as reported in many papers [7,47]. A similar approach was exploited using thermal or laser vaporization cluster sources [6,48]. sp carbon has also been produced by ion irradiation of amorphous carbon [49] and by femtosecond (fs) laser irradiation of a graphite target [50]. fs laser pulses were used to produce amorphous carbon films containing sp, sp^2 and sp^3 fractions, however control over their relative quantities was not demonstrated [51]. Isolated wires can be produced by laser ablation (with both fs and ns pulses) of carbon solid targets or suspensions in liquids and particularly in the polyyne-like form with an even number of carbon atoms [7,46]. With reference to polyynes in solution, an easy-to-use and cost-effective technique is the arc discharge in liquids developed by Cataldo [52]. This technique also allows for the control of the chain termination by selecting suitable solvents [53].

Various chemical techniques have been used to synthesize a large number of sp carbon chains terminated with different molecular groups as reported in the review by Szafert and Gladysz [54]. Among the most commonly employed chemical routes are: dehydropolycondensation of acetylene, the Glaser reaction based on the oxidative coupling reaction of ethynyl groups by copper salts, polycondensation reactions of halides, and dehydrohalogenation of polymers such as the chemical carbonization of poly(vinylidene halides) (PVDH). Wire formation via self-assembly of carbon atoms in the presence of Pt atoms on graphene has been recently reported by Kano et al. [55].

With reference to top-down methods, the only technique proposed so far is electron bombardment, sometimes even accompanied by application of axial stress, in systems such as carbon nanotubes [56] or a single graphene flake. The electron beam of a TEM allows the selective removal of carbon atoms until a single atomic chain is formed as a junction between nanotubes or connecting two separate graphene edges [13]. Other systems of carbon wires connected to graphene edges have also been reported by some authors [57-59].

One of the major problems arising during the synthesis of sp-carbon wires is the stability of the structures. A viable route for the synthesis of stable structures is the stabilization of preformed wires and a few attempts have been made in this direction so far. We demonstrated that H-terminated polyynes could be embedded in a solid assembly of Ag nanoparticles resulting in a sample which is stable for several weeks at room temperature under ambient conditions [60]. Hayashi and co-workers showed that it is possible to produce a polymeric composite (i.e., poly(vinyl alcohol)) containing polyynes stabilized by Ag nanoparticles [61].

Due to their high stability, polyynes in liquids (up to 14–16 carbon atoms) can now be synthesized even in the form of size-selected samples [5,62,63] and with well-defined end groups [54]. Solid-state samples have been also produced in powder form [64] and Chalifoux and Tykwinski recently reported the synthesis of chains of up to 44 carbon atoms terminated by bulky groups [65]. The latter system is stable in air and at room temperature in the form of a solid sample. On the contrary, cumulenes seem more difficult to produce and fewer works report their observation. For instance, both cumulenes and polyynes have been detected in a pure sp–sp^2 cluster-assembled system [9,66] and the higher tendency of cumulenes to undergo sp^2 transformation has been outlined [45,67,68]. By modification of the termination-induced electronic arrangement, short cumulenic structures can be produced, as reported by Cataldo [69] and extensively discussed in the review by Cadierno et al. [70]. A significant step in the preparation of long cumulenic chains was very recently presented by the group of Tykwinski [43,44]: by adopting different synthesis procedures, long cumulenes chains (up to 8 sp-carbon atoms) have been selectively obtained. Again, the end caps play a fundamental role for two reasons. The first is that due to their chemical nature, they promote the formation of a double bond on the first bond of the sp chain, as required to induce a cumulenic structure. Secondly, they are chosen to be bulky enough to prevent interactions among sp chains, thus avoiding cross-linking and degradation.

Raman spectroscopy of carbon-atom wires

As pointed out when discussing the structural and electronic properties, the vibrational properties (notably Raman activity [71,72]) of CAWs are similar to other one-dimensional, poly-conjugated carbon systems, such as polyacetylene and polyenes. The Raman spectra of these π-electron systems have been extensively investigated [26,28,36-38] and show a peculiar behavior. In particular, the dominant feature originates from the oscillation of the BLA which is an out-of-phase C–C stretching and is named the “R mode” or “ECC mode”, according to the effective conjugation coordinate (ECC) model [26,28,36,37]. The spectral peak shifts to a lower wavenumber and with an increased intensity for an increasing wire length (i.e., number of carbon atoms). In addition, recent theoretical analysis carried out with DFT suggests that for long wires under axial strain along the sp-chain, anharmonicity may also drastically affect the Raman spectra, resulting in an interesting interplay with Peierls distortion effects [73].

Examples of the extreme sensitivity of Raman spectroscopy to the carbon hybridization state, electronic structure and local order, are shown in Figure 3, where different carbon systems are characterized by well-defined Raman scattering features. In contrast to the other forms of carbon (e.g., fullerenes, nanotubes, graphene), the Raman spectra of sp-carbon chains has been only recently investigated in detail, and a consistent description has just begun to emerge. The Raman spectrum of polyynes shows a similar behavior to polyenes with a very intense feature named the “α line” by some authors [62] which corresponds to the ECC mode. In addition a second, minor band (β line) is often observed. These fingerprints lie in the 1800–2300 cm^{-1} region and they are related to different collective stretching vibrations of sp-hybridized C–C bonds (i.e., BLA oscillation modes), which have been discussed in detail in [32] through theoretical analysis and first-principles calculations. This spectral region is particular to sp carbon, since none of the other carbon nanostructures have peaks in this region (see Figure 3). Within this spectral region cumulenes exhibit lower overall Raman signals than polyynes. DFT calculations have quantitatively shown that for realistic systems of finite length, the strong electron–phonon coupling is responsible for the red-shift of the Raman mode when increasing the length [31,33,35,41].

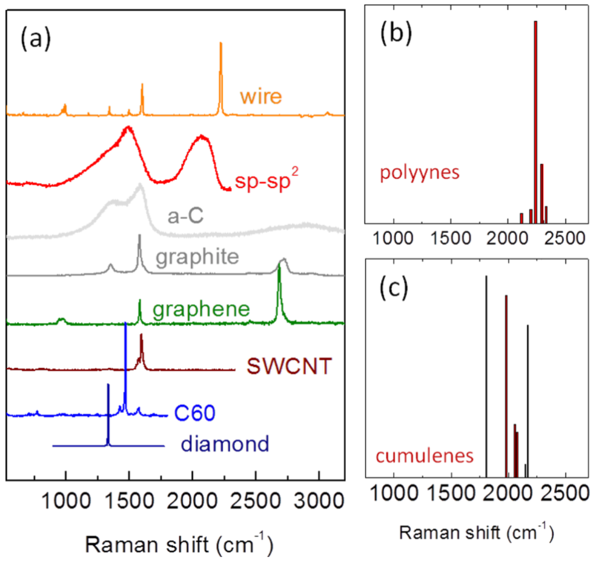

Figure 3: (a) Experimental Raman spectra of carbon solids and nanostructures. (b,c) DFT-computed Raman peaks for finite polyynes and cumulenes of different lengths. Figure adapted with permission from [40], copyright 2010 John Wiley & Sons.

Furthermore, a first interpretation has been carried out by taking into account the infinite chain model, which allows interpretation of the α and β lines on the basis of the longitudinal optical (LO) phonon dispersion branches of an infinite, Peierls-distorted, carbon chain (i.e., with two atoms in the unit cell). Similar to the tendency of the electronic structure (where the band gap is modulated by the BLA, showing a transition from semiconducting (BLA $\neq$ 0) to metallic states (BLA = 0)), the LO phonon branch is also strongly modulated by the BLA and shows a Kohn anomaly at Γ in the case of a cumulenic chain [30-33,35]. This behavior can be interpreted on the basis of the modulation of the ECC mode force constant, driven by the occurrence of increasingly more π-electron delocalization with decreasing BLA. This point has been theoretically demonstrated by means of the Hückel model [29,32,33], which highlights the important role of long-range vibrational interactions among C–C stretching coordinates in the sp-carbon chain. As in the case of standard polymer systems, the wavenumbers associated with LO vibrations in finite length chains can be correlated to the LO branch of the respective infinite model at different points of the first Brillouin zone. This procedure, reported elsewhere in detail [33,72], consists of analyzing the displacement vectors associated with C–C stretching normal modes, finding the nodal pattern and associating the corresponding phonon wavevector. For polyynes, the ECC modes of a finite chain characterized by a given BLA can be correlated to the LO dispersion branch obtained for the same BLA value. This ideal model can be successfully adopted to give an interpretation of the Raman spectra of hydrogen-capped chains of increasing length [30,31] and long polyynes (containing up to 20 conjugated triple bonds) capped with bulky groups [72]. The same approach also allows the Raman spectra of cumulenic species to be modeled [40]. The latter case is particularly interesting since it highlights the inherent weakness of the infinite chain model. The possibility of detecting cumulenic chains by Raman spectroscopy has been often challenged based on the fact that an infinite chain with equivalent double bonds would be a monoatomic chain with no optical phonon branch. However, the existence of cumulenic molecular systems has been revealed by Raman spectroscopy for mixed sp/sp^2 carbon nanostructures [9,47,66]. This apparent contradiction can be solved by relaxing the infinite chain model. While only phonons at Γ have non-negligible Raman activity for an infinite polymer, for finite chains, vibrations located on the LO branch at different points of the 1st Brillouin zone can also be Raman active, due to end effects (which are obviously lacking when periodic boundary conditions are assumed). For instance, the Raman spectra of several DFT-computed cumulenic (C_N) chains are reported in [40]. Many vibrational transitions show non-negligible Raman intensity, thus demonstrating the possibility of detecting cumulenic chains by means of Raman spectroscopy. Interestingly, the interplay between the activation of out-of-Γ normal modes and the molecular parameters governing Raman activity [29,74] generates a detectable Raman signal for LO modes other than ECC in cumulenes, as shown in Figure 3(b,c). In reference to cumulenes, it has to be observed by Liu et al. that finite cumulenes have a well-defined torsional stiffness. Therefore, the relative twisting vibrations of the CH_2 end groups should be considered as potential Raman signals useful for the characterization of these systems, given that their respective force constant decreases with 1/length [75]. However, in this respect, calculations of the Raman response of these modes [40] have revealed that such modes are expected to be very weak (or inactive) compared to the bending modes which occur in a close wavenumber range and have been observed in [67], thus hindering the detection of these CH_2 twisting modes.

Based on the above discussion, it should be clear how end effects might affect the overall properties of sp-carbon chains, not only by modifying the molecular structure (i.e., BLA) but also by influencing the electronic and vibrational properties. By properly choosing the end groups, one can modulate the structure of the chain with the aim of modulating the band gap of the system. This effect can be spectroscopically probed due to the evolution of the distinct marker bands observed in the Raman spectra. Hence, Raman spectroscopy, enhanced by the strong predictive power of first-principles simulations, constitutes a powerful, non-invasive characterization technique, which can provide valuable information on the molecular properties of sp-carbon systems.

We now introduce a few case studies where Raman spectroscopy proved to be particularly insightful for the characterization of sp-carbon systems. For two cases (hydrogen- and phenyl-terminated polyynes) we will show that Raman spectroscopy allows the identification of CAWs of different lengths. Furthermore, by comparing Raman and SERS we will discuss the occurrence of charge transfer between CAWs and metal nanoparticles used as the SERS active medium. Such charge transfer results in a change of the electronic configuration of the wire that evolves towards a more equalized structure (i.e., cumulenic).

H-terminated polyynes were produced by the submerged arc discharge technique, as described in detail in [64]. When the discharge is operated in methanol it is possible to obtain polyynes with an even number of carbon atoms ($6 \leq C \leq 16$) terminated by one hydrogen atom on each side. The size distribution obtained from HPLC complemented with UV–vis spectroscopy is reported in Figure 4. Even at low concentration it is possible to obtain a Raman spectrum from the liquid sample as shown in Figure 4a, where the low intensity of the sp signal is clear when compared to the signal of the solvent (methanol). The sp signal consititutes an asymmetrical band extending from 2000 cm^{-1} to 2250 cm^{-1} as a result of the contribution of wires of different lengths.

As previously mentioned the vibrational features are strongly dependent on the wire length which is clearly shown in the theoretical spectrum obtained by computing the active Raman modes for single wires with 6–18 carbon atoms. The wavenumber of the Raman modes decreases for longer wires while the Raman intensity increases. Although the correct Raman intensity behavior as a function of chain length is not very accurately captured by the DFT calculations, by summing the different contributions and properly weighting by their quantity, we can obtain a fair representation of the experimental spectrum. Hydrogen-terminated polyynes show limited stability with time since they easily undergo a transition towards sp^2 as a consequence of cross-linking reactions [77]. It is known that end groups bulkier than hydrogen, such as phenyls or even

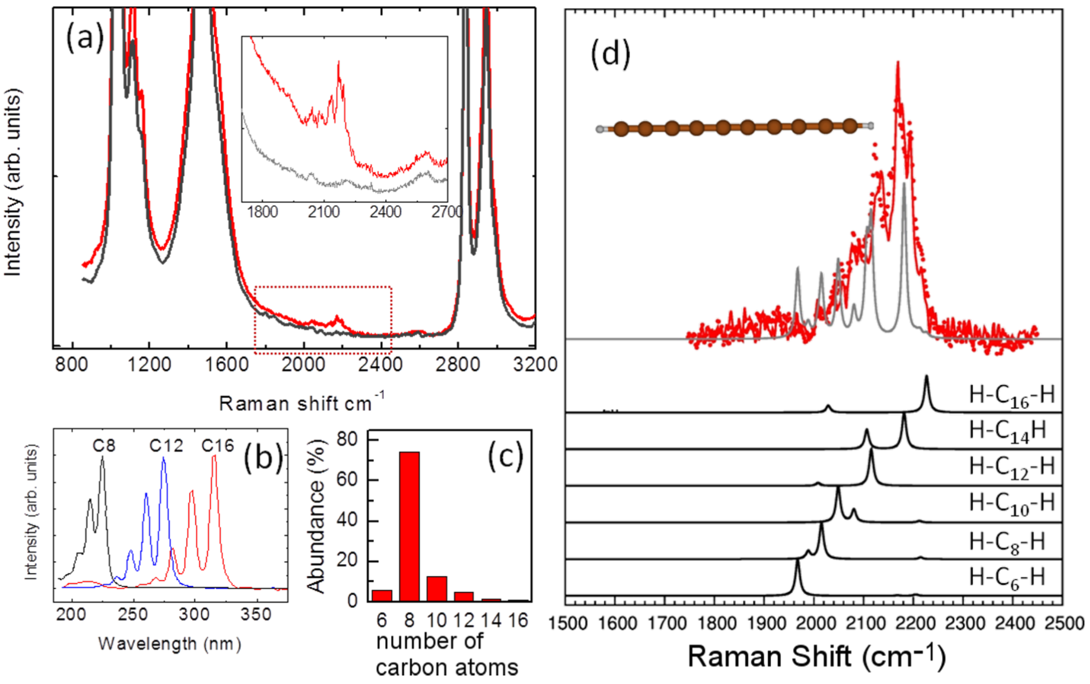

Figure 4: (a) Experimental Raman spectrum (1064 nm) of H-capped polyynes in methanol (5 × 10^{-3} M), with the pure solvent shown for comparison. (b,c) UV–vis spectra for polyynes of different lengths and size distribution in the sample solution. (d) DFT-computed Raman peaks for polyynes present in the sample weighted by their correspondent abundance and comparison with the experimental spectrum. Figure adapted with permission from [76], copyright 2006 Elsevier.

larger caps [65], impart stability to CAWs. Phenyl-terminated polyynes were produced by chemical synthesis with details given in [78]. Due to the termination type, these systems are stable at ambient conditions even when the solvent is completely removed and the sample is in the solid state, as shown in Figure 5. The Raman spectrum of diphenyl-polyynes is characterized by well-resolved peaks in the 2050–2250 cm^{-1} region. Also in this case, this is due to the size distribution of polyynes in the sample and is confirmed by the spectrum of the size-selected sample with 4 carbon atom wires. The additional peak at 1600 cm^{-1} is related to the stretching of the phenyl ring, hence, it is a marker of the termination with sp^2 character.

DFT calculations of the Raman spectra of several phenyl-capped polyynes of selected length allow the assignment of each observed peak to a given size of the sp chain. In this case, a significant red shift of the ECC mode for increasing chain lengths is also observed, which is consistent with an increase of π-conjugation. The Raman intensities of the computed spectra reported in Figure 5d are normalized to allow a better comparison with the experimental spectra.

A peculiar effect is observed when polyynes (both H- and phenyl-terminated wires) interact with metal nanoparticles (i.e., silver and gold), such as those employed in SERS to increase the sensitivity of the Raman technique. Interaction with metal nanoparticles has been investigated both in solution and on surfaces. SERS in solution has been carried out by adding silver and gold colloids to the sample solution while for surface SERS (S-SERS), silver and gold nanoislands supported on silicon and glass substrates have been used [39]. It was observed that the SERS spectrum is radically different from the Raman spectrum. A shift in the main Raman peak locations is accompanied by the appearance of new spectral features at lower wavenumbers (below 2000 cm^{-1}), as shown in Figure 6 for the case of silver nanoparticles. This occurs also in the case of gold nanoparticles for different excitation wavelengths ranging from NIR (1064 nm) to blue (458 nm) wavelengths, illustrating that this is not a resonance-activated effect [39].

When interacting with metal nanoparticles in solution, H-terminated polyynes promote colloid aggregation, which causes the plasmon resonance to broaden and shift from the visible to the NIR. This effectively allows SERS to be performed at different excitation wavelengths. This behavior of H-terminated polyynes can be rationalized by assuming a strong chemical interaction with metal particles or even substitution of the hydrogen with silver. This effect can also justify the increased stability observed after mixing with silver nanoparticles [60]. Phenyl-capped polyynes show similar aggregation when mixed with metal nanoparticles.

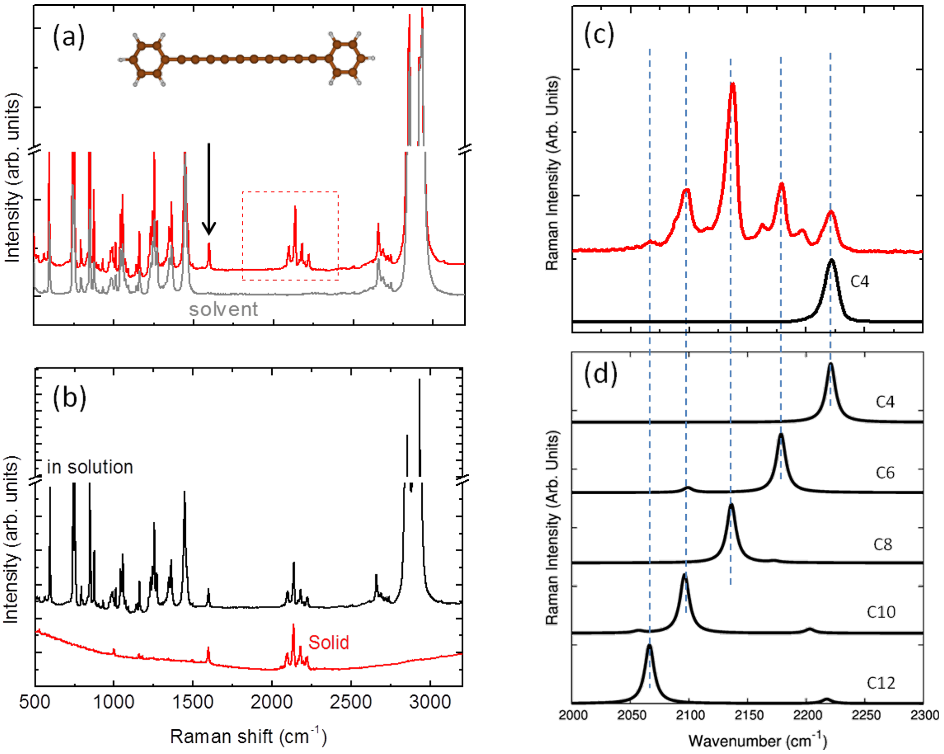

Figure 5: (a) Experimental Raman spectrum (1064 nm) of phenyl-capped polyynes in decalin (10^{-2} M) with the pure solvent shown for comparison. The peak related to the phenyl termination is marked with an arrow. (b) The Raman spectrum of phenyl-capped polyynes after solvent removal to show the stability of the sample. (c) Detail of the experimental Raman spectrum of panel (a). The spectrum of size-selected phenyl-capped polyyne with 4 carbon atoms is also reported. (d) Peaks corresponding to different wire lengths according to DFT calculations of the Raman modes [39]. Figure adapted with permission from [39], copyright 2011 American Chemical Society.

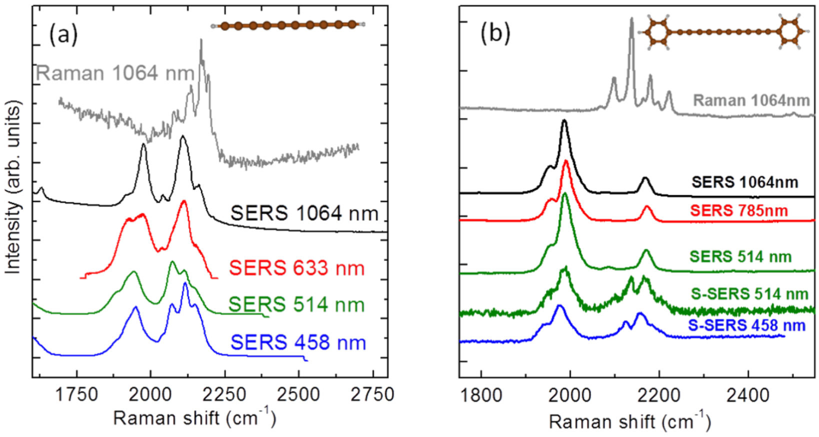

Figure 6: Raman and SERS spectra of H-capped (a) and phenyl-capped (b) polyynes in solution at different excitation wavelengths. SERS on solid surfaces (S-SERS) of phenyl-capped polyynes are also reported. The Raman spectra (at 1064 nm) of both systems are shown for direct comparison. Figure adapted with permission from [39], copyright 2011 American Chemical Society.

The changes occurring in the vibrational properties of wires upon interaction with metal nanoparticles (i.e., observed comparing Raman with SERS) suggest a chemical SERS effect with total enhancement factors up to 10^6, as observed in the case of H-capped polyynes [76]. In order to explain this observation, the possibility of a charge transfer between the metal and the carbon wire has been proposed [39]. Computing the Raman shift of CAWs of different lengths and comparing neutral CAWs with charged ones, it is straightforward to observe a relevant softening of the ECC Raman modes and an increase of their Raman activity, which is promoted for larger conjugation, as reported in Figure 7.

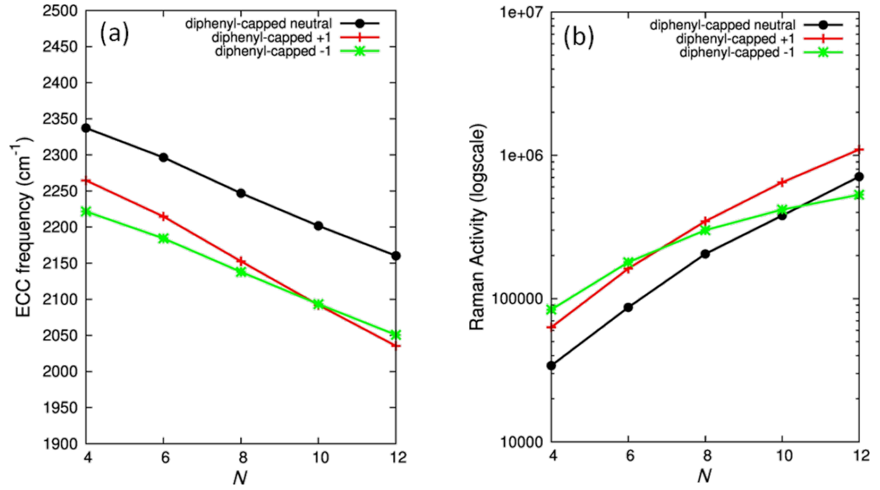

Figure 7: (a) Modulation of the DFT-computed [39] vibrational frequency and (b) Raman activity of the ECC band for phenyl-capped polyynes of different lengths (*N*) and charge states (0, +1, –1). Figure adapted with permission from [39], copyright 2011 American Chemical Society.

For instance, for a wire of a given size, a decrease of about 100 cm^{-1} is predicted when the wire is charged, both by adding or removing one electron. The trend in both peak location and Raman intensity is similar even though the shifting effect is slightly different upon oxidation/reduction in long/short chains. By consequence, in both positively or negatively charged diphenyl-capped polyynes, new bands would appear in the spectra at lower wavenumbers and with a larger Raman activity, which can explain the recorded experimental SERS spectra.

Figure 8a reports the energy E^{ion} required for the formation of the two possible charged configurations for each wire length, namely Ag$^+$ [Ph–C$_N$–Ph]$^-$ and Ag$^-$ [Ph–C$_N$–Ph]$^+$. Given a pair of ionic species A$^+$..B$^-$, E^{ion} is defined as $E^{\text{ion}} = \text{IP(A)} - |\text{EA(B)}|$, where IP(A) is the ionization potential of A and EA(B) is the electron affinity of B. By evaluating this term for the two charged configurations indicated above, we can determine the direction of the charge transfer since the complex possessing the lower value of E^{ion} would be preferentially formed.

IP and EA have been calculated for neutral and charged diphenyl-capped polyynes: in particular "adiabatic" IP (AIP) and EA (AEA) are reported by considering the total energy of

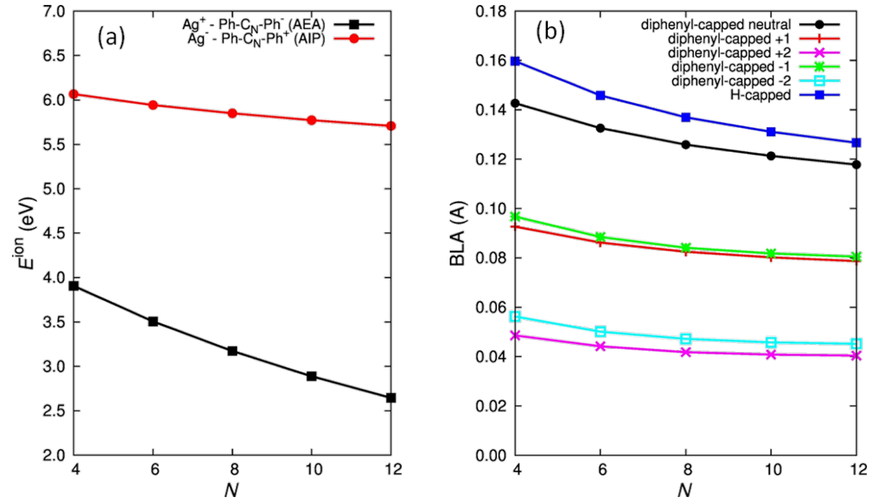

Figure 8: (a) Plot of the DFT-computed energy [39] required for the formation of the charged species (E_{ion} = IP(A) − |EA(B)| where IP(A) is the ionization potential of A and EA(B) is the electron affinity of B) for the two possible cases Ag$^+$ [Ph–C$_N$–Ph]$^-$ and Ag$^-$ [Ph–C$_N$–Ph]$^+$ of phenyl-capped polyynes of different chain lengths (*N*). The following experimental values for the work function and EA have been used in the case of Ag: IP = 4.6 eV and EA = −1.30 eV for EA [34] (b) Modulation of the DFT-computed [39] BLA for phenyl-capped polyynes of different lengths (*N*) and charge states (0, +1, −1). Figure adapted with permission from [39], copyright 2011 American Chemical Society.

the charged species in their minima, thus including geometry-relaxation effects upon charge transfer. For Ag we have considered the experimental values of IP and EA [39].

Based on this calculation and Figure 8a, it is clear that the configuration with a positively charged metal and negatively charged wire is favored. Furthermore, E^{ion} is also modulated by π conjugation in this case. For increasing chain lengths (i.e., larger conjugation) the energy required for the formation of charged species decreases, thus favoring the charge transfer process.

In addition, since charge transfer obviously alters the electronic structure of the wire, we can expect some effect also on the molecular structure. This is due to the strong, characteristic electron–phonon coupling existing in π-conjugated systems which connects the electronic effects with the structure of the sp chain. This indeed occurs, as demonstrated by the BLA values computed for the neutral and charged species (Figure 8b). Charge transfer induces a BLA decrease in the polyyne structure, which evolves towards a more equalized structure. In other words, upon charge transfer the wire moves from an alternating (polyyne) to an equalized (cumulene) wire configuration. The reduction amounts to more than 30% for a singly charged wire and more than 60% for a doubly charged wire, reaching a lower value of 0.04 Å for 12 carbon atoms. It is important to notice that for finite-length wires, the ideal cumulene structure with BLA = 0 Å is not realistic due to the influence of the terminations. The end effects are stronger in shorter wires, as shown in Figure 2f where the BLA of finite cumulenes is reported. Vinylidene-capped systems have a BLA which ranges from about 0.05 Å to 0.02 Å moving from 4 to 10 carbon atoms. Uncapped C_N cumulenes show a BLA below 0.02 Å even though they represent a model system that is experimentally unfeasible, except in extreme conditions. As a reference, this result agrees with theoretical calculations by Weimer et al. [79] reporting an increase in the BLA in cumulene wires from 0.006 to 0.048 when the chain length is decreased from 40 to 4 atoms.

This approach gives only a qualitative evaluation of the charge transfer since it does not include the effect of the wire-to-metal interaction in the calculation. The proposed effect is reasonable, although a more complete model should consider the whole wire and metal system and their interaction. This is indeed extremely complex and time consuming from a calculation point of view due to the large numbers of atoms and the need to consider electronic and vibrational properties.

Conclusion

sp-carbon-atom wires show appealing properties for fundamental studies and applied research. They represent an additional player in the family of carbon nanostructures and can be potentially integrated with graphene and nanotubes to take advantage of their widely tunable electronic and optical properties. We have reviewed the present understanding of structure–property relationship and the use of Raman and SERS for a detailed investigation of wire structure and electronic properties. Although stable polyynes are currently being synthesized, for technological applications, additional work is needed to reveal the properties of wires assembled in thin films. Cumulenes are particularly appealing as a 1D metal. Even though their synthesis remains challenging, novel cumulenic systems have been recently obtained by control of sp-chain capping [43]. Another strategy in this direction is the modification of the structure of polyynes through the control of charge transfer effects.

sp carbon has also attracted interest as a molecular junction, as shown in a number of theoretical investigations and a few experimental works regarding wires connected to graphene and nanotubes. These have shown interesting electronic and transport properties [80-84]. While experimental work is still focused on the synthesis and structural investigation of different CAWs, mixed sp–sp^2 systems are attracting the attention of the carbon community as hypothetical, novel, hybrid carbon allotropes [85]. Among possible sp–sp^2 hybrids theoretically predicted, we mention graphyne systems, as outlined by Hirsch [1]. Such structures are 2D carbon layers where sp^2 rings form a network through sp, linear connections. For some of these systems, peculiar properties are expected such as the existence of Dirac cones in the electronic band structure and extremely high electron mobility [86].

References

1. Hirsch, A. *Nat. Mater.* **2010,** *9,* 868–871. doi:10.1038/nmat2885
2. Avouris, P. *Phys. Today* **2009,** 34. doi:10.1063/1.3074261
3. Novoselov, K. S.; Fal'ko, V. I.; Colombo, L.; Gellert, P. R.; Schwab, M. G.; Kim, K. *Nature* **2012,** *490,* 192. doi:10.1038/nature11458
4. Ahn, J.-H.; Hong, B. H. *Nat. Nanotechnol.* **2014,** *9,* 737. doi:10.1038/nnano.2014.226
5. Cataldo, F., Ed. *Polyynes Synthesis, properties and Applications;* Taylor and Francis, 2006.
6. Wakabayashi, T.; Ong, A.-L.; Strelnikov, D.; Krätschmer, W. *J. Phys. Chem. B* **2004,** *108,* 3686–3690. doi:10.1021/jp0376572
7. Ravagnan, L.; Mazza, T.; Bongiorno, G.; Devetta, M.; Amati, M.; Milani, P.; Piseri, P.; Coreno, M.; Lenardi, C.; Evangelista, F.; Rudolf, P. *Chem. Commun.* **2011,** *47,* 2952. doi:10.1039/c0cc03778h
8. Zaidi, A. A.; Hu, A.; Wesolowski, M. J.; Fu, X.; Sanderson, J. H.; Zhou, Y.; Duley, W. W. *Carbon* **2010,** *48,* 2517–2520. doi:10.1016/j.carbon.2010.03.026
9. Ravagnan, L.; Siviero, F.; Lenardi, C.; Piseri, P.; Barborini, E.; Milani, P.; Casari, C. S.; Li Bassi, A.; Bottani, C. E. *Phys. Rev. Lett.* **2002,** *89,* 285506. doi:10.1103/PhysRevLett.89.285506

10. Tabata, H.; Fujii, M.; Hayashi, S. *Carbon* **2006,** *44,* 522–529. doi:10.1016/j.carbon.2005.08.007
11. Tabata, H.; Fujii, M.; Hayashi, S. *Chem. Phys. Lett.* **2006,** *420,* 166. doi:10.1016/j.cplett.2005.12.054
12. Zhao, X.; Ando, Y.; Liu, Y.; Jinno, M.; Suzuki, T. *Phys. Rev. Lett.* **2003,** *90,* 187401. doi:10.1103/PhysRevLett.90.187401
13. Jin, C.; Lan, H.; Peng, L.; Suenaga, K.; Iijima, S. *Phys. Rev. Lett.* **2009,** *102,* 205501. doi:10.1103/PhysRevLett.102.205501
14. Heimann, R. B.; Evsyukov, S. E.; Kavan, L., Eds. *Carbyne and Carbynoid structures;* Physics and Chemistry of Materials with Low-Dimensional Structures, Vol. 21; Kluwer: Springer Netherlands, Netherlands, 1999. doi:10.1007/978-94-011-4742-2
15. El Goresy, A.; Donnay, G. *Science* **1968,** *161,* 363. doi:10.1126/science.161.3839.363
16. Greenville Whittaker, A.; Kintner, P. L. *Science* **1969,** *165,* 589. doi:10.1126/science.165.3893.589
17. Greenville Whittaker, A. *Science* **1978,** *200,* 763. doi:10.1126/science.200.4343.763
18. Smith, P. P. K.; Buseck, P. R. *Science* **1982,** *216,* 984. doi:10.1126/science.216.4549.984
19. Greenville Whittaker, A. *Science* **1985,** *229,* 485. doi:10.1126/science.229.4712.485
20. Smith, P. P. K.; Buseck, P. R. *Science* **1985,** *229,* 486. doi:10.1126/science.229.4712.486
21. Kroto, H. *Rev. Mod. Phys.* **1997,** *69,* 703. doi:10.1103/RevModPhys.69.703
22. Malard, L. M.; Pimenta, M. A.; Dresselhaus, G.; Dresselhaus, M. S. *Phys. Rep.* **2009,** *473,* 51–87. doi:10.1016/j.physrep.2009.02.003
23. Ferrari, A. C. *Solid State Commun.* **2007,** *143,* 47–57. doi:10.1016/j.ssc.2007.03.052
24. Lang, N. D.; Avouris, P. *Phys. Rev. Lett.* **2000,** *84,* 358. doi:10.1103/PhysRevLett.84.358
25. Tongay, S.; Senger, R. T.; Dag, S.; Ciraci, S. *Phys. Rev. Lett.* **2004,** *93,* 136404. doi:10.1103/PhysRevLett.93.136404
26. Zerbi, G. In *Vibrational Spectroscopy of Polymers: Principles and Practice;* Everall, N. J.; Chalmers, J. M.; Griffiths, P. R., Eds.; Wiley: Chichester, United Kingdom, 2007; pp 487–537.
27. Kertesz, M.; Choi, C. H.; Yang, S. *Chem. Rev.* **2005,** *105,* 3448–3481. doi:10.1021/cr990357p
28. Del Zoppo, M.; Castiglioni, C.; Zuliani, P.; Zerbi, G. In *Handbook of Conductive Polymers;* Skotheim, T.; Eisenbaumer, R. L.; Reynoilds, J., Eds.; Dekker: New York, NY, U.S.A., 1998.
29. Milani, A.; Tommasini, M.; Zerbi, G. *J. Raman Spectrosc.* **2009,** *40,* 1931. doi:10.1002/jrs.2342
30. Milani, A.; Tommasini, M.; Del Zoppo, M.; Castiglioni, C.; Zerbi, G. *Phys. Rev. B* **2006,** *74,* 153418. doi:10.1103/PhysRevB.74.153418
31. Tommasini, M.; Fazzi, D.; Milani, A.; Del Zoppo, M.; Castiglioni, C.; Zerbi, G. *J. Phys. Chem. A* **2007,** *111,* 11645. doi:10.1021/jp0757006
32. Tommasini, M.; Milani, A.; Fazzi, D.; Del Zoppo, M.; Castiglioni, C.; Zerbi, G. *Physica E* **2008,** *40,* 2570. doi:10.1016/j.physe.2007.07.016
33. Milani, A.; Tommasini, M.; Zerbi, G. *J. Chem. Phys.* **2008,** *128,* 064501. doi:10.1063/1.2831507
34. Tommasini, M.; Fazzi, D.; Milani, A.; Del Zoppo, M.; Castiglioni, C.; Zerbi, G. *Chem. Phys. Lett.* **2007,** *450,* 86. doi:10.1016/j.cplett.2007.10.100
35. Milani, A.; Tommasini, M.; Fazzi, D.; Castiglioni, C.; Del Zoppo, M.; Zerbi, G. *J. Raman Spectrosc.* **2008,** *39,* 164. doi:10.1002/jrs.1850
36. Castiglioni, C.; Lopez Navarrete, J. T.; Zerbi, G.; Gussoni, M. *Solid State Commun.* **1988,** *65,* 625. doi:10.1016/0038-1098(88)90352-3
37. Castiglioni, C.; Tommasini, M.; Zerbi, G. *Philos. Trans. R. Soc. London, A* **2004,** *362,* 2425. doi:10.1098/rsta.2004.1448
38. Ehrenfreund, E.; Vardeny, Z.; Brafman, O.; Horovitz, B. *Phys. Rev. B* **1987,** *36,* 1535. doi:10.1103/PhysRevB.36.1535
39. Milani, A.; Lucotti, A.; Russo, V.; Tommasini, M.; Cataldo, F.; Li Bassi, A.; Casari, C. S. *J. Phys. Chem. C* **2011,** *115,* 12836–12843. doi:10.1021/jp203682c
40. Innocenti, F.; Milani, A.; Castiglioni, C. *J. Raman Spectrosc.* **2010,** *41,* 226–236. doi:10.1002/jrs.2413
41. Yang, S.; Kertesz, M.; Zólyomi, V.; Kürti, J. *J. Phys. Chem. A* **2007,** *111,* 2434. doi:10.1021/jp067866x
42. Yang, S.; Kertesz, M. *J. Phys. Chem. A* **2008,** *112,* 146. doi:10.1021/jp076805b
43. Januszewski, J. A.; Wendinger, D.; Methfessel, C. D.; Hampel, F.; Tykwinski, R. R. *Angew. Chem., Int. Ed.* **2013,** *52,* 1817–1821. doi:10.1002/anie.201208058
44. Januszewski, J. A.; Tykwinski, R. R. *Chem. Soc. Rev.* **2014,** *43,* 3184–3203. doi:10.1039/c4cs00022f
45. Ravagnan, L.; Piseri, P.; Bruzzi, M.; Miglio, S.; Bongiorno, G.; Baserga, A.; Casari, C. S.; Li Bassi, A.; Lenardi, C.; Yamaguchi, Y.; Wakabayashi, T.; Bottani, C. E.; Milani, P. *Phys. Rev. Lett.* **2007,** *98,* 216103. doi:10.1103/PhysRevLett.98.216103
46. Bogana, M.; Ravagnan, L.; Casari, C. S.; Zivelonghi, A.; Baserga, A.; Li Bassi, A.; Bottani, C. E.; Vinati, S.; Salis, E.; Piseri, P.; Barborini, E.; Colombo, L.; Milani, P. *New J. Phys.* **2005,** *7,* 81. doi:10.1088/1367-2630/7/1/081
47. Casari, C. S.; Li Bassi, A.; Ravagnan, L.; Siviero, F.; Lenardi, C.; Piseri, P.; Bongiorno, G.; Bottani, C. E.; Milani, P. *Phys. Rev. B* **2004,** *69,* 075422. doi:10.1103/PhysRevB.69.075422
48. D'Urso, L.; Compagnini, G.; Puglisi, O.; Scandurra, A.; Cataliotti, R. S. *J. Phys. Chem. C* **2007,** *111,* 17437–17441. doi:10.1021/jp075817u
49. Compagnini, G.; Battiato, S.; Puglisi, O.; Barratta, G. A.; Strazzulla, G. *Carbon* **2005,** *43,* 3025–3028. doi:10.1016/j.carbon.2005.06.025
50. Hu, A.; Rybachuk, M.; Lu, Q.-B.; Duley, W. W. *Appl. Phys. Lett.* **2007,** *91,* 131906. doi:10.1063/1.2793628
51. Hu, A.; Lu, Q.-B.; Duley, W. W.; Rybachuk, M. *J. Chem. Phys.* **2007,** *126,* 154705. doi:10.1063/1.2727450
52. Cataldo, F. *Carbon* **2003,** *41,* 2671. doi:10.1016/S0008-6223(03)00345-2
53. Cataldo, F. *Tetrahedron* **2004,** *60,* 4265–4274. doi:10.1016/j.tet.2004.03.033
54. Szafert, S.; Gladysz, J. A. *Chem. Rev.* **2003,** *103,* 4175–4205. doi:10.1021/cr030041o
55. Kano, E.; Takeguchi, M.; Fujita, J.-i.; Hashimoto, A. *Carbon* **2014,** *80,* 382–386. doi:10.1016/j.carbon.2014.08.077
56. Troiani, H. E.; Miki-Yoshida, M.; Camacho-Bragado, G. A.; Marques, M. A. L.; Rubio, A.; Ascencio, J. A.; Jose-Yacaman, M. *Nano Lett.* **2003,** *3,* 751. doi:10.1021/nl0341640
57. Chuvilin, A.; Meyer, J. C.; Algara-Siller, G.; Kaiser, U. *New J. Phys.* **2009,** *11,* 083019. doi:10.1088/1367-2630/11/8/083019
58. Cretu, O.; Botello-Mendez, A. R.; Janowska, I.; Pham-Huu, C.; Charlier, J.-C.; Banhart, F. *Nano Lett.* **2013,** *13,* 3487. doi:10.1021/nl4018918
59. Casillas, G.; Mayoral, A.; Liu, M.; Ponce, A.; Artyukhov, V. I.; Yakobson, B. I.; Jose-Yacaman, M. *Carbon* **2014,** *66,* 436. doi:10.1016/j.carbon.2013.09.019
60. Casari, C. S.; Russo, V.; Li Bassi, A.; Bottani, C. E.; Cataldo, F.; Lucotti, A.; Tommasini, M.; Del Zoppo, M.; Castiglioni, C.; Zerbi, G. *Appl. Phys. Lett.* **2007,** *90,* 13111. doi:10.1063/1.2430676

61. Okada, S.; Fujii, M.; Hayashi, S. *Carbon* **2011,** *49,* 4704–4709. doi:10.1016/j.carbon.2011.06.074
62. Tabata, H.; Fujii, M.; Hayashi, S.; Doi, T.; Wakabayashi, T. *Carbon* **2006,** *44,* 3168–3176. doi:10.1016/j.carbon.2006.07.004
63. Lucotti, A.; Tommasini, M.; Fazzi, D.; Del Zoppo, M.; Chalifoux, W. A.; Ferguson, M. J.; Zerbi, G.; Tykwinski, R. R. *J. Am. Chem. Soc.* **2009,** *131,* 4239–4244. doi:10.1021/ja078198b
64. Cataldo, F.; Casari, C. S. *J. Inorg. Organomet. Polym. Mater.* **2007,** *17,* 641–651. doi:10.1007/s10904-007-9150-3
65. Chalifoux, W. A.; Tykwinski, R. R. *Nat. Chem.* **2010,** *2,* 967–971. doi:10.1038/nchem.828
66. Ravagnan, L.; Manini, N.; Cinquanta, E.; Onida, G.; Sangalli, D.; Motta, C.; Devetta, M.; Bordoni, A.; Piseri, P.; Milani, P. *Phys. Rev. Lett.* **2009,** *102,* 245502. doi:10.1103/PhysRevLett.102.245502
67. Casari, C. S.; Li Bassi, A.; Baserga, A.; Ravagnan, L.; Piseri, P.; Lenardi, C.; Tommasini, M.; Milani, A.; Fazzi, D.; Bottani, C. E.; Milani, P. *Phys. Rev. B* **2008,** *77,* 195444. doi:10.1103/PhysRevB.77.195444
68. Yildizhan, M. M.; Fazzi, D.; Milani, A.; Brambilla, L.; Del Zoppo, M.; Chalifoux, W. A.; Tykwinski, R. R.; Zerbi, G. *J. Chem. Phys.* **2011,** *134,* 124512. doi:10.1063/1.3571451
69. Cataldo, F. *J. Inorg. Organomet. Polym. Mater.* **2006,** *16,* 15. doi:10.1007/s10904-006-9031-1
70. Cadierno, V.; Gimeno, J. *Chem. Rev.* **2009,** *109,* 3512–3560. doi:10.1021/cr8005476
71. Lucotti, A.; Tommasini, M.; Chalifoux, W. A.; Fazzi, D.; Tykwinski, R. R.; Zerbi, G. *J. Raman Spectrosc.* **2012,** *43,* 95–101. doi:10.1002/jrs.2992
72. Agarwal, N. R.; Lucott, A.; Fazzi, D.; Tommasini, M.; Castiglioni, C.; Chalifoux, W. A.; Tykwinsk, R. R. *J. Raman Spectrosc.* **2013,** *44,* 1398–1410. doi:10.1002/jrs.4300
73. Artyukhov, V. I.; Liu, M.; Yakobson, B. I. *Nano Lett.* **2014,** *14,* 4224. doi:10.1021/nl5017317
74. Castiglioni, C.; Milani, A.; Fazzi, D.; Negri, F. *J. Mol. Struct.* **2011,** *993,* 26. doi:10.1016/j.molstruc.2010.12.021
75. Liu, M.; Artyukhov, V. I.; Lee, H.; Xu, F.; Yakobson, B. I. *ACS Nano* **2013,** *7,* 10075. doi:10.1021/nn404177r
76. Lucotti, A.; Tommasini, M.; Del Zoppo, M.; Castiglioni, C.; Zerbi, G.; Cataldo, F.; Casari, C. S.; Li, A.; Russo, V.; Bogana, M.; Bottani, C. E. *Chem. Phys. Lett.* **2006,** *417,* 78. doi:10.1016/j.cplett.2005.10.016
77. Lucotti, A.; Casari, C. S.; Tommasini, M.; Li Bassi, A.; Fazzi, D.; Russo, V.; Del Zoppo, M.; Castiglioni, C.; Cataldo, F.; Bottani, C. E.; Zerbi, G. *Chem. Phys. Lett.* **2009,** *478,* 45–50. doi:10.1016/j.cplett.2009.06.030
78. Cataldo, F.; Ursini, O.; Angelini, G.; Tommasini, M.; Casari, C. *J. Macromol. Sci., Part A: Pure Appl. Chem.* **2010,** *47,* 739–746. doi:10.1080/10601325.2010.491749
79. Weimer, M.; Hieringer, W.; Della Sala, F.; Görling, A. *Chem. Phys.* **2005,** *309,* 77–87. doi:10.1016/j.chemphys.2004.05.026
80. Zanolli, Z.; Onida, G.; Charlier, J.-C. *ACS Nano* **2010,** *4,* 5174–5180. doi:10.1021/nn100712q
81. Wang, C.; Batsanov, A. S.; Bryce, M. R.; Martın, S.; Nichols, R. J.; Higgins, S. J.; García-Suárez, V. M.; Lambert, C. J. *J. Am. Chem. Soc.* **2009,** *131,* 15647–15654. doi:10.1021/ja9061129
82. Moreno-García, P.; Gulcur, M.; Manrique, D. Z.; Pope, T.; Hong, W.; Kaliginedi, V.; Huang, C.; Batsanov, A. S.; Bryce, M. R.; Lambert, C.; Wandlowski, T. *J. Am. Chem. Soc.* **2013,** *135,* 12228. doi:10.1021/ja4015293
83. Standley, B.; Bao, W.; Zhang, H.; Bruck, J.; Lau, C. N.; Bockrath, M. *Nano Lett.* **2008,** *8,* 3345. doi:10.1021/nl801774a
84. Yuzvinsky, T. D.; Mickelson, W.; Aloni, S.; Begtrup, G. E.; Kis, A.; Zettl, A. *Nano Lett.* **2006,** *6,* 2718. doi:10.1021/nl061671j
85. Diederich, F.; Kivala, M. *Adv. Mater.* **2010,** *22,* 803–812. doi:10.1002/adma.200902623
86. Malko, D.; Neiss, C.; Viñes, F.; Görling, A. *Phys. Rev. Lett.* **2012,** *108,* 086804. doi:10.1103/PhysRevLett.108.086804

License and Terms

The definitive version of this article is the electronic one which can be found at:
doi:10.3762/bjnano.6.49

BEILSTEIN JOURNAL OF NANOTECHNOLOGY

Entropy effects in the collective dynamic behavior of alkyl monolayers tethered to Si(111)

Christian Godet§

Full Research Paper

Address:
Institut de Physique de Rennes, UMR 6251 CNRS - Université de Rennes 1, 35042 Rennes Cedex, France

Email:
Christian Godet - christian.godet@univ-rennes1.fr

§ Phone: +33 2 23 23 57 06; Fax: +33 2 23 23 61 98

Keywords:
admittance spectroscopy; dipolar relaxation; entropy; gauche defect; organic monolayer

Beilstein J. Nanotechnol. **2015,** *6,* 583–594.
doi:10.3762/bjnano.6.60

Received: 23 July 2014
Accepted: 05 February 2015
Published: 26 February 2015

This article is part of the Thematic Series "Self-assembly of nanostructures and nanomaterials".

Guest Editor: I. Berbezier

Abstract

Dynamic properties of *n*-alkyl monolayers covalently bonded to Si(111) were studied by broadband admittance spectroscopy as a function of the temperature and the applied voltage using rectifying Hg/$C_{12}H_{25}$/n-type Si junctions. Partial substitution of methyl end groups by polar (carboxylic acid) moieties was used to enhance the chain end relaxation response. Two thermally activated dissipation mechanisms (B1 and B2, with $f_{B1} < f_{B2}$) are evidenced for all reverse bias values. The strong decrease of both relaxation frequencies with increasing reverse dc bias reveals increasing motional constraints, attributed to electrostatic pressure applied to the densely-packed nanometer-thick monolayer. Spectral decomposition of the frequency response shows a power-law dependence of their activation energies on $|V_{DC}|$. A large reverse bias reversibly increases the B2 response attributed to the distribution of gauche defects, in contrast with the constant strength of the acid dipole loss (B1). A trans–gauche isomerization energy of 50 meV is derived from the temperature dependence of the B2 dipolar strength. For both dissipation mechanisms, the observed linear correlation between activation energy and logarithm of pre-exponential factor is consistent with a multi-excitation entropy model, in which the molecular reorientation path is strongly coupled with a large number of low energy excitations (here the *n*-alkyl bending vibrational mode) collected from the thermal bath. This collective dynamic behavior of alkyl chains tethered to Si is also confirmed by the asymmetric relaxation peak shape related to many-body interactions in complex systems.

Introduction

Self-assembled monolayers (SAM) and organic molecular layers (OML) have attracted great interest over the past two decades because surface functionalization offers great flexibility for a molecular-level control of surface chemistry, surface energy, biocompatibility, friction, corrosion, liquid chromatography, interfacial interactions and electronic transport [1-6].

More recent studies have been focused on the functionalization of nanostructures. However, in spite of a large number of experimental and simulation studies, it is not yet clear how the layer structure affects the measured properties of such functionalized surfaces. In particular, a number of structural and conformational models have been proposed to describe mechanical [7-24] and electron transport [7,25-32] properties.

In order to understand the behavior of nanometer-thick 2D assemblies of molecules tethered to metallic or semiconductor surfaces, the concepts developed for bulk organic solids should be revisited by also considering molecular coverage, lateral (in-plane) inhomogeneity and transverse gradient of disorder [3].

As far as disorder is concerned, in model systems made of linear alkyl chains tethered in a densely packed array, experiments and simulations indicate that a quasi-perfect order can be obtained (at least locally) at low temperature, in the most stable all-trans conformation of the $(CH_2)_n$ molecular backbone [17,22]. However, increasing temperature has a strong influence on the tethered polymethylene OML structure because new chain configurations can be reached from this free energy minimum by a trans–gauche isomerization mechanism (rotation around the C–C axis). Hence, although some topological order is imposed by the head group binding at particular sites of a crystalline substrate, orientational order induced by lateral chain interactions (e.g., van der Waals, electrostatic and dipolar forces) is progressively lost for chain segments located away from the head towards the molecular tail. The strain-induced formation of gauche defects, initiating at outer bonds (end-gauche) and proceeding inward (kinks and gauche–gauche conformers) [3,17,22] results into a disorder gradient.

Another important issue related to energy dissipation mechanisms is the behavior of tethered OML under compressive and shear forces, as found in nano-tribology experiments, where external forces can cause conformational changes. Again, a disorder gradient results from the formation of gauche defects which can be reverted when the atomic force microscope (AFM) tip is moved away (laterally or vertically) [7,9-16,18,21,23,24].

In the field of molecular electronics, many studies were performed by using junctions made of alkyl OML tethered to oxide-free silicon surfaces through chemically stable non-polar Si–C bonds [4,33-35]. These robust densely packed insulating molecular layers play the role of nanometer-thick tunnel barriers [25,27,31,32,36-39]. Although conformational changes are intrinsic to soft matter, the consequences of temperature-induced [25-27,31] and pressure-induced [7,9] conformational changes on electron transport properties have rarely been explicitly described.

In this context, this admittance spectroscopy study emphasizes a collective dynamic behavior of linear saturated (*n*-alkyl) chains tethered to Si(111). Dynamic properties are very sensitive to structure and conformation of the OML. In contrast with alternative dynamic probes, such as nuclear magnetic resonance, which are limited by a poor signal-to-noise ratio and require functionalization of 3D nanoparticles or porous solids [3], admittance spectroscopy is sensitive to 0.3 picomoles of carboxylic acid dipoles [40] and measurements can be performed in a well-defined metal/OML/semiconductor planar configuration, which is relevant for molecular electronics devices. Admittance spectroscopy provides insights in the modulation of localized charge density and dipole reorientation in a system submitted to a time-dependent electric field. Dissipation (energy loss) mechanisms can be described by using equivalent representations of the complex admittance, including the dielectric permittivity ε^* and electrical modulus M^*. Dipole reorientation requires an activation of the system with energy barriers related either to local or more collective reorientation mechanisms.

Previous admittance spectroscopy studies of metal/*n*-alkyl/Si junctions have shown changes in peak shape and frequency of the molecular relaxation signature with increasing forward bias, which were attributed to an enhanced rigidity of OML [29,30]. Recently, the temperature dependence of the molecular relaxation frequency (at low reverse bias) has revealed the sensitivity of its activation energy to end-group functionalization, namely increased motional constraints with carboxylic acid substitution to methyl groups [40].

This extension of our previous work [40] to large reverse dc bias applied to $Hg/C_{12}H_{25}/Si$ tunnel junctions, resulting in a change in the distribution of topological defects, reveals a collective behavior of linear saturated (*n*-alkyl) chains tethered to the Si(111) surface. The effects of both temperature and applied dc bias on the dynamics of a monolayer of *n*-alkyl chains tethered to Si(111) are studied by broadband admittance spectroscopy (0.1 Hz to 10 MHz) using a partial substitution of methyl (CH_3) end groups (0.1 Debye) by carboxylic acid (COOH) dipolar moieties (1.74 Debye) in order to enhance the chain end relaxation response. Here, a mixed alkyl/acid-functionalized monolayer with 5% acid molar fraction (in the liquid phase) was chosen to avoid acid–acid dipole interactions at the OML surface (Figure 1). Using low-doped n-type Si (1–10 Ω·cm) provides strong rectification [27,32,38-40] with a very low dc current in the reverse bias regime at low temperatures (130–300 K). In addition, low doping is interesting for providing a low depletion capacitance, which increases the high frequency cutoff (typically 1 MHz) arising from the series resistance R_S (due to bulk Si and rear contact resistance) [40,41].

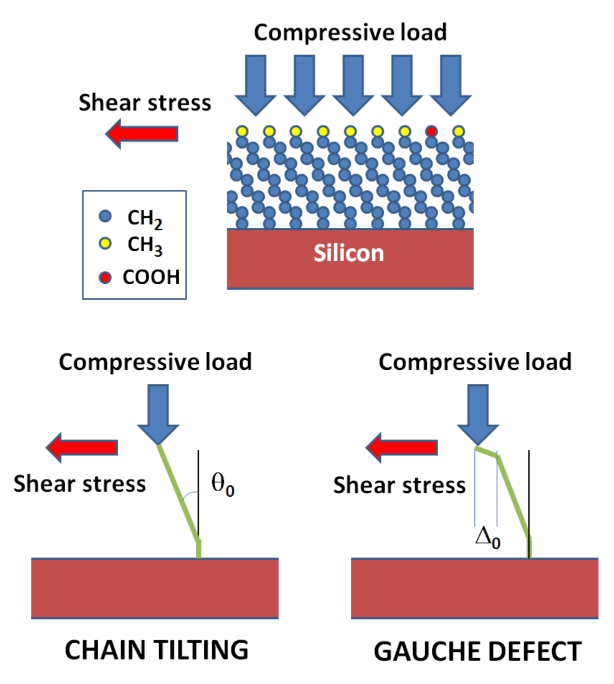

Figure 1: Top: the electrostatic pressure resulting from a dc voltage drop on the insulating molecular monolayer is described by a normal compressive load. Bottom: the mechanical response to the induced shear stress may lead to global chain axis tilting (left panel) or formation of gauche defects preferentially localized at chain ends (right panel).

In the experimental admittance $Y(V,T,\omega)$ characteristics, two bias-dependent relaxation peaks (B1 and B2, with $f_{B1} < f_{B2}$) are observed in addition to a bias-independent peak A near 10^3 Hz, previously attributed to adventitious water condensation [32,40]. With increasing reverse bias, the slowing down of both relaxation frequencies f_{B1} and f_{B2} reveals increasing motional constraints, which are attributed to electrostatic pressure effects. The magnitude of this electrostatic pressure remains well below the applied tip pressure used in AFM experiments (0.03–60 GPa) [21,24]. Since the dipolar relaxation peaks, B1 and B2, overlap with peak A, a spectral decomposition is mandatory to obtain the intensities and frequencies of dipolar relaxation peaks, along with the asymmetric peak shapes in the context of Dissado–Hill (DH)/Jonscher theories for many-body interactions [42-46]. Arrhenius plots of the relaxation frequencies show that the apparent activation energies and pre-exponential factors strongly increase with applied dc voltage, $|V_{DC}|$.

The dynamics of the tethered OML will be discussed in terms of a collective behaviour, with three complementary approaches: a) The DH model addresses spatial correlations between “embedded dipoles” in order to describe the asymmetric relaxation peak shapes [45,46]. b) The multi-excitation entropy model proposed by Yelon, Movaghar and Crandall (YMC) [47,48] considers a thermodynamic description of the dipole reorientation path strongly coupled with elementary excitations collected from a thermal bath. c) The applied bias dependence of activation energies is tentatively related to compression and shear stresses expected for an OML considered as a continuous medium submitted to a compressive force (Figure 1) [49]. Finally, on the basis of the bias dependence of the relaxation peak intensities, relaxation mechanisms B1 and B2 will be, respectively, attributed to acid end-group dipoles and to gauche defect configurations.

Results

As reported previously [32], several techniques were used to obtain complementary information on the conformal coverage (STM, AFM), OML thickness (spectroscopic ellipsometry, SE), molecular packing density and possible interface oxidation of the Si substrate (X-ray photoelectron spectroscopy). The surface density of acid groups (0.4×10^{14} cm^{-2}) and the total organic layer (acid + alkyl) coverage (2.6×10^{14} cm^{-2}) were obtained by XPS using, respectively, the C 1s (COOH) signal and the total C 1s peak area. The thickness ($d_{SE} = 1.06 \pm 0.1$ nm) obtained from SE data indicates a rather large average tilt angle (40°) of the chain axis with respect to the normal direction.

Dipolar relaxation is investigated in a wide frequency range (from 1×10^{-1} Hz to 1×10^7 Hz). To observe dipolar relaxation mechanisms, low temperature and reverse bias were imposed to obtain low dc conductance and a relaxation frequency of the space-charge layer below 1 Hz [32]. The complex admittance, $Y^*(V_{DC},T,\omega) = G_m + j\omega\, C_m$, can be analyzed by using either the capacitance $C^* = (Y^*/j\omega)$ or the electrical modulus $M^* = (\varepsilon^*)^{-1} = j\omega\, C_0/Y^*$ (here $C_0 = C^*/\varepsilon^*$ is arbitrarily set to 100 pF). The characteristic frequencies of the loss peaks in imaginary modulus, $M''(\omega)$, or in imaginary permittivity, $\varepsilon''(\omega)$, data correspond to a delay between the electric field and local charge modulation or dipole rotation [32,39,40,50].

In the following, the low dc bias situation is briefly recalled, before considering the effect of increasing the reverse bias, $|V_{DC}|$, and the spectral analysis method.

Dipolar relaxation at low applied bias

Two classes of relaxation mechanisms, A and B, have been identified with, respectively, a weak (f_A) and a strong (f_B) temperature dependence of the relaxation frequencies [32]. At low temperatures ($T < 150$ K), only mechanism A is observed at intermediate frequencies ($f_A \approx 4 \times 10^3$ Hz in Figure 2b). The characteristic frequency f_A is basically bias-independent and has very small values for activation energy (E_A = 29.6 ± 1 meV) and pre-exponential factor ($f_A{}^0 \approx (7 \pm 2) \times 10^3$ Hz). Its small modulus intensity, $M''_{MAX} \approx 0.02$, and dipolar relaxation strength, $\Delta\varepsilon \approx 0.09$, decrease weakly as a function of the increasing temperature (Figure 6b in [32]). The asymmetric $M''(\omega)$ peak shape is defined by an apparent pre-peak slope $m_{DH}(A) \approx 0.86 \pm 0.05$ and a post-peak slope $(1 - n_{DH}(A)) \approx 0.61 \pm 0.05$.

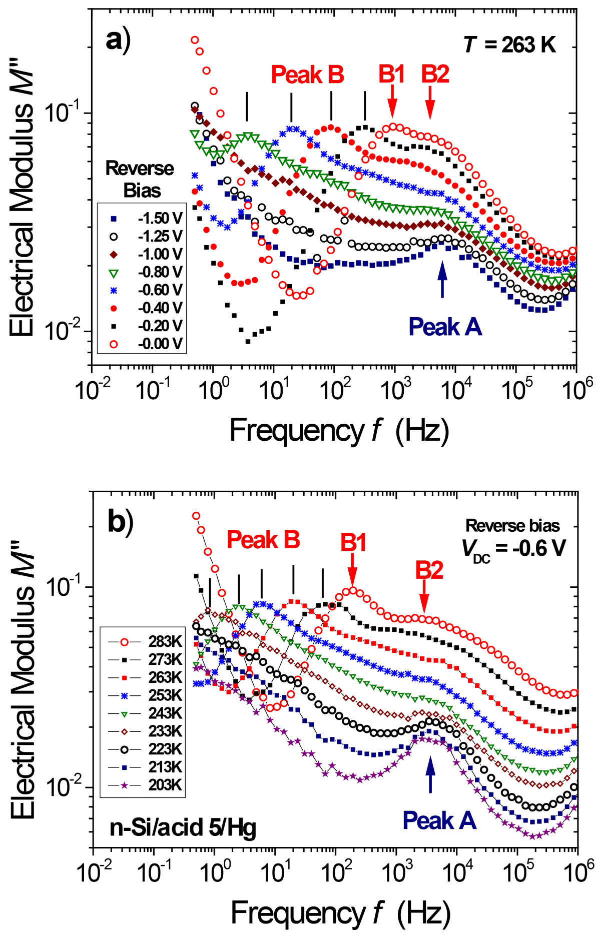

Figure 2: Imaginary electrical modulus $M''(\omega)$ of the Hg/acid 5/n-type Si junction: a) reverse-bias dependence at T = 263 K; b) temperature dependence (203–283 K) under strong reverse bias (V_{DC} = −0.6 V). The admittance data show (i) a bias-independent relaxation peak A ($f_A \approx 5$ kHz) with a weak T dependence, and (ii) two bias-dependent peaks (B1 and B2) at lower frequency with strong bias and temperature dependence.

With increasing temperature mechanism B also appears. As a matter of fact, two relaxation peaks B1 and B2 ($f_{B1} < f_{B2}$) are clearly observed in junctions with diluted carboxyl end group dipoles (Si/acid 5), a larger M''_{MAX} intensity being found for the lower-frequency B1 peak (Figure 2). For the stronger peak B1, the relaxation frequency f_{MAX} taken at the M''_{MAX} peak maximum exhibits an activated behavior $f_{MAX} = f_B{}^0 \times \exp(-E_B/kT)$ with high values for the activation energy, $E_B \approx 0.40$ eV, and the pre-exponential factor ($f_B{}^0 \approx 10^{10}$ Hz) [32]. As shown below, the spectral decomposition method (E_{B1} = 0.37 eV) confirms this result; at low bias, a small but significant difference in activation energy values is also found between mechanisms B1 (E_{B1} = 0.37 eV) and B2 (E_{B2} = 0.32 eV). In the following, bias-dependent relaxation data will be helpful to elucidate their identification.

Bias dependence of dipolar relaxation

With increasing reverse bias, a strong slowing down of both relaxation mechanisms at frequencies f_{B1} and f_{B2} is observed. Figure 2a illustrates this behavior at T = 263 K, along with the constant strength of the B1 relaxation mechanism. In the reverse-bias regime, both B1 and B2 peak frequencies show a stronger temperature dependence, as illustrated in Figure 2b, at V_{DC} = −0.6 V. The ratio between the respective frequencies of peaks B1 and B2 being less than 20 for all investigated temperatures, they strongly overlap. Note that peak A is also present in the available frequency window, although it clearly appears only at very low temperature and strong reverse bias.

Spectral decomposition

The analysis of the relaxation data requires some fitting of admittance spectra with a large number of unknown parameters (characteristic frequencies, peak intensity M''_{MAX} or dipolar relaxation strength $\Delta\varepsilon$, peak shape exponents). Hence, measurements with wide frequency windows at low temperatures are crucial experimental conditions. To describe the relaxation peak shapes, we assume that all three relaxation mechanisms follow the same type of many-body interactions (although with different parameters) consistent with a collective response of the densely-packed assembly of tethered organic chains.

To account for the typically observed deviations from the ideal Debye relaxation, Dissado–Hill and Jonscher have elaborated the theoretical description of many-body interactions in complex systems on the basis of an ideal structure that interlinks the dipoles and can be represented by perturbations on different length scales [45,46]. The relaxation rate β_{iN} of an individual dipole is defined by its interactions within a cluster of size N_i formed by its surrounding inactive neighbors. The occurrence of correlated-cluster regions with sizes M_j depending on the strength of dipolar screening [42,44] takes place at the mesoscopic level. The macroscopic average over all cooperative mesoscopic regions provides the universal relaxation, given by the dielectric susceptibility [29,30,45,46,51]:

$$\varepsilon(\omega)-\varepsilon_{\infty}(\omega)=\Delta\varepsilon\left(1-j\omega/\omega_{\mathrm{DH}}\right)^{-1+n_{\mathrm{DH}}}\times\frac{{}_2F_1\left[1-n_{\mathrm{DH}},1-m_{\mathrm{DH}};2-n_{\mathrm{DH}};\left(1-\mathrm{j}\omega/\omega_{\mathrm{DH}}\right)^{-1}\right]}{{}_2F_1\left[1-n_{\mathrm{DH}},1-m_{\mathrm{DH}};2-n_{\mathrm{DH}};1\right]}, \qquad (1)$$

where the Gauss hypergeometric function ${}_2F_1[\ ,\ ;\ ;\ ]$ is defined by $0 \le m \le 1$ and $0 \le n \le 1$, ω is the frequency and ω_{DH} is the peak frequency. Asymptotic limits, ω^m for $\omega << \omega_{\mathrm{DH}}$ and ω^{n-1} for $\omega >> \omega_{\mathrm{DH}}$, are fully consistent with Jonscher [42-44] and Havriliak–Negami [52,53] expressions.

Fitting the four parameters ($\Delta\varepsilon$, ω_{DH}, m_{DH}, n_{DH}) for each relaxation mechanism is performed using the complex permittivity (Equation 1) by minimizing the error function EF($\Delta\varepsilon$, ω_{DH}, m_{DH}, n_{DH}) given by the sum over the fitting range of $[\mathrm{Ln}\ (M''_{\mathrm{EXP}}/M''_{\mathrm{CALC}})]^2$. In the following, we address the dependence of peaks B1 and B2 on temperature and bias, including their dipolar strength $\Delta\varepsilon = \varepsilon_0 - \varepsilon_\infty$, along with the shapes resulting from their collective response.

Admittance data analysis

Fitting procedure: Decomposition of admittance spectra into three asymmetric relaxation peaks (A, B1 and B2) was performed by adjusting the Dissado–Hill parameters (Equation 1), excluding data in the low-frequency region where the dc current is strong and data in the high frequency regime ($f > 0.1$ MHz) where series resistance effects are significant. Because each relaxation peak is defined by four characteristic parameters (frequency, dipolar relaxation strength and two characteristic slope exponents) an unambiguous decomposition is not straightforward.

Since the activation energy and the pre-exponential factor of the relaxation frequency $f_{\mathrm{A}}(T)$ are readily obtained from low-temperature data, according to f_{A} (Hz) = $1.5 \times 10^4 \exp(-0.0296/kT)$, the frequency of peak A can be extrapolated to higher T and fixed in the further parameter adjustment. Note that any error (e.g., underestimation) made in the fixed f_{A} value influences (decreases) the fitted n_{B2} value. Some parameter adjustment was allowed for the slopes ($m_{\mathrm{A}} = 0.9 \pm 0.1$, $n_{\mathrm{A}} = 0.65 \pm 0.1$) and the relaxation strength, $\Delta\varepsilon = 0.15 \pm 0.05$ of peak A.

In a first step of spectral decomposition, the slopes (m_{DH} and $1-n_{\mathrm{DH}}$) were fixed in order to fit the two peak frequencies (f_{B1} and f_{B2}) and the three peak strengths (A, B1 and B2). It was ensured that the change in the other (fitted) parameters remained small when the fixed m_{B2} value is changed by ±0.1 (typically at 0.7 or at 0.8). This constraint on m_{B2} is helpful to decrease some fluctuations in the fitted peak strength $\Delta\varepsilon$ as a function of the temperature. A representative example of data fitting is given in Figure 3 (with fixed values for $m_{\mathrm{A}} = 1$ and $n_{\mathrm{A}} = 0.53$) showing that an accurate decomposition into three peaks is obtained even for experimental spectra with substantial peak overlap; in this particular example, peaks B1 and B2 are separated by one decade (e.g., at $V_{\mathrm{DC}} = -0.6$ V, the peak frequency ratio $f_{\mathrm{B2}}/f_{\mathrm{B1}} = 20 \pm 5$).

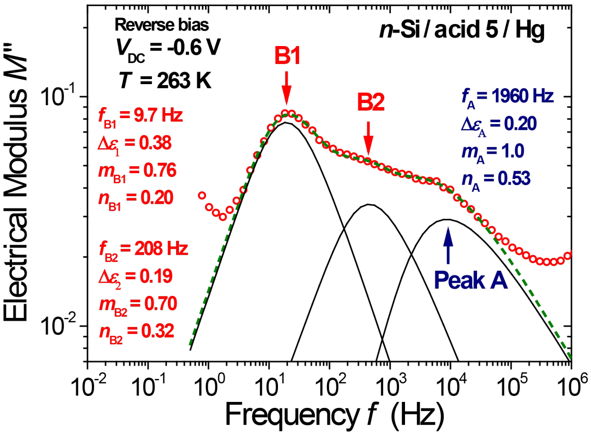

Figure 3: Decomposition of the electrical modulus $M''(\omega)$ obtained at T = 263 K and $V_{\mathrm{DC}} = -0.6$ V into three dipolar relaxation peaks using the peak shape given by the Dissado–Hill theory (Equation 1). The dashed line is the peak sum fitted to the data (open circles).

In a second fitting step, the slopes were considered as additional free parameters to refine the spectral decomposition. The latter conditions improve the error function by a factor of about two. Note that the improvement of this error function value is limited by a few noisy data near 50 and 100 Hz.

Peak shape: The shapes of peaks B1 and B2 in log(M'') vs log(ω) plots are rather independent of the measurement temperature. However, pre-peak slopes must be compared in the higher T range, where m_{B1} is obtained with a good accuracy, while post-peak slopes must be compared in the lower T range, where n_{B2} is obtained with a good accuracy. In contrast, peak overlap provides larger error bars on the fitted n_{B1} and m_{B2} parameters.

The pre-peak slopes m_{B1} and m_{B2} are quite similar, and the small difference, $m_{\mathrm{B2}} \approx 0.70 \le m_{\mathrm{B1}} \approx 0.78 \pm 0.05$ observed over many T and V_{DC} values, remains within the experimental and the fitting error. No systematic change of m_{B1} and m_{B2} with applied bias is detected. In the Dissado–Hill model, high values of pre-peak slopes indicate a large degree of disorder at the inter-cluster scale, i.e., at longer relaxation times.

In contrast, a larger difference appears in the fitted values of the post-peak slopes ($n_{B1} \approx 0.15 \pm 0.1 << n_{B2} \approx 0.6 \pm 0.2$). Although large errors bars are obtained for the fitted n_{B2} values, due to some frequency overlap with peak A, the difference is quite significant. In the Dissado–Hill model, a high value of the post-peak slope $|n_{B1} - 1|$ for mechanism B1 indicates a large degree of disorder at the intra-cluster scale (i.e., at shorter relaxation times), approaching the situation $n \approx 0$ where dipoles relax independently (leading to the Debye classical model, in contrast with $n \approx 1$, where reorientations are fully correlated).

In summary, over the whole investigated temperature range, while little difference in long-range order (pre-peak slopes $m_{B1} \approx m_{B2}$) is observed between mechanisms B1 and B2, short-range order (post-peak slopes $n_{B1} < n_{B2}$) is more developed for mechanism B2.

Activation energy: The activation energy of the relaxation peak frequency is interpreted in terms of motional constraints for dipole reorientation. For each V_{DC} value, the relaxation frequencies (f_{B1}, f_{B2}) reported in Figure 4 exhibit an Arrhenius dependence on the temperature, $f_B = f_B^0 \times \exp(-E_B/kT)$ over three decades. An important observation is the evidence of a so-called "focal point" at which the Arrhenius lines (extrapolated to high T) tend to converge; within the experimental error. A similar focal (or isokinetic) temperature $T_F = 320 \pm 10$ K is found for both mechanisms B1 and B2 (Figure 4). The consequences of this result on the pre-exponential factor behavior are discussed below.

Since the activation energies for relaxation peaks B1 and B2 both increase with the applied $|V_{DC}|$ values, the temperature fitting range becomes narrower and the resulting error bars increase. As a consequence, the analysis of relaxation data is limited to $|V_{DC}| \le 1$ V. The resulting activation energies, E_{B1} and E_{B2} summarized in Figure 5, strongly depend on the applied dc bias, with a superlinear behavior. The bias dependence is slightly stronger for E_{B2} as compared to E_{B1}. Both activation energies can be reasonably described by power law functions $|V_{DC}|^q$, with $q \ge 2$. If the exponents $q_1 = 2.0$ and $q_2 = 2.5$ are forced in this power-law dependence, one obtains E_{B1} (eV) = 0.35 + 0.85 $|V_{DC}|^2$ and E_{B2} (eV) = 0.32 + 0.90 $|V_{DC}|^{2.5}$ (Figure 5).

A strong correlation between activation energy (in the range of 0.3–1.3 eV) and pre-exponential factor (range 10^{10} to 10^{24} Hz) is found in Figure 6, showing a linear dependence of log $f_B^0(V_{DC})$ vs $E_B(V_{DC})$, up to very high values of the pre-exponential factor. A remarkable feature is that both relaxation mechanisms follow the same linear correlation, with inverse slope $kT^* = 28.1$ meV ($T^* = 325$ K). The similar values found

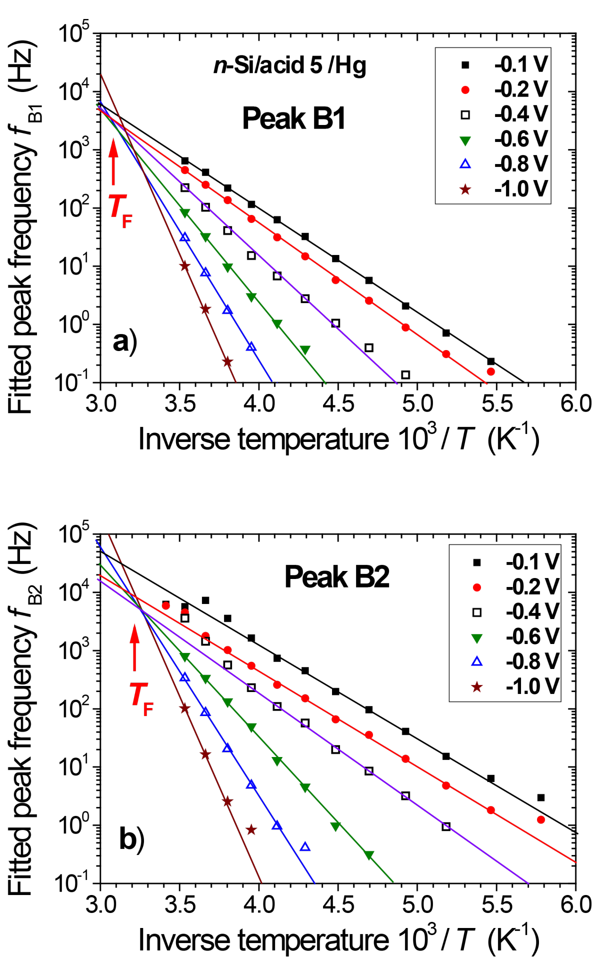

Figure 4: Temperature dependence of the dipolar relaxation frequencies f_{B1} (a) and f_{B2} (b) obtained for the Hg/acid 5/*n*-type Si junction at different reverse bias values (V_{DC} range from −0.1 V to −1.0 V). The lines are Arrhenius fits to the data, showing the existence of a "focal point" near $T_F \approx 320$ K.

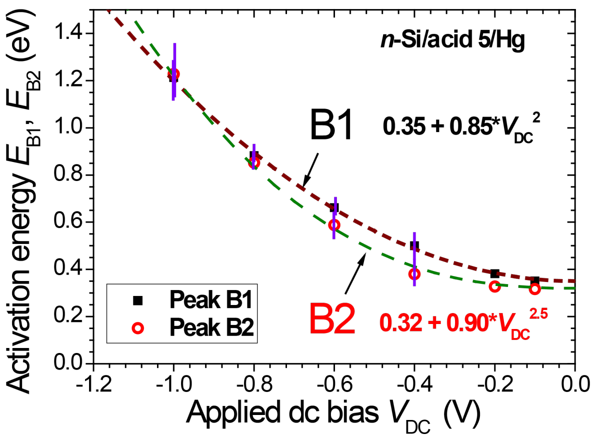

Figure 5: Bias dependence of dipolar relaxation activation energies, E_{B1} (squares) and E_{B2} (circles). The lines are power-law functions with forced exponent values: E_{B1} (eV) = 0.35 + 0.85 $|V_{DC}|^2$; E_{B2} (eV) = 0.32 + 0.90 $|V_{DC}|^{2.5}$.

for the inverse slope temperature T^* (Figure 6) and the "focal point" temperature T_F given by Arrhenius plots (Figure 4) will be discussed below.

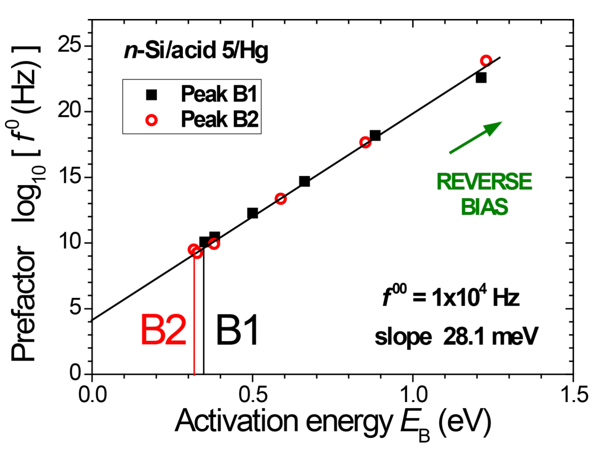

Figure 6: Linear correlation between activation energy and pre-exponential factor values derived from Figure 4, for peaks B1 (squares) and B2 (circles). The inverse slope is kT^* = 28.1 meV (T^* = 325 K).

Dipolar relaxation strength: Since the rather weak peak B2 overlaps with peaks B1 and A, respectively, at lower and higher frequencies, the fitted strength, Δε, of peak B2 is lower than its apparent value at the peak frequency, as shown in Figure 4. The dipolar relaxation strengths of mechanisms B1 and B2 show a different behavior as a function of the temperature, as illustrated in Figure 7 for several reverse bias values. For a given V_{DC} value, whereas the peak strength of B1 is basically constant, the peak strength of B2 increases (by a factor of about three) with increasing temperature in the range from 130 to 280 K; for smaller applied bias values, a larger slope is observed above 230 K.

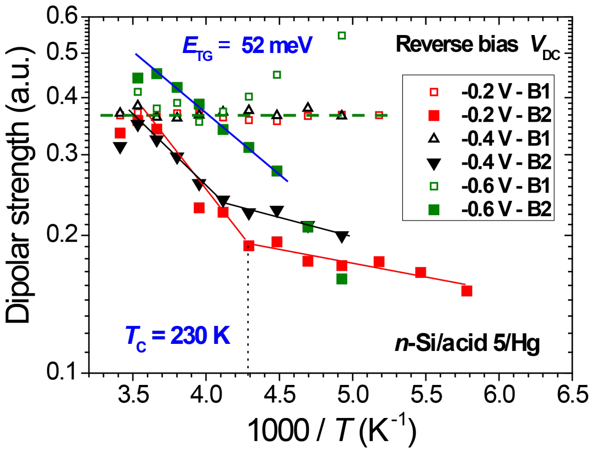

Figure 7: Temperature dependence of the dipolar relaxation strength Δε of peaks B1 and B2, measured at reverse bias values V_{DC} = −0.2, −0.4, and −0.6 V. At low applied bias, two different regimes appear, below and above 230 K.

Discussion

The dynamics of the Si/acid 5 junction shows two different relaxation mechanisms with similar activation energies, both increasing with applied reverse dc bias. In this section, we attribute both relaxation mechanisms to dipolar units in the OML, namely acid end groups (B1) and gauche defects (B2), and we argue that the electrostatic pressure (induced by the dc voltage drop over the insulating monolayer) is responsible for both increasing motional constraints and increasing the number of gauche defects. In addition, both dipole relaxation mechanisms reveal a strong coupling of the dipole reorientation path with the molecular vibrational modes and manifest a collective dynamic response.

Trans–gauche isomerization

Over the whole investigated temperature range, the strength of relaxation peak B1 is remarkably stable (Figure 7), as expected for a constant number of carboxylic acid dipoles. This indicates that the weak electrostatic pressure does not induce strong effects on their dipolar strength, which could arise, e.g., from a collapse of the organic monolayer.

In contrast, mechanism B2 attributed to gauche defects is enhanced at high temperatures and high dc bias. This temperature dependence supports previous modeling of C_{18} alkyl monolayers tethered to Si(111), showing an increase of gauche defects density by a factor of about five over the range 100–300 K [17]: (i) At low temperatures, little space is available for molecular reorientations and trans–gauche isomerization is restricted. (ii) With increasing temperature the number of chain gauche conformers rises and some disordering originates in the chain end regions and propagates towards the middle of the chain. The latter calculations are also consistent with vibrational and NMR spectroscopies [3,19,31,54].

In this admittance study, peak shapes do not show any evidence of ordering at low temperatures. Large values of the pre-peak slopes ($m_{B1} \approx m_{B2}$) are characteristic of long-range disorder for both mechanisms B1 and B2. In contrast, the post-peak slopes ($n_{B1} < n_{B2}$) indicate that the chain ends (B1) are more disordered while they simultaneously experience larger motional constraints (smaller frequency, larger activation energy) than the gauche defects (B2).

Assuming a constant dipolar strength for all gauche defects, the dependence of the gauche defect response on temperature (range 220–280 K) provides a value of 52 ± 5 meV for the activation energy of $\Delta\varepsilon$ (B2) (Figure 7). This trans–gauche isomerization energy for tethered *n*-alkyl chains is larger than the value deduced from the density of vibrational states for short *n*-alkanes in the liquid phase (34 meV) [55,56] and comparable to that of perfluoro-*n*-alkanes (44 meV) [57].

However, an accurate quantification of the number of gauche defects would require an estimate of the dipole moments for all non-centrosymmetric methylene conformations, which will depend on details of the trans–gauche sequences. Vibrational spectroscopy and molecular dynamics studies of tethered alkyl monolayers have shown that the distribution of gauche defects at internal chain positions (kinks, gauche–gauche) and at chain ends (end-gauche) depends both on chain packing, chain length and temperature [58,59]. Interestingly, for the smaller applied bias, a weaker temperature dependence of $\Delta\varepsilon$ (B2) is observed below 230 K. Note that for longer *n*-alkyl tethered chains (C_{12} and above), a steady increase of the number of internal gauche defects was found from 100 to 300 K, while the density of end-gauche defects was very weakly dependent on the temperature [59]. The slope change observed near 230 K in Figure 7 may thus reveal the presence of end-gauche conformers at low temperatures, and an increase in internal gauche configurations (including kinks and double-gauche conformers) at higher temperatures. However, additional defects arising from disordered domain boundaries cannot be excluded.

Multiexcitation entropy model of relaxation frequency

With increasing reverse bias, slowing down of both relaxation frequencies f_{B1} and f_{B2} due to motional constraints is related to a simultaneous increase of both activation energy (E_B) and pre-exponential factor (f_B^0) values. Hence, a kind of "compensation" occurs, namely the frequency decrease is less dramatic than that which would arise from a change in activation energy only. More precisely, we have shown in Figure 6 that the relaxation mechanisms B1 and B2 follow the same linear correlation (with inverse slope kT^*) between E_B (in the range of 0.3–1.3 eV) and $\log(f_B^0)$ (in the range from 10^{10} to 10^{24} Hz). The latter apparent prefactor values exceed typical phonon frequencies (10^{13} Hz) by more than ten decades.

This "compensation law" observed for solid-state phenomena with a large activation energy in many areas (physics, mechanics, chemistry, biology) has been rationalized by a multi-excitation entropy model, in the strong coupling limit, which incorporates the entropy of low energy excitations collected from a thermal bath [47]. In the YMC model, when the entity which is being excited and the excitation reservoir (the lattice and its vibrations) are so strongly coupled as to be indistinguishable, the excitation must be treated by using the transition state theory and the Eyring equation, with a free energy for the transition, $\Delta G = \Delta E - T\Delta S$ that includes the large entropy associated with this fluctuation. Hence, the resulting frequency expression $f_B = f_B^0 \exp(\Delta S/k)\cdot\exp(-\Delta E/kT)$ may explain very large apparent prefactor values, $f_B^0 \exp(\Delta S/k)$; a linear relationship between ΔS and ΔE is thus a sufficient condition to obtain a linear compensation law (as found in Figure 6).

In the YMC model, when a large activation enthalpy barrier ΔE is obtained from a bath of elementary excitations, the number necessary to pass the barrier can be estimated from $n \approx \Delta E/\hbar\omega$, where $\hbar\omega$ is the average energy of the bath excitations (typically tens of meV). To evaluate the number Ω of configurational paths, considered as equally probable, Yelon, Movaghar and Crandall consider an interaction volume [48] containing N excitations, where N is the number that must be available in order to provide the n excitations to be annihilated. The change in entropy

$$\Delta S = k\ln(\Omega) = k\ln\left[\frac{N!}{n!(N-n)!}\right]$$

is approximated by

$$\Delta S = \frac{\Delta E}{\hbar\omega}k\ln\left(\frac{N}{n}\right),$$

if $N >> n$ (Stirling's approximation). Since the larger the value of N, the more likely the process, the YMC model emphasizes that N may be treated as a coupling constant, between the external force and the microscopic motion at the molecular level. If the coupling with the thermal bath is not strongly dependent on ΔE, this relation predicts the existence of a "focal point" in the Arrhenius plot at the temperature

$$T_F = \frac{\hbar\omega}{k\ln(N/n)}$$

along with a linear relationship between activation energy and logarithm of the pre-exponential factor with slope kT_F.

In the framework of the multiexcitation entropy model, the temperature $T^* = 325$ K found in this work provides the energy (28 meV or 227 cm^{-1}) of the collected excitations available from the thermal bath (divided by a number of the order of 1). Hence, as $|V_{DC}|$ increases, increasingly large number of vibrational excitations (in the range of 10–50) is required to overcome the activation barrier for collective molecular reorientation.

Coupling with vibrational modes

Thermal bath excitations (227 ± 10 cm^{-1}) revealed by dipolar relaxation dynamics can be compared with vibrational energies of *n*-alkanes, either in the liquid phase or in a two-dimensionally tethered phase.

For *n*-alkanes in the liquid phase, low vibration energies correspond to skeletal deformations, i.e., torsion or expansion/contraction [60]. Calculated spectra of the density of vibrational states for short *n*-alkanes, taking into account the distribution of conformational configurations resulting from the trans–gauche isomerization [55,56], show a C–C stretching band centered around 900 cm^{-1}, obviously too high to account for our results, whereas torsion modes of CH_2–CH_2 units occur at too low energies (150 cm^{-1}). In contrast, the CCC bending region centered near 220 cm^{-1} is related to the LAM-1 mode (single node longitudinal acoustic mode), which is also called “accordion” mode because all CCC angles change in phase. Disorder effects in the LAM modes were studied by Raman spectroscopy; the frequency in the solid ordered phase (all-trans configuration) is smaller (200 cm^{-1}) than in the liquid phase (broad band near 240 cm^{-1}) in which a disordered-LAM (or D-LAM) scattering is taken as the envelope of a statistical distribution of LAM-1 modes of short trans planar sequences [61].

The first LAM-*k* frequencies (*k* being the number of nodes) have been computed for *n*-alkane molecules of variable length tethered to a solid surface [62], showing very good agreement of the C_{12} alkane LAM-1 frequency (226 cm^{-1}) with our results. Some molecular dynamics studies of tethered *n*-alkanes also reveal similar vibrational energies in the velocity autocorrelation function [63].

In summary, the dynamics of the Si/acid 5 junction reveal a cooperative coupling of thermal excitations to dipolar relaxation of the tethered *n*-alkane OML. The characteristic wavenumber of 227 cm^{-1} is related to the longitudinal acoustical mode (LAM-1) of the chain skeleton rather than to the higher energy CC stretching mode. Since the LAM frequency of the accordion mode is length dependent [62], this model predicts that the "focal point" temperature T_F should decrease with increasing *n*-alkane length.

OML mechanics: compressive and shear forces

In this section, the molecular layer is considered as a continuous medium submitted to a compressive electrostatic pressure, proportional to V_I^2, where V_I is the potential drop across the insulating OML with thickness d_{OML} and dielectric permittivity ε_I:

$$P\left(\text{N}\cdot\text{m}^{-2}\right)=\left(\varepsilon_0\varepsilon_I/2\right)\left(V_I/d_{OML}\right)^2. \qquad (2)$$

This electrostatic force leads to compressive and shear stress components, respectively, normal and parallel to the substrate.

Furthermore, each molecule is considered as a rigid elastic rod, tilted at some angle with respect to the normal to the surface and submitted to forced oscillations. The mechanical response to normal compression load has been tabulated for a number of geometries [49]. For a rod that is fixed on one side and free on the other side (fixed–free conditions), as occurs for linear tethered molecules, stress and strain depend on the spring constant $k = (P/E\cdot I)^{1/2}$ where I is the moment of inertia of the rod, E its Young modulus, and P the normal compression load.

In the context of a molecular layer submitted to compression, conformational changes of the molecules must be taken into account (Figure 1). A gauche defect (B2) such as a kink conformer is depicted as a laterally displaced bond with respect to the plane of the alkyl chain, while a tilted chain corresponds to a global angular displacement of the molecule backbone axis and hence of the end-group dipole (B1). Specific transverse shear moments result from these two situations [49]. In the case (B2) of a rod submitted to axial compression P plus externally created lateral displacement Δ_0, the transverse shear is proportional to the product $(P\cdot k)$, i.e., $P^{3/2}$, because the angular tilt $\theta_A \approx \Delta_0\cdot k$. In the case (B1) of a rod submitted to axial compression plus externally created angular displacement θ_0, the transverse shear is simply proportional to P, assuming that the angular tilt $\theta_A \approx \theta_0$ is independent of axial compression.

This simple nano-mechanical model for the fixed–free rod conditions thus predicts a stronger normal pressure dependence of the transverse shear for (kink) gauche defects as compared to end group dipoles. This corresponds qualitatively to the larger sensitivity to the applied bias found for E_{B2} as compared to E_{B1}, shown in Figure 5. Although $|V_I|$ is expected to increase with $|V_{DC}|$, the fact that V_I is not directly measured in our experiments precludes further conclusions.

Conclusion

This fundamental admittance spectroscopy study provides new guidelines to identify the contribution of activated dipolar relaxation mechanisms and to discriminate the response of electrically active interface defects in organic monolayer/semiconductor assemblies.

Dynamic properties of tethered *n*-alkyl molecules were studied using a Hg/$C_{12}H_{25}$/n-type Si(111) junction with partial substitution of methyl end groups by polar acid moieties. Two temperature-activated relaxation mechanisms have been attributed to dipole end groups (B1) and gauche defects (B2). The temperature dependence of peak B2 dipolar strength provides a trans–gauche isomerization energy of 50 meV for tethered *n*-alkyl molecules. The enhanced B2 peak density, observed with increasing applied bias, is attributed to the formation of gauche defects as a means of reducing the stress due to electrostatic pressure across the nanometer-thick insulating layer. This effect is expected to be stronger with shorter alkyl chains (thinner OML in Equation 2) with possible implications on electron transport through molecular tunnel barriers. Further work is required to investigate its dependence on the OML packing density.

Arrhenius plots of relaxation frequencies show that activation energies and pre-exponential factors strongly increase with applied dc voltage, $|V_{DC}|$. This "compensation law", which governs the relaxation frequencies for both dissipation mechanisms (Figure 6), reveals a strong coupling of end-group dipoles and gauche defects with the longitudinal acoustic mode (LAM-1, bending vibration) of the C_{12} alkyl chain. In the context of a multi-excitation entropy model, the isokinetic temperature T_F, related to the energy of elementary excitations of the bath (here the *n*-alkyl accordion-like vibration), is expected to decrease with increasing *n*-alkyl chain length.

Since entropic contributions in the cooperative backbone mobility of tethered molecular layers also appear in the friction dissipation processes (coupling between external shear and internal molecular modes of relaxation) [24], a comparative study of tribological and electrostatic compression responses might be fruitful.

This collective dynamic behavior of alkyl chains tethered to Si is also consistent with the asymmetric relaxation peak shapes related to many-body interactions in complex relaxing systems. In this study, peak shape analysis indicates better short-range order (along with weaker motional constraints) for gauche defects as compared with end-group dipoles.

Experimental

Covalent immobilization of mixed alkyl/acid OML

Covalent OML grafting was performed on hydrogen-terminated Si(111):H surfaces using linear alkene molecules with a UV-assisted liquid phase process [40,64]. A low-doped n-type Si (phosphorus doped, 1–10 Ω·cm resistivity, Siltronix) was chosen to obtain rectifying junctions. After etching, the Si(111):H surface was used immediately for covalent binding of the mixed *n*-dodecyl/undecanoic acid-terminated monolayer (denoted as Si/acid 5), using the photochemical reaction at 300 nm for 3 h of Si(111):H with a mixture of undecylenic acid/1-dodecene (molar ratio 5/95).

Admittance measurements

Admittance measurements were performed with a frequency response analyzer (Alpha-A High Resolution, Novocontrol Technologies). The sample holder was inserted in a two terminal active cell with the impedance converter mounted directly above the sample.

The junction was placed into a cryostat under dry nitrogen flow to avoid extensive water condensation and to minimize surface oxidation during electrical measurements [39,40]. An ohmic back contact was obtained by applying a silver paste electrode on the scratched Si rearside and a mercury top electrode (99.999% Fluka, contact area $S = 5 \times 10^{-3}$ cm^2) was used to avoid electrical shorts through possible pinholes in the OML. A solid Hg electrode is obtained in the low temperature range ($T < 233$ K) but no discontinuity is observed in the junction properties at this particular temperature.

The ac modulation amplitude V_{AC} was set at 20 mV. The capacitance (4.5 pF) of the empty Teflon cell in parallel with the molecular junction was subtracted to obtain C_m. At high frequencies, useful information on dipolar mechanisms is limited by the series resistance R_S (due to bulk Si and back contact resistance). Acquisition of dipolar relaxation data was performed in the reverse bias regime of the rectifying metal/OML/Si junction, with decreasing temperature steps and, at each temperature, the dc bias was scanned from the reverse regime ($V_{DC} = -2$ V) towards the forward regime ($V_{DC} = +1$ V).

The trans–gauche isomerization reactions are nearly reversible under our experimental conditions. To illustrate this point, the weak spectral changes observed upon return to room temperature (293 K) after the low temperature scan have been analyzed: peak B1 (respectively B2) is slightly shifted to higher frequency by a factor of 2.2 (respectively a factor of 2.8); while the peak strength ratio $\Delta\varepsilon(B2)/\Delta\varepsilon(B1)$ has increased by about 10% (at −0.6 V).

Acknowdedgements

Bruno Fabre (SCR, University of Rennes 1) is acknowledged for molecular grafting experiments. The author is also grateful to A.B. Fadjie-Djomkam and S. Ababou-Girard (IPR, University of Rennes 1) for their participation in the admittance measurements.

References

1. Schreiber, F. *Prog. Surf. Sci.* **2000,** *65,* 151–257. doi:10.1016/S0079-6816(00)00024-1
2. Unger, K. K., Ed. *Packings and stationary phases in chromatographic techniques;* Chromatographic Science Series, Vol. 47; Marcel Dekker: New York, 1990.
3. Badia, A.; Lennox, R. B.; Reven, L. *Acc. Chem. Res.* **2000,** *33,* 475–481. doi:10.1021/ar9702841
4. Vuillaume, D. *C. R. Phys.* **2008,** *9,* 78–94. doi:10.1016/j.crhy.2007.10.014
5. Vilan, A.; Yaffe, O.; Biller, A.; Salomon, A.; Kahn, A.; Cahen, D. *Adv. Mater.* **2010,** *22,* 140–159. doi:10.1002/adma.200901834
6. Ghosh, A. W. Electronics with molecules. In *Comprehensive Semiconductor Science and Technology;* Bhattacharya, P.; Fornari, R.; Kamimura, H., Eds.; Elsevier: Amsterdam, 2011; pp 383–479. doi:10.1016/B978-0-44-453153-7.00033-X
7. Salmeron, M.; Neubauer, G.; Folch, A.; Tomitori, M.; Ogletree, D. F.; Sautet, P. *Langmuir* **1993,** *9,* 3600–3611. doi:10.1021/la00036a041
8. Siepmann, J. I.; McDonald, I. R. *Phys. Rev. Lett.* **1993,** *70,* 453–456. doi:10.1103/PhysRevLett.70.453
9. Dürig, U.; Züger, O.; Michel, B.; Häussling, L.; Ringsdorf, H. *Phys. Rev. B* **1993,** *48,* 1711–1717. doi:10.1103/PhysRevB.48.1711
10. Tupper, K. J.; Brenner, D. W. *Langmuir* **1994,** *10,* 2335–2338. doi:10.1021/la00019a051
11. Du, Q.; Xiao, X.-d.; Charych, D.; Wolf, F.; Frantz, P.; Shen, Y. R.; Salmeron, M. *Phys. Rev. B* **1995,** *51,* 7456–7463. doi:10.1103/PhysRevB.51.7456
12. Chaudhury, M. K. *Curr. Opin. Colloid Interface Sci.* **1997,** *2,* 65–69. doi:10.1016/S1359-0294(97)80009-X
13. Lio, A.; Morant, C.; Ogletree, D. F.; Salmeron, M. *J. Phys. Chem. B* **1997,** *101,* 4767–4773. doi:10.1021/jp963807f
14. Burns, A. R.; Houston, J. E.; Carpick, R. W.; Michalske, T. A. *Phys. Rev. Lett.* **1999,** *82,* 1181–1184. doi:10.1103/PhysRevLett.82.1181
15. Tutein, A. B.; Stuart, S. J.; Harrison, J. A. *Langmuir* **2000,** *16,* 291–296. doi:10.1021/la991225u
16. Clear, S. C.; Nealey, P. F. *Langmuir* **2001,** *17,* 720–732. doi:10.1021/la000650g
17. Zhang, L.; Wesley, K.; Jiang, S. *Langmuir* **2001,** *17,* 6275–6281. doi:10.1021/la0106337
18. Chandross, M.; Grest, G. S.; Stevens, M. J. *Langmuir* **2002,** *18,* 8392–8399. doi:10.1021/la025598y
19. Berg, O.; Klenerman, D. *J. Am. Chem. Soc.* **2003,** *125,* 5493–5500. doi:10.1021/ja027128w
20. Martin, P.; Marsaudon, S.; Thomas, L.; Desbat, B.; Aimé, J.-P.; Bennetau, B. *Langmuir* **2005,** *21,* 6934–6943. doi:10.1021/la050288b
21. Devraprakasam, D.; Biswas, S. K. *Phys. Rev. B* **2005,** *72,* 125434. doi:10.1103/PhysRevB.72.125434
22. Mukhopadhyay, R.; Mitra, S.; Johnson, M.; Rajeev Kumar, V. R.; Pradeep, T. *Phys. Rev. B* **2007,** *75,* 075414. doi:10.1103/PhysRevB.75.075414
23. Subhalakshmi, K.; Devaprakasam, D.; Math, S.; Biswas, S. K. *Tribol. Lett.* **2008,** *32,* 1–11. doi:10.1007/s11249-008-9353-y
24. Knorr, D. B., Jr.; Widjaja, P.; Acton, O.; Overney, R. M. *J. Chem. Phys.* **2011,** *134,* 104502. doi:10.1063/1.3556668
25. Selzer, Y.; Salomon, A.; Cahen, D. *J. Phys. Chem. B* **2002,** *106,* 10432–10439. doi:10.1021/jp026324m
26. Seitz, O.; Böcking, T.; Salomon, A.; Gooding, J. J.; Cahen, D. *Langmuir* **2006,** *22,* 6915–6922. doi:10.1021/la060718d
27. Salomon, A.; Shpaisman, H.; Seitz, O.; Boecking, T.; Cahen, D. *J. Phys. Chem. C* **2008,** *112,* 3969–3974. doi:10.1021/jp710985b
28. Frederiksen, T.; Munuera, C.; Ocal, C.; Brandbyge, M.; Paulsson, M.; Sanchez-Portal, D.; Arnau, A. *ACS Nano* **2009,** *3,* 2073–2080. doi:10.1021/nn9000808
29. Pleutin, S.; Clément, N.; Guérin, D.; Vuillaume, D. *Phys. Rev. B* **2010,** *82,* 125436. doi:10.1103/PhysRevB.82.125436
30. Clement, N.; Pleutin, S.; Guerin, D.; Vuillaume, D. *Phys. Rev. B* **2010,** *82,* 035404. doi:10.1103/PhysRevB.82.035404
31. Shpaisman, H.; Seitz, O.; Yaffe, O.; Roodenko, K.; Scheres, L.; Zuilhof, H.; Chabal, Y. J.; Sueyoshi, T.; Kera, S.; Ueno, N.; Vilan, A.; Cahen, D. *Chem. Sci.* **2012,** *3,* 851–862. doi:10.1039/c1sc00639h
32. Fadjie-Djomkam, A. B.; Ababou-Girard, S.; Godet, C. *J. Appl. Phys.* **2012,** *112,* 113701. doi:10.1063/1.4767121
33. Linford, M. R.; Chidsey, C. E. D. *J. Am. Chem. Soc.* **1993,** *115,* 12631–12632. doi:10.1021/ja00079a071
34. Boukherroub, R. *Curr. Opin. Solid State Mater. Sci.* **2005,** *9,* 66–72. doi:10.1016/j.cossms.2006.03.006
35. Li, Y.; Calder, S.; Yaffe, O.; Cahen, D.; Haick, H.; Kronik, L.; Zuilhof, H. *Langmuir* **2012,** *28,* 9920–9929. doi:10.1021/la3010568
36. Kar, S.; Miramond, C.; Vuillaume, D. *Appl. Phys. Lett.* **2001,** *78,* 1288–1290. doi:10.1063/1.1351530
37. Faber, E. J.; de Smet, L. C. P. M.; Olthuis, W.; Zuilhof, H.; Sudhölter, E. J. R.; Bergveld, P.; van den Berg, A. *ChemPhysChem* **2005,** *6,* 2153–2166. doi:10.1002/cphc.200500120
38. Salomon, A.; Boecking, T.; Chan, C. K.; Amy, F.; Girshevitz, O.; Cahen, D.; Kahn, A. *Phys. Rev. Lett.* **2005,** *95,* 266807. doi:10.1103/PhysRevLett.95.266807
39. Fadjie-Djomkam, A. B.; Ababou-Girard, S.; Hiremath, R.; Herrier, C.; Fabre, B.; Solal, S.; Godet, C. *J. Appl. Phys.* **2011,** *110,* 083708. doi:10.1063/1.3651401
40. Godet, C.; Fadjie-Djomkam, A.-B.; Ababou-Girard, S.; Tricot, S.; Turban, P.; Li, Y.; Pujari, S. P.; Scheres, L.; Zuilhof, H.; Fabre, B. *J. Phys. Chem. C* **2014,** *118,* 6773–6787. doi:10.1021/jp411937t
41. Godet, C.; Fadjie-Djomkam, A.-B.; Ababou-Girard, S. *Solid-State Electron.* **2013,** *80,* 142–151. doi:10.1016/j.sse.2012.10.012
42. Jonscher, A. K. *Dielectric Relaxation in Solids;* Dielectric Press: London, 1983.
43. Jonscher, A. K. *J. Phys. D* **1999,** *32,* R57. doi:10.1088/0022-3727/32/14/201
44. Jonscher, A. K.; Jurlewicz, A.; Weron, K. *Contemp. Phys.* **2003,** *44,* 329–339.
45. Dissado, L. A.; Hill, R. M. *Nature* **1979,** *279,* 685–689. doi:10.1038/279685a0
46. Dissado, L. A.; Hill, R. M. *Proc. R. Soc. London, Ser. A* **1983,** *390,* 131–180. doi:10.1098/rspa.1983.0125
47. Yelon, A.; Movaghar, B.; Crandall, R. S. *Rep. Prog. Phys.* **2006,** *69,* 1145–1194. doi:10.1088/0034-4885/69/4/R04
48. Yelon, A.; Movaghar, B. *Phys. Rev. Lett.* **1990,** *65,* 618–620. doi:10.1103/PhysRevLett.65.618
49. Young, W. C.; Budynas, R. G. *Roark's formulas for stress and strain,* 7th ed.; McGraw-Hill: New York, 2002.
50. Barsoukov, E.; Macdonald, J. R. *Impedance Spectroscopy,* 2nd ed.; Wiley: Hoboken, NJ, 2005; p 188. doi:10.1002/0471716243
51. Usacheva, T. M.; Lifanova, N. V.; Zhuravlev, V. I.; Matveev, V. K. *Russ. J. Phys. Chem. A* **2010,** *84,* 1194–1201. doi:10.1134/S0036024410070198
52. Havriliak, S.; Negami, S. *J. Polym. Sci., Part C: Polym. Symp.* **1966,** *14,* 99–117. doi:10.1002/polc.5070140111

53. Havriliak, S.; Negami, S. *Polymer* **1967,** *8,* 161–210. doi:10.1016/0032-3861(67)90021-3
54. Badia, A.; Cuccia, L.; Demers, L.; Morin, F.; Lennox, R. B. *J. Am. Chem. Soc.* **1997,** *119,* 2682–2692. doi:10.1021/ja963571t
55. Snyder, R. G. *J. Chem. Soc., Faraday Trans.* **1992,** *88,* 1823–1833. doi:10.1039/ft9928801823
56. Cates, D. A.; Strauss, H. L.; Snyder, R. G. *J. Phys. Chem.* **1994,** *98,* 4482–4488. doi:10.1021/j100067a041
57. Snyder, R. G. *J. Chem. Phys.* **1982,** *76,* 3921–3927. doi:10.1063/1.443508
58. Luedtke, W. D.; Landman, U. *J. Phys. Chem. B* **1998,** *102,* 6566–6572. doi:10.1021/jp981745i
59. Singh, S.; Wegmann, J.; Albert, K.; Müller, K. *J. Phys. Chem. B* **2002,** *106,* 878–888. doi:10.1021/jp012979w
60. Lin-Vien, D.; Colthup, N. B.; Fateley, W. G.; Grasselli, J. G. *Handbook of Infrared and Raman Characteristic Frequencies of Organic Molecules;* Academic Press: New York, 1991; p 16.
61. Brambilla, L.; Zerbi, G. *Macromolecules* **2005,** *38,* 3327–3333. doi:10.1021/ma047390k
62. Levin, C. S.; Janesko, B. G.; Bardhan, R.; Scuseria, G. E.; Hartgerink, J. D.; Halas, N. J. *Nano Lett.* **2006,** *6,* 2617–2621. doi:10.1021/nl062283k
63. Klatte, S. J.; Beck, T. L. *J. Phys. Chem.* **1993,** *97,* 5727–5734. doi:10.1021/j100123a044
64. Cordier, S.; Fabre, B.; Molard, Y.; Fadjie-Djomkam, A.-B.; Tournerie, N.; Ledevna, A.; Naumov, N. G.; Moreac, A.; Turban, P.; Tricot, S.; Ababou-Girard, S.; Godet, C. *J. Phys. Chem. C* **2010,** *114,* 18622–18633. doi:10.1021/jp1071007

License and Terms

BEILSTEIN JOURNAL OF NANOTECHNOLOGY

Self-assembled anchor layers/polysaccharide coatings on titanium surfaces: a study of functionalization and stability

Ognen Pop-Georgievski[*,‡1], Dana Kubies[‡1], Josef Zemek[2], Neda Neykova[2,3], Roman Demianchuk[1], Eliška Mázl Chánová[1], Miroslav Šlouf[1], Milan Houska[1] and František Rypáček[1]

Full Research Paper

Open Access

Address:
[1]Institute of Macromolecular Chemistry, Academy of Sciences of the Czech Republic, Heyrovsky sq. 2, 16206 Prague 6, Czech Republic, [2]Institute of Physics, Academy of Sciences of the Czech Republic, Cukrovarnicka 10, 16253 Prague 6, Czech Republic and [3]Czech Technical University in Prague, Faculty of Nuclear Sciences and Physical Engineering, Trojanova 13, 12000 Prague 2, Czech Republic

Email:
Ognen Pop-Georgievski[*] - georgievski@imc.cas.cz

* Corresponding author ‡ Equal contributors

Keywords:
alginate; biomimetic surfaces; bisphosphonates; neridronate; poly(dopamine); spectroscopic ellipsometry; surface characterization; surface modification; titanium; XPS

Beilstein J. Nanotechnol. **2015,** *6,* 617–631.
doi:10.3762/bjnano.6.63

Received: 31 July 2014
Accepted: 05 February 2015
Published: 02 March 2015

This article is part of the Thematic Series "Self-assembly of nanostructures and nanomaterials".

Guest Editor: I. Berbezier

Abstract

Composite materials based on a titanium support and a thin, alginate hydrogel could be used in bone tissue engineering as a scaffold material that provides biologically active molecules. The main objective of this contribution is to characterize the activation and the functionalization of titanium surfaces by the covalent immobilization of anchoring layers of self-assembled bisphosphonate neridronate monolayers and polymer films of 3-aminopropyltriethoxysilane and biomimetic poly(dopamine). These were further used to bind a bio-functional alginate coating. The success of the titanium surface activation, anchoring layer formation and alginate immobilization, as well as the stability upon immersion under physiological-like conditions, are demonstrated by different surface sensitive techniques such as spectroscopic ellipsometry, infrared reflection–absorption spectroscopy and X-ray photoelectron spectroscopy. The changes in morphology and the established continuity of the layers are examined by scanning electron microscopy, surface profilometry and atomic force microscopy. The changes in hydrophilicity after each modification step are further examined by contact angle goniometry.

Introduction

Titanium and titanium alloys are widely used in medicine and dentistry to replace and support hard tissues [1]. The absence of toxic alloying metals [1], extraordinary specific strength, appropriate Young's modulus, outstanding biocompatibility and excellent corrosion resistance make commercially pure titanium a highly favored, biocompatible, metallic material [2].

The biocompatibility and corrosion resistance of titanium surfaces is closely related to the presence of a spontaneously formed 3–6 nm thick layer of titanium oxides, mostly in the form of titanium(IV) oxide (TiO_2). The outermost surface of the oxide is covered with a 2.8–9.5 Å thick hydroxy group layer [3], which determines the reactivity of titanium surfaces [4] and sets their isoelectric point in the range of 3.5–6.2 [5-7].

Different surface modifications have been proposed to take the advantage of the titanium surface properties and to promote beneficial interactions at tissue–titanium implant interfaces. Established techniques use modifications of the titanium surface morphology and variations in the inorganic surface chemistry [8]. Procedures based on electrostatically driven adsorption [9-11], covalent coupling [12], electrochemical surface modifications [13], self-organized organic layers [14,15], etc. have been extensively studied for the immobilization of biologically active molecules [16] on titanium surfaces. Bio-related titanium surface modifications based on polysaccharides and synthetic polymers have been performed by physisorption and electrostatic interactions. In comparison with polylactide coatings, physisorbed alginate coatings are capable of exhibiting pronounced cell adhesion [17]. Chitosan/alginate, multilayered, 3D networks prepared by the layer-by-layer method enabled encapsulation of bone marrow stromal cells on the surface of dental or joint implants [18]. Polyelectrolyte (chitosan, poly(L-glutamic acid), and poly-L-lysine) coatings increased the surface ionic nature and wettability of the surface, yielding enhanced osteoblast differentiation [19].

The success of these modifications is highly dependent on the chemical state, reactivity and surface concentration of the hydroxy groups, as well as the presence of contaminants [12]. Therefore, one of the main objectives of this contribution is to perform and precisely characterize the activation of commercially pure titanium substrates for the realization of reactive titanium surfaces without contaminants. Such activated surfaces can be further functionalized by the covalent immobilization of self-assembled anchoring layers of different organic compounds, providing functional groups for further modification. Covalent bonding, which provides a stable fixation of immobilized compounds, is an alternative approach to coatings based on adsorption processes. The most common strategies for the formation of anchoring layers are thiol-based self-assembled monolayers (SAMs) [20] and silanes [21,22]. Despite the ease of preparation and high uniformity of the resulting layers, the thiol–SAMs provide an anchoring chemistry scheme limited only to noble metals. Furthermore, the established thiol bond is prone to oxidation and can be displaced from the surface [23,24]. Alkoxy- and chloro-silanes are widely used for the modification of different surface oxides. The mechanism of the layer formation includes replacement of a silane group by the transfer of a proton from the activated surface hydroxy group. This leads to the elimination of alcohol or hydrochloric acid, depending on whether alkoxysilane or chlorosilane, respectively, is used. In most cases the alkoxysilane treatment results in a 3D polymer network and extra precaution needs to be taken for the creation of a monolayer [22,25]. Surface treatments using 3-aminopropyltriethoxysilane (APTES) can result in several surface structures such as covalent attachment, self-assembly, multilayer formation by surface-initiated (SI) polymerization and particle adsorption [22]. The obstacles and limitations inherent to thiol–SAMs and silanes can be circumvented by the use of moieties bearing phosphonate [14,26,27] and bisphosphonate (BP) [28,29] groups. Upon hydrolysis, these form strong mono- and bi-dentate coordination bonds with metal surfaces [30]. Inspired by the composition of mussel adhesive proteins, Messersmith et al. [31] proposed the formation of poly(dopamine) (PDA) confluent films as a substrate-independent modification approach. The ability of PDA to adhere to solid surfaces stems from the reactivity of ortho-quinone/catechol moieties that form coordination bonds with surface metal oxides and covalent bonds with nucleophilic groups. In addition to this, the different PDA units can establish a wide range of non-covalent bonds through π stacking, hydrogen bonding, and van der Waals- and hydrophobic-interactions. PDA films have been used as the anchor layers of non-fouling polymer brushes [32-34], substrates for cell adhesion [35,36] and as platforms for controlled cell adhesion [37]. The presence of amine groups in PDA has been used for functionalization with moieties for photo-induced grafting reactions [38,39].

In this work, we study the immobilization of three compounds to the titanium surface: bisphosphonate neridronate, APTES and PDA. The neridronate covalent coupling leads to immobilization of the particular self-assembled molecules, whereas the immobilization of APTES or dopamine monomers results in the formation of partially or fully polymerized layers of APTES siloxane or PDA, respectively. The reactive amino end groups present in these anchor layers can be further utilized for the covalent bonding of a biofunctional coating of compounds bearing negatively charged functional groups. To this end, an anionic polysaccharide alginate extracted from the cell walls of brown algae (Phaeophyceae) was chosen as a model natural polymer, which satisfies the set prerequisites. This polysaccharide is biocompatible and degradable under normal physiological conditions [40] and has been used in various biomedical applications [41,42]. The presence of carboxyl groups in the structure of β-D-mannuronate and α-L-guluronate monomer units can be utilized for the immobilization of the polysaccharide chains to the anchor layer amine groups through the creation of amide bonds.

The success of the performed modifications and their short-term stability in a phosphate buffer at 37 °C was probed by different surface sensitive techniques such as X-ray photoelectron spectroscopy (XPS), spectroscopic ellipsometry (SE) and infrared reflection–absorption spectroscopy (IRRAS). The changes in topography and the established continuity of the layers were revealed by scanning electron microscopy (SEM), stylus profilometry (SP) and atomic force microscopy (AFM). The changes in hydrophilicity after each modification and immersion step are further examined by contact angle goniometry.

Results and Discussion

Surface analysis of activated titanium surfaces

The surface concentration of elements present on pristine, activated and flat titanium surfaces, as determined by XPS, is summarized in Table 1. Considerable amounts of aluminum and silicon were observed on the pristine surfaces, most likely from the polishing pastes used by the producer. In order to produce a consistent and reproducible titanium oxide surface layer, four different chemical treatments were tested in both alkaline (using alkaline piranha or 0.5 M NaOH) and acidic conditions (using mixtures of H_2SO_4/HCl or H_2SO_4/H_2O_2). The chemical treatments were followed by 5 min oxygen plasma treatments. The tested activation procedures significantly decreased the concentration of inorganic contaminants and caused a beneficial increase in the surface concentration of titanium and oxygen. The surfaces were free of inorganic contaminants when alkaline piranha ($NH_4OH:H_2O_2:H_2O$) was used for the cleaning and activation process. However, despite the rigorous chemical and oxygen plasma treatments, as well as the precautions taken during the sample preparation, it was not possible to completely avoid hydrocarbon contamination. We presume that the hydrocarbon contamination takes place mainly during the transfer of the freshly oxidized titanium samples from the plasma reactor to the desiccator. Irrespective of the surface treatment, the high resolution C 1s spectra centered at 285.0 eV lacked the expected titanium carbide contribution at 281.6 eV. Furthermore, the surfaces were free of metallic titanium (peak at 454.1 eV). Similar to the observations on rough [19] and ultra-flat titanium surfaces performed by template striping [43], our high resolution titanium 2p spectra in the region of 450–468 eV showed the characteristic Ti 2p spin-split doublet structure, with a separation of approximately 6 eV between the Ti $2p_{1/2}$ and Ti $2p_{3/2}$ peaks (Figure 1). The binding energies of the contributions within the Ti $2p_{3/2}$ envelope were found at 458.9 ± 0.1 and 457.4 ± 0.1 eV and were assigned to TiO_2 and Ti_2O_3, respectively. The activation treatments increased the TiO_2 concentration from 80% for the pristine surfaces to more than 97% for the activated titanium surfaces.

Figure 1 also reports the high resolution oxygen 1s XPS spectra of the studied titanium surfaces. The O 1s envelope could be resolved into surface oxide contributions at 530.3 ± 0.1 eV, 531.5 ± 0.1 eV and 533.0 ± 0.3 eV arising from titanium oxides (TiO_2 and Ti_2O_3), Al_2O_3 and SiO_2, respectively. The presence of hydroxy groups on the surface was evidenced by the presence of the peak at 531.8 ± 0.2 eV. The performed activation treatments increased the contribution of the hydroxy from the observed 2% for the pristine surfaces to more than 6% for the activated titanium surfaces (Supporting Information File 1, Table S1). This was evidenced by the change in the ratio between surface hydroxy and oxide from 0.04 for the untreated titanium surfaces to values in the range 0.1–0.2 for the activated ones. The careful analysis of the obtained high resolution O 1s spectra enabled the estimation of the concentration of hydroxy groups on the titanium surfaces according the method proposed by McCafferty and Wightman [3]. The performed activation treatments increased the surface density of the hydroxy groups from the initial 2–4 hydroxy groups per nm^2 on the pristine titanium surfaces to 4–14 hydroxy groups per nm^2. These values are consistent with the range of values of 5–15 hydroxy groups per nm^2 reported for titanium foils [3] and titanium dioxide powders [44]. The observed concomitant increase in concentration of surface hydroxy groups and decrease in the presence of surface contaminants inevitably leads to higher re-

Table 1: Influence of the surface treatments on the surface concentration of elements present on pristine, activated and flat titanium surfaces, as determined by XPS. The ratio between the surface oxides and hydroxides determined from the analysis of the high resolution O 1s spectra is also reported.

Treatment	Ti	O	C (atom %)	Al	Si	MtOH/Oxide
Pristine	7.9	50.3	28.8	7.3	5.7	0.04
$NH_4OH:H_2O_2:H_2O$	18.0	59.0	23.0	–	–	0.2
NaOH	17.0	58.4	21.5	3.1	–	0.1
HCl/H_2SO_4	17.8	58.6	19.3	4.4	–	0.1
H_2SO_4/H_2O_2	18.0	55.5	24.6	–	1.9	0.2
Flat surface	19.5	56.7	23.8	–	–	0.2

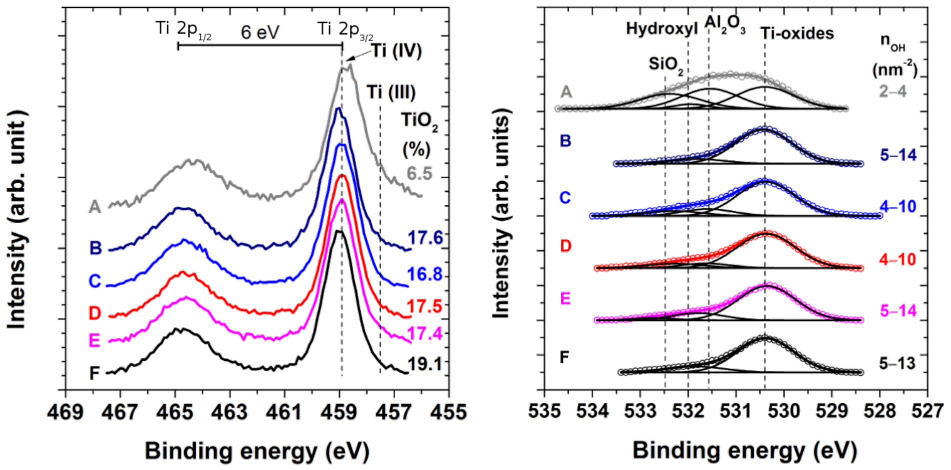

Figure 1: High resolution Ti 2p (left) and O 1s (right) XPS spectra of pristine titanium surfaces (A) and surfaces treated using alkaline piranha (B), 0.5 M NaOH (C), a HCl/H_2SO_4 mixture (D) and piranha solution (H_2SO_4/H_2O_2) (E). The spectrum of flat titanium surfaces deposited on silicon substrates (F) is given for comparison. The dominant contribution (more than 96.7%) within the Ti $2p_{3/2}$ envelope appears at 458.9 ± 0.1 eV and is identified as TiO_2. The measured O 1s spectra (points) was fitted (solid, colored lines) by resolving the individual surface oxide contributions (black lines) centered at 530.3 ± 0.1, 531.5 ± 0.1 and 533.0 ± 0.3 eV arising from titanium oxides (TiO_2 and Ti_2O_3), Al_2O_3 and SiO_2, respectively. The hydroxy groups on the surface gave rise to the peak at 531.8 ± 0.2 eV. The figure also reports the surface density of hydroxy groups (n_{OH}).

activity of the treated surfaces [4,44]. In addition to an increase in the number of surface sites available for binding, SEM (Supporting Information File 1, Figure S1) and stylus profilometry (Supporting Information File 1, Table S2) analysis showed an increased microscale texture for all treated surfaces (alkaline piranha, 0.5 M NaOH, and piranha (H_2SO_4/H_2O_2)) except for those treated with a H_2SO_4/HCl solution. Microscale texturing similar to that reported here has been obtained by treatments such as machining [45,46], anodic oxidation [45,46] and chemical oxidation using piranha [12]. The increase in the surface roughness and the creation of a specific microscale texture due to oxidative treatments as observed in our study have been shown to enhance the rate of bone formation [12,45,46].

The decreased organic contamination and increased surface density of hydroxy groups on the activated surfaces is further evidenced by the higher hydrophilicity of the treated surfaces (Supporting Information File 1, Table S2). The activation treatments decrease the measured advancing water contact angles from about 50° for the pristine titanium surfaces to values lower than 30°. Almost completely wettable surfaces were obtained when alkaline piranha was used as the surface activation treatment.

It is worth mentioning that the chemical activation using alkaline piranha simultaneously led to augmentation of the surface composition, surface reactivity, topography and hydrophilicity. Therefore, this chemical activation treatment is a potentially valuable step in the treatment of titanium surfaces and possible implants based on this material. Importantly, the evaporation-deposited, flat, titanium reference samples (R_{RMS} < 1.0 nm) have the same surface composition and surface density of hydroxy groups (Table 1 and Figure 1) as the activated pure titanium surfaces. Therefore, it is reasonable to consider the flat surfaces as a representative reference surface of the activated pristine titanium for the verification of the surface modifications based on thin anchor layers and on the alginate monolayer. The absence of surface irregularities on these mirror-like substrates enables techniques such as SE, IRRAS and AFM to be used for the characterization of sub- and mono-molecular, organic overlayers.

Anchor layer deposition

The reproducibility in terms of continuity, uniformity, reactivity and adhesion properties of the anchor layers is a prerequisite for the creation of grafted adlayers with defined properties [34]. The attachment of the anchor layers of three FDA approved, organic compounds (neridronate, APTES and dopamine) were performed on oxygen plasma-activated, flat titanium substrates. As previously observed by XPS, the exposure of titanium and titanium oxide surfaces to air resulted in a thin adherent layer of organic contaminants. The presence of such an organic contaminant layer influences the optical dispersion function of the titanium films. These ill-defined optical parameters of the titanium substrates decrease the precision of the ellipsometric data analysis during subsequent surface modifications. A practical way to circumvent this problem is to perform the SE measurements in different solvents (ethanol, isobutanol, toluene), a method referred as the multiple-environment method. Due to the refractive index matching between the solvents and the adsorbed organic contaminants, and the possible dissolution of the contaminants, the multiple-environment method revealed the intrinsic optical dispersion function of the flat titanium surfaces. The measured data of a neat titanium layer in different solvents was simultaneously fitted with the parameters of a Drude–Lorentz and two Lorentz oscillator functions as discussed in Supporting Information File 1, Figure S2.

The SE analysis showed formation of a 0.9 ± 0.3 nm thick monolayer of neridronate. The concomitant processes of the self-assembly of dopamine and its intermediates (dopamine-quinone, 5,6-dihydroxyindole, etc.), of SI polymerization and of adsorption of the resulting polymer molecules resulted in a 15.2 ± 0.5 nm thick confluent PDA layer. Despite the precautions taken during the APTES deposition for the formation of the SAM [21] (freshly distilled reagents, dry titanium substrates and elevated temperature during the capping reaction), a 12.4 ± 1.7 nm thick APTES siloxane polymer multilayer was formed [21]. The presence of the anchor layers increased the water contact angles of completely wettable flat titanium surfaces (oxygen plasma treated) to 40 ± 1°, 72 ± 1° and 60 ± 5° for the substrates containing neridronate, APTES and PDA, respectively. Here, the lower hydrophilicity is caused by the presence of organic molecules with increased hydrophobicity in comparison to the neat titanium surface.

The surface immobilization of these organic moieties and their covalent structure was further verified by independent IRRAS and XPS measurements. The IR spectra of the resulting anchor layers showed the characteristic in-plane bending modes, $\delta_{\text{in-plane}}$(NH), of free and H-bonded amino groups in the region 1600–1650 cm^{-1}. The covalent immobilization of the BP molecules is verified by the significant changes in the IRRAS spectra (Figure 2A) of the original sodium neridronate powder and the neridronate self-assembled monolayer on the titanium surface. Similarly to the observations on different free phosphonic acids in aqueous solution [47,48] and phosphonic acids adsorbed on bentonite [49], the 2000–800 cm^{-1} region in our IR spectrum of sodium neridronate powder was characterized by different stretching (ν) and bending (δ) modes of P=O, P–O(H) and P–O– units of sodium phosphonate and free phosphonic acid. The initially observed spectrum of the sodium neridronate powder significantly changed upon tethering of the molecules to the titanium surface. The neridronate monolayer immobilized to the titanium surface gives rise to the asymmetric and symmetric ν_{as} P–OTi of $R(PO_3)$, ν_s P–OTi of $R(PO_3)$, ν_s P–O, ν_s P–O of $R(PO_3{}^{2-})$, ν_{as} P–OH of $R(HPO_3{}^{2-})$ modes at 1121, 1038, 996, 978 and 960 cm^{-1}, respectively. The observed absence and/or reduced intensity of the strong bands of ν_{as} (P–O) and ν_s (P–O) of $P(OH)_2$ in the region below 960 cm^{-1} indicates that the neridronate molecules are covalently bound to the titanium surface by forming not only monodentate, but also bidentate complexes.

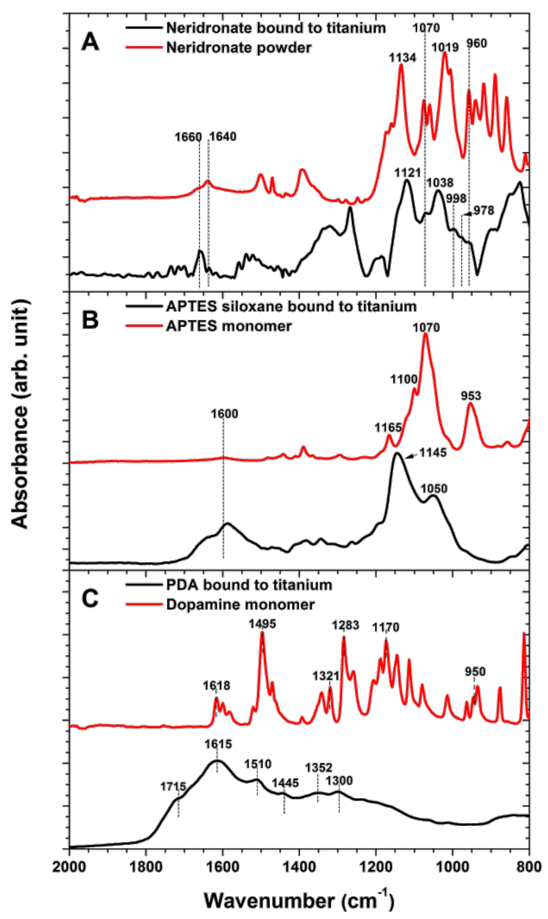

Figure 2: FTIR spectra of starting neridronate (A), APTES (B) and dopamine (C) organic moieties in their native state (red) and corresponding immobilized films on activated flat titanium surfaces (black). The spectra of the immobilized films were taken in IRRAS mode against backgrounds of bare titanium.

The IR spectrum of the liquid APTES monomer is characterized by the ν(Si–O–C) stretching modes at 1165, 1100, 1070 and 953 cm^{-1} (Figure 2B). The formation of the 12.4 ± 1.7 nm thick adherent polymer layer of APTES siloxane was further evidenced by the IRRAS measurements. The dominant vibrations of the APTES films were observed at 1145 and 1050 cm^{-1}. These contributions were assigned to the ν(Si–O–Si) stretching modes. As initially described by Kurth and Bein [21], the presence of these vibrations verify not only the immobilization of the APTES molecules to the surface, but also proves the presence of the siloxane polymer network. The network is formed by SI polymerization from non-hydrolyzed ethoxy groups (which can give rise to silanol groups) and free silanols that did not undergo a dehydration condensation reaction with surface hydroxy groups. Both possible mechanisms are accompanied by adsorption and further condensation between the surface reactive species and APTES siloxane aggregates formed in the reactive solution. The presence of ethoxy groups, resulting in an incomplete cross-linking of the APTES siloxane polymer network, can be seen by the significant broadening of the dominate IR contributions toward the initially observed main peaks of APTES "monomer". This may be a source of the hydrolytical layer instability. In a water environment, the primary amines present in the network can intra- or inter- molecularly coordinate to a silicon center and catalyze the hydrolysis reaction.

The spectrum of a solid dopamine monomer (Figure 2C) is characterized by skeletal vibration modes of aromatic double bonds (1650–1400 cm^{-1}), stretching ν(C–O) modes of the catechol moieties at 1283 cm^{-1}, in-plane bending $\delta_{\text{in-plane}}$(C–H) at 1170 cm^{-1} and stretching modes ν(C–C–N) of the aminoethyl chain at 935 cm^{-1} [50]. The oxidative polymerization of dopamine and the surface attachment of different monomer units (dopamine-quinone, 5,6-dihydroxyindole, etc.) caused evident changes in the IR spectra (Figure 2C) and resulted in a confluent layer of PDA [32-34,51]. Similar to previous studies on PDA modified materials [32-34,52], the spectrum of PDA immobilized onto titanium substrates is characterized by poorly resolved bands of many overlapping vibration modes of the different monomer units. The most prominent contributions at 1615, 1510, 1445 cm^{-1} originate from the C=C vibrations of the different monomer units, whereas the shoulder at 1715 cm^{-1} indicates the presence of quinone groups. The shift in frequency, the broadening of the initial contributions, as well as the appearance of new bands with respect to the IR spectra of dopamine, proves not only the polymer nature of the resulting films, but also their complex highly conjugated covalent structure.

The complementary XPS measurements further verified the successful formation of surface adherent films and their covalent structure. The determined elemental compositions of the neridronate, APTES siloxane and PDA anchor layers is reported in Table 2. The covalent tethering of the organic moieties caused an increase in the contributions of carbon and was associated with the significant decrease in the surface concentration of titanium. In the case of the thick polymer anchor films of APTES and PDA, the contributions arising from the titanium substrate were negligible. Importantly, the XPS spectra verified the presence of nitrogen on the surface of different anchor layers. Moreover, the obtained relative ratios N/P = 0.57 for the neridronate and N/Si = 0.65 for APTES siloxane are reasonably close to the expected values of 0.5 and 1, respectively. Figure 3 reports the high resolution carbon 1s XPS spectra for the neridronate, APTES siloxane and PDA adherent films immobilized on the flat titanium surfaces. The C 1s envelope of the anchor layers could be resolved into contributions centered at 285 ± 0.1 eV arising from sp^3 carbon (C–C and C–H functionalities), at 285.9 ± 0.1 eV arising from the C–N species of amines and at 286.6 ± 0.2 eV arising from the C–O contribution of hydroxy groups present in neridronate, the non-hydrolyzed ethoxy groups of APTES and catechols of poly(dopamine). The spectrum of APTES has an additional contribution at 284.3 ± 0.2 eV from the C–Si functionality. The PDA shows contributions at 284.5 ± 0.1, 288.0 ± 0.2, 289.3 ± 0.3 and 291.2 ± 0.2 eV arising from the carbon species of sp^2 carbon (C=C functionality), the C=O functionality of the quinons, the carboxylic carbon functionality (O–C=O groups) and the π–π* transition (shake-up), respectively [53,54]. A rather unexpected peak at 288.4 ± 0.1 eV was observed in the high resolution C 1s spectra of neridronate and APTES siloxane. Although with a large uncertainty, Acres et al. have tentatively assigned this peak to the C–C=O functionality [55]. A similar contribution was observed for micro-plasma polymerized APTES layers [56] and was attributed to amide contribution. Since our immobilization protocols lack harsh plasma deposition treatments, we tentatively attribute this functionality to carbamate-like structures, which form due to the scrubbing effect of amines on CO$_2$ from air [57].

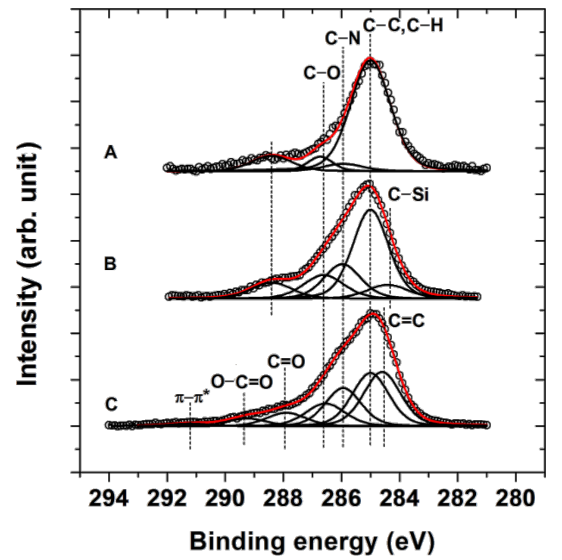

Figure 3: High resolution C 1s XPS spectra of neridronate (A), APTES siloxane (B) and PDA (C) films on the surfaces of activated flat titanium substrates (black). The unfilled circles represent the measured data, while the red lines represent the fitted data. The individual contributions to the fitted data of different functional groups present in the films are represented with black lines.

The topography and homogeneity of the resulting anchor layers on titanium substrates was monitored via AFM. The corresponding images are presented in Figure 4. The AFM data clearly evidence the functionalization of the flat titanium surfaces with confluent anchor layers free of pinholes. The self-assembly of neridronate molecules resulted in a fine-grained

Table 2: Elemental compositions of anchor layers (neridronate, APTES siloxane and PDA) and ALG layers tethered to these surfaces, as determined by XPS.

Modification	Ti	O	C	N	P	Si
			(atom %)			
Neat, flat titanium surface	19.5	56.7	23.8	–	–	–
Neridronate	13.8	55.6	25.9	1.7	3.0	–
APTES siloxane	–	27.1	54.6	7.2	–	11.1
PDA	0.4	22.1	70.7	6.8	–	–
ALG/neridronate	1.8	22.2	70.1	5.8	–	–
ALG/APTES siloxane	0.6	27.9	60.5	6.3	–	4.7
ALG/PDA	–	30.7	61.9	7.4	–	–

topography similar to the activated titanium surface (Figure 4A and Figure 4B). The processes of self-assembly, SI polymerization and adsorption of aggregates from the reactive solution during adsorption and formation of the APTES siloxane and PDA layers led to surfaces with an increased roughness of 1.1 ± 0.2 nm and 3.6 ± 1.2 nm, respectively (Figure 4C and Figure 4D). The immobilized polymer surfaces exhibited a more pronounced grain structure with nanoparticles having average diameter of 12 nm for the APTES siloxane and of 38 nm for PDA anchor layers. While such a pronounced surface topography is considered to be an inherent characteristic of the PDA films [34,53], the presence of such surface objects on APTES layers is rarely discussed. However, even in the case when a APTES SAM was achieved [58], the presence of surface adherent objects resembling aggregates having average diameter of up 30 nm was inevitable. We presume that the observed APTES siloxane aggregates are formed in the reactive solution and further adsorbed and even grafted onto the surface.

Covalent binding of alginate

The tethering of alginate (ALG) chains by reaction of the carboxyl groups to the amine-functionalized titanium surfaces was performed by following standard EDC/NHS protocols. The binding reaction resulted in the formation of 5.0 ± 1.9 nm thick alginate films, irrespective of the anchor layer. The grafting density, calculated from the ellipsometric thickness and the molecular weight of ALG (1.5×10^6 g·mol^{-1}), was $1.3–3.0 \times 10^{11}$ chains/cm^2. The presence of the polysaccharide chains was obvious from the significant increase in the surface hydrophilicity. The immobilization of hydrophilic alginate chains resulted in a decrease in the contact angles from the values determined for the anchor layers to 13 ± 3°, 19 ± 3° and 13 ± 1° for the alginate films bound to neridronate, APTES and PDA, respectively.

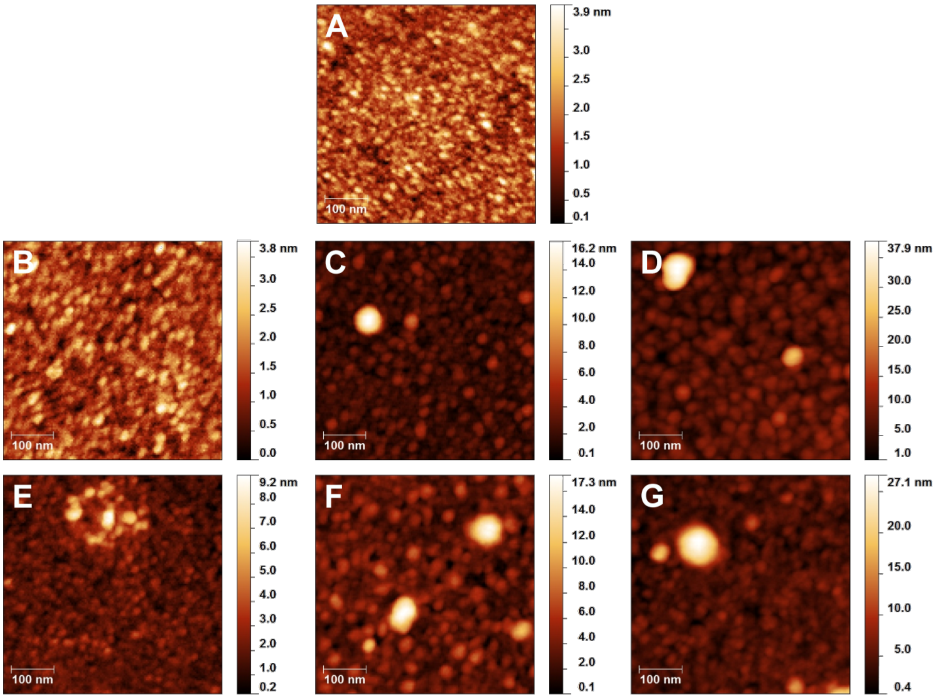

Figure 4: AFM images of the neat, flat titanium surface (R_{RMS} = 0.5 ± 0.3 nm) (A), and confluent anchor layers of neridronate (R_{RMS} = 0.5 ± 0.2 nm) (B), APTES (R_{RMS} = 1.1 ± 0.2 nm) (C) and PDA (R_{RMS} = 3.6 ± 1.2 nm) (D). The figure also reports AFM images of ALG layers grafted onto neridronate (R_{RMS} = 0.7 ± 0.3 nm) (E), APTES (R_{RMS} = 1.8 ± 0.2 nm) (F) and PDA (R_{RMS} = 2.9 ± 1.0 nm) (G) anchor layers. The AFM measurements on the ALG surfaces were performed on predominantly flat regions with R_{RMS} values similar to those of the initial anchor layers.

The covalent tethering of the polysaccharide chains and the formation of amide bonds between the activated carboxyl groups of ALG and the amines present in the anchor layer were probed by IRRAS measurements. A representative IR spectrum of free alginate deposited on the flat titanium surface is presented in Figure 5. The spectrum is dominated by the symmetric ν_{sym} (C=O) and asymmetric ν_{asym} (C=O) modes of charged carboxyl groups at 1630 and 1420 cm^{-1}, respectively, in addition to the stretching ν(C–O) modes of the pyranosyl ring, β-(1-4)-glycosidic bonds and hydroxy groups of the polysaccharide in the 1200–1000 cm^{-1} region. The established covalent bonds between the carboxyl groups of the alginate chains and the amines present on the surface are evidenced by the appearance of the highly specific amide I and amide II bands at 1650 and 1540 cm^{-1}, respectively (Figure 5). Additionally, the differential spectra of ALG bound to neridronate and PDA show the carbonyl band (1730 cm^{-1}) and the bands characteristic for the polysaccharide moieties (1200–1000 cm^{-1}). In the same region, the differential spectrum of ALG bound to the siloxane anchor layer is characterized by a valley at 1580 cm^{-1} arising from decreased in-plane bending $\delta_{in\text{-}plane}$(NH) of amine contributions and at 1145 and 1037 cm^{-1} from decreased ν(Si–O–Si) stretching contributions. The appearance of these bands is associated with the amine-catalyzed hydrolysis of the siloxane bonds of the polymer network [22] during the 24 h immersion in MES buffer.

The IRRAS results of the immobilization of ALG to the anchor layers are further supported by XPS measurements. The formation of the 5 nm thick polysaccharide layer on the surfaces with different anchors serves to further decrease the contributions from the titanium substrate. This corresponds to a concomitant increase in the presence of the elements from the organic moieties (Table 2). Compared to the high resolution C 1s spectra of the anchor layers (Figure 3), the spectra of the bound alginate films (Figure 6) show increased contributions at 286.5 ± 0.1 eV arising from the C–O moiety of the pyranosyl ring, β-(1-4)-glycosidic bonds and hydroxy groups of the polysaccharide in addition to a peak at 289.2 ± 0.1 eV arising from the O–C=O functionality of carboxylic groups. Importantly, the presence of the peak at 288.1 ± 0.2 eV verifies the formation of amide bonds (N–C=O) between the activated carboxyl groups of ALG and the amines present in the anchor layers. Thus, the XPS studies strongly prove the covalent immobilization of the alginate films.

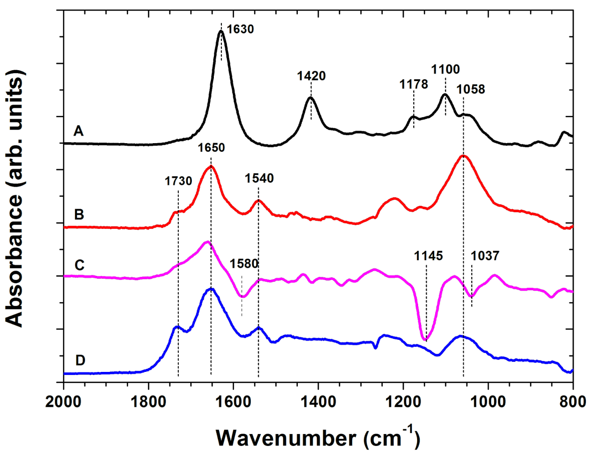

Figure 5: Differential IRRAS spectra of free alginate adsorbed onto a flat titanium surface (A) and covalently bound alginate molecules to the amines of the neridronate (B), APTES (C) and PDA (D) anchor layers. The IRRAS spectra of covalently bound alginate films was characterized by the presence of the carbonyl band (1730 cm^{-1}), amide I (1650 cm^{-1}), amide II band (1540 cm^{-1}) and ν(C–O) stretching modes of the pyranosyl ring, β-(1-4)-glycosidic bonds and hydroxy groups of the polysaccharide (1200–1000 cm^{-1}). The spectra were referenced to corresponding background spectra of bare titanium and titanium bearing different anchor layers.

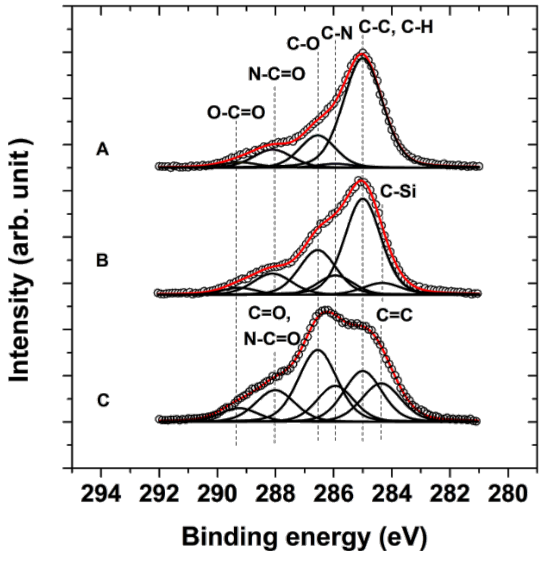

Figure 6: High resolution C 1s XPS spectra of alginate coatings on neridronate (A), APTES siloxane (B) and PDA (C) anchoring layers. The unfilled circles represent the measured data, while the red lines represent the fitted data. The individual contributions to the fitted data of different functional groups present in the films are represented with black lines.

The tethering of ALG resulted in surfaces with a predominantly flat topography (Figure 4E–G) similar to those observed for the corresponding anchor layers (Figure 4B–D). The ALG films on neridronate, APTES siloxane and PDA were characterized by R_{RMS} values of 0.7 ± 0.3 nm, 1.8 ± 0.2 nm and 2.9 ± 1.0 nm, respectively. The increase in the ellipsometric thickness of 5 nm combined with the AFM findings of the surface roughness (similar to the values characteristic for the anchor layers) indicates the formation of continuous ALG films, which merely replicate the surface underneath. However, although only occasionally observed, the AFM measurement also showed the presence of regions of surface-immobilized ALG aggregates composed of particles with an average diameter exceeding 40 nm (Supporting Information File 1, Figure S3). The observed nanoparticle aggregates may have a physisorbed fraction of loosely bound ALG chains that are a potential source of instability and defects when these surfaces are exposed to physiological conditions.

Stability of alginate films

The stability of the anchor layers and anchored ALG films is crucial for their performance especially when biomedical and tissue engineering applications are in question. The deterioration of these surface confluent layers could affect the surface concentration of free carboxylic end groups that are essential in the envisaged applications. Furthermore, the instability of the layers that are in intimate contact with the titanium surface could result in complete delamination of the potentially surface adherent alginate gels.

The stability tests of the neat, anchor layers and the ALG/anchor layers on flat titanium substrates were performed by immersion in PBS buffer at 37 °C for a period of 7 days. The ellipsometric thickness and water contact angles were measured on dry films after 1, 3 and 7 days of incubation (Figure 7 and Supporting Information File 1, Figure S4). The thickness of the ALG adlayers was obtained from an optical model that considered a constant thickness of the neridronate and PDA anchor layers as determined before the grafting. The adopted optical model conforms with the observed stability of neat neridronate and PDA films during the immersion in PBS (Supporting Information File 1, Figures S4 and S5). When the polysaccharide layer was bound to the APTES siloxane, the optical model considered the instability of the APTES anchor in accordance with the SE, CA (Supporting Information File 1, Figure S4) and IRRAS findings (Supporting Information File 1, Figure S5). This methodology enabled monitoring of the stability of the ALG adlayer in the two-layer stack.

During the 7 days of incubation, only a minor decrease in the measured ellipsometric thickness was observed (Figure 7). We presume that the reduction in the ALG thickness is mainly caused by the release of a physisorbed fraction present in the surface adherent ALG aggregates. However, the water contact angles of the ALG coatings remained rather constant. This indicates that the observed, small decrease in thickness due to deterioration of the ALG films does not reveal the less-wettable anchor layers underneath (Supporting Information File 1, Figure S4). The stability of the ALG/anchor layers and the neat anchor layers was further verified by IRRAS measurements (Figure 8 and Supporting Information File 1, Figure S5). The IRRAS data enabled monitoring of the changes in the covalent structure of the whole ALG/anchor double layer and allowed for the contributions of both constituents of the stack to be separately resolved. As depicted in Figure 8, the polysaccharide films bound to neridronate and PDA anchors are rather stable without any significant changes in the position and intensity of the main vibrations of the double layer components. However, the ALG films anchored to APTES showed continuous deterioration during the 7 days of immersion. The main reduction in intensity was observed for the bands centered at 1146 and 1046 cm^{-1} arising from the ν(Si–O–Si) stretching modes of the APTES siloxane polymer network. The position of these bands corresponds to the positions of the decreased contributions in the IRRAS spectra of the deteriorated neat APTES siloxane films (Supporting Information File 1, Figure S5). This implies that the main components released during the immersion are of siloxane nature. At the same time, the spectral contributions of ALG were affected to a minor extent, most likely due to the several grafting points through which the polysaccharide chains are bound to the surface. However, the previously discussed hydrolytic instability of the APTES siloxane anchor layer would eventually lead to a complete cleavage of the polysaccharide layer from the titanium surface during a long-term immersion.

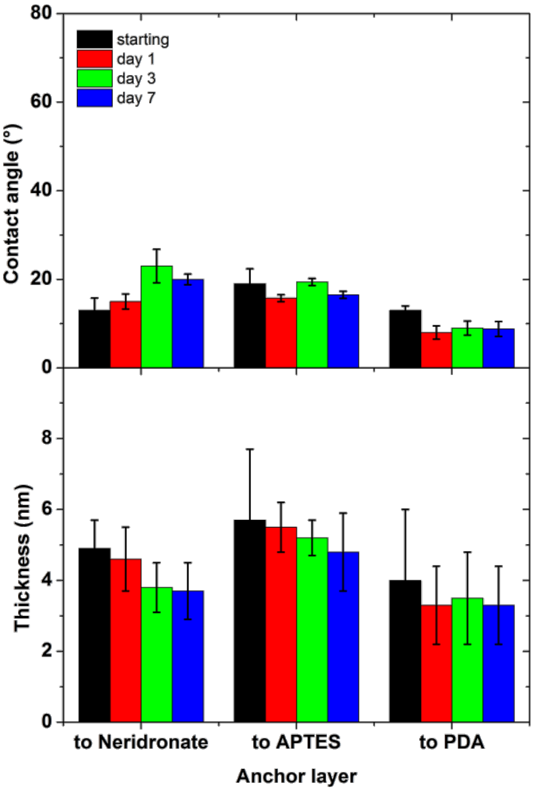

Figure 7: Ellipsometric thickness and water contact angle evolution of ALG bound to neridronate, APTES siloxane and PDA during the immersion in PBS (37 °C, pH = 7.4) (mean value ± SD, n = 15).

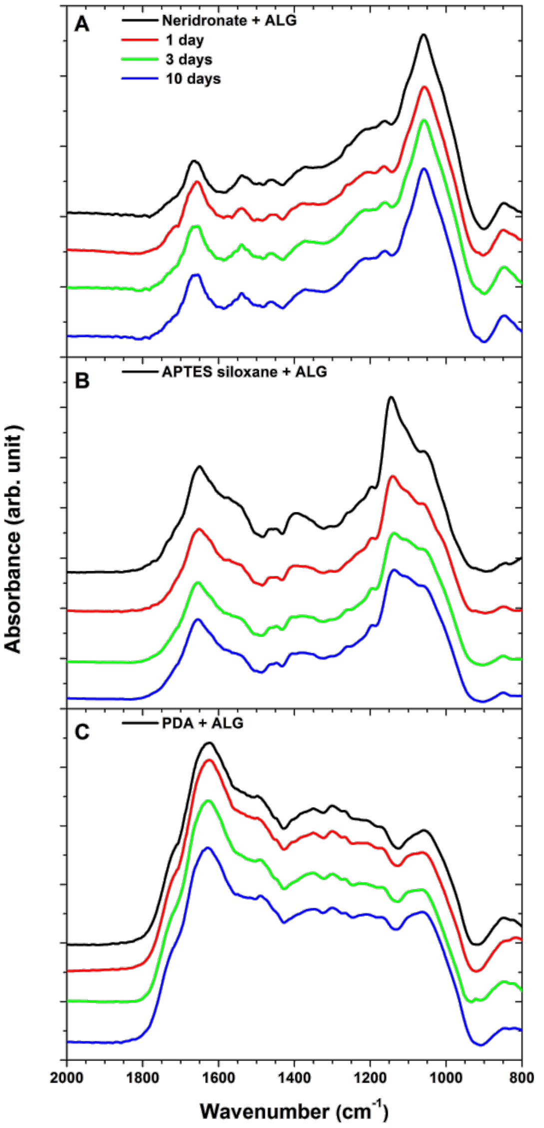

Figure 8: Evolution of IRRAS spectra of ALG bound to neridronate (A), to APTES siloxane (B) and to PDA (C) upon immersion in PBS at 37 °C for 7 days.

Based on the stability observations, the alginate monolayers bound to the neridronate or PDA anchor layers can be potentially used for the immobilization of a thin alginate hydrogel carrier of bioactive compounds (such as calcium phosphates or other biologically active molecules) formed by ionic cross-linking [40]. The proposed architecture is envisaged to enhance adhesion, proliferation, differentiation of osteoblasts, and thus ultimately, to achieve a better integration of the titanium implant into the bone tissue.

Conclusion

In the present contribution, we demonstrated the successful covalent attachment of ALG chains to neridronate, APTES and PDA anchor layers immobilized on activated titanium surfaces. The formation of the ALG and anchor layer films was investigated utilizing SE, AFM and contact angle goniometry. The IRRAS analysis further evidenced the established amide bonds between the carboxyl groups of ALG and amine groups of the anchor layers. The immobilization of the organic moieties, as well as the changes in the surface composition of pristine titanium surfaces after different surface activation treatments, was probed by XPS measurements. The changes in the surface morphology and roughness parameters during the activation of titanium surfaces were monitored by SEM and SP analysis. The 5 nm thick ALG layers anchored to neridronate and PDA were stable during immersion under physiological-like conditions for 7 days. The hydrolysis of the anchoring APTES siloxane network led to a higher deterioration tendency of the ALG/APTES double layer. The presented surface modification strategy of titanium can be an effective path for the formation of ALG-based hydrogel coatings enriched with bioactive compounds for bone tissue engineering applications.

Experimental

Materials

Dopamine hydrochloride (98.5%) was purchased from Sigma and 3-triethoxysilylpropan-1-amine from Aldrich. 3-(Ethyliminomethyleneamino)-*N*,*N*-dimethylpropan-1-amine (EDC), 1-hydroxy-2,5-pyrrolidinedione (NHS) and 2-(morpholin-4-yl)ethanesulfonic acid (MES) were obtained from Fluka. Sodium alginate salt (ALG) derived from brown algae was purchased from Sigma. The molecular weight of ALG was determined by size exclusion chromatography (SEC) on a gradient Knauer system with diode array detection (DAD) and an Alltech 3300 evaporative light scattering detection (ELSD) system. The SEC measurement was performed on a PolySept GFC-P linear column using an isocratic system of 0.03 M ammonium acetate buffer in acetonitrile/water (20/80 v/v). The determined average molecular weight of ALG was 1.5×10^6 g·mol^{-1} (PDI = 2.45) with the column calibration carried out using PEO standards. The ALG peak had a unimodal distribution without the presence of low molecular weight degradation products.

All organic solvents (petroleum ether, methanol, ethanol, isobuthanol and toluene) were of analytical grade (Lach-Ner, Czech Republic) and used as received. Ultrapure water was obtained with a Millipore Milli-Q system.

Substrate preparation

Clean, single-side-polished silicon wafers (CZ, orientation <100>, B-doped, resistivity 5–20 Ω·cm) with a ≈50 nm SiO_2 thermal overlayer (Siegert Consulting e.K., Germany) were used as substrates for the preparation of ultraflat titanium surfaces. Flat, titanium reference surfaces (50 nm thickness) were obtained by evaporation deposition (rate = 0.35 Å·s^{-1}, pressure = 6.66 × 10^{-6} Pa) using a COV AP SQC-310C deposition device (Angstrom Engineering, Canada). The coated substrates were cut into 1.2 cm × 1.2 cm pieces, sonicated in methanol, and deionized in water for 15 min, followed by oxygen plasma oxidization (25 W, Plasma Cleaner/Sterilizer, Harrick, USA) for 5 min directly before the anchor layer immobilization.

Commercially available, paste-polished, pure titanium surfaces (Beznoska, Czech Republic) were used to probe the presence of inorganic and organic surface contaminants and to determine the surface concentration of introduced hydroxy groups. After the initial sonication in petrolether, methanol and deionized water for 15 min, the following surface cleaning and activation procedures were investigated: alkaline piranha treatment (mixture of 25% NH_3, 30% H_2O_2 and water at 1:1:5 v/v/v, at 70 °C for 15 min), immersion in 0.5 M NaOH (60 °C for 24 h), immersion in a mixture of concentrated HCl and H_2SO_4 (1:1 v/v, at room temperature for 20 min) and a piranha cleaving treatment utilizing concentrated H_2SO_4 and 30% H_2O_2 (1:1 v/v, at room temperature for 20 min). The substrates were subsequently thoroughly rinsed with ultrapure water, blow-dried using nitrogen, and exposed to an oxygen plasma (25 W) for 5 min just before the XPS analysis or the binding of the anchor layers (Scheme 1).

Formation of anchoring layers

Neridronate monosodium salt ((6-amino-1-hydroxy-1-phosphonohexyl)-hydroxyphosphinate sodium) was prepared according previous reports [59]. The immobilization on the flat titanium surfaces proceeded from a 0.005 M neridronate solution in water at 100 °C for 48 h. Afterwards, the samples were rinsed in water 3 times for 5 min to remove the physisorbed molecules, then blow-dried and kept in vacuum until further use.

Siloxane anchor layers were prepared by exposing the activated titanium substrates to 0.1% v/v APTES solutions in dry toluene at 70 °C. After 12 h of exposure, the samples were sonicated in dry toluene for 15 min to remove the physisorbed siloxane particles, then blow-dried and kept in vacuum until further use.

A poly(dopamine) coating was deposited from a 2 mg·mL^{-1} solution prepared by dissolution of dopamine hydrochloride in an air-saturated 10 mM Tris hydrochloride (pH 8.5) buffer. After 3 h of polymerization, the PDA-coated surfaces were rinsed with water, sonicated in water for 15 min and blow-dried in a stream of nitrogen.

Stability tests were performed on alginate-containing and neat-anchor layers deposited on flat titanium substrates, incubated in PBS (pH 7.4, containing 0.02 wt % sodium azide) at 37 °C for 7 days. After the immersion period, the substrates were rinsed with copious amounts of water and blow-dried in a stream of nitrogen.

Tethering of alginate onto titanium layers containing anchor layers

The tethering of the alginate chains to the amine-functionalized flat titanium substrates was performed employing a modified EDC/NHS protocol based on the work of Rowley et al. [60]. Alginate was dissolved in mixture of 0.1 M MES and 0.15 M NaCl, at pH 5, at a concentration of 1 wt %. Next, EDC was added and the solution was stirred for 15 min. Afterwards, NHS was added and the solution was stirred for an additional 15 min until the production of bubbles diminished. The molar ratio between reactants was uronic units/EDC/NHS (1:20:20). The titanium substrates bearing the neridronate, APTES siloxane and PDA anchors were placed in 12-well cultivation plates and 0.8 mL of the reaction solution was deposited on the surface and allowed to react for 24 h. Subsequently the alginate-grafted substrates were rinsed with water and blow-dried in a stream of nitrogen.

Methods

Spectroscopic ellipsometry (SE): Ex situ and in situ ellipsometric data were acquired using a spectroscopic imaging, auto-nulling ellipsometer (EP^3-SE, Nanofilm Technologies, Germany) equipped with a liquid cell (V_{internal} = 0.7 mL) in 4-zone mode in the wavelength range of 398.9–811.0 nm (source: Xe arc lamp, wavelength step: 10 nm) at an angle of incidence of 60°. The cell windows (strain-free, optical BK-7 glass from Qioptiq, Germany) exhibited only small birefringence and dichroism causing errors in the ellipsometric angles Δ and Ψ smaller than 0.3° and 0.1°, respectively. These errors were corrected following the method of Azzam and Bashara [61]. To increase the measurement precision and exclude errors from the variations of layer thickness throughout the substrate area, a 10× objective and position-calibrated sample stage were utilized to perform repeated ex situ and in situ measurements over the same sample area (1 × 2 mm). The obtained data were analyzed with multilayer models using the EP^4-SE analysis software (Accurion GmbH, Germany).

The thickness and refractive index of the resulting organic layers were obtained from simultaneous fitting of the obtained ellipsometric data using the Cauchy dispersion function ($n = A_n + B_n/\lambda$, $k = 0$ with $A_n = 1.412 \pm 0.010$, $B_n = 5900 \pm 80$ nm^2 for neridronate and $A_n = 1.413 \pm 0.009$, $B_n = 6270 \pm 70$ nm^2 for APTES and $A_n = 1.4714 \pm 0.008$, $B_n = 13200 \pm 1000$ nm^2 for

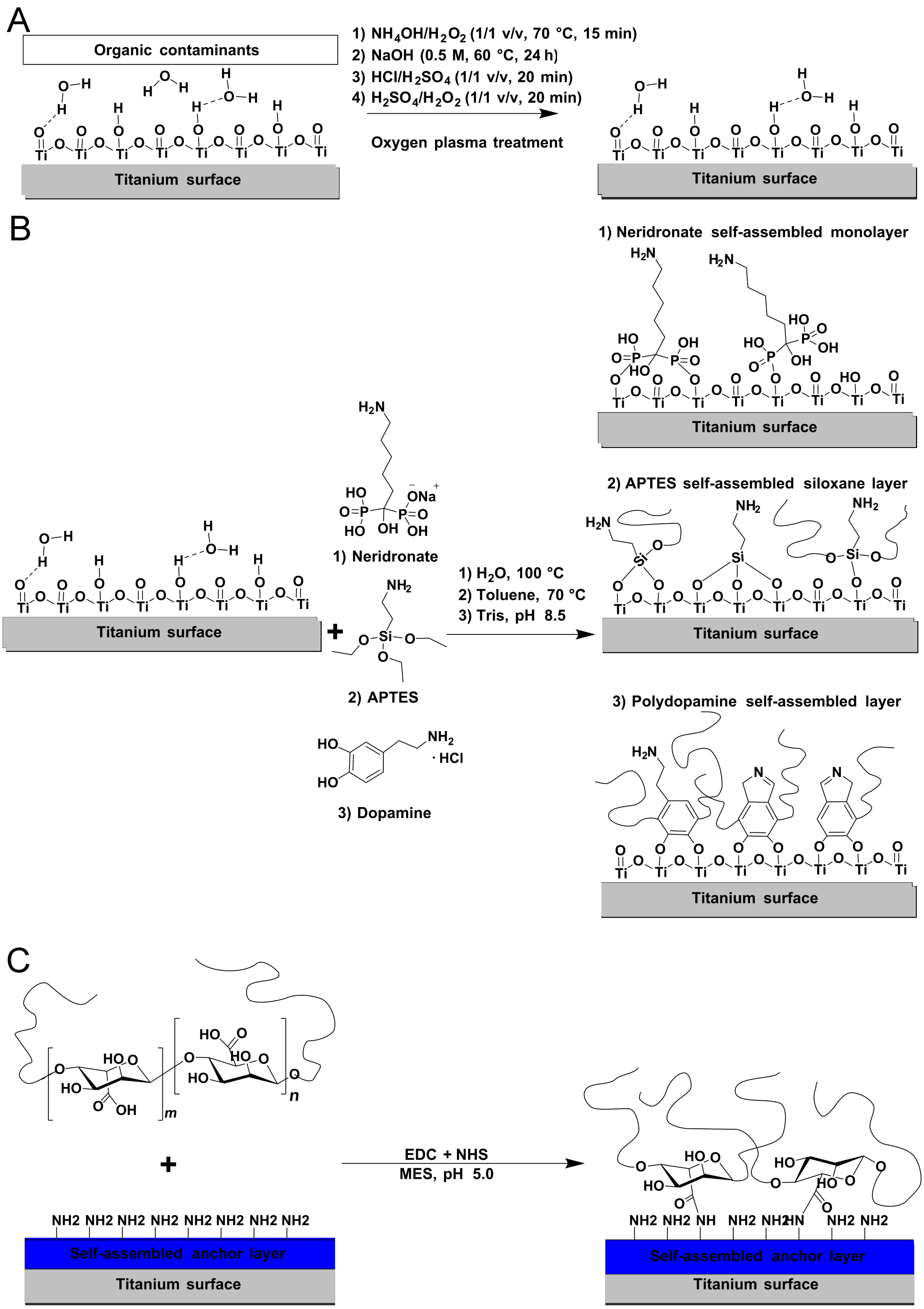

Scheme 1: Performed surface treatments and subsequent reactions for the activation and modification of titanium surfaces. (A) Cleaning and activation procedures for the removal of inorganic and organic contaminants from the titanium surface and to increase the number of free hydroxy groups. (B) Immobilization of neridronate, APTES siloxane and poly(dopamine) anchor layers through surface specific reactions between the phosphonate, silane and catechol groups of corresponding compounds and hydroxy groups on the surface. (C) Covalent binding of ALG chains to amino groups present in the anchor layers by the EDC/NHS coupling reaction.

the ALG layers). The optical dispersion functions of PDA, silicon dioxide and silicon were taken from previous reports [34,62]. The optical dispersion functions of ethanol, isobutanol, toluene and titanium dioxide were taken from the EP^4-SE database.

Contact angle measurement*:* The wettability of the organic surfaces on flat, titanium reference surfaces was examined by a static sessile water drop method using a DataPhysics OCA 20 contact angle system. Each sample was characterized using four 3 µL drops of material. The data were evaluated using the Young–Laplace method.

The wettability of the commercially available, rough titanium substrates upon different treatments was estimated by measuring the advancing and receding water contact angles utilizing the dynamic Wilhelmy plate method. The measurements were performed on a Kruss K12 (Germany) tensiometer.

Infrared reflection–absorption spectroscopy (IRRAS): The infrared spectra of neridronate, APTES and dopamine moieties were recorded using a Perkin Elmer, Paragon 1000PC, FTIR spectrometer, equipped with a MCT detector and a single reflection, monolithic diamond, Golden Gate ATR accessory (Specac, England). The spectra of the dry organic films formed on titanium surfaces were recorded using a Bruker IFS 55 FTIR spectrometer (Bruker Optics, Germany) equipped with a MCT detector. The measurements were performed at a grazing angle (80°, p-polarization) using the reflection spectroscopy accessory. The measurement chamber was continuously purged with dry air. The acquisition time was approximately 20 min at a resolution of 2 cm^{-1}. The spectra are reported as $-\log(R/R_0)$, where R is the reflectance of the sample and R_0 is the reflectance of bare titanium reference surfaces.

Atomic force microscopy (AFM): AFM characterization was performed on a Dimension ICON (Bruker, USA) system in peak force tapping mode in air using silicon probes (TAP150A, Bruker, USA) with a typical force constant of 5 N·m^{-1}. The images were taken using a scan rate in the range of 0.5−1.2 Hz and a peak force set point of 0.02−0.2 V.

Surface profilometry: Macroscopic surface roughness and waviness measurements were performed using a Tencor P-10 (Texas, USA) surface profiler with 1 mm long scans at a speed of 20 µm·s^{-1} and a sampling rate of 200 Hz using a maximum stylus force of 0.02 N.

Scanning electron microscopy (SEM): The SEM analysis was performed on a Quanta 200 FEG (FEI, Czech Republic) microscope. All micrographs presented are secondary electron images taken under high vacuum using an accelerating voltage of 30 kV.

X-ray photoelectron spectroscopy (XPS): The core-level photoelectron spectra were recorded using an angle-resolved photoelectron spectrometer, ADES 400 (VG Scientific, UK), operating at a base pressure of 1.33 × 10^{-7} Pa. The system was equipped with an X-ray excitation source and a rotatable hemispherical electron energy analyzer. The photoelectron spectra were recorded using Mg Kα radiation with a pass energy of 100 eV or 20 eV (high-energy resolution). The incidence angle was 70° with respect to the sample surface normal and the emission angle along the surface normal. The atomic concentrations of carbon, oxygen and nitrogen were determined from the C 1s, O 1s, and N 1s photoelectron peak areas after a Shirley inelastic background subtraction. Assuming a simple model of a semi-infinite solid of homogeneous composition, the peak areas were corrected for the photoelectric cross-sections [63], the inelastic mean free paths of the electrons in question [64], and the transmission function of the spectrometer [65]. The experimental uncertainties in the quantitative analysis of XPS were assessed in separate experiments with several standard materials and were estimated to be below 7%. This value encompasses the overall uncertainties of the method that are typically introduced by the background subtraction.

Supporting Information

Supporting Information File 1

Additional Experimental Information.
[http://www.beilstein-journals.org/bjnano/content/supplementary/2190-4286-6-63-S1.pdf]

Acknowledgements

The authors acknowledge the support of the Grant Agency of the Ministry of Health of the Czech Republic (grant number: NT/13297–4), of the Ministry of Education, Youth and Sports of the Czech Republic (grant number: SGS No. 10/297/OHK4/3T/14, EE2.3.30.0029 and the project “BIOCEV – Biotechnology and Biomedicine Centre of the Academy of Sciences and Charles University” CZ.1.05/1.1.00/02.0109), and the Czech Science Foundation (grant number: P108/11/1857).

References

1. Elias, C. N.; Lima, J. H. C.; Valiev, R.; Meyers, M. A. *JOM* **2008,** *60,* 46–49. doi:10.1007/s11837-008-0031-1
2. Park, J. B.; Bronzino, J. D., Eds. *Biomaterials - Principles and Applications;* CRC Press: Boca Raton, FL, USA, 2003.

3. McCafferty, E.; Wightman, J. P. *Surf. Interface Anal.* **1998,** *26,* 549–564. doi:10.1002/(SICI)1096-9918(199807)26:8<549::AID-SIA396>3.0.CO;2-Q
4. Tanaka, Y.; Saito, H.; Tsutsumi, Y.; Doi, H.; Imai, H.; Hanawa, T. *Mater. Trans.* **2008,** *49,* 805–811. doi:10.2320/matertrans.MRA2007317
5. Kataoka, S.; Gurau, M. C.; Albertorio, F.; Holden, M. A.; Lim, S.-M.; Yang, R. D.; Cremer, P. S. *Langmuir* **2004,** *20,* 1662–1666. doi:10.1021/la035971h
6. Roessler, S.; Zimmermann, R.; Scharnweber, D.; Werner, C.; Worch, H. *Colloids Surf., B* **2002,** *26,* 387–395. doi:10.1016/S0927-7765(02)00025-5
7. Parks, G. A. *Chem. Rev.* **1965,** *65,* 177–198. doi:10.1021/cr60234a002
8. Schliephake, H.; Scharnweber, D. *J. Mater. Chem.* **2008,** *18,* 2404–2414. doi:10.1039/b715355b
9. Tosatti, S.; De Paul, S. M.; Askendal, A.; VandeVondele, S.; Hubbell, J. A.; Tengvall, P.; Textor, M. *Biomaterials* **2003,** *24,* 4949–4958. doi:10.1016/S0142-9612(03)00420-4
10. Schuler, M.; Owen, G. Rh.; Hamilton, D. W.; De Wild, M.; Textor, M.; Brunette, D. M.; Tosatti, S. G. P. *Biomaterials* **2006,** *27,* 4003–4015. doi:10.1016/j.biomaterials.2006.03.009
11. Tosatti, S.; Schwartz, Z.; Campbell, C.; Cochran, D. L.; VandeVondele, S.; Hubbell, J. A.; Denzer, A.; Simpson, J.; Wieland, M.; Lohmann, C. H.; Textor, M.; Boyan, B. D. *J. Biomed. Mater. Res., Part A* **2004,** *68A,* 458–472. doi:10.1002/jbm.a.20082
12. Nanci, A.; Wuest, J. D.; Peru, L.; Brunet, P.; Sharma, V.; Zalzal, S.; McKee, M. D. *J. Biomed. Mater. Res.* **1998,** *40,* 324–335. doi:10.1002/(SICI)1097-4636(199805)40:2<324::AID-JBM18>3.0.CO;2-L
13. Jimbo, R.; Ivarsson, M.; Koskela, A.; Sul, Y.-T.; Johansson, C. *J. Oral Maxillofac. Res.* **2010,** *1,* e3. doi:10.5037/jomr.2010.1303
14. Zorn, G.; Gotman, I.; Gutmanas, E. Y.; Adadi, R.; Sukenik, C. N. *J. Mater. Sci.: Mater. Med.* **2007,** *18,* 1309–1315. doi:10.1007/s10856-006-0117-7
15. Heijink, A.; Schwartz, J.; Zobitz, M. E.; Crowder, K. N.; Lutz, G. E.; Sibonga, J. D. *Clin. Orthop. Relat. Res.* **2008,** *466,* 977–984. doi:10.1007/s11999-008-0117-7
16. Kaigler, D.; Avila, G.; Wisner-Lynch, L.; Nevins, M. L.; Nevins, M.; Rasperini, G.; Lynch, S. E.; Giannobile, W. V. *Expert Opin. Biol. Ther.* **2011,** *11,* 375–385. doi:10.1517/14712598.2011.554814
17. Bagno, A.; Genovese, M.; Luchini, A.; Dettin, M.; Conconi, M. T.; Menti, A. M.; Parnigotto, P. P.; Di Bello, C. *Biomaterials* **2004,** *25,* 2437–2445. doi:10.1016/j.biomaterials.2003.09.018
18. Wu, M.-Y.; Chen, N.; Liu, L.-K.; Yuan, H.; Li, Q.-L.; Chen, S.-H. *J. Bioact. Compat. Polym.* **2009,** *24,* 301–315. doi:10.1177/0883911509105848
19. Park, J. H.; Schwartz, Z.; Olivares-Navarrete, R.; Boyan, B. D.; Tannenbaum, R. *Langmuir* **2011,** *27,* 5976–5985. doi:10.1021/la2000415
20. Chapman, R. G.; Ostuni, E.; Yan, L.; Whitesides, G. M. *Langmuir* **2000,** *16,* 6927–6936. doi:10.1021/la991579l
21. Kurth, D. G.; Bein, T. *Langmuir* **1995,** *11,* 3061–3067. doi:10.1021/la00008a035
22. Smith, E. A.; Chen, W. *Langmuir* **2008,** *24,* 12405–12409. doi:10.1021/la802234x
23. Flynn, N. T.; Tran, T. N. T.; Cima, M. J.; Langer, R. *Langmuir* **2003,** *19,* 10909–10915. doi:10.1021/la035331e
24. Sung, I.-H.; Kim, D.-E. *Tribol. Lett.* **2004,** *17,* 835–844. doi:10.1007/s11249-004-8091-z
25. Xiao, S.-J.; Textor, M.; Spencer, N. D.; Sigrist, H. *Langmuir* **1998,** *14,* 5507–5516. doi:10.1021/la980257z
26. Dubey, M.; Weidner, T.; Gamble, L. J.; Castner, D. G. *Langmuir* **2010,** *26,* 14747–14754. doi:10.1021/la1021438
27. Silverman, B. M.; Wieghaus, K. A.; Schwartz, J. *Langmuir* **2005,** *21,* 225–228. doi:10.1021/la048227l
28. Lecollinet, G.; Delorme, N.; Edely, M.; Gibaud, A.; Bardeau, J.-F.; Hindré, F.; Boury, F.; Portet, D. *Langmuir* **2009,** *25,* 7828–7835. doi:10.1021/la8039576
29. Yoshinari, M.; Oda, Y.; Ueki, H.; Yokose, S. *Biomaterials* **2001,** *22,* 709–715. doi:10.1016/S0142-9612(00)00234-9
30. Luschtinetz, R.; Gemming, S.; Seifert, G. *Eur. Phys. J. Plus* **2011,** *126,* 98. doi:10.1140/epjp/i2011-11098-4
31. Lee, H.; Dellatore, S. M.; Miller, W. M.; Messersmith, P. B. *Science* **2007,** *318,* 426–430. doi:10.1126/science.1147241
32. Pop-Georgievski, O.; Rodriguez-Emmenegger, C.; de los Santos Pereira, A.; Proks, V.; Brynda, E.; Rypáček, F. *J. Mater. Chem. B* **2013,** *1,* 2859–2867. doi:10.1039/c3tb20346h
33. Pop-Georgievski, O.; Verreault, D.; Diesner, M.-O.; Proks, V.; Heissler, S.; Rypáček, F.; Koelsch, P. *Langmuir* **2012,** *28,* 14273–14283. doi:10.1021/la3029935
34. Pop-Georgievski, O.; Popelka, S.; Houska, M.; Chvostova, D.; Proks, V.; Rypáček, F. *Biomacromolecules* **2011,** *12,* 3232–3242. doi:10.1021/bm2007086
35. Ku, S. H.; Ryu, J.; Hong, S. K.; Lee, H.; Park, C. B. *Biomaterials* **2010,** *31,* 2535–2541. doi:10.1016/j.biomaterials.2009.12.020
36. Ryu, J.; Ku, S. H.; Lee, H.; Park, C. B. *Adv. Funct. Mater.* **2010,** *20,* 2132–2139. doi:10.1002/adfm.200902347
37. Proks, V.; Jaroš, J.; Pop-Georgievski, O.; Kučka, J.; Popelka, Š.; Dvořák, P.; Hampl, A.; Rypáček, F. *Macromol. Biosci.* **2012,** *12,* 1232–1242. doi:10.1002/mabi.201200095
38. Kaupp, M.; Quick, A. S.; Rodriguez-Emmenegger, C.; Welle, A.; Trouillet, V.; Pop-Georgievski, O.; Wegener, M.; Barner-Kowollik, C. *Adv. Funct. Mater.* **2014,** *24,* 5649–5661. doi:10.1002/adfm.201400609
39. Rodriguez-Emmenegger, C.; Preuss, C. M.; Yameen, B.; Pop-Georgievski, O.; Bachmann, M.; Mueller, J. O.; Bruns, M.; Goldmann, A. S.; Bastmeyer, M.; Barner-Kowollik, C. *Adv. Mater.* **2013,** *25,* 6123–6127. doi:10.1002/adma.201302492
40. Becker, T. A.; Kipke, D. R.; Brandon, T. *J. Biomed. Mater. Res.* **2001,** *54,* 76–86. doi:10.1002/1097-4636(200101)54:1<76::AID-JBM9>3.0.CO;2-V
41. Li, Z.; Ramay, H. R.; Hauch, K. D.; Xiao, D.; Zhang, M. *Biomaterials* **2005,** *26,* 3919–3928. doi:10.1016/j.biomaterials.2004.09.062
42. Chen, T. W.; Chang, S. J.; Niu, G. C.-C.; Hsu, Y. T.; Kuo, S. M. *J. Appl. Polym. Sci.* **2006,** *102,* 4528–4534. doi:10.1002/app.24945
43. Rossetti, F. F.; Reviakine, I.; Textor, M. *Langmuir* **2003,** *19,* 10116–10123. doi:10.1021/la034280i
44. Feng, B.; Chen, J. Y.; Qi, S. K.; He, L.; Zhao, J. Z.; Zhang, X. D. *J. Mater. Sci.: Mater. Med.* **2002,** *13,* 457–464. doi:10.1023/A:1014737831371
45. Larsson, C.; Thomsen, P.; Aronsson, B.-O.; Rodahl, M.; Lausmaa, J.; Kasemo, B.; Ericson, L. E. *Biomaterials* **1996,** *17,* 605–616. doi:10.1016/0142-9612(96)88711-4
46. Larsson, C.; Thomsen, P.; Lausmaa, J.; Rodahl, M.; Kasemo, B.; Ericson, L. E. *Biomaterials* **1994,** *15,* 1062–1074. doi:10.1016/0142-9612(94)90092-2
47. Chapman, A. C.; Thirlwell, L. E. *Spectrochim. Acta* **1964,** *20,* 937–947. doi:10.1016/0371-1951(64)80094-1

48. Zenobi, M. C.; Luengo, C. V.; Avena, M. J.; Rueda, E. H. *Spectrochim. Acta, Part A: Mol. Biomol. Spectrosc.* **2008,** *70,* 270–276. doi:10.1016/j.saa.2007.07.043
49. Zenobi, M. C.; Luengo, C. V.; Avena, M. J.; Rueda, E. H. *Spectrochim. Acta, Part A: Mol. Biomol. Spectrosc.* **2010,** *75,* 1283–1288. doi:10.1016/j.saa.2009.12.059
50. Lagutschenkov, A.; Langer, J.; Berden, G.; Oomens, J.; Dopfer, O. *Phys. Chem. Chem. Phys.* **2011,** *13,* 2815–2823. doi:10.1039/c0cp02133d
51. Proks, V.; Brus, J.; Pop-Georgievski, O.; Večerníková, E.; Wisniewski, W.; Kotek, J.; Urbanová, M.; Rypáček, F. *Macromol. Chem. Phys.* **2013,** *214,* 499–507. doi:10.1002/macp.201200505
52. Müller, M.; Keßler, B. *Langmuir* **2011,** *27,* 12499–12505. doi:10.1021/la202908b
53. Pop-Georgievski, O.; Neykova, N.; Proks, V.; Houdkova, J.; Ukraintsev, E.; Zemek, J.; Kromka, A.; Rypaček, F. *Thin Solid Films* **2013,** *543,* 180–186. doi:10.1016/j.tsf.2012.11.128
54. Clark, M. B., Jr.; Gardella, J. A., Jr.; Schultz, T. M.; Patil, D. G.; Salvati, L., Jr. *Anal. Chem.* **1990,** *62,* 949–956. doi:10.1021/ac00208a011
55. Acres, R. G.; Ellis, A. V.; Alvino, J.; Lenahan, C. E.; Khodakov, D. A.; Metha, G. F.; Andersson, G. G. *J. Phys. Chem. C* **2012,** *116,* 6289–6297. doi:10.1021/jp212056s
56. Bashir, M.; Rees, J. M.; Bashir, S.; Zimmerman, W. B. *Thin Solid Films* **2014,** *564,* 186–194. doi:10.1016/j.tsf.2014.06.004
57. Gray, M. L.; Soong, Y.; Champagne, K. J.; Pennline, H.; Baltrus, J. P.; Stevens, R. W., Jr.; Khatri, R.; Chuang, S. S. C.; Filburn, T. *Fuel Process. Technol.* **2005,** *86,* 1449–1455. doi:10.1016/j.fuproc.2005.01.005
58. Pasternack, R. M.; Amy, S. R.; Chabal, Y. J. *Langmuir* **2008,** *24,* 12963–12971. doi:10.1021/la8024827
59. Kieczykowski, G. R.; Jobson, R. B.; Melillo, D. G.; Reinhold, D. F.; Grenda, V. J.; Shinkai, I. *J. Org. Chem.* **1995,** *60,* 8310–8312. doi:10.1021/jo00130a036
60. Rowley, J. A.; Madlambayan, G.; Mooney, D. J. *Biomaterials* **1999,** *20,* 45–53. doi:10.1016/S0142-9612(98)00107-0
61. Azzam, R. M. A.; Bashara, N. M. *Ellipsometry and Polarized Light,* 5th ed.; Elsevier: Amsterdam, Netherlands, 2003.
62. Herzinger, C. M.; Johs, B.; McGahan, W. A.; Woollam, J. A.; Paulson, W. *J. Appl. Phys.* **1998,** *83,* 3323–3336. doi:10.1063/1.367101
63. Band, I. M.; Kharitonov, Yu. I.; Trzhaskovskaya, M. B. *At. Data Nucl. Data Tables* **1979,** *23,* 443–505. doi:10.1016/0092-640X(79)90027-5
64. Tanuma, S.; Powell, C. J.; Penn, D. R. *Surf. Interface Anal.* **1994,** *21,* 165–176. doi:10.1002/sia.740210302
65. Jiříček, P. *Czech. J. Phys.* **1994,** *44,* 261–267. doi:10.1007/BF01694490

License and Terms

BEILSTEIN JOURNAL OF NANOTECHNOLOGY

Simple approach for the fabrication of PEDOT-coated Si nanowires

Mingxuan Zhu[1,2,3], Marielle Eyraud[*4,§], Judikael Le Rouzo[1], Nadia Ait Ahmed[5], Florence Boulc'h[4], Claude Alfonso[1], Philippe Knauth[4] and François Flory[1,2]

Full Research Paper

Open Access

Address:
[1]Aix-Marseille University, Institut Matériaux Microélectronique Nanosciences de Provence-IM2NP, CNRS-UMR 7334, équipe OPTO-PV, Domaine Universitaire de Saint-Jérôme, Service 231, 13397 Marseille Cedex 20, France, [2]Ecole Centrale Marseille, 38 rue Joliot Curie, 13451 Marseille Cedex 20, France, [3]Shanghai Institute of Technical Physics, Chinese Academy of Sciences, 500 Yutian Road, 200240 Shanghai, China, [4]Aix-Marseille University, CNRS, MADIREL UMR 7246, équipe Electrochimie des Matériaux, 13397 Marseille Cedex 20, France, and [5]Université Abderrahmane Mira, Lab. d'Electrochimie, Corrosion et de Valorisation énergétique, 06000 Bejaia, Algeria

Email:
Marielle Eyraud* - marielle.eyraud@univ-amu.fr

* Corresponding author
§ Tel.: +33 4 13 55 18 21

Keywords:
conductive polymer; core–shell structure; electrodeposition; hybrid material; SiNW

Beilstein J. Nanotechnol. **2015,** *6,* 640–650.
doi:10.3762/bjnano.6.65

Received: 21 July 2014
Accepted: 06 February 2015
Published: 04 March 2015

This article is part of the Thematic Series "Self-assembly of nanostructures and nanomaterials".

Guest Editor: I. Berbezier

Abstract

The synthesis of a conformal poly(3,4-ethylenedioxythiophene) (PEDOT) layer on Si nanowires was demonstrated using a pulsed electrodeposition technique. N-type Si nanowire (SiNWs) arrays were synthesized using an electroless metal-assisted chemical etching technique. The dependence of the SiNW reflection on the concentration of the $AgNO_3$ solution was identified. A reflection of less than 2% over the entire visible spectral range was obtained for these structures, evidencing their excellent antireflective properties. The etched SiNWs nanostructures can be further modified by using a tapering technique, which further preserves the strong light trapping effect. P-type PEDOT was grown on these SiNWs using electrochemical methods. Since the polymerization reaction is a very fast process with regards to monomer diffusion along the SiNW, the conformal deposition by classical, fixed potential deposition was not favored. Instead, the core–shell heterojunction structure was finally achieved by a pulsed deposition method. An extremely large shunt resistance was exhibited and determined to be related to the diffusion conditions occurring during polymerization.

Introduction

Silicon nanowires (SiNWs) are a current, active research topic for many applications such as photovoltaics [1], lithium batteries [2], hydrogen storage [3] and optoelectronic devices [4] due to their unique properties with respect to visible light management [5-7]. Using an electroless etching method, a reflectivity as low as 1.3% over the entire visible spectrum can be achieved for SiNWs [8]. As far as the device fabrication is concerned, a core–shell arrangement of p–n junction forming materials is promising for the optimization of the electronic charge collection capability. This is due to the nature of the core–shell structure, which allows the transport path along the radial direction of photogenerated carriers to be greatly shortened without sacrificing light absorption [9].

However, the high aspect ratio of SiNWs makes it difficult to realize a radial p–n junction, where each individual Si wire in the array would need to be individually coated. Various fabrication efforts have been attempted to achieve a true core–shell p–n junction. For example, chemical vapor deposition (CVD) [10,11] and atomic layer deposition (ALD) [12] are methods that can be employed to obtain this type of nanostructured junction, however, they suffer from high cost. The combination of spin-on doping (SOD) and rapid thermal annealing (RTM) was also attempted to achieve a core–shell Si homojunction [13,14], but this method failed to precisely control the thickness of the shell. Core–shell, radial p–n junctions can also be realized by simply spin coating poly(3,4-ethylenedioxythiophene)/polystyrene sulfonate (PEDOT/PSS) (a successful, commercial, conducting polymer) onto a SiNW array. This gave very promising results for photovoltaic cells based on this heterojunction, with a photon capture efficiency (PCE) of 6.72% [15]. The resulting SiNW/PEDOT/PSS heterojunction showed rectification behavior with a large saturation current density. A relatively low shunt resistance and a high saturation current are displayed by devices produced using the spin coating method. This is because the PEDOT:PSS only partially covers the SiNWs array, leaving most of the SiNW surface uncovered [16]. In order to improve the junction quality, a conformal PEDOT shell should be introduced to eliminate charge transport paths parallel to the diode.

Compared with the spin coating technique, the electrochemical polymerization of PEDOT provides the possibility of excellent polymer morphology control by tuning the thickness and reaction rate. Template polymerization of PEDOT has already been investigated on nanostructures such as ZnO [17], TiO_2 [18], GaAs [19], AAO [20]. However, using a SiNW array as template for PEDOT deposition is an unexplored research field with only a few existing publications [21,22]. Some relevant questions are: (i) What is the role of nanostructured Si in PEDOT nucleation and growth? (ii) How do the deposition conditions influence the PEDOT properties? (iii) How can the diode quality be improved?

In this paper, we will first present the influence of the $AgNO_3$ concentration on the antireflection properties of SiNWs that were etched with the electroless metal-assisted chemical etching (EMACE) method. To determine the optimum electrodeposition parameters, a preliminary study was performed for 3,4-ethylenedioxythiophene (EDOT) oxidation on vitreous carbon (a conductive, non-electroactive, and easily-polished substrate). This was followed by EDOT oxidation on SiNW substrates. Optical and electrical properties, as well as morphology and composition of the samples, were determined using spectroscopy, current density–voltage curves, scanning electron and transmission electron microcopies, energy-dispersive X-ray analysis, and IR spectroscopy.

Results and Discussion

Effect of tapering on SiNW antireflection

The SiNWs, as prepared from an n-type Si substrate according to the process described in the Experimental section, can be seen in Figure 1. The geometry of the wires depends strongly on the experimental conditions and can be controlled. This work on SiNWs includes a detailed study of the dimensions of these structures as related to their properties. For instance, the length of the SiNW can be easily controlled by the etching duration and the concentration of the $AgNO_3$ solution influences the morphology. However, for this study, only those SiNWs that exhibit good optical performance (low reflection at the surface, i.e., a light trapping effect) which were suitable for PEDOT deposition (using a KOH solution after the EMACE process) were addressed. The chosen experimental conditions resulted in a dense array of smooth Si nanowires, 2 μm in length, approximately 100 nm thick, and oriented perpendicular to the Si substrate. In this case, the space between the wires was quite small. TEM observation of the nanowires allows the dimensions to be measured more precisely. The polydispersity of the diameter is low with a diameter of 130 ± 5 nm (see Figure 2). The effect of the duration of the tapering step on the shape, length and density of the SiNWs is shown by comparing Figure 1a (without tapering) with Figure 1b–d, where the etching time increases from b to d. Clearly, by increasing the tapering duration, the space between wires is increased, the density of wires is reduced, and their top becomes sharper.

Spectrophotometric measurements were performed on these samples to determine their light absorption properties (Figure 3). Due to the strong light trapping effect [1], the SiNWs produced without tapering exhibit a reflection of less

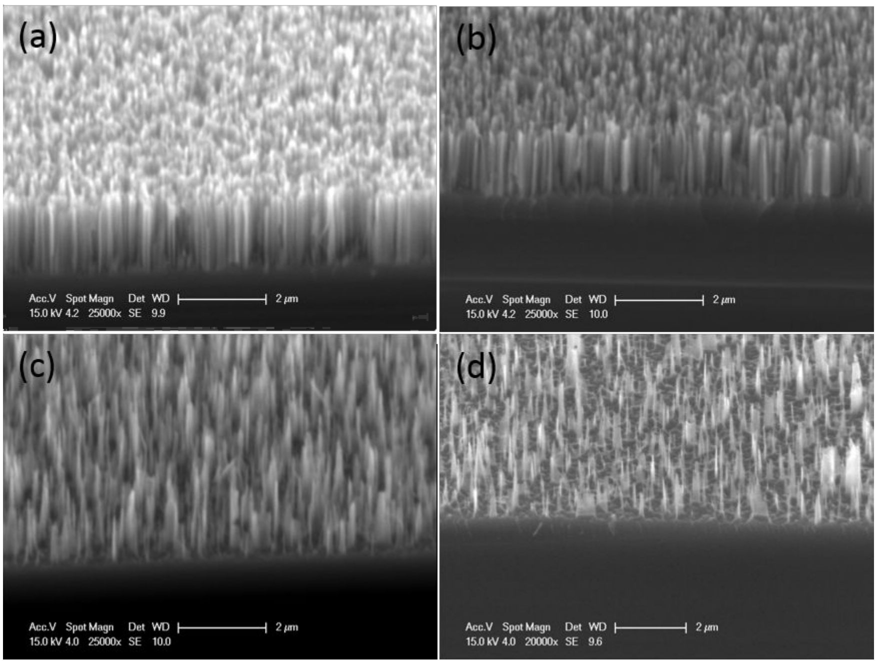

Figure 1: Tilted-view, SEM observations of SiNW samples without tapering (a) and for different tapering times: (b) 10 s, (c) 30 s, (d) 50 s.

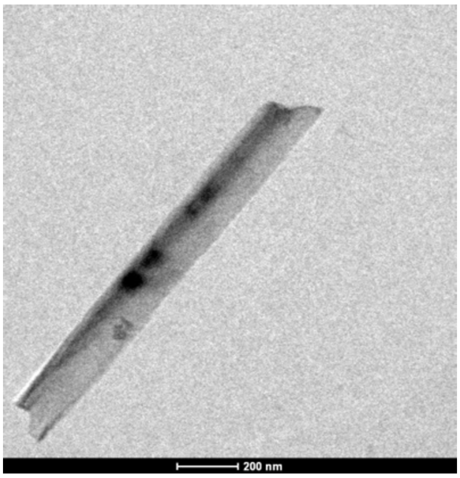

Figure 2: TEM image of a silicon nanowire obtained using the same conditions as those in Figure 1a.

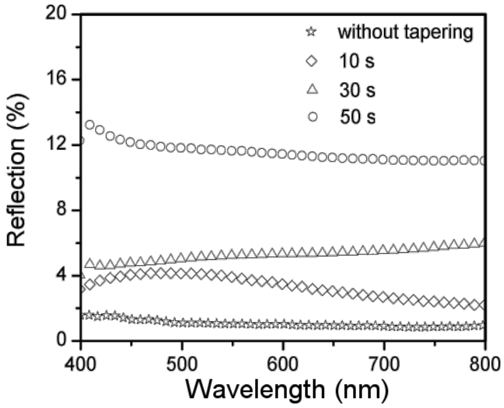

Figure 3: Reflection spectra of SiNWs in the visible spectral range without tapering and after 10, 30, and 50 s of tapering.

than 2% over the entire visible range. The reflection of the tapered samples increases with the tapering duration. After 50 s of tapering, the SiNWs have a reflection greater than 10% due to the reduced nanowire density on the substrate. For a tapering time of less than 30 s, the reflectance does not show significant change: a 10 s tapering leads to a reflection of less than 5% and a 30 s tapering to a reflection of less than 6%. This suggests that there is still a strong light trapping effect in the tapered SiNWs, although the morphology has been obviously modified. By tuning the interspace volume, the EDOT diffusion effect on the morphology of PEDOT can be further investigated, as will be discussed later.

Cyclic voltammetry and FTIR analysis for PEDOT deposition on vitreous carbon

Cyclic voltammetry (CV) experiments on vitreous carbon from EDOT containing solutions, starting from −1.5 to 1.5 V for 2 successive cycles, are shown in Figure 4. During the first scan (solid line), no current is observed up to a potential value of 1.3 V. Between 1.3 and 1.5 V, the first EDOT oxidation peak appears (see the Ox2 label in Figure 4), which is in good agreement with the literature [23,24]. This leads to the rapid synthesis of PEDOT according to the reaction in Scheme 1.

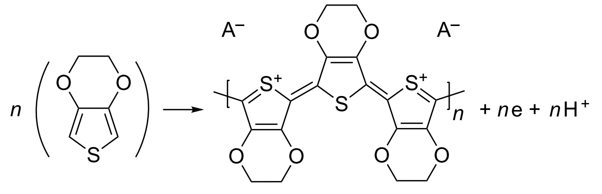

Scheme 1: Polymerization reaction scheme for PEDOT synthesis.

When the potential is reversed, a crossover point between the forward and the backward current is observed between 1.3 and 1.1 V. This effect appears because it is easier to deposit PEDOT on PEDOT (during the reverse scan), than to deposit PEDOT on vitreous carbon (during the forward scan). This CV curve form is called a nucleation loop and implies that the PEDOT film completely covered the initial vitreous carbon surface. When the potential was decreased below 0.5 V, a small reduction peak (Red 1 in Figure 4) was exhibited during the reverse scan showing that the polymer can be reduced according to the reaction [24] in Scheme 2.

During the second scan (dashed line), a new oxidation peak (Ox1) appears around 0.5 V corresponding to the oxidization of PEDOT. The oxidation of EDOT into PEDOT near Ox2 appears at a lower potential than during the first scan (1.1 V), and no nucleation loop is observed. This is because the vitreous carbon substrate is completely covered by the PEDOT film during the first cycle. At the end of the experiment, the electrode is completely covered with a blue film.

Figure 5 presents 10 successive cycles performed on vitreous carbon. The increase of both the cathodic and anodic current densities for the Red1 (left arrow) and Ox1 (right arrow) peaks with increasing number of cycles is obvious, and is correlated with the thickening of the PEDOT film. On the contrary, the current at Ox2 due to the EDOT to PEDOT transformation is constant, indicating the good conductivity of the film.

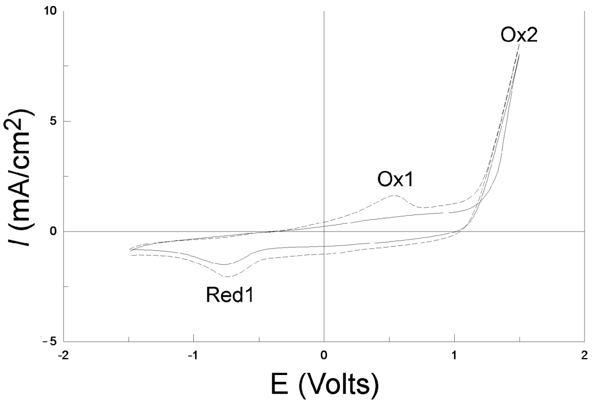

Figure 4: Two successive CVs performed on vitreous carbon with 10 mM EDOT and 0.1 M $LiClO_4$ in acetonitrile solution. Scan rate: 100 mV/s. The solid line corresponds to the 1st scan and the dashed line to the 2nd scan.

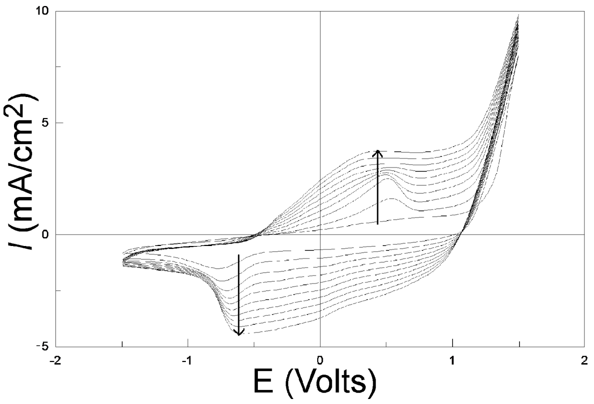

Figure 5: 10 successive CVs performed on vitreous carbon with 10 mM EDOT and 0.1 M $LiClO_4$ in acetonitrile solution. Scan rate: 100 mV/s. The arrow direction indicates increasing scan numbers.

To prove that a PEDOT film can be obtained under these conditions, a fixed voltage of 1.5 V was applied for 5 s in a 10 mM EDOT acetonitrile (ACN) solution with 0.1 M $LiClO_4$ and the reflection FTIR spectra were recorded in the wavenumber region 1400–800 cm^{-1} (Figure 6). Additionally, Table 1

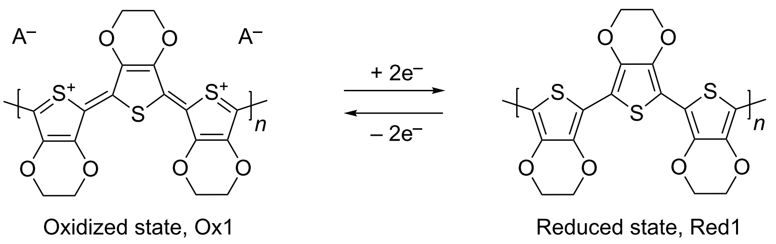

Scheme 2: Polymer reduction reaction scheme for PEDOT.

presents the principal assignments reported in literature for similar polythiophene films. Vibrations at 830, 930 and 970 cm^{-1} originate from the C–S bond in the thiophene ring [17,25,26]. Moreover, vibrations at 1040 cm^{-1}, 1130 cm^{-1}, 1180 cm^{-1} and 1300 cm^{-1} are assigned to stretching in the alkylenedioxy group [17,25,26]. These results confirm that the electrodeposited thin blue films are PEDOT.

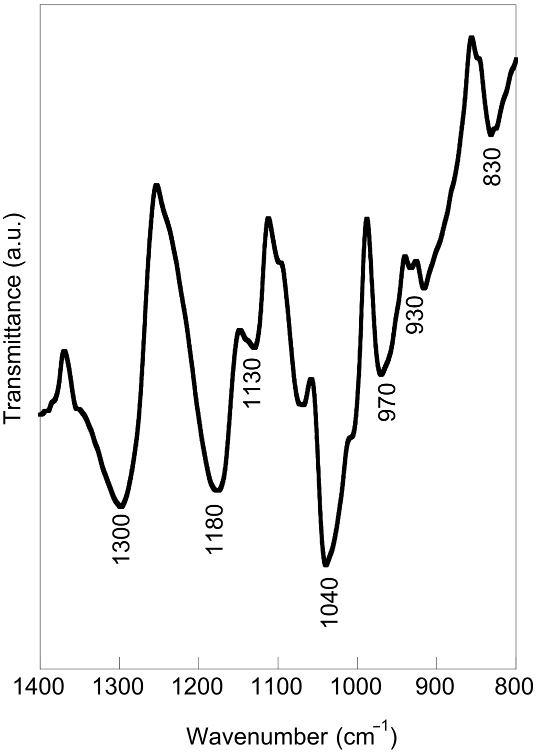

Figure 6: FTIR spectrum of a PEDOT film electropolymerized onto vitreous carbon.

Table 1: Proposed assignments for the main vibrations of polythiophene films.

Wavenumber (cm^{-1})	Assignment^{a}	Reference
830 cm^{-1}	C–S	[17,25,26]
930 cm^{-1}	C–S	[25]
970 cm^{-1}	C–S	[17]
1040 cm^{-1}	C=C / CO–R–OC	[25,26]
1130 cm^{-1}	CO–R–OC	[25,26]
1180 cm^{-1}	CO–R–OC	[25]
1300 cm^{-1}	CO–R–OC	[17]

^{a}R represents CH_2–CH_2.

Cyclic voltammetry of PEDOT deposition on SiNWs

Illumination by a concentrated light source is necessary for PEDOT polymerization on SiNWs electrodes. Indeed, the comparison of the CV curves in Figure 7 for EDOT under ambient light (curve a) shows that the current density is almost zero, much lower than that after illumination (curve b). The reason is that illumination may provide electron holes that increase the conductivity of the n-type SiNW substrate under anodic polarization. For all further experiments, the SiNW substrate was kept under constant illumination.

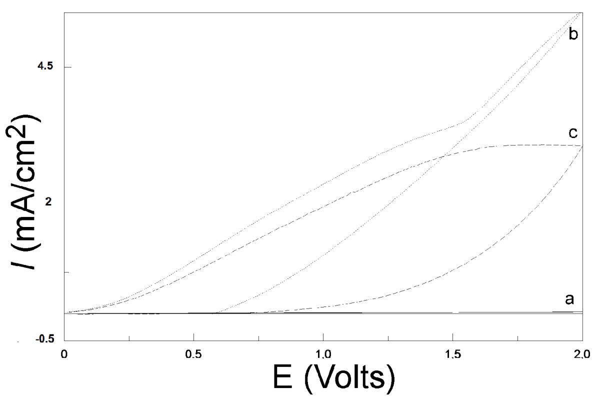

Figure 7: CVs of PEDOT deposition on SiNWs under various conditions. Scan rate: 100 mV/s. (a) 10 mM EDOT with 0.1 M $LiClO_4$ in acetonitrile solution, without illumination; (b) 10 mM EDOT with 0.1 M $LiClO_4$ in acetonitrile solution, under illumination; (c) 0.1 M $LiClO_4$ in acetonitrile solution, under illumination.

The CV measurement in an EDOT-containing solution (Figure 7, curve b) presents a characteristic inflection point at 1.3 V where the EDOT monomer begins to be oxidized and polymerized. After this inflection point, the current density in the EDOT-containing solution is much higher than that measured in the EDOT-free solution (curve c), suggesting that it arises from PEDOT polymerization. The first oxidation current that appears between 0 and 1.3 V in both EDOT-free (curve c) and EDOT-containng solutions (curve b) (absent in the glassy carbon substate, Figure 4) can be related to the oxidation of SiNWs to silica. The absence of the nucleation loop previously observed during the first cycle on vitreous carbon (Figure 4) is noted, and is likely due to this first large oxidation current.

Figure 8 presents two successive cycles corresponding to PEDOT deposition on SiNWs. Several notable differences appear between the two scans. First, the disappearance of the first large peak due to the oxidation of Si in SiO_2 can be observed. This could happen because the PEDOT layer obtained during the first scan already covers the substrate. Also, the small peak around 0.5 V corresponds to the oxidation of the previously reduced PEDOT layer. It can also be observed that polymerization of EDOT in PEDOT is achieved at a lower anodic potential (0.9 V) than previously (1.3 V). Finally, a large decrease in the PEDOT formation current in comparison with that obtained during the first cycle can be observed, likely due to the presence of the insulating silica sublayer.

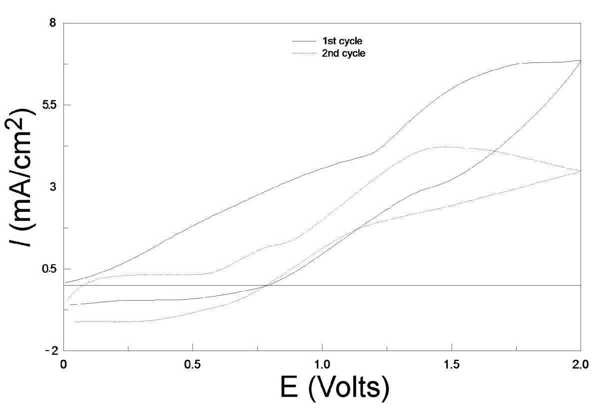

Figure 8: Two successive CVs performed on SiNWs under illumination with 10 mM EDOT and 0.1 M $LiClO_4$ in acetonitrile solution. Scan rate: 100 mV/s.

PEDOT deposition on SiNWs using 1.5 V constant potential

For PEDOT deposition, a constant potential deposition was preferred over cycling in order to avoid a silica layer that was thicker than desired. Indeed, during CV deposition, the oxidation of Si in SiO_2 was observed before the deposition of PEDOT, while at fixed potential, simultaneous Si and EDOT oxidation occurred.

SEM experiments and EDX analysis were then performed on a PEDOT deposit on SiNW substrate (Figure 9a,b). The SiNWs were fabricated using the EMACE method described in the Experimental section. The PEDOT was electrochemically deposited in a potentiostatic manner at a fixed 1.5 V potential for 5 s in a 10 mM EDOT ACN solution with 0.1 M $LiClO_4$.

The SEM image in Figure 9a shows a damaged area which occurred during the cutting of the sample. A continuous film is formed on the top of silicon wires. The presence of S and C in the EDX spectra of Figure 9b proves that the film is primarily PEDOT. The space between the Si nanowires seems not to be filled by the polymer. This is caused by the competition between PEDOT polymerization on the tips and EDOT diffusion from solution to the inner space at the bottom. EDOT monomer that is more highly oxidized is produced in proximity of the tips of silicon wires. This is because the sharper morphology of the wire can lead to a much more intense electric field, resulting in an increase in polymer volume at the tips, and finally producing a mushroom-like morphology. With regards to the expanded polymer blocks of EDOT diffusion into the space, the 2D spread of PEDOT along the wire surface towards the bottom might also be prevented due to the lack of sufficient EDOT monomer.

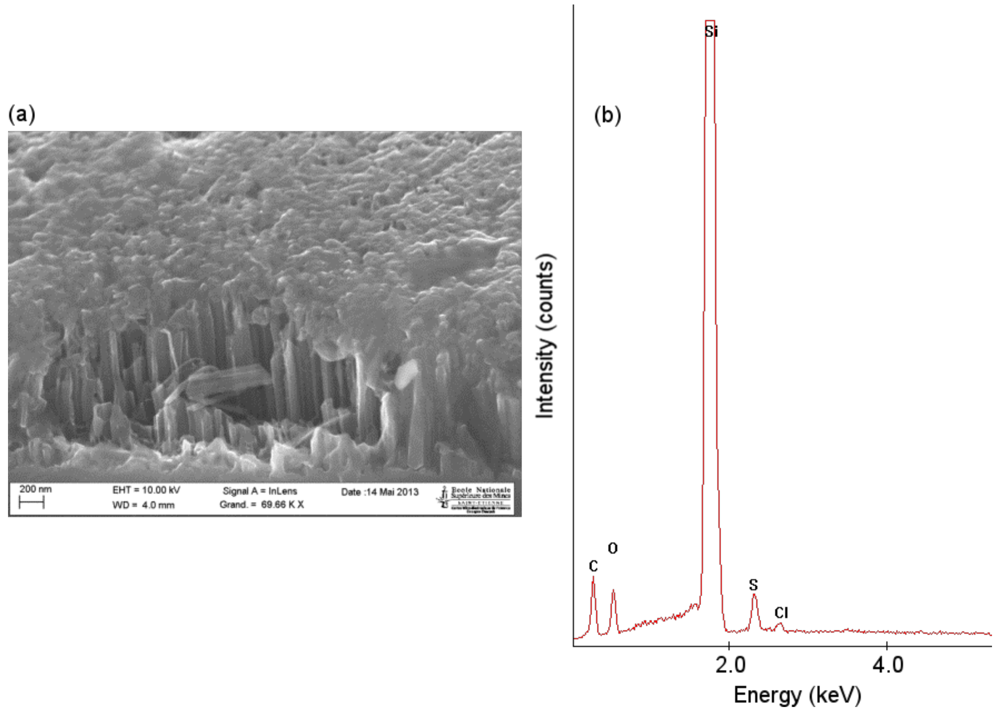

Figure 9: (a) SEM tilted-view of PEDOT covering the top of a SiNW array after 5 s of electrodeposition; (b) corresponding EDX spectrum.

Effect of EDOT diffusion on PEDOT morphology

In order to achieve a conformal deposition, the previously discussed tapering method for the SiNWs was coupled with pulse deposition (5 cycles of 1 s on-time at 1.5 V and 10 s off-time at open circuit potential) in an attempt to force the EDOT oxidation along the entire SiNW. As described in the tapering process, the interspace volume between wires was changed by tuning the tapering durations to 0, 10, 30, and 50 s (see Figure 1). These tapered SiNWs samples were then dipped into the EDOT solution and the pulse method was performed to develop the polymer (see Figure 10a–d). Compared with the shorter tapering times (and therefore, a weaker diffusion effect) in Figure 10a and Figure 10b, the PEDOT films in Figure 10c and Figure 10d are thicker and PEDOT can be seen at the bottom and between wires. In contrast, for the samples presented in Figure 10a and Figure 10b, the space between the wires is very narrow; EDOT molecules cannot diffuse along the wires, and a mushroom-like morphology is obtained.

These results are more evident in Figure 11, which shows high-resolution SEM images for two tapering durations (10 and 30 s). Figure 11a shows a cross section of the 10 s tapered sample, where the PEDOT is mainly concentrated on the top of

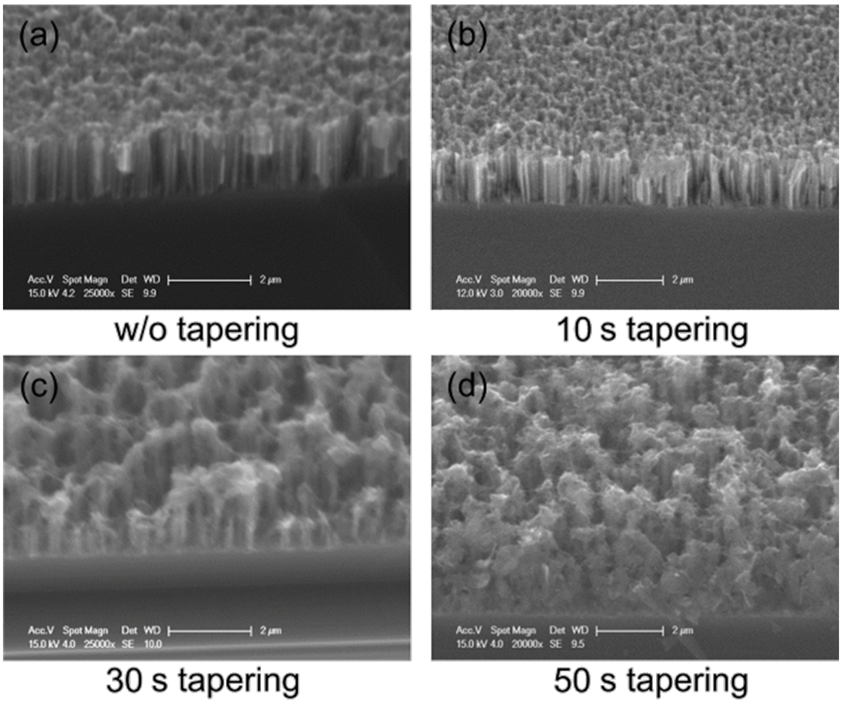

Figure 10: Tilted-view SEM images of SiNWs after PEDOT deposition at 1.5 V pulse deposition with a 10 mM EDOT + 0.1 M $LiClO_4$ in acetonitrile solution (a) without tapering, (b) after 10 s tapering, (c) after 30 s tapering and (d) after 50 s tapering.

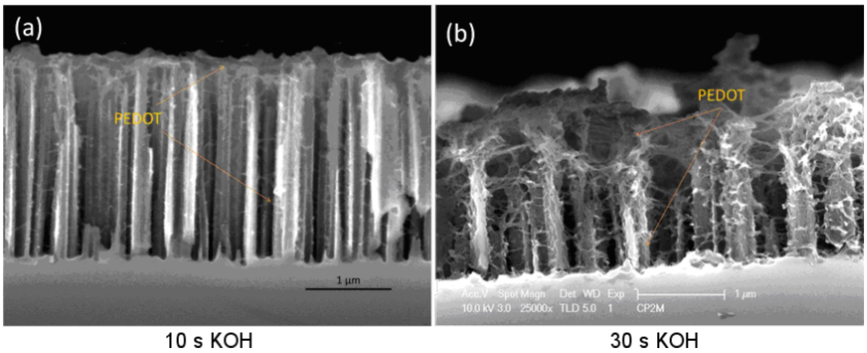

Figure 11: Cross-sectional view of HRSEM images of SiNWs/PEDOT sample after 10 s tapering (a) and 30 s tapering (b).

the wires and only a small amount of PEDOT is formed at the bottom. This leads to an increased roughness of the tubes. However, Figure 11b presents a cross section of the 30 s tapered sample, where the tubes appear to be highly roughened due to the complete wrapping of the PEDOT from the top to the bottom. Moreover, the TEM image in Figure 12 of this 30 s tapered sample further demonstrates that the entire surface of a wire is wrapped with the polymer. The increased space between wires allows more EDOT to diffuse into the bottom space of wires during the electrodeposition and finally leads to a more conformal PEDOT covering layer.

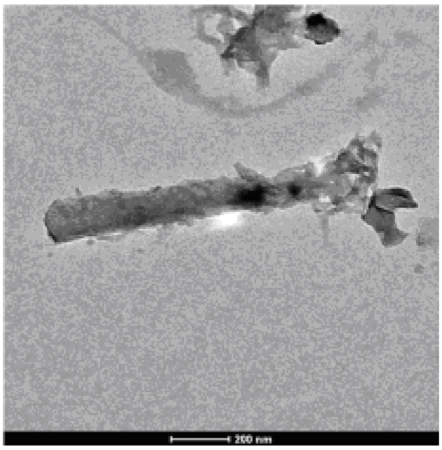

Figure 12: TEM image of a single SiNW/PEDOT after 30 s of tapering (corresponding to the sample in 11b).

The morphology of PEDOT on SiNWs is usually dependent on the synthesis conditions. Path A in Figure 13 identifies a continuous deposition that corresponds to CV or potentiostatic deposition experiments. Path B in Figure 13 corresponds to a stepwise deposition, which favors EDOT monomer diffusion into the space between the wires and thus results in a conformal layer.

Effect of EDOT diffusion on diode quality

We further characterized the two PEDOT/SiNWs diodes with SiNWs tapered for 10 s and 30 s. As can be seen in Figure 14, both the 10 s and 30 s tapered devices show a distinct diode behavior with a constant reverse current–density curve in the negative voltage range. This is an indication that most of the shunt paths for charge transport at reverse voltages are blocked. An extremely large shunt resistance (R_{sh} > 1 M·Ω·cm^2) and a very low leakage current density (J_{lk}, on the order of μA/cm^2) could be realized with this electrochemical method. The R_{sh} is three orders of magnitude higher than that of the reported diodes made by spin coating PEDOT onto SiNWs arrays [27]. This may be attributed to a much more conformal coating and much better adhesion of electrodeposited PEDOT on the Si nanowires. Indeed, it was found that the deposited PEDOT is difficult to remove from the Si surface with a taper because of the strong adhesion to Si.

The ultrahigh shunt resistance is directly related to the morphology of PEDOT surrounding the Si wire. In the current–potential characterization of a SiNWs/PEDOT diode in Figure 14, the R_{sh} and the J_{lk} for the 30 s sample are better than for the 10 s tapered diode. Since the primary shunt path can be formed by a top metal contact directly touching the n-doped Si through the PEDOT layer, a continuous PEDOT layer that sepa-

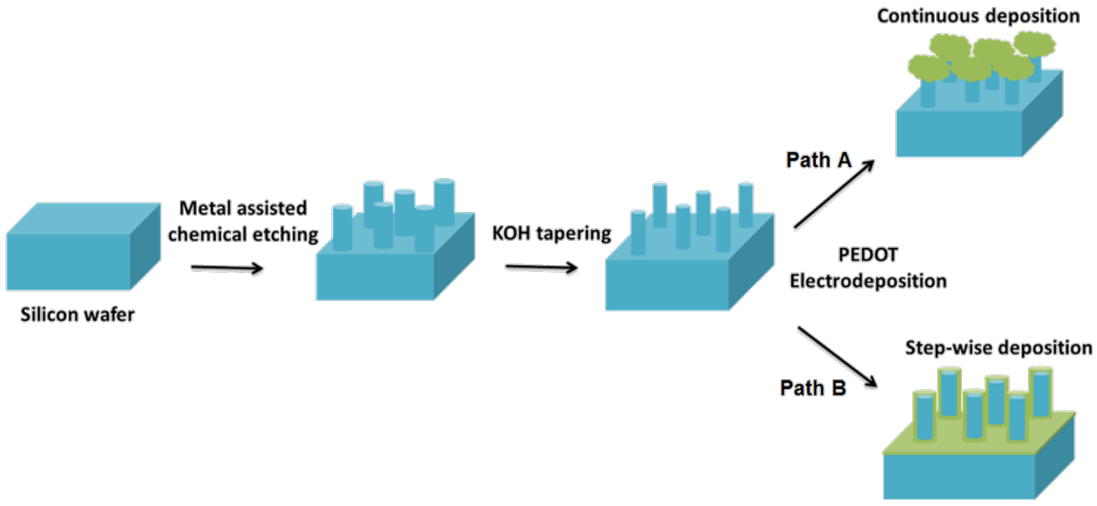

Figure 13: Schematic illustration of the processes resulting in PEDOT/SiNW hybrid structures. (a) Continuous electrodeposition leads to a mushroom-like morphology of PEDOT (green) on the tips of SiNW (blue), while (b) a step-wise deposition aids in the formation of a conformal PEDOT layer (green) surrounding each individual SiNW (blue).

rates n-doped Si from the top contact may prevent charge from tunneling through PEDOT. Therefore, the thicker layer formed after 30 s of tapering reduces the saturation current more than in the case of the 10 s tapered SiNW diode. We note that the forward current density for both diodes is relatively low: this could be due to the PEDOT conductivity, which is currently under study.

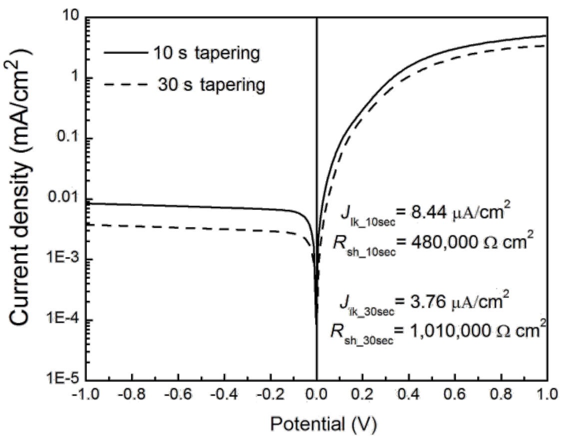

Figure 14: Current–potential characterization of the diodes with SiNW arrays tapered for 10 s (solid line) and 30 s (dashed line).

Conclusion

In the present study, the preparation of a hybrid SiNW/PEDOT material using both chemical and electrochemical methods has been studied. The resulting structures based on silicon nanowires show interesting antireflective properties, with a reflection as low as 2% in the visible spectral range of 400–800 nm. PEDOT electrodeposition was successfully performed on illuminated, n-type SiNWs. The SEM images of the samples reveal that using a continuous deposition technique, the PEDOT layer covers primarily only the top of the Si wires due to the EDOT diffusion which affects the morphology of the polymer film. For a conformal, uniform deposition, pulse techniques were combined with etching of the SiNWs which allowed the monomer to better diffuse along the wires. The main advantage of this approach lies in the simplicity of both the SiNWs and PEDOT, both allowing for efficient and low-cost methods such as chemical etching and electrochemical deposition. To our knowledge, these two processes have never been combined for the production of such a hybrid material.

Experimental

SiNW etching and tapering

Before chemical etching, the Si wafers (phosphorus-doped, <100> oriented, resistivity 1–10 Ω·cm, thickness 255–305 μm) were ultrasonically cleaned for 15 min in acetone and isopropanol. After several rinsing steps in deionized water, the wafers were immersed in piranha solution (H_2SO_4:H_2O_2 3:1 v/v) and subsequently in deionized water for 15 min.

The EMACE technique is described in the literature [28] and is presented briefly here. During the Ag plating step (Step 1), the Si wafers were immersed into an aqueous solution of 4.8 M HF and 4 mM $AgNO_3$ for 1 min. During the SiNW etching step (Step 2), the Ag-plated wafer was transferred to another solution of 0.3 M H_2O_2 and 4.8 M HF. The Ag network acts as a catalyst for the SiNWs etching, which was carried out for 2 min. The Ag catalyst was finally (Step 3) dissolved by immersion into 69% HNO_3 for 30 min. The chemical reactions associated to each step are the following:

Step 1: $4Ag^+ + Si + 6F^- \rightarrow 4Ag + SiF_6^{2-}$

Step 2: $2H_2O_2 + 4H^+ + Si + 6F^- \rightarrow 4H_2O + SiF_6^{2-}$

Step 3: $3Ag + NO_3^- + 4H^+ \rightarrow 3Ag^+ + NO + 2H_2O$

A tapering process was used to increase the EDOT diffusion by increasing the space between wires. The etched SiNWs were immersed into a KOH aqueous solution containing isopropyl alcohol (IPA) (31.2 g KOH + 25 mL IPA in 100 mL deionized water) for 10, 30 and 50 s. The addition of IPA was used to reduce the tapering rate [29].

Core–shell structure realization

The PEDOT deposition was conducted in an electrochemical cell with a three-electrode configuration. The reference electrode was Ag/AgCl and the counter electrode was a platinum plate. All the potentials were indicated versus the Ag/AgCl reference electrode ($E_{Ag/AgCl}$ = 0.192 V/SHE). A disc of vitreous carbon or the n-type SiNW array was set as the working electrode. For the latter, an illumination source consisting of a 150 W halogen lamp was used during the PEDOT polymerization to render the n-type Si substrate conductive in the anodic area. The deposition was controlled by a Solartron SI 1287 with a computer running CorrWare software.

A non-aqueous medium was preferred over the classical sodium polystyrene sulfonate (NaPSS) aqueous environment in order to avoid the important silicon oxidation during PEDOT deposition. An EDOT solution containing 10 mM EDOT and 0.1 M $LiClO_4$ in anhydrous acetonitrile was used.

During the CV measurements, the potential scan was varied linearly in time in the direction from the cathodic to the anodic region, then the potential sweep was reversed to the beginning.

This ramp in potential was repeated several times. The scan rate was 100 mV/s.

The deposit was first realized using a continuous deposition mode with a constant 1.5 V potential for 5 s. The pulse deposition technique was also used with the aim to improve the coverage of the nanowires with the polymer. The pulses consisted of 5 cycles of 1 s on-time at 1.5 V and 10 s off-time where the system was held at its open circuit potential. The total duration for the PEDOT deposition was the same (5 s) as that used for the continuous deposition technique.

After electrodeposition, the PEDOT on SiNW sample was rinsed with acetonitrile several times to remove excess EDOT monomer. The PEDOT/SiNWs sample was rinsed thoroughly with ethanol and then dried with an air stream.

Characterization methods

The spectrophotometric measurements were performed with an integrating sphere provided by Sphereoptics. The SEM images and EDX spectroscopy were recorded with a Philips XL ESEM. The TEM observations were made with a TECNAÏ G20 instrument. Reflection FTIR spectra of PEDOT thin films were obtained using a VERTEX 70 spectrophotometer. Current–potential curves were measured using a Keithley 2400 instrument in a dark environment.

Acknowledgements

The authors would like to gratefully acknowledge the financial support from the research project between the Chinese Scholarship Council (CSC) and the Ecoles Centrale of Lille, Lyon, Marseille, Nantes, and Paris.

References

1. Garnett, E. C.; Brongersma, M. L.; Cui, Y.; McGehee, M. D. *Annu. Rev. Mater. Res.* **2011,** *41,* 269–295. doi:10.1146/annurev-matsci-062910-100434
2. Chan, C. K.; Peng, H.; Liu, G.; McIlwrath, K.; Zhang, X. F.; Huggins, R. A.; Cui, Y. *Nat. Nanotechnol.* **2008,** *3,* 31–35. doi:10.1038/nnano.2007.411
3. Hochbaum, A. I.; Yang, P. *Chem. Rev.* **2010,** *110,* 527–546. doi:10.1021/cr900075v
4. Li, Y.; Qian, F.; Xiang, J.; Lieber, C. M. *Mater. Today* **2006,** *9,* 18–27. doi:10.1016/S1369-7021(06)71650-9
5. Garnett, E.; Yang, P. *Nano Lett.* **2010,** *10,* 1082–1087. doi:10.1021/nl100161z
6. Brönstrup, G.; Jahr, N.; Leiterer, C.; Csáki, A.; Fritzsche, W.; Christiansen, S. *ACS Nano* **2010,** *4,* 7113–7122. doi:10.1021/nn101076t
7. Hu, L.; Chen, G. *Nano Lett.* **2007,** *7,* 3249–3252. doi:10.1021/nl071018b
8. Ozdemir, B.; Kulekci, M.; Turan, R.; Unalan, H. E. *Nanotechnology* **2011,** *22,* 155606. doi:10.1088/0957-4484/22/15/155606
9. Kayes, B. M.; Atwater, H. A.; Lewis, N. S. *J. Appl. Phys.* **2005,** *97,* 114302. doi:10.1063/1.1901835
10. Tian, B.; Zheng, X.; Kempa, T. J.; Fang, Y.; Yu, N.; Yu, G. *Nature* **2007,** *449,* 885–889. doi:10.1038/nature06181
11. Tsakalakos, L.; Balch, J.; Fronheiser, J.; Korevaar, B.; Sulima, O.; Rand, J. *Appl. Phys. Lett.* **2007,** *91,* 233117. doi:10.1063/1.2821113
12. Jia, G.; Steglich, M.; Sill, I.; Falk, F. *Sol. Energy Mater. Sol. Cells* **2012,** *96,* 226–230. doi:10.1016/j.solmat.2011.09.062
13. Hwang, J.; Kao, M.; Shiu, J.; Fan, C.; Ye, S.; Yu, W. *J. Phys. Chem. C* **2011,** *115,* 21981–21986. doi:10.1021/jp205151d
14. Jung, J.-Y.; Guo, Z.; Jee, S.-W.; Um, H.-D.; Park, K.-T.; Hyun, M. S. *Nanotechnology* **2010,** *21,* 445303. doi:10.1088/0957-4484/21/44/445303
15. Bai, F.; Li, M.; Huang, R.; Li, Y.; Trevor, M.; Musselman, K. *RSC Adv.* **2014,** *4,* 1794–1798. doi:10.1039/c3ra45473h
16. He, L.; Jiang, C.; Wang, H. *IEEE Electron Device Lett.* **2011,** *32,* 1406–1408. doi:10.1109/LED.2011.2162222
17. Döbbelin, M.; Tena-Zaera, R.; Carrasco, P. M.; Sarasua, J.-R.; Cabañero, G.; Mecerreyes, D. *J. Polym. Sci., Part A: Polym. Chem.* **2010,** *48,* 4648–4653. doi:10.1002/pola.24251
18. Dehaudt, J.; Beouch, L.; Peralta, S.; Plesse, C.; Aubert, P.-H.; Chevrot, C. *Thin Solid Films* **2011,** *519,* 1876–1881. doi:10.1016/j.tsf.2010.10.052
19. Mariani, G.; Wang, Y.; Wong, P.-S.; Lech, A.; Hung, C.-H.; Shapiro, J. *Nano Lett.* **2012,** *12,* 3581–3586. doi:10.1021/nl301251q
20. Xiao, R.; Il Cho, S.; Liu, R.; Lee, S. B. *J. Am. Chem. Soc.* **2007,** *129,* 4483–4489. doi:10.1021/ja068924v
21. Yao, Y.; Liu, N.; McDowell, M.; Pasta, M.; Cui, Y. *Energy Environ. Sci.* **2012,** *5,* 7927–7930. doi:10.1039/c2ee21437g
22. Kim, Y.; Baek, J.; Kim, M.-H.; Choi, H.-J.; Kim, E. *Ultramicroscopy* **2008,** *108,* 1224–1227. doi:10.1016/j.ultramic.2008.04.054
23. Kirchmeyer, S.; Reuter, K. *J. Mater. Chem.* **2005,** *15,* 2077–2088. doi:10.1039/b417803n
24. Randriamahazaka, H.; Noel, V.; Chevrot, C. *J. Electroanal. Chem.* **1999,** *472,* 103–111. doi:10.1016/S0022-0728(99)00258-2
25. Rodriguez-Moreno, J.; Navarrete-Astorga, E.; Martín, F.; Schrebler, R.; Ramos-Barrado, J. R.; Dalchiele, E. A. *Thin Solid Films* **2012,** *525,* 88–92. doi:10.1016/j.tsf.2012.10.067
26. Kvarnström, C.; Neugebauer, H.; Blomquist, S.; Ahonen, H. J.; Kankare, J.; Ivaska, A. *Electrochim. Acta* **1999,** *44,* 2739–2750. doi:10.1016/S0013-4686(98)00405-8
27. Jeong, S.; Garnett, E. C.; Wang, S.; Yu, Z.; Fan, S.; Brongersma, M. L. *Nano Lett.* **2012,** *12,* 2971–2976. doi:10.1021/nl300713x
28. Huang, Z.; Geyer, N.; Liu, L.; Li, M.; Zhong, P. *Nanotechnology* **2010,** *21,* 465301. doi:10.1088/0957-4484/21/46/465301
29. Seidel, H.; Csepregi, L.; Heuberger, A.; Baumgärtel, H. *J. Electrochem. Soc.* **1990,** *137,* 3612–3626. doi:10.1149/1.2086277

License and Terms

The definitive version of this article is the electronic one which can be found at:
doi:10.3762/bjnano.6.65

BEILSTEIN JOURNAL OF NANOTECHNOLOGY

Manipulation of magnetic vortex parameters in disk-on-disk nanostructures with various geometry

Maxim E. Stebliy, Alexander G. Kolesnikov, Alexey V. Ognev*, Alexander S. Samardak and Ludmila A. Chebotkevich

Full Research Paper

Open Access

Address:
Laboratory of Thin Film Technologies, School of Natural Sciences,
Far Eastern Federal University, Vladivostok 690950, Russia

Email:
Alexey V. Ognev* - ognevav@gmail.com

* Corresponding author

Keywords:
hysteresis; magnetic vortex; magnetization reversal; micromagnetic structure

Beilstein J. Nanotechnol. **2015,** *6,* 697–703.
doi:10.3762/bjnano.6.70

Received: 17 September 2014
Accepted: 09 February 2015
Published: 10 March 2015

This article is part of the Thematic Series "Self-assembly of nanostructures and nanomaterials".

Guest Editor: I. Berbezier

Abstract

Magnetic nanostructures in the form of a sandwich consisting of two permalloy (Py) disks with diameters of 600 and 200 nm separated by a nonmagnetic interlayer are studied. Magnetization reversal of the disk-on-disk nanostructures depends on the distance between centers of the small and big disks and on orientation of an external magnetic field applied during measurements. It is found that manipulation of the magnetic vortex chirality and the trajectory of the vortex core in the big disk is only possible in asymmetric nanostructures. Experimentally studied peculiarities of a motion path of the vortex core and vortex parameters by the magneto-optical Kerr effect (MOKE) magnetometer are supported by the magnetic force microscopy imaging and micromagnetic simulations.

Introduction

Magnetic nanostructures have a wide range of unique properties that facilitate their practical implementation in real functional devices. For instance, magnetoresistive memory is used in aviation systems requiring the high reliability, nonvolatility and data write/read rate. Nanomagnets with stable and controllable spin configurations can be used to produce the magnetic logic elements. However, micromagnetic stability decreases with the reduction of the size of a nanomagnet resulting in a lack of controllability the spin configurations [1]. Therefore, the development of reliable methods for the manipulation of micromagnetic structures in nanomagnets is an important topic not only for fundamental physics, but mostly for high-tech sectors of economics including electronics, data storage and sensor technologies.

Nanomagnets in the shape of disks attract huge scientific attention, because of the possibility to realize the four stable magnetic vortex states with different combinations of polarity and chirality [2]. Polarity (up or down out-of-plane component of magnetization in the central core of the vortex state) can be controlled by an external magnetic field aligned perpendicular to a disk plane. This method is complicated to be used for microelectronic applications due to the high value of an applied field (usually, larger than 1 kOe [3]).

The in-plane component of the vortex state is characterized by the clockwise (CW) or counterclockwise (CCW) magnetization rotation or chirality. The majority of methods of chirality manipulation are based on an application of magnetic asymmetry in disks through cutting of a part of the disk, forming of a hole or producing a magnetization gradient [4-7]. However, the modified shape or magnetization asymmetry of a disk results in significant changes in the values of vortex nucleation and annihilation fields. Moreover, the trajectory of a vortex core is distorted and its gyrotropic motion frequency changes significantly.

Recently, by using magnetic force microscopy (MFM), we have demonstrated a reliable method to control the vortex parameters in a big disk if a disk with smaller diameter is placed on its top [8]. In this paper, we present results of the impact of the small disk position relative to a symmetry axis of the “small disk on big disk” nanostructure. By using a measurement method based on the magneto-optical Kerr effect (MOKE), the vortex chirality in disks has been reliably defined. Peculiarities of the vortex nucleation process as well as the vortex core trajectory under an impact of bias fields have been observed. Experimental findings have been interpreted by micromagnetic simulations [9].

Results and Discussion

Figure 1a shows scanning electron microscopy (SEM) images of disk-on-disk nanostructures with different distances between its centers, s, which range from 0 (small disk in the center) to 230 nm (small disk at the edge of big disk). We have experimentally studied the effect of the orientation of the disk-on-disk nanostructure relatively to an external magnetic field on the magnetization reversal in dependence on s. The angle φ, defining the orientation of an applied magnetic field, was counted from the selected x-axis, passing through the centers of the disks. The results are shown in Figure 1b. It was found that the magnetization reversal changes qualitatively. For symmetric nanostructures with $s = 0$ the M–H curve is anhysteretic (Figure 1c, loop s_0^0) and its shape does not depend on the orientation of the external field (Figure 1b). In asymmetric nanostructures ($s \neq 0$) the angular dependence is strongly uniaxial with the maxima at 90° and −90°: $M_r/M_s > 0$ (where M_r is the remanence and M_s is the saturation magnetization) and the hysteresis loop is open (Figure 1c, loop s_{170}^{90}). There are two local maxima at $\varphi = 0$ and 180° surrounded by two minima, Figure 1b. In the field, aligned at an angles 0 and 180°, the hysteresis loop has an inverted shape, i.e., $M_r/M_s < 0$. The maximum change of M_r/M_s was observed in nanostructures with $s = 170$ nm.

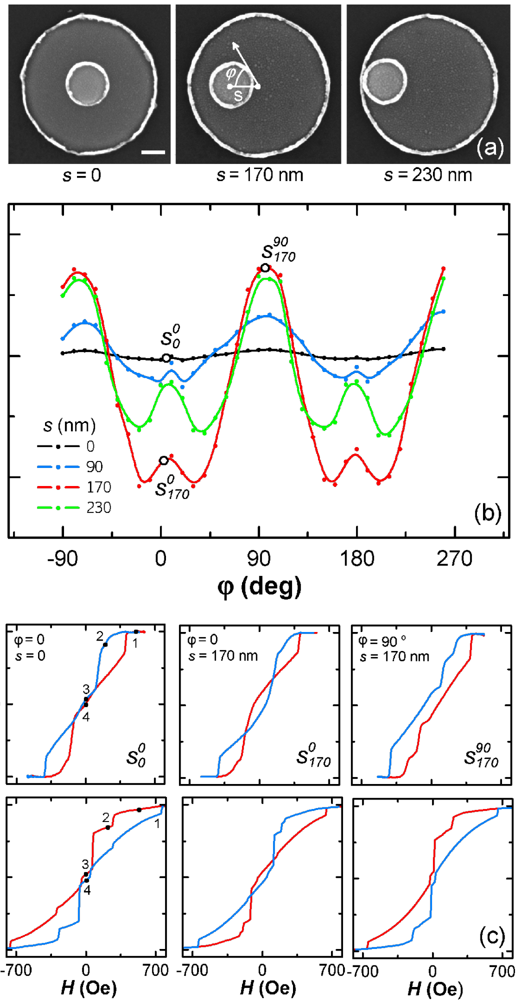

Figure 1: (a) SEM images of the disk-on-disk nanostructure with s = 0, 170 and 230 nm; (b) Dependence of M_r/M_s on the magnetic field orientation relatively to the x-axis; (c) experimental (upper row) and simulated (bottom row) hysteresis loops for following cases: (i) s = 0 and φ = 0, (ii) s = 170 nm and φ = 0, (iii) s = 170 nm and φ = 90°.

To understand the physics of magnetization reversal in disk-on-disk nanostructures, micromagnetic simulations and MFM measurements were conducted. Calculated hysteresis loops are shown in the bottom row of Figure 1c. As can be observed seen, the shapes of the loops, as well as the critical fields, are in a good agreement with the experimental data presented in the upper row of Figure 1c. There are several areas with a sharp jump in magnetization at values of H of about 150 and 230 Oe.

Magnetic properties of symmetric nanostructures

Let us consider the magnetization reversal in a case when $s = 0$. Figure 2 shows the results of MFM study and calculated spin configurations at magnetic fields marked with numbers in the hysteresis loop (Figure 1c, loop s_0^0). With the reduction of the external field from the positive saturation, H_s (point 1), the disk-on-disk system turns from a homogeneous magnetic state into the state with antiparallel magnetization due to the magnetization switching in the small disk (point 2). As can be observed, there is a step in the hysteresis loop. With further decrease of the field the magnetic vortex emerges in the big disk, meanwhile the "C-shape" state is formed in the small disk (point 3). If the external field is increased from negative saturation, $-H_s$, the magnetization reversal does not change qualitatively, but at $H = 0$ (point 4 in Figure 1c) the magnetization in the small disk becomes opposite to the field orientation. Vortex chirality switches from CW to CCW direction (Figure 2, case 4). There is an intercoupling between the vortex chirality in the big disk and the magnetization in the small disk. If in the small disk the "C-shape" state has CCW chirality, than the big disk will have CW chirality, and vice versa. Thus, applying a positive or negative field along φ = 0, one could control the vortex chirality in the big disk. However, in a symmetric disk-on-disk system the formation of "C-shape" state in the small disk and the vortex nucleation in the big disk are equally probable. Therefore, it is impossible to reliably control the chirality in the big disk.

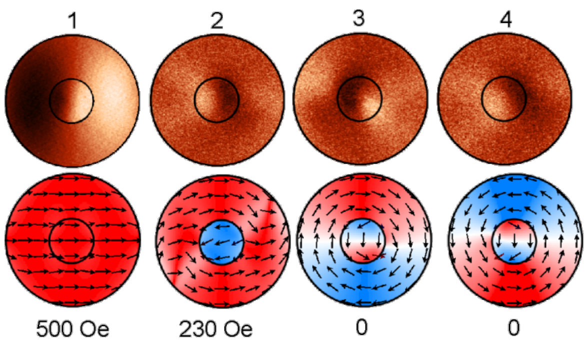

Figure 2: MFM images of magnetic structure (upper row) and corresponding spin configurations (bottom row) in the field oriented at φ = 0.

Magnetic properties of asymmetric nanostructures

In the case of asymmetric nanostructures with $s \neq 0$, the magnetization reversal depends on the orientation of the field relatively to the direction of s. (Figure 1c, loops s_{170}^0 and s_{170}^{90}). The MFM study showed that the magnetization reversal is similar to the processes in a symmetric structure: The single-domain state forms in the small disk, and the vortex forms in the big disk. However, there are some features caused by asymmetry.

Remagnetization in the magnetic field at φ ≈ 0

Let us consider the case in which the field H_x is applied at an angle φ ≈ 0, i.e., directed along the selected x-axis. MFM contrast, formed by the single-domain state of the small disk, dominates over the weak contrast of the vortex state in the big disk. Therefore, to analyze the MFM data, micromagnetic simulations of spin configurations were used (Figure 3). At saturation (H_s > 500 Oe) disks are in single-domain states with collinear orientation of magnetization. At a field of H ≈ 230 Oe the small disk is in single-domain state with the magnetization, oriented antiparallel to the magnetization in the big disk. In the field H ≈ 150 Oe the vortex nucleates at the edge of the big disk. With the decrease of the field down to zero the vortex core is shifted to the center of the disk. With the rise of negative fields, the vortex core is shifted to the lower edge of the disk and then it annihilates.

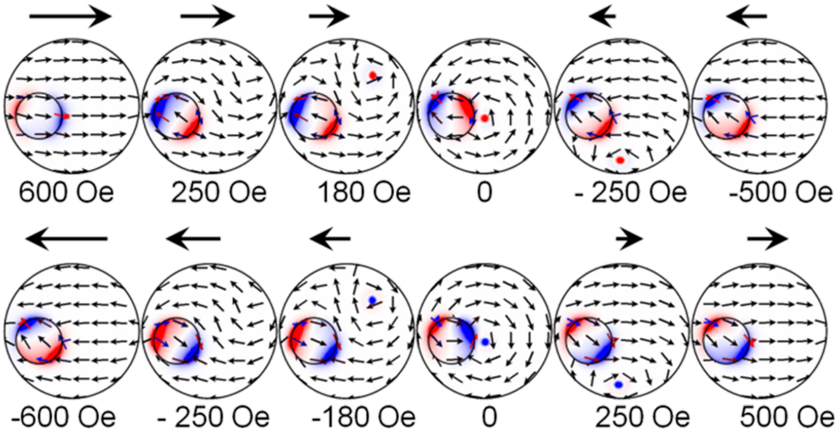

Figure 3: Spin configurations realized in the disk-on-disk nanostructure in dependence on an external magnetic field H applied at φ ≈ 0.

If the magnetization reversal of the disk-on-disk nanostructure in the fields ranging from $-H_s$ to $+H_s$ is analyzed, the quality of the reversal process does not change. But at $H = 0$, the magnetization in the small disk is oriented in the direction opposite to the field. The chirality of the vortex is reversed and becomes rotated clockwise. The asymmetric structure enables one to control the magnetic vortex chirality in the big disk through the orientation of the magnetic field. How to use the magneto-optical Kerr effect to define the magnetic vortex chirality in the disk-on-disk nanostructure will be discussed below.

According to the micromagnetic simulations, the vortex nucleates in the same place of the big disk, regardless of the orientation of H_x. Then the vortex core along a path that does not intersect the small disk (see inset in Figure 4a). As can be observed, there are no steps in the hysteresis loop due to the magnetostatic interaction of the small disk and the vortex core. Applying the constant magnetic field H_y perpendicular to the *s* direction (i.e., along the *y*-axis), the vortex-core trajectory changes. The direction of displacement of the vortex core depends on its chirality. The outline of this process is shown in the inset of Figure 4c and Figure 4d. In the case of CCW chirality (Figure 4c), the vortex core is deflected to the small disk. Passing under the small disk, the vortex core interacts with it. This affects the magnetic hysteresis loop in which a characteristic step appears. If the chirality has CW rotation, the vortex core is deflected to the right side without any interaction with the small disk (Figure 4d).

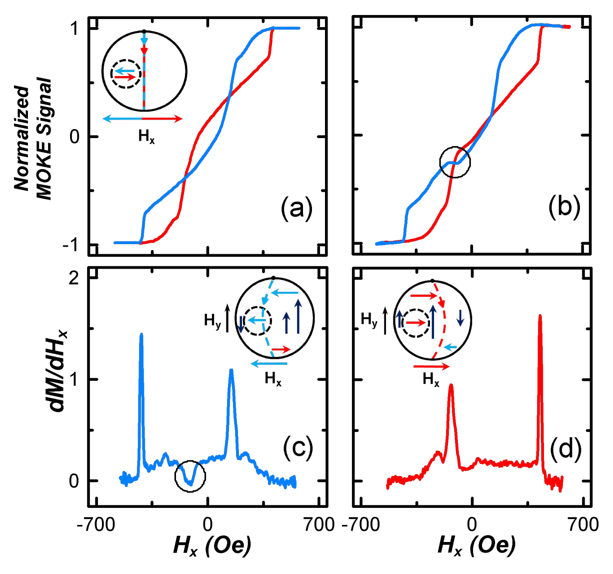

Figure 4: Hysteresis loops corresponding to the magnetization reversal of the disk-on-disk nanostructure without (a) and with bias field H_y (b). (c,d) The first derivative curves dM/dH_x defined for different branches of the hysteresis loop with bias field H_y. Insets show the trajectory of the vortex core motion with the magnetization reversal without (a) and with bias field H_y (c,d). Insets illustrate the schematic view of trajectories of the vortex core in dependence on the applied magnetic fields.

Figure 4 shows the magnetic hysteresis loops measured only in the field H_x (Figure 4a) and in the presence of a bias field H_y (Figure 4b). As can be observed, the loop becomes asymmetric under impact of H_y. During magnetization reversal in the fields from $+H_s$ to $-H_s$ (blue curve) ranging from −86 to −146 Oe, a typical step, characterized by a constant magnetization in dependence on the field magnitude, appears in the loop. In the dM/dH_x curve, shown in Figure 4c, the change of the magnetization velocity is zero matching the pinning of the vortex core by the small disk (marked by the circle). The shifted trajectory of the vortex core is shown in the inset in Figure 4c. There is no step on the return curve (when the field changing from $-H_s$ to $+H_s$) due to a vortex core pinning, because the core is moving away from the small disk (see the inset in Figure 4d). The velocity of the vortex in the fields ranging from 20 to 350 Oe is almost constant (Figure 4d). The preservation of the loop asymmetry during multiple magnetization reversals shows that if the field is changed from $+H_s$ to $-H_s$, the vortex chirality exhibits only CCW rotation, and from $-H_s$ to $+H_s$ the chirality is rotated clockwise.

Remagnetization in magnetic field at φ ≈ 90°

Let us consider a case in which the magnetic field is oriented perpendicular to the *s*-direction, i.e., $\varphi \approx 90°$. MOKE results and calculated loops for this case are shown in Figure 1c. Micromagnetic simulations (Figure 5) and MFM data point out that the magnetizations of the small and big disks at saturation are oriented along the applied field direction. With the field is reduced down to 300 Oe, the single-domain state switches in the small disk leading to an antiparallel alignment of the magnetic moments in adjacent layers (AP state). This change of the magnetic state causes the first step in the hysteresis loop. Then, the vortex with CCW chirality nucleates in the big disk from the small disk side. When the magnetic field is decreased to zero, the vortex core is shifted to the center of the small disk. This is reflected in a relative small change of the magnetization in the field ranging from H_n to 0. At $H = 0$ the vortex core is shifted from the disk center, so the remanence is positive (no inversion as in the previous case). In the negative fields the vortex core gets out from under the small disk, moves through the center of the disk to the edge and then annihilates.

When the magnetization reversal occurs under a field between $-H_s$ and 0, the magnetization of the small disk is directed opposite to the field. The vortex in the big disk also nucleates from the side of the small disk, but the vortex chirality in the big disk changes and the magnetization vector rotates clockwise. Thus, because of the asymmetry of the magnetization distribution in

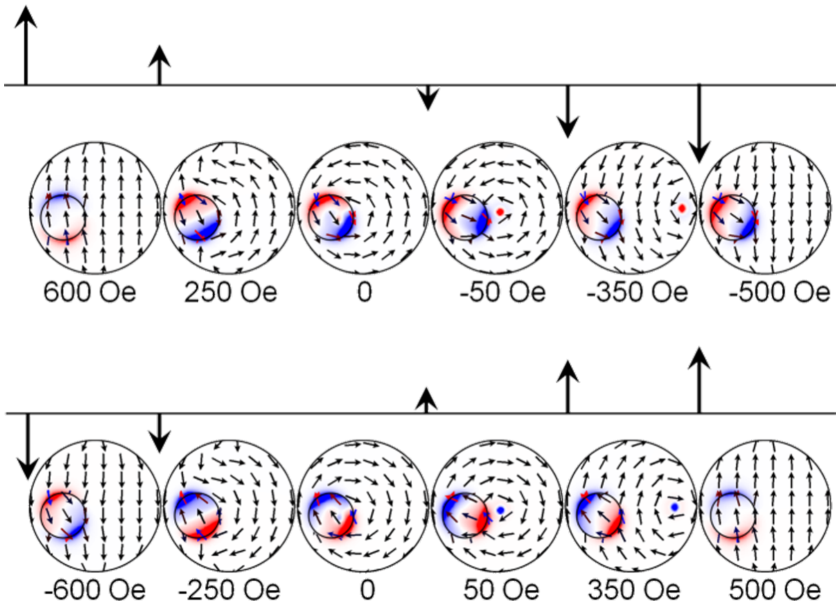

Figure 5: Spin configurations in the disk-on-disk nanostructure during the magnetization reversal under the applied magnetic field *H* oriented at φ ≈ 90°.

the nanostructure, the vortex chirality depends on the direction of an applied magnetic field, and the vortex nucleation always occurs on the side of the small disk and does not depend on the field orientation.

For experimental verification of the vortex chirality and trajectory of the core movement, MOKE measurements were used. The results are shown in Figure 6. The local magnetization loop in the field ranging from +500 to −50 Oe was measured. The M/M_S curve (blue line) in the field ranging from +500 to −50 Oe matches the full hysteresis loop (black line). The reverse curve (red line) in the range from −50 to +500 Oe differs from the reverse branch of the hysteresis loop.

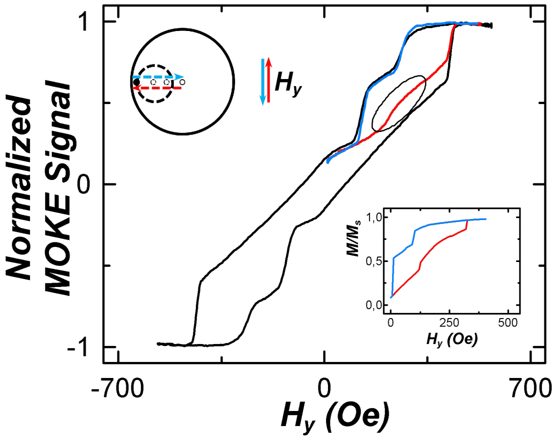

Figure 6: Hysteresis loops measured under a field ranging from +500 to −500 Oe (black line), as well as under an asymmetric field changing from +500 to −50 Oe (colored lines). Insets represent the schematic view of trajectories of the vortex core (top) and the result of micromagnetic simulations of the hysteresis loop (bottom).

Results of the micromagnetic simulations show that in fields changing from +500 to −50 Oe, the transition of the spin configuration is the same as in Figure 5. Vortex nucleates under the small disk with the following core movement to the center of the big disk (blue arrow in the upper insert in Figure 6). When the field switches to the opposite direction (from −50 to +500 Oe), the core is moving to the nucleation site where the vortex annihilates (red arrow in the upper inset in Figure 6). Passing under the small disk, the vortex core interacts with its magnetic poles. This is reflected in the simulated hysteresis loop in the form of a step (red curve in the lower inset in the Figure 6). This step is seen in the experimental local loop (marked by the oval on the red curve). A similar dependence is observed when the field is changing from −500 to 50 Oe.

Thus, when the field H is directed at φ ≈ 90°, the vortex nucleates only under the small disk, and the orientation of the single-domain state in the small disk and the vortex chirality in the big disk depend on the direction of the external magnetic field [8].

It is clear that one can control the vortex chirality in the big disk by changing the direction of an external magnetic field. However, it is crucial to the break the symmetry of the system with respect to chirality. That is why in case of symmetric nanostructures the chirality control is impossible. In the asymmetric nanostructure, the inhomogeneous magnetostatic field is induced between the small disk in single-domain state or “C-shape” state and the big disk. This leads to a breaking of the circular symmetry and, consequently, gives an opportunity to control the chirality and nucleation point of the vortex.

Figure 7 shows the scheme of the location of vortex nucleation sites depending on the direction of an external field for nanostructures with s = 170 nm. To construct the scheme the experimental data $M_r/M_s = f(\varphi)$ (see Figure 1a), and the micromagnetic simulation results were used. When $M_r/M_s < 0$, the magnetic field is applied under an angle from 70 to −70° (indicated by the blue arrow in Figure 7) and the vortex nucleation sites are located in the blue sectors, being perpendicular to the field orientation (marked with blue points in the scheme). Here, for a vortex nucleation in the upper and lower sectors, the field H has to be directed at $\varphi > 0$ and $\varphi < 0$, correspondingly. As seen in Figure 3, the nanostructure is slightly turned at the angle $\varphi = 5°$ and the vortex nucleates in the upper sector. As for this direction of the field the vortex nucleation site is constant, the variation of the field from $+H_s$ to 0 or from 0 to $-H_s$ leads to a controlled change of the vortex chirality: CCW or CW, respectively. If apply the field is applied at $\varphi = 0$, which is difficult to implement experimentally, the probability of vortex nucleation in the upper and lower sectors is equal and the chirality control fails.

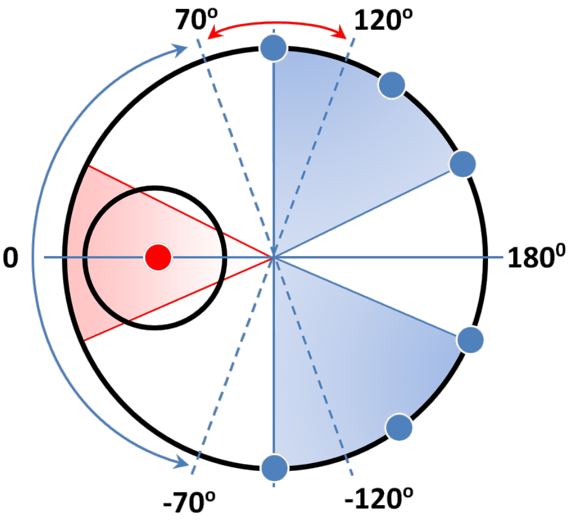

Figure 7: Scheme explaining the interplay between the orientation of an external magnetic field (angles are marked by the blue and red arrows) and location of the vortex nucleation sites in the big disk (blue and red points).

If $M_r/M_s > 0$, the field has to be applied at an angle between 70 and 120° (the range indicated by the red arrow in Figure 7). In this case, the vortex nucleation site is located only in the red sector. The micromagnetic calculations show that for the given configuration of the magnetic field, the vortex nucleation is energetically favorable under the small disk (marked with the red point in the scheme). This fact has been confirmed experimentally by MOKE measurements (see Figure 6). To control the chirality of the vortex, as in the case discussed above, the field has to be applied at an angle different from 90°. For example, Figure 5 shows the simulation results for the case in which H is oriented at $\varphi = 95°$. Then for a magnetization reversal from $+H_s$ to 0, the vortex has a CCW chirality, and from $-H_s$ to 0 it has CW chirality.

Conclusion

The magnetic behavior of disk-on-disk nanostructures with various geometries is demonstrated. The magnetization reversal of disk nanostructures depends on the distance between the centers of the small and big disks as well as on the orientation of an applied magnetic field. The inverted character of hysteresis loops in the case of an asymmetric geometry of the disk-on disk nanostructures was found. Maximum inversion of the remanence value was observed for s = 170 nm. It is shown that at remanence the big disk has the vortex configuration, meanwhile the small disk is in the single-domain state. The reliable control of spin configurations in the disks at remanence can be uniquely specified by the orientation of the external magnetic field. The formation of stable vortex configurations with a desired chirality was experimentally demonstrated. Our study shows that the vortex chirality in the asymmetric disk-on-disk nanostructures can be explicitly defined by MOKE measurements. Our findings open new opportunities for practical implementation of the vortex-based devices such as memory cells [10] and ternary logic elements [11].

Experimental

The experimental study was conducted for disk-on-disk nanostructures consisting of two permalloy (Py or $Ni_{80}Fe_{20}$) nanodisks with a thickness of 35 nm. The big (bottom) and small (upper) disks with diameters of 600 and 200 nm, respectively, were separated by a 3 nm thick Cu interlayer. The nanostructures were fabricated on naturally oxidized Si(111) substrates by means of electron-beam lithography, magnetron sputtering and standard lift-off process. Geometry and surface roughness were checked with scanning electron (SEM, Supra, Carl Zeiss) and atomic force (AFM, Ntegra Aura, NT-MDT) microscopes. Magnetic properties were studied by using a magneto-optical Kerr effect (MOKE, NanoMOKE II) magnetometer and a magnetic force microscope (MFM, Ntegra Aura, NT-MDT). Micromagnetic simulations were performed by using OOMMF software [9] with standard parameters for Py: M_s = 860 Gs, exchange stiffness $A = 1.38 \cdot 10^6$ erg/cm, damping factor α = 0.05 [11]. The magnetic anisotropy was chosen zero in order not to insert an asymmetry of magnetic properties into the system. Dimension of the simulated disk-on-disk nanostructure matched the experimental sample. Cell size was taken as $3 \times 3 \times 35$ nm^3.

Acknowledgements

This study was supported by the Russian Ministry of Education and Science (Contracts 14.575.21.0039 (RFMEFI57514X0039) and NIR 559), Russian Foundation for Basic Research (15-02-05302/15) and Far Eastern Federal University.

References

1. Coffey, W. T.; Kalmykov, Y. P. *J. Appl. Phys.* **2012,** *112,* 121301. doi:10.1063/1.4754272
2. Guslienko, K. Yu.; Novosad, V.; Otani, Y.; Shima, H.; Fukamichi, K. *Phys. Rev. B* **2001,** *65,* 024414. doi:10.1103/PhysRevB.65.024414
3. Kikuchi, N.; Okamoto, S.; Kitakami, O.; Shimada, Y.; Kim, S. G.; Otani, Y.; Fukamichi, K. *J. Appl. Phys.* **2001,** *90,* 6548. doi:10.1063/1.1416132
4. Zhong, Z.; Zhang, H.; Tang, X.; Jing, Y.; Jia, L.; Liu, S. *J. Magn. Magn. Mater.* **2009,** *321,* 2345–2349. doi:10.1016/j.jmmm.2009.02.030
5. Dumas, R. K.; Gredig, T.; Li, C.-P.; Schuller, I. K.; Liu, K. *Phys. Rev. B* **2009,** *80,* 014416. doi:10.1103/PhysRevB.80.014416
6. Cambel, V.; Karapetrov, G. *Phys. Rev. B* **2011,** *84,* 014424. doi:10.1103/PhysRevB.84.014424
7. Liu, Y.; Du, A. *J. Appl. Phys.* **2010,** *107,* 013906. doi:10.1063/1.3268423
8. Stebliy, M. E.; Ognev, A. V.; Samardak, A. S.; Diga, K. S.; Chebotkevich, L. A. *IEEE Trans. Magn.* **2012,** *48,* 4406. doi:10.1109/TMAG.2012.2196269
9. OOMMF Project at NIST. http://math.nist.gov/oommf (accessed Sept 16, 2014).
10. Kim, S.-K.; Lee, K.-S.; Yu, Y.-S.; Choi, Y.-S. *Appl. Phys. Lett.* **2008,** *92,* 022509. doi:10.1063/1.2807274
11. Stebliy, M. E.; Ognev, A. V.; Samardak, A. S.; Kolesnikov, A. G.; Chebotkevich, L. A.; Han, X. *Appl. Phys. Lett.* **2014,** *104,* 112405. doi:10.1063/1.4869024

License and Terms

The definitive version of this article is the electronic one which can be found at:
doi:10.3762/bjnano.6.70

BEILSTEIN JOURNAL OF NANOTECHNOLOGY

Observation of a photoinduced, resonant tunneling effect in a carbon nanotube–silicon heterojunction

Carla Aramo*[1], Antonio Ambrosio[2], Michelangelo Ambrosio*[1], Maurizio Boscardin[3], Paola Castrucci[4], Michele Crivellari[3], Marco Cilmo[1], Maurizio De Crescenzi[4], Francesco De Nicola[4], Emanuele Fiandrini[5], Valentina Grossi[6], Pasqualino Maddalena[7], Maurizio Passacantando[6], Sandro Santucci[6], Manuela Scarselli[4] and Antonio Valentini[8]

Full Research Paper

Address:
[1]INFN, Sezione di Napoli, Via Cintia 2, 80126 Napoli, Italy, [2]CNR-SPIN U.O.S. di Napoli and Dipartimento di Scienze Fisiche, Università degli Studi di Napoli “Federico II”, Via Cintia 2, 80126 Napoli, Italy, [3]Centro per Materiali e i Microsistemi Fondazione Bruno Kessler (FBK), Trento, Via Sommarive 18, 38123 Povo di Trento, Italy, [4]INFN, Sezione di Roma “Tor Vergata”, Dipartimento di Fisica, Università degli Studi di Roma “Tor Vergata”, Via della Ricerca Scientifica 1, 00133 Roma, Italy, [5]INFN, Sezione di Perugia, Dipartimento di Fisica, Università degli Studi di Perugia, Piazza Università 1, 06100 Perugia, Italy, [6]INFN, Sezione di L’Aquila, Dipartimento di Scienze Fisiche e Chimiche, Università degli Studi dell’Aquila, Via Vetoio, 67100 Coppito, L’Aquila, Italy, [7]INFN, Sezione di Napoli and Dipartimento di Scienze Fisiche, Università degli Studi di Napoli “Federico II”, Via Cintia 2, 80126 Napoli, Italy, and [8]INFN, Sezione di Bari and Dipartimento di Fisica, Università degli Studi di Bari, Via Amendola 173, 70126 Bari, Italy

Email:
Carla Aramo* - aramo@na.infn.it; Michelangelo Ambrosio* - ambrosio@na.infn.it

* Corresponding author

Keywords:
heterojunction; multiwall carbon nanotubes; NDR; photodetector; tunneling

Beilstein J. Nanotechnol. **2015,** *6,* 704–710.
doi:10.3762/bjnano.6.71

Received: 30 September 2014
Accepted: 12 February 2015
Published: 10 March 2015

This article is part of the Thematic Series "Self-assembly of nanostructures and nanomaterials".

Guest Editor: I. Berbezier

Abstract

A significant resonant tunneling effect has been observed under the 2.4 V junction threshold in a large area, carbon nanotube–silicon (CNT–Si) heterojunction obtained by growing a continuous layer of multiwall carbon nanotubes on an n-doped silicon substrate. The multiwall carbon nanostructures were grown by a chemical vapor deposition (CVD) technique on a 60 nm thick, silicon nitride layer, deposited on an n-type Si substrate. The heterojunction characteristics were intensively studied on different substrates, resulting in high photoresponsivity with a large reverse photocurrent plateau. In this paper, we report on the photoresponsivity characteristics of the device, the heterojunction threshold and the tunnel-like effect observed as a function of applied voltage and excitation wavelength. The experiments are performed in the near-ultraviolet to near-infrared wavelength range. The high conversion efficiency of light radiation into photoelectrons observed with the presented layout allows the device to be used as a large area photodetector with very low, intrinsic dark current and noise.

Introduction

Negative differential resistance (NDR), where the current decreases as a function of voltage, has been observed in the current–voltage curves of several types of structures (e.g., heavily doped p–n junction, double and triple barrier, quantum well, quantum wires and quantum dots, nanotubes and graphene) [1-7]. In general, it has been associated with the occurrence of a process at the junction that allows the electrons to tunnel between energy levels that are aligned only at a certain applied voltage. In the case of carbon nanotubes (CNTs), a number of cases have been reported in which this effect has been observed both for single-walled as well as for double-walled CNTs [3-5].

In this work, a photosensitive junction was fabricated which exhibits a current–voltage characteristic showing a marked tunneling-like shape with a NDR in the region between 1.5 and 2.2 V of excitation light. In fact, in this region, the observed current decreases and varies with the incident photon wavelength. The effect of the incident radiation is so strong it allows the carriers to cross the junction through the 2.4 V barrier, even at voltages of a few hundred mV.

The optoelectronic properties of semiconducting carbon nanotubes are advantageous for the development of photodetector devices in the near-to-mid-infrared region (from ≈1 to ≈15 μm) [8]. The mechanisms behind the infrared sensitivity of CNTs have been discussed by various authors [9,10]. The photoconductivity of individual CNTs, as well as ropes and films of CNTs have been studied extensively both in the visible [11] and the infrared [12] range. The variations in the photoconductivity of CNT-based devices have been attributed to the photon-induced generation of charge carriers in single-wall CNTs and the subsequent charge separation across the carbon nanotube–metal contact interface [11]. To the best of our knowledge, there is a lack of measurements in the UV region [8], and moreover, there are no reports on the observation of the NDR generated by light radiation to date.

In this paper, we report on the device characteristics, optoelectronic properties and, for the first time, a portion of the I–V curve showing a bell-shape tunneling behavior with a marked presence of a NDR. The tunneling current is generated by the incident radiation and it is function of the wavelength and the incident power intensity.

Experimental

In a similar manner to that described [13], the photodevice was realized by growing a film of multiwall carbon nanotubes (MWCNTs) on an n-doped silicon substrate. The substrates used to build the photodetector were fabricated by Fondazione Bruno Kessler (FBK) in Povo, Trento (Italy), unlike the substrate of the devices shown in Figure 1 of [13]. On the upper part of the n-doped silicon wafer (1 × 1 cm^2, 300 μm thickness and resistivity of 3–12 Ω·cm) an insulating layer of 60 nm of silicon nitride (Si_3N_4) is grown by plasma-enhanced chemical vapor deposition (PECVD). Two, circular, metallic Ti/Pt electrodes of 1 mm in diameter are placed at a distance of 4 mm from each other (Figure 1a) on the silicon nitride surface. A

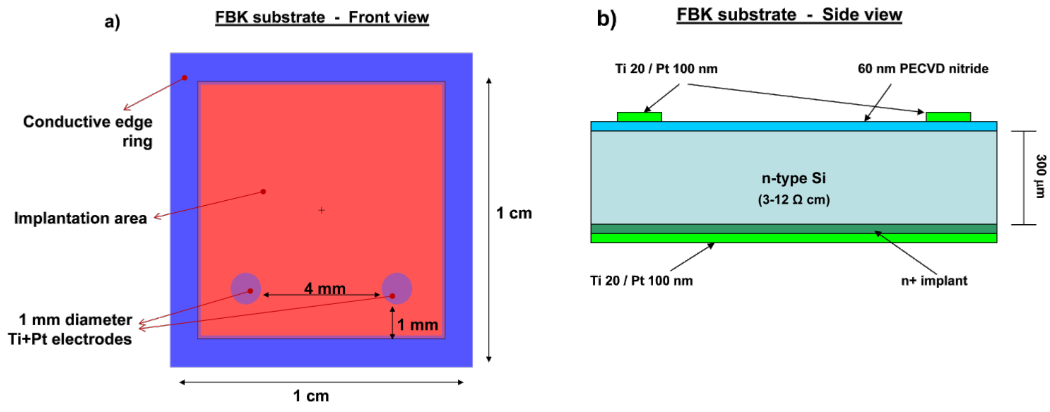

Figure 1: (a) Schematic front view and (b) side view of the Si substrate produced by Fondazione Bruno Kessler (FBK) in Povo, Trento (Italy).

metallic guard ring, 1 mm wide, serves to inhibit superficial current dispersions during electrical measurements. In the bottom part of the silicon wafer, a thin n^+ implanted layer ensures ohmic contact between the silicon and the metallic Ti/Pt electrodes, covering the entire back surface (Figure 1b). Thus, the main differences between the FBK substrate used in this work and the substrate used in [13] are: the Si_3N_4 insulation layer on the upper part of the Si is much thinner (60 nm instead of 140 nm), the different thickness of Si (300 µm instead of 500 µm), the different Si resistivity (3–12 Ω·cm instead of 40 Ω·cm) and the absence of a Si_3N_4 insulating layer in the bottom part of the Si layer. Due to these differences, the results from this work are different from those obtained in earlier work reported in [13].

The FBK substrate was then covered with a uniform layer of MWCNTs grown on the implantation area by CVD. The MWCNTs grow due to the presence of catalytic particles of about 60 nm in diameter, which are obtained by annealing a 3 nm thick Ni film at 700 °C for 20 min in a hydrogen atmosphere. The film was deposited on the substrate by thermal evaporation at a pressure of 10^{-6} Torr. The diffusion of Ni on Pt guarantees the absence of catalyst particles directly on the electrodes, and the growth of MWCNTs only on the Si_3N_4 substrate. The MWCNTs were grown by keeping the substrate at a temperature of 700 °C for 10 min in an acetylene atmosphere. In Figure 2a, a scanning electron microscopy image of the resulting MWCNT is reported and in the inset a Raman spectrum of MWCNT exhibits two main peaks attributed to the D- and G-bands. The G-band at ≈1600 cm^{-1} corresponds to the splitting of the E_{2g} stretching mode of graphite. The intense D-band indicates the presence of defective graphitic structures or amorphous carbon [14].

Regarding the electrical measurements performed, a drain voltage was applied between the topside and backside of the electrodes (Figure 2b). The topside electrodes were both connected to ground. The investigation of the device behavior as a radiation detector was performed with continuous emitting laser diodes (LDs) at several wavelengths. The LD intensity was controlled by a low voltage power supply and measured with a power meter. Measurements were performed at room temperature, at LD powers from 0.1 to 1.0 mW with a 0.1 mW step, with a drain voltage ranging from −5 to 30 V with a step of 0.1 V, and at fixed excitation wavelengths of 378, 405, 532, 650, 685, 785, 880 and 980 nm. The current was measured with a Keithley 2635 source meter, which also provided the drain voltage. The measurement procedure was controlled by LabView routines running on a PC.

Results and Discussion

Measurements were carried out on both the CNT–Si heterojunction and the Si substrates to compare the behavior of the pure substrate and the CNT–Si junction. Figure 3 shows the comparison between the dark currents of the bare substrate and of the CNT–Si heterojunction. The curves were obtained after stressing the junctions through different sweep voltages in the

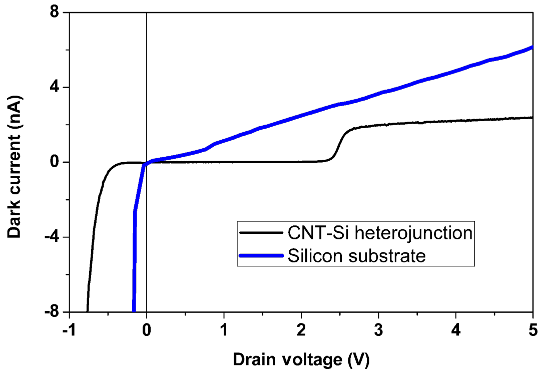

Figure 3: Dark current comparison of the Si substrate and the CNT–Si heterojunction.

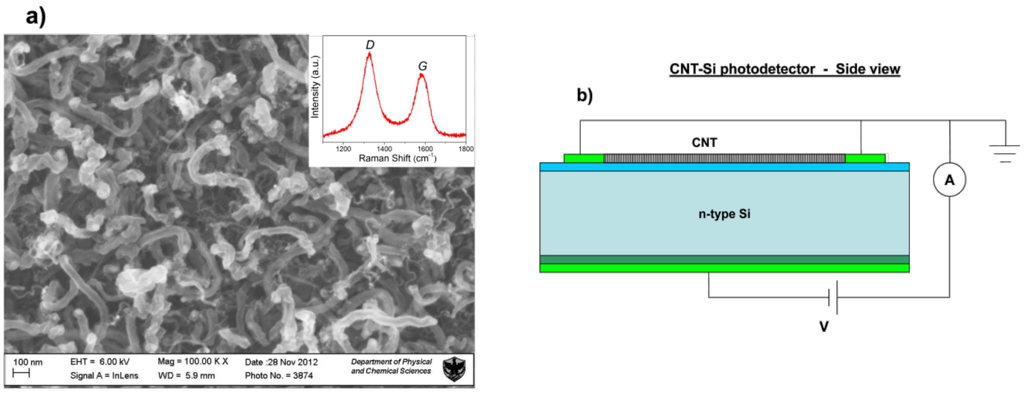

Figure 2: (a) Scanning electron microscopy (SEM) image of MWCNT samples grown on the implantation area. The inset shows a Raman spectrum of the same sample (b) Side view of electrical readout connections.

range between −30 and 30 V. Both of the devices showed a rectifying behavior after the conditioning – an indication that the conduction channels are open through the nitride layer by the voltage sweeps.

The reverse current for positive voltages, however, is very different. As the substrate shows a linear trend due to internal thermionic emission and a low shunt resistance, the CNT–Si junction exhibits a null dark current until a threshold is reached. For this device, the threshold was found at 2.4 V. Above this threshold, the current assumes a linear trend. In any case, the thermionic current through the heterojunction is less than that present in the substrate alone.

The detailed characteristics of the dark current around the threshold voltage are shown in Figure 4a, and Figure 4b shows the plot of the capacitance–voltage (C–V) measurement, which evidence the rapid decrease of the charge accumulation layer of the heterojunction around the threshold.

The CNT–Si junction exhibits interesting photosensitivity properties. While the substrate is light insensitive, the device with CNT deposited on the Si_3N_4 layer is greatly sensitive to radiation in the range from 378 to 980 nm.

Figure 5a reports the photocurrent measured in the configuration shown in Figure 2b. When the drain voltage exceeds the threshold voltage shown in Figure 3, the reverse photocurrent begins to grow linearly until reaching a plateau, which is constant over a large voltage range. The photocurrent depends quite linearly on the intensity of the illumination, as shown in Figure 5b. No saturation effects were observed up to tens of mW. The photodetector is sensitive to light radiation over a wide range of wavelengths.

Figure 5c shows the measured photoresponsivity (photocurrent generated by 1 mW of light intensity) for incident light of wavelengths ranging from 378 to 980 nm. When illuminated by the monochromatic intensity of a filtered xenon lamp, the external quantum efficiency (EQE) trend is similar to that of the LED illuminated experiment, as shown in Figure 5d.

It should be noted the efficiency of the detector for near-ultraviolet radiation is well above that of the Si photodetectors. This effect was observed in several similar devices as reported in [13,15-17]. However, in this report, there are some relevant, new aspects to be noted. The first one is that the EQE of the present device exhibits a maximum around 700 nm, which is at a wavelength much shorter than observed in earlier works [13]. In addition, the EQE shape is more symmetric over a large wavelength range and remains high at wavelengths from the near-UV to near-IR. The second important difference is the smaller threshold value obtained in this case. Both of these results lead to improved performance of the current device. Moreover, for these devices, we observed for the first time a non-zero current in the reverse voltage region below the 2.4 eV junction threshold under light. The shape of the current–voltage curve presents a NDR and resembles that of a resonant tunneling junction.

Figure 6b–d shows the photocurrent measured at three incident light powers (0.1, 0.5 and 1.0 mW) for three wavelengths (378, 650 and 980 nm). The drain voltage at maximum photocurrent varies weakly as a function of the wavelength of the incident radiation and is at about 1.8 V for 378 nm, 1.5 V for 650 nm and 1.7 V for 980 nm. The ratio between the peak and valley tunnel photocurrent depends on the light intensity and wavelength, as well as the NDR. The peak current is proportional to the EQE of photoconversion to any intensity and any wave-

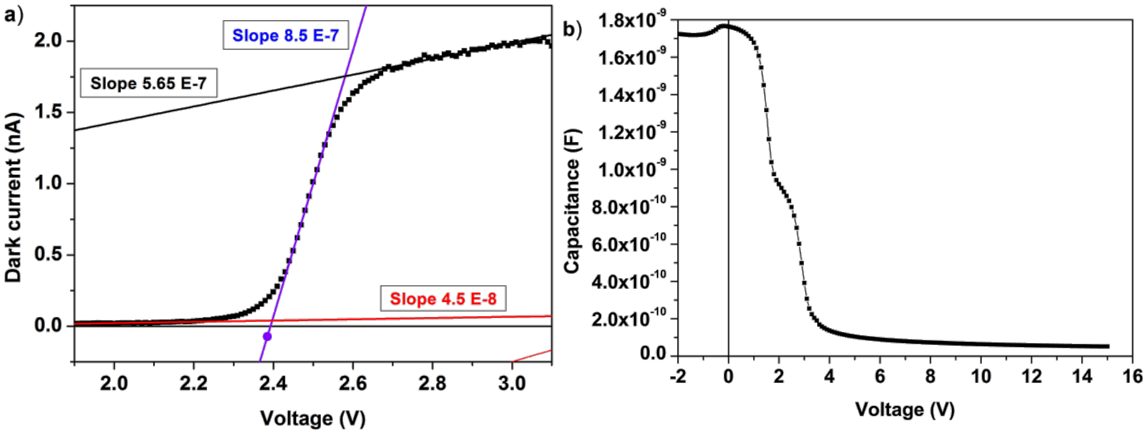

Figure 4: (a) Details of the dark current around the threshold voltage with a curve fit. (b) C–V plot of the heterojunction.

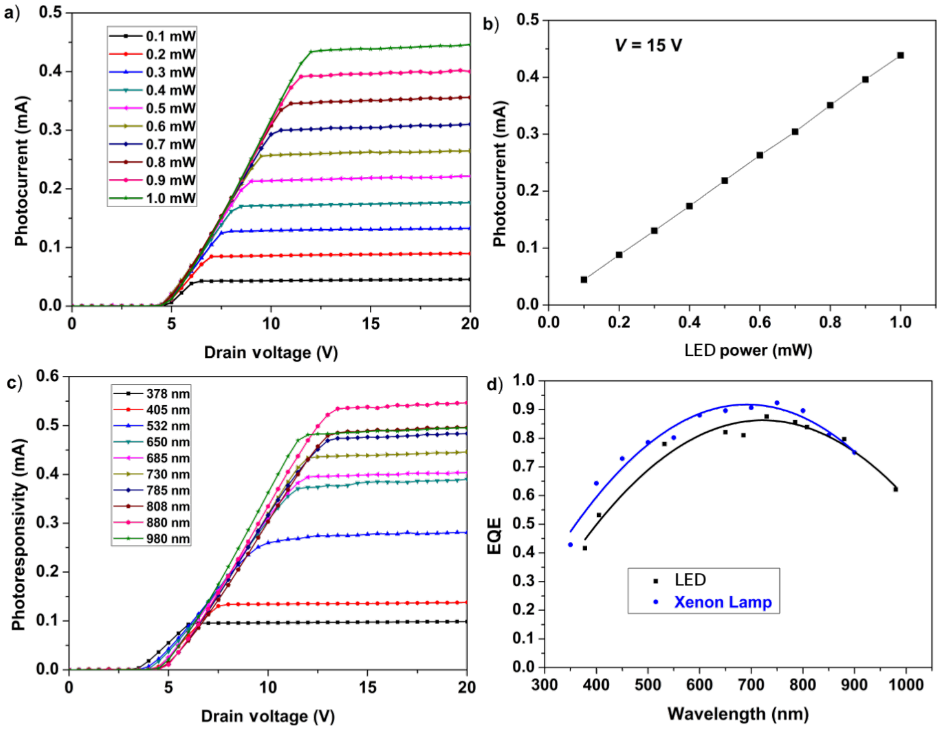

Figure 5: (a) Photocurrent induced by a 730 nm continuous wave, low power light source at various illumination intensities. (b) Photocurrent linearity at a drain voltage 15 V and wavelength of 730 nm. (c) Photocurrent induced at different wavelengths. (d) Comparison between the device external quantum efficiency (EQE) measured with an LD and a xenon lamp, filtered at different wavelengths.

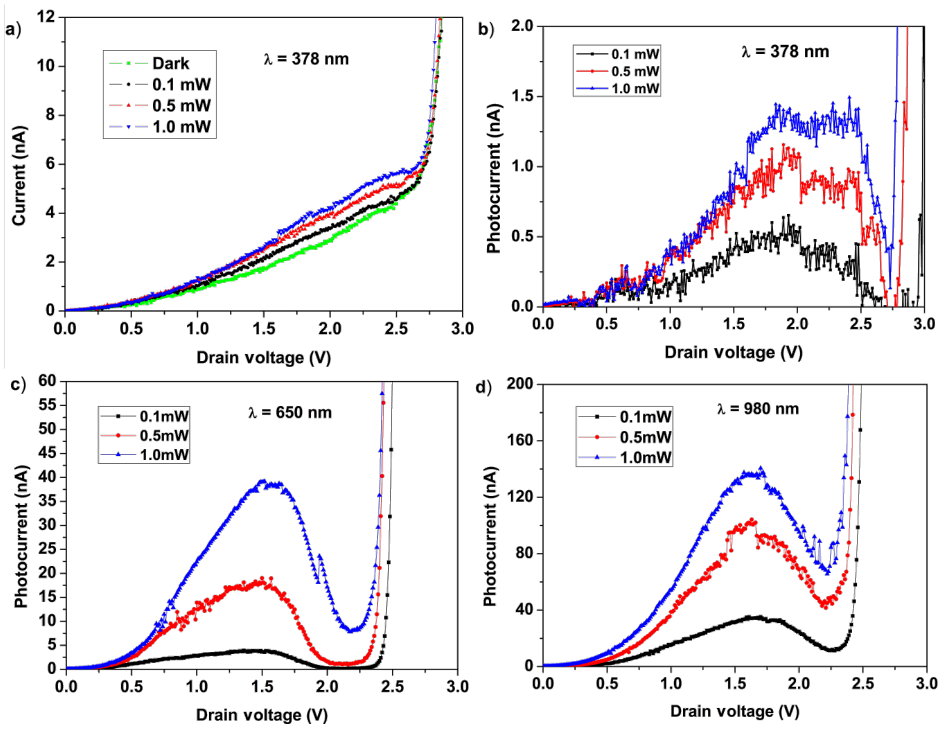

Figure 6: (a) Dark current and photocurrent tunneling in a CNT–Si heterojunction under 378 nm light illumination at different intensities. (b) The same as in (a) after subtracting the dark current. (c) The same as in (b) but for 650 nm and (d) 980 nm.

length, and is about 5 × 10^{-4} times the corresponding reverse current (at plateau) for all intensities and at all wavelengths. These effects were tested in a number of samples. Figure 5 and Figure 6 show the data obtained for two of these samples. Thus, the values reported for the ratio between the NDR peak current and the reverse current at plateau cannot be calculated given the current values reported in the two figures.

These observations clearly indicate that incident light and (as a consequence) the photogenerated charges play a fundamental role in the heterojunction behavior. The similarity in the current shape with that of a typical resonant tunneling junction suggests that a kind of electronic resonance process induced by the photogenerated charges may be present. Recently, Castrucci et al. [18] stressed that multiwall CNTs can contribute to the photocurrent because their density of states shows the same van Hove singularities as the single-walled CNTs. The excitation of electron–hole pairs is the responsible for this effect in each single wall of the multiwall CNT. In the present case, the incident light produces the sizeable absorption band observed around 1.5–2.4 eV that is a convolution of the several electronic transitions occurring in each nanotube. The contacts among the nanotubes ensure the charge transfer between the nanotubes and the observation in the I–V curve. The bell shape of the absorption band detected in the I–V spectra mimics that observed in the tunneling effect between a highly doped p–n junction; however, in our case, the physics behind this process is completely different. However, several questions are still open regarding the interpretation of the experimental data, for which we cannot exclude the presence of different mechanisms.

Conclusion

In this paper, we report the results of a negative differential resistance behavior generated by the incident radiation, which varies as a function of wavelength and incident power intensity for a new photosensitive device consisting of MWCNTs grown at 700 °C on a Si substrate. The junction presents rectifying properties with a 2.4 V threshold to the flow of reverse current, a strong photosensitivity to light radiation at wavelengths between 378 and 980 nm, a very broad plateau extended over a large range of drain voltages, and a good linearity of the photoresponsivity versus light intensity. The conversion efficiency of light radiation to photocurrent is maximum at 730 nm, with an external quantum efficiency of ≈92%, and an EQE of ≈43% at 378 nm. No saturation phenomena were observed at high intensity, and no significant differences between the diffuse light of a xenon lamp and the directed light of LDs were observed.

The most surprising result was the observation of a remarkable photoinduced resonant tunneling-like current, which was completely absent in dark conditions, and which was absent in the substrate without CNTs. Therefore, the resonant tunnel-like current is generated only under light radiation and it is function of the wavelength as well as of the power intensity. The ratio between the resonant tunneling-like peak photocurrent and the plateau of the reverse photogenerated current was about 5 × 10^{-4} for all intensities and wavelengths. These features, which are currently still under investigation, suggest the potential use of the device for optoelectronics applications.

Acknowledgements

The authors thank P. Di Meo, A. Pandalone and A. Vanzanella for their precious assistance in data acquisition and experimental instrumentation and B. Alfano for the data acquisition programs. This work has been supported by the Istituto Nazionale di Fisica Nucleare (INFN) in the framework of project PARIDE (Pixel Array for Radiation Imaging DEtector).

References

1. Sze, S. M. *Physics of Semiconductor devices;* John Wiley & Sons: New York, NY, USA, 1969.
2. Davies, J. *The physics of low dimensional semiconductors. An introduction;* Cambridge University Press: Cambridge, United Kingdom, 1998.
3. Liu, Q.; Yu, L.; Li, H.; Qin, R.; Jing, Z.; Zheng, J.; Gao, Z.; Lu, J. *J. Phys. Chem. C* **2011,** *115,* 6933–6938. doi:10.1021/jp112285t
4. Liu, Q.; Luo, G.; Qin, R.; Li, H.; Yan, X.; Xu, C.; Lai, L.; Zhou, J.; Hou, S.; Wang, E. *Phys. Rev. B* **2011,** *83,* 155442. doi:10.1103/PhysRevB.83.155442
5. Rinkiö, M.; Johansson, A.; Kotimäki, V.; Törmä, P. *ACS Nano* **2010,** *4,* 3356. doi:10.1021/nn100208v
6. Nguyen, P. D.; Nguyen, T. C.; Hossain, F. M.; Huynh, D. H.; Evans, R.; Skafidas, E. *Nanoscale* **2015,** *7,* 289. doi:10.1039/C4NR05133E
7. Britnell, L.; Gorbachev, R. V.; Geim, A. K.; Ponomarenko, L. A.; Mishchenko, A.; Greenaway, M. T.; Fromhold, T. M.; Novoselov, K. S.; Eaves, L. *Nat. Commun.* **2013,** *4,* No. 1794. doi:10.1038/ncomms2817
8. Konstantatos, G.; Sargent, E. H. *Nat. Nanotechnol.* **2010,** *5,* 391. doi:10.1038/nnano.2010.78
9. Kenny, J. T.; Pollock, H. R. *Infrared Phys. Technol.* **2001,** *42,* 385–390. doi:10.1016/S1350-4495(01)00097-4
10. Itkis, M. E.; Borondics, F.; Yu, A.; Haddon, R. C. *Science* **2006,** *312,* 413. doi:10.1126/science.1125695
11. Lu, S.; Panchapakesan, B. *Nanotechnology* **2006,** *17,* 1843. doi:10.1088/0957-4484/17/8/006
12. Levitsky, I. A.; Euler, W. B. *Appl. Phys. Lett.* **2003,** *83,* 1857. doi:10.1063/1.1606099
13. Ambrosio, A.; Aramo, C.; Battiston, R.; Castrucci, P.; Cilmo, M.; De Crescenzi, M.; Fiandrini, E.; Grossi, V.; Guarino, F.; Maddalena, P.; Nappi, E.; Passacantando, M.; Pignatel, G.; Santucci, S.; Scarselli, M.; Tinti, A.; Valentini, A.; Ambrosio, M. *J. Instrum.* **2012,** *7,* P08013. doi:10.1088/1748-0221/7/08/P08013
14. Passacantando, M.; Bussolotti, F.; Grossi, V.; Santucci, S.; Ambrosio, A.; Ambrosio, M.; Ambrosone, G.; Carillo, V.; Maddalena, P.; Perillo, E.; Raulo, A. *Appl. Phys. Lett.* **2008,** *93,* 051911. doi:10.1063/1.2968203

15. Tinti, A.; Righetti, F.; Ligonzo, T.; Valentini, A.; Nappi, E.; Ambrosio, A.; Ambrosio, M.; Aramo, C.; Maddalena, P.; Castrucci, P.; Scarselli, M.; De Crescenzi, M.; Fiandrini, E.; Grossi, V.; Santucci, S.; Passacantando, M. *Nucl. Instrum. Methods Phys. Res., Sect. A* **2011,** *629,* 377–381. doi:10.1016/j.nima.2010.11.097
16. Aramo, C.; Ambrosio, A.; Ambrosio, M.; Battiston, R.; Castrucci, P.; Cilmo, M.; De Crescenzi, M.; Fiandrini, E.; Grossi, V.; Guarino, F.; Maddalena, P.; Nappi, E.; Passacantando, M.; Pignatel, G.; Santucci, S.; Scarselli, M.; Tinti, A.; Valentini, A. *Nucl. Instrum. Methods Phys. Res., Sect. A* **2013,** *718,* 554–556. doi:10.1016/j.nima.2012.10.107
17. Aramo, C.; Ambrosio, A.; Ambrosio, M.; Battiston, R.; Castrucci, P.; Cilmo, M.; De Crescenzi, M.; Fiandrini, E.; Grossi, V.; Guarino, F.; Maddalena, P.; Nappi, E.; Passacantando, M.; Pignatel, G.; Santucci, S.; Scarselli, M.; Tinti, A. *EPJ Web Conf.* **2013,** *53,* 08014. doi:10.1051/epjconf/20135308014
18. Castrucci, P.; Scilletta, C.; Del Gobbo, S.; Scarselli, M.; Camilli, L.; Simeoni, M.; Delley, B.; Continenza, A.; De Crescenzi, M. *Nanotechnology* **2011,** *22,* 115701. doi:10.1088/0957-4484/22/11/115701

License and Terms

The definitive version of this article is the electronic one which can be found at:
doi:10.3762/bjnano.6.71

BEILSTEIN JOURNAL OF NANOTECHNOLOGY

Production, detection, storage and release of spin currents

Michele Cini

Full Research Paper

Open Access

Address:
Dipartimento di Fisica and Istituto Nazionale di Fisica Nucleare, Università di Roma Tor Vergata, Via della Ricerca Scientifica 1, I-00133 Rome, Italy

Email:
Michele Cini - michele.cini@roma2.infn.it

Keywords:
quantum pumping; quantum transport; spin current

Beilstein J. Nanotechnol. **2015,** *6,* 736–743.
doi:10.3762/bjnano.6.75

Received: 05 November 2014
Accepted: 16 February 2015
Published: 13 March 2015

This article is part of the Thematic Series "Self-assembly of nanostructures and nanomaterials".

Guest Editor: I. Berbezier

Abstract

Background: Quantum rings connected to ballistic circuits couple strongly to external magnetic fields if the connection is not symmetric. Moreover, properly connected rings can be used to pump currents in the wires giving raise to a number of interesting new phenomena. At half filling using a time-dependent magnetic field in the plane of the ring one can pump a pure spin current, excited by the the spin–orbit interaction in the ring.

Results: Such a magnetic current is even under time reversal and produces an electric field instead of the usual magnetic field. Numerical simulations show that one can use magnetizable bodies as storage units to concentrate and save the magnetization in much the same way as capacitors operating with charge currents store electric charge. The polarization obtained in this way can then be used on command to produce spin currents in a wire. These currents show interesting oscillations while the storage units exchange their polarizations.

Conclusion: The magnetic production of spin currents can be a useful alternative to optical excitation and electric field methods.

Introduction

The time-honored field of quantum transport has been evolving in the past 15 years in such a way that spin–orbit interaction effects and spin currents have become one of the main directions, also in view of promising applications to the new field of spintronics. An excellent review has been provided by Žutić and co-workers [1]. In recent years there has been in the literature a growing interest in the relation between magnetic and transport properties of materials [2]. On the other hand, other promising themes of research on spin currents remain largely to be explored.

One is the spin version of quantum pumping – something that is not possible classically. A seminal paper by Thouless [3] pointed out that quantum mechanics gives the possibility of propagating a charge current in a circuit without an applied bias. It became clear later that quantum pumping obtained by varying one parameter in the Hamiltonian requires a nonlinear dependence of the current on the dynamics. Romeo and Citro [4] have discussed memory and pumping effects in oscillators coupled to parasitic nonlinear dynamics. These ideas must be extended to spin currents.

As another example, systems containing rings and having a nontrivial topology are another important direction of research that has been given relatively little attention to date in this context. Nevertheless, it is clear that such systems will soon occupy the front of stage when the focus will shift on the mechanical effects of magnetic fields in nanoscopic systems. The interest in quantum ring properties is rather fundamental since they show striking deviances from classical properties [5] and also because of the growing role of topological effects in this field.

The present paper belongs to a series devoted to the magnetic properties of quantum rings linked tangentially to ballistic circuits. The geometry is explained in Figure 1. If the ring-wire connection is asymmetric, a current in the external circuit selects a chirality in the ring and produces a magnetic moment. As we shall see, the reverse is also true, namely, a chiral current in the ring can pump charge in the wire. By the same token, a symmetrically connected quantum ring inserted in a circuit cannot choose a chirality and has zero magnetic moment when a current flows through it. A symmetric connection (Figure 1 right) is unfavorable for quantum pumping. This is why a maximally asymmetrical connection is relevant in this respect. I call this geometry a laterally connected ring (see Figure 1 left).

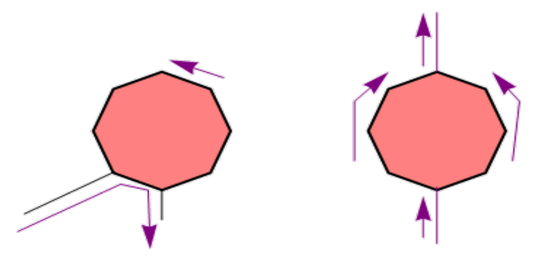

Figure 1: Left: Lateral connection of a quantum ring ($N_{\text{ring}} = 8$) to external wires (any even number of sides greater or equal than four can be considered, since the graph is bipartite, see below.) The flow of a current in the external wire selects a chirality in the ring and produces a magnetic moment. Right: a symmetric connection to the external wire. No magnetic moment is produced.

The effects described in the present paper are purely quantum mechanical, because spins are involved and also because pumping phenomena are classically forbidden. Even spinless models with laterally connected rings give raise to pumping [6]. One method for pumping a charge current while leaving the ring neutral is based on the introduction of integer numbers of fluxons. The magnetic moment of the ring also deviates strongly from classical theory [5]. While one-parameter pumping is forbidden in a linear system [7], quantum effects produce nonlinearity and pumping. In the adiabatic limit there is no pumping at all, as shown in a beautiful general analysis by Avron, Raveh and Zur [8]. However, if a flux of the order of a flux quantum is inserted in a time of the order of the electron hopping time, an electron is pumped in response of an inserted flux of the order of a fluxon [6]. The present treatment neglects interactions. However, the above phenomena were studied within the Luttinger liquid [9] approach. It was found that the pumping phenomena persist unhindered in the presence of the interactions [10].

In [11], it was shown that laterally connected rings have peculiar properties for quantum pumping. One can pump spin-polarized currents into the wires by using rotating magnetic fields or letting the ring rotate around the wire. This method works without any need for a spin–orbit interaction, and without stringent requirements about the conduction band filling. Besides, they can be used to pump spin, rather than just charge. In principle, quantum mechanics allows us to build a device to achieve that in more than one way. One can also build a ring device that can produce a pure spin current, that is, a magnetic current without any charge current associated to it [12].

In the present paper, I concentrate on the last thought experiment in order to better clarify the physical meaning of the spin current obtained in this way. This can be done by more thought experiments. The results suggest that one can transfer magnetization between two distant bodies directly through a lead, without moving any charges. Also, one can we detect the spin currents by the field they produce around the wire. Moreover, one can use a spin current to magnetize bodies and later use the magnetized bodies to excite a pure spin current in a wire. The experimental realization of a magnetic current could also be useful for the ongoing research of an electric dipole moment of the electron. Moreover such theoretical ideas, once realized in a practical device, would offer new strategies to attack the problems connected to spintronic applications.

Alternative mechanisms for generating pure spin currents have been proposed. Bhat and Sipe [13] proposed using circularly propagating light beams to excite polarized spin currents. Brataas and coworkers [14] predicted that precessing ferromagnets inject spin currents in semiconductors. The spin Hall effect [15,16] uses an electric field. The novel mechanism based on laterally connected rings is driven by a time-dependent magnetic field.

Geometry and dynamics of spin current generation

In this Section, I recall the Hamiltonian H_{prod}, the same as in [12], which, in the half filling case, describes the magnetic production of the spin current based on a quantum pumping effect in the absence of an external bias. Below, H_{prod} will be complemented with other terms to allow for spin current storage and release.

$$H_{\text{prod}} = H_{\text{D}} + H'_{\text{B}} , \tag{1}$$

where H_{D} is the device Hamiltonian and H'_{B} the in-plane magnetic term. Here,

$$H_{\text{D}} = H_{\text{wires}} + H_{\text{ring}} + H_{\text{ring-wires}} \cdot \tag{2}$$

The polygonal ring, with an even number N_{ring} of sides, which ensure a bipartite lattice, is represented by

$$H_{\text{ring}} = \sum_{i \in \text{ring}} H_{\text{ring}}(i), \tag{3}$$

where, with the identification of ring site $N_{\text{ring}} + 1$ with site 1, we may write

$$H_{\text{ring}}(i) = \left(t_{\text{ring}} \sum_{\sigma} \exp\left[i\sigma\alpha_{\text{SO}} \right] c^{\dagger}_{i+1,\sigma} c_{i,\sigma} + \text{h.c.} \right). \tag{4}$$

Here α_{SO} is a phase due to the spin–orbit interaction [17], and can be of order unity or smaller.

Figure 1 left shows the geometry for a ring of $N_{\text{ring}} = 8$ vertices, but any polygon with even N_{ring} grants a pure spin current. The vertices of the polygon represent sites and are acted upon by the spin–orbit interaction and by the external magnetic field $B(t)$. The side length may be taken to be of order of a few angstroms. All sites are connected to the first neighbors by spin-diagonal matrix elements.

The Hamiltonian for the left and right wires is a standard tight-binding model

$$H_{\text{wires}} = H_{\text{L}} + H_{\text{R}} = t_h \sum_{n,\sigma} c^{\dagger}_{n,\sigma} c_{n+1,\sigma} + \text{h.c.} \tag{5}$$

Finally, the ring–wires contacts are modeled in $H_{\text{ring-wires}}$ whereby the ring has a nearest neighbor connection to the leads via a tunneling Hamiltonian with hopping matrix elements t_{lr} in the obvious way.

The magnetic interaction due to $B(t)$ acts exclusively on spin and is:

$$H'_{\text{B}} = \mu_{\text{B}} B(t) \sum_{i \in \text{ring}} \left(c^{\dagger}_{i,\uparrow} c_{i,\downarrow} + c^{\dagger}_{i,\downarrow} c_{i,\uparrow} \right), \tag{6}$$

with the Bohr magneton $\mu_{\text{B}} = 5.79375 \cdot 10^{-5}$ eV/T. The time-dependent field lies in the plane of the ring and has no flux through it. However, it couples to the electron spins in the ring, where the magnetic spin-flip combined with the spin–orbit interaction excites the spin current that is pumped to the external wires. Finally, I note that in this formulation there are no mean-free-path effects. This is appropriate to systems that are small compared to the mean free path. In such cases the transport is ballistic.

Numerical evolution and calculation of the currents

For $t < 0$, $B = 0$ and the system is in thermal equilibrium with a spin-independent chemical potential E_{F} at temperature T. The natural time unit for this problem is $\tau = \hbar / t_h$. In the code the Hamiltonian is constant during time slices of 0.2τ and jumps to the next value at the end. In this way, the many-electron Schrödinger equation is integrated by a succession of sudden approximations.

Taking the spin quantization axis along z (orthogonal to the plane of the ring), the number current operator may be written as:

$$J_{m,\sigma} = \frac{i t_h}{\hbar} \left(c^{\dagger}_{m+1,\sigma} c_{m,\sigma} - c^{\dagger}_{m,\sigma} c_{m+1,\sigma} \right). \tag{7}$$

I calculate the time-dependent number current by the partition-free approach [18], namely,

$$J_{n,\sigma}(t) = -2 \frac{t_h}{h} \operatorname{Im}\left(G^{<}_{n,\sigma,n-1,\sigma} \right) \tag{8}$$

where, in terms of the retarded function $g^{r}_{i,j}$,

$$G^{<}_{i,j}(t) = \sum_{q} n^{0}_{q} g^{r}_{i,q}(t,0) g^{r*}_{j,q}(t,0), \tag{9}$$

where q runs over the ground state spin-orbitals for $B = 0$ and n^{0}_{q} is the Fermi function.

In the numerical calculations below I take $t_h = t_{\text{ring}} = t_{\text{lr}} = 1$ eV as a reasonable order-of-magnitude, and the temperature is absolute zero. My codes calculate number currents taking $t_h = 1$. If this is interpreted to mean that $t_h = 1$ eV, which corresponds to the frequency $2.42 \cdot 10^{14}$ s^{-1}, a current $J = 1$ from the code means $2.42 \cdot 10^{14}$ electrons per second, which corresponds to a charge current of $3.87 \cdot 10^{-5}$ A. We also need a characteristic magnetic field. Recalling that $\phi_0 = h/e \approx 4.134\ 10^{-15}$ in MKSA units, we introduce the magnetic field B_ϕ such that $B_\phi S(N) = \phi_0$ where

$$S(N) = \frac{Na^2}{4\tan\left(\pi/N\right)}$$

is the ring area. Thus,

$$B_\phi[\mathrm{T}] = \frac{1.65 \cdot 10^6}{a^2}\frac{\tan(\pi/N)}{N},$$

with a in angstroms.

In the present geometry both spin directions orthogonal to the ring are treated on the same footing. The spin symmetry is broken by α_{SO} which provides a driving force. For any time dependence of $V(t) = \mu_B B_{\parallel}(t)$ the charge current vanishes identically at half filling and a pure spin current obtains.

A good analytic understanding of the purely spin current, of its non-adiabatic character, and of its topological origin was achieved in [12]. The absence of a charge current can be deduced from the invariance of the problem under a canonical transformation that exchanges electrons with holes, spin-up with spin-down and changes sign to one of the sublattices. The exact analytical results of [12] need not be repeated here. However, I note that the proof of the absence of a charge current can be extended to finite temperatures simply by replacing the ground state average used there by a Grand-Canonical one.

Numerical results obtained with an odd N_{ring} show a partial spin polarization, in line with the fact that they do not correspond to bipartite lattices. The extra atom produces a charge current that becomes small when the ring gets large. Below we consider even N_{ring}.

Field produced by a stationary spin current

A line of dipole moments polarized along z and extending along the x-axis would be described by the magnetic moment linear density

$$\vec{m}(\vec{r}) = \rho_M(x)\delta(y)\delta(z)\hat{z}, \tag{10}$$

where $\hat{z}$ is the unit vector along z, $\rho_M(x)$ is a magnetization density and $\delta(x)$ is Dirac's delta. This will produce a vector potential that we can write in the form

$$\vec{A}(\vec{r}) = \frac{\mu_0}{4\pi}\int \frac{d\vec{m} \wedge (\vec{r} - \vec{r}')}{|\vec{r} - \vec{r}'|^3}. \tag{11}$$

Here μ_0 is the vacuum susceptibility. For a constant distribution ρ_M the integral yields, in components,

$$\vec{A}(\vec{r}) = \frac{\mu_0\rho_M}{2\pi}\left(\frac{y}{y^2+z^2}, 0, 0\right). \tag{12}$$

If the line of dipole moments moves along the x-axis with speed u, in the stationary system the dipole density is $\rho'_M = \gamma\rho_M$ with $\gamma = 1/[1 - (u^2/c^2)]^{(1/2)}$, while the four-potential is found by a Lorentz transformation. It reads $\left(V/c, \vec{A}'\right)$ where $\vec{A}' = \gamma\vec{A}$, and the scalar potential is

$$V = -\frac{\mu_0\rho_{M'}u}{2\pi}\frac{y}{y^2+z^2}. \tag{13}$$

One can represent a time-independent spin-current semiclassically by two superimposed lines of opposite polarization moving with opposite speeds. Their vector potentials cancel each other out and one is left with a scalar potential

$$V(\vec{r}) = -\frac{\mu_0\rho_{M'}u}{\pi}\frac{y}{y^2+z^2}. \tag{14}$$

This shows a duality between the electric current producing a magnetic field and the magnetic current producing an electric field. This duality has already been pointed out [19] in a different model, but in view of the possibility to obtain pure spin currents in nanoscopic objects (where due to the nanoscopic dimensions, intense fields prevail at short distances from the wire) it acquires an extra significance, as we shall see. To begin with, although these treatments are semiclassical and approximate, the vanishing of the magnetic field is exact, since the pure spin current is even under the time reversal operator T while the magnetic field is odd.

In polar coordinates, with $y = r\cos(\theta)$, $z = r\sin(\theta)$, the electric field components are given by:

$$\left(E_y, E_z\right) = \frac{\mu_0\rho_{M'}u}{\pi}\frac{1}{r^2}\left(\cos(2\theta), \sin(2\theta)\right). \tag{15}$$

The pattern is shown in Figure 2. Note that all the black arrows represent the direction of $\vec{E}$ at a fixed distance from the lead (central disk) and start from the light blue circle. However, if one starts from the y-axis (direction of $\vec{B}$) and makes an angle of π, the direction of $\vec{E}$ rotates by 2π.

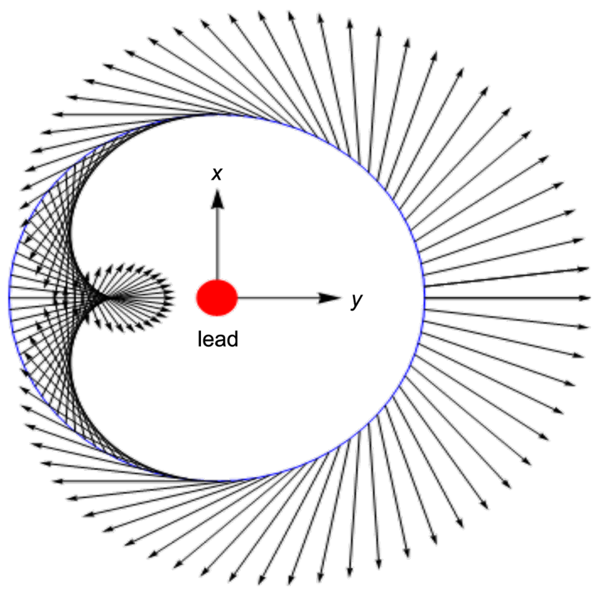

Figure 2: Pattern in the *y*–*z*-plane of the electric field produced by a pure spin current flowing in the lead, parallel to the *x*-axis, represented here by the disk at the origin. The magnetic field is along the *y*-axis.

This field is without divergence and rotation outside the singular line of the lead. No charge distribution could yield this pattern. This field symmetry could in principle be used to detect and measure the spin current, even if it were in combination with a normal charge current.

However, the experimental realization of a pure spin current would have a more fundamental significance, because of its time-reversal invariance. It is T-even, while an electric current is trivially T-odd. Particle physicists are trying to measure, or put constraints on, the electric dipole moment of the electron [20] by using strong fields in molecular [21] or solid-state measurements [22]. Formally, the electron anomalous magnetic moment is describes in Dirac's theory by a term proportional to $F_{\mu\nu}\sigma^{\mu\nu}\psi$, where ψ is Dirac's spinor, $F_{\mu\nu}$ and $\sigma^{\mu\nu}$ are the electromagnetic and spin tensors, respectively [23]. A term in $F_{\mu\nu}\sigma^{\mu\nu}\gamma_5\psi$ would yield the effects of an electric dipole moment. However, this would be odd under time-reversal, and it was originally discarded for this reason. No experimental fact supports its existence. Now, however, such a term would be most wanted by people looking for new physics, and is predicted by several theories trying to explain, e.g., the excess of matter over antimatter in the universe. If such a term exists, it should produce a T-odd term in the pure spin current and a magnetic field that could be sought for. A recent [20] upper limit for the electron dipole moment is $8.3 \cdot 10^{-17}\mu_B$. Can we do better in this way? Since in the present approach the time dependence $B(t)$ is arbitrary one can also consider a time-dependent spin current radiating electromagnetic waves. The quantitative estimate of the accuracy of this method is beyond the scope of the present paper and is a rather demanding task. Detailed calculations are under way.

Storage, detection and delayed release of the spin current

The possibility of exciting a pure spin current suggests that a magnetization transfer without charging of the kind outlined in the Introduction should be feasible by using a laterally connected polygonal ring and a magnetic field in the same plane as the ring. It should be possible to store and possibly concentrate the spin current in the form of a long-lived static polarization of a storage electron gas for later use. Actually the polarization would be permanent in the absence of the spin–orbit interaction in the reservoirs. In materials with low atomic numbers the polarization could be long-lived enough to make interesting experiments on it and maybe even technological applications. A measurement of the magnetic moment of the storage bodies would also serve to detect and measure the time integral of the spin current.

Here, I wish to present computer experiments aimed at this target, in which the storage bodies are cubes of various sizes. The total Hamiltonian is given as:

$$H = H_{\text{prod}} + H_{\text{ext}} + H_{L,\text{store}}(t) + H_{R,\text{store}}(t). \qquad (16)$$

Here, H_{prod} is the above described Hamiltonian with a 6-site ring. The field parallel to the y-axis was taken to grow linearly form 0 to 32 T at time $t = 80\ \tau$. I recall that time is measured in units of $\tau = \hbar / t_h$. The spin–orbit constant was taken to be $\alpha_{SO} = 1$. The additional terms in Equation 16 describe the left and right storage units $H_{L,\text{store}}(t)$, $H_{R,\text{store}}(t)$ and the external wire H_{ext} of the same form as Equation 5 connecting the identical storage unit.

Below, the storage units will be taken to be 2 × 2 × 2 or 3 × 3 × 3 cubic clusters of sites, which are bipartite. One must choose $H_{L,\text{store}}(t)$ and $H_{R,\text{store}}(t)$ such that the whole graph is bipartite, and the storage units will be half filled initially and for all times. Here $H_{L,\text{store}}(t)$ and $H_{R,\text{store}}(t)$ also contain the connections to the external wire and to the respective wires to the ring, and these depend on the time according to the following pattern.

Initially, the whole system is in equilibrium in the absence of external fields. Then the direct cube–cube connection is removed and the external field in the plane of the ring starts to excite a spin current that will polarize the cubes in the opposite way. Indeed, the numerical results confirm that a pure spin current flows in the wires from the ring to the cubes, and its polarization axis is in the y–z-plane. Then, the cubes are isolated and the spin current is stored in them as a constant magnetization. Finally, the direct connection through a 6-site lead is established. Then, a spin current is excited in the connecting lead while the up and down spin populations in both rings oscillate.

The sum of spin-up and spin-down populations in each cube was constant and the two uncharged rings are oppositely polarized. The pattern was similar when the spin quantization axis was taken along y or along z. These oscillations look similar to those already observed in spin-injection experiments, described by Albert Fert in his Nobel lecture [24]. Those observed thus far are in the microwave range, while in the present approach the characteristic frequency is proportional to the hopping integral. This suggests that higher frequencies than those reported in the literature could be attained.

In Figure 3 and Figure 4, the storage rings have 27 sites, the ring-cubes connections have 13 sites and the cube–cube connection has 6 sites. The populations start from half filling, that is, 13.5 electrons per spin. Then the left cube receives an up-polarization and the polarization of the right ring is opposite. One could engineer the timing of the process and the size of the storage units if the aim is to maximize the polarization. From $t_1 = 15\tau$ to $t_2 = 30\tau$ the cubes are isolated and polarization is constant, as it should be. In both cases, the polarization transfer without charging is quite substantial. The cubes remain strictly neutral like the rest of the system. At t_2 the cubes are connected through a wire which has a hopping integral $t_{\text{ext}} = 0.25\ t_h$ in Figure 3 and $t_{\text{ext}} = 0.75\ t_h$ in Figure 4. The upper panels show the evolution of the spin-up occupation, while the lower panel shows the spin-oscillating currents in the wires connecting the reservoirs. The spin-down currents are opposite. The current oscillates because the reservoirs exchange their polarizations. In Figure 4, the 6-site connection between the reservoirs has a larger hopping constant and produces a stronger and faster spin polarization exchange.

The spin-up current in the cube–cube connection in a similar numerical experiment with 8-site cubes is shown in Figure 5. It starts at time $t = 30\tau$ when the cubes are connected via a 6-sites wire and shows oscillations. It should be interesting to observe the spectrum and polarization of electromagnetic waves emitted by these oscillating magnetic currents. This would be another way to detect the spin current.

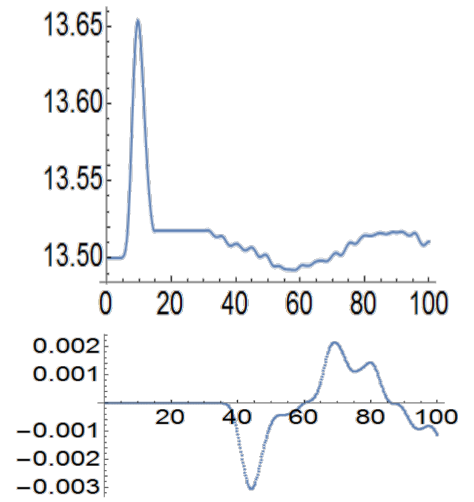

Figure 3: Upper panel: up-spin population of the left storage cube versus time measured in units of τ. Lower panel: spin-up current in the wire connecting the two 27-site cubes, where the hopping integral is $t_{\text{ext}} = 0.25\ t_h$.

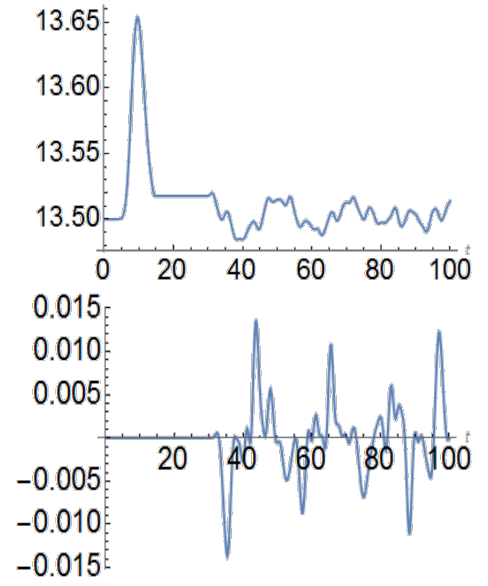

Figure 4: Upper panel: up-spin population on the left storage cube versus time measured in units of τ. Lower panel: spin-up current in the wire connecting the two 27-site cubes, where the hopping integral is $t_{\text{ext}} = 0.75\ t_h$.

Conclusion

I presented a theoretical study of tight-binding model devices consisting of a ring laterally connected to a wire and designed to produce spin polarized currents at half filling. A tangent time-dependent magnetic field in the plane of the ring can be used to pump a magnetic, i.e., purely spin current, excited by

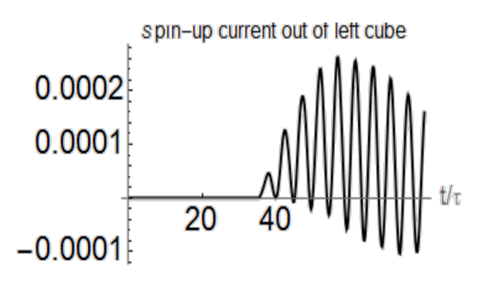

Figure 5: Spin-up current from the left storage cube in the cube–cube connection, when both storage cubes have eight sites. The hopping integral in the cube–cube wire is $t_{\text{ext}} = 0.05\ t_h$. The spin-down current is opposite.

the spin–orbit interaction in the ring. This behavior is analytically described in [12] and is found to be robust with respect to temperature and small deviations from half filling.

The main results of the present paper concern possible schemes to detect, store, gather, and then release magnetization. Suitable reservoirs or storage units have been shown to work with spin currents in analogy with capacitors for common charge currents. The spin polarization can be stored without charging the reservoir and then used on demand to produce pure spin currents in a wire. These currents show oscillations while the storage units exchange their polarizations and the intensity and amplitude of the oscillations can be modified by changing the conductivity of the link between the polarized units. The experimental realization of a magnetic current could also be relevant for the ongoing research of time-reversal violating new physics. Detailed calculations of such fields are under way.

The present model neglects electron–electron interactions, but it is physically reasonable that adding to the Hamiltonian a correlation term such as $U(\hat{n}_\uparrow + \hat{n}_\downarrow - 1)^2$ would tend to reinforce the charge pinning effects described here. At any rate, in the Hartree approximation, it would change nothing since its average at half filling vanishes strictly during the evolution of the system as a consequence of the theorem of [12].

In the present work the currents were generated by the action of a magnetic field, without the need of an external bias. However, the results have implications on the general problem of quantum transport in ballistic, topologically non-trivial circuits. Compelling physical arguments based on thought experiments [5] suggest that the magnetic moment of a quantum ring is not obtained by substituting the quantum current in the classical formula [25]. The basic reason is that any measurement of the magnetic moment of the ring requires the measurement of a force exerted on the ring by a probe flux, which according to quantum mechanics has an influence on the current. Actually, rephrasing the conclusions of [5], the magnetic moment is given by the operator

$$\hat{M}(\phi) = \frac{\partial H_{\text{ring}}^{G}}{\partial \phi} + \Delta^{\dagger} H_{\text{ring}}^{G} + H_{\text{ring}}^{G} \Delta\,, \qquad (17)$$

where ϕ is the probe magnetic flux through the ring, H_{ring}^{G} is the grand-canonical ring Hamiltonian referenced to the equilibrium chemical potential of the system and $\Delta = \Delta = \partial / \partial\phi$. As a consequence, when the circuit is biased by a small potential difference V_{bias} and a small current flows, $\langle \hat{M} \rangle$ is found [5] to go with V_{bias}^3 while one classically expects $M \sim V_{\text{bias}}$ in a linear circuit. Indeed, at small V_{bias} the quantum effects favor a laminar current which is not coupled to the magnetic field. The main subject of the present work can also be considered a complementary way to study the quantum effects of [6] in the reversed situation when $V_{\text{bias}} = 0$ and it is the interaction of the ring with a magnetic field that produces a current in the external circuit.

The above theoretical effort leads to several intriguing possibilities from the viewpoint of basic research and possible applications and I hope that this will stimulate experimentalists to work on the magnetic properties of laterally connected quantum rings.

References

1. Žutić, I.; Fabian, J.; Das Sarma, S. *Rev. Mod. Phys.* **2004,** *76,* 323–410. doi:10.1103/RevModPhys.76.323
2. Amico, L.; Fazio, R.; Osterloh, A.; Vedral, V. *Rev. Mod. Phys.* **2008,** *80,* 517–576. doi:10.1103/RevModPhys.80.517
3. Thouless, D. J. *Phys. Rev. B* **1983,** *27,* 6083–6087. doi:10.1103/PhysRevB.27.6083
4. Romeo, F.; Citro, R. *Phys. Rev. B* **2010,** *82,* 085317. doi:10.1103/PhysRevB.82.085317
5. Cini, M.; Perfetto, E.; Stefanucci, G. *Phys. Rev. B* **2010,** *81,* 165202. doi:10.1103/PhysRevB.81.165202
6. Cini, M.; Perfetto, E. *Phys. Rev. B* **2011,** *84,* 245201. doi:10.1103/PhysRevB.84.245201
7. Brouwer, P. W. *Phys. Rev. B* **1998,** *58,* R10135–R10138. doi:10.1103/PhysRevB.58.R10135
8. Avron, J. E.; Raveh, A.; Zur, B. *Rev. Mod. Phys.* **1988,** *60,* 873–915. doi:10.1103/RevModPhys.60.873
9. Haldane, F. D. M. *J. Phys. C: Solid State Phys.* **1981,** *14,* 2585. doi:10.1088/0022-3719/14/19/010
10. Perfetto, E.; Cini, M.; Bellucci, S. *Phys. Rev. B* **2013,** *87,* 035412. doi:10.1103/PhysRevB.87.035412
11. Cini, M.; Bellucci, S. *J. Phys.: Condens. Matter* **2014,** *26,* 145301. doi:10.1088/0953-8984/26/14/145301
12. Cini, M.; Bellucci, S. *Eur. Phys. J. B* **2014,** *87,* 106. doi:10.1140/epjb/e2014-50073-9
13. Bhat, R. D. R.; Sipe, J. E. *Phys. Rev. Lett.* **2000,** *85,* 5432–5435. doi:10.1103/PhysRevLett.85.5432

14. Brataas, A.; Tserkovnyak, Y.; Bauer, G. E. W.; Halperin, B. I. *Phys. Rev. B* **2002,** *66,* 060404. doi:10.1103/PhysRevB.66.060404
15. Hirsch, J. E. *Phys. Rev. Lett.* **1999,** *83,* 1834–1837. doi:10.1103/PhysRevLett.83.1834
16. Zhang, S. *Phys. Rev. Lett.* **2000,** *85,* 393–396. doi:10.1103/PhysRevLett.85.393
17. Zvyagin, A. A. *Phys. Rev. B* **2012,** *86,* 085126. doi:10.1103/PhysRevB.86.085126
18. Cini, M. *Phys. Rev. B* **1980,** *22,* 5887–5899. doi:10.1103/PhysRevB.22.5887
    Erratum: Cini, M. *Phys. Rev. B* **2014,** *89,* 239902. 10.1103/PhysRevB.89.239902.
19. Sun, Q.-f.; Guo, H.; Wang, J. *Phys. Rev. B* **2004,** *69,* 054409. doi:10.1103/PhysRevB.69.054409
20. Commins, E. D. *J. Phys. Soc. Jpn.* **2007,** *76,* 111010. doi:10.1143/JPSJ.76.111010
21. Hudson, J. J.; Kara, D. M.; Smallman, I. J.; Sauer, B. E.; Tarbutt, M. R.; Hinds, E. A. *Nature* **2011,** *473,* 493–496. doi:10.1038/nature10104
22. Lamoreaux, S. K. *Phys. Rev. A* **2002,** *66,* 022109. doi:10.1103/PhysRevA.66.022109
23. Greiner, W. *Relativistic quantum mechanics;* Springer: Berlin, Germany, 1990.
24. Albert Fert - Nobel Lecture: The Origin, Development and Future of Spintronics. http://www.nobelprize.org/nobel_prizes/physics/laureates/2007/fert-lecture.html (accessed Nov 3, 2014).
25. Jackson, J. D. Magnetostatics. *Classical electrodynamics;* John Wiley & Sons: New York, NY, U.S.A., 1962; pp 132–168.

License and Terms

BEILSTEIN JOURNAL OF NANOTECHNOLOGY

Combination of surface- and interference-enhanced Raman scattering by CuS nanocrystals on nanopatterned Au structures

Alexander G. Milekhin*[1,2], Nikolay A. Yeryukov[1,2], Larisa L. Sveshnikova[1], Tatyana A. Duda[1], Ekaterina E. Rodyakina[1,2], Victor A. Gridchin[1,3], Evgeniya S. Sheremet[1,4] and Dietrich R. T. Zahn[1,4]

Full Research Paper

Open Access

Address:
[1]A. V. Rzhanov Institute of Semiconductor Physics, pr. Lavrentieva, 13, Novosibirsk 630090, Russia, [2]Novosibirsk State University, Pirogov str. 2, Novosibirsk 630090, Russia, [3]Novosibirsk State Technical University, pr. Karl Marx, 20, Novosibirsk, 630092, Russia and [4]Semiconductor Physics, Technische Universität Chemnitz, D-09107 Chemnitz, Germany

Email:
Alexander G. Milekhin* - milekhin@isp.nsc.ru

* Corresponding author

Keywords:
copper sulfide (CuS) nanocrystals; interference-enhanced Raman spectroscopy; phonons; surface-enhanced Raman spectroscopy

Beilstein J. Nanotechnol. **2015,** *6,* 749–754.
doi:10.3762/bjnano.6.77

Received: 12 September 2014
Accepted: 17 February 2015
Published: 17 March 2015

This article is part of the Thematic Series "Self-assembly of nanostructures and nanomaterials".

Guest Editor: I. Berbezier

Abstract

We present the results of a Raman study of optical phonons in CuS nanocrystals (NCs) with a low areal density fabricated through the Langmuir–Blodgett technology on nanopatterned Au nanocluster arrays using a combination of surface- and interference-enhanced Raman scattering (SERS and IERS, respectively). Micro-Raman spectra of one monolayer of CuS NCs deposited on a bare Si substrate reveal only features corresponding to crystalline Si. However, a new relatively strong peak occurs in the Raman spectrum of CuS NCs on Au nanocluster arrays at 474 cm^{-1}. This feature is related to the optical phonon mode in CuS NCs and manifests the SERS effect. For CuS NCs deposited on a SiO$_2$ layer this phonon mode is also observed due to the IERS effect. Its intensity changes periodically with increasing SiO$_2$ layer thickness for different laser excitation lines and is enhanced by a factor of about 30. CuS NCs formed on Au nanocluster arrays fabricated on IERS substrates combine the advantages of SERS and IERS and demonstrate stronger SERS enhancement allowing for the observation of Raman signals from CuS NCs with an ultra-low areal density.

Introduction

Investigations of Raman scattering in nanostuctures such as nanocrystals (NCs) are limited by a low Raman cross-section because of the very low scattering volume of the nanostructures. Surface-enhanced Raman spectroscopy (SERS) taking advantage of plasmonics leads to a remarkable increase of the Raman sensitivity as shown for several semiconductor NC types [1-13].

The SERS effect by longitudinal optical (LO) phonons of CdS in Ag–CdS composite nanoparticles in solution and on a solid substrate was demonstrated [1,2]. Resonant SERS enhancement by LO phonons of CdSe was observed in core–shell CdSe/ZnS NCs deposited on commercially available nanostructured Au substrates [3]. Later, the SERS effect by LO phonons in CdSe in CdSe/ZnS NCs was realized on non-ordered nanostructured Ag surfaces [4]. Very recently, Lee et al. [5] reported the observation of SERS by surface optical (SO) and LO phonon modes in a CdSe core and the transverse optical (TO) phonon mode in a ZnS shell of core–shell CdSe/ZnS NCs attached to the surface of a Au nanowire. The spectrum of optical and interface phonons was obtained from the analysis of SERS spectra of pure CdSe NCs, core–shell CdSe/CdS, and CdSe/CdZnS NCs deposited on Ag SERS substrates [6]. A prominent enhancement of Raman scattering by LO phonons was observed in Au-ZnO NC nanocomposites [7] and ZnO NCs covered by Ag [8] excited near resonance with the interband electronic transitions in ZnO NCs.

Anomalously enhanced Raman scattering by LO phonons in epitaxial GaN and ZnO NC thin films covered with Ag was also explained by SERS [9]. A pronounced 10^4-fold SERS enhancement by surface optical phonons was observed for ZnO NCs excited in resonance with localised surface plasmon in Ag nanoclusters deposited on ZnO NCs and out of the resonance [10,11]. SERS by LO phonons of CdTe was investigated in mixed Ag-CdTe NCs with a controllable Ag nanoparticle/CdTe NC mixture ratio [12]. The first report on the observation of the SERS effect by optical phonons in CuS NCs on ordered arrays of Au nanoclusters fabricated in a nanolithography process was published recently [13]. CuS NCs were synthesised by using the Langmuir–Blodgett (LB) technique, which allows the formation of arrays of CuS NCs with variable areal density. It was established that the variation of Au nanocluster size and shape in the nanostructured Au arrays governs the local surface plasmon resonance energy enabling resonance SERS in absorbates deposited on the arrays [13-17]. Moreover, CuS NCs are resistant against intense laser excitation even under resonant conditions. This is important for micro-Raman experiments with the NCs on nanostructured Au arrays under excitation in the green spectral region. These two issues make CuS NCs an attractive model system for SERS investigations of inorganic analytes. As it was demonstrated in [18], extremely thin absorbing coatings deposited on an antireflection layer (typically 100 nm SiO_2 on Si) exhibit interference-enhanced Raman scattering (IERS) thus providing an alternative opportunity to enhance the Raman response by phonons in absorbates.

In this paper we present the results of both IERS and SERS and their combination by optical phonons in CuS NCs deposited on metal and semiconductor structures aiming at a maximal enhancement of the phonon response from CuS NCs.

Results and Discussion

Conventional Raman scattering

A typical Raman spectrum of a dense array of CuS NCs deposited by LB technology on a Au substrate is shown in Figure 1. The average thickness of CuS NC film is about 32 nm, which corresponds to 5–6 monolayer (ML) coverage by CuS NCs. The spectrum reveals a pronounced peak at 474 cm^{-1}, which is assigned to vibrational (stretching) modes from the covalent S–S bonds [19] and a much weaker peak at about 270 cm^{-1} attributed to the Cu–S bond vibration [19]. Therefore, the main attention was paid to the analysis of the Raman intensity of the most intense mode at 474 cm^{-1}.

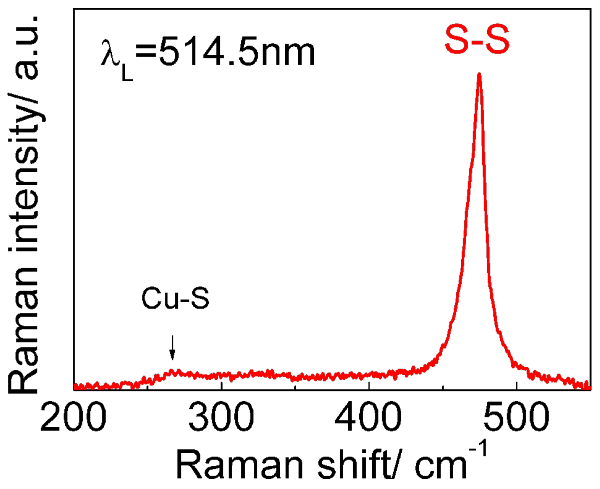

Figure 1: A typical Raman spectrum of the dense ensemble of CuS NCs (about 5–6 MLs) on a Au substrate excited with 514.5 nm.

Interference-enhanced Raman scattering

It was already established that thickness and refractive index of the SiO_2 layer determine conditions for laser light interference, and thus for IERS by absorbates deposited on the sample surface [18,20]. Since these two parameters are crucial for the enhancement of the Raman scattering by the absorbing NC layer, we used spectroscopic ellipsometry to determine the precise value of the SiO_2 layer thickness that gives the maximal IERS signal. The data on optical properties of CuS NC layer are also absent in literature, therefore, a wedge-shaped SiO_2 layer with the thickness varying in the range from 0 to 570 nm was fabricated. This sample served as a substrate for the deposition of CuS NCs by using the LB technique and for further Raman experiments.

The micro-Raman scattering study was performed in a backscattering geometry using a moving stage for precise positioning along the wedge-shaped sample in the direction of increasing thickness. Figure 2 shows the Raman spectra of CuS NCs recorded from areas with different SiO_2 thickness. A significant periodic enhancement of the Raman scattering intensity by the phonon mode of CuS NCs indicates the presence of the IERS phenomenon. As the interference conditions inside the transparent oxide layer for the incident light wavelength changes with oxide thickness, a noticeable enhancement of the Raman scattering by the Si phonon (about 30%) also takes place. The periodic variation of the enhancement factor of the phonon mode in CuS NCs as a function of SiO_2 layer thickness (Figure 3) was established for different laser excitation lines (632.8, 514.5, and 325 nm). Here, the intensity of the phonon mode of CuS NCs on a bare Si should be taken as a reference. However, it is worth mentioning that the intensity of the phonon mode is equal or below the noise level. Therefore, only an estimate of the IERS (as well as SERS) enhancement factor is possible. The maximal estimated IERS enhancement for the excitation wavelength of 632.8 nm reaches a value of at least 30 for a SiO_2 layer thickness of 75 nm. As expected, the IERS enhancement maximum is observed for thicker SiO_2 layers with increasing laser excitation wavelength. This SiO_2 layer thickness (75 nm) was used for further combined IERS and SERS experiments.

Surface-enhanced Raman scattering

A typical SEM image of the edge of a periodic Au nanocluster array on a Si substrate with deposited CuS NCs is presented in Figure 4a. One can see that the CuS NCs are homogeneously distributed on the Au nanocluster array and on the bare Si

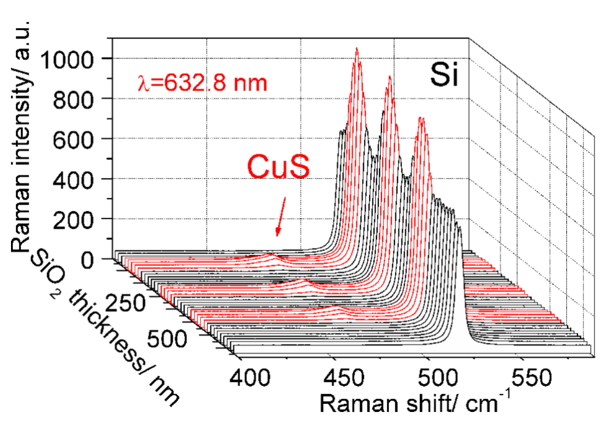

Figure 2: Raman spectra of CuS NCs (of about 1 ML coverage) fabricated on a Si substrate with a SiO_2 layer of variable thickness. Raman spectra were taken using 514.5 nm excitation wavelength.

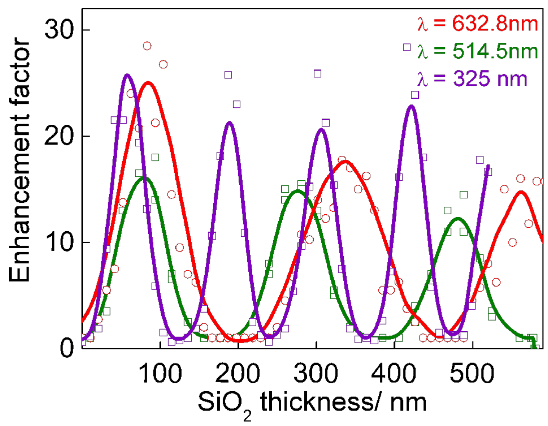

Figure 3: The dependence of the IERS enhancement factor of phonon modes in CuS NCs on the thickness of the SiO_2 layer determined for laser excitation lines at 632.8, 514.5, and 325 nm.

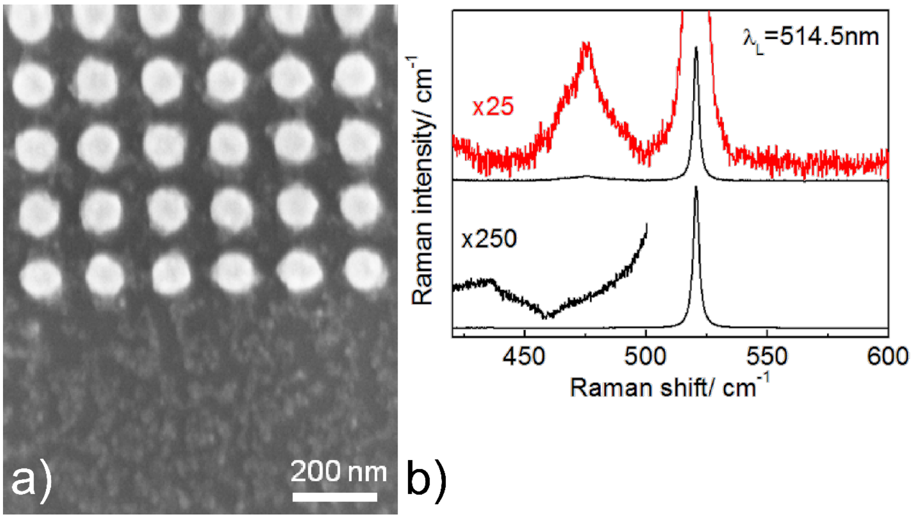

Figure 4: a) SEM image and b) micro-Raman spectra of CuS NCs deposited on Si (lower part) and Au nanocluster array (upper part).

surface with an average thickness of about 1 ML. The Raman spectrum measured from the area where CuS NCs are formed on bare Si (lower part in Figure 4a) shows only one strong Raman line at 521 cm^{-1} related to the Si substrate (lower curve in Figure 4b). Weak Raman features located in the spectral range of 400–500 cm^{-1} are also typical for monocrystalline Si [21] while no evidence of the phonon modes from CuS NCs is detected. However, a strong Raman band centred near 474 cm^{-1} arises when the Raman spectra are acquired from the area where CuS NCs are deposited on the nanocluster array. The SERS enhancement factor can hardly be determined since no reference signal from CuS NCs is detected on bare Si. However, depending on the NC areal density the SERS enhancement factor was estimated as 30–50, which is comparable to that of IERS.

Combination of SERS and IERS

In order to achieve even stronger enhancement of Raman scattering by phonons in CuS NCs by both IERS and SERS, CuS NCs were deposited on arrays of Au nanoclusters fabricated using nanolithography on a 75 nm thick SiO_2 layer. Obviously, the LSPR energy of the Au nanocluster arrays fabricated on a SiO_2 layer and on a Si substrate can be different due to the difference of dielectric functions of SiO_2 and Si [22,23] that determine the LSP energy. Indeed, the CuS NCs on Au nanocluster arrays fabricated on a Si substrate excited with 514.5 nm demonstrate a prominent SERS signal from optical phonons of CuS NCs with the same effective coverage (of about 1 ML) (Figure 4), while no signal is detected when Au nanoclusters were fabricated on a SiO_2 layer (not shown here). Most probably the shift of the LSPR energy in Au arrays fabricated on SiO_2 layer is responsible for the absence of CuS phonon modes in Raman spectra excited with 514.5 nm. The situation changes when the Raman scattering of the same structures was investigated under excitation with a red laser line (632.8 nm). CuS NCs on Au nanocluster arrays fabricated on Si exhibit noticeable SERS signal with an intensity comparable with that of the IERS signal when CuS NCs are deposited on a bare 75 nm thick SO_2 layer or an array of Au (Figure 5, curves 2 and 3, respectively). Note, that again no Raman signal is detected for NCs deposited on a bare Si substrate (Figure 5, curve 1). However, CuS NCs on Au nanocluster arrays fabricated on a SiO_2 layer (Figure 5, curve 4) reveal further significant enhancement of Raman scattering (a factor of about 6). According to [24] the electromagnetic field has a maximum in the vicinity of an adsorbate/oxide interface due to constructive interference. The SERS intensity is proportional to the forth order of electromagnetic field and, therefore, can be significantly enhanced for the adsorbate (or CuS NCs) located in the local field. The constructive interference in oxide layers was successfully used for achieving the maximum field enhancement for optical antennas [25], for realising the effect of co-enhanced IERS and SERS by organic molecules [26] and graphene [27], as well as for designing a chip for single molecular detection [28]. Thus, the use of the combination of SERS and IERS is preferable for the detection of a weak Raman response from a tiny amount of a material such as CuS NCs of an ultra-low areal density.

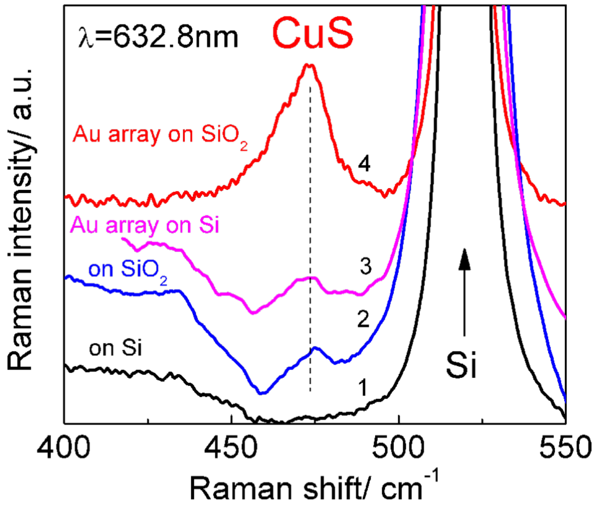

Figure 5: Raman spectra of CuS NCs deposited on bare Si, 75 nm SiO_2 layer on Si, and on Au arrays fabricated on Si and SiO_2 layer on Si measured with 632.8 nm.

Figure 6 shows a SEM image of homogeneously deposited CuS NCs with an areal density about ten times lower than that determined for the sample presented in Figure 4a. The SERS spectrum of the CuS NCs with ultra-low areal density shows a Raman phonon response at the same frequency position (about 474 cm^{-1}) with an intensity about 25 times weaker than for 1 ML of CuS NCs. This low intensity is explained by the smaller number of CuS NCs taking part in the SERS process. It is important to emphasise that the full width at half-maximum (FWHM) decreases from 17 to 9 cm^{-1} with decreasing areal density. This can be explained by the decreasing interaction between individual CuS NCs in the ensembles with the ultra-low areal density and by the reduced number of agglomerates of CuS NCs.

Conclusion

A periodical enhancement of Raman scattering by optical phonons from one monolayer of CuS nanocrystals fabricated by the Langmuir–Blodgett technology on a SiO_2 layer deposited on a Si substrate was observed with the variation of the SiO_2 layer thickness due to interference-enhanced Raman scattering. The pronounced enhancement of the Raman scattering from the nanocrystal ensembles deposited on arrays of Au nanoclusters evidences the surface enhanced Raman scattering effect. The

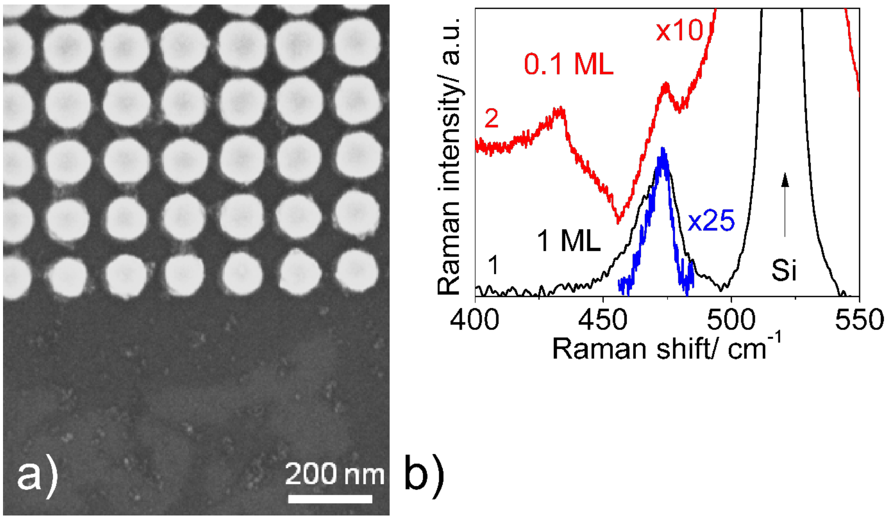

Figure 6: a) SEM image of CuS NCs with an ultra-low areal density deposited on Au arrays on SiO_2 layer and b) SERS-IERS Raman spectra measured with 632.8 nm. SERS spectrum of CuS NCs with 1 ML coverage on Au arrays formed on SiO_2 layer (curve 1) together with the Raman response of the CuS NCs of ultra-low areal density (denoted as 0.1 ML, curve 2). The 25 times enlarged fragment of curve 2 is shown for comparison.

combination of interference- and surface-enhanced Raman scattering led to a stronger enhancement of the phonon response by a factor of at least 180, and was successfully applied for probing the phonon spectrum of CuS nanocrystals with an ultra-low areal density.

Experimental

The layer of thermally grown SiO_2 with gradually varying thickness (from 0 to 570 nm) was prepared on a Si substrate in a wet chemical process by controlled dipping of a Si substrate covered by a homogeneous 600 nm thick SiO_2 layer into HF solution in H_2O (with bulk ratio 2:5) and served as IERS substrate. The thickness of the SiO_2 layer was determined from spectroscopic ellipsometry measurements averaging over an area of about 1 mm.

Periodic Au nanocluster arrays with a size of 10 × 10 μm^2 were fabricated as reported previously [13] on Si and 75 nm thick SiO_2 layers by direct electron beam writing (Raith-150, Germany) of a 130 nm spin-coated resist film (polymethyl methacrylate 950 K). A 40 nm Au film with a 5 nm Ti underlayer for better adhesion was deposited by electron beam evaporation on the patterned positive resist. Finally, the resist was removed by a lift-off process in dimethylformamide resulting in a periodic array of Au nanoclusters. As a result, the fabricated SERS-active substrates consist of areas of Au nanoclusters with a period of 150 nm.

CuS NCs were fabricated on the IERS and SERS substrates using the Langmuir–Blodgett technology as reported in [29]. Briefly, at the first stage behenic acid dissolved in hexane was spread onto the water surface in a LB bath using a $CuSO_4$ solution as a subphase. The copper behenate films formed were then transferred (Y-type) from the water surface onto a bare silicon substrate or SERS-active substrates. The typical thickness of copper behenate films ranged from 200 to 4 monolayers (MLs) corresponding to an average NC film thickness from 33 to 0.7 nm. At the second stage, the nucleation of CuS NCs in the organic matrix took place by sulfidizing the samples. At the last stage, 4 h of annealing at a temperature of 150 °C under argon atmosphere resulted in the removal of the organic matrix and the formation of free-standing CuS NCs on the substrates.

The morphology of the samples was determined using scanning electron microscopy (SEM). SEM images were obtained using a Raith-150 system at 10 kV acceleration voltage, 30 μm aperture and 6 mm working distance. It was found that the size of Au nanoclusters varied from array to array from 20 to 130 nm, while the height is fixed to 55 ± 5 nm. CuS NCs have a spherical shape and an average size in the range of 5–8 nm.

Raman experiments were carried out using Horiba T64000 and Labram HR800 spectrometers equipped with microscopes (the laser beam was focused to a spot with a size of 1 μm^2) in a backscattering geometry at room temperature. He-Cd, Ar$^+$, DPSS Cobolt$^®$, and He–Ne lasers with wavelengths of 325, 514.5, 514.7, and 632.8 nm, respectively, and power below 2 mW were used for excitation.

Acknowledgements

The work was supported by the DFG project ZA146/22-1, DFG Research Unit 1713 “Sensoric Micro- and Nanosystems”, Russian science foundation (project 14-12-01037), the cfAED cluster of excellence, by the Ministry of Education and Science of the Russian Federation, and CKP. Special thanks to K. P. Mogil'nikov for ellipsometry measurements of SiO_2 layers with gradual thickness and determination of SiO_2 thickness.

References

1. Honma, I.; Sano, T.; Komiyama, H. *J. Phys. Chem.* **1993,** *97,* 6692–6695. doi:10.1021/j100127a020
2. Milekhin, A. G.; Yeryukov, N. A.; Sveshnikova, L. L.; Duda, T. A.; Kosolobov, S. S.; Latyshev, A. V.; Surovtsev, N. V.; Adichtchev, S. V.; Himcinschi, C.; Zenkevich, E. I.; Jian, W.-B.; Zahn, D. R. T. *J. Phys. Chem. C* **2012,** *116,* 17164–17168. doi:10.1021/jp210720v
3. Hugall, J. T.; Baumberg, J. J.; Mahajan, S. *Appl. Phys. Lett.* **2009,** *95,* 141111. doi:10.1063/1.3243982
4. Chursanova, M. V.; Dzhagan, V. M.; Yukhymchuk, V. O.; Lytvyn, O. S.; Valakh, M. Ya.; Khodasevich, I. A.; Lehmann, D.; Zahn, D. R. T.; Waurisch, C.; Hickey, S. G. *Nanoscale Res. Lett.* **2009,** *5,* 403–409. doi:10.1007/s11671-009-9496-2
5. Lee, Y.-b.; Lee, S. H.; Lee, S.; Lee, H.; Kim, J.; Joo, J. *Appl. Phys. Lett.* **2013,** *102,* 033109. doi:10.1063/1.4788926
6. Todescato, F.; Minotto, A.; Signorini, R.; Jasieniak, J. J.; Bozio, R. *ACS Nano* **2013,** *7,* 6649–6657. doi:10.1021/nn402022z
7. Wang, X.; Kong, X.; Yu, Y.; Zhang, H. *J. Phys. Chem. C* **2007,** *111,* 3836–3841. doi:10.1021/jp064118z
8. Shan, G.; Xu, L.; Wang, G.; Liu, Y. *J. Phys. Chem. C* **2007,** *111,* 3290–3293. doi:10.1021/jp066070v
9. Liu, C. Y.; Dvoynenko, M. M.; Lai, M. Y.; Chan, T. H.; Lee, Y. R.; Wang, J.-K.; Wang, Y. L. *Appl. Phys. Lett.* **2010,** *96,* 033109. doi:10.1063/1.3291041
10. Milekhin, A. G.; Yeryukov, N. A.; Sveshnikova, L. L.; Duda, T. A.; Zenkevich, E. I.; Kosolobov, S. S.; Latyshev, A. V.; Himcinschi, C.; Surovtsev, N. V.; Adichtchev, S. V.; Feng, Z. C.; Wu, C. C.; Wuu, D. S.; Zahn, D. R. T. *J. Exp. Theor. Phys.* **2011,** *113,* 983–991. doi:10.1134/S1063776111140184
11. Rumyantseva, A.; Kostcheev, S.; Adam, P.-M.; Gaponenko, S. V.; Vaschenko, S. V.; Kulakovich, O. S.; Ramanenka, A. A.; Guzatov, D. V.; Korbutyak, D.; Dzhagan, V.; Stroyuk, A. L.; Shvalagin, V. V. *ACS Nano* **2013,** *7,* 3420–3426. doi:10.1021/nn400307a
12. Wang, Y.; Li, M.; Jia, H.; Song, W.; Han, X.; Zhang, J.; Yang, B.; Xu, W.; Zhao, B. *Spectrochim. Acta, Part A* **2006,** *64,* 101–105. doi:10.1016/j.saa.2005.07.003
13. Yeryukov, N. A.; Milekhin, A. G.; Sveshnikova, L. L.; Duda, T. A.; Rodyakina, E. E.; Sheremet, E. S.; Ludemann, M.; Latyshev, A. V.; Zahn, D. R. T. *Thin Solid Films* **2013,** *543,* 35–40. doi:10.1016/j.tsf.2013.03.070
14. Li, J.-H.; Chen, S.-W.; Chou, Y.; Wu, M.-C.; Hsueh, C.-H.; Su, W.-F. *J. Phys. Chem. C* **2011,** *115,* 24045–24053. doi:10.1021/jp203307f
15. Kahl, M.; Voges, E.; Kostrewa, S.; Viets, C.; Hill, W. *Sens. Actuators, B* **1998,** *51,* 285–291. doi:10.1016/S0925-4005(98)00219-6
16. Guillot, N.; Shen, H.; Frémaux, B.; Péron, O.; Rinnert, E.; Toury, T.; Lamy de la Chapelle, M. *Appl. Phys. Lett.* **2010,** *97,* 023113. doi:10.1063/1.3462068
17. Alvarez-Puebla, R.; Cui, B.; Bravo-Vasquez, J.-P.; Veres, T.; Fenniri, H. *J. Phys. Chem. C* **2007,** *111,* 6720–6723. doi:10.1021/jp070906s
18. Nemanich, R. J.; Tsai, C. C.; Connell, G. A. N. *Phys. Rev. Lett.* **1980,** *44,* 273–276. doi:10.1103/PhysRevLett.44.273
19. Ishii, M.; Shibata, K.; Nozaki, H. *J. Solid State Chem.* **1993,** *105,* 504–511. doi:10.1006/jssc.1993.1242
20. Yoon, D.; Moon, H.; Son, Y.-W.; Choi, J. S.; Park, B. H.; Cha, Y. H.; Kim, Y. D.; Cheong, H. *Phys. Rev. B* **2009,** *80,* 125422. doi:10.1103/PhysRevB.80.125422
21. Kolobov, A. V.; Maeda, Y.; Tanaka, K. *J. Appl. Phys.* **2000,** *88,* 3285–3289. doi:10.1063/1.1289818
22. Marsillac, S.; Little, S. A.; Collins, R. W. *Thin Solid Films* **2011,** *519,* 2936–2940. doi:10.1016/j.tsf.2010.11.065
23. Aspnes, D. E.; Theeten, J. B. *J. Electrochem. Soc.* **1980,** *127,* 1359–1365. doi:10.1149/1.2129899
24. Nemanich, R. J. Interference-enhanced Raman scattering from thin films and interfaces. In *Microbeam Analysis;* Russell, P. E., Ed.; San Francisco Press: San Francisco, CA, USA, 1989; pp 141–145.
25. Seok, T. J.; Jamshidi, A.; Kim, M.; Dhuey, S.; Lakhani, A.; Choo, H.; Schuck, P. J.; Cabrini, S.; Schwartzberg, A. M.; Bokor, J.; Yablonovitch, E.; Wu, M. C. *Nano Lett.* **2011,** *11,* 2606–2610. doi:10.1021/nl2010862
26. Min, Q.; Pang, Y.; Collins, D. J.; Kuklev, N. A.; Gottselig, K.; Steuerman, D. W.; Gordon, R. *Opt. Express* **2011,** *19,* 1648–1655. doi:10.1364/OE.19.001648
27. Gao, L.; Ren, W.; Liu, B.; Saito, R.; Wu, Z.-S.; Li, S.; Jiang, C.; Li, F.; Cheng, H.-M. *ACS Nano* **2009,** *3,* 933–939. doi:10.1021/nn8008799
28. Wang, D.; Zhu, W.; Best, M. D.; Camden, J. P.; Crozier, K. B. *Nano Lett.* **2013,** *13,* 2194–2198. doi:10.1021/nl400698w
29. Milekhin, A.; Sveshnikova, L.; Duda, T.; Surovtsev, N.; Adichtchev, S.; Ding, L.; Zahn, D. R. T. *J. Vac. Sci. Technol., B* **2010,** *28,* C5E22. doi:10.1116/1.3442799

License and Terms

The definitive version of this article is the electronic one which can be found at:
doi:10.3762/bjnano.6.77

BEILSTEIN JOURNAL OF NANOTECHNOLOGY

Statistics of work and orthogonality catastrophe in discrete level systems: an application to fullerene molecules and ultra-cold trapped Fermi gases

Antonello Sindona*[1,2], Michele Pisarra[1,2], Mario Gravina[1,2], Cristian Vacacela Gomez[1,2], Pierfrancesco Riccardi[1,2], Giovanni Falcone[1,2] and Francesco Plastina[1,2]

Full Research Paper

Open Access

Address:
[1]Dipartimento di Fisica, Università della Calabria, Cubo 30C, 87036 Rende (CS), Italy and [2]INFN, sezione LNF, Gruppo collegato di Cosenza, Cubo 31C, 87036 Rende (CS), Italy

Email:
Antonello Sindona* - antonello.sindona@fis.unical.it

* Corresponding author

Keywords:
nanostructured systems; non-equilibrium thermodynamics; orthogonality catastrophe; sudden quench; ultra-cold Fermi gases; work distribution

Beilstein J. Nanotechnol. **2015,** *6,* 755–766.
doi:10.3762/bjnano.6.78

Received: 30 September 2014
Accepted: 09 February 2015
Published: 18 March 2015

This article is part of the Thematic Series "Self-assembly of nanostructures and nanomaterials".

Guest Editor: I. Berbezier

Abstract

The sudden introduction of a local impurity in a Fermi sea leads to an anomalous disturbance of its quantum state that represents a local quench, leaving the system out of equilibrium and giving rise to the Anderson orthogonality catastrophe. The statistics of the work done describe the energy fluctuations produced by the quench, providing an accurate and detailed insight into the fundamental physics of the process. We present here a numerical approach to the non-equilibrium work distribution, supported by applications to phenomena occurring at very diverse energy ranges. One of them is the valence electron shake-up induced by photoionization of a core state in a fullerene molecule. The other is the response of an ultra-cold gas of trapped fermions to an embedded two-level atom excited by a fast pulse. Working at low thermal energies, we detect the primary role played by many-particle states of the perturbed system with one or two excited fermions. We validate our approach through the comparison with some photoemission data on fullerene films and previous analytical calculations on harmonically trapped Fermi gases.

Introduction

Closed many-particle systems and their out-of-equilibrium dynamics after a quench have been attracting considerable interest over the past years, with particular attention to the brutal disturbance of the equilibrium properties of a Fermi gas, induced by the sudden introduction of localized scattering potential in the system [1-4]. Notwithstanding the weakness of the perturbation, its effect can be so pronounced that the final state of the gas loses essentially any overlap with the initial unperturbed one, as the number of particles approaches the thermodynamic limit. This *orthogonality catastrophe* predicted by

Anderson [5] was first witnessed by the anomalous response of conduction electrons to core level ionization through X-ray absorption, and the subsequent emission of a core electron from simple metals [6,7]. The corresponding kinetic energy spectrum was observed to have an asymmetric peak at the binding energy of the core level with a power-law singularity, which has then become known as the *Fermi edge singularity* [7]. Similar patterns were afterwards identified in a large number of core-ionized systems [8,9], including organic molecules [10] and carbon-based nanomaterials [11-19], where an additional signature of the Anderson orthogonality catastrophe are the secondary peaks, or shake-up satellites, in the core level spectra. Despite the diversity of contexts in which Fermi edge resonance and Anderson orthogonality catastrophe occur [20-30], the same generic physics has been recently observed in the controllable domain of ultra-cold trapped gases, as a response to the embedding of a single probe qubit, i.e., a two-level impurity [31,32]. Furthermore the intrinsic out-of-equilibrium dynamics induced by the impurity has been thoroughly analyzed by treating the quench as a thermodynamic transformation [33], and using the full statistics of the work done on the gas [34,35]. Interestingly enough, X-ray absorption and emission spectra from noninteracting quantum dots have been interpreted in terms of the quantum work distribution, and linked to the corresponding fluctuation relations in statistical mechanics [36]. To explore more of such a connection, we present here a comparison of the statistics of the work done in the C_{60} molecule, following the core ionization of a carbon atom, and a harmonically trapped Fermi gas, following the sudden switch on of a localized perturbation, assumed to have an s-wave-like character. In particular, we propose a numerical approach suitable for low-temperature regimes to compute the work distribution (Section 1), based on the knowledge of the initial ground state and the low-lying final perturbed states of the systems (Section 2). To treat the fullerene molecule, we use density-functional theory (DFT) and simulate the sudden creation of a core state, by replacing a 1s electron pair with the effective pseudo-potentials of neutral and ionized atomic carbon (Section 2.1). In the harmonically trapped Fermi gas, on the other hand, we assume a contact scattering potential with a spatially structure-less form, localized at the center of the harmonic trap, and express the potential strength in terms of a dimensionless parameter, which turns out to be the critical parameter governing the sudden quench process (Section 2.2). We then determine the one-fermion structures of the systems in the absence or presence of the perturbation, and compute the many-body overlap between the initial unperturbed ground state and the final perturbed states, with not more than two excited fermions (Section 3). The work distribution obtained with such contributions accounts for more than 95% of the shake-up process, which let us select the suitable parameters in the Fermi gas with a shake-up content similar to that of fullerene. We test the accuracy of the methods through the comparison with available X-ray photoemission experiments [12,13], in the fullerene case, and previous analytical calculations [32,35], in the Fermi gas case. Finally, we draw some conclusions on the results obtained in the two applications (Section Conclusion).

Results and Discussion

1 Work distribution and energy spectrum in a sudden quench

We begin by reviewing some concepts regarding non-equilibrium thermodynamics in a suddenly quenched Fermi gas. Consider a many-fermion system in a well-defined Gibbs state

$$\hat{\rho} = \frac{e^{-\beta(\hat{H}-\mu\hat{N})}}{\mathrm{tr}[e^{-\beta(\hat{H}-\mu\hat{N})}]},$$

at inverse temperature β and chemical potential μ. The equilibrium is set by the initial Hamiltonian $\hat{H}$ and the number operator $\hat{N}$, which are diagonal in the same basis of eigenstates $|\Phi_i\rangle$ having the eigenvalues E_i and N_i, respectively. After removing the contact with the thermal reservoir, suppose some *work* is performed by taking the system out of equilibrium through the abrupt introduction of an external perturbation $\hat{V}$. Now the perturbed system is characterized by the final Hamiltonian $\hat{H}' = \hat{H} + \hat{V}$, specified by the eigenstates $|\Phi'_f\rangle$ and the eigenenergies E'_f. In this picture, the work done is not a quantum mechanical observable, but rather a stochastic variable distributed according to a probability distribution $P_\beta(W)$ [34]. The definition of such a distribution requires two projective measurements: the first projects onto the eigenbasis of the initial Hamiltonian, with the system in thermal equilibrium. The system then suddenly evolves, before the second measurement projects onto the eigenbasis of the final Hamiltonian. Accordingly, the probability to do the work $W = E'_f - E_i$ is given by the probability $\langle\Phi_i|\hat{\rho}|\Phi_i\rangle$ of obtaining E_i for the first measurement outcome, followed by the conditioned probability $|\langle\Phi_i|\Phi'_f\rangle|^2$ of obtaining E'_f for the second. The work distribution is therefore obtained as [33]

$$P_\beta(W) = \sum_{i,f} \frac{e^{-\beta E_i}}{Z} |\langle\Phi_i|\Phi'_f\rangle|^2 \delta\left[W - \left(E'_f - E_i\right)\right]. \quad (1)$$

At the absolute zero, only the unperturbed ground state remains in the initial state summation

$$P(W) = \sum_f |\langle\Phi_0|\Phi'_f\rangle|^2 \delta\left[W - \left(E'_f - E_0\right)\right], \quad (2)$$

and the work distribution tends to the initial state average $P(W) = \langle \Phi_0 \,|\, \delta[W - (\hat{H}' - E_0)] \,|\, \Phi_0 \rangle$, which coincides with the emission spectrum of the system in response to the sudden perturbation [37,38]. Interestingly enough, the cross-section for the ionization of a core level ε_c due to absorption of an X-ray photon of energy $\hbar\omega$ in matter results from two factors [39]: core-electron photo-ejection and valence-electron dynamic screening. The former is expressed by the photo-current probability, involving the initial core state and the final photo electron state. The latter is manifested by the work distribution in Equation 2, which can be interpreted as the probability density that the work $W = \hbar\omega + \varepsilon_c - \varepsilon$ is used to excite valence electrons at the expense of the kinetic energy of the photoelectron, ε [17-19]. Indeed, $P(W)$ accounts for the $N - 1$ electrons that do not directly participate in the ionization process. This *spectator electron* approach is particularly suitable for mono-energetic X-rays that cause deep core-level photoelectrons to be ejected from the sample ($\hbar\omega \gg |\varepsilon_c|$).

2 Initial and final Hamiltonians

We have seen that the key ingredients of the work distribution (Equation 2) are the many-body states of the unperturbed and perturbed Fermi systems. In the following we will take the different physical situations set forth above. Specifically, we will first investigate the valence electronic structure of a fullerene molecule in the absence or presence of a 1s core hole, whose fast creation induces an abrupt attractive perturbation of the electrons of the system. Then, we will shift the focus to a harmonically trapped gas of fermionic atoms with an embedded impurity, whose fast excitation can be modeled by a suddenly introduced repulsive δ-potential.

2.1 The fullerene molecule

Consider a cluster of 60 carbon atoms arranged in a fullerene molecule of radius 3.1573 Å, whose equilibrium geometry and characteristic bond lengths (of 1.4474 and 1.3696 Å, respectively) are reported Figure 1. We can do some *work* on the cluster by core-ionizing one of its atoms to form a molecular cation. The valence electrons are then thrown out of equilibrium, tending to dynamically relax and compensate for the presence of a positive charge. To depict the rearrangement of the valence electronic structure, we use a DFT approach in which we replace the core electrons of a specific atom in the molecule with an effective core potential (ECP) of the Stevens–Basch–Krauss (SBK) type [40], whose parameters are adjusted to describe neutral and core-ionized atomic carbon [10]. The valence electrons in this reference atom are described by a d-polarized double split-valence pseudo-basis, being specifically designed for the considered ECP and optimized for the neutral (C_{60}) and ionized (C^*_{60}) clusters [18,19]. As for the core and valence electrons of all other atoms in the compound, we select the d-polarized triple split-valence basis set denoted 6-311G* [41]. We then perform a spin-restricted DFT calculation [42-44], working under the generalized gradient approximation (GGA) for electron exchange and correlation, parameterized by the Perdew–Burke–Ernzerhof (PBE) functional

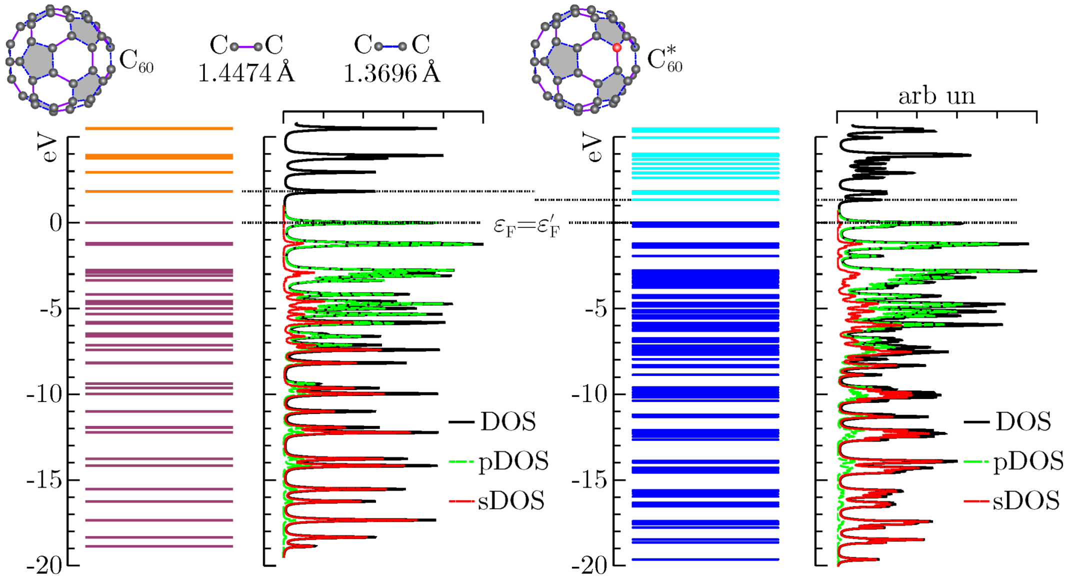

Figure 1: Valence levels and (broadened) DOS for the neutral (C_{60}) and ionized (C^*_{60}) fullerene molecules, as computed with the DFT approach outlined in the main text. In C_{60} the projected density of s and p states contribute for 44.2% and 55.3% of the occupied DOS, respectively. In C^*_{60} the s-DOS and p-DOS contributions change to 51.1% and 48.8%, respectively. The residual part (not shown) is left to the projected density of polarized d-states.

[45,46]. All electron spin pairs from the clusters are explicitly taken into account except for the one removed from the reference atom. Convergence for C_{60} and C^*_{60} leads to optimized ground state wave functions made of single Slater determinants of 179 pairs of occupied molecular orbitals (MOs), which are linear combinations of 1135 contracted Gaussians from both the ECP basis, localized at the reference atom, and the 6-311G* basis centered on all other atoms. To simplify the notation we denote such composite basis sets as $\left|\overrightarrow{g^{\mathrm{ECP}}_{6\text{-}311}}\right\rangle$ for C_{60}, and $\left|\overrightarrow{g^{\mathrm{ECP}*}_{6\text{-}311}}\right\rangle$ for C^*_{60}. The corresponding coefficients (eigenvectors) are computed from the secular equations following DFT energy minimization.

The electron spin pairs occupy 59 core levels, that is, one per carbon atom excluding the reference atom, and 120 valence levels. The core MOs are mainly given by linear combinations of the s-contracted Gaussians of the ECP+6-311G* basis set, where the valence coefficients of the ECP set tend to compensate for the absence of the core electrons in the reference atom. The core eigenvalues are nearly degenerate with a percentage standard deviation below 0.15%. The average core energy ε_c for C_{60} overestimates the experimental C 1s energy by a percentage error of about 7%. Possible causes for this discrepancy are discussed in [18]. The valence states are of the form $|v\rangle = \vec{v}\cdot\left|\overrightarrow{g^{\mathrm{ECP}}_{6\text{-}311}}\right\rangle$ and $|v'\rangle = \vec{v}'\cdot\left|\overrightarrow{g^{\mathrm{ECP}}_{6\text{-}311}}\right\rangle$, where $\vec{v}$ and $\vec{v}'$ are the valence-eigenvectors of coefficients for C_{60} and C^*_{60}, respectively. As shown in Figure 1, the valence electronic structure of the neutral and ionized clusters is made of discrete energy levels separated by an average energy difference of about 0.2 eV. The predicted band gap value of 1.82 eV for C_{60} is consistent with experiments [47] and previous calculations [18]. Core ionization leads to a decrease of the band gap in C^*_{60} of about 0.5 eV (Table 1).

In order to determine the symmetry of the valence MOs, we compute a density of state (DOS) distribution from the superposition of Lorentzian lines of equal height, centered at the occupied/empty MO energy values. We then use the valence coefficients to construct a weighted sum yielding the *projected* distributions arising from the s, p, and d components of the ECP+6-311G* basis set. The normalized profiles of the total DOS, the s-DOS, and the p-DOS for both the neutral and ionized molecules are also displayed in Figure 1, where a broadening width of about 0.5 eV is applied. We see that the lowest occupied valence MOs, with energies in the range of ca. 10–20 eV below the Fermi level, have a dominant s character. At higher energies, up to about 2–3 eV below the Fermi energy, the p components become more and more significant, tending to compete with the s components and forming sp^2 and sp^3 bonds. On the other hand, the valence MOs close to the Fermi energy are mainly made of p orbitals pointing along the radial directions of the buckyball. Based on the analysis of the relative areas of the projected densities of states, we may infer that core ionization produces an enhancement of the s component with respect to the p component of about 5%, while polarization effects due to the d orbitals play a marginal role. This is not surprising given the s character of the core hole. The key feature of the many-electron response to core ionization is given by the squared overlaps between the valence MOs of C_{60} and C^*_{60}. The latter are straightforwardly computed from the 1135 × 1135 overlap matrix $\left|\overrightarrow{g^{\mathrm{ECP}*}_{6\text{-}311}}\right\rangle\left\langle\overrightarrow{g^{\mathrm{ECP}}_{6\text{-}311}}\right|$, by left (right) multiplication with the valence eigenvectors $\vec{v}$ and $\vec{v}'$, respectively. To have a more clear idea of the change of the valence electrons wavefunctions in the surrounding of the core-hole site, we focus on the ends of the occupied valence spectra. In particular, we consider the highest and lowest occupied MOs of the neutral molecule and some MOs of the ionized molecule to

Table 1: Squared overlap integrals between the lowest and highest occupied valence states in the neutral C_{60} molecule ($v = 1$, $\varepsilon_1 = -18.8575$ eV and $v = v_F = 120$, $\varepsilon_{120} = \varepsilon_F = 0$, respectively) and some valence states in the ionized C_{60} molecule (where $\varepsilon'_F = -3.132$ eV). The reported values confirm the remarkable non adiabatic effects induced by core hole creation (see also below in Figure 2).

v'	$\varepsilon_{v'} - \varepsilon'_F$	$\lvert\langle v' \mid v = 1\rangle\rvert^2$	v'	$\varepsilon_{v'} - \varepsilon'_F$	$\lvert\langle v' \mid v = 120\rangle\rvert^2$
1	−19.6357	0.428741	115	−1.2163	0.000219
2	−18.6425	0.554975	116	−0.2204	0.791579
3	−18.4765	0.009811	117	−0.0762	$<10^{-6}$
4	−18.4765	$<10^{-6}$	118	−0.0653	0.004186
5	−17.7799	0.003615	119	−0.0163	$<10^{-6}$
6	−17.5758	0.000141	$v'_F = 120$	0	$<10^{-6}$
7	−17.5214	$<10^{-6}$	121	1.3361	0.042688
8	−17.4262	0.000096	122	1.6871	$<10^{-6}$
9	−17.4126	$<10^{-6}$	123	1.8096	0.000134
10	−16.5364	0.000784	124	2.6232	0.012468
11	−16.4248	0.000091	125	2.8799	$<10^{-6}$

have similar binding energies relative to the perturbed Fermi level. The squared overlap between these states are listed in Table 1, while some of their orbital shapes are shown in Figure 2.

We see that core ionization has more direct influence on the bottom of the valence band, inducing the lowest occupied state $|v=1\rangle$ of C_{60} to get mostly mixed with the first two occupied states of C_{60}^*, namely $|v'=1\rangle$ and $|v'=2\rangle$. Significant modifications, however, affect also the unperturbed Fermi state $|v_F=120\rangle$, which looses essentially any correlation with the perturbed Fermi state $|v'_F=120\rangle$, and is mainly mapped to the $|v'=116\rangle$-state keeping some non negligible leakage to some other perturbed states with similar energies. This is a clear signature of the highly non-adiabatic behavior inherent to the process. As a global measure of the disturbance brought by the core hole, we take the valence electron ground states $|\Phi_0\rangle$ and $|\Phi'_0\rangle$, for the neutral and ionized molecule, respectively, and compute their squared overlap

$$\left|\langle \Phi_0|\Phi'_0\rangle\right|^2 = \left|\det\left\{\langle v|v'\rangle\right\}_{v,v'=1,\ldots,120}\right|^2,$$

which denotes the ground-state survival probability. Complementarily, the shake-up probability is given by $1-\left|\langle \Phi_0|\Phi'_0\rangle\right|^2$ and takes a value of 19.10%.

2.2 The harmonically trapped Fermi gas

We now take a spin 1/2 gas of weakly interacting atoms in a parabolic potential of a typical length x_0 and trapping frequency ω. Neglecting the inter-particle forces, the one-fermion Hamiltonian is that of a harmonic oscillator

$$H(x) = \frac{\hbar\omega}{2}\left(-\frac{x_0^2\partial^2}{\partial x^2}+\frac{x^2}{x_0^2}\right), \tag{3}$$

with eigenvalues $\varepsilon_v = \hbar\omega(v+1/2)$, and eigenstates $|v\rangle$, which have the coordinate representation

$$\langle x|v\rangle = \frac{H_v\left(x/x_0\right)}{2^{v/2}\,v!^{1/2}\,\pi^{1/4}x_0^{1/2}}\,e^{-\frac{x^2}{2x_0^2}}, \tag{4}$$

expressed in terms of the Hermite polynomials $H_v(x/x_0)$ of order v = 0,1,…. We now add a two-level impurity trapped in an auxiliary potential and brought in contact with the gas. The impurity is initially in its ground state with a negligible scattering interaction with the fermions in their equilibrium configuration set by $H(x)$. We suppose doing some *work* on the system by quickly exciting the impurity. Then, the gas feels a sudden perturbation $V(x,t)$ = $V(x)\theta(t)$, assumed to have an

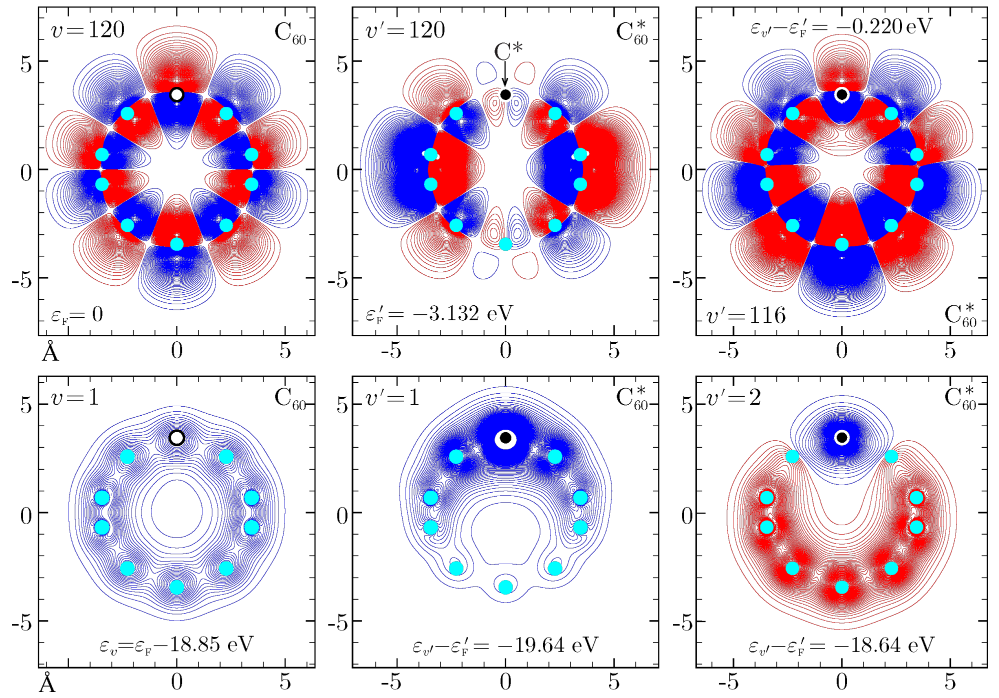

Figure 2: Lowest and highest occupied valence states for the neutral fullerene molecule (C_{60}) and corresponding valence states in the ionized fullerene molecule (C_{60}^*). The sudden switching mechanism leads most of the content of the unperturbed Fermi state to be found in a state lying about 0.22 eV below the perturbed Fermi level. On the other hand, the lowest- energy unperturbed valence state gets mainly mixed with the first two occupied perturbed valence states (see also Table 1).

s-wave like character. Further details on how this set-up can efficiently describe an ultra-cold Fermi gas probed by a two-level impurity, with the parabolic potential mimicking the magneto-optical trapping potential, may be found for example in [25,28,31,32,48]. Let us further assume that the perturbation is spatially structure-less and localized at the center of the trap, e.g., $V(x) = \pi V_0 x_0 \delta(x)$. The perturbation strength V_0 can be parameterized as $V_0 = \hbar\omega\alpha^{1/2}\left(\nu_F + 1/2\right)^{1/2}$, where ν_F is the Fermi number (corresponding to $2(\nu_F + 1)$ fermions, and α a dimensionless parameter, which turns out to be the critical parameter of the theory [32,35,49].

The simple structure of $V(x)$ allows one to handle the diagonalization of the total Hamiltonian $H'(x) = H(x) + V(x)$, which describes the gas after switching on the potential. In particular, the perturbed eigenfunctions in presence of the excited impurity can be written in terms of the parabolic cylinder functions

$$\left\langle x \middle| \nu' \right\rangle = \frac{\eta_{\nu'} D_{\nu'}\left(\sqrt{2}\left|x\right|/x_0\right)}{\Gamma\left(\nu'+1\right)^{1/2}\pi^{1/4}x_0^{1/2}}, \tag{5}$$

with normalization constants $\eta_{\nu'}$ and associated level energies $\varepsilon_{\nu'} = \hbar\omega(\nu' + 1/2)$. We see that $\left\langle x \middle| \nu' \right\rangle = \left\langle x \middle| \nu \right\rangle$ and $\varepsilon_{\nu'} = \varepsilon_\nu$ when the perturbed quantum number ν' takes non-negative integer values. Furthermore, due to the fact that $\left\langle x = 0 \middle| \nu \right\rangle = 0$, for $\nu = 1,3,\ldots$, the odd harmonic oscillator eigenfunctions and eigenenergies are left unaffected by the δ-potential, i.e., $\nu' = \nu = 1,3,\ldots$. As for the perturbed wave functions corresponding to $\nu = 0,2,\ldots$, the stationary Schrödinger equation for $H'(x)$ leads the implicit condition [35,50]:

$$\frac{2}{\pi\alpha^{1/2}\sqrt{\frac{1}{2}+\nu_F}} + \frac{\Gamma\left(-\frac{\nu'}{2}\right)}{\Gamma\left(\frac{1-\nu'}{2}\right)} = 0, \tag{6}$$

which ensures the physically correct behavior for $\left\langle x \middle| \nu' \right\rangle$. Now, since the Γ-function has poles for negative integer values, Equation 6 leads to $\nu' \to \nu$ for $\alpha \to 0$, and $\nu' \to \nu + 1$ for $\alpha \to \infty$. Then, ν' takes a real values in the range $[\nu, \nu + 1]$ for $\nu = 0,2,\ldots$. More importantly, each fixed values of α and ν_F yields a one-to-one mapping of $\left|\nu\right\rangle$, ε_ν onto $\left|\nu'\right\rangle$, $\varepsilon_{\nu'}$. This means that we can first obtain the ν' values by numerically solving Equation 6, compute the perturbed energies $\varepsilon_{\nu'}$ and the normalization constants $\eta_{\nu'}$, and then find the perturbed states $\left|\nu'\right\rangle$. In Figure 3 and Figure 4 we show an example of gas with 122 fermions ($\nu_F = 120$) in absence and presence of an impurity potential characterized by the critical parameter $\alpha = 0.1$. Similar to the fullerene case, we see that the sudden perturbation is more efficient on the lower part of the energy spectrum, which corresponds to a more pronounced shifting of the perturbed even levels towards the unperturbed odd ones. This is also attested by comparing the unperturbed and perturbed density of levels, obtained by superimposing Gaussian functions of width $0.15\hbar\omega$, centered at the occupied/empty energy values. A more quantitative analysis comes from the squared overlaps $\left|\left\langle \nu \middle| \nu' \right\rangle\right|^2$, some of which are numerically computed and reported in Table 2. In contrast to the C_{60}/C_{60}^* case, we notice that the states involved is the $\varepsilon_\nu, \left|\nu\right\rangle \leftrightarrow \varepsilon_{\nu'}, \left|\nu'\right\rangle$ mapping are always strongly correlated by a squared overlap value larger than $\left|\left\langle \nu = 0 \middle| \nu' = 0 \right\rangle\right|^2 \approx 0.74$.

Nonetheless, a much more regular dynamic screening is experienced by the gas, involving single fermion states with squared overlaps $\left|\left\langle \nu \middle| \nu' \right\rangle\right|^2 > 0.01$. Indeed we observe a non-negligible leakage of the unperturbed wave function onto the perturbed eigenfunctions, having an energy larger than $5\hbar\omega$ than the unperturbed energy value. With the two eigenbases $\left\{\left|\nu\right\rangle\right\}$ and $\left\{\left|\nu'\right\rangle\right\}$, we can form Slater determinants and compute the many-body states of the gas. In particular, the unperturbed and perturbed ground states include the lowest occupied $2(\nu_F + 1)$ one-particle states, and the ground-state survival probability can be computed from

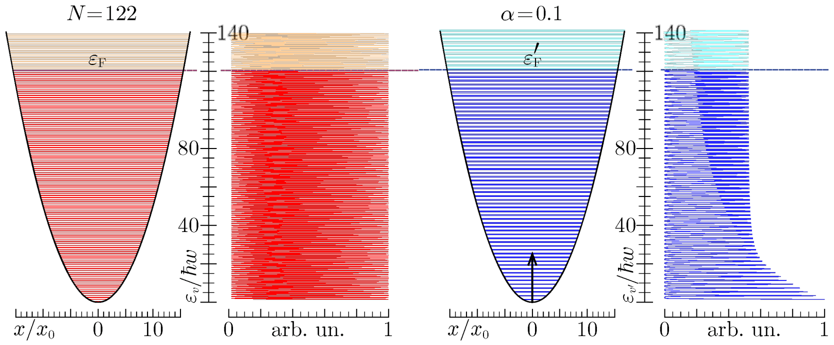

Figure 3: Energy levels and (broadened) density of states for a trapped gas of spin 1/2 fermions having a number of occupied states (N = 122) similar to that of the valence band of C_{60}. The critical parameter is set to α = 0.1, which corresponds to an impurity potential height of $V_0 = 3.47\hbar\omega$.

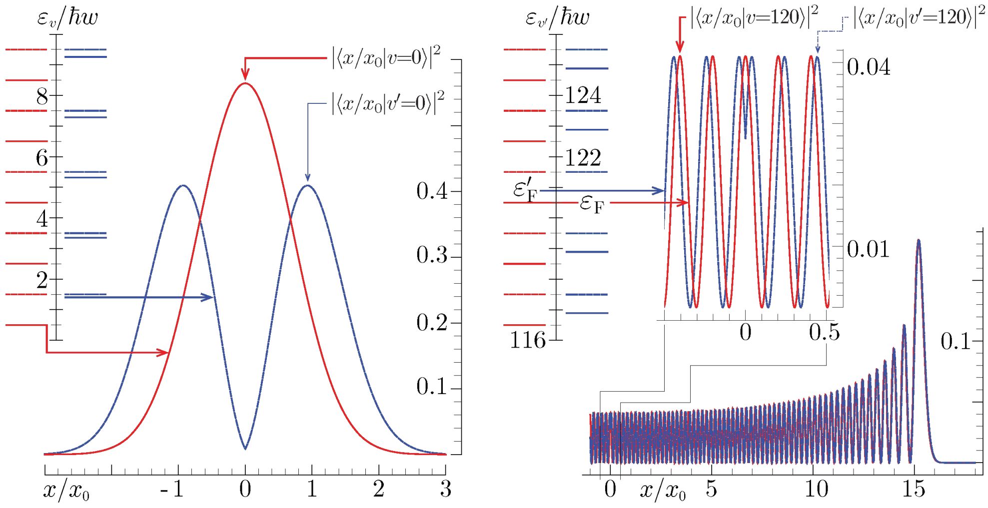

Figure 4: Lowest and highest occupied one-particle wave functions and levels for a harmonically trapped gas of $N = 122$ fermions in absence and presence of the excited impurity, whose perturbation is characterized by the critical parameter $\alpha = 0.1$ (see also Figure 3 and Table 2). The unperturbed and perturbed Fermi levels, relative to the lowest occupied one-particle state, are $\varepsilon_F = 120.5\hbar\omega$ and $\varepsilon'_F = 120.838\hbar\omega$, respectively.

Table 2: Squared overlap integrals in a spin 1/2 trapped gas of 122 particles with a sudden switching impurity potential characterized by the critical exponent value $\alpha = 0.1$ (see also Figure 3). The lowest occupied ($v = 0$, $\varepsilon_0 = 0.5$ eV) and highest occupied ($v = 120$, $\varepsilon_{120} = \varepsilon_F = 120.5$) states are mostly correlated to the corresponding perturbed states. Shake-up effects though involve the perturbed states which are closer in energy.

v'	$\varepsilon_{v'}$ / $\hbar\omega$	$\left|\langle v'|v=0\rangle\right|^2$	v'	$\varepsilon_{v'}$ / $\hbar\omega$	$\left|\langle v'|v=120\rangle\right|^2$
0	1.38233	0.742291	110	110.85	0.00147324
2	3.32392	0.108816	112	112.848	0.00234289
4	5.28188	0.046455	114	114.845	0.00429914
6	7.24826	0.0265519	116	116.843	0.010353
8	9.22	0.017436	118	118.84	0.0518994
10	11.1955	0.0124231	120	120.838	0.882784
12	13.1739	0.00934134	122	122.836	0.0234252
14	15.1546	0.00729833	124	124.834	0.00692288
16	17.137	0.00586813	126	126.831	0.00325807
18	19.121	0.00482476	128	128.829	0.00188445
20	21.1063	0.00403857	130	130.827	0.00122525

$$\left|\langle\Phi_0|\Phi'_0\rangle\right|^2 = \left|\det\left\{\langle v|v'\rangle\right\}_{v,v'\le v_F+1}\right|^2.$$

The shake-up probability $1-\left|\langle\Phi_0|\Phi'_0\rangle\right|^2$ increases with increasing height of the impurity potential barrier. In the example considered here (Figure 3 and Figure 4) this probability takes a percentage value of 19.26%, which is extraordinarily similar to that of fullerene. Suppose we keep the critical exponent constant, i.e., we fix $\alpha = 0.1$, but reduce the number of fermions in the gas to $N = 38$ first, and then to $N = 16$. The corresponding shake-up probabilities will decrease to 15.36% and 12.17%, respectively. Suppose, as a complement, we keep the particle number constant, say, $N = 122$, and increase α to 0.2 first, and then to 0.3. The corresponding shake-up probabilities will increase to 29.3% and 35.7%, respectively.

3 Work distribution decomposition and many-fermion shake-up

To characterize the zero-temperature features of the work distribution (Equation 2), we decompose it according to the number of fermions excited to the final states by the external potential. In other words, we re-arrange the final state summation in Equation 2 to write it in the form

$$P(W) = \sum_{k=0}^{\infty} P_k(W)$$

where $P_k(W)$ accounts for the work done in all processes which lead the system to occupy a final state with k fermions above the Fermi level. Now, we use the formalism of creation and annihilation operators, denoted $c_{v'}^{\dagger}$ and $c_{v'}$, respectively, acting on the perturbed ground state, to express the $P_k(W)$ distributions as shown in Equation 7 (see below).

Here, the squared overlaps can be reduced to the calculation of matrix determinants involving the unperturbed and perturbed one-fermion eigenstates of the initial and final Hamiltonians, i.e., the unperturbed ground state set $\{\langle v|\}_{v \le v_{\mathrm{F}}}$ and the perturbed set obtained by taking $\{|v'\rangle\}_{v < v_{\mathrm{F}}+1}$ and replacing the elements $v'_1,\ldots,v'_k$ with $u'_1,\ldots,u'_k$. We also need to point out that in the work distribution of fullerene we do not include the core electrons, which do not take part in the photo-ejection. Indeed, the overlap between the initial and final many-body states of the "spectator" core levels is 1, within a numerical error of ca. 10^{-6}. This fact is not surprising, notwithstanding the differences in the one-electron core states (Figure 2), because excitations from the core to the valence part of the one-electron initial and final spectra are not allowed.

The situations that we have considered so far encompass relatively weak external perturbations, for which the most prominent contribution is the no-shake line

$$P_0(W) = \left|\langle \Phi_0 | \Phi'_0 \rangle\right|^2 \delta\left[W - \left(E'_0 - E_0\right)\right]. \tag{8}$$

This term corresponds to a process in which the work $W = E'_0 - E_0$ is used to distort the initial ground state, and leave all the particles in the system relaxed into the final ground state. Indeed, as already pointed out in the previous section and emphasized by the results shown in Table 3, the no-shake intensity, i.e., the ground-state survival probability, takes percentage values of the order of about 80% either in the core-ionized fullerene molecule or in the Fermi gas with $N = 122$ particles, shaken up by a δ-potential of critical exponent $\alpha = 0.1$. The $P_{k \ge 1}$ distributions define the shake-up process, with k fermions jumping between the (unperturbed) ground state and the (perturbed) excited states in response to the perturbation [35].

Also from Table 3, we can see that the largest part of the fermion shake up lies in one-fermion excitations processes, e.g.,

$$P_k(W) = \sum_{\substack{v'_1,\ldots,v'_k \\ \varepsilon_{v'_1} \le \varepsilon'_{\mathrm{F}},\ldots,\varepsilon_{v'_1} \le \varepsilon'_{\mathrm{F}}}} \; \sum_{\substack{u'_1,\ldots,u'_k \\ \varepsilon_{u'_1} > \varepsilon'_{\mathrm{F}},\ldots,\varepsilon_{u'_1} > \varepsilon'_{\mathrm{F}}}} \left|\langle \Phi_0 | c_{v'_1} \ldots c_{v'_k} c^{\dagger}_{u'_1} \ldots c^{\dagger}_{u'_k} | \Phi'_0 \rangle\right|^2$$
$$\times \delta\left[W - \left(E'_0 + \varepsilon_{u'_1} + \ldots + \varepsilon_{u'_k} - E_0 - \varepsilon_{v'_1} - \ldots - \varepsilon_{v'_k}\right)\right]. \tag{7}$$

Table 3: Ground-state survival probability and shake-up probabilities involving excited states with 1–3 particles above the Fermi level. The closure relation $\sum_n |\Phi'_n\rangle\langle\Phi'_n| = 1$, projected onto the unperturbed ground state, is verified with an error of less than 5% in all cases.

	C_{60}	$\alpha = 0.1$ $N = 122$	$\alpha = 0.1$ $N = 84$	$\alpha = 0.1$ $N = 38$	$\alpha = 0.1$ $N = 16$
no shake (%) $\int dW P_0(W) = \left|\langle \Phi_0 | \Phi'_0 \rangle\right|^2$	80.899	80.739	81.876	84.635	87.834
one body (%) $\int dW P_1(W)$	17.031	14.975	13.736	11.614	8.091
two body (%) $\int dW P_2(W)$	0.249	0.211	0.147	0.067	0.012
three body (%) $\int dW P_3(W)$	$\approx 10^{-3}$	$\approx 10^{-5}$	$\approx 10^{-7}$	$\approx 10^{-7}$	$\approx 10^{-8}$
$\sum_f \left|\langle \Phi_0 | \Phi'_f \rangle\right|^2$ (%) $\approx \sum_{i=1}^{3} \int dW P_i(W)$	98.450	95.929	95.759	96.317	95.937

in $P_1(W)$, while a residual contribution is from two-fermion excitations, included in $P_2(W)$, and three-fermion shake up may be generally neglected. The unitarity relation

$$\sum_f \left| \left\langle \Phi_0 \middle| \Phi'_f \right\rangle \right|^2 = 1$$

is verified within ca. 95–98% by restricting the *f*-summation to final states involving not more than two electrons excited at the considered energies. These features are supported by the plots in Figure 5, where we show how the partial components P_0, P_1 and P_2 contribute to the zero-temperature work distribution (Equation 2). Besides the primary line, i.e., the no-shake intensity, we observe a sequence of secondary lines accounting, respectively, for one- and two-fermion transitions that are separated by 1–2 order of magnitudes. The three-fermion response lines (not shown) have maximum intensities smaller than 10^{-5}% and 10^{-7}%, in the two cases discussed here. Not visible enough, the shake lines of the harmonically trapped Fermi gas are almost uniformly spaced in steps of $2\hbar\omega$. The non-perfect periodicity is due to the slight changes in the perturbed one-fermion energies (see also Table 2), which where not caught by the perturbation model of [32,35].

To finalize the analysis, we briefly discuss how to include temperature effects into Equation 2, approximated as

$$P(W) \approx \sum_{k=1}^{3} P_k(W)\,.$$

As shown in the perturbation model of [32,35], the role of the temperature is mostly accounted for by a Gaussian broadening characterized by the variance

$$\delta_\beta^2 = \sum_\nu \frac{\left| \left\langle \nu \middle| \hat{V} \middle| \nu \right\rangle \right|^2}{e^{-\beta(\varepsilon_\nu - \mu)} + e^{\beta(\varepsilon_\nu - \mu)} + 2}\,,$$

which is related to the particle–hole statistics, as well as to the diagonal matrix element of the external potential. In the fullerene case, another source of broadening is given by the core-hole lifetime. Besides, to cope with real photoemission experiments a further Gaussian term due to experimental uncertainties is needed [18,19]. Working at low thermal energies, we can therefore set $P_\beta(W) \approx P(W) \otimes B(W)$, with $B(W)$ denoting a broadening function, which includes the "thermal" Gaussian of standard deviation δ_β. In Figure 6, we apply these considerations to determine the low-temperature profile of the work distributions for the core-ionized fullerene molecule and the shaken-up Fermi gas. Comparing the fullerene distribution with the experimental C 1s line shape from a thick C_{60} film, we find a significant match of the low-energy satellite structure, at excitation energies below about 4 eV, with the theoretical spectrum, apart from a peak position shift of 0.31 eV. As a further comparison, in Figure 6 (left panel) we report the work distribution obtained from the C_{60} and C_{60}^* eigensystems with a three-parameter hybrid functional by Becke [51] (the B3LYP functional) instead of the PBE functional. Both the PBE and B3LYP results appear to be consistent within a peak position shift of about 1 eV, though the relative peak position structure of the experimental satellites seems to be better reproduced by the B3LYP functional. The Lorenztian broadening of the spectra are consistent with the calculated life-time broadening of the C 1s level in graphite [52].

On the other hand, the numerical shake-up response of the harmonically trapped Fermi gas is in excellent agreement with

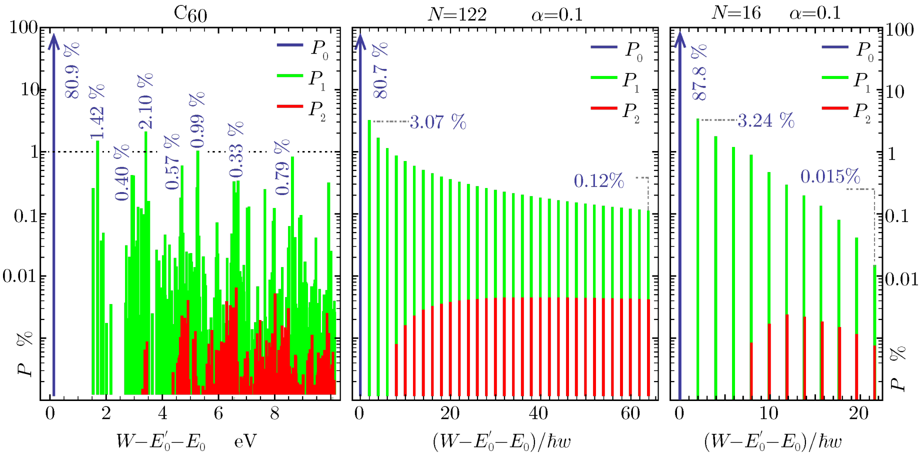

Figure 5: Zero-temperature work-distribution components (Equation 7) for a C_{60} molecule undergoing core ionization, and a Fermi gas of *N* = 16, 122 particles, shaken-up by a perturbation of critical index α = 0.1. Vertical values are give in percent, following Table 3.

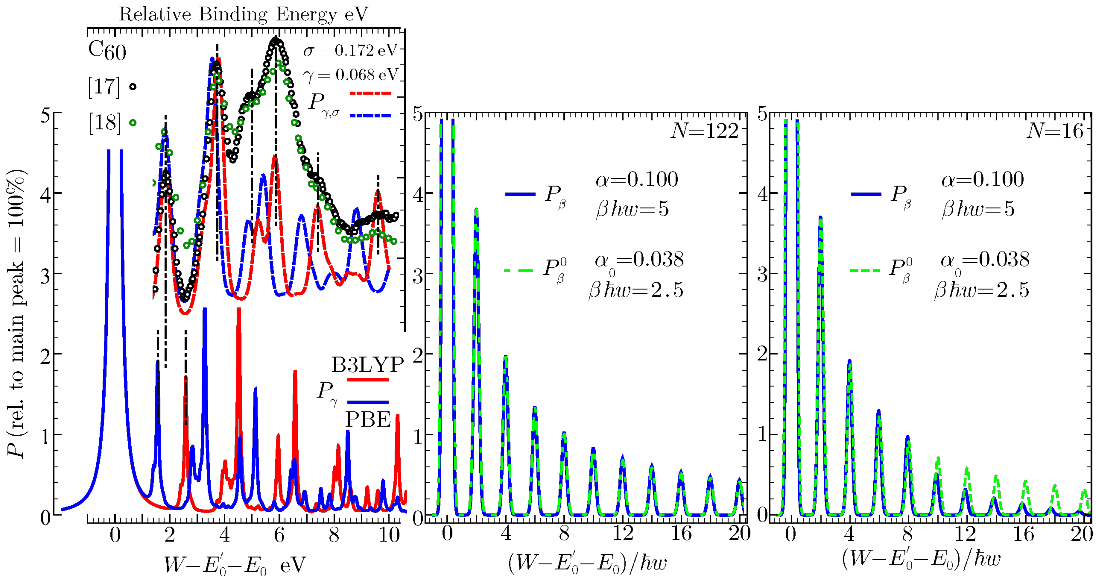

Figure 6: Low-temperature work distributions for: (left) a C_{60} molecule undergoing core-ionization; (center,right) a Fermi gas of N = 16, 122 particles shaken-up by a perturbation of critical index α = 0.1. In the C_{60} case, P_γ is the zero-temperature distribution $P(W) \approx \sum_{k=1}^{3} P_k(W)$ broadened by a Lorentzian of width γ = 0.05 eV; $P_{\gamma,\sigma}$ is obtained by convoluting $P(W)$ with a Voigt distribution [18,19], whose Gaussian standard deviation σ = 0.172 eV and Lorentzian width γ = 0.068 eV are adjusted to some measurements on thick fullerene films. The experimental data are taken from [12,13] and plotted on the same arbitrary unit scale [18,19]. The theoretical distributions are computed with the DFT approach outlined in Section 2.1, using both the PBE and the B3LYP functionals. In the two examples of the Fermi gas, the zero-temperature work distributions are broadened with a Gaussian whose standard deviation δ_β corresponds to $\beta\hbar\omega = 5$, and compared with the analytical model of [32,35]. Vertical values are given in percent relative to the no-shake peak.

the analytical model presented in [32,35], in which a compact form was given to the characteristic function of work

$$\chi^0_\beta(t) \approx e^{-\delta^2_{0\beta}t^2/2}\left[\frac{e^{2\tau_0\omega}-1}{e^{2\omega(\tau_0+it)}-1}\right]^{\alpha_0}$$

being the Fourier transform of the work distribution, and including all possible excited states, i.e., all possible components (Equaiton Equation 7). Two differences, inherent to the perturbation method, lie in the non-perfect periodic sequence of the shake-up peaks, which is significant only for low particle numbers, and in the critical exponent of the perturbation approach denoted α_0 giving rise to the thermal broadening δ^0_β. Accordingly, the effective temperatures corresponding to the numerical and analytical curves are different. When the perturbation series giving rise to $\chi^0_\beta(t)$ is summed over all orders, α_0 will be eventually renormalized to α, and $\delta_{0\beta}$ to δ_β.

Conclusion

We have presented a numerical approach towards the calculation of the work distribution for a many-fermion system, shaken up by the sudden quench of a work parameter. To show the versatility of the method, we have discussed applications in two very diverse energy ranges, namely: (i) a fullerene molecule, where the absorption of a photon leads to a critical rearrangement of the ground state of the interacting valence electrons, witnessed by the Anderson orthogonality catastrophe; and (ii) a non-interacting gas of harmonically trapped fermions, where the catastrophe can be simulated in a controlled fashion by the appropriate embedding of a single probe qubit. We have suitably selected the parameters of the Fermi gas, in order to have roughly the same overall shake-up content as the fullerene molecule. In the plots of Figure 5 and Figure 6, we have explored the detailed features of the Anderson orthogonality catastrophe in the sequence of the shake-up satellites. The comparison with experiments on C_{60} indicates the reliability of the approach, putting emphasis on the present capability of DFT codes in predicting the excited state structure of molecules and solids [53]. On the other hand the comparison of the results from the trapped Fermi gas with the analytical model of [32,35] is suggestive of a deeper analysis into the definition of the critical exponent of the model, leaving open the possibility for further investigations in the weak-coupling regime.

References

1. Jarzynski, C. *J. Stat. Phys.* **2000,** *98,* 77–102. doi:10.1023/A:1018670721277
2. Jarzynski, C. *Phys. Rev. Lett.* **1997,** *78,* 2690–2693. doi:10.1103/PhysRevLett.78.2690
3. Campisi, M.; Hänggi, P.; Talkner, P. *Rev. Mod. Phys.* **2011,** *83,* 771–791. doi:10.1103/RevModPhys.83.771

4. Plastina, F.; Alecce, A.; Apollaro, T. J. G.; Falcone, G.; Francica, G.; Galve, F.; Lo Gullo, N.; Zambrini, R. *Phys. Rev. Lett.* **2014,** *113,* 260601. doi:10.1103/PhysRevLett.113.260601
5. Anderson, P. W. *Phys. Rev. Lett.* **1967,** *18,* 1049–1051. doi:10.1103/PhysRevLett.18.1049
6. Mahan, G. D. *Phys. Rev.* **1967,** *163,* 612–617. doi:10.1103/PhysRev.163.612
7. Nozières, P.; De Dominicis, C. T. *Phys. Rev.* **1969,** *178,* 1097–1107. doi:10.1103/PhysRev.178.1097
8. Citrin, P. H.; Wertheim, G. K.; Baer, Y. *Phys. Rev. B* **1977,** *16,* 4256–4282. doi:10.1103/PhysRevB.16.4256
9. Ohtaka, K.; Tanabe, Y. *Rev. Mod. Phys.* **1990,** *62,* 929–991. doi:10.1103/RevModPhys.62.929
10. Karlsen, T.; Børve, K. J. *J. Chem. Phys.* **2000,** *112,* 7979. doi:10.1063/1.481398
11. Sette, F.; Wertheim, G. K.; Ma, Y.; Meigs, G.; Modesti, S.; Chen, C. T. *Phys. Rev. B* **1990,** *41,* 9766–9770. doi:10.1103/PhysRevB.41.9766
12. Enkvist, C.; Lunell, S.; Sjögren, B.; Svensson, S.; Brühwiler, P. A.; Nilsson, A.; Maxwell, A. J.; Mårtensson, N. *Phys. Rev. B* **1993,** *48,* 14629–14637. doi:10.1103/PhysRevB.48.14629
13. Leiro, J. A.; Heinonen, M. H.; Laiho, T.; Batirev, I. G. *J. Electron Spectrosc. Relat. Phenom.* **2003,** *128,* 205. doi:10.1016/S0368-2048(02)00284-0
14. Gao, B.; Wu, Z.; Luo, Y. *J. Chem. Phys.* **2008,** *128,* 234704. doi:10.1063/1.2943676
15. Petaccia, L.; Goldoni, A.; Lizzit, S.; Larciprete, R. *J. Electron Spectrosc. Relat. Phenom.* **2005,** *144–147,* 793–797. doi:10.1016/j.elspec.2005.01.067
16. Hentschel, M.; Guinea, F. *Phys. Rev. B* **2007,** *76,* 115407. doi:10.1103/PhysRevB.76.115407
17. Sindona, A.; Plastina, F.; Cupolillo, A.; Giallombardo, C.; Falcone, G.; Papagno, L. *Surf. Sci.* **2007,** *601,* 2805. doi:10.1016/j.susc.2006.12.055
18. Sindona, A.; Pisarra, M.; Naccarato, F.; Riccardi, P.; Plastina, F.; Cupolillo, A.; Ligato, N.; Caputi, L. S.; Falcone, G. *J. Phys.: Condens. Matter* **2013,** *25,* 115301. doi:10.1088/0953-8984/25/11/115301
19. Sindona, A.; Naccarato, F.; Pisarra, M.; Riccardi, P.; Falcone, G. *Thin Solid Films* **2013,** *543,* 41–47. doi:10.1016/j.tsf.2013.02.137
20. Anderson, P. W.; Yuval, G. *Phys. Rev. Lett.* **1969,** *23,* 89–92. doi:10.1103/PhysRevLett.23.89
21. Sindona, A.; Baragiola, R. A.; Falcone, G.; Oliva, A.; Riccardi, P. *Phys. Rev. A* **2005,** *71,* 052903. doi:10.1103/PhysRevA.71.052903
22. Sindona, A.; Rudi, S. A.; Maletta, S.; Baragiola, R. A.; Falcone, G.; Riccardi, P. *Surf. Sci.* **2007,** *601,* 1205. doi:10.1016/j.susc.2006.12.027
23. Riccardi, P.; Pisarra, M.; Cupolillo, A.; Commisso, M.; Sindona, A.; Baragiola, R. A.; Dukes, C. A. *J. Phys.: Condens. Matter* **2010,** *22,* 305004. doi:10.1088/0953-8984/22/30/305004
24. Ubbelohde, N.; Roszak, K.; Hohls, F.; Maire, N.; Haug, R. J.; Novotný, T. *Sci. Rep.* **2012,** *2,* No. 374. doi:10.1038/srep00374
25. Knap, M.; Shashi, A.; Nishida, Y.; Imambekov, A.; Abanin, D. A.; Demler, E. *Phys. Rev. X* **2012,** *2,* 041020. doi:10.1103/PhysRevX.2.041020
26. Dóra, B.; Pollmann, F.; Fortágh, J.; Zaránd, G. *Phys. Rev. Lett.* **2013,** *111,* 046402. doi:10.1103/PhysRevLett.111.046402
27. Baeten, M.; Wouters, M. *Phys. Rev. B* **2014,** *89,* 245301. doi:10.1103/PhysRevB.89.245301
28. Campbell, S.; García-March, M. A.; Fogarty, T.; Busch, T. *Phys. Rev. A* **2014,** *90,* 013617. doi:10.1103/PhysRevA.90.013617
29. Schiró, M.; Mitra, A. *Phys. Rev. Lett.* **2014,** *112,* 246401. doi:10.1103/PhysRevLett.112.246401
30. Ossipov, A. *Phys. Rev. Lett.* **2014,** *113,* 130402. doi:10.1103/PhysRevLett.113.130402
31. Goold, J.; Fogarty, T.; Lo Gullo, N.; Paternostro, M.; Busch, T. *Phys. Rev. A* **2011,** *84,* 063632. doi:10.1103/PhysRevA.84.063632
32. Sindona, A.; Goold, J.; Lo Gullo, N.; Lorenzo, S.; Plastina, F. *Phys. Rev. Lett.* **2013,** *111,* 165303. doi:10.1103/PhysRevLett.111.165303
33. Talkner, P.; Lutz, E.; Hänggi, P. *Phys. Rev. E* **2007,** *75,* 050102(R). doi:10.1103/PhysRevE.75.050102
34. Silva, A. *Phys. Rev. Lett.* **2008,** *101,* 120603. doi:10.1103/PhysRevLett.101.120603
35. Sindona, A.; Goold, J.; Lo Gullo, N.; Plastina, F. *New J. Phys.* **2014,** *16,* 045013. doi:10.1088/1367-2630/16/4/045013
36. Heyl, M.; Kehrein, S. *Phys. Rev. Lett.* **2012,** *108,* 190601. doi:10.1103/PhysRevLett.108.190601
37. Schönhammer, K.; Gunnarsson, O. *Phys. Rev. B* **1978,** *18,* 6606–6614. doi:10.1103/PhysRevB.18.6606
38. Brako, R.; Newns, D. M. *J. Phys. C: Solid State Phys.* **1981,** *14,* 3065. doi:10.1088/0022-3719/14/21/023
39. Doniach, S.; Sondheimer, E. H. *Green's Functions For Solid State Physicists;* Imperial College Press: London, United Kingdom, 1988. Reprinted 1998, World Scientific Pub Co: Singapore.
40. Stevens, W. J.; Basch, H.; Krauss, K. *J. Chem. Phys.* **1984,** *81,* 6026. doi:10.1063/1.447604
41. Krishnan, R.; Binkley, J. S.; Seeger, R.; Pople, J. A. *J. Chem. Phys.* **1980,** *72,* 650. doi:10.1063/1.438955
42. Schmidt, M. W.; Baldridge, K. K.; Boatz, J. A.; Elbert, S. T.; Gordon, M. S.; Jensen, J. H.; Koseki, S.; Matsunaga, N.; Nguyen, K. A.; Su, S. J.; Windus, T. L.; Dupuis, M.; Montgomery, J. A. *J. Comput. Chem.* **1993,** *14,* 1347–1363. doi:10.1002/jcc.540141112
43. Gordon, M. S.; Schmidt, M. W. Advances in electronic structure theory: GAMESS a decade later. In *Theory and Applications of Computational Chemistry, the First Forty Years;* Dykstra, C. E.; Frenking, G.; Kim, K. S.; Scuseria, G. E., Eds.; Elsevier: Amsterdam, Netherlands, 2005; pp 1167–1189.
44. *GAMESS,* Aug 11, 2011; Mark Gordon's Quantum Theory Group: Ames Laboratory: Iowa State University, USA, 2011.
45. Perdew, J. P.; Burke, K.; Ernzerhof, M. *Phys. Rev. Lett.* **1996,** *77,* 3865–3868. doi:10.1103/PhysRevLett.77.3865
46. Perdew, J. P.; Burke, K.; Ernzerhof, M. *Phys. Rev. Lett.* **1997,** *78,* 1396. doi:10.1103/PhysRevLett.78.1396
47. Pradhan, N. A.; Liu, N.; Silien, C.; Ho, W. *Phys. Rev. Lett.* **2005,** *94,* 076801. doi:10.1103/PhysRevLett.94.076801
48. Bloch, I.; Dalibard, J.; Zwerger, W. *Rev. Mod. Phys.* **2008,** *80,* 885–964. doi:10.1103/RevModPhys.80.885
49. Plastina, F.; Sindona, A.; Goold, J.; Lo Gullo, N.; Lorenzo, S. *Open Syst. Inf. Dyn.* **2013,** *20,* 1340005. doi:10.1142/S1230161213400052
50. Goold, J.; Busch, T. *Phys. Rev. A* **2008,** *77,* 063601. doi:10.1103/PhysRevA.77.063601
51. Becke, A. D. *J. Chem. Phys.* **1993,** *98,* 5648–5652. doi:10.1063/1.464913
52. Mele, E. J.; Ritsko, J. J. *Phys. Rev. Lett.* **1979,** *43,* 68–71. doi:10.1103/PhysRevLett.43.68
53. Pisarra, M.; Riccardi, P.; Sindona, A.; Cupolillo, A.; Ligato, N.; Giallombardo, C.; Caputi, L. *Carbon* **2014,** *77,* 796. doi:10.1016/j.carbon.2014.05.084

License and Terms

BEILSTEIN JOURNAL OF NANOTECHNOLOGY

Magnetic properties of self-organized Co dimer nanolines on Si/Ag(110)

Lisa Michez[1], Kai Chen[2], Fabien Cheynis[1], Frédéric Leroy[1], Alain Ranguis[1], Haik Jamgotchian[1], Margrit Hanbücken[1] and Laurence Masson*[1]

Full Research Paper

Open Access

Address:
[1]Aix Marseille Université, CNRS, CINaM UMR 7325, 13288 Marseille, France and [2]Synchrotron SOLEIL, L'Orme des Merisiers, Saint-Aubin – BP 48, 91192 Gif-sur-Yvette Cedex, France

Email:
Laurence Masson* - laurence.masson@cinam.univ-mrs.fr

* Corresponding author

Keywords:
nanomagnetism; one-dimensional nanostructures; scanning tunneling microscopy (STM); self-organization; X-ray magnetic circular dichroism (XMCD)

Beilstein J. Nanotechnol. **2015,** *6,* 777–784.
doi:10.3762/bjnano.6.80

Received: 17 September 2014
Accepted: 17 February 2015
Published: 19 March 2015

This article is part of the Thematic Series "Self-assembly of nanostructures and nanomaterials".

Guest Editor: I. Berbezier

Abstract

We demonstrate the kinetically controlled growth of one-dimensional Co nanomagnets with a high lateral order on a nanopatterned Ag(110) surface. First, self-organized Si nanoribbons are formed upon submonolayer condensation of Si on the anisotropic Ag(110) surface. Depending on the growth temperature, individual or regular arrays (with a pitch of 2 nm) of Si nanoribbons can be grown. Next, the Si/Ag(110) system is used as a novel one-dimensional Si template to guide the growth of Co dimer nanolines on top of the Si nanoribbons, taking advantage of the fact that the thermally activated process of Co diffusion into the Si layer is efficiently hindered at 220 K. Magnetic characterization of the Co nanolines using X-ray magnetic circular dichroism reveals that the first atomic Co layer directly adsorbed onto the Si nanoribbons presents a weak magnetic response. However, the second Co layer exhibits an enhanced magnetization, strongly suggesting a ferromagnetic ordering with an in-plane easy axis of magnetization, which is perpendicular to the Co nanolines.

Introduction

In the last fifteen years, bottom-up approaches have provided promising routes for creating a wide range of nanostructures with new magnetic, electronic, photonic or catalytic properties. Such approaches are based on growth phenomena after atoms and molecules are deposited from the vapor phase onto surfaces. Taking advantage of the intrinsic structural properties of atomically well-defined surfaces, the self-ordering of atoms and molecules allows the fabrication of patterns with nanometer dimensions and precise control over the shape, composition and mesoscale organization of the structures formed.

As growth occurs in many cases under non-equilibrium conditions, the resulting structures result from a competition between kinetics and thermodynamics. With respect to metallic nanostructures, the morphology is essentially determined by kinetics and results from a complex balance of many competing processes occurring at the atomic scale. Each of these processes is thermally activated and characterized by an activation energy. By tuning the growth parameters, such as the substrate temperature or the deposition rate during the deposition of matter, atomistic processes can be selectively promoted or hindered. Using a pre-patterned substrate, networks of metastable, metallic nanostructures exhibiting different geometries can be fabricated on metallic substrates by self-organized growth. Self-ordering proceeds by the preferential nucleation of species on regular-spaced surface traps, which can exist as steps [1,2], atomic sites [3], or the combination of both [4,5], chemical species [6] or dislocation networks [7]. In contrast, when molecules are deposited onto surfaces, the growth is more driven by thermodynamics and molecular arrangements are the result of a delicate balance between lateral interactions between molecules and molecule–substrate coupling. Considering the capability of chemical synthesis to create artificial molecules with a potentially large variety of functionalities, supramolecular [8-11] and covalent [12] assemblies with tailor-made properties can be produced by self-assembly. It has also been reported that nanotemplates can be successfully used to form well-ordered molecular arrays [9,13-17]. Finally, the growth of semiconductor nanostructures is an intermediate case where the pattern is governed by the complex interplay between kinetics and thermodynamics.

The last twenty years have seen an unprecedented rise in the interest in magnetic nanostructures. Besides the interest to potential technological applications, such as magnetic field sensors or magnetic data storage, numerous studies have been devoted to fundamental investigations of magnetism at the nanoscale. Since the discovery of the magnetoresistance effect in 1988, this field has been constantly developing novel nanosystems with unusual physical properties, highlighting the need to study structures of low dimensionality for a fundamental understanding of the physics of the magnetic state. Although less developed, the fabrication of nanostructures of true atomic dimension using a bottom-up approach can result in a deeper insight into the fundamental understanding of their intrinsic properties. For instance, the study of surface-supported two-dimensional (2D) and one-dimensional (1D) Co nanostructures has shown that magnetic properties are highly size dependent, due to the low coordination of the atoms of atomic-scale nanostructures [1,18]. For such nanostructures, enhanced magnetic anisotropy energy (MAE) and orbital moment have been evidenced as compared to the bulk material. Concerning 1D nanostructures, additional effects, especially with regards to magnetic anisotropy, are expected, related to their anisotropic shape [1,19,20]. Since metallic substrates are known to strongly influence the magnetic properties of the supported transition metal nanostructures, it appears interesting to also study the growth of such objects on a non-metallic template. We underline that since self-organized growth allows the fabrication of a high-density of nanostructures with a narrow size distribution, this route of nanofabrication opens up the possibility to investigate their properties using either local or macroscopic integration probes.

In this paper, we show how kinetically controlled growth methods allow for the fabrication of identical, highly ordered, 1D, Co nanostructures on a pre-patterned Ag(110) substrate. For the first step, individual Si nanoribbons (NRs) and high-density arrays (5×10^6 cm^{-1}) of Si NRs are formed on Ag(110) upon submonolayer condensation of Si at room temperature (RT) and 460 K, respectively. We have recently shown that Co deposition on the Si/Ag(110) system at RT leads to the self-organized growth of Co dimer nanolines on top of the Si NRs, reproducing the 1D pattern of the Si template. This, however, is limited by defects induced by Co incorporation into the Si NRs [21]. In the experiments reported herein, Co was deposited at 220 K to kinetically block this Co incorporation process and obtain long, defect-free, Co nanolines. The first magnetic characterization results of the Co nanolines using X-ray magnetic circular dichroism (XMCD) are reported, revealing that the atomic Co layer directly adsorbed onto the Si nanoribbons presents a weak magnetic response. The second Co layer exhibits an enhanced magnetization, strongly suggesting a ferromagnetic ordering with an in-plane easy axis of magnetization, perpendicular to the Co nanolines.

Results and Discussion

Self-organized growth of Si nanoribbons on Ag(110)

Depending on the temperature of the silver substrate (T_{sub}) during Si deposition, different geometries of 1D Si nanostructures can be grown on the bare Ag(110) substrate, ranging from isolated, ultrathin, Si NRs to massive 1D nanostuctures corresponding to silver surface faceting [22]. All of these nanostructures are perfectly aligned along the $\left[1\bar{1}0\right]$ direction of Ag(110). In the following, we will focus on the formation of the Si NRs, which are stable below 550 K and are subsequently used to guide the growth of the Co nanolines.

In their pioneering work, Leandri et al. reported that upon submonolayer Si deposition at RT on the anisotropic Ag(110) surface, isolated Si NRs spontaneously form [23]. As can be viewed in the STM image presented in Figure 1a, the Si NRs are parallel to the atomically dense $\left[1\bar{1}0\right]$ rows of Ag(110) and have been shown to display a 2× periodicity along their edges ($2 \cdot a_{\text{Ag}\|} \approx 0.6$ nm) [23]. These NRs, denoted hereafter as single

NRs, are composed of two rows of round protrusions [24]. We note that these protrusions are too large to represent individual atoms. We have recently shown that neither STM nor non-contact atomic force microscopy (nc-AFM) probes can straightforwardly resolve the inner atomic structure of the Si NRs [25]. All NRs, varying only in length, present the same width of $2 \cdot a_{\mathrm{Ag}\perp}$ (≈0.8 nm) and the same apparent height: the corrugation measured by STM varies from 50 to 150 pm, depending on tunneling conditions [26]. As shown in Figure 1a, the self-organized Si NRs deposited at RT are randomly distributed on the Ag terraces. Only a few of the grown Si NRs (those corresponding to four row protrusions) present a width of $4 \cdot a_{\mathrm{Ag}\perp}$ (≈1.6 nm). We emphasize that these NRs differ only in width from the single ones and will be denoted hereafter double NRs. The ratio between double and single NRs increases with T_{sub} [24,26]. At T_{sub} = 460 K, double NRs are predominantly formed upon Si deposition. These double NRs are self-organized in a regular array with a 5× periodicity in the [001] direction, perpendicular to the NRs (see Figure 1b). At submonolayer coverage, the silver substrate is thus progressively covered upon Si deposition by elongated 2D islands corresponding to the 5 × 2 Si grating. Remarkably, this extremely dense Si NR array has a very low density of defects corresponding to isolated defects or single NRs (more rarely triple NRs ($6 \cdot a_{\mathrm{Ag}\perp}$)).

At completion of this 5 × 2 arrangement, the entire silver substrate is covered by an ultrathin Si film consisting of a self-organized Si NR array (pitch: $5 \cdot a_{\mathrm{Ag}\perp} \approx 2$ nm) with a single domain orientation. This structure was confirmed by surface diffraction techniques (low energy electron diffraction, LEED and grazing incidence X-ray diffraction, GIXD) and large scale STM images [24,26]. The sharp spots of the 5 × 2 superstructure displayed in LEED patterns and the narrow GIXD diffraction peaks associated with the 5× periodicity of the superlattice confirm the high structural order of the Si grating. It should be noted that to date, despite the numerous experimental and theoretical investigations on the Si/Ag(110) interface, no reliable atomic structural model for the Si NRs has been proposed.

Self-organized growth of Co dimer nanolines on Si/Ag(110)

Recent studies have shown that Si NRs grown on Ag(110) can be used as a template for the formation at RT of 1D nanostructures composed of transition metals such as Co [21] or Mn [27]. In both studies, a preferential adsorption on top of the Si NRs with respect to the surrounding uncovered silver areas was reported. Co and Mn are known to easily react with silicon to form silicides. The thermally activated process of Co and Mn diffusion into the Si NRs, which is the first step of the silicide formation, was found to be partially hindered at RT in both systems. This gives rise to the formation of 1D nanostructures, reproducing the 1D pattern of the Si/Ag(110) template.

First, we reference the results already obtained in our group concerning Co adsorption at RT [21,28,29]. The STM image of Figure 2c shows a typical 1D Co nanostructure formed after Co deposition at RT on isolated Si NRs, partially covering the Ag(110) surface. The grown 1D nanostructures correspond to Co nanolines composed of dimers oriented perpendicular to the axis of the Si NRs. A Co dimer of the second layer can also be observed. The Co–Co distance in a dimer, as measured by STM, is ≈0.4 nm (i.e., $\approx a_{\mathrm{Ag}\perp}$) and the distance between two dimers along the nanoline is ≈0.43 nm (i.e., $\approx 1.5 \cdot a_{\mathrm{Ag}\parallel}$). The apparent height of both Co layers is ≈50 pm, suggesting single-atom-thick layers. Interestingly, it has been reported that the Co nanoline growth proceeds in a nearly layer-by-layer growth,

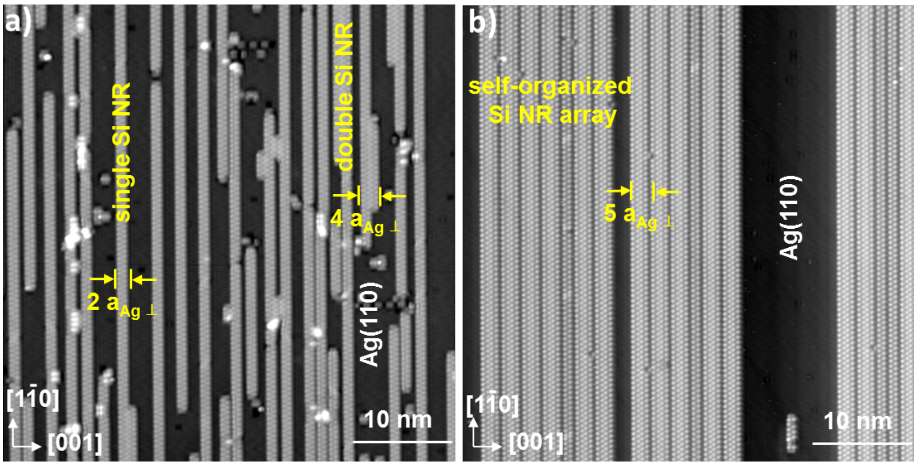

Figure 1: STM images recorded at 77 K at submonolayer Si coverage showing single and double Si nanoribbons (NRs) grown on Ag(110) upon Si deposition at (a) T_{sub} = RT, I = 300 pA, V_{sample} = 1V and (b) T_{sub} = 460 K, I = 200 pA, V_{sample} = 140 mV. The pitch of the Si array is $5 \cdot a_{\mathrm{Ag}\perp}$ ($a_{\mathrm{Ag}\perp}$ = 0.409 nm, the Ag(110) lattice parameter in the [001] direction).

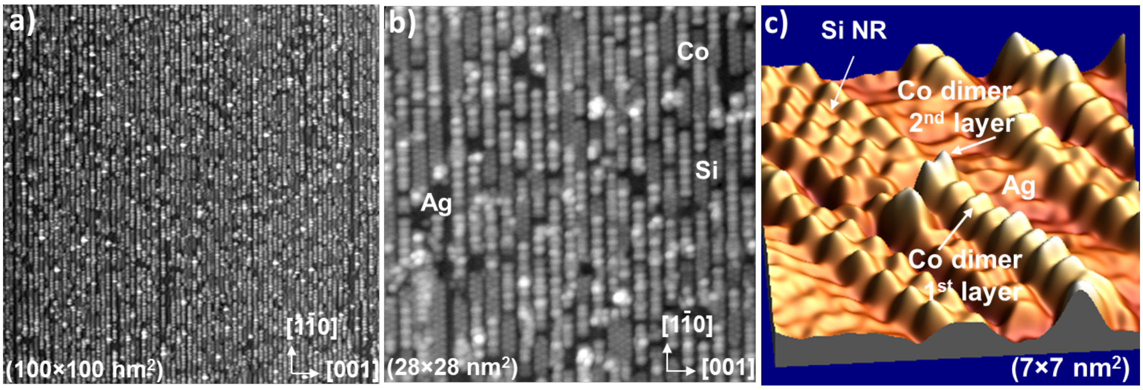

Figure 2: (a,b) STM images at different magnification scales, recorded at 77 K for a Co coverage of approx. 0.6 monolayers, showing the formation of identical and highly ordered Co dimer nanolines on the Si nanoribbon array grown on Ag(110) after Co deposition at 220 K. *I* = 90 pA, V_{sample} = −1 V. (c) High-resolution STM image of a Co dimer nanoline grown at RT on a Si nanoribbon (NR). *I* = 1.3 nA, V_{sample} = 0.55 V.

reproducing the 1D pattern of the Si template up to five monolayers thick. The width of the Co dimer nanolines is similar to the width of a single Si NR. Co adsorption on double Si NRs leads to the formation of nanolines identical to those observed on single Si NRs, except that most of them are coupled by two on the same double NRs.

Despite the fact that the kinetics of Co diffusion into the Si NRs has been observed to be low at RT at the timescale of our experiments, it has been shown that the length of the Co nanolines is governed by this atomic process of Co in-diffusion rather than the surface diffusion of the adsorbed Co atoms [21]. The incorporation of Co leads to the local destruction of the Si NRs, leaving bare Ag(110) areas. As the activation energy for Co surface diffusion is expected to be lower than that of Co in-diffusion, Co deposition at a lower temperature was performed in the experiments presented here to form longer, defect-free, Co nanolines. The STM images in Figure 2a,b show the formation of identical and highly ordered Co dimer nanolines on the Ag(110) surface completely covered with the Si NR array grown on Ag(110), upon Co deposition at T_{sub} = 220 K. The Co coverage is 0.6 ± 0.1 of a monolayer of Co (ML_{Co}). 1 ML_{Co} corresponds to the 5 × 2 Si NR array completely covered with Co nanolines and equals 0.6 monolayers (ML) in silver (110) surface atom density. It can be observed that only few, bare silver areas remain, suggesting that the process of Co incorporation into the Si NRs is efficiently blocked at this temperature. In the following section, magnetic characterization of such assemblies of Co nanolines using XMCD is reported.

Magnetic characterization of the Co dimer nanolines

X-ray absorption spectroscopy (XAS) spectra were recorded at normal incidence in a magnetic field of 6 T for parallel (σ^+) and antiparallel (σ^-) alignment of the X-ray helicity with respect to the sample magnetization. Magnetic hysteresis measurements at the L_3 resonance confirm that the sample magnetization is saturated at 6 T. The strong non-magnetic background signal coming from the Ag substrate was subtracted from the Co $L_{2,3}$ XAS spectra presented in this paper. The spectra are also normalized to the incident beam intensity, which is set to zero at the L_3 pre-edge and to one far above the L_2 edge. Figure 3a,b shows the XAS spectra for both helicities (upper panel) for ≈1 ML_{Co} and ≈2 ML_{Co}, respectively. Two broad absorption resonances are clearly visible at the L_3 and L_2 edges. A shoulder peak, indicated in the XAS spectra of Figure 3 by a dotted line, is also present at about 4 eV above the L_3 edge, located at 779.4 eV. The XAS spectra, which clearly show no trace of cobalt silicides [30,31], are characteristic of metallic Co [32]. Such a lineshape has been seen in numerous structures composed of a thin Co layer grown on a metallic substrate [1,4,32-34] or an insulating support [35]. Although the shoulder at +4 eV from the L_3 edge can be observed for other Co nanostructures (e.g., an ultrathin 1.25 ML Co film grown on Rh(111) [33] or a superlattice of 0.35 ML 2D Co nanoparticles on Au(788) [4]) this feature is more pronounced in the case of our Co nanolines, especially for low Co coverage. It seems reasonable to exclude the formation of a Co silicide or a Co oxide, since in these cases, a more structured absorption spectrum is expected [30,36,37]. The XAS signal around this energy may be enhanced by the presence of interface states for Co atoms located at the Co/Si interface as suggested by Pong et al. [30]. For both 1 ML_{Co} and 2 ML_{Co}, the XAS spectra are similar. However, appreciable differences are present in the XMCD signals reported in the lower panels of Figure 3a,b. The XMCD signal that represents the difference between the XAS spectra for left- and right-handed polarized light gives access to the magnetization direction and magnitude of a specific element. According to the magnetic sum rules [38,39], the spin

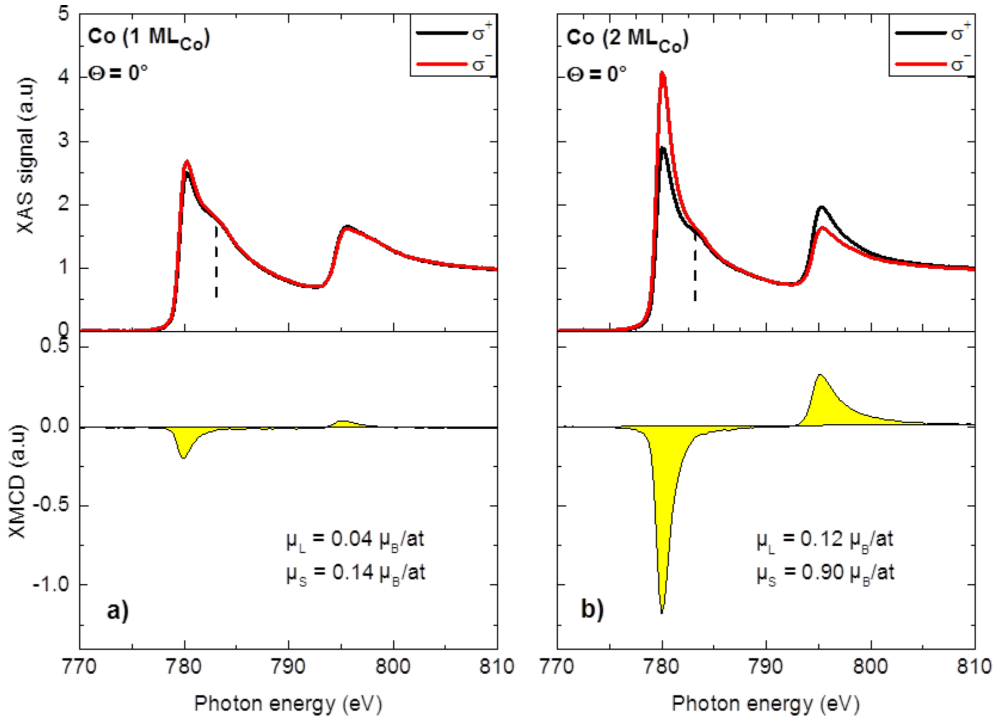

Figure 3: XAS spectra taken at normal incidence (Θ = 0°) for both helicities (σ^+ and σ^-) at 4 K with a magnetic field of 6 T and corresponding XMCD signals for (a) 1 ML$_{Co}$ and (b) 2 ML$_{Co}$ on Si/Ag(110). Orbital and spin magnetic moments in both structures were determined by applying the sum rules.

(μ_S) and orbital (μ_L) moments can indeed be quantitatively determined. In this work, we have applied the formalism described by Chen et al. [35] in order to evaluate the spin and orbital contributions to the magnetization of the Co nanolines. The number of holes in the Co 3d band is estimated to be 2.5, which corresponds to the average theoretical value for bulk Co [40,41]. Note that a similar value of 2.4 has been found for the case of Co adatoms on Pt(111) [18]. For 1 ML$_{Co}$, we obtain a spin moment of 0.14 Bohr magneton (μ_B) and an orbital moment of 0.04 · μ_B, values, which are considerably smaller than the bulk values given in [35]. The very low dichroism for 1 ML$_{Co}$ reveals a weak magnetic order in this structure when Co is directly adsorbed on Si. Interestingly, a similar Co coverage grown on metallic substrates exhibits a strong magnetic response [1,19,33]. Our results thus evidence that the ultrathin Si layer decouples the Co nanostructures from the metallic substrate, which leads to a drastic decrease of both the orbital and spin magnetic moments.

The deposition of a second ML$_{Co}$ leads to a strong enhancement of the XMCD signal. The spin and orbital moments of the ultrathin 2 ML$_{Co}$ film derived from our measurements are 0.90 · μ_B and 0.12 · μ_B, respectively. Taking into account the values found for 1 ML$_{Co}$ and considering that they remain the same in the first layer of the 2 ML$_{Co}$ film, the moments of the Co atoms in the second layer can be estimated as μ_S = 1.66 · μ_B and μ_L = 0.20 · μ_B. These values, which are close to those of the bulk material (μ_S = 1.55 · μ_B and μ_L = 0.153 · μ_B) [35], strongly suggest a ferromagnetic ordering. This structure is therefore used to study the magnetic anisotropy in the Co nanolines. The hysteresis loops, obtained from the XMCD signal, were recorded at 4 K for different angles Θ varying from normal incidence (Θ = 0°) to grazing incidence (Θ = 70°) using the measurement geometry presented in Figure 4b. Note that at grazing incidence, the magnetic field is oriented perpendicularly to the Co lines. The hysteresis loops for the two extreme configurations (Θ = 0° and 70°) are presented in Figure 4a and the details of the zero-field region show an opening in the *M–H* curve recorded at Θ = 70°. The square shape of the magnetization curve confirms the presence of significant exchange coupling in the Co film. The angular dependence of the magnetization measured at 0.5 T and normalized to the saturation value is plotted in Figure 4c. The results clearly evidence the presence of an in-plane easy axis of magnetization, perpendicular to the Co nanolines (i.e., along the Co dimer direction). Theoretical [20] and experimental [42] studies related to the 1D Co nanostructures deposited on metallic substrates revealed that the easy axis of magnetization considerably depends on the transverse width of the wires and on the interaction with the substrate. In both cases, an easy axis of magnetization perpen-

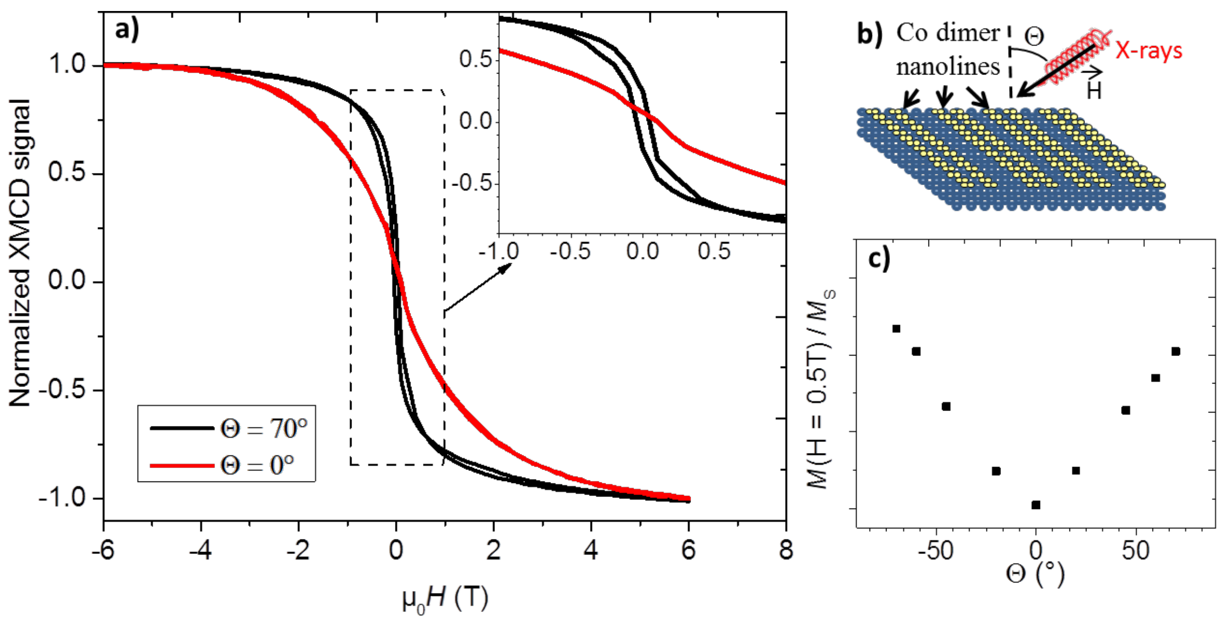

Figure 4: (a) Hysteresis loops of 2 ML_{Co} on Si/Ag(110) measured at 4 K at normal (Θ = 0°) and grazing (Θ = 70°) incidences. The curves have been normalized to their saturation value. (b) Schematic representation of the measurement configuration: incident light and magnetic field are parallel and form an angle Θ with the surface normal in the plane perpendicular to the Co nanolines. (c) Variation of the magnetization at 0.5 T normalized to the saturation magnetization (M_S) as a function of the incidence angle, Θ.

dicular to the wires is reported for two-atom-wide wires, in-plane in the case of Co deposited on Pd(110) [20], and with an out-of-plane component for Co bi-chains decorating the steps of the Pt(997) surface [42]. Although the interaction with the underlying layer is expected to be different in our system, our results are consistent with these reported findings. However, our system differs in MAE, which can be estimated from the hysteresis curves [33]. Bearing in mind the very weak dichroic signal recorded for the 1 ML_{Co} deposit, for this calculation, we consider that only the second Co layer contributes to the *M–H* curve. The total magnetic moment has been taken as the sum of both the spin and orbital moments in the second Co layer, which gives 1.86 · μ_B per atom. The MAE can be derived from the hysteresis curves displayed in Figure 4a using Equation 2 in [33]. We obtain an in-plane MAE of 0.07 meV per Co atom. This value is small compared to the large out-of-plane anisotropy of Co bi-chains on Pt(997) [42] and to the in-plane anisotropy of Co bi-atomic chains grown on Pd(110) [20]. However, a study of the magnetization angular dependence in the surface plane is required in order to fully characterize the anisotropy of our system and understand its origin.

Conclusion

In this work, we demonstrated that by tuning the temperature of the silver substrate during Co deposition, the nanopatterned Ag(110) surface consisting of a regular array of Si nanoribbons can be used to guide the self-organized growth of identical Co dimer nanolines with a high lateral order. XMCD measurements revealed that the proximity of the Si template does not affect the metallic character of the Co nanostructures. However, the magnetic properties of the Co nanolines are considerably reduced for low Co coverage when Co is directly adsorbed on Si. The study of the magnetization angle dependence evidences the presence of an in-plane easy axis of magnetization perpendicular to the Co nanolines (i.e., along the Co dimer direction). Another in-plane anisotropy (for instance, along the nanolines) is not excluded, but its demonstration requires further measurements. We stress that due to the presence of a magnetic Co–Si dead layer on the Si template, an efficient decoupling of the Co nanostructures from the metallic silver substrate can be achieved for the upper Co layers, allowing for the characterization of their intrinsic properties.

Experimental

All experiments were performed in situ in ultra high vacuum (UHV, base pressure, 10^{-10} Torr). The STM images and LEED patterns were recorded at the CINaM in Marseille using an Omicron Nanotechnology STM, working at 77 K and RT. XMCD experiments were performed at the DEIMOS [43] beamline at the French national synchrotron facility (SOLEIL), which operates in the soft X-ray range. XAS was performed in total electron yield mode at the Co $L_{2,3}$ edges. The spectra were recorded at 4 K, under a variable magnetic field of up to 6 T, collinear with the incident X-ray direction. To probe the magnetic anisotropy, the sample was rotated with respect to the magnetic field by an angle Θ, where Θ is the angle between the surface normal and the light beam ranging from 0° (normal incidence) to 70° (grazing incidence), as represented in Figure 4b. The Co/Si/Ag(110) system was obtained using standard procedures for growth experiments in UHV. The Ag(110) sample was prepared by repeated cycles of Ar^+ sputtering and annealing at 770 K. Si was evaporated on the silver substrate at two different substrate temperatures (RT and 460 K) from either a thermally heated crucible using a commercial Omicron Nanotechnology e-beam evaporator or a direct current heated piece of silicon wafer kept at 1520 K. The Co was deposited using a Co rod (purity 99.99%) inserted in a commercial Omicron Nanotechnology e-beam evaporator. For XMCD measurements, Co was deposited at 220 K on the silver substrate covered with the Si NR grating. The Co coverages in XMCD experiments have been estimated using combined measurements with Auger electron spectroscopy (AES), XAS at the Co L_3 edge and STM. All STM images were obtained in the constant current mode. The STM data were processed using WSxM and Gwyddion software. The lattice parameters of Ag(110) are denoted $a_{Ag\|} = 0.289$ nm in the $\left[1\bar{1}0\right]$ direction and $a_{Ag\perp} = 0.409$ nm in the [001] direction.

Acknowledgements

The authors thank Vincent Repain for fruitful discussions during the experiments performed at the DEIMOS-SOLEIL beamline. The support from the DEIMOS beamline staff is greatly acknowledged.

References

1. Gambardella, P.; Dallmeyer, A.; Maiti, K.; Malagoli, M. C.; Eberhardt, W.; Kern, K.; Carbone, C. *Nature* **2002,** *416,* 301. doi:10.1038/416301a
2. Moyen, E.; Macé, M.; Agnus, G.; Fleurence, A.; Maroutian, T.; Houzé, F.; Stupakiewicz, A.; Masson, L.; Bartenlian, B.; Wulfhekel, W.; Beauvillain, P.; Hanbücken, M. *Appl. Phys. Lett.* **2009,** *94,* 233101. doi:10.1063/1.3148782
3. Repain, V.; Baudot, G.; Ellmer, H.; Rousset, S. *Europhys. Lett.* **2002,** *58,* 730. doi:10.1209/epl/i2002-00410-4
4. Weiss, N.; Cren, T.; Epple, M.; Rusponi, S.; Baudot, G.; Rohart, S.; Tejeda, A.; Repain, V.; Rousset, S.; Ohresser, P.; Scheurer, F.; Bencok, P.; Brune, H. *Phys. Rev. Lett.* **2005,** *95,* 157204. doi:10.1103/PhysRevLett.95.157204
5. Borca, B.; Fruchart, O.; Kritsikis, E.; Cheynis, F.; Rousseau, A.; David, P.; Meyer, C.; Toussaint, J. C. *J. Magn. Magn. Mater.* **2010,** *322,* 257. doi:10.1016/j.jmmm.2009.09.003
6. Boishin, G.; Sun, L. D.; Hohage, M.; Zeppenfeld, P. *Surf. Sci.* **2002,** *512,* 185. doi:10.1016/S0039-6028(02)01390-0
7. Brune, H.; Giovannini, M.; Bromann, K.; Kern, K. *Nature* **1998,** *394,* 451. doi:10.1038/28804
8. Yokoyama, T.; Yokoyama, S.; Kamikado, T.; Okuno, Y.; Mashiko, S. *Nature* **2001,** *413,* 619. doi:10.1038/35098059
9. Theobald, J. A.; Oxtoby, N. S.; Phillips, M. A.; Champness, N. R.; Beton, P. H. *Nature* **2003,** *424,* 1029. doi:10.1038/nature01915
10. Stepanow, S.; Lingenfelder, M.; Dmitriev, A.; Spillmann, H.; Delvigne, E.; Lin, N.; Deng, X.; Cai, C.; Barth, J. V.; Kern, K. *Nat. Mater.* **2004,** *3,* 229. doi:10.1038/nmat1088
11. Schlickum, U.; Klappenberger, F.; Decker, R.; Zoppellaro, G.; Klyatskaya, S.; Ruben, M.; Kern, K.; Brune, H.; Barth, J. V. *J. Phys. Chem. C* **2010,** *114,* 15602–15606. doi:10.1021/jp104518h
12. Lackinger, M.; Heckl, W. M. *J. Phys. D: Appl. Phys.* **2011,** *44,* 464011. doi:10.1088/0022-3727/44/46/464011
13. Weckesser, J.; De Vita, A.; Barth, J. V.; Cai, C.; Kern, K. *Phys. Rev. Lett.* **2001,** *87,* 96101. doi:10.1103/PhysRevLett.87.096101
14. Otero, R.; Naitoh, Y.; Rosei, F.; Jiang, P.; Thostrup, P.; Gourdon, A.; Lœgsgaard, E.; Stensgaard, I.; Joachim, C.; Besenbacher, F. *Angew. Chem., Int. Ed.* **2004,** *43,* 2092. doi:10.1002/anie.200353586
15. Cañas-Ventura, M. E.; Xiao, W.; Wasserfallen, D.; Müllen, K.; Brune, H.; Barth, J. V.; Fasel, R. *Angew. Chem., Int. Ed.* **2007,** *46,* 1814–1818. doi:10.1002/anie.200604083
16. Berner, S.; Corso, M.; Widmer, R.; Groening, O.; Laskowski, R.; Blaha, P.; Schwarz, K.; Goriachko, A.; Over, H.; Gsell, S.; Schreck, M.; Sachdev, H.; Greber, T.; Osterwalder, J. *Angew. Chem., Int. Ed.* **2007,** *46,* 5115. doi:10.1002/anie.200700234
17. Aït-Mansour, K.; Ruffieux, P.; Gröning, P.; Fasel, R.; Gröning, O. *J. Phys. Chem. C* **2009,** *113,* 5292–5299. doi:10.1021/jp8101749
18. Gambardella, P.; Rusponi, S.; Veronese, M.; Dhesi, S. S.; Grazioli, C.; Dallmeyer, A.; Cabria, I.; Zeller, R.; Dederichs, P. H.; Kern, K.; Carbone, C.; Brune, H. *Science* **2003,** *300,* 1130. doi:10.1126/science.1082857
19. Yan, L.; Przybylski, M.; Yafeng, L.; Wang, W. H.; Barthel, J.; Kirschner, J. *Appl. Phys. Lett.* **2005,** *86,* 102503. doi:10.1063/1.1870127
20. Félix-Medina, R.; Dorantes-Dávila, J.; Pastor, G. M. *New J. Phys.* **2002,** *4,* 100. doi:10.1088/1367-2630/4/1/3a0
21. Dettoni, F.; Sahaf, H.; Moyen, E.; Masson, L.; Hanbücken, M. *EPL* **2011,** *94,* 28007. doi:10.1209/0295-5075/94/28007
22. Ronci, F.; Serrano, G.; Gori, P.; Cricenti, A.; Colonna, S. *Phys. Rev. B* **2014,** *89,* 115437. doi:10.1103/PhysRevB.89.115437
23. Leandri, C.; Le Lay, G.; Aufray, B.; Girardeaux, C.; Avila, J.; Dávila, M. E.; Asensio, M. C.; Ottaviani, C.; Cricenti, A. *Surf. Sci.* **2005,** *574,* L9. doi:10.1016/j.susc.2004.10.052
24. Bernard, R.; Leoni, T.; Wilson, A.; Lelaidier, T.; Sahaf, H.; Moyen, E.; Assaud, L.; Santinacci, L.; Leroy, F.; Cheynis, F.; Ranguis, A.; Jamgotchian, H.; Becker, C.; Borensztein, Y.; Hanbücken, M.; Prévot, G.; Masson, L. *Phys. Rev. B* **2013,** *88,* 121411. doi:10.1103/PhysRevB.88.121411
25. Leoni, T.; Bernard, R.; Ranguis, A.; Borensztein, Y.; Prévot, G.; Masson, L. *ECS Trans.* **2014,** *64,* 89. doi:10.1149/06406.0089ecst
26. Sahaf, H.; Masson, L.; Léandri, C.; Aufray, B.; Le Lay, G.; Ronci, F. *Appl. Phys. Lett.* **2007,** *90,* 263110. doi:10.1063/1.2752125
27. De Padova, P.; Ottaviani, C.; Ronci, F.; Colonna, S.; Olivieri, B.; Quaresima, C.; Cricenti, A.; Dávila, M. E.; Hennies, F.; Pietzsch, A.; Shariati, N.; Le Lay, G. *J. Phys.: Condens. Matter* **2013,** *25,* 014009. doi:10.1088/0953-8984/25/1/014009
28. Sahaf, H.; Léandri, C.; Moyen, E.; Macé, M.; Masson, L.; Hanbücken, M. *EPL* **2009,** *86,* 28006. doi:10.1209/0295-5075/86/28006
29. Masson, L.; Sahaf, H.; Amsalem, P.; Dettoni, F.; Moyen, E.; Koch, N.; Hanbücken, M. *Appl. Surf. Sci.* **2013,** *267,* 192. doi:10.1016/j.apsusc.2012.09.155

30. Pong, W. F.; Chang, Y. K.; Mayanovic, R. A.; Ho, G. H.; Lin, H. J.; Ko, S. H.; Tseng, P. K.; Chen, C. T.; Hiraya, A.; Watanabe, M. *Phys. Rev. B* **1996,** *53,* 16510. doi:10.1103/PhysRevB.53.16510
31. Lerch, P.; Jarlborg, T.; Codazzi, V.; Loupias, G.; Flank, A. M. *Phys. Rev. B* **1992,** *45,* 11481. doi:10.1103/PhysRevB.45.11481
32. Brune, H.; Gambardella, P. *Surf. Sci.* **2009,** *603,* 1812. doi:10.1016/j.susc.2008.11.055
33. Lehnert, A.; Dennler, S.; Błoński, P.; Rusponi, S.; Etzkorn, M.; Moulas, G.; Bencok, P.; Gambardella, P.; Brune, H.; Hafner, J. *Phys. Rev. B* **2010,** *82,* 094409. doi:10.1103/PhysRevB.82.094409
34. Böske, T.; Clemens, W.; Carbone, C.; Eberhardt, W. *Phys. Rev. B* **1994,** *49,* 4003. doi:10.1103/PhysRevB.49.4003
35. Chen, C. T.; Idzerda, Y. U.; Lin, H.-J.; Smith, N. V.; Meigs, G.; Chaban, E.; Ho, G. H.; Pellegrin, E.; Sette, F. *Phys. Rev. Lett.* **1995,** *75,* 152. doi:10.1103/PhysRevLett.75.152
36. Regan, T. J.; Ohldag, H.; Stamm, C.; Nolting, F.; Lüning, J.; Stöhr, J.; White, R. L. *Phys. Rev. B* **2001,** *64,* 214422. doi:10.1103/PhysRevB.64.214422
37. Gragnaniello, L.; Agnoli, S.; Parteder, G.; Barolo, A.; Bondino, F.; Allegretti, F.; Surnev, S.; Granozzi, G.; Netzer, F. P. *Surf. Sci.* **2010,** *604,* 2002. doi:10.1016/j.susc.2010.08.012
38. Thole, B. T.; Carra, P.; Sette, F.; van der Laan, G. *Phys. Rev. Lett.* **1992,** *68,* 1943. doi:10.1103/PhysRevLett.68.1943
39. Carra, P.; Thole, B. T.; Altarelli, M.; Wang, X. *Phys. Rev. Lett.* **1993,** *70,* 694. doi:10.1103/PhysRevLett.70.694
40. Wu, R.; Wang, D.; Freeman, A. J. *Phys. Rev. Lett.* **1993,** *71,* 3581. doi:10.1103/PhysRevLett.71.3581
41. Guo, G. Y.; Ebert, H.; Temmerman, W. M.; Durham, P. J. *Phys. Rev. B* **1994,** *50,* 3861. doi:10.1103/PhysRevB.50.3861
42. Gambardella, P.; Dallmeyer, A.; Maiti, K.; Malagoli, M. C.; Rusponi, S.; Ohresser, P.; Eberhardt, W.; Carbone, C.; Kern, K. *Phys. Rev. Lett.* **2004,** *93,* 77203. doi:10.1103/PhysRevLett.93.077203
43. Ohresser, P.; Otero, E.; Choueikani, F.; Chen, K.; Stanescu, S.; Deschamps, F.; Moreno, T.; Polack, F.; Lagarde, B.; Daguerre, J.-P.; Marteau, F.; Scheurer, F.; Joly, L.; Kappler, J.-P.; Muller, B.; Bunau, O.; Sainctavit, P. *Rev. Sci. Instrum.* **2014,** *85,* 013106. doi:10.1063/1.4861191

License and Terms

BEILSTEIN JOURNAL OF NANOTECHNOLOGY

Applications of three-dimensional carbon nanotube networks

Manuela Scarselli*[1], Paola Castrucci[1], Francesco De Nicola[1], Ilaria Cacciotti[2], Francesca Nanni[3], Emanuela Gatto[4], Mariano Venanzi[4] and Maurizio De Crescenzi[1]

Full Research Paper

Address:
[1]Dipartimento di Fisica, Università di Roma Tor Vergata, Via della Ricerca Scientifica 1, 00133 Roma, Italy, [2]Università di Roma Niccolò Cusano (INSTM-UdR), Via Don Carlo Gnocchi 3, 00166 Roma, Italy, [3]Dipartimento di Ingegneria dell'Impresa, Università di Roma Tor Vergata (INSTM-UdR Roma Tor Vergata), Via del Politecnico 1, 00133 Roma, Italy and [4]Dipartimento di Scienze e Tecnologie Chimiche, Università di Roma Tor Vergata, Via della Ricerca Scientifica 1, 00133 Roma, Italy

Email:
Manuela Scarselli* - manuela.scarselli@roma2.infn.it

* Corresponding author

Keywords:
carbon nanotube sponge; electrochemical; hydrophobicity; lipophilicity

Beilstein J. Nanotechnol. **2015,** *6,* 792–798.
doi:10.3762/bjnano.6.82

Received: 30 September 2014
Accepted: 26 February 2015
Published: 23 March 2015

This article is part of the Thematic Series "Self-assembly of nanostructures and nanomaterials".

Guest Editor: I. Berbezier

Abstract

In this paper, we show that it is possible to synthesize carbon-based three-dimensional networks by adding sulfur, as growth enhancer, during the synthesis process. The obtained material is self-supporting and consists of curved and interconnected carbon nanotubes and to lesser extent of carbon fibers. Studies on the microstructure indicate that the assembly presents a marked variability in the tube external diameter and in the inner structure. We study the relationship between the observed microscopic properties and some potential applications. In particular, we show that the porous nature of the network is directly responsible for the hydrophobic and the lipophilic behavior. Moreover, we used a cut piece of the produced carbon material as working electrode in a standard electrochemical cell and, thus, demonstrating the capability of the system to respond to incident light in the visible and near-ultraviolet region and to generate a photocurrent.

Introduction

In the last years, there has been growing interest in developing natural and synthetic three-dimensional architectures rather than two-dimensional ones because of the increase of active surface area throughout the entire 3D structure. Hydrogels, organogels, and aerogels based on silica [1] or carbon [2] and consisting of micro-, and macroscopic assemblies are reported in the literature. In particular, self-sustaining assemblies that show high porosity [3], structural stability, and good electrical conductivity [4] are the best candidates for environmental applications such as filtration [5], separation [6], biological sensors [7], and oil-spill remediation [8] but also as mechanical actuators [9], catalytic supports [10], and super capacitors [11]. In this research field, architectures based on carbon nanotubes (CNTs) are the focus of intense research activity [2]. Since CNTs are one-dimensional structures with well-known electrical and mechanical properties, they are the ideal building blocks for constructing three-dimensional random meshes from their overlapping. Recently, Gui and co-workers [6] fabricated CNT-sponges through a chemical vapor deposition (CVD) process during which a catalyst precursor (ferrocene) dissolved in dichlorobenzene, which acted as carbon precursor, was injected in the reactor chamber. They obtained millimeter-thick CNT-assemblies in which individual nanotubes were stacked in a random manner to form the bulk material.

Similarly, in this paper, we show that through carrying out a CVD synthesis with different precursors it is possible to synthesize three-dimensional carbon networks consisting of randomly interconnected nanostructures. The bulk carbon nanostructures display a structural flexibility rarely observed in other high-porosity materials, e.g., bulk carbon aerogels [12] or aligned CNT arrays [3]. The pristine CNT-sponges are super-hydrophobic (i.e., a water contact angle greater than 150°) and oleophilic as reported recently [13,14]. Therefore, in this paper, we show that the structural and electronic features of the network are directly responsible for the hydrophobic and the lipophilic behavior.

In addition, to test the capability of the system to respond to incident light and generate a photocurrent, we cut a piece of the CNT-sponge, which has a self-sustainable structure, and used it as the working electrode in a standard electrochemical cell. In this manner, it was possible to register a good photo-response of the CNT-network in the visible and near-ultraviolet range.

Results and Discussion

The produced CNT-sponges are light and porous, and can be cut into pieces of the desired size as shown in Figure 1. The micro-porosity of the synthesized material is responsible for its very low density of about 15 mg/cm^3 and its good conductivity (electrical resistance of about 40 Ω·cm^{-1}). These values are comparable to those reported in the literature for similar samples [6].

Figure 1: Photograph of a dish containing CNT-sponges, and two cut pieces of few cubic mm.

Scanning electron microscopy (SEM) analysis of the interior of the samples reveals that the material is made of randomly self-assembled, long and interconnected tubular nanostructures, with pore sizes from several nanometers to a few micrometers (Figure 2a). The high number of interconnections indicated by the arrows in Figure 2b is caused by the presence of topological defects in the carbon sp^2 lattice that originate during the growth process. In particular, the addition of sulfur to the synthesis process induces the formation of pentagonal and heptagonal carbon rings [15,16] that favors the bent geometry of the nanostructures. No structural differences are observed along the whole sample within this morphological characterization.

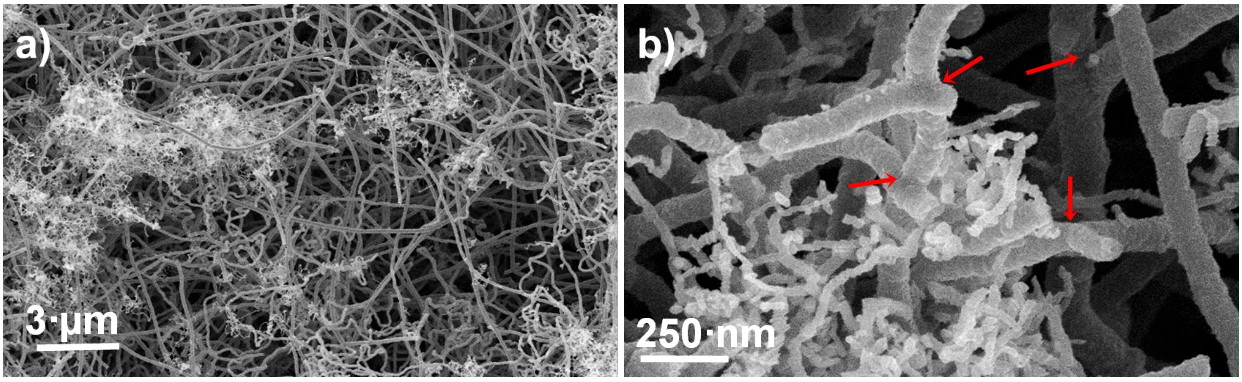

Figure 2: SEM micrographs showing the entangled structure of the network acquired at two different magnifications (a,b). The red arrows in panel (b) point to junctions between CNTs.

In the case of the sample reported in Figure 2, the statistical analysis gives a double distribution of the external diameter centered at 91 ± 3 nm, and 418 ± 5 nm, respectively. The length of the tubes can vary from few nanometers to millimeters, and the CNTs have a high number of walls as evidenced by a transmission electron microscopy studies described in [13]. SEM micrographs obtained at higher magnification evidence the presence of interconnected and curled CNTs as shown in Figure 2b. The electron energy loss spectroscopy analysis performed in reflection mode further supports the predominance of C-sp^2 hybridization in the nanotubes, as indicated by the electron microscopy studies. In fact, the spectrum in Figure 3, displays two peaks at 6 eV and 24.5 eV. These are contributions coming from the π and $\pi + \sigma$ plasmons, respectively, of the sp^2 lattice [17]. In particular, the energy positions of both features are downshifted in energy loss compared to those of the highly oriented pyrolytic graphite (7 eV and 28 eV, respectively). This behavior is due to the low dimensionality of the system similar to that reported for multi-walled CNTs [18].

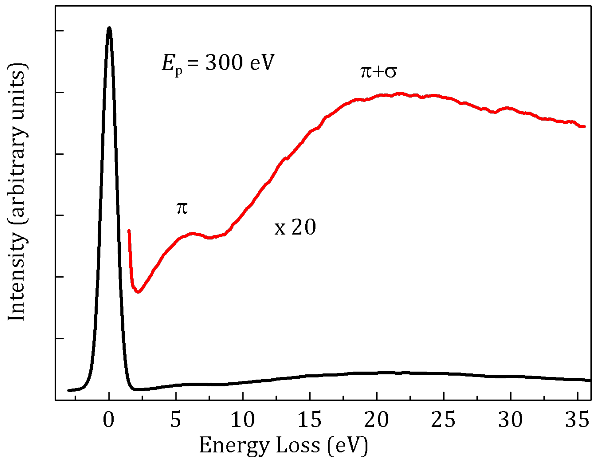

Figure 3: Electron energy loss spectra (E_p = 300 eV) obtained on the CNT-sponge. The π and π + σ plasmons have been emphasized for better view (red line).

The micro-porosity of the synthesized material is responsible of its low weight and its capability to sustain high compression loads as recently reported for our samples [14]. Furthermore, two interesting properties that originate from the high porosity and the presence of numerous interconnected one-dimensional nanostructures are the hydrophobicity and oleophilicity. To better characterize the hydrophobicity one can measure the advanced static contact angle at room temperature for water droplets of different volumes ranging from 5 to 20 µL, as shown in Figure 4a.

The presence of a composite solid–liquid–air interface explains the high value of the measured contact angle (Θ = 175°), as evaluated in Figure 4b, with no observable roll-off angle, even when the substrate is turned upside down, see Figure 5a. Therefore, we infer that the contact angle hysteresis is sufficiently high to pin the water droplet on the MWCNT surface. It is possible to estimate the adhesive force in length units of a surface in contact with water from the equation [19]:

$$F_{\mathrm{adh}} = \gamma_{\mathrm{LV}}\left(1+\cos\Theta\right), \qquad (1)$$

where γ_{LV} denotes the surface tension of the liquid–vapor (LV) interface for water γ_{LV} = 72.5 mN/m, and Θ is the measured contact angle (Θ = 175°). The estimated adhesion force of the water droplet (20 µL) reported in Figure 4b, is about 50 µN.

Measuring the variation of the static contact angle as a function of the time at room temperature shows a reduction of the initial value of less than 2% after 100 min, due to water evaporation. This proves the stability of the super-hydrophobic state (Figure 5b). These findings indicate that the CNT-sponge wettability is well described by a Cassie–Baxter model [20] for which a quite rough surface allows air trapping and ensures the high contact angle measured. In particular, in such a system pores in the random network (i.e., void fraction) favor air trapping due to the strong capillary force that the surface exerts on the liquid. The water drop can be viewed as sitting on a

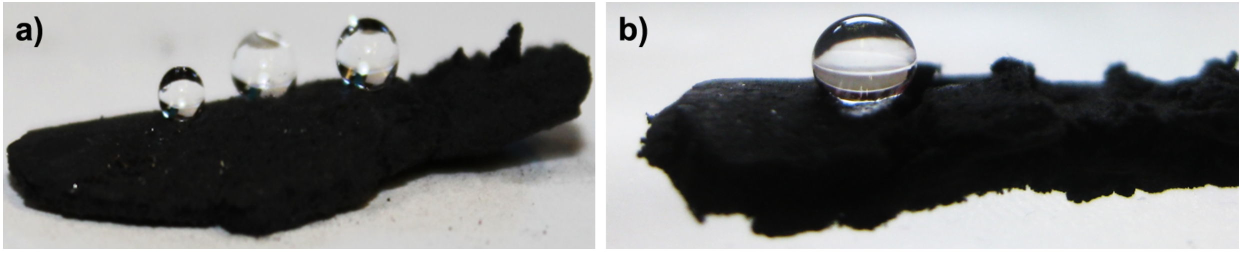

Figure 4: Photographs of water droplets of different volumes (a) and contact angle profile of a single drop (b) on the bulk material.

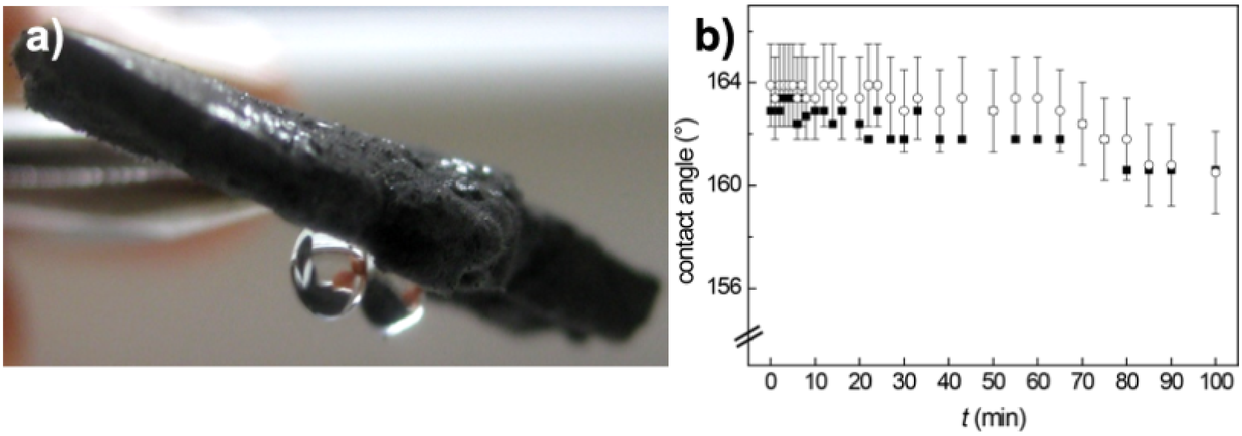

Figure 5: Stability of the super-hydrophobic state. No roll-off angle was measured, even when the substrate is turned upside down (a). Variation of the measured contact angle for a 10 µL water droplet as a function of the time, the vertical scale has been expanded for better view (b).

composite surface consisting of solid and air. Therefore, one can describe the wetting properties of the sponge surface in the super-hydrophobic regime using the Cassie-Baxter equation [20]:

$$\cos\theta^* = (1-\phi)\cos\theta - \phi; \quad 1 = \phi + \phi_s, \tag{2}$$

where ϕ_s and ϕ are the fractions of solid and air contacting the water droplet, θ^* is the apparent contact angle, and θ is the Young's contact angle of the surface, with $\cos\theta$ defined as:

$$\cos\theta = \frac{\gamma_{SV} - \gamma_{SL}}{\gamma_{LV}}, \tag{3}$$

where γ_{SV}, γ_{SL}, and γ_{LV} denote the surface tension of the solid–vapor (SV), the solid–liquid (SL), and the liquid–vapor (LV) interface, respectively. If we insert in Equation 2 the Young's contact angle measured experimentally for a MWCNT [21,22] (from Nanocyl, NC7000, diameter: 5–50 nm) random network film, $\theta \cong 92°$, and as apparent contact angle the average value $\theta^* = 175°$, we obtain a surface air fraction of $\phi \cong 0.98$.

This value indicates that the wet fractional area of the drop base in contact with the sponge surface is very low and thus large amount of air pockets formed, because of the fakir effect [23] induced by the high roughness of the CNT random network.

On the other hand, the CNT-sponge shows a high absorption capacity towards oils (e.g., vegetable and mineral oil). The contact angle is significantly less than 90° and therefore the CNT-sponge is lipophilic [6]. In Figure 6a the beginning of the removal of mineral oil (from AGIP company, ISO46) spreading on the water surface using the as-prepared three-dimensional material is shown. It is possible to evaluate the adsorption capacity of the sponge, from the ratio between the final and initial weight after full adsorption [6]. As an example, a CNT-sponge of 2 mg is able to selectively uptake vegetable oil up to 16 times of its initial weight. The observed high value of the uptake efficiency can be ascribed to the presence of both (i) carbon sp^2 species (e.g., nanofibers), characterized by a rough surface, and (ii) the high porosity. In fact, it is known that irregular surfaces make adsorption of organics much easier than smooth ones [24]. The adsorbed oil can easily be removed after the sponge is saturated simply through squeezing it from the sponge or through burning it. In Figure 6b, the oil-saturated sponge is ignited, the fire burns the oil and the sponge is ready to be reused.

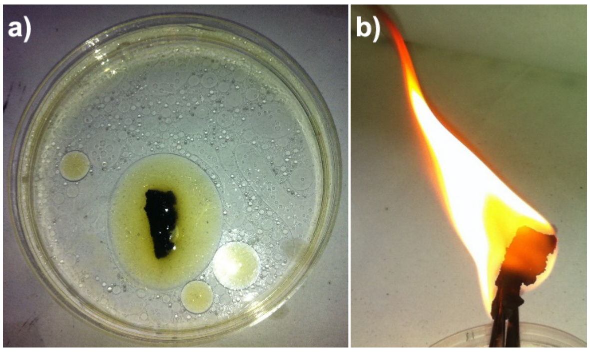

Figure 6: Burning and reuse of the CNT-sponge. Photograph of the starting of the oil-adsorption process (a), and burning after the sponge got saturated with oil (b).

We investigated with SEM on the nanostructure properties before and after oil adsorption and the subsequent burning process. Figure 7a and Figure 7b show two SEM micrographs

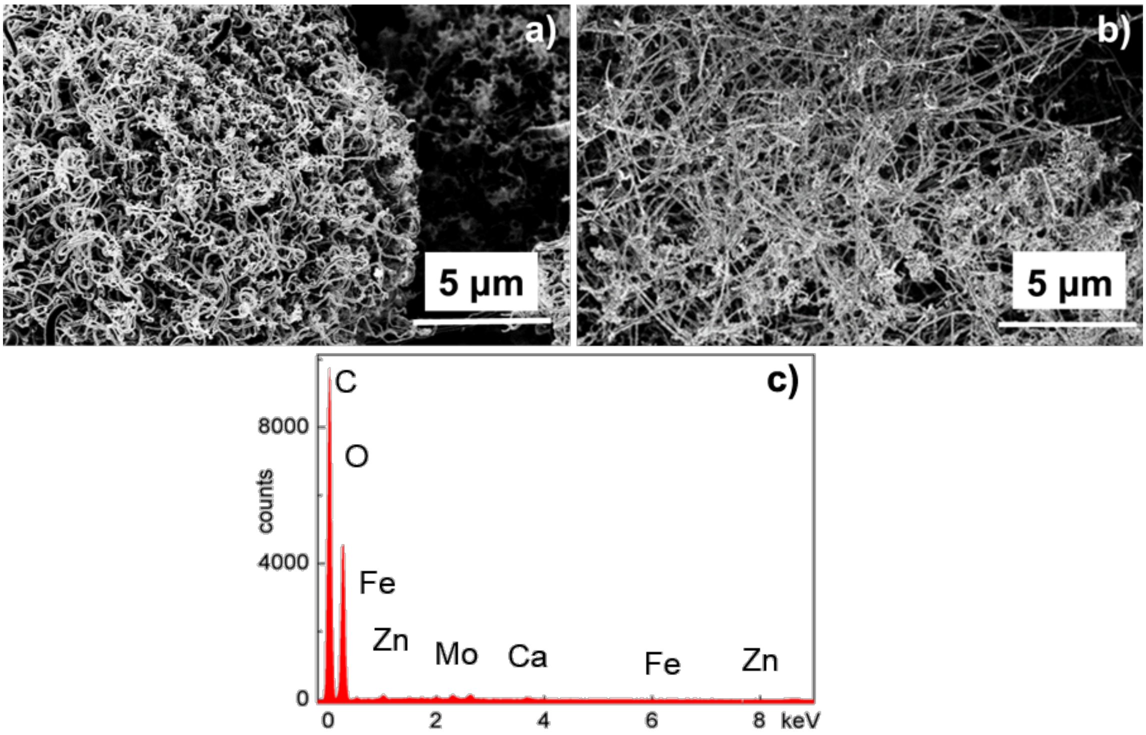

Figure 7: SEM micrographs of the CNT-sponge surface after one (a) and two (b) burning processes. Correspondent EDX spectrum collected from sample (a) showing some constituents of the adsorbed oil together with the main components of the CNT-sponge (c).

obtained from the surface of the CNT-sponge after one and two adsorption–burning processes, respectively. While the porous assembly appears almost entirely preserved, the nanostructures composing the network are partially covered by some oil residues. This finding is confirmed by EDX spectrum collected on the network of Figure 7a, that shows contributions from: the CNT-nanostructures (C and Fe), some of the constituents the oil used in the experiment (Zn, Mo) and small traces of Ca from water, Figure 7c. No sulfur signal was detected in the network, indicating that the sulfur content is too small. Therefore, we can assume that almost no sulfur was trapped in the network, in accordance to what was reported for similar CNT-networks [25].

A sponge-like multiwall-CNT framework was recently used as the catalytic layer of a counter electrode for a dye-sensitized solar cell (DSC) [26]. The CNT-sponge was directly transferred onto a conductive substrate to make a counter electrode (CE), exploiting its good electrical and mechanical properties. A photoelectric conversion efficiency of about 6.2% was achieved for the DSC with a CNT-sponge CE, compared to 7.6% of that with Pt CEs.

Recently, our research group showed that 2D films made of pristine MWCNTs can be used as optically active medium for light energy conversion in a solar cell device [27]. Accordingly, we performed a similar measurement using a piece of CNT-sponge, which possesses a self-supporting structure, as the working electrode in a standard electrochemical cell. The photo-response was measured as a function of the incident photon wavelength and expressed in terms of IPCE (incident-photon-to-current efficiency) (Figure 8). In the same figure, the response obtained from a MWCNT film grown on a silicon substrate [27-29] is reported for comparison. The samples show a photo response to the incident light with a similar IPCE trend. It is noteworthy that the signal coming from the CNT-sponge has a maximum around 420 nm, red-shifted with respect to that obtained from CNTs film of around 360 nm. The observed difference can be ascribed to the highly complex microscopic structure of the sponge compared to that of the MWCNTs composing the film. Indeed, not only the CNT-sponge presents a marked variability in the tube diameter but also carbon few fibers are present in the network. These structural fluctuations give different response to incident light.

Conclusion

A chemical vapor deposition process can be used to synthesize three-dimensional porous structures composed of CNTs. The obtained CNT material exhibits a sponge-like structure and has a low density. The capability to adsorb and remove different

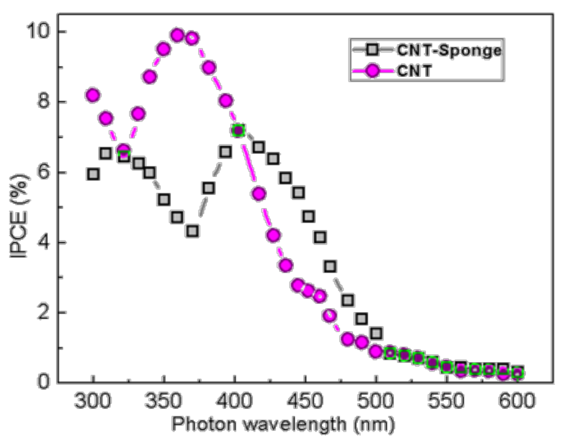

Figure 8: Incident-photon-to-current efficiency (IPCE, %) obtained from a MWCNT 2D film (purple circles), and for a CNT-sponge sample (grey squares) as function of incident photon wavelength.

types of oil has been demonstrated and can be considered very interesting for environmental applications. In addition, the CNT network shows a good photo response to incident light in the visible and near ultraviolet range, thus proving its potential application in photon-energy conversion devices. The collected results enable us to predict that the produced CNT-sponges are an interesting example of nanostructured materials that may be employed in new emerging fields of applications such as environmental sector, sensing and electromechanical transduction. At the same time, a thorough study on the correlation between the observed properties and the structural and electronic features of the network is ongoing.

Experimental

Chemical vapor deposition process for the growth of 3D CNT networks: The chemical vapor deposition process was carried out in a horizontal hot-wall quartz furnace. Prior to the experiment, argon gas was flushed into the growth chamber, to restore an ambient inert pressure (760 Torr). Ferrocene (2.3 wt %) and tiophene (1.5 wt %) were dissolved in ethanol to be used as catalyst and sulfur precursors, respectively. The obtained solution was placed in a 10 mL glass syringe and injected into the growth chamber at a constant rate of 7 mL/h through a flux of argon and acetylene (500/200 sccm), which act as gas carrier and carbon precursor, respectively. The vaporized solution and the gas mixture were injected through a stainless tube directly into the high temperature region of the quartz tube furnace. The CNT synthesis was carried out at a temperature of 900 °C, measured by an optical pyrometer.

Microstructure investigation: The morphology of the CNT-sponges was examined with a field emission gun scanning electron microscope (FEG-SEM, Leo Supra 35) equipped with energy dispersion spectroscopy (EDX).

Electron energy loss analysis: Electron energy loss (EELS) was recorded in reflection mode ex situ in an ultrahigh vacuum system (base pressure about 2×10^{-10} Torr) equipped with an electron gun ($E_p = 300$ eV, $\Delta E = 1.0$ eV).

Contact angle measurements: Static advanced contact angles were measured from optical images and analyzed with the open-source software ImageJ.

Evaluation of the oil-adsorption capacity: A cut piece of CNT-sponge was laid down onto the surface of a vessel containing water over which drops of mineral oil (from AGIP Company, Italy) have been deposited. By measuring the ratio between the mass of the dry CNT bulk material and the mass after oil adsorption, the oil-adsorption capacity was evaluated. The adsorbed oil in the material was then removed burning it in air and then was used to repeat the above process for many cycles.

Photocurrent measurements: Photo-electrochemical measurements were carried out at room temperature with a standard three-arm photo-electrochemical cell, using a platinum (Pt) wire as the counter electrode, a saturated calomel electrode (SCE) as the reference electrode and the sample as working electrode. Measurements have been performed on MWCNT films grown on a Si(111) substrate and a cut piece of CNT-sponge. A 0.5 M KI and 0.01M I_2 in acetonitrile solution was used as the electrolyte. Samples were irradiated with light coming from a 200 W Xe lamp (Osram) equipped with a monochromator ($\lambda > 300$ nm) and a PG-310 potentiostat (HEKA Elektronik, Lambrecht, Germany) measured the photo-current. The intensity of the photo-current signal was normalized to the irradiated sample area and the incident light power and expressed as IPCE (incident-photon-to-current efficiency) [27-29]. The light intensity near the electrode surface was estimated to be about 50 $\text{mW}\cdot\text{cm}^{-2}$ by azobenzene actinometry [30].

Acknowledgements

The European Office of Aerospace Research and Development (EOARD) through the Air Force Office of Scientific Research (AFOSR) under Grant No. FA9550-14-1-0047 funded this project.

References

1. Zhao, D.; Yang, P.; Melosh, N.; Feng, J.; Chmelka, B. F.; Stucky, G. D. *Adv. Mater.* **1998,** *10,* 1380–1385. doi:10.1002/(SICI)1521-4095(199811)10:16<1380::AID-ADMA1380>3.0.CO;2-8

2. Nardecchia, S.; Carriazo, D.; Ferrer, M. L.; Gutiérrez, M. C.; del Monte, F. *Chem. Soc. Rev.* **2013,** *42,* 794–830. doi:10.1039/C2CS35353A
3. Lee, J.; Kim, J.; Hyeon, T. *Adv. Mater.* **2006,** *18,* 2073–2094. doi:10.1002/adma.200501576
4. Gui, X.; Wei, J.; Wang, K.; Cao, A.; Zhu, H.; Jia, Y.; Shu, Q.; Wu, D. *Adv. Mater.* **2010,** *22,* 617–621. doi:10.1002/adma.200902986
5. Li, H.; Gui, X.; Zhang, L.; Wang, S.; Ji, C.; Wei, J.; Wang, K.; Zhu, H.; Wu, D.; Cao, A. *Chem. Commun.* **2010,** *46,* 7966–7968. doi:10.1039/c0cc03290e
6. Gui, X.; Li, H.; Wang, K.; Wie, J.; Jia, Y.; Li, Z.; Fan, L.; Cao, A.; Zhu, H.; Wu, D. *Acta Mater.* **2011,** *59,* 4798–4804. doi:10.1016/j.actamat.2011.04.022
7. Qian, W.; Gu, Z.-Z.; Fujishima, A.; Sato, O. *Langmuir* **2002,** *18,* 4526–4529. doi:10.1021/la0118199
8. Moura, F. C. C.; Lago, R. M. *Appl. Catal., B* **2009,** *90,* 436–440. doi:10.1016/j.apcatb.2009.04.003
9. Cao, A.; Dickrell, P. L.; Sawyer, W. G.; Ghasemi-Nejhad, M. N.; Ajayan, P. M. *Science* **2005,** *310,* 1307–1310. doi:10.1126/science.1118957
10. García-Martínez, J.; Lancaster, T. M.; Ying, J. Y. *Adv. Mater.* **2008,** *20,* 288–292. doi:10.1002/adma.200602977
11. You, B.; Jiang, J.; Fan, S. *ACS Appl. Mater. Interfaces* **2014,** *6,* 15302–15308. doi:10.1021/am503783t
12. Bryning, M. B.; Milkie, D. E.; Islam, M. F.; Hough, L. A.; Kikkawa, J. M.; Yodh, A. G. *Adv. Mater.* **2007,** *19,* 661–664. doi:10.1002/adma.200601748
13. Camilli, L.; Pisani, C.; Gautron, E.; Scarselli, M.; Castrucci, P.; D'Orazio, F.; Passacantando, M.; Moscone, D.; De Crescenzi, M. *Nanotechnology* **2014,** *25,* 065701. doi:10.1088/0957-4484/25/6/065701
14. Camilli, L.; Pisani, C.; Passacantando, M.; Grossi, V.; Scarselli, M.; Castrucci, P.; De Crescenzi, M. *Appl. Phys. Lett.* **2013,** *102,* 183117. doi:10.1063/1.4804385
15. Tibbetts, G. G.; Bernard, C. A.; Gorkiewicz, D. W.; Alig, R. L. *Carbon* **1994,** *32,* 569–576. doi:10.1016/0008-6223(94)90074-4
16. Romo-Herrera, J. M.; Sumpter, B. G.; Cullen, D. A.; Terrones, H.; Cruz-Silva, E.; Smith, D. J.; Meunier, V.; Terrones, M. *Angew. Chem., Int. Ed.* **2008,** *47,* 2948–2953. doi:10.1002/anie.200705053
17. Calliari, L.; Fanchenko, S.; Filippi, M. *Carbon* **2007,** *45,* 1410–1418. doi:10.1016/j.carbon.2007.03.034
18. Castrucci, P.; Scilletta, C.; Del Gobbo, S.; Scarselli, M.; Camilli, L.; Simeoni, M.; Delley, B.; Continenza, A.; De Crescenzi, M. *Nanotechnology* **2011,** *22,* 115701. doi:10.1088/0957-4484/22/11/115701
19. Adamson, W.; Gast, A. P. *Physical Chemistry of Surfaces;* John Wiley & Sons: New York, 1997.
20. Cassie, A. B. D.; Baxter, S. *Trans. Faraday Soc.* **1944,** *40,* 546–551. doi:10.1039/tf9444000546
21. De Nicola, F.; Castrucci, P.; Scarselli, M.; Nanni, F.; Cacciotti, I.; De Crescenzi, M. *Nanotechnology* **2015,** *26,* 145701. doi:10.1088/0957-4484/26/14/145701
22. De Nicola, F.; Castrucci, P.; Scarselli, M.; Nanni, F.; Cacciotti, I.; De Crescenzi, M. *Sci. Rep.* **2015,** *5,* 8583. doi:10.1038/srep08583
23. Quéré, D. *Nat. Mater.* **2002,** *1,* 14–15. doi:10.1038/nmat715
24. Peng, X.; Li, Y.; Luan, Z.; Di, Z.; Wang, H.; Tian, B.; Jia, Z. *Chem. Phys. Lett.* **2003,** *376,* 154–158. doi:10.1016/S0009-2614(03)00960-6
25. Shan, C.; Zhao, W.; Lu, X. L.; O'Brien, D. J.; Li, Y.; Cao, Z.; Elias, A. L.; Cruz-Silva, R.; Terrones, M.; Wei, B.; Suhr, J. *Nano Lett.* **2013,** *13,* 5514–5520. doi:10.1021/nl403109g
26. Chen, J.; Meng, F.; Gui, X.; Sun, H.; Zeng, H.; Li, Z.; Zhou, Y.; Tang, Z. *Carbon* **2012,** *50,* 5624–5627. doi:10.1016/j.carbon.2012.08.002
27. Castrucci, P.; Tombolini, F.; Scarselli, M.; Speiser, E.; Del Gobbo, S.; Richter, W.; De Crescenzi, M.; Diociaiuti, M.; Gatto, E.; Venanzi, M. *Appl. Phys. Lett.* **2006,** *89,* 253107. doi:10.1063/1.2408648
28. Scarselli, M.; Camilli, L.; Matthes, L.; Pulci, O.; Castrucci, P.; Gatto, E.; Venanzi, M.; De Crescenzi, M. *Appl. Phys. Lett.* **2012,** *101,* 241113. doi:10.1063/1.4771125
29. Scarselli, M.; Castrucci, P.; Camilli, L.; Del Gobbo, S.; Casciardi, S.; Tombolini, F.; Gatto, E.; Venanzi, M.; De Crescenzi, M. *Nanotechnology* **2011,** *22,* 035701. doi:10.1088/0957-4484/22/3/035701
30. Kuhn, H. J.; Braslavsky, S. E.; Schmidt, R. *Pure Appl. Chem.* **1989,** *61,* 187–210. doi:10.1351/pac198961020187

License and Terms

BEILSTEIN JOURNAL OF NANOTECHNOLOGY

Nanostructuring of GeTiO amorphous films by pulsed laser irradiation

Valentin S. Teodorescu[1], Cornel Ghica[1], Adrian V. Maraloiu[1], Mihai Vlaicu[1], Andrei Kuncser[1], Magdalena L. Ciurea*[1,2], Ionel Stavarache[1], Ana M. Lepadatu[1], Nicu D. Scarisoreanu[3], Andreea Andrei[3], Valentin Ion[3] and Maria Dinescu[3]

Full Research Paper

Address:
[1]National Institute of Materials Physics, 105 bis Atomistilor Street, 077125 Bucharest-Magurele, Romania, [2]Academy of Romanian Scientists, Bucuresti 050094, Romania and [3]National Institute of Plasma Lasers and Radiation, 409 Atomistilor Street, 077125 Bucharest-Magurele, Romania

Email:
Magdalena L. Ciurea* - ciurea@infim.ro

* Corresponding author

Keywords:
fast diffusion; GeTiO film; nanostructuring; pulsed laser annealing; cross-sectional transmission electron microscopy (XTEM)

Beilstein J. Nanotechnol. **2015,** *6,* 893–900.
doi:10.3762/bjnano.6.92

Received: 17 September 2014
Accepted: 24 February 2015
Published: 07 April 2015

This article is part of the Thematic Series "Self-assembly of nanostructures and nanomaterials".

Guest Editor: I. Berbezier

Abstract

Laser pulse processing of surfaces and thin films is a useful tool for amorphous thin films crystallization, surface nanostructuring, phase transformation and modification of physical properties of thin films. Here we show the effects of nanostructuring produced at the surface and under the surface of amorphous GeTiO films through laser pulses using fluences of 10–30 mJ/cm^2. The GeTiO films were obtained by RF magnetron sputtering with 50:50 initial atomic ratio of Ge:TiO$_2$. Laser irradiation was performed by using the fourth harmonic (266 nm) of a Nd:YAG laser. The laser-induced nanostructuring results in two effects, the first one is the appearance of a wave-like topography at the film surface, with a periodicity of 200 nm and the second one is the structure modification of a layer under the film surface, at a depth that is related to the absorption length of the laser radiation. The periodicity of the wave-like relief is smaller than the laser wavelength. In the modified layer, the Ge atoms are segregated in spherical amorphous nanoparticles as a result of the fast diffusion of Ge atoms in the amorphous GeTiO matrix. The temperature estimation of the film surface during the laser pulses shows a maximum of about 500 °C, which is much lower than the melting temperature of the GeTiO matrix. GeO gas is formed at laser fluences higher than 20 mJ/cm^2 and produces nanovoids in the laser-modified layer at the film surface. A glass transition at low temperatures could happen in the amorphous GeTiO film, which explains the formation of the wave-like topography. The very high Ge diffusivity during the laser pulse action, which is characteristic for liquids, cannot be reached in a viscous matrix. Our experiments show that the diffusivity of atomic and molecular species such as Ge and GeO is very much enhanced in the presence of the laser pulse field. Consequently, the fast diffusion drives the formation of amorphous Ge nanoparticles through the segregation of Ge atoms in the GeTiO matrix. The nanostructuring effects induced by the laser irradiation can be used in functionalizing the surface of the films.

Introduction

Laser pulse processing of surfaces and thin films is a useful tool for purposes such as the amorphous thin films crystallization [1-6], surface nanostructuring [7-10], laser-induced thin film dewetting [11,12], phase transformation and modification of physical properties of thin films [13-16]. The laser fluence values used for these applications are below the ablation threshold of the irradiated material in order to prevent a loss of material during laser processing.

The absorption length of ultraviolet (UV) laser radiation is in the range of tens of nanometers for many materials [17]. The laser pulse energy is deposited in a very thin layer beneath the surface of the laser target, which has a thickness of the order of magnitude of the laser absorption length. If the irradiated film thickness is greater than the laser radiation absorption length, the laser annealing takes place only in a surface layer of the film, and a gradual modification of the nanostructure or a crystallization can be induced in the film [18,19].

The surface heating of the film during the laser pulse action can be estimated if the physical properties of the films are known. The most important are the absorption coefficient of the laser radiation in the films and the heat diffusivity. Some of these parameters can be considered to be similar to those in bulk material, but in many cases of amorphous or multi-component films there are no corresponding bulk materials. The laser radiation absorptivity for many amorphous films is not known. Even in the case when the properties can be optically measured, they change at the beginning of each laser pulse, i.e., every successive laser pulse will see a different surface nanostructure with different absorptivity and different thermal diffusivity. Finally, the surface structure stabilizes after a number of laser pulses, which generally happens in the case of films crystallization. In addition to the thermal effect of the UV absorption in the target, the UV radiation can also induce photonic effects, such as the diffusivity enhancement of atomic species due to the lattice bonds softening [20-22] in the strong field of the laser pulse. High values of atomic diffusivity were observed for Ge diffusion in the case of laser crystallization annealing of SiGe amorphous film [18].

In this paper, we report about the nanostructuring at the surface and under the surface of amorphous GeTiO films by laser pulse action. The cross sectional study gives evidence of a fast diffusion effect, i.e., the formation of amorphous Ge nanoparticles through the segregation of Ge atoms in the GeTiO matrix.

Experimental

Amorphous GeTiO films with a thickness of 330 nm were deposited by RF magnetron sputtering on Si(100) wafer substrates using Ge:TiO_2 with 50:50 atomic ratio. Details on the film deposition are found in [23]. These GeTiO amorphous films were irradiated with laser fluences from 10 to 30 mJ/cm^2 and different numbers of laser pulses in the range from 10 to 500. The laser irradiations were performed by using the fourth harmonic (λ = 266 nm) radiation of a Nd:YAG laser (Surellite II, "Continuum", USA) working in TEM00 mode, giving a maximum pulse energy of 100 mJ for the fourth harmonic with a pulse length of 5–7 ns and an adjustable repetition rate of 1–10 Hz. The experimental value of the laser average fluence is measured with an energymeter (Gentec QE 65 LP, Noise Level Energy 10 μJ, maximum frequency 100 Hz).

The laser irradiations were performed in air, perpendicularly to the film surface, using the central part of the laser beam, with a diameter of 7 mm having a rather homogeneous intensity. However, at the micrometer scale the laser beam is not homogeneous, because the high coherence of the Nd:YAG laser radiation gives rise to interference effects on the target surface, which induces local intensification of the laser fluence. Under these conditions, the film surface temperature during the laser pulse duration can only be estimated as an average value.

The nanostructuring of the amorphous GeTiO films starts at very low laser fluences, and the evolution of their morphology cannot be considered as a sign of melting. All laser treatments were conducted at low fluences, so that the films remain practically in the solid state phase, as the surface temperature estimation shows.

Before and after laser irradiation, the nanostructure of the film surfaces was observed by scanning electron microscopy (SEM) and atomic force microscopy (AFM). The structure in the depth of the irradiated films was studied by cross-section transmission electron microscopy (XTEM). The specimens for XTEM were prepared by the conventional method: Small pieces cut from the irradiated area of the film sample were glued face to face, followed by mechanical polishing and ion milling in a Gatan PIPS model 691 aparatus. Transmission electron microscopy was performed by using a Jeol ARM 200F electron microscope, performing normal TEM imaging, scanning transmission electron microscopy-high angle annular dark field (STEM-HAADF) imaging and energy-dispersive X-ray spectroscopy (EDX). The estimation of the film surface temperature was performed by using the Heat Flow software [24].

Results

A quasi-coherent wave relief with a periodicity of about 200 nm and 10 nm amplitude was observed on the surface of the GeTiO film, after irradiation with 100 laser pulses with a fluence of

15 mJ/cm^2. This periodicity is smaller than the 266 nm wavelength of the laser radiation. Figure 1 shows the SEM (Figure 1a) and AFM (Figure 1b) images of the irradiated surface area of the film.

Figure 2 shows low-magnification XTEM images of the film before (Figure 2a) and after (Figure 2b) laser irradiation with 100 pulses at low laser fluence (15 mJ/cm^2). The wave relief is visible in the XTEM specimen because the film sample was cut perpendicular to the wave relief formed on the film surface. The film structure remains amorphous after laser irradiation, but a small increase of the volume is observed at the film surface due to the laser pulse action.

The morphology and the structure of the modified film surface layer strongly depend on the laser fluence (Figure 3a and

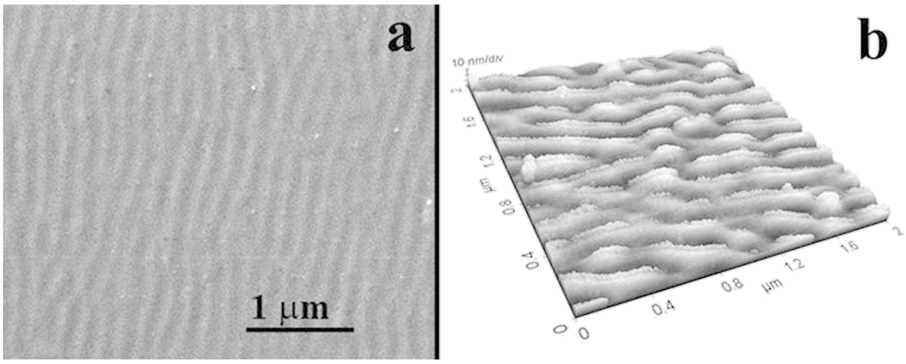

Figure 1: Surface relief of the GeTiO film after laser irradiation with 100 laser pulses at 15 mJ/cm^2 fluence. (a) SEM image and (b) AFM image.

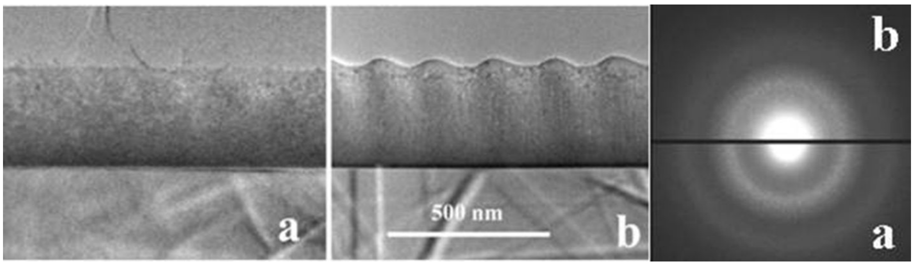

Figure 2: Low-magnification XTEM images of the amorphous GeTiO film, before (a) and after (b) laser irradiation at low fluence (15 mJ/cm^2). A small, but evident, increase of the film volume happens. The film structure remains amorphous after laser irradiation, as can be seen from the corresponding SAED patterns.

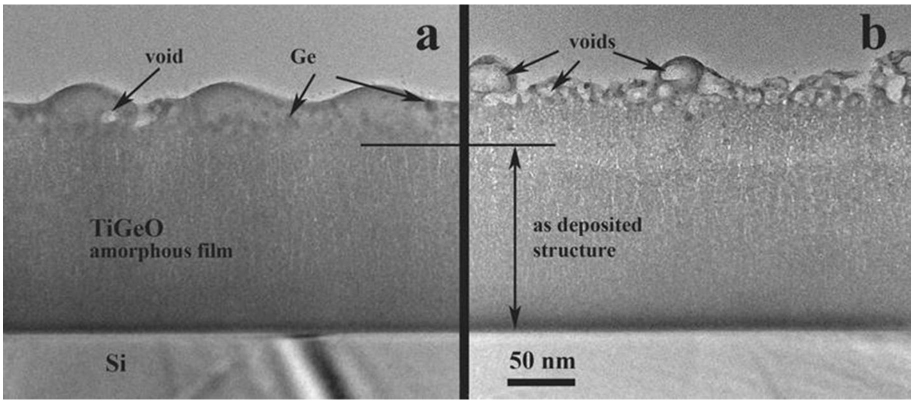

Figure 3: XTEM images of the amorphous GeTiO RF film after laser irradiation with 266 nm laser radiation. (a) Low fluence (15 mJ/cm^2) and (b) higher laser fluence (20 mJ/cm^2). The film structure morphology is transformed in a depth of about 50 nm.

Figure 3b). At a higher fluence (20 mJ/cm^2), the wave relief disappears and an irregular structure of nanovoids appears in the surface layer. A closer look at the transformed surface layer (see Figure 3) reveals the formation of spherical nanoparticles and nanovoids. The formed nanovoids contribute to the small volume increase even at 15 mJ/cm^2 (Figure 3a).

The most interesting transformation happened beneath the film surface, as revealed by detailed observations (Figure 4). The film structure is modified over a depth of about 50 nm and all the rest of film remains unchanged. The structure of the modified layer is also amorphous.

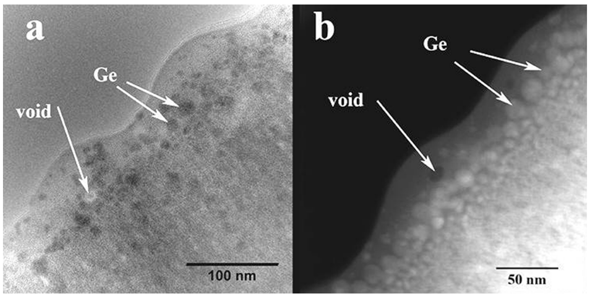

Figure 4: Morphology details of the GeTiO film surface layer structure revealed by the cross sectional observations. (a) XTEM conventional image and (b) a similar area viewed by STEM-HAADF method.

During laser pulse irradiation, the morphology of the film surface layer affected by the laser pulse actions gradually changes. Spherical amorphous Ge nanoparticles are formed by Ge atoms segregation. These spherical Ge nanoparticles have 5 nm diameters at the interface with the region of the unchanged amorphous film structure (region III in Figure 5) and grow up to about 20 nm in the middle of the laser-transformed layer (region II in Figure 5). The first 10 nm layer under the film surface (region I in Figure 5) contains less Ge and only very few spherical Ge nanoparticles, as it can be observed from the HAADF-STEM images in Figure 4b and Figure 5.

The EDX line scan analysis, performed along the green line shown in Figure 5, reveals the majority of Ge content of the amorphous spherical nanoparticle, arrowed in the image, where the Ge signal is much higher than the Ti signal. The spherical amorphous Ge nanoparticles formed at the interface with the non-modified amorphous film (interface between region II and region III), have a minimum size of 5 nm. The size grows to about 20 nm in the middle of the layer affected by laser (see region II in Figure 5). The size distribution of the Ge nanoparticles is shown in Figure 6. The size range is between 5 and 25 nm and the average size is 11.5 nm.

The average composition of the modified layer and of the non-modified GeTiO film was measured by EDX using an electron spot-size of about 50 nm in diameter, which integrates the content of the total thickness of the laser transformed surface layer (see Figure 7).

The overall content of Ge in the modified top layer is less than in the middle of the film. So, in the modified surface layer, the Ge:Ti atomic ratio is between 2 and 2.3 depending on the site of measurement, while in the middle of the film it is close to 3 as it results from the RF magnetron sputtering films preparation. This shows that about 1/3 of the Ge content is lost from the

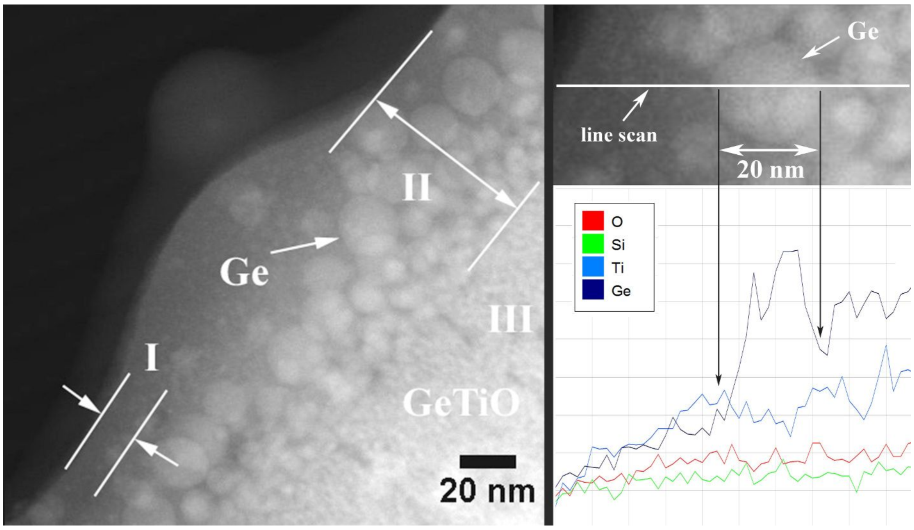

Figure 5: STEM-HAADF image (left) and a detail from the same image correlated with line scan EDX analyse (right) performed on the XTEM specimen prepared from the GeTiO film irradiated with 100 laser pulses at a fluence of 15 mJ/cm^2.

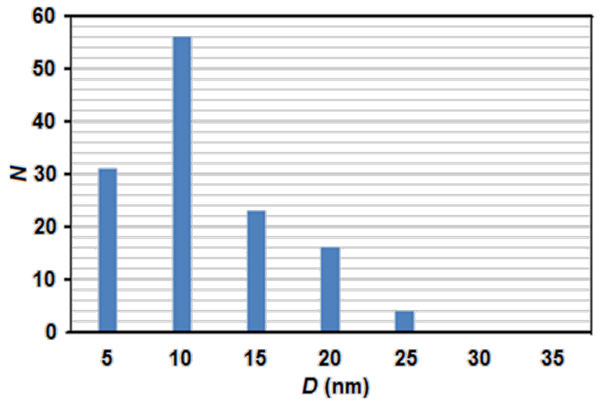

Figure 6: Size distribution of the Ge nanoparticles in region II of the laser transformed layer. The distribution is made from 130 nanoparticles counted on STEM images in which the Ge content is revealed by the *Z*-contrast. The average size is 11.5 nm.

surface layer affected by the laser radiation, and 2/3 of it can be segregated in amorphous Ge nanoparticles.

Discussion

The nanostructure formed at the GeTiO film surface by pulsed laser irradiation shows that several effects are produced during the laser pulse action. The first one is the wave-like relief formed on the film surface, which has a periodicity of about 200 nm, less than the laser radiation wavelength. The second one is the segregation of the Ge nanoparticles under the film surface by a fast diffusion process in the surface layer related to the laser absorption depth.

The formation of periodic ripples due to laser pulse irradiation was already reported a long time ago [25,26], and in the case of perpendicular laser irradiation, the period of the ripple is equal to the laser wavelength or harmonics [27]. This happens at all wavelengths and pulse durations, as in the case of femtosecond laser irradiation [28].

The stress-induced periodic-ripples mechanism demonstrated for crystalline Si [29] could be used for amorphous materials if we define a stress yield for plastic flow. Such a mechanism can be imagined based on the shear transformation-zone theory of plastic deformation near the glass transition [30].

The temperature due to the laser heating was estimated by using the Heat Flow software [24]. Figure 8 shows the temperature variation at different depths of the surface layer during the laser pulse action. For the calculation, the physical parameters were set to maximize the temperature. The absorption coefficient

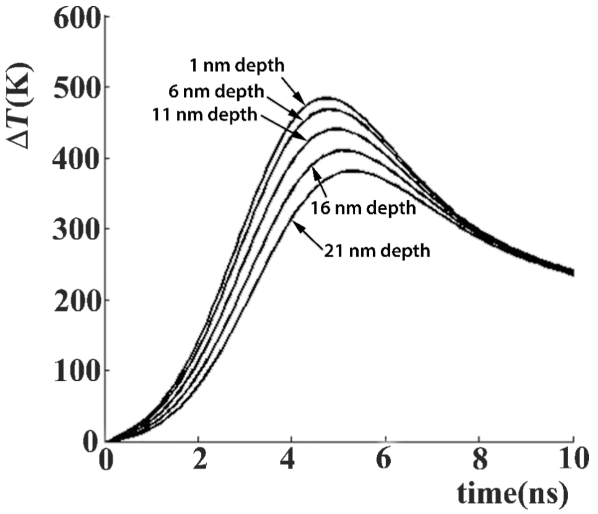

Figure 8: Temperature estimation for different depths beneath the GeTiO film surface during the laser pulse action, considering a Gaussian shape of the laser pulse with a total duration of 7 ns and a laser fluence of 30 mJ/cm^2.

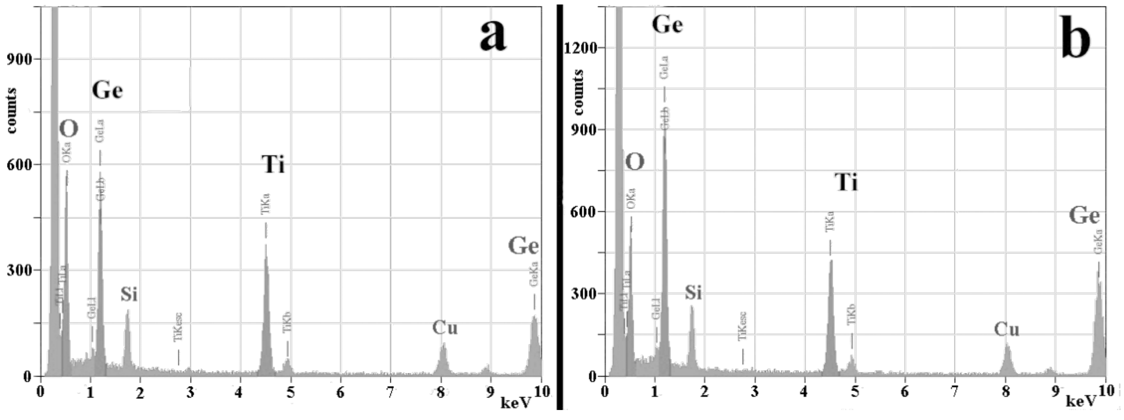

Figure 7: EDX spectra collected on the cross section specimen with an electron beam of 50 nm diameter. (a) Spectrum of the laser-modified layer, and (b) spectrum from a similar specimen area located in the middle of the GeTiO film, where the amorphous structure is not modified by the laser pulse action. The Cu signal comes from the Cu grid and Si peak is due to the redeposition during the ion thinning process.

used is 10^6 cm^{-1} (similar to Ge [17]), and the heat diffusivity is similar to that of TiO_2 (0.02 cm^2/s). Even under these conditions, the temperature grows up to about 500 °C for a laser fluence of 30 mJ/cm^2, which is about double of the average fluence measured for the laser beam. Under these conditions, it is clear that the film surface does not melt during the laser pulse action. The melting temperature for Ge is about 900 °C [17], and of GeO_2 and TiO_2 is much higher [31].

However, the wave relief formed at the surface at low laser fluence, reveals a possible viscous character of the film surface, which probably happens in amorphous films in which a glass transformation process could happen [32]. For amorphous Ge, the temperature of glass transformation is around 600 °C [33], and probably the GeTiO structure has a similar behaviour. The glass transition of the GeTiO amorphous structure can be triggered under the laser pulse action.

At higher laser fluences, the wave relief disappears and a many small spherical (20–30 nm) nanovoids and a few larger ones (40–50 nm) appear at the film surface. We consider that these nanovoids are formed by the aggregation of the molecular GeO gas produced in the film matrix, during laser beam action. GeO gas can be formed around 600 °C [34].

The formation of Ge nanoparticles in a dielectric matrix was also evidenced in amorphous GeTiO films annealed in a conventional furnace [23]. The annealing at about 600 °C leads to the formation of Ge nanocrystals in the film matrix, which is formed by a crystallized mixture of two phases, the Ge in TiO_2 anatase phase and the rutile phase (Ti in GeO_2 rutile phase). If annealing is performed at 700 °C, the $(GeTi)O_2$ rutile phase decomposes and a layer of GeO_2 nanocrystallites appears on the film surface. This clearly shows that Ge diffuses out of the film as GeO.

In the case of laser annealing (irradiation), a fraction of Ge escapes from the top surface layer as revealed by the EDX measurements. We consider that the thickness of the surface layer which contains less Ge nanoparticles (zone I in Figure 4) reveals the diffusion length of Ge species during laser pulse annealing. In the inner zone II, the fast diffusion of Ge under the laser pulse field induces the formation of the amorphous Ge spherical nanoparticles. The Ge nanoparticles formation can be explained only by assuming the fast diffusion of Ge in a surface layer with its thickness being related to the laser radiation absorption length. The laser pulse duration is $\tau = 7$ ns, and the normal diffusivity of the Ge species in the solid state phase is of the order of $D = 10^{-14}$ m^2/s at temperatures of about 900 °C [35]. For a total duration of 100 pulses the total diffusion length of the Ge species can be of the order of $(D\cdot\tau)^{1/2} = 10$ pm. Normally, a diffusion or segregation of Ge atoms in the solid phase cannot be expected. However, the experimental data show that the diffusion length of Ge atoms is about 10 nm during the laser pulse action, corresponding to a diffusivity in the range of 10^{-5} to 10^{-6} m^2/s, which is typical for the liquid phase. In the viscous phase the diffusivities are much smaller than in the liquid phase as the fraction of the broken bonds in the viscous phase is much smaller than in the liquid phase. The fast diffusion of Ge in the solid matrix was also evidenced in the case of laser irradiation of amorphous SiGe films [18].

The prolonged high-resolution TEM observation of the amorphous spherical Ge nanoparticles situated in the very thin areas of the XTEM specimen induces local heating and the crystallization of the amorphous Ge nanoparticles. Figure 9a shows such a spherical Ge nanoparticle crystallized during observation. If the electron irradiation continues for several minutes, the spherical crystallite becomes larger through a crystal growth process, as shown in Figure 9b.

The fast Fourier transform (FFT) pattern inserted in Figure 9b shows a quadratic structure for the larger crystallite. By comparing the lattice fringes of the crystallized particle, before and after the crystal growth process (detail in Figure 10) we observe a contraction of the lattice fringe spacing from 0.326 to 0.317 nm, and a small rotation (about 2°) of the lattice fringes direction. The 0.326 nm lattice spacing is characteristic for the cubic Ge and the crystallized particle has the size of the initial spherical Ge amorphous particle. After the crystal growth process, the crystallized area becomes larger and the visible lattice spacing becomes 0.317 nm. The 0.317 nm lattice spacing suggests the formation of the $(GeTi)O_2$ rutile structure [23].

The initial Ge amorphous nanoparticles are produced by laser annealing which in turn initiates the segregation of Ge atoms. This segregation can start around a Ge-rich cluster in the GeTiO amorphous matrix. The crystallization of the Ge phase under electron beam irradiation is an indirect proof that these Ge amorphous particles are practically formed only by Ge atoms. The subsequent crystal growth process developed after the Ge crystallization will use the surrounding GeTiO material which has a smaller Ge content. The high-resolution TEM observations show that the crystalline planes of the cubic Ge (111) with a spacing of 0.326 nm are parallel to the (110) planes of the $(GeTi)O_2$ rutile structure having a spacing of 0.317 nm. This means that around the Ge spherical crystallite, the crystal growth process favours the growth of the rutile structure.

Conclusion

We investigated the effects of nanostructuring produced by the pulsed-laser irradiation at the surface and beneath the surface of

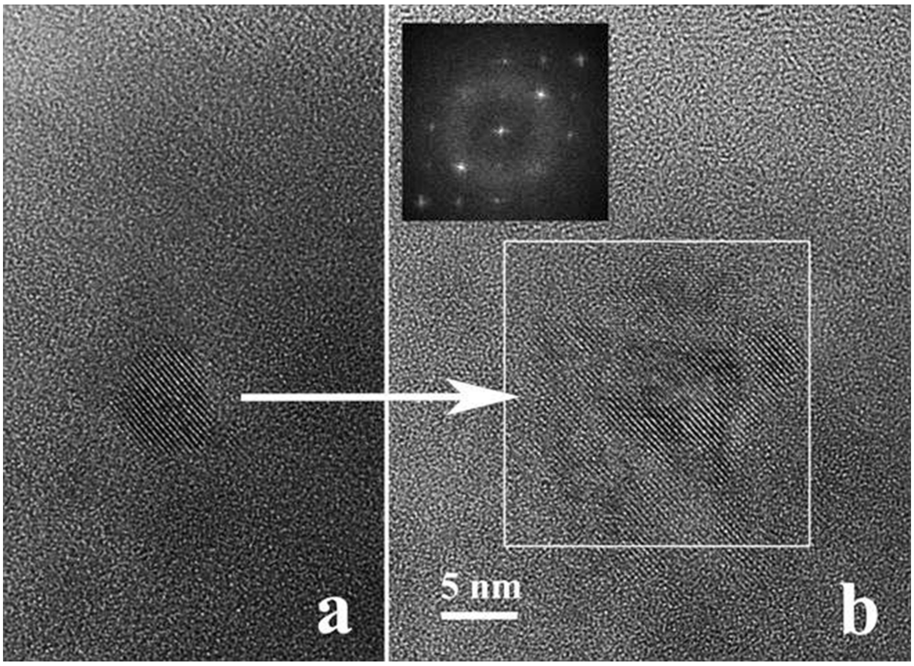

Figure 9: Crystallization (a) and subsequent crystal growth (b) of the Ge amorphous nanoparticle under the high density electron beam irradiation in the microscope. The FFT inserted in the (b) shows a pattern characteristic for the $(GeTi)O_2$ rutile structure.

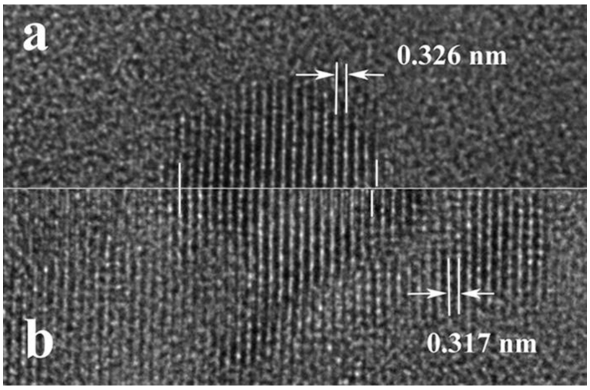

Figure 10: High-resolution TEM images comparing details of the initial crystallized particle (a) and the same area of the particle after the crystal growth process (b). The lattice fringe spacing in panel (b) is smaller than that in panel (a).

amorphous magnetron sputtered GeTiO films. The nanostructuring consists of two simultaneous processes, namely the laser-induced nanostructuring, i.e., the appearance of a wave-like topography on the film surface and the structure modification beneath the film surface, in a depth that is correlated with the laser radiation absorption length. The periodicity of the wave-like relief is smaller than the laser wavelength. The laser annealing of the amorphous GeTiO films results in an unusual segregation of Ge atoms leading to formation of amorphous Ge nanoparticles beneath the film surface due to the fast diffusion of Ge atomic species.

The laser irradiation at low fluences used in our experiments heats the film surface only up to several hundred degrees (less than 500 °C), which is far from the melting point of the amorphous matrix. A glass transition effect is expected in the amorphous GeTiO film, transforming the matrix in a viscous one. This is supposed to favor the formation of the wave relief at the film surface.

We show that the Ge segregation takes place through fast Ge diffusion, at diffusivity values typical for the liquid phase. The viscous behavior of the modified layer is not enough to explain the high Ge diffusivity.

Acknowledgements

The paper was supported by the PNII ID project No 289/2011 and PN II-PT-PCCA-9/2012. The authors are grateful to Dr. E. F. Wagner (EPFL) for the permission to use the Heat Flow software for the simulation of the laser heating.

References

1. Stehle, M. *J. Non-Cryst. Solids* **1997,** *218,* 218–222. doi:10.1016/S0022-3093(97)00293-7
2. Van Overschelde, O.; Snyders, R.; Wautelet, M. *Appl. Surf. Sci.* **2007,** *254,* 971–974. doi:10.1016/j.apsusc.2007.08.018

3. Sandu, C. S.; Teodorescu, V. S.; Ghica, C.; Canut, B.; Blanchin, M. G.; Roger, J. A.; Brioude, A.; Bret, T.; Hoffman, P.; Garapon, G. *Appl. Surf. Sci.* **2003,** *208,* 382–387. doi:10.1016/S0169-4332(02)01412-5
4. Falk, F.; Andrä, G. *J. Cryst. Growth* **2006,** *287,* 397–401. doi:10.1016/j.jcrysgro.2005.11.052
5. Ganz, D.; Gaparro, G.; Aegerter, M. A. *J. Sol-Gel Sci. Technol.* **1998,** *13,* 961–967. doi:10.1023/A:1008634902289
6. Teodorescu, V. S.; Ghica, C.; Sandu, C. S.; Maraloiu, A. V.; Blanchin, M.-G.; Canut, B.; Roger, J. *Dig. J. Nanomater. Biostruct.* **2006,** *1,* 60–69.
7. Sheglov, D. V.; Gorokhov, E. B.; Volodin, V. A.; Astankova, K. N.; Latyshev, A. V. *Nanotechnology* **2008,** *19,* 245302. doi:10.1088/0957-4484/19/24/245302
8. Perez del Pino, A.; György, E.; Marcus, I. C.; Roqueta, J.; Alonso, M. I. *Nanotechnology* **2011,** *22,* 295304. doi:10.1088/0957-4484/22/29/295304
9. Tokarev, V. N.; Khomich, V. Yu.; Shmakov, V. A.; Yamshchikov, V. A. *Dokl. Phys.* **2008,** *53,* 206–210. doi:10.1134/S1028335808040083
10. Joya, Y. F.; Liu, Z. *Appl. Phys. A* **2011,** *102,* 91–97. doi:10.1007/s00339-010-6151-9
11. Trice, J.; Thomas, D.; Favazaa, C.; Sureshkumar, R.; Kalyanaraman, R. *Phys. Rev. B* **2007,** *75,* 235439. doi:10.1103/PhysRevB.75.235439
12. Krishma, H.; Favazza, C.; Gangopadhyay, A. K.; Kalyanaraman, R. *JOM* **2008,** *60,* 37–42. doi:10.1007/s11837-008-0115-y
13. Sivakov, V.; Petersen, C.; Daniel, C.; Shen, H.; Mücklich, F.; Mathur, S. *Appl. Surf. Sci.* **2005,** *247,* 513–517. doi:10.1016/j.apsusc.2005.01.088
14. Starbova, K.; Mankov, V.; Starbov, N.; Popov, D.; Nihtianova, D.; Kolev, K.; Laude, L. D. *Appl. Surf. Sci.* **2001,** *173,* 177–183. doi:10.1016/S0169-4332(00)00830-8
15. Kim, K.; Kim, S.; Lee, S. Y. *Curr. Appl. Phys.* **2012,** *12,* 585–588. doi:10.1016/j.cap.2011.09.006
16. Marin, D. V.; Volodin, V. A.; Gorotkhov, E. B.; Shcheglov, D. V.; Latyshev, A. V.; Vergnat, M.; Koch, J.; Chichkov, B. N. *Tech. Phys. Lett.* **2010,** *36,* 439–442. doi:10.1134/S1063785010050159
17. Bäuerle, D. *Laser Processing and Chemistry,* 3rd ed.; Springer: Berlin, Germany, 2000. doi:10.1007/978-3-662-04074-4
18. Teodorescu, V. S.; Ghica, C.; Maraloiu, A. V.; Lepadatu, A.-M.; Stavarache, I.; Ciurea, M. L.; Scarisoreanu, N. D.; Andrei, A. Nanoscale fast Ge diffusion in laser irradiated SiGe thin films. In *Proceedings Nanotech Conference & Expo,* Washington, DC, May 12–16, 2013; pp 109–112.
19. Sandu, C. S.; Teodorescu, V. S.; Ghica, C.; Hoffman, P.; Bret, T.; Brioude, A.; Blanchin, M. G.; Roger, J. A.; Canut, B.; Croitoru, M. *J. Sol-Gel Sci. Technol.* **2003,** *28,* 227–234. doi:10.1023/A:1026037301769
20. Craciun, V.; Singh, R. K.; Boyd, I. W. *J. Electron. Mater.* **2002,** *31,* 1325–1329. doi:10.1007/s11664-002-0116-5
21. Lim, G.; Kar, A. *Mater. Sci. Eng., B* **2011,** *176,* 660–668. doi:10.1016/j.mseb.2011.02.011
22. Garcia, B. J.; Martinez, J.; Piqueras, J.; Castaño, J. L.; Muñoz-Yagüe, A. *Appl. Phys. A* **1988,** *46,* 191–196. doi:10.1007/BF00939263
23. Stavarache, I.; Lepadatu, A.-M.; Teodorescu, V. S.; Galca, A. C.; Ciurea, M. L. *Appl. Surf. Sci.* **2014,** *309,* 168–174. doi:10.1016/j.apsusc.2014.04.212
24. Wagner, E. Selective light induced chemical vapour deposition of titanium dioxide thin films. Ph.D. Thesis, École polytechnique fédérale de Lausanne, Switzerland, 2002. doi:10.5075/epfl-thesis-2650
25. Guosheng, Z.; Fauchet, P. M.; Siegman, A. E. *Phys. Rev. B* **1982,** *26,* 5366–5381. doi:10.1103/PhysRevB.26.5366
26. Sipe, J. E.; Young, J. F.; Preston, J. S.; van Driel, H. M. *Phys. Rev. B* **1983,** *27,* 1141–1154. doi:10.1103/PhysRevB.27.1141
27. Barborica, A.; Mihailescu, I. N.; Teodorescu, V. S. *Phys. Rev. B* **1994,** *49,* 8385–8395. doi:10.1103/PhysRevB.49.8385
28. Tsibidis, G. D.; Barberoglou, M.; Loukakos, P. A.; Stratakis, E.; Fotakis, C. *Phys. Rev. B* **2012,** *86,* 115316. doi:10.1103/PhysRevB.86.115316
29. Tsibidis, G. D.; Stratakis, E.; Aifantis, K. E. *J. Appl. Phys.* **2012,** *111,* 053502. doi:10.1063/1.3688020
30. Langer, J. S. *Phys. Rev. E* **2008,** *77,* 021502. doi:10.1103/PhysRevE.77.021502
31. Van Overschelde, O.; Delsate, T.; Snyders, R. *J. Appl. Phys.* **2012,** *111,* 123108. doi:10.1063/1.4728159
32. Ojovan, M. I. *Adv. Condens. Matter Phys.* **2008,** No. 817829. doi:10.1155/2008/817829
33. Richet, P. *Phys. Chem. Miner.* **1990,** *17,* 79–88. doi:10.1007/BF00209228
34. Pauleau, Y.; Remy, J.-C. *J. Less-Common Met.* **1975,** *42,* 199–208. doi:10.1016/0022-5088(75)90005-3
35. Choi, W. K.; Ho, V.; Ng, V.; Ho, Y.; Ng, S. P.; Chim, W. K. *Appl. Phys. Lett.* **2005,** *86,* 143114. doi:10.1063/1.1891290

License and Terms

BEILSTEIN JOURNAL OF NANOTECHNOLOGY

Fabrication of high-resolution nanostructures of complex geometry by the single-spot nanolithography method

Alexander Samardak*, Margarita Anisimova, Aleksei Samardak and Alexey Ognev

Full Research Paper

Address:
Laboratory of Thin Film Technologies, School of Natural Sciences,
Far Eastern Federal University, 8 Sukhanova St., Vladivostok 690950,
Russia

Email:
Alexander Samardak* - samardak.as@dvfu.ru

* Corresponding author

Keywords:
electron-beam lithography; exposure dose; high-resolution lithography; nanomagnets; nanostructure; overexposure; PMMA; polymer; resist carbonization

Beilstein J. Nanotechnol. **2015,** *6,* 976–986.
doi:10.3762/bjnano.6.101

Received: 17 September 2014
Accepted: 25 March 2015
Published: 17 April 2015

This article is part of the Thematic Series "Self-assembly of nanostructures and nanomaterials".

Guest Editor: I. Berbezier

Abstract

The paper presents a method for the high-resolution production of polymer nanopatterns with controllable geometrical parameters by means of a single-spot electron-beam lithography technique. The essence of the method entails the overexposure of a positive-tone resist, spin-coated onto a substrate where nanoscale spots are exposed to an electron beam with a dose greater than 0.1 pC per dot. A single-spot enables the fabrication of a nanoring, while a chain of spots placed at distance of 5–30 nm from each other allows the production of a polymer pattern of complex geometry of sub-10 nm resolution. We demonstrate that in addition to the naturally oxidized silicon substrates, gold-coated substrates can also successfully be used for the single-spot nanopattering technique. An explanation of the results related to the resist overexposure was demonstrated using Monte Carlo simulations. Our nanofabrication method significantly accelerates (up to 10 times) the fabrication rate as compared to conventional lithography on positive-tone resist. This technique can be potentially employed in the electronics industry for the production of nanoprinted lithography molds, etching masks, nanoelectronics, nanophotonics, NEMS and MEMS devices.

Introduction

The continuous growth of the nanotechnology and microelectronic industries requires the development of new approaches and methods for the formation of nanoscale structures of desired geometry with a spatial resolution of less than 100 nm. One of the most advanced and in-demand technologies is mask-free or direct-write lithography based on the interaction of an electron beam with a polymer resist [1].

Under normal conditions, electron-beam lithography (EBL) enables the production of polymer patterns with an ≈20–30 nm spatial resolution (e.g., line width or dot diameter) of smallest elements [2]. Under certain conditions (exposure at an acceleration voltage >50 kV, development at low temperatures, using a dose correction mechanism, etc.), a resolution of 5 nm for single lines and dots can be achieved [3-5]. Since this is the absolute best-case resolution, it is almost impossible to obtain, for example, rectangular or triangular nanoobjects with sharp edges and low roughness. For drawing arrays consisting of more than 10,000 nanoscale elements, the time required for a template pattering can be estimated to be on the order of hours or even tens of hours. Often, during such a long exposure, a pattern generator will produce an error due to a buffer overflow because of the large data exchange. Moreover, the main drawback of EBL is the exposure speed (usually 10^7 pixels per second) [6] and the expense involved in the mass production process. One possible solution to these mentioned issues is to use the dual-tone property of polymer resists, which depends on the exposure dose and enables the fast and inexpensive fabrication of high-resolution nanopatterns of complex shape.

The effect of high-dose electron irradiation on the chemical properties of polymers (resulting in hardening or overexposure) was observed in different types of positive resists: DQN [7], AZ-PF514 [8], and PMMA [9,10]. Poly(methyl methacrylate) (PMMA) is the most prevalent EBL resist employed due to its high-resolution capability, good lift-off performance, stability, excellent adhesion to substrates and compatibility with the other processing steps. PMMA consists of long polymer chains that are broken into smaller, more soluble fragments by scission with the electron beam. Depending on the exposure dose, PMMA can act as a positive or negative resist [9,10]. PMMA's dual-tone resist capability opens up a simple and inexpensive route to produce a range of polymer nanostructures using direct overexposure of the electron beam [11-15].

In this paper we report on the low acceleration voltage (<30 kV) fabrication of polymer nanopatterns of different geometry consisting of both the individual elements and arrays of nanostructures with sub-20 nm resolution on semiconductor and metallic surfaces.

Results and Discussion

Single-spot pattering of polymeric micro- and nano-rings on silicon substrates

In the first experiments, the naturally oxidized, monocrystalline silicon substrates were spin-coated with PMMA 950k A2 positive-tone resist to a thickness of 150 nm. The acceleration voltage of the electron beam was 10 kV. The magnitude of the acceleration voltage determines the energy of the electron beam, and hence the penetration depth into the resist and substrate. The exposure dose refers to the number of inserted electrons in the primary electron beam. In the beginning, it was empirically found that at single spot doses less than 0.2 pC, the PMMA resist behaves as positive-tone resist. The high solubility of the positive-tone resist in the exposed areas was observed after development in a 1:3 4-methyl-2-pentanone (MIBK)/IPA solution for 30 s under normal conditions. Soaking the resist in acetone for 30 s leads to the complete removal of any remaining resist. At single-spot doses in the range 0.2–100 pC, the exposed and developed samples showed the dual-tone resist behavior.

As seen in Figure 1a, the pattern prepared with a single electron-beam spot is ring-shaped: the resist remains in the center surrounded by a clean substrate area. The main reason for the formation of the ring is the overexposure of the resist at the irradiation point followed by its carbonization [11,13]. Thus, the overexposed, positive resist acts as a negative resist. The distribution of electrons in a resist due to forward and back scattering is Gaussian in nature. This means that only the central part of the exposed area receives a dose with a value above the threshold for the carbonization process. This fact is confirmed by the high chemical resistance of the ring core to developer and solvents such as acetone and EBR remover. The surrounding resist receives a significantly lower dose and remains as a positive-tone resist that can be easily removed with developer

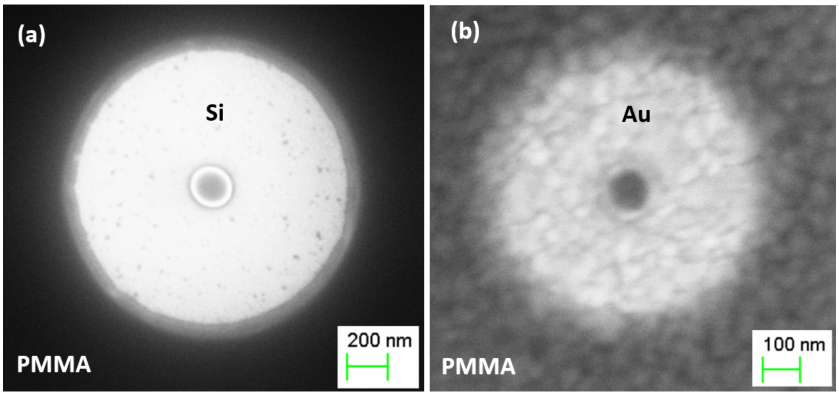

Figure 1: SEM images demonstrating the effect of substrate on the single-spot overexposure of a ring at a dose of 1 pC on 150 nm thick PMMA at an acceleration voltage of 10 kV: (a) single-crystal Si substrate; (b) Si substrate coated with a 200 nm Au film. Note the difference in scale between the two images.

or acetone. As discussed below, the diameter of the core and the outer ring size depend not only on the exposure dose, but also on the thickness of the resist, acceleration voltage of the electron beam, and the atomic number, roughness and crystal structure of substrate materials.

The substrate material has an important role in the formation of polymer patterns. Carbonized ring cores, formed on Si and Au surfaces (Figure 1a,b), have the same round shape, while the diameter and the quality of core and outer edges vary significantly. In the case of a monocrystalline Si substrate, the ring has a sharp edge with a small resist undercut (Figure 1a). As seen in Figure 1b, exposure of the resist on the polycrystalline Au film leads to a deep undercut and rough edges after development.

The physics behind the single-spot overexposure and development process is schematically illustrated in Figure 2. The main impact area of the incident electron beam falls on the small central area, followed by the forward scattering of electrons in resist, which makes the beam diameter larger and leads to resist overexposure at high doses. The surrounding area of the resist is exposed due to backscattered and secondary electrons after large angle collisions in a substrate. These scattered electrons re-emerge into the resist at some distance from the point at which they left it. Forward and backscattered electrons have a distinct energy density distribution in the substrate [13], which defines the pattern profile after development.

Since elastic collisions of primary electrons in a substrate depend on the atomic number, *Z*, of the substrate material, the distribution of backscattered electrons in a Au film ($Z = 79$) will be significantly different than in Si ($Z = 14$) (Figure 3). As

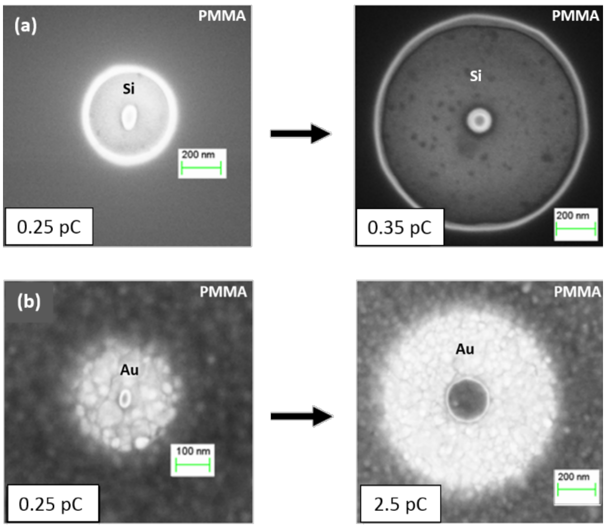

Figure 3: Effect of the exposure dose and substrate material on the single-spot pattern formation: (a) the ring prepared on a single-crystal Si substrate at a dose of 0.25 pC (left) and 0.35 pC (right); (b) the ring patterned on a polycrystalline Au film at a dose of 0.25 pC (left) and 2.5 pC (right).

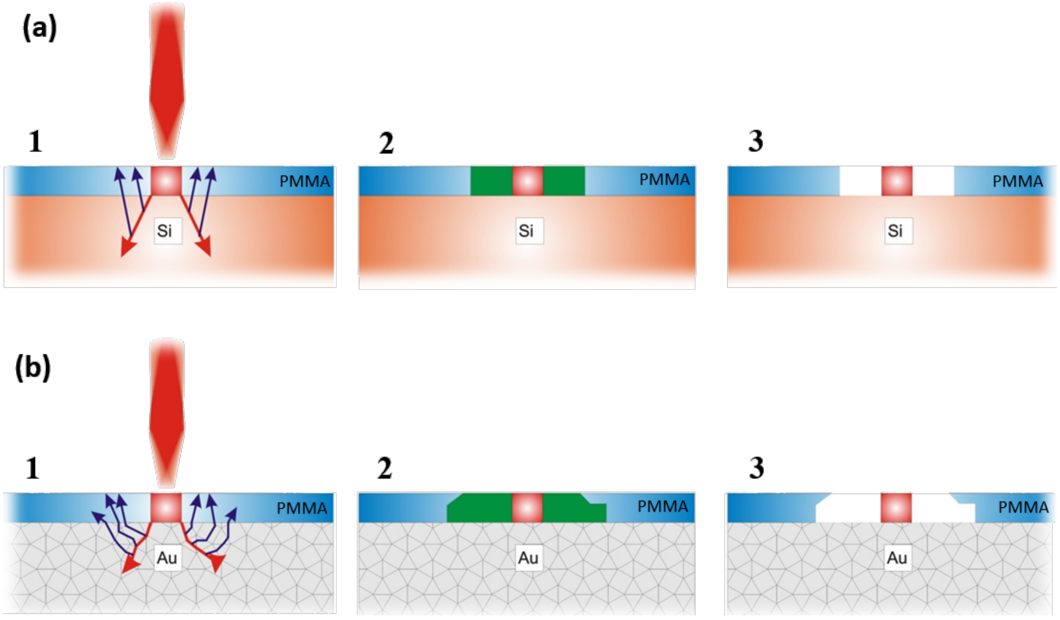

Figure 2: Single-spot overexposure of a ring dependening on the substrate type: (a) a single-crystal Si substrate and (b) a Si substrate coated with a 200 nm Au film. 1: an interaction of forward- and back-scattered electrons with positive resist; the overexposed area shown in red. 2: a normal exposure of resist areas highlighted in green. 3: the expected pattern profile after development.

shown in [16], the backscattering coefficient, which defines a fraction of primary electrons that are backscattered in a substrate, varies significantly with Z. As Si is lighter than Au, the maximum of the backscattered electron emission is very broad and corresponds to the normalized energy, $W = E/E_0 = 0.5$, where E and E_0 are the energy of backscattered and primary electrons, respectively. For Au, $W = 0.95–0.98$. As a result, in the case of the Au substrate, the rings have a much smaller outer diameter compared to the Si substrate (Figure 3). Even at a dose of 2.5 pC, the ring on the Au substrate is still smaller than that patterned onto the Si substrate at a dose 0.35 pC.

Our experimental findings are supported by Monte Carlo simulations performed with NanoPECS software [17]. In the case of the Si substrate, most of the electrons penetrate the resist via forward scattering at small angles, which broadens the primary beam size (Figure 4a). The energy distribution of electrons in Figure 4b shows that the central part of the resist is overexposed. Afterwards, the electrons enter into the Si substrate, where they collide with the nuclei of the atoms. If an electron has kinetic energy above the interaction treshold, three random scenarios are possible: small-angle forward scattering, wide-angle back scattering or secondary electron emission. Backscattered electrons are the main cause of the subsequent exposure of resist areas a few hundred nanometers away from the incident beam point (Figure 4a,b).

For the Au substrate (Figure 4c,d), significant wide-angle scattering occurs near the surface for a smaller interaction volume because of the heavy Au nucleus. Hence, a large fraction of

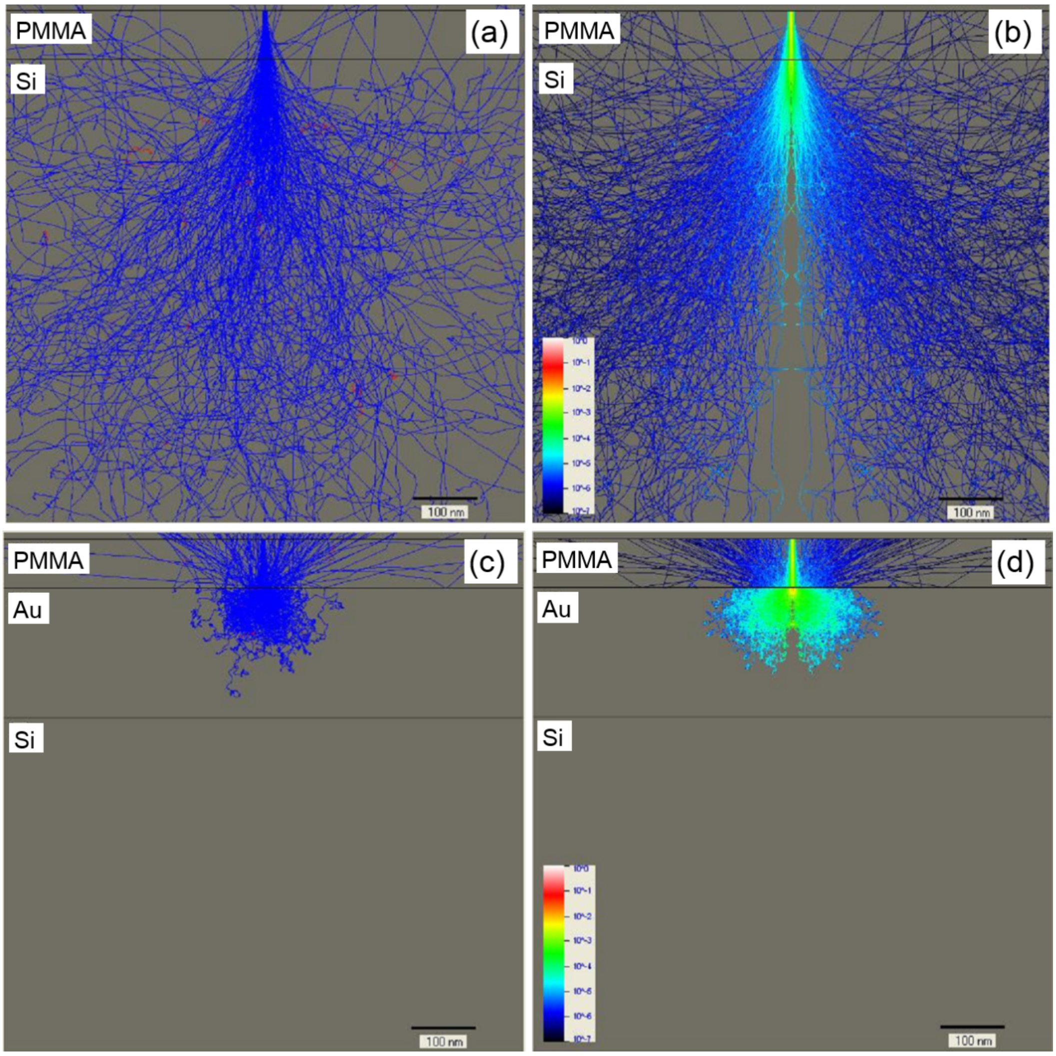

Figure 4: (a,c) Monte Carlo simulation of 250 electron scattering trajectories at 10 keV incident energy in a 75 nm thick PMMA layer on bulk Si and on 200 nm Au-coated substrates, respectively. (b,d) Electron energy distribution at 10 keV incident energy in a 75 nm thick PMMA layer on bulk Si and 200 nm Au-coated substrates, respectively. Trajectories that leave the sample represent backscattered electrons.

incident electrons are backscattered to the resist not far away from the point where they penetrate into the Au film. As result, the outer edge of a ring patterned on a Au film has a smaller diameter than that on a Si substrate and becomes blurred. In contrast, for a single-crystal Si substrate, the electron scattering occurs with less variation (Figure 4a,b), which increases the sharpness of the core and outer edge (Figure 3).

The spatial structure and profile of a ring measured by atomic force microscopy are shown in Figure 5. As seen in Figure 5c, after development, the height of the central pillar of the ring was reduced relative to the surrounding resist. It exhibits the characteristic centered peak, indicating the place where the incident electron beam interacted with resist. One explanation for this reduced height effect is the gradual dissipation of primary electrons that penetrate the resist. The single spot with Gaussian shape matching the electron beam diameter has the size of 2 nm on the resist surface. As it passes through the PMMA layer, the electron beam becomes broader because of the forward scattering arising from electron–electron interactions, and it carbonizes more resist volume being closer to the substrate. Thus, a trajectory distribution of electrons produced by Monte Carlo simulations shows that the upper third part of the pillar is very narrow and can be easily removed by developer (Figure 4).

Figure 6 shows the experimental dependence of the outer diameter d_{out} and the core diameter d_{in} on the radiation dose for silicon and gold-coated substrates with respect to resist thickness. Increasing the dose leads to an increase in both diameters. Thus, rings with much larger diameters can be patterned on the silicon substrate at a lower dose. As Au is a material with a much higher Z as compared to Si, the elastic scattering of the electrons in the Au substrate plays a key role. It leads to a large decrease of the interaction value, causing much smaller d_{out} and d_{in} values for the rings patterned using the same parameters on a Si substrate [16]. Moreover, it was experimentally found that the thickness of the resist also significantly contributes to the formation of the nanostructures. Thus, with increasing resist thickness, the values of d_{out} and d_{in} increase for both substrates. Primarily, this is caused by the increased broadening of the incident beam due to inelastic forward scattering of primary electrons in thicker resists, leading to a larger interaction volume in the substrate below. As shown in Figure 6b, the ring core begins to appear in the thinnest of the resists at a dose of 0.2 pC for

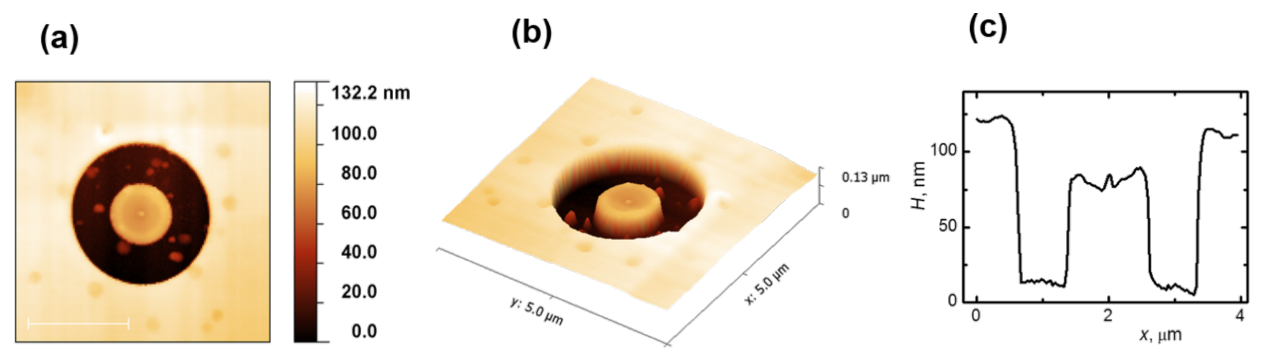

Figure 5: AFM images of the ring, patterned on the silicon substrate coated by a 120 nm thick PMMA A2 resist: (a) top view; (b) 3D view; (c) ring profile.

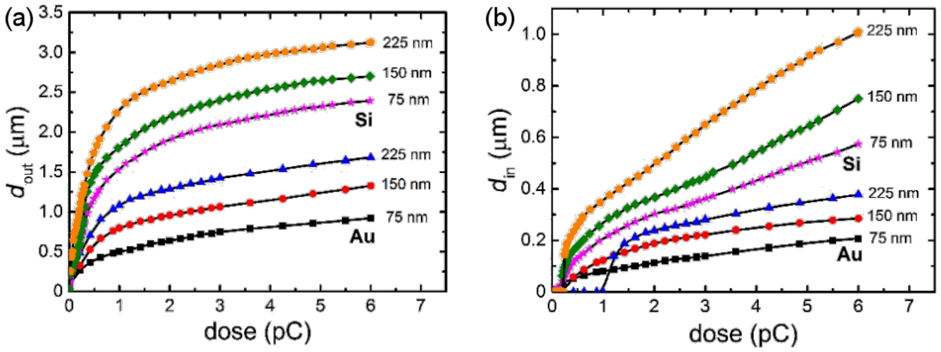

Figure 6: Dependence of d_{out} (a) and d_{in} (b) on the exposure dose at an acceleration voltage of 10 kV for different thicknesses of PMMA (from 75 to 225 nm) for Si and Au substrates.

both Si and Au substrates. For the thickest of the resists, this occurs at doses of 0.25 and 1.2 pC for Si and Au substrates, respectively.

As seen in Figure 6, the use of a polycrystalline conductive substrate, such as bulk Si coated with a thin Au film, gives the advantage of fabrication of rings with an outer diameter of less than 1 µm due to the saturation effect caused by a partial absorption of electrons in the metal film. However, for a single-crystal semiconductor substrate, such as Si, patterned rings of high resolution covering a wide range of possible diameters is feasible. The intentional change in the film thickness and crystallinity (grain size, lattice type) of the metal substrate enables the reflection and absorption of electrons to be manipulated and can be used for precise tuning of the parameters of the pattern.

Patterning of complex nanostructures of various geometries

For the fabrication of polymer nanostructure patterns of complex geometry, the Si substrate was spin-coated with a PMMA A2 resist. Before exposure, a special digital nanostructure pattern was prepared. Such a pattern consisted of a number of single spots with designated doses of 0.1 pC or higher. The dose 0.1 pC corresponds to the single-line dose of 10^5 µC/cm, which is 100 times higher than the positive-tone regime in conventional lithography. The spots were arranged in the form of the desired nanostructure. It was experimentally discovered that the distance between neighboring spots, d_s, must be ≤30 nm. At these values the carbonized cores coalesce during overexposure. After development, the surrounding area, which still behaves as a positive resist, is removed and the remaining carbonized resist forms a nanostructure in accordance with the digital pattern (Figure 7). In the case of the Si substrate, the smaller the d_s, the higher the resolution, as demonstrated in Figure 7a–c. For the Au-coated substrate, larger distances up to d_s = 30 nm lead to higher resolution, as shown in Figure 7e–g. Since the electron beam diameter is approximately 2 nm, there is no advantage in designing a d_s less than 4 nm. For d_s > 30 nm, the links between overexposed areas are broken, leading to formation of separated islands of carbonized resist for both substrates (Figure 7d,h).

A few examples of nanostructures with a line width ranging from 10–30 nm patterned on Si and Au-coated substrates are shown in Figure 8. Patterns having the same resolution can be produced on monocrystalline Si and polycrystalline Au substrates, but at different values of d_s. In the case of the Au substrate, d_s is three times larger than for Si. This enables a much faster fabrication of nanopatterns of the same dimension and quality on polycrystalline conductive substrates. The main reason for the highest resolution at d_s = 30 nm on the Au substrate is that the electron backscattering coefficient for bulk Au is about three times larger than for bulk Si at an acceleration voltage of 10 kV [18].

The electron beam energy plays a very important role in the fabrication process because of its strong effect on the electron penetration depth and the number of inelastic collisions occurring in the resist. On the one hand, with an increase of the electron energy, the penetration depth increases, giving a narrow energy density distribution of primary electrons in the resist. On the other hand, at higher voltages, the number of polymer chain scissions per electron decreases. In Figure 9 the effect of the acceleration voltage on a nanopattern is represented. As seen in

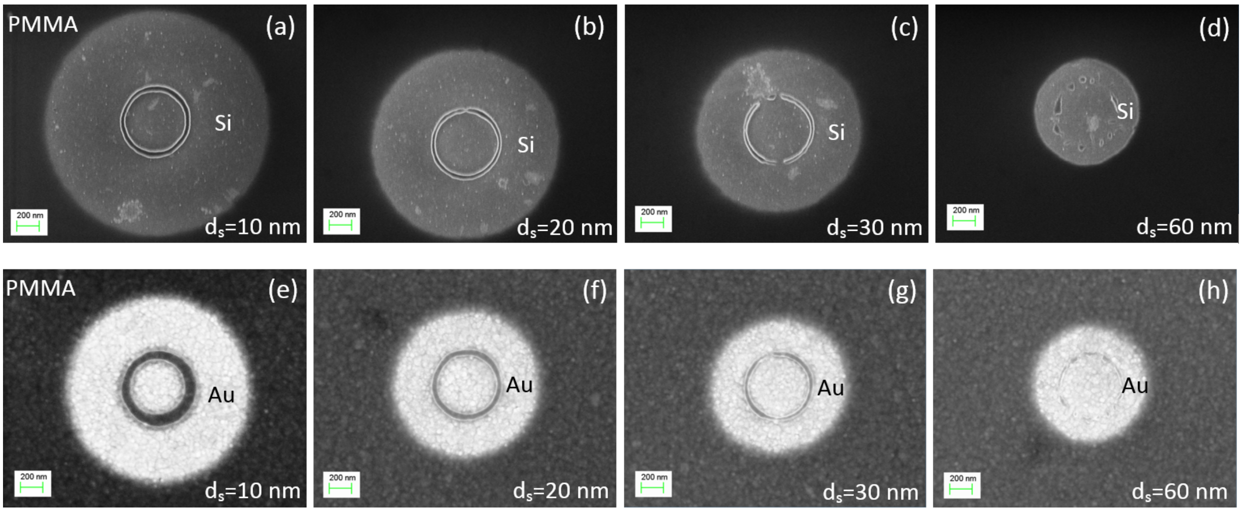

Figure 7: SEM images demonstrating the effect of changing the d_s between the electron beam spots with a dose of 0.1 pC on the formation of circles on Si (a–d) and Au (e–h) substrates coated with PMMA of 75 nm thickness at an acceleration voltage of 10 kV.

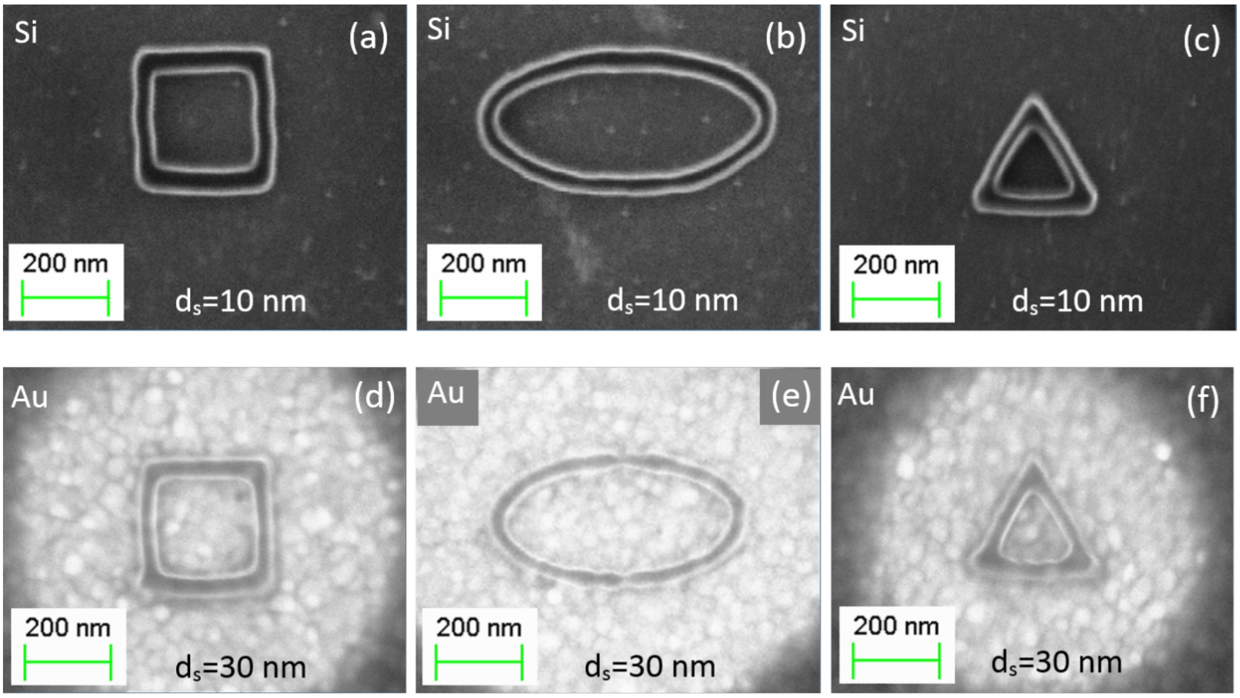

Figure 8: Polymer nanostructures fabricated on a PMMA A2 resist of 75 nm thickness at an acceleration voltage of 10 kV and exposure dose of 0.1 pC with d_s = 10 nm and 30 nm for Si (a–c) and Au (d–f) substrates, respectively. Patterned (a,d) square, (b,e) oval, and (c,f) triangle shapes possible using the methods described herein.

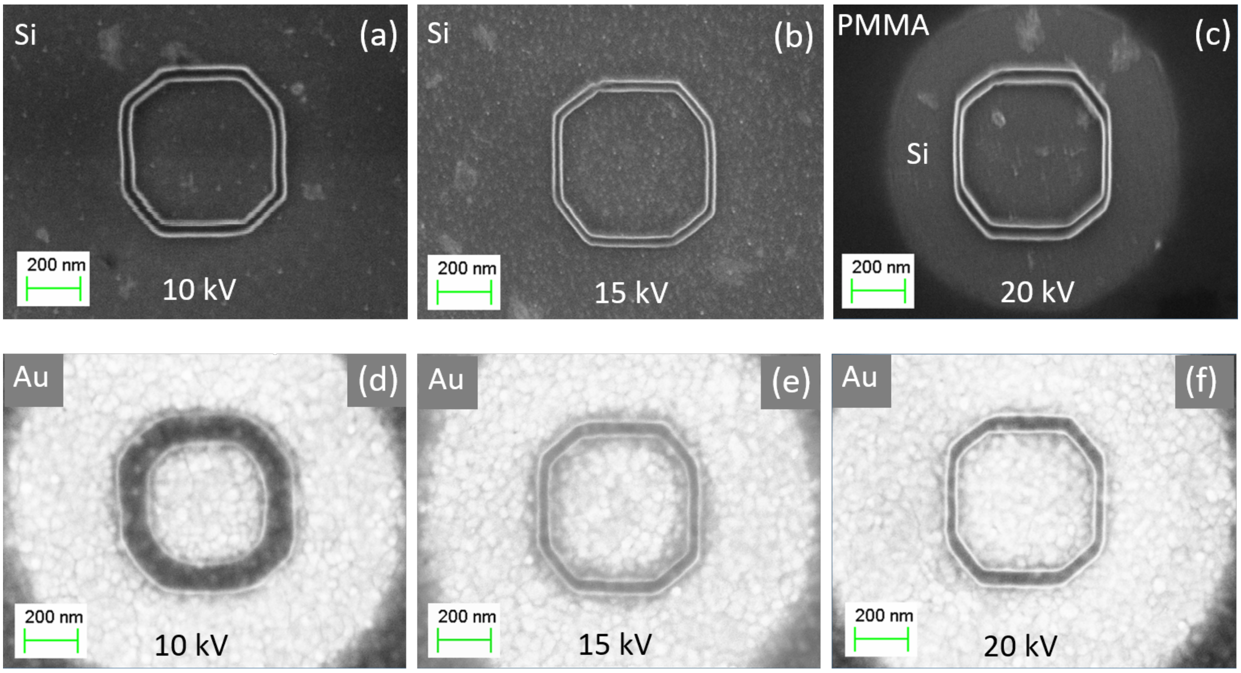

Figure 9: Effect of the acceleration voltage on the formation of polygons on Si (a–c) and Au (d–f) substrates coated with PMMA of 75 nm thickness and d_s = 10 nm.

Figure 9a–c for a Si substrate, an increase in the acceleration voltage from 10 to 20 kV does not significantly change the resolution of the polygon. However, for the Au-coated substrate a completely different situation is observed (Figure 9d–f): with the increase of the acceleration voltage, the resolution/resist contrast is drastically improved.

The dependence of the spot lithography resolution for a 75 nm thick PMMA layer on the acceleration voltage in the range of 10–20 kV can be illustrated with results from Monte Carlo simulations, as presented in Figure 4 and Figure 10. There are no significant differences in the energy distribution of electrons penetrating the resist for the Si substrate (Figure 4b and Figure 10a,b). However, for the Au substrate (in the case of a 10 kV acceleration voltage), the large angle backscattered and secondary electrons strongly contribute to the overexposure of the central pillar (Figure 4d). With an increase in the acceleration voltage, this effect diminishes due to the increase in the fraction of small angle backscattered electrons that expose the resist away from the central pillar (Figure 10c,d).

Figure 11 provides three dimensional images of rings with round and square shapes made of carbonized resist. As can be seen, the nanostructures have flat outer and inner lateral sides with a thickness of about 20 nm, demonstrating the high resolution and spatial quality possible with this technique.

An example of the proximity effect is shown in Figure 12. If the nanostructures are close enough to one another, then surrounding areas, which behave as a positive-tone resist, are affected too. The black and grey contrast corresponds to PMMA and Si, respectively.

As has been shown above, the low energy single-spot electron-beam lithography method overcomes the disadvantages of conventional lithography on positive-tone resist. This method enables the formation of complex polymer nanostructures of any shape with a minimum line width of 10 nm not only on semiconductor substrates, but also on conductive surfaces such

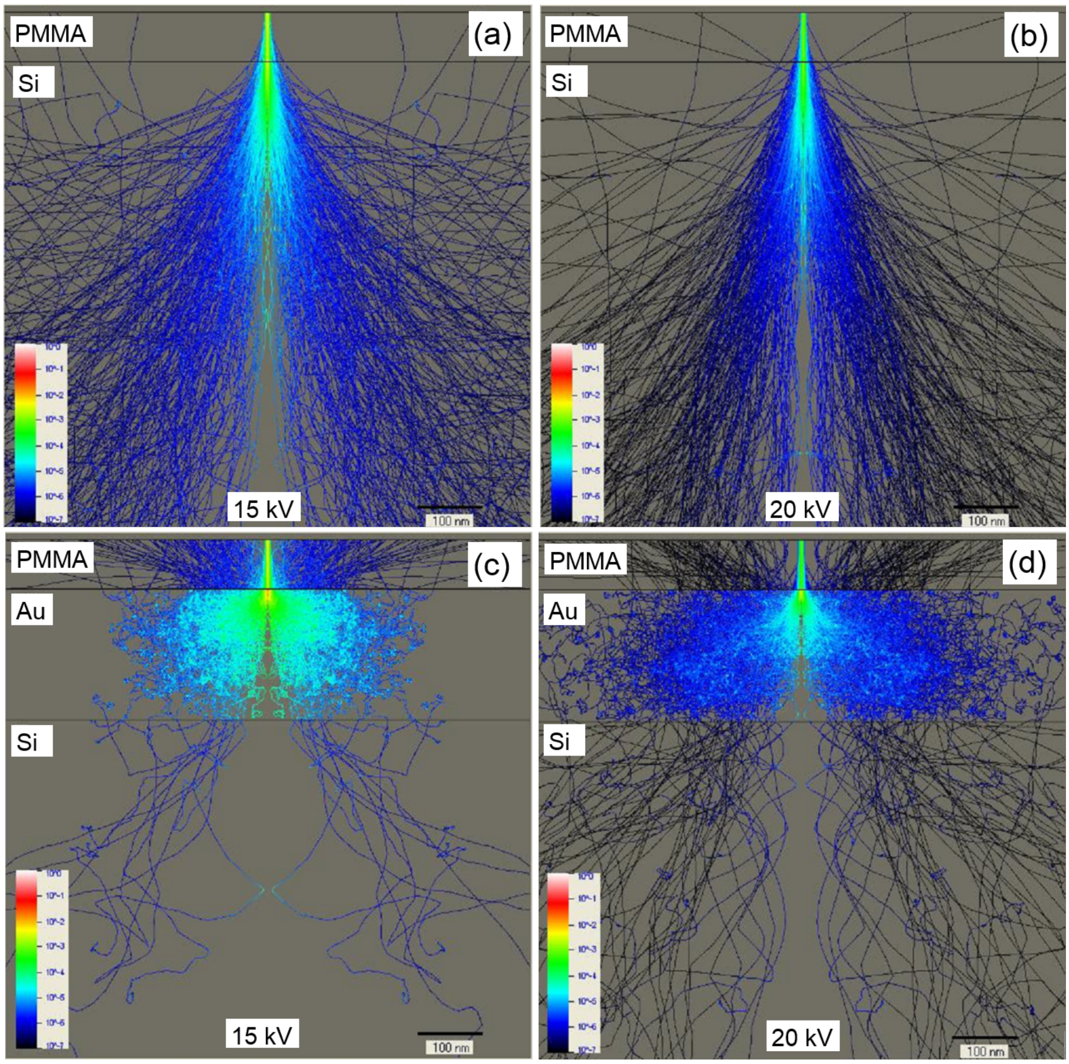

Figure 10: (a,b) Electron energy distribution in a 75 nm thick PMMA layer on a bulk Si substrate at 15 and 20 kV incident energies, respectively. (c, d) Energy distribution in a 75 nm thick PMMA layer on a Si substrate coated with a 200 nm Au film at 15 and 20 kV incident energies, respectively.

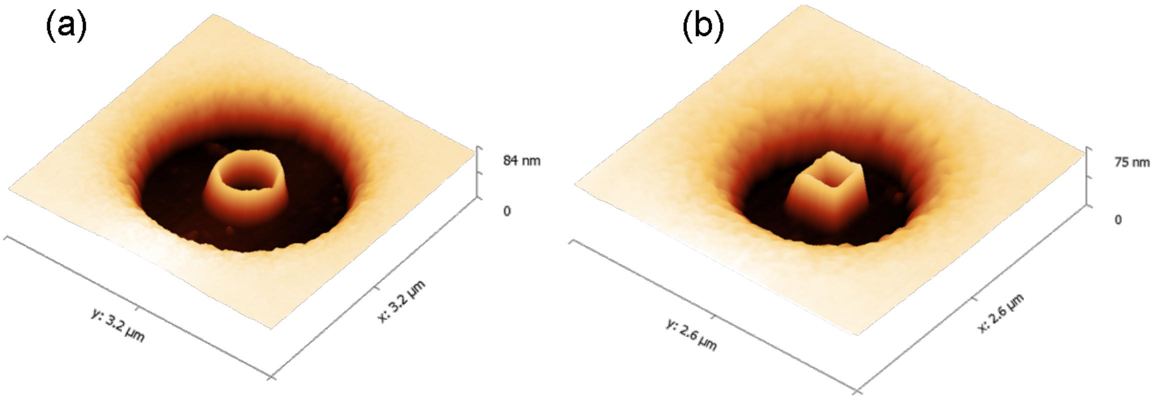

Figure 11: 3D AFM images of polymer nanostructures fabricated on PMMA A2 resist with thickness of 75 nm on Si substrates at an acceleration voltage of 10 kV, exposure dose of 0.1 pC and d_s = 10 nm: (a) circular ring with a line width of 20 nm; (b) square ring with a line width of 22 nm.

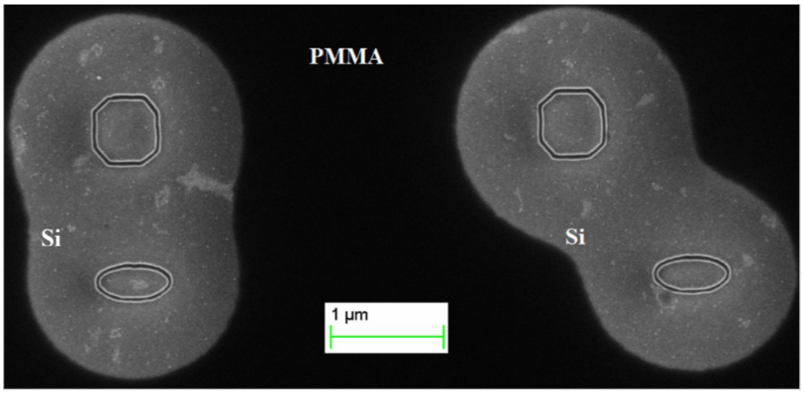

Figure 12: Demonstration of the proximity effect using nanostructures fabricated on a PMMA A2 resist with a thickness of 75 nm at a cathode acceleration voltage of 10 kV, exposure dose of 0.1 pC and d_s = 10 nm.

as a Au thin film. A similar sub-20 nm resolution is possibly using state-of-the-art, high-energy e-beam lithography systems with a beam acceleration of 50–100 kV on positive and negative resists [19]. In the single-spot nanolithography, there are no limitations in the use of thin metal films such as Au, Pt, Al, Cu, Ti or Cr. The minimum line width, given an electron beam diameter of 2 nm, is limited only by the length of the polymer chain (≈5 nm) and the thickness of the resist. We have empirically found that the thinner the resist, the higher the resolution of the single-spot lithography.

Another advantage is that the lines of patterned nanostructures are substantially defect-free, as shown in Figure 13. Our method enables the production of high-quality carbonized patterns of sub-20 nm resolution using the positive resist only. The transfer of patterns onto the substrates using wet chemical or plasma etching is possible due to the high chemical and mechanical resistance of the carbonized templates.

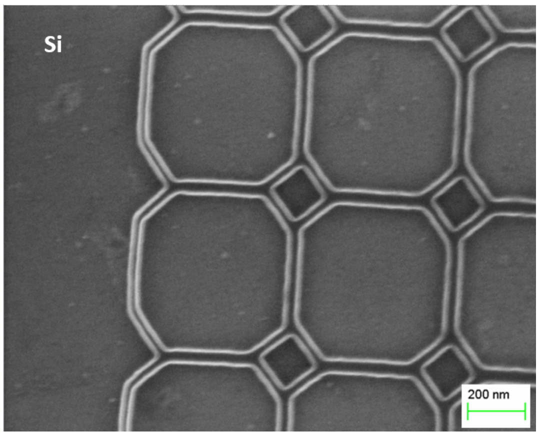

Figure 13: An example of a complex polymer pattern with a minimum line width of 15 nm fabricated at an acceleration voltage of 10 kV, exposure dose of 0.1 pC and d_s = 10 nm.

An example of a practical application of the single-spot lithography method is shown in Figure 14. The patterned polymer nanostructures were sputtered with a magnetron in vacuum with a 20 nm-thick cobalt film. This resulted in 3D magnetic nanostructures with unusual spin configurations that potentially can be used in magnetic sensing technologies, memory, logic and biomedical applications [20]. Moreover, the single-spot nanolithography method is very promising for fabrication of high-quality, artificial, spin-ice lattices [21,22], magnonic [23] and photonic [24] crystals on large scale.

An important additional advantage of the proposed method is the fast patterning of a template as compared with the exposure time required for the reversed pattern on positive resist using conventional lithography techniques, where a sequential scan of the selected area is required. To fabricate a template in the form of an array of 25 × 25 (625 elements in total) equilateral triangles with a length of 210 nm and a line width of 40 nm, only 17.6 s are required. In contrast, the exposure of the same pattern using conventional lithography techniques on a positive resist requires 152 s, that is 8.6 times longer, but with reduced resolution.

Conclusion

The fast and simple fabrication of polymer nanopatterns of various geometries with sub-10 nm resolution on semiconductor and metallized substrates using the single-spot nanofabrication was demonstrated at low-energy acceleration voltages. The resulting nanostructures have sharp edges and defect-free lines. Arrays of nanoelements or complex nanostructures can be easily scaled to large areas, with the distinct advantage of a reduced exposure time of up to ten times as compared to the conventional electron-beam lithography process on positive resist. The single-spot electron-beam lithography method enables the overexposure of selected areas of a positive resist with a dose higher then 0.1 pC and a distance between the spots of less than 30 nm. The resulting nanostructures are patterned in accordance with a digital pattern to produce the desired carbonized nanostructures. The high acid and plasma resistance as well as the presumably high mechanical durability of the carbonized nanostructures make them very attractive for the fabrication of hard nanoimprint lithography molds and etching masks, as well as for nanoelectronic and nanophotonic applications, MEMS and NEMS devices.

Experimental

Sample preparation

All the preparation procedures were conducted in a class 10,000 clean room. The PMMA A2 resist (MicroChem Corp., 950 K, 2 wt % in anisole) was spin-coated at different rates in range from 1000–4000 rpm for 1 min in order to produce the desired thickness on standard-cleaned undoped Si(111) substrates without and with a Au thin film of 200 nm thickness. The Au thin film was deposited by thermal evaporation of pure gold (99.99 atom %) from a Mo crucible at a base pressure of 10^{-5} Torr. The samples were baked on a hot plate at 180 °C for 90 s in order to harden the resist, to remove the residual solvent, and to raise the adhesion between PMMA and the substrate surface. Immediately after baking, the samples were exposed in E-Line EBL system (Raith, Germany). The spot size, cathode acceleration voltage, beam current and aperture size were 2 nm, 10 kV, 0.072 nA and 30 µm, respectively. Some experiments were performed at an acceleration voltage of 15 and 20 kV. The vacuum pressure in the work chamber was 1.5×10^{-6} Torr. Prior to exposure, a digital pattern of the desired nanostructures was prepared based on the single-spot overexposure. The samples were developed with 1:3 MIBK/IPA at 20 °C for 45 s, then rinsed in pure IPA and distilled water for 10 s, and finally dried with nitrogen gas.

Characterization

The thickness and surface morphology of the PMMA and Au films were measured with an Ntegra Aura (NT-MDT, Russia) atomic force microscope. The evolution of the resist before and after development was studied with a Supra (Carl Zeiss, Germany) scanning electron microscope at an acceleration voltage of 10 kV. Monte Carlo simulations were performed with the NanoPECS software package.

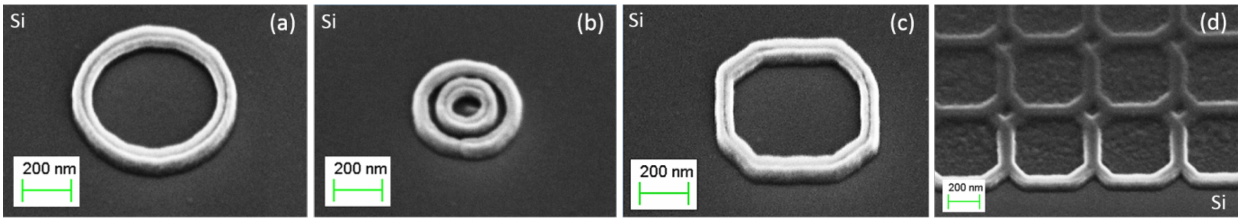

Figure 14: SEM images of Co nanostructures formed on the pre-patterned Si substrate: (a) circle, (b) double circle, (c) polygon, (d) complex polymer pattern shown in Figure 13.

Acknowledgements

The authors acknowledge the support of the Russian Ministry of Education and Science under the state task 559 and Far Eastern Federal University. A.S. thanks Dr Maksim Stebliy for the magnetron sputtering of the magnetic film over PMMA patterns.

References

1. Biswas, A.; Bayer, I. S.; Biris, A. S.; Wang, T.; Dervishi, E.; Faupel, F. *Adv. Colloid Interface Sci.* **2012,** *170,* 2–27. doi:10.1016/j.cis.2011.11.001
2. Grigorescu, A. E.; Hagen, C. W. *Nanotechnology* **2009,** *20,* 292001–292032. doi:10.1088/0957-4484/20/29/292001
3. Küpper, D.; Küpper, D.; Wahlbrink, T.; Bolten, J.; Lemme, M. C.; Georgiev, Y. M.; Kurz, H. *J. Vac. Sci. Technol., B* **2006,** *24,* 1827–1832. doi:10.1116/1.2214709
4. Yasin, S.; Hasko, D. G.; Ahmed, H. *Appl. Phys. Lett.* **2001,** *78,* 2760–2762. doi:10.1063/1.1369615
5. Arjmandi, N.; Lagae, L.; Borghs, G. *J. Vac. Sci. Technol., B* **2009,** *27,* 1915–1918. doi:10.1116/1.3167367
6. Broers, A. N. *Philos. Trans. R. Soc., A* **1995,** *353,* 291–311. doi:10.1098/rsta.1995.0101
7. Livesay, W. R.; Rubiales, A. L.; Ross, M. F.; Woods, S. C.; Campbell, S. Electron beam hardening of photo resist. In *Proc. SPIE 1925,* Advances in Resist Technology and Processing X, San Diego, CA, USA, Feb 28, 1993; Hinsberg, W. D., Ed.; SPIE: Bellingham, WA, USA, 1993; pp 426–430. doi:10.1117/12.154778
8. de Koning, H.; Zandbergen, P.; Verheijen, M. J.; Biermann, U. K. P. *Microelectron. Eng.* **1995,** *27,* 421–424. doi:10.1016/0167-9317(94)00138-K
9. Zailer, I.; Frost, J. E. F.; Chabasseur-Molyneux, V.; Ford, C. J. B.; Pepper, M. *Semicond. Sci. Technol.* **1996,** *11,* 1235–1238. doi:10.1088/0268-1242/11/8/021
10. Hoole, A. C. F.; Welland, M. E.; Broers, A. N. *Semicond. Sci. Technol.* **1997,** *12,* 1166–1171. doi:10.1088/0268-1242/12/9/017
11. Duan, H.; Zhao, J.; Zhang, Y.; Xie, E.; Han, L. *Nanotechnology* **2009,** *20,* 135306–135314. doi:10.1088/0957-4484/20/13/135306
12. Duan, H.; Winston, D.; Yang, J. K. W.; Cord, B. M.; Manfrinato, V. R.; Berggren, K. K. *J. Vac. Sci. Technol., B* **2010,** *28,* C6C58. doi:10.1116/1.3501353
13. Gautsch, S.; Studer, M.; de Rooij, N. F. *Microelectron. Eng.* **2010,** *87,* 1139–1142. doi:10.1016/j.mee.2009.10.046
14. Gautsch, S.; de Rooij, N. F. *Microelectron. Eng.* **2011,** *88,* 2533–2536. doi:10.1016/j.mee.2011.02.012
15. Adeyenuwo, A. P.; Stepanova, M.; Dew, S. K. *J. Vac. Sci. Technol., B* **2011,** *29,* 06F312. doi:10.1116/1.3657512
16. Goldstein, J.; Newbury, D. E.; Joy, D. C.; Lyman, C. E.; Echlin, P.; Lifshin, E.; Sawyer, L. C.; Michael, J. R. *Scanning Electron Microscopy and X-Ray Microanalysis,* 3rd ed.; Springer: New York, NY, USA, 2003. doi:10.1007/978-1-4615-0215-9
17. Robin, F. Electron-Beam Lithography Applications at ETH Zurich, Raith application note. Raith GmbH, 2006, 1–4.
18. Dapor, M. *Phys. Rev. B* **1992,** *46,* 618–625. doi:10.1103/PhysRevB.46.618
19. Wu, C. S.; Makiuchi, Y.; Chen, C. D. High-energy Electron Beam Lithography for Nanoscale Fabrication. In *Lithography;* Wang, M., Ed.; InTech Europe: Rijeka, Croatia, 2010; pp 41–266. doi:10.5772/8179
20. Shukla, S.; Deheri, P. K.; Ramanujan, R. V. Magnetic Nanostructures: Synthesis, Properties, and Applications. In *Springer Handbook of Nanomaterials;* Vajtai, R., Ed.; Springer: Berlin, Germany, 2013; pp 473–514. doi:10.1007/978-3-642-20595-8_12
21. Phatak, C.; Petford-Long, A. K.; Heinonen, O.; Tanase, M.; De Graef, M. *Phys. Rev. B* **2011,** *83,* 174431–174435. doi:10.1103/PhysRevB.83.174431
22. Hügli, R. V.; Duff, G.; O'Conchuir, B.; Mengotti, E.; Fraile Rodríguez, A.; Nolting, F.; Heyderman, L. J.; Braun, H. B. *Philos. Trans. R. Soc., A* **2012,** *370,* 5767–5782. doi:10.1098/rsta.2011.0538
23. Kruglyak, V. V.; Demokritov, S. O.; Grundler, D. *J. Phys. D: Appl. Phys.* **2010,** *43,* 264001–264014. doi:10.1088/0022-3727/43/26/264001
24. Joannopoulos, J. D.; Johnson, S. G.; Winn, J. N.; Meade, R. D. *Photonic Crystals: Molding the Flow of Light,* 2nd ed.; Princeton University Press: Princeton, NJ, USA, 2008.

License and Terms

BEILSTEIN JOURNAL OF NANOTECHNOLOGY

Interaction of electromagnetic radiation in the 20–200 GHz frequency range with arrays of carbon nanotubes with ferromagnetic nanoparticles

Agylych Atdayev, Alexander L. Danilyuk and Serghej L. Prischepa*

Full Research Paper

Open Access

Address:
Belarusian State University of Informatics and Radioelectronics, P. Browka St. 6, 220013 Minsk, Belarus

Email:
Serghej L. Prischepa* - prischepa@bsuir.by

* Corresponding author

Keywords:
carbon nanotubes; electromagnetic radiation; ferromagnetic nanoparticles; magnetic dipole; magnetic nanocomposite; resonance circuit

Beilstein J. Nanotechnol. **2015,** *6,* 1056–1064.
doi:10.3762/bjnano.6.106

Received: 16 September 2014
Accepted: 30 March 2015
Published: 24 April 2015

This article is part of the Thematic Series "Self-assembly of nanostructures and nanomaterials".

Guest Editor: I. Berbezier

Abstract

The interaction of electromagnetic radiation with a magnetic nanocomposite based on carbon nanotubes (CNT) is considered within the model of distributed random nanoparticles with a core–shell morphology. The approach is based on a system composed of a CNT conducting resistive matrix, ferromagnetic inductive nanoparticles and the capacitive interface between the CNT matrix and the nanoparticles, which form resonance resistive–inductive–capacitive circuits. It is shown that the influence of the resonant circuits leads to the emergence of specific resonances, namely peaks and valleys in the frequency dependence of the permeability of the nanocomposite, and in the frequency dependence of the reflection and transmission of electromagnetic radiation.

Introduction

Magnetic nanocomposites consisting of ferromagnetic nanoparticles embedded into a matrix material are currently the subject of intensive study. The properties of such materials can be tuned by the external magnetic field, spin-polarized current or electromagnetic radiation. In conventional ferromagnetic materials, the magnetic properties are determined by the domain structure and domain walls within the grains. In nanostructured materials, the magnetic properties and the static and dynamic magnetic behavior are controlled by the interparticle exchange interaction, which gives rise to a new generation of devices with improved characteristics and new functionalities. Such magnetic nanocomposites are prospects for memory storage, emission and high frequency devices.

New magnetic nanocomposites based on carbon nanotubes (CNTs) [1-3] are very promising for high frequency applications [4-14] such as transmission lines, mixtures and detectors [15-17], antennas and absorbing materials [18-26]. The absorption properties of CNT-based nanocomposites are primarily determined by the dielectric loss [27]. However, the intercalation of magnetic nanoparticles into the CNT matrix leads to the increase of the absorption properties due to the induced magnetic loss [24,28-31]. In order to predict the absorption properties of CNT-based nanocomposites, the realization of a wide variety of experimental investigations and the development of theoretical approaches, which take into account the different parameters of nanocomposites, are necessary.

In particular, the interaction of electromagnetic radiation (EMR) with CNT-based magnetic nanocomposites is developed in several directions [4-8]. One of the main problems is related to the elucidation of the absorption mechanisms of the EMR by such complex nanocomposites composed of a porous carbon matrix, ferromagnetic nanoparticles and the interfaces between them [8]. In such systems, accounting for the properties of the carbon matrix, nanoparticles and interfaces becomes of great importance [8]. This issue can be taken into account when considering the CNT-based nanocomposite as a system of such components comprised of a CNT conducting resistive matrix, ferromagnetic inductive nanoparticles and the capacitive interfaces between the CNT matrix and the nanoparticles. Therefore, the development of models to adequately describe the absorption properties of CNT-based magnetic nanocomposites in a wide frequency range is an important task.

Based on a previously developed approach [8], in this paper, the interaction of EMR with a CNT-based nanocomposite in the frequency range 20–200 GHz is theoretically studied. Special attention is given to the role of the resonance resistive–inductive–capacitive ($R_iL_iC_i$) circuits, which leads to a deeper understanding of the problem. Such nanocomposites can be easily synthesized in situ during the CNT growth by chemical vapor deposition, which involves carbon decomposition of an organic precursor with 3*d* catalytic metals such as Fe, Ni and Co [32].

Model

Before describing our theoretical approach in detail, we first specify the object of investigation targeted in this work. We consider the CNT-based nanocomposite synthesized by floating catalyst chemical vapor deposition (FCCVD) employing ferrocene $Fe(C_5H_5)_2$ as the source of catalytic iron-based nanoparticles (NPs). Under standard FCCVD conditions (i.e., synthesis temperature: 1150 K, ferrocene concentration: 5–10 wt %, injection rate of the Ar carrier gas: 100 cm^3/min, growth duration: 1 min), the multiwall CNTs are formed. The height of the structure is approximately 50 μm and the average CNT diameter is less than 40 nm [8]. The conductivity of such samples is usually in the range of 100–120 $(\Omega\cdot m)^{-1}$ at room temperature [8] and at liquid helium temperature, this decreases to 40–50 $(\Omega\cdot m)^{-1}$. The catalytic, single crystalline, iron-based NPs for the above mentioned ferrocene content are distributed both inside and outside the CNTs and are covered by a carbon shell which prevents their oxidation [8,32,33]. The average size of the NPs is slightly less than the CNT diameter, and lies in the range of a = 20–30 nm [34], and are therefore considered as a single domain [35]. The main phase of the NPs is iron carbide (Fe_3C) with an orthorhombic crystalline structure, and their saturation magnetization at room temperature is $M_{sat} \approx 90$ A·m^2/kg and the Curie temperature was measured as $T_C = 481$ K [32]. Raman spectroscopy can usually reveal slight defects in such CNTs [8,33,34].

The model of the interaction of EMR with CNT-based nanocomposite used in this work is based on a previously developed approach [8]. This approach relies on the modified Bruggeman effective medium theory, which takes into account the conductive magnetic particles randomly distributed in the medium [36,37], and was developed to determine the reflection (R) and transmission (T) coefficients of the EMR for nanostructured magnetic composites at frequencies above 1 GHz. It takes into account both the magnetic properties of the NPs and the transport, structural and magnetic properties of the CNT matrix. The interface between the NPs and the CNT matrix was also considered and characterized by the wave impedance, Z_i. The calculated R and T coefficients adequately describe the experimental data for the X and K_a bands [8].

Here, we modify this approach [8] by specifying the expressions for the permeability and permittivity of the nanocomposite taking into account the possible resistive, capacitive and inductive coupling between the components of the sample. Indeed, in the frequency range of tens or hundreds of GHz, the microwave properties of the nanocomposite should strongly depend not only on the magnetic and dielectric properties of the CNT matrix material and magnetic inclusions, but also on the contribution of the resistive–inductive–capacitive coupling (circuits) which arise in such a complex system. These couplings, which are due to the presence of eddy currents in the nanocomposite, could be described by $R_iL_iC_i$ contours. On the other hand, the CNT-based nanocomposite can be represented as a matrix of CNTs in which ferromagnetic NPs are randomly distributed [8]. Each NP is coated by a protective shell (interface) according to the experimental findings [32,33]. We suppose that the $R_iL_iC_i$ contours are formed primarily due to the resistance of the CNT matrix, the NP inductance, and the capacitance of the interfaces. For simplicity, we also assume that the R_i, L_i, and C_i model parameters are constant for each of the cases considered in this article. Physically, this means that all the NPs are of the same size and all interfaces have the same capacitance. Under these assumptions, the $R_iL_iC_i$ circuit describing the nanocomposite properties is resonant, that is, it has its own resonance frequency.

To model the permeability of such a nanostructured composite, we obtained the following modified expression:

$$\mu(\omega) = \frac{-B_\mu + \sqrt{B_\mu^2 + 8\mu_1 Q_\mu}}{4Q_\mu} \tag{1}$$

where

$$B_\mu = \frac{(3-5N) - \mu_1 Q_\mu (6-7N)}{(3-2N)} \tag{2}$$

$$Q_\mu = \frac{1}{\mu_2} - \frac{\mathrm{i}\omega \cdot a\mu_0}{2Z_i(\omega)}, \tag{3}$$

μ_1 and μ_2 are the relative permeabilities of the carbon matrix and the ferromagnetic NPs respectively, a is the NP diameter, ω is cyclic frequency of EMR, μ_0 is magnetic constant, and N is the volume NP concentration.

For the permittivity, the following modified expression was deduced:

$$\varepsilon(\omega) = \frac{-B_\varepsilon + \sqrt{B_\varepsilon^2 + 8\varepsilon_1 Q_\varepsilon}}{4Q_\varepsilon} + \mathrm{i}(\sigma/\omega), \tag{4}$$

where

$$B_\varepsilon = \frac{(3-5N) - \varepsilon_1 Q_\varepsilon (6-7N)}{(3-2N)}, \tag{5}$$

$$Q_\varepsilon = \frac{Z_i\omega \cdot a\varepsilon_0}{Z_i\omega \cdot a\varepsilon_0\varepsilon_2 + 2\mathrm{i}}, \tag{6}$$

ε_1 and ε_2 are the relative permittivities of the carbon matrix and the NP, respectively, ε_0 is permittivity of vacuum, and σ is the specific conductivity of CNT-based nanocomposite.

The reflection coefficient is determined as

$$R(\omega) = 20\log\left|\frac{Z(\omega) - Z_0}{Z(\omega) + Z_0}\right| \tag{7}$$

where $Z(\omega) = \sqrt{\mu_0\mu(\omega)/\varepsilon_0\varepsilon(\omega)}$, and $Z_0 = 377\ \Omega$ is the characteristic impedance of the plane wave in vacuum.

The transmission coefficient, which determines the efficiency of shielding, consists of the absorption, reflection, and multireflection processes,

$$\begin{aligned} T(\omega) = 8.86\,\mathrm{Re}(\gamma) + 20\log\left|(Z_0 + Z)^2/4Z_0 Z\right| \\ +20\log\left|1 + \exp\left[-d\,\mathrm{Re}(\gamma)\right](Z_0 - Z)^2/(Z_0 + Z)^2\right|, \end{aligned} \tag{8}$$

where d is the nanocomposite thickness, and

$$\gamma(\omega) = \mathrm{i}\omega\sqrt{\mu_0\mu(\omega)\varepsilon_0\varepsilon(\omega)}$$

is the propagation coefficient.

The impedance of the nanocomposite depends on the contribution of the resonance circuits containing active resistance, R_i, inductance, L_i, and capacitance, C_i. Their resonant frequency is $\omega_0 = 1/\sqrt{L_i C_i}$. We considered both the series and parallel connection of these elements that form the circuits, where the impedances are determined by known expressions.

For the series circuit, the impedance is

$$Z_i = R_i + \mathrm{i}(\omega L_i - 1/\omega C_i). \tag{9}$$

For the partially parallel, $R_iL_iC_i$ circuit (assuming the resistance R_i is in series with the inductance L_i), the impedance is

$$Z_i = \left[R_i + \mathrm{i}\omega L_i\right] / \left\{(\mathrm{i}\omega C_i)\left[R_i + \mathrm{i}(\omega L_i - 1/\omega C_i)\right]\right\}. \tag{10}$$

For the series–parallel circuit (L_i and C_i are in parallel and R_i is in series with them), the impedance is expressed as

$$Z_i = R_i + 1/(\mathrm{i}\omega C_i + 1/\mathrm{i}\omega L_i). \tag{11}$$

For a fully parallel circuit (L_i, C_i and R_i are in parallel), the impedance is

$$Z_i = \left[R_i^{-1} + \mathrm{i}(\omega C_i - 1/\omega L_i)\right]^{-1}. \tag{12}$$

Equations 1, 4, 7 and 8, together with Equations 2, 3, 5, 6 and 9–12 were applied for the calculation of the frequency dependent $\varepsilon(\omega)$ [38], $\mu(\omega)$, $R(\omega)$ and $T(\omega)$. For all results reported in this work, the specific conductivity was set as σ = 120 (Ω·m)$^{-1}$ [8].

Other model parameters were similar to that reported in [8], but for the sake of convenience, we summarize them together in Table 1 with the parameters of the $R_iL_iC_i$ circuits used in the calculations. The dimensions and properties of the nanocomposite components provide a range of L_i and C_i parameters corresponding to the pH and pF, respectively, and R_i values in the range of mΩ. This choice of circuit parameters matches with the specified frequency range of 20–200 GHz.

Results and Discussion

For the case of the series circuit, for which the impedance is expressed by Equation 9, the nonlinearity of μ(ω) close to the resonance frequency and, consequently, of R(ω) and T(ω) were obtained (Figure 1a,b, curves 1 and 2). In particular, at some values of the circuit parameters, a strong reduction of the μ(ω) dependence is observed, followed by smooth peak (Figure 1a). Correspondingly, the reflectivity and transmission first increase significantly and then drop (Figure 1b). Consequently, depending on the circuit parameters, one can observe either a gradual change in the resonance for reflection and transmission,

Table 1: Values of input parameters used in the model.

Parameter	Unit	Values			
a	nm	20–30			
N	a.u.	0.1 ± 0.01			
μ_1	a.u.	(3 ± 0.5) + i(0.35 ± 0.1)			
μ_2	a.u.	(7 ± 2) + i(0.5 ± 0.2)			
ε_1	a.u.	(10 ± 0.5) + i(0.1 ± 0.05)			
ε_2	a.u.	(2 ± 0.2) + i(0.1 ± 0.05)			
Re(ε_a[a])	a.u.	14 ± 2			
		Type of circuit			
		series	partially parallel	series–parallel	fully parallel
R_i	Ω	0.003–0.02	0.01–0.02	0.005–0.01	0.002–0.01
C_i	pF	2–20	1–15	1–15	1–10
L_i	pH	0.2–2	0.01–0.1	0.01–0.12	0.01–0.15

[a]Permittivity of the nanocomposite.

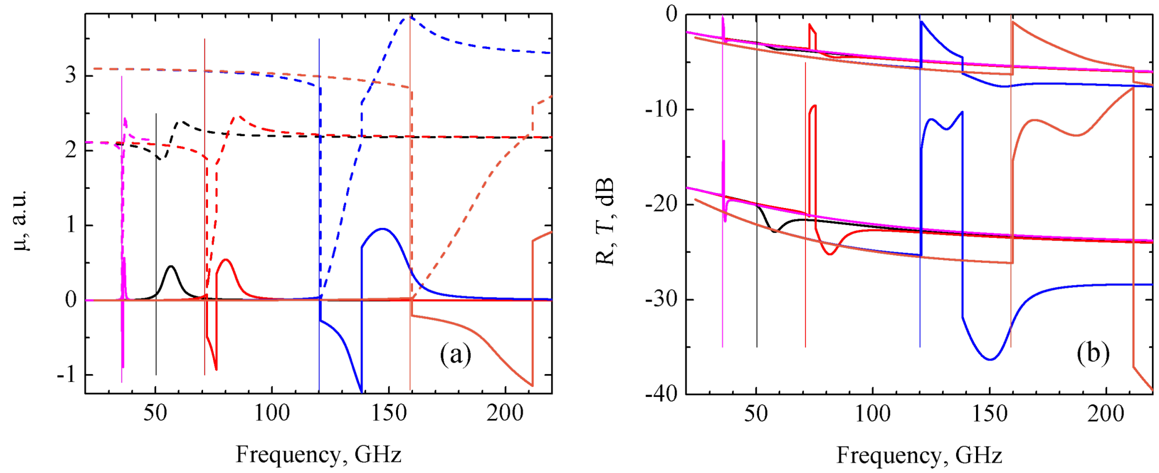

Figure 1: Frequency dependence of the real (dashed lines) and imaginary (solid lines) parts of the permeability (a), and of the reflection, *R* (upper curves), and transmission, *T* (lower curves), coefficients (b) for the CNT-based nanocomposite consisting of a series $R_iL_iC_i$ circuit. From left to right: R_i = 0.015 Ω, L_i = 2 pH, C_i = 10 pF (ω_0 = 35.6 GHz) (magenta lines); R_i = 0.015 Ω, L_i = 0.5 pH, C_i = 20 pF (ω_0 = 50.3 GHz) (black lines); R_i = 0.015 Ω, L_i = 0.5 pH, C_i = 20 pF (ω_0 = 71.2 GHz) (red lines); R_i = 0.012 Ω, L_i = 0.35 pH, C_i = 5 pF (ω_0 = 120.3 GHz) (blue lines); R_i = 0.012 Ω, L_i = 0.2 pH, C_i = 5 pF (ω_0 = 159.1 GHz) (orange lines). The resonance frequency of the $R_iL_iC_i$ circuit, ω_0, is represented by a vertical line of corresponding color.

or a sharp change of these coefficients. The second type of resonance is characterized by large steps in the *R* and *T* frequency dependence; namely, *R* increases almost to 0 dB, and *T* changes from −22 dB to −10 dB. The step width could reach 10–15 GHz.

It was found that the reduction of L_i and C_i results in a broadening and shift of the peaks towards higher frequencies. This result is depicted in Figure 1a,b. Note that the nanocomposite resonance always occurs at a frequency close to the resonance frequency of the circuit, ω_0. The resonance frequency is depicted in Figure 1 by thin vertical lines. The increase in the inductance by several orders of magnitude results in the narrowing of the resonance and the reduction of the resonance frequency.

For the partially parallel circuit consisting of a R_i and L_i series connection and C_i in parallel with them, the appearance of distinct steps in the μ, *R* and *T* spectra were obtained for a given set of circuit parameters, as shown in Figure 2. Here, the real part of the permeability reduces to almost zero and its imaginary part becomes negative. The reflection coefficient increases abruptly almost to zero and the transmission coefficient increases from −22 to −10 dB.

Qualitatively, the frequency behavior of the μ, *R* and *T* coefficients is similar to that of the series circuit. However, the width of the valley is much wider in this case and reached the value of 400 GHz. This result is shown in Figure 2a for μ(ω) and in Figure 2b for *R*(ω) and *T*(ω). In subsequent subsections for the other circuit configuration, only μ(ω) curves will be presented.

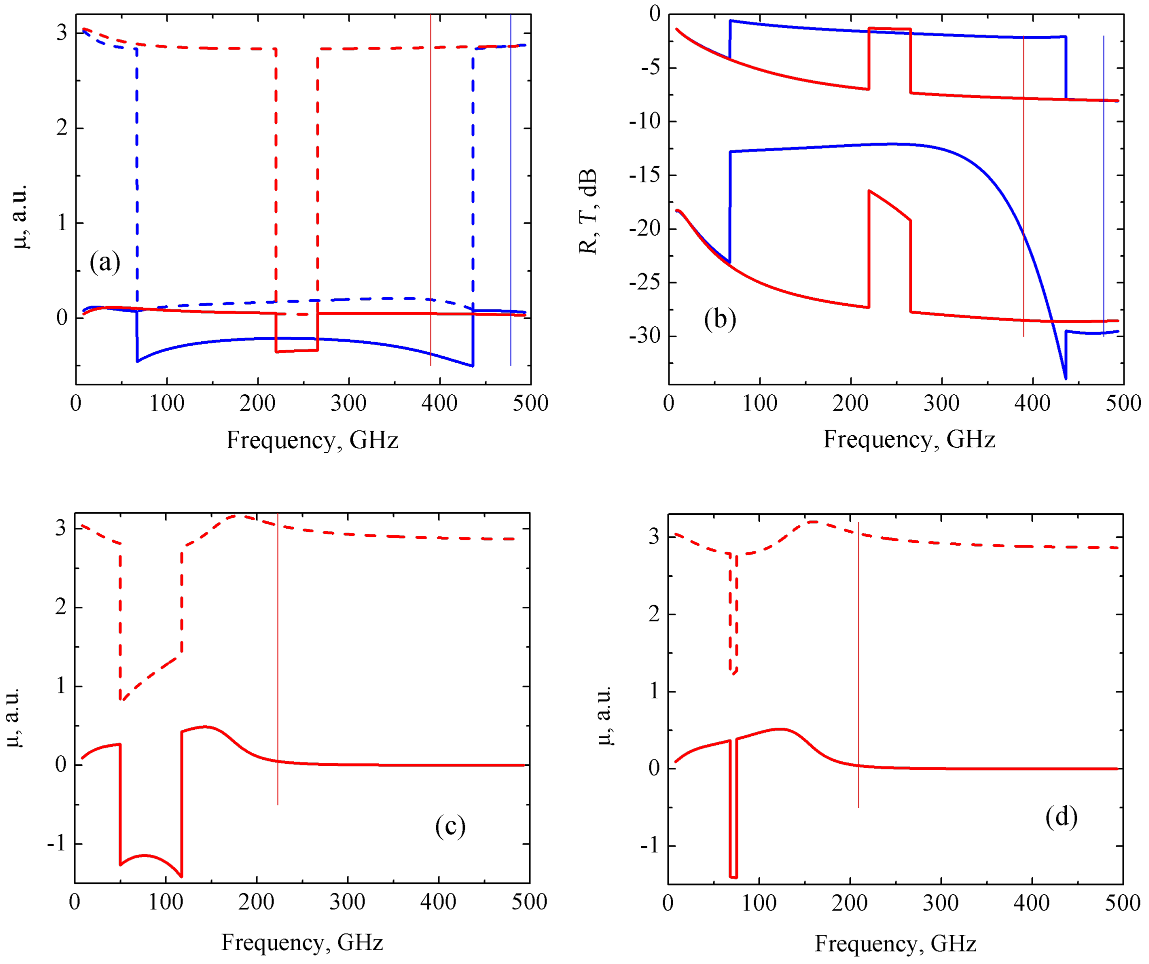

Figure 2: Frequency dependencies of the real (dashed lines) and imaginary (solid lines) parts of the permeability (a,c,d), and of the reflection *R* (upper curves) and transmission *T* (lower curves) coefficients (b) of the CNT based nanocomposite consisting of partially parallel circuit:
(a) – R_i = 0.01 Ω, L_i = 0.01 pH, C_i = 10 pF (ω_0 = 477.5 GHz) – blue curves; R_i = 0.02 Ω, L_i = 0.01 pH, C_i = 10 pF (ω_0 = 390.0 GHz) – red curves;
(b) – R_i = 0.01 Ω, L_i = 0.01 pH, C_i = 10 pF (ω_0 = 477.5 GHz) – blue curves; R_i = 0.02 Ω, L_i = 0.01 pH, C_i = 10 pF (ω_0 = 390.0 GHz) – red curves;
(c) – R_i = 0.01 Ω, L_i = 0.05 pH, C_i = 10 pF (ω_0 = 223.0 GHz); (d) – R_i = 0.01 Ω, L_i = 0.0569 pH, C_i = 10 pF (ω_0 = 209.0 GHz). Resonance frequencies of the $R_iL_iC_i$ circuits ω_0 are drawn by vertical lines of corresponding colors.

This wide valley occurs for the following set of given parameters: $R_i = 0.01\ \Omega$, $L_i = 0.01$ pH, and $C_i = 10$ pF. If we then hold R_i and C_i constant and vary L_i towards higher values, the valley in the μ(ω) dependence is shifted to lower frequencies and narrows, as shown in Figure 2c,d. For values greater than $L_i = 0.0569$ pH, the valley disappears (not shown here). A similar behavior is obtained when holding R_i and L_i constant and varying C_i in the range 10–41 pF. If instead we set $L_i = 0.01$ pH and $C_i = 10$ pF and increase R_i to $0.02\ \Omega$ (instead of $0.01\ \Omega$), the valley in the μ(ω) dependence is shifted to the frequency range between 200 and 300 GHz with a corresponding contraction in the middle of the range. This result is depicted in Figure 2a by red line. Note that for the partially parallel circuit, the resonance occurs at frequencies lower than the frequency of the resonance $R_iL_iC_i$ circuit.

For the series–parallel circuit, two types of resonances were observed. The first one is related to the valley in the μ(ω) dependence. However, in contrast to the previous cases, the real part of the permeability does not drop to zero, as can be seen in Figure 3a. This valley is related to the increase of both the *R* and *T* coefficients as depicted in Figure 3b by the solid lines. The width of this growth reached a value of 30–40 GHz. The second type of resonance yields a smooth increase of the permeability at higher frequencies (Figure 1a). Therefore, both the abrupt and smooth resonances are observed simultaneously. An increase in any one of the parameters of the $R_iL_iC_i$ circuit causes a narrowing of this valley (Figure 3c), and eventually, its disappearance (Figure 3d). In particular, from Figure 3d it follows that for the parameters $R_i = 0.007\ \Omega$, $L_i = 0.075$ pH and $C_i = 15$ pF, only the smooth resonance remains, which is

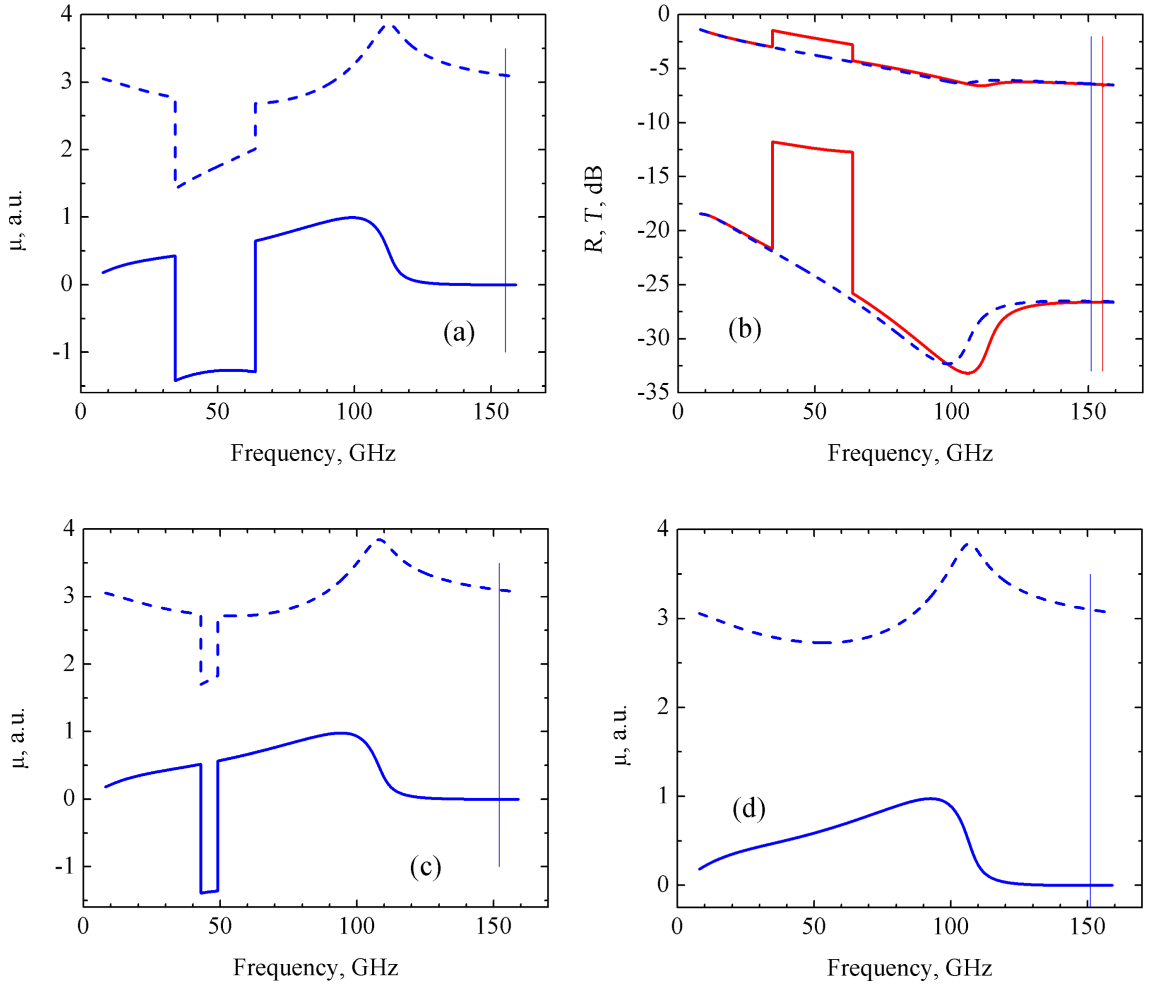

Figure 3: Frequency dependence of the real (dashed lines) and imaginary (solid lines) parts of the permeability (a,c,d), and of the reflection *R* (upper curves) and transmission *T* (lower curves) coefficients (b) of the CNT-based nanocomposite consisting of a series–parallel circuit. (a) $R_i = 0.007\ \Omega$, $L_i = 0.07$ pH, $C_i = 15$ pF ($\omega_0 = 155.3$ GHz); (b) $R_i = 0.007\ \Omega$, $L_i = 0.07$ pH, $C_i = 15$ pF ($\omega_0 = 155.3$ GHz) (red solid lines) and $R_i = 0.007\ \Omega$, $L_i = 0.075$ pH, $C_i = 15$ pF ($\omega_0 = 151.1$ GHz) (blue dashed lines); (c) $R_i = 0.007\ \Omega$, $L_i = 0.073$ pH, $C_i = 15$ pF ($\omega_0 = 152.1$ GHz); (d) $R_i = 0.007\ \Omega$, $L_i = 0.075$ pH, $C_i = 15$ pF ($\omega_0 = 151.1$ GHz). The resonance frequency of the $R_iL_iC_i$ circuits, ω_0, are indicated by vertical lines.

reflected in the smooth $R(\omega)$ and $T(\omega)$ dependence (Figure 3b, dashed lines). Note that in this case, the $\mu(\omega)$ behavior is very sensitive to the circuit parameters. In particular, the change in the induction from 0.07 pH (Figure 3a) to 0.075 pH (Figure 3d) results in the complete disappearance of the valley in the $\mu(\omega)$ dependence.

In the case of the fully parallel circuit, the steps in the $\mu(\omega)$, $R(\omega)$ and $T(\omega)$ dependence were observed similar to those in the partially parallel circuit of Figure 4. In general, the frequency behavior of the permeability and of the R and T coefficients differs significantly from that previously observed. In fact, the real part of the permeability first gradually approaches zero, then sharply increases to a value of approximately 3 at $\omega \approx 50$ GHz, while the imaginary part of μ is negative at $\omega < 50$ GHz and becomes 0 for $\omega > 50$ GHz (Figure 4a). The corresponding behavior of the reflectivity and transmission coefficients is shown in Figure 4b by solid red lines.

It was found that the variation of R_i and C_i within the whole range of interest (see Table 1) does not lead to a noticeable change in the $\mu(\omega)$ curves. Only a variation of L_i produces a qualitative change in the $\mu(\omega)$ function. Indeed, when L_i becomes larger than 0.095 pH, the $\mu(\omega)$ curves become smooth, as shown in Figure 4d. The corresponding frequency behavior of the reflectivity and transmission is depicted in Figure 4b by dashed blue lines.

In our opinion, one of the main results of this work is the observation of intense, wide valleys in the permeability. The reason for the abrupt decrease in the $\mu(\omega)$ dependence at some combination of the $R_iL_iC_i$ circuit parameters is related to the complex

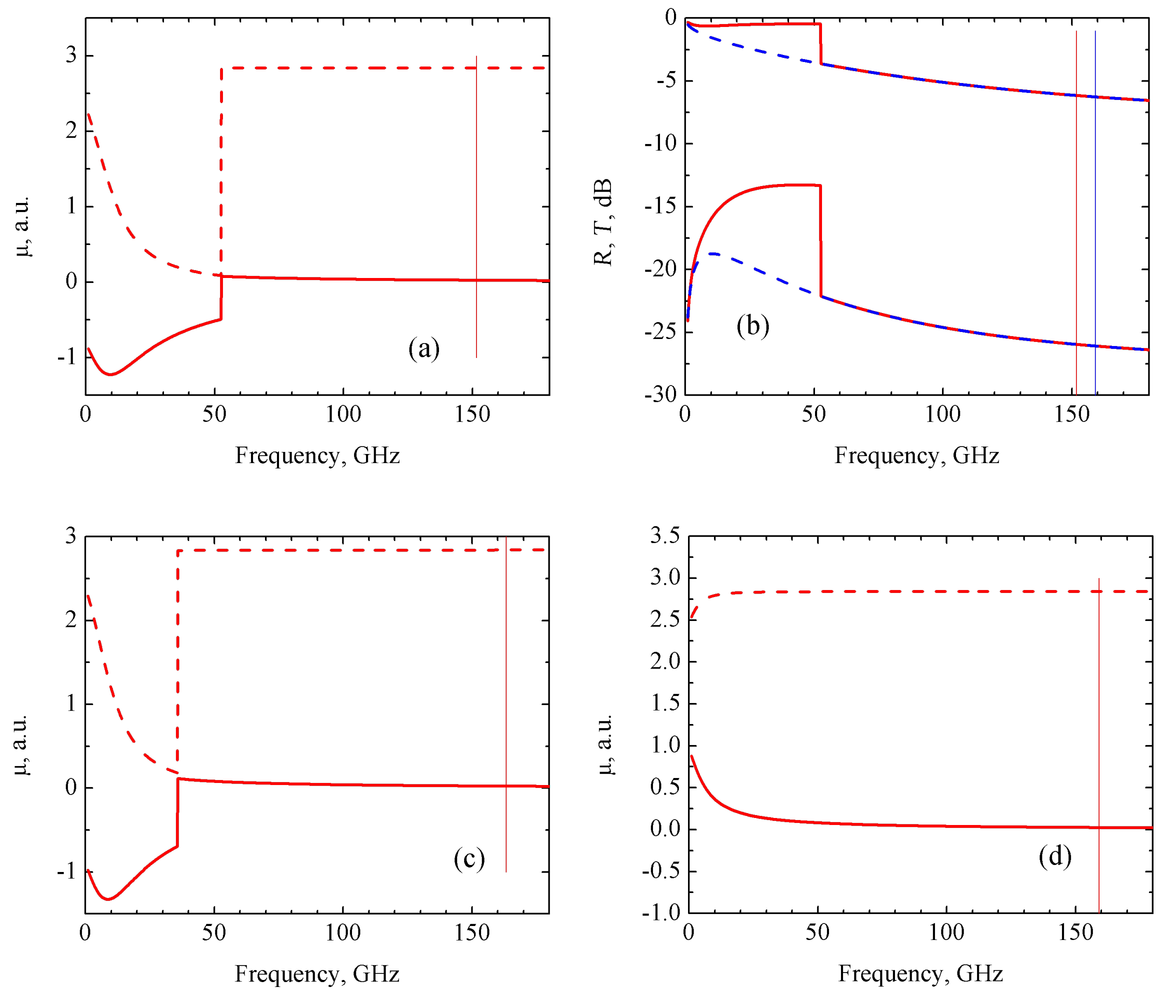

Figure 4: Frequency dependence of the real (dashed lines) and imaginary (solid lines) parts of the permeability (a,c,d), and of the reflection R (upper curves) and transmission T (lower curves) coefficients (b) of the CNT-based nanocomposite consisting of a fully parallel circuit. (a) $R_i = 0.01\ \Omega$, $L_i = 0.09$ pH, $C_i = 10$ pF ($\omega_0 = 151.7$ GHz); (b) $R_i = 0.01\ \Omega$, $L_i = 0.09$ pH, $C_i = 10$ pF ($\omega_0 = 151.7$ GHz) (solid red lines) and $R_i = 0.01\ \Omega$, $L_i = 0.1$ pH, $C_i = 10$ pF ($\omega_0 = 159.2$ GHz) (dashed blue lines); (c) $R_i = 0.01\ \Omega$, $L_i = 0.095$ pH, $C_i = 10$ pF ($\omega_0 = 163.3$ GHz); (d) $R_i = 0.01\ \Omega$, $L_i = 0.1$ pH, $C_i = 10$ pF ($\omega_0 = 159.2$ GHz). The resonance frequencies of the $R_iL_iC_i$ circuits, ω_0, are represented by the vertical lines.

contribution to the permeability of the nanocomposite from the circuit and the magnetic NPs. Indeed, the permeability of the nanocomposite is conditioned by 3 main contributions: the superposition of the permeabilities of the carbon matrix, the NPs and the wave impedance of the nanocomposite, as given in Equations 1–3. Here, the permittivity is almost constant. Therefore, the effective nanocomposite parameters are determined both by the carbon matrix parameters and by the polarization of the electrical and magnetic dipoles created by magnetic NPs. These dipoles placed into the carbon matrix cause additional electromagnetic fields which influence the shielding properties of the nanocomposite. Apparently, the determination of the permeability of such nanocomposites should be performed by taking the polarization of such dipoles into account. In our case, the magnetic polarization of dipoles formed by the magnetic NPs is determined by the permeability of the NP and by the impedance of the interface. As a result, during the interaction of the EMR with a composite material having intercalated magnetic metallic NPs of diameter less than the EMR wavelength, additional fields arise in the sample on the length scale much smaller than the EMR wavelength, but larger than the nanoparticle size. These fields are conditioned by the electric and magnetic dipoles created by the metallic NPs. These additional fields should be taken into account when considering the R and T coefficients. They are accounted for via the effective values of the permittivity and permeability. The values of these fields, or the polarizability, are determined by the nanoparticle–interface–carbon matrix system impedance. At some combination of the resonance circuit parameters and the permeability of the NP, compensation for the absorption occurs and the real part of the permeability goes to zero and its imaginary part becomes negative. In other words, the nanocomposite impedance compensates for the magnetic moment created by the NP in the carbon matrix at a fixed frequency range. When no valley is present in the $\mu(\omega)$ dependence, the impedance of the magnetic dipole (and consequently, its polarizability) is determined by the permeability of the NP and of the nanocomposite, which are both positive.

Conclusion

Problems related to the influence of the conductive carbon matrix, the inductive ferromagnetic NPs and the capacitive interface between the carbon matrix and the embedded ferromagnetic nanoparticles in CNT-based nanocomposites on the interaction of these materials with the EMR in the 20–200 GHz frequency range were numerically considered by applying a modified model. A distinctive feature of this model is the introduction of resonant resistive–inductive–capacitive circuits with different connections between the elements to describe the parameters of the nanocomposite. In particular, the circuits were modeled as resonant circuits having resistance, inductance and capacitance with series, parallel and mixed connections.

It was shown that for the series resonance circuit, both smooth and sharp resonances occur in the frequency dependent μ, R and T coefficients. Depending on the given model parameters, the width of the resonance varied from 1 to 50 GHz. These phenomena occur close to the resonance frequency of the circuit, which is always less than the resonance frequency of the nanocomposite. For the partially parallel circuits, the wide valleys in the frequency dependent μ spectra were obtained. There, the real part of the permeability drops to almost zero, followed by a sharp increase to the value determined by the permeability of the nanocomposite. As a result, over some frequency range, the nanocomposite becomes much more transparent to the EMR. The width of this range reaches hundreds of GHz and it appears at frequencies lower than the resonance frequency of the circuit. For the series–parallel circuits, the nonlinear dependence of μ, R and T on frequency was obtained. Also, a combination of the nonlinear dependence and the valley-like dependence could be observed for this case depending on the parameters given for the circuits. The valley width reached values of 40 GHz and is extremely sensitive to the model parameter values. They are observed far below the resonance frequency. Finally, for the fully parallel circuit, the $\mu(\omega)$, $R(\omega)$ and $T(\omega)$ dependencies are step-like, but with a slight increase of the resonance frequency of the circuit, these steps disappear and the dependence become gradual.

It is worth mentioning that the obtained effects are in the range of tens and hundreds of GHz due to the characteristic values of the passive elements of the interfaces (pH and pF). Sudden decreases in the $\mu(\omega)$ coefficient for different $R_iL_iC_i$ circuits are explained in terms of the interaction of the magnetic dipole formed by the ferromagnetic metallic NPs and the $R_iL_iC_i$ circuits, which leads to the compensation of the resonant absorption of EMR by magnetic dipole.

An experimental observation of the predicted phenomena is possible given improved control of the CNT-based nanocomposite parameters such as size, concentration of NPs embedded into the CNT matrix, NPs localization in the CNT matrix, etc. Further work related to the investigation of the influence of the distribution of the model parameters on the absorption process of EMR by CNT-based magnetic nanocomposite is currently under progress now.

Acknowledgements

This work was partially supported by the Belarusian Foundation for Fundamental Research, grant #F13F-002 and #F15LIT-009.

References

1. Saito, R.; Dresselhaus, G.; Dresselhaus, M. S. *Physical Properties of Carbon Nanotubes;* Imperial College Press: London, U.K., 2003.
2. Marulanda, J. M. *Carbon Nanotubes: Applications on Electron Devices;* InTech: New York, 2011.
3. Rao, C. N. R.; Govindaraj, A. *Nanotubes and Nanowires;* Royal Society of Chemistry: Cambridge, U.K., 2005.
4. Federici, J.; Moeller, L. *J. Appl. Phys.* **2010,** *107,* 111101. doi:10.1063/1.3386413
5. Crespo, M.; Méndez, N.; González, M.; Baselga, J.; Pozuelo, J. *Carbon* **2014,** *74,* 63–72. doi:10.1016/j.carbon.2014.02.082
6. Ye, H.; Wang, X. J.; Lin, W.; Wong, C. P.; Zhang, Z. M. *Appl. Phys. Lett.* **2012,** *101,* 141909. doi:10.1063/1.4757395
7. Qin, F.; Brosseau, C. *J. Appl. Phys.* **2012,** *111,* 061301. doi:10.1063/1.3688435
8. Labunov, V. A.; Danilyuk, A. L.; Prudnikava, A. L.; Komissarov, I.; Shulitski, B. G.; Speisser, C.; Antoni, F.; Le Normand, F.; Prischepa, S. L. *J. Appl. Phys.* **2012,** *112,* 024302. doi:10.1063/1.4737119
9. Lehman, J.; Sanders, A.; Hanssen, L.; Wilthan, B.; Zeng, J.; Jensen, C. *Nano Lett.* **2010,** *10,* 3261–3266. doi:10.1021/nl100582j
10. Yang, Z.-P.; Ci, L. J.; Bur, J. A.; Lin, S.-Y.; Ajayan, P. M. *Nano Lett.* **2008,** *8,* 446–451. doi:10.1021/nl072369t
11. Wang, X. J.; Wang, L. P.; Adewuyi, O. S.; Cola, B. A.; Zhang, Z. M. *Appl. Phys. Lett.* **2010,** *97,* 163116. doi:10.1063/1.3502597
12. Shi, H.; Ok, J. G.; Baac, H. W.; Guo, L. J. *Appl. Phys. Lett.* **2011,** *99,* 211103. doi:10.1063/1.3663873
13. Wang, X. J.; Flicker, J. D.; Lee, B. J.; Ready, W. J.; Zhang, Z. M. *Nanotechnology* **2009,** *20,* 215704. doi:10.1088/0957-4484/20/21/215704
14. Yang, Z.-P.; Hsieh, M.-L.; Bur, J. A.; Ci, L.; Hanssen, L. M.; Wilthan, B.; Ajayan, P. M.; Lin, S.-Y. *Appl. Opt.* **2011,** *50,* 1850–1855. doi:10.1364/AO.50.001850
15. Miano, G.; Villone, F. *IEEE Trans. Antennas Propag.* **2006,** *54,* 2713–2724. doi:10.1109/TAP.2006.882170
16. Appenzeller, J.; Frank, D. J. *Appl. Phys. Lett.* **2004,** *84,* 1771–1773. doi:10.1063/1.1655696
17. Rosenblatt, S.; Lin, H.; Sazonova, V.; Tiwari, S.; McEuen, P. L. *Appl. Phys. Lett.* **2005,** *87,* 153111. doi:10.1063/1.2103391
18. Nefedov, I. S. *Phys. Rev. B* **2010,** *82,* 155423. doi:10.1103/PhysRevB.82.155423
19. Zhang, M.; Zhang, H. Y.; Zeng, G. X. *Adv. Mater. Res. (Durnten-Zurich, Switz.)* **2011,** *194–196,* 520–523. doi:10.4028/www.scientific.net/AMR.194-196.520
20. Dresselhaus, M. S. *Nature* **2004,** *432,* 959–960. doi:10.1038/432959a
21. Hanson, G. W. *IEEE Trans. Antennas Propag.* **2005,** *53,* 3426–3435. doi:10.1109/TAP.2005.858865
22. Burke, P. J.; Li, S.; Yu, Z. *IEEE Trans. Nanotechnol.* **2006,** *5,* 314–334. doi:10.1109/TNANO.2006.877430
23. Nemilentsau, A. M.; Slepyan, G. Ya.; Maksimenko, S. A. *Phys. Rev. Lett.* **2007,** *99,* 147403. doi:10.1103/PhysRevLett.99.147403
24. Watts, P. C. P.; Ponnampalam, D. R.; Hsu, W. K.; Barnes, A.; Chambers, B. *Chem. Phys. Lett.* **2003,** *378,* 609–614. doi:10.1016/j.cplett.2003.07.002
25. Ye, Z.; Li, Z.; Roberts, J. A.; Zhang, P.; Wang, J. T.; Zhao, G. L. *J. Appl. Phys.* **2010,** *108,* 054315. doi:10.1063/1.3477195
26. Li, Z.; Ye, Z.; Roberts, J. A.; Zhao, G. L. *J. Appl. Phys.* **2011,** *110,* 074107. doi:10.1063/1.3646405
27. Wang, L.; Zhou, R.; Xin, H. *IEEE Trans. Microwave Theory Tech.* **2008,** *56,* 499–506. doi:10.1109/TMTT.2007.914627
28. Cojocaru, C. S.; Senger, A.; Le Normand, F. *J. Nanosci. Nanotechnol.* **2006,** *6,* 1331–1338. doi:10.1166/jnn.2006.144
29. Vovchenko, L.; Matzui, L.; Oliynyk, V.; Launetz, V.; Le Normand, F. *Physica E* **2012,** *44,* 928–931. doi:10.1016/j.physe.2011.10.018
30. Xie, G.; Wang, Z.; Cui, Z.; Shi, Y. *Carbon* **2005,** *43,* 3181–3183. doi:10.1016/j.carbon.2005.07.024
31. Ghasemi, A.; Shirsath, S. E.; Li, X.; Morisako, A. *J. Appl. Phys.* **2011,** *109,* 07A507. doi:10.1063/1.3551727
32. Danilyuk, A. L.; Prudnikava, A. L.; Komissarov, I. V.; Yanushkevich, K. I.; Derory, A.; Le Normand, F.; Labunov, V. A.; Prischepa, S. L. *Carbon* **2014,** *68,* 337–345. doi:10.1016/j.carbon.2013.11.010
33. Danilyuk, A. L.; Komissarov, I. V.; Labunov, V. A.; Le Normand, F.; Derory, A.; Hernandez, J. M.; Tejada, J.; Prischepa, S. L. *New J. Phys.* **2015,** *17,* 023073. doi:10.1088/1367-2630/17/2/023073
34. Prischepa, S. L.; Danilyuk, A. L.; Prudnikava, A. L.; Komissarov, I. V.; Labunov, V. A.; Yanushkevich, K. I.; Le Normand, F. Magnetic Properties of Nanocomposites Based on Magnetically Functionalized Carbon Nantotubes. In *Nanomagnetism;* Gonzalez Estevez, J. M., Ed.; One Central Press: Manchester, UK, 2014; pp 227–245.
35. Leslie-Pelecky, D. L.; Rieke, D. R. *Chem. Mater.* **1996,** *8,* 1770–1783. doi:10.1021/cm960077f
36. Bohren, C. V.; Huffman, D. R. *Absorption and Scattering of Light by Small Particles;* John Wiley & Sons: New York, USA, 1998. doi:10.1002/9783527618156
37. Ponomarenko, V. P. *Radiotekh. Elektron. (Moscow, Russ. Fed.)* **2000,** *45,* 869–870. (in Russian).
38. For the permittivity, only the imaginary part depends on frequency as σ/ω. Therefore, this result was not presented in the text.

License and Terms

The definitive version of this article is the electronic one which can be found at:
doi:10.3762/bjnano.6.106

BEILSTEIN JOURNAL OF NANOTECHNOLOGY

Nanomechanical humidity detection through porous alumina cantilevers

Olga Boytsova*[1,2], Alexey Klimenko[1], Vasiliy Lebedev[1], Alexey Lukashin[1]
and Andrey Eliseev[1]

Full Research Paper

Open Access

Address:
[1]Lomonosov Moscow State University, 119992, Moscow, Russia and
[2]Kurnakov Institute of General and Inorganic Chemistry of The
Russian Academy of Science, 119991, Moscow, Russia

Email:
Olga Boytsova* - boytsova@gmail.com

* Corresponding author

Keywords:
anodic aluminium oxide; atomic force microscopy (AFM); cantilever arrays; humidity; mechanical sensor; porous alumina

Beilstein J. Nanotechnol. **2015,** *6,* 1332–1337.
doi:10.3762/bjnano.6.137

Received: 18 September 2014
Accepted: 20 May 2015
Published: 16 June 2015

This article is part of the Thematic Series "Self-assembly of nanostructures and nanomaterials".

Guest Editor: I. Berbezier

Abstract

We present here the behavior of the resonance frequency of porous anodic alumina cantilever arrays during water vapor adsorption and emphasize their possible use in the micromechanical sensing of humidity levels at least in the range of 10–22%. The sensitivity of porous anodic aluminium oxide cantilevers ($\Delta f/\Delta m$) and the humidity sensitivity equal about 56 Hz/pg and about 100 Hz/%, respectively. The approach presented here for the design of anodic alumina cantilever arrays by the combination of anodic oxidation and photolithography enables easy control over porosity, surface area, geometric and mechanical characteristics of the cantilever arrays for micromechanical sensing.

Introduction

The last two decades have seen a surge in resonant micro- and nanomechanical engineering raised by the creation of high-performance and cost-effective detection systems. Highly elastic silicon and, in contrast, soft polymer cantilevers were implemented to chemical sensors with resonance shift assay [1-3]. To date, the determination of trace amounts of adsorbed biological, chemical and other multiplex substances through micromechanical sensing still holds a tremendous potential [4-8]. To improve the shifts of the resonant frequency one needs to enlarge the active surface area of the sensor while preserving its mechanical stiffness. This necessitates the use of the porous systems with “open through porosity”. One promising porous system exhibiting all the necessary characteristics is anodic aluminium oxide (AAO). Its huge surface area offers an enormous number of binding sites.

The adsorption of chemicals on the surface of the cantilever manifests itself by the shift of the resonance frequency in dynamic vibration mode. The loading mass can be calculated from the change of resonance frequencies after (f_1) and before (f_0) adsorption as follows [9,10]:

$$\Delta m = \frac{k}{\pi^2}\left(\frac{1}{f_1^2} - \frac{1}{f_0^2}\right). \qquad (1)$$

Here, the spring constant k is given by $k = (E \cdot w \cdot t^3)/(4 \cdot l^3)$, where w, t and l are the width, thickness and length of the cantilever and E is the Young's modulus of the cantilever [11]. According to Equation 1, the more molecules are adsorbed on the surface of a cantilever, the larger is the shift of the resonance frequency. Therefore AAO cantilevers hold a great promise for the development of micromechanical sensor arrays.

In the present work we concentrated on the elaboration of experimental methods for the fabrication of anodic alumina cantilever arrays and their testing for adsorption of water vapors.

Results and Discussion

The proposed procedure for the fabrication of cantilever arrays combines anodic oxidation of aluminium foil with a conventional photolithography process (Figure 1).

Using the lithography approach for AAO pattern formation mostly becomes possible due to selective and anisotropic etching of anodic alumina films on aluminium in basic solutions. On the other hand anodic oxidation itself enables easy control over channel diameter and interpore distance of the porous film over a wide range (pore diameter from 15 to 200 nm; interpore distance from 50 to 500 nm, film thicknesses up to 200 micrometers) [3]. Moreover the thickness of AAO films can be regulated precisely by using conventional electrochemistry methods by controlling the total electric quantity and assuming a current efficiency of 90% [12]. Thus, the proposed approach enables easy control over porosity, surface area, and geometric characteristics of cantilever arrays which provide wide opportunities for the design of micromechanical sensors with specific mechanical response.

To predict the behavior of the cantilever in the gas/liquid phase we investigated alterations of the amplitude–frequency characteristics when changing pressure and humidity. The frequency response of elastic beam is strongly dependent on the fluid it is vibrating in [2]. In vacuum, when the vapors are absent, the measurement of the resonance frequency is routinely made compared to measurements in viscous media. At first we emphasized the damping effect on cantilever vibration for porous AAO and standard Si cantilevers explored in the real system (air) and in model (vacuum). The amplitude–frequency profiles of rectangular cantilevers made of Si and porous anodic aluminium oxide are provided in Figure 2. Their characteristics are summarized in Table 1. The Q factor for both types of beams significantly increases after change air media to vacuum. Natural shifts to high-frequency region are observed for the porous cantilever as well for the Si cantilever.

For comparison we also studied the effect of the water content on the vibration of the cantilever from the AAO membrane obtained at 40 V in 0.3 M oxalic acid. Figure 3 shows the experimental results using a cantilever with a length of 800 µm and 10% porosity.

The resonant frequency decreases from 117.7 kHz at 10% to 116.5 kHz at 21% humidity. Changing the humidity from 21 to 10% increases the resonant frequency by 1120 Hz and quality factor of the AAO cantilever increases from 61 to 82, respectively (Figure 3).

Using Equation 1 and the Young's modulus of AAO of 340 GPa one can evaluate the quantity of water adsorbed onto the anodic alumina surface. The calculation gives a result of Δm = 20 pg at a sensitivity $\Delta f/\Delta m$ of 56 Hz/pg. On the other hand, the amount of absorbed water can be estimated from the Langmuir monolayer absorption isotherm. Taking into account the total area of the cantilever of $1.74 \cdot 10^{-6}$ m^2 ($1.58 \cdot 10^{-6}$ m^2

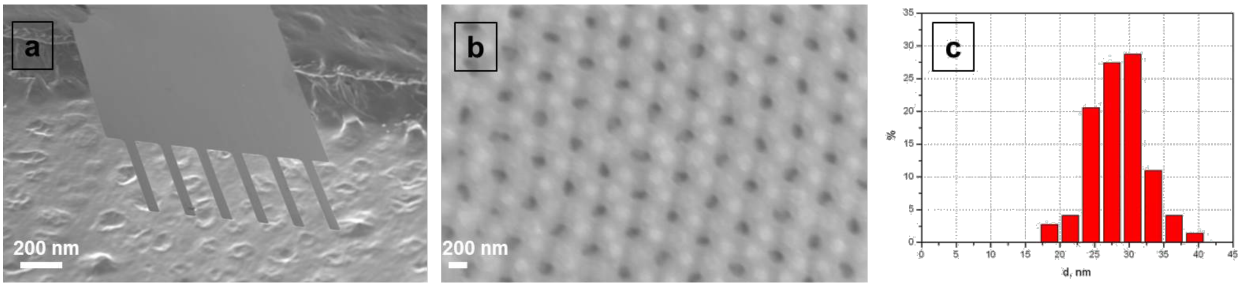

Figure 1: SEM images of a six-cantilevers array (2 µm thickness) obtained through chemical photolithography: (a) general view, (b) porous structure of AAO cantilever with 30 nm average pore diameter and 105 nm average interpore distances and (c) pore size distribution.

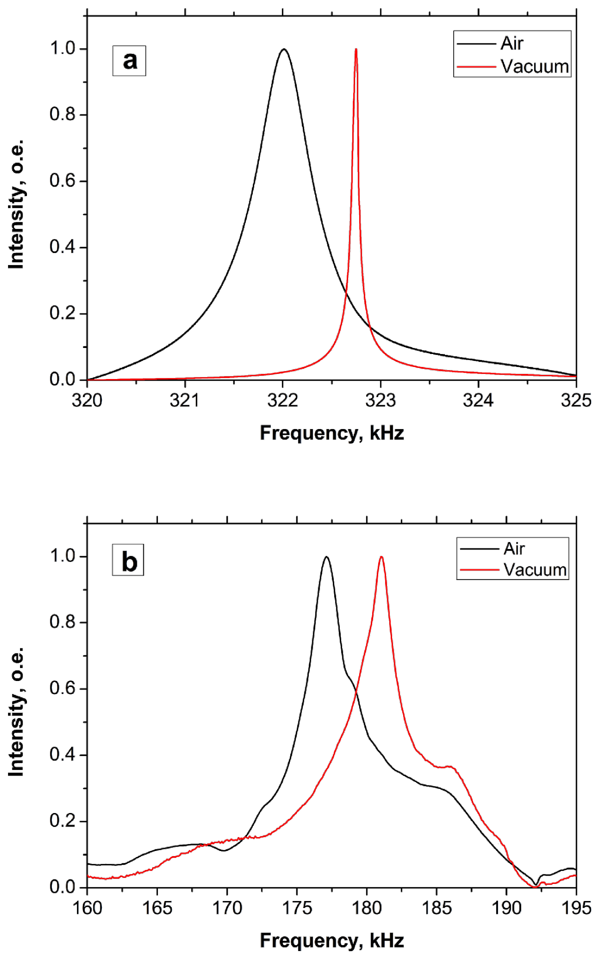

Figure 2: a) Frequency responses of Si rectangular cantilever (2 µm thick, 100 µm long and 30 µm wide) in the air (black line) and in vacuum (red solid line). The frequency shift is 780 Hz. b) Frequency responses of AAO cantilever (2 µm thick, 800 µm long and 100 µm wide) in the air (black line) and in vacuum (red solid line). The shift here is 3900 Hz.

interior and $1.63 \cdot 10^{-7}$ m^2 exterior area) and the density of the active sites of 4.8 nm^{-2} the maximal mass of a water monolayer adsorbed onto cantilever surface is 250 pg. This results in an increase of the experimental water surface coverage of about 8% within the experimental humidity levels.

From the Langmuir sorption isotherm a humidity change from 10 to 22% should result in growth of the surface coverage by

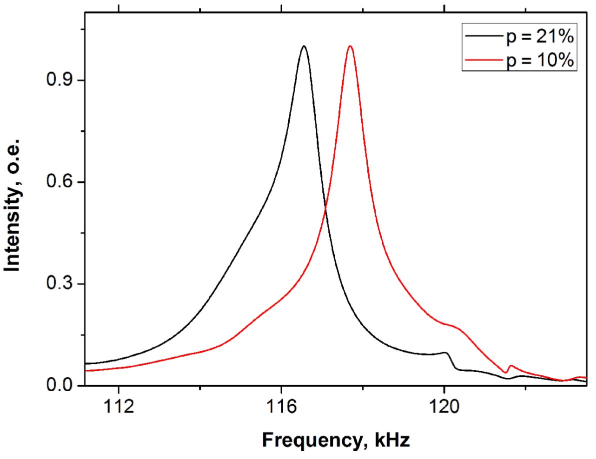

Figure 3: Frequency responses of AAO rectangular cantilever (2 µm thick, 800 µm long and 100 µm wide) at relative humidities of 10 and 21% (1120 Hz shift).

8.9%, which fits well to the obtained value. However, despite the good agreement between the estimations we should stress that they can be far from being realistic due to a strong chemical interaction of water molecules with AAO surface and pore curvature.

Figure 4 illustrates the resonant frequency dependence on air humidity. The experimental points were obtained by measuring the resonant frequency with decreasing humidity levels from 22 to 10% (at 298 K).

After each humidity decrement the system was left to reach equilibrium for 10–30 min. Equilibration criterion was resonant frequency creep below 1 Hz/min. The curve indicates a linear behavior approximated by $f = 118.99 \cdot (1 + 0.00198H)^{-1/2}$ (red line), which correlates well with Equation 1. The humidity sensitivity of the AAO cantilever in the linear range estimated by the slope of the experimental curve equals about 100 Hz/%. Hysteresis was not observed for the considered range close to equilibrium. The resonance frequency for the same value of humidity measured after a cycle of increasing and decreasing humidity is well reproduced within the error of 30 Hz. We believe this error corresponds to an inaccuracy of setting up the desired humidity value and a slight deviation from equilibrium during measurements. The plateau at low humidity levels

Table 1: Shifts of resonance frequency and quality factors *Q* for Si and AAO cantilevers under different pressure (vacuum and air, humidity 22%).

cantilever material	Si		AAO	
condition	air	vacuum (10^{-5} mbar)	air	vacuum (10^{-5} mbar)
Q factor	350	3230	39	52
resonant frequency *f*, kHz	322.01	322.79	177.12	181.02

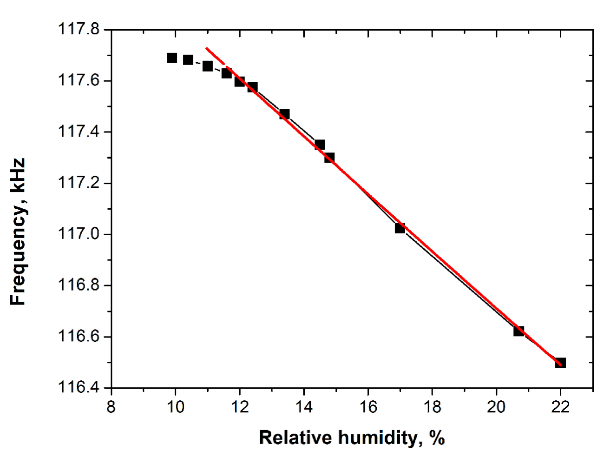

Figure 4: Resonance frequency of the AAO cantilevers (2 µm thick, 800 µm long and 100 µm wide) as function of relative humidity from 10 to 22%. Red line: approximation of the linear part as $f = 118.9972 \cdot (1 + 0.00198H)^{-1/2}$. Inaccuracy of frequency detection is below the size of the symbols.

demonstrates a moisture detection limit of 10%. This likely occurs due to residual native water absorbed on the AAO surface, which cannot be removed without heating. Linear behavior of environmental humidity on the resonance frequency of the cantilever oscillation allows us to use AAO cantilevers as humidity sensors at least in the humidity range of 10–22%.

Conclusion

The proposed combination of anodic oxidation and photolithography processes enables the successful formation of porous alumina cantilevers with desired geometric characteristics. Because of the high surface area of the pores the cantilevers exhibit an exceptional sensitivity to absorbed mass. The resonance frequency shift in water vapor absorption experiments over a humidity range of 10–22% fits well to the monolayer adsorption isotherm. A strong response to environmental change enables the use of AAO cantilever arrays in microsensors with ultra-low detection limits. The study has to be considered as an initial experiment to focus on the profound understanding of micromechanical behavior of anisotropic porous materials having a high specific surface area, such as anodic alumina films.

Experimental

Preparation of the cantilever array

AAO layer formation was carried out in 0.3 M $H_2C_2O_4$ (98%, Aldrich) at a constant voltage of 40 V. The electrolyte was pumped through the two-electrode cell by a peristaltic pump, and its temperature was kept constant (2 °C) during anodization. The films with a thickness of 2 µm were obtained by controlling the total electric charge. To define the shapes of the cantilever array the pattern of the photolithographic mask was directly transferred onto the AAO surface (spin-coat with S1818 microposit, 6 s at 500 rpm and than 20 s at 5000 rpm, 5 min of drying at 110 °C, 315 mJ of UV radiation [13]). Then unmasked AAO was etched away with 0.5% KOH for 10 min. The mask was removed after drying the samples at 160 °C for 10 min with acetone. Finally the remaining aluminium was dissolved in 0.5 M $CuCl_2$ acidic solution (5 vol % HCl). The size of the obtained microcantilevers equals 800 × 100 × 2 μm^3 (Figure 5).

One should note that these dimensional characteristics can be simply tuned by choosing lithographical mask with the desired cantilever shapes and varying of anodization charge. Films were characterized by optical (Nikon Eclipse 600pol) and scanning electron (LEO Supra 50VP) microscopes. The density of anodic alumina was determined by measuring sample hydrostatic weight.

Resonance frequency measurement

Mechanical measurements with air, vacuum and wet media were carried out by AFM (NTEGRA Aura) in the range of

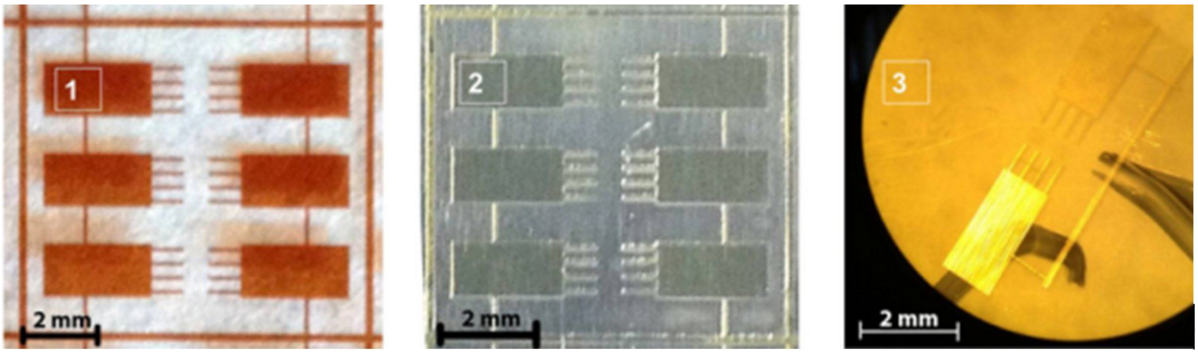

Figure 5: Photomask (1); cantilever arrays as formed on Al-foil (2); free-standing anodic alumina cantilevers (3).

0–600 kHz. The experimental setup used in this study is shown on Figure 6. The AFM is equipped with vacuum chamber Ar-flow controllers as well as humidity and temperature sensors.

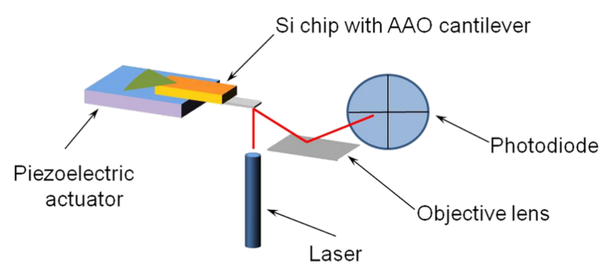

Figure 6: Scheme of measurement cell in atomic force microscope with an integrated optical read-out.

The desired moisture level was obtained by controlling the humidity at 25 °C with saturated salt-water and $CaCl_2$ dryer. Saturated salt-water was used to reach high relative humidity in the microscope chamber. After stabilization of humidity equilibrium in the system we start measurements of the resonance frequency over a $CaCl_2$ dryer down to the lowest possible humidity level. The microscope determined the upper limit of humidity level. Typically around 10 min have been needed to stabilize the cantilever to a fixed baseline. Humidity levels were varied in the range of 10–22%. An example of the resonance spectrum of porous alumina cantilevers detected with the AFM is shown in Figure 7.

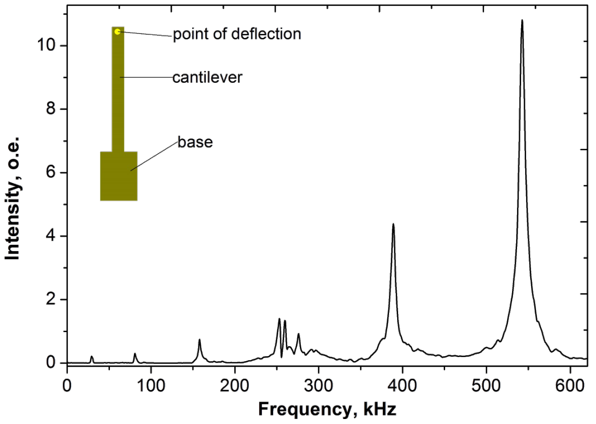

Figure 7: Spectrum of lateral (in-plane) modes corresponding to an alumina cantilever 2 µm thick, 800 µm long and 100 µm wide.

The arrays were supported by Si tips before measurements. The reflectivity of the surface of anodic aluminium oxide is sufficient for detecting vibrations without additional metal reflective coating. According to the exhibited behavior, adequate level of sample reproducibility has been demonstrated by the fabrication procedure described. The frequency does not shift for different points along the one cantilever. In contrast, intensity and a uniform vibration were indicated along the whole cantilever independently from where the AFM beam was detected. The magnitude of the maximal resonance frequency (about 545 kHz) predictably decreases when the optical beam of AFM moves to base of array. Experimentally we established the excitation of mechanical vibrations perpendicular to the cantilever surface as torsion. The thickness of cantilever arrays influences on stiffness and may also cause an increasing in resonance frequency: from 500 kHz for 2 µm thick cantilevers to 670 kHz for 30 µm thick cantilevers.

Acknowledgements

The work was partially supported with the grant of RFBR 13-08-01382 and by M. V. Lomonosov Moscow State University Program of Development. The authors would like to thank Dr. K. S. Napolskii for help with discussion and insightful comments.

References

1. Pellejero, I.; Agustí, J.; Urbiztondo, M. A.; Sesé, J.; Pina, M. P.; Santamaría, J.; Abadal, G. *Sens. Actuators, B* **2012,** *168,* 74–82. doi:10.1016/j.snb.2012.01.041
2. Lavrik, N. V.; Sepaniak, M. J.; Datskos, P. G. *Rev. Sci. Instrum.* **2004,** *75,* 2229–2253. doi:10.1063/1.1763252
3. Boisen, A.; Dohn, S.; Keller, S. S.; Schmid, S.; Tenje, M. *Rep. Prog. Phys.* **2011,** *74,* 036101. doi:10.1088/0034-4885/74/3/036101
4. Binning, G.; Quate, C. F.; Gerber, C. *Phys. Rev. Lett.* **1986,** *56,* 930–933. doi:10.1103/PhysRevLett.56.930
5. Goeders, K. M.; Colton, J. S.; Bottomley, L. A. *Chem. Rev.* **2008,** *108,* 522–542. doi:10.1021/cr0681041
6. Pina, M. P.; Mallada, R.; Arruebo, M.; Urbiztondo, M.; Navascués, N.; de la Iglesia, O.; Santamaria, J. *Microporous Mesoporous Mater.* **2011,** *144,* 19–27. doi:10.1016/j.micromeso.2010.12.003
7. Hosaka, S.; Chiyoma, T.; Ikeuchi, A.; Okano, H.; Sone, H.; Izumi, T. *Curr. Appl. Phys.* **2006,** *6,* 384–388. doi:10.1016/j.cap.2005.11.024
8. Kuroyanagi, T.; Terada, Y.; Takei, K.; Akita, S.; Arie, T. *Appl. Phys. Lett.* **2014,** *104,* 193104. doi:10.1063/1.4876959
9. Yang, J.; Ono, T.; Esashi, M. *Sens. Actuators, A* **2000,** *82,* 102–107. doi:10.1016/S0924-4247(99)00319-2
10. Chen, G. Y.; Thundat, T.; Wachter, E. A.; Warmack, R. J. *J. Appl. Phys.* **1995,** *77,* 3618–3622. doi:10.1063/1.359562
11. Sarid, D. *Scanning Force Microscopy;* Oxford University Press: New York, NY, U.S.A., 1991.
12. Petukhov, D. I.; Napolskii, K. S.; Eliseev, A. A. *Nanotechnology* **2012,** *23,* 335601. doi:10.1088/0957-4484/23/33/335601
13. Brevnov, A. D.; Mardilovich, P. Electrochemical Micromachining and Microstructuring of Aluminum and Anodic Alumina. In *Electrodeposition;* Djokic, S. S., Ed.; Modern Aspects of Electrochemistry, Vol. 48; Springer: Berlin, Germany, 2010; pp 215–249. doi:10.1007/978-1-4419-5589-0_5

License and Terms